Advanced Ceramic Materials

Scrivener Publishing
100 Cummings Center, Suite 541J
Beverly, MA 01915-6106

Advanced Materials Series

The Advanced Materials Series provides recent advancements of the fascinating field of advanced materials science and technology, particularly in the area of structure, synthesis and processing, characterization, advanced-state properties, and applications. The volumes will cover theoretical and experimental approaches of molecular device materials, biomimetic materials, hybrid-type composite materials, functionalized polymers, supramolecular systems, information- and energy-transfer materials, biobased and biodegradable or environmental friendly materials. Each volume will be devoted to one broad subject and the multidisciplinary aspects will be drawn out in full.

Series Editor: Ashutosh Tiwari
Biosensors and Bioelectronics Centre
Linköping University
SE-581 83 Linköping
Sweden
E-mail: ashutosh.tiwari@liu.se

Managing Editors: Sachin Mishra and Sophie Thompson

Publishers at Scrivener
Martin Scrivener (martin@scrivenerpublishing.com)
Phillip Carmical (pcarmical@scrivenerpublishing.com)

Advanced Ceramic Materials

Edited by

Ashutosh Tiwari,
Rosario A. Gerhardt and
Magdalena Szutkowska

WILEY

Copyright © 2016 by Scrivener Publishing LLC. All rights reserved.

Co-published by John Wiley & Sons, Inc. Hoboken, New Jersey, and Scrivener Publishing LLC, Beverly, Massachusetts.
Published simultaneously in Canada.

No part of this publication may be reproduced, stored in a retrieval system, or transmitted in any form or by any means, electronic, mechanical, photocopying, recording, scanning, or otherwise, except as permitted under Section 107 or 108 of the 1976 United States Copyright Act, without either the prior written permission of the Publisher, or authorization through payment of the appropriate per-copy fee to the Copyright Clearance Center, Inc., 222 Rosewood Drive, Danvers, MA 01923, (978) 750-8400, fax (978) 750-4470, or on the web at www.copyright.com. Requests to the Publisher for permission should be addressed to the Permissions Department, John Wiley & Sons, Inc., 111 River Street, Hoboken, NJ 07030, (201) 748-6011, fax (201) 748-6008, or online at http://www.wiley.com/go/permission.

Limit of Liability/Disclaimer of Warranty: While the publisher and author have used their best efforts in preparing this book, they make no representations or warranties with respect to the accuracy or completeness of the contents of this book and specifically disclaim any implied warranties of merchantability or fitness for a particular purpose. No warranty may be created or extended by sales representatives or written sales materials. The advice and strategies contained herein may not be suitable for your situation. You should consult with a professional where appropriate. Neither the publisher nor author shall be liable for any loss of profit or any other commercial damages, including but not limited to special, incidental, consequential, or other damages.

For general information on our other products and services or for technical support, please contact our Customer Care Department within the United States at (800) 762-2974, outside the United States at (317) 572-3993 or fax (317) 572-4002.

Wiley also publishes its books in a variety of electronic formats. Some content that appears in print may not be available in electronic formats. For more information about Wiley products, visit our web site at www.wiley.com.

For more information about Scrivener products please visit www.scrivenerpublishing.com.

Cover design by Russell Richardson

Library of Congress Cataloging-in-Publication Data:

ISBN 978-1-119-24244-4

Printed in the United States of America

10 9 8 7 6 5 4 3 2 1

Contents

Part 3 Functional and Applied Ceramics

Preface

Ceramic materials are inorganic and nonmetallic porcelains, tiles, enamels, cements, glasses and refractory bricks. Today, the term "ceramics" has gained a wider meaning as a new generation of materials which influence our lives; electronics, computers, communications, aerospace and other industries rely on them for a number of uses. In general, advanced ceramic materials include electroceramics, optoelectronic ceramics, superconductive ceramics and the more recently developed piezoelectric and dielectric ceramics. Due to their features, including their mechanical properties and decorative textures, they can be considered for environmental uses and energy applications, as well as for use in bioceramics, composites, functionally graded materials, intelligent ceramics and so on. This book has a transdisciplinary readership that spans students, engineers, scholars, scientists, physicists, chemists, life scientists and beyond. The volume brings together innovative methodologies and strategies adopted in the research and development of advanced ceramic materials and offers a comprehensive view of cutting-edge research on ceramic materials and technologies.

A wide range of processing methods used to generate ceramic materials for a variety of functional, structural and biomedical applications are described in this book. The book starts with an excellent review of solution-based methods that can be used to deposit epitaxial films of oxide nanomaterials for microelectronics applications and is followed by a detailed description of tantalum oxides and related phases and their potential use in solar cells and other applications. In the next chapter there is a discussion of the basics of microwave processing which contains a brief summary of its history in various materials and a description of the recent work on hybrid microwave sintering of metal matrix composites containing absorbing ceramic materials.

The next chapters focus on structural applications, starting with a description of continuous fiber ceramic matrix composites, where typical matrix and filler materials are discussed along with the interfacial layers needed to induce crack deflection and improved fracture toughness. The following two chapters deal with the addition of carbon

nanotubes (single-wall and multiwall) into bulk alumina and zirconia and how the characteristics of the nanotubes as well as the processing methods used can affect the resultant properties. Next the detection of crack healing in MAX phase ceramics and their enhanced properties as a result of the incorporation of these unique materials are discussed.

Additional chapters investigate the effect of the additives on manufacturability and biocompatibility. In the first chapter of this section, waste materials from a variety of industries are incorporated into ceramic brick for sustainable manufacturing. The authors propose the use of an artificial neural network optimization program for identifying the conditions that work best for each additive. The next chapter focuses on the importance of different additives to improve the bioactivity of calcium orthophosphates used in medical implants, followed by a chapter investigating the effect of silver additions to hydroxyapatite for improved antifungal and antibacterial responses using a variety of surface controlled schemes.

This book is written for readers from diverse backgrounds across the fields of chemistry, physics, materials science and engineering, medical science, pharmacy, environmental technology, biotechnology, and biomedical engineering.

Editors
Ashutosh Tiwari, PhD, DSc
Rosario Gerhardt, PhD
Magdalena Szutkowska, PhD
July, 2016

Part 1

DESIGN, PROCESSING, AND PROPERTIES

Ashutosh Tiwari, Rosario A. Gerhardt and Magdalena Szutkowska (eds.) Advanced Ceramic Materials, (1–2) © 2016 Scrivener Publishing LLC

1

Development of Epitaxial Oxide Ceramics Nanomaterials Based on Chemical Strategies on Semiconductor Platforms

A. Carretero-Genevrier[1]*, R. Bachelet[1], G. Saint-Girons[1], R. Moalla[1], J. M. Vila-Fungueiriño[2], B. Rivas-Murias[2], F. Rivadulla[2], J. Rodriguez-Carvajal[3], A. Gomez[4], J. Gazquez[4], M. Gich[4] and N. Mestres[4]

[1]Institut des Nanotechnologies de Lyon (INL) CNRS—Ecole Centrale de Lyon, Ecully, France
[2]Centro de Investigación en Química Biológica y Materiales Moleculares (CIQUS), Universidad de Santiago de Compostela, Santiago de Compostela, Spain
[3]Institut Laue-Langevin, Grenoble Cedex 9, France
[4]Institut de Ciència de Materials de Barcelona ICMAB, Consejo Superior de Investigaciones Científicas CSIC, Campus UAB Catalonia, Spain

Abstract

The technological impact of combining substrate technologies with the properties of functional advanced oxide ceramics is colossal given its relevant role in the development of novel and more efficient devices. However, the precise control of interfaces and crystallization mechanisms of dissimilar materials at the nanoscale needs to be further developed. As an example, the integration of hybrid structures of high-quality epitaxial oxide films and nanostructures on silicon remains extremely challenging because these materials present major chemical, structural and thermal differences. This book chapter describes the main promising strategies that are being used to accommodate advanced oxide nanostructured ceramics on different technological substrates via chemical solution deposition (CSD) approaches. We will focus on novel examples separated into two main sections: (i) epitaxial ceramic nanomaterials entirely performed by soft chemistry, such as nanostructured piezoelectric quartz thin films on silicon or 1D complex oxide nanostructures epitaxially grown on silicon, and (ii) ceramic materials prepared by combining soft chemistry and physical techniques, such as epitaxial perovskite

**Corresponding author*: adrien.carretero-genevrier@ec-lyon.fr

Ashutosh Tiwari, Rosario A. Gerhardt and Magdalena Szutkowska (eds.) Advanced Ceramic Materials, (3–32) © 2016 Scrivener Publishing LLC

oxide thin films on silicon using the combination of soft chemistry and molecular beam epitaxy. Consequently, this chapter will cover cutting-edge strategies based on the potential of combining epitaxial growth and CSD to develop oxide ceramics nanomaterials with novel structures and improved physical properties.

***Keywords*:** Epitaxial growth, thin-film growth, silicon, perovskites, solution chemistry, molecular beam epitaxy, oxide nanostructures, magnetic oxide nanowires, quartz thin films, octahedral molecular sieves

1.1 Introduction

Single-crystalline thin films of functional oxides exhibit a rich variety of properties such as ferroelectricity, piezoelectricity, superconductivity, ferro- and antiferro-magnetism, and nonlinear optics that are highly appealing for new electronic, opto-electronic and energy applications [1, 2]. Over the past few years, tremendous progress has been achieved in the growth of functional oxides on oxide substrates (such as $LaAlO_3$, $SrTiO_3$, Al_2O_3, MgO, and scandates) [3, 4]. As a result, to date, it is possible to control the epitaxial growth at the unit cell level, which has led to new phenomena arising from the engineering of novel interfaces [5–8]. However, to fully exploit their properties, functional oxides should be effectively integrated on a semiconductor platform like silicon, germanium or III/V substrates, which are compatible with the electronics industry. The controlled epitaxial growth of functional oxide layers on semiconductor substrates is a challenging task as a result of the strong structural, chemical, and thermal dissimilarities existing between these materials. In spite of the difference in lattice parameters and thermal expansion coefficients, the major difficulty to engineer epitaxy is linked to the necessity of preventing the formation of an amorphous interfacial layer during the first stages of the growth (e.g. SiO_2 or silicates on Si, depending of the atmosphere), which hinders any further epitaxy. Additionally, the cations of most oxide compounds can easily interdiffuse into the silicon substrate giving rise to the formation of spurious phases at the interface [9]. To overcome these major challenges, it is required to use a stable buffer layer, which can act simultaneously as a chemical barrier preventing ionic inter-diffusion and as a structural template favoring epitaxy.

In this context, McKee *et al.* [10] demonstrated the possibility to grow epitaxial $SrTiO_3$ (STO) films on Si(001) by molecular beam epitaxy (MBE) with Sr passivation strategy. This work sets the basis to integrate STO and related perovskites on silicon for monolithic devices. Consequently, most

of the research on crystalline functional oxides such as STO [11], lead zirconate titanate $PbZr_{0.52}Ti_{0.48}O_3$(PZT) [12], $BaTiO_3$ (BTO) [13–17], $LaCoO_3$ (LCO) [18], and $La_{0.7}Sr_{0.3}MnO_3$ (LSMO) [19] integrated with Si has been based on an STO buffer layer epitaxially grown on Si(001) by MBE.

For decades, the integration of functional oxides onto a silicon platform has been identified as an important route to improve and widen the performances of microelectronics and nanoelectronics devices. A clear example is the successful preparation of two-dimensional electron gas at interfaces between $LaAlO_3$ and $SrTiO_3$ (STO) on Si(001). In this case, the STO film acts simultaneously as a buffer layer and as an active part of the functional heterostrucuture [20]. Moreover, 2D electron gases at the interface have also been demonstrated using $LaTiO_3$ [21] and $GdTiO_3$ [22, 23] grown on STO-buffered Si. Functional non-volatile BTO-based ferroelectric tunnel junctions (FTJ) on Si(001) substrates with a tunneling electroresistance (TER) ratio over 10,000% have been recently demonstrated by pulsed laser deposition (PLD) [24] and MBE [25] growth methods. In both cases, this was accomplished by including a thin layer of STO as an epitaxial template on silicon. In addition, concomitant ferroelectric and antiferromagnetic behaviors were demonstrated on single-crystal $BiFeO_3$ (BFO) films grown on STO on Si(100) using PLD [26] and MBE [27].

Integration of self-assembled vertical epitaxial nanocomposites thin films on Si substrates has been reported for multiferroic or magnetic memory and logic devices. The growth of $La_{0.7}Sr_{0.3}MnO_3$–ZnO perovskite–wurtzite and CeO_2–BTO fluorite–perovskite vertical nanocomposites on a Si substrate by PLD was described using a $TiN/SrTiO_3$ bilayer buffer layer [28, 29]. The respective magnetoresistance and ferroelectric properties matched those of similar films grown on single-crystal STO. In addition, perovskite–spinel magneto-electric BFO–CFO vertical nanocomposites were successfully integrated on Si using two different buffered substrates: $Sr(Ti_{0.65}Fe_{0.35})O_3/CeO_2$/YSZ/Si and 8 nm STO/Si [30].

The integration of functional oxides on germanium has recently received a great attention for high-speed and low-power device applications [31], as a result of the higher electron and hole mobility of germanium over silicon [32]. Indeed, a germanium-based ferroelectric field effect transistor was produced recently [33]. In this case, an ultrathin (20 Å) STO layer was first deposited on the Ge substrate. This layer imposes an in-plane compressive strain on BTO to overcome the tensile strain caused by the thermal expansion mismatch between both materials, therefore providing BTO films on Ge with out-of-plane polarization.

The development of freestanding oxide devices based on microelectromechanical systems (MEMS) technologies using standard silicon

micromachining techniques was possible from $SrTiO_3$/Si structures. Thus, the fabrication of integrated free-standing LSMO microbridges for low-power consumption pressure sensors [34] and uncooled bolometers [35] was recently demonstrated.

The direct growth of functional oxide film on silicon has proved to be also an effective way of integration without epitaxy. In this context, a field effect transistor preserving magnetoelectric functionality on a silicon-integrated device based on a $La_{0.825}Sr_{0.175}MnO_3/Pb_{0.2}Zr_{0.8}TiO_3$ (LSMO/PZT) bilayer directly grown by PLD on non-processed Si substrate has been demonstrated by Fina *et al.* [36]. The measured modulation of the magnetic and transport properties of LSMO upon PZT ferroelectric switching is large, despite the polycrystalline nature of the structure.

Yttrium-stabilized zirconia (YSZ) has also shown to be a very effective buffer layer to integrate functional oxide layers on Si(001) despite a lattice mismatch of about 5% and because it scavenges the native oxide on the substrate surface and reduces the native SiO_2 oxide layer, with controlled oxygen partial pressure. These characteristics favor the formation of an epitaxial relation with the silicon substrate [37–39], thus making possible the integration of functional ferromagnetic spinel oxides [40–42] and ferroelectric perovskite oxides [43]. The use of an YSZ template substrate has also permitted the fabrication of all-oxide, free-standing, heteroepitaxial, and piezoelectric MEMS on silicon by using $PbZr_{0.52}Ti_{0.48}O_3$ as the active functional material [44]. Recently, optimized growth conditions and subsequent functional oxides deposition have been shown on a silicon wafer scale (>4") using PLD [45].

The opportunities of combining functional oxides with integrated photonic devices and circuits are equally enormous. In spite of the recent advances made on silicon photonics, many limitations still need to be solved [46]. The integration of electro-optical active oxides will allow extending the silicon photonics platform to engineer nonlinear materials, which can be effectively used for tuning, switching, and modulating light in extremely dense photonic circuits. Examples of that are: the fabrication of electro-optical switches based on oxides with metal-to-insulator transitions (e.g. VO_2) [47], optical insulators based on magnetic oxides (e.g. Co-substituted $CeO_{2-\delta}$ and Co/Fe-substituted $SrTiO_{3-\delta}$) [48], and high-speed modulators based on oxides with the strong Pockels coefficients (e.g. $BaTiO_3$) [49, 50]. Moreover, the integration of PZT layers on GaAs substrates is highly interesting for optoelectronic applications considering, for instance the modulation of the optical properties of GaAs-based heterostructures through the strain induced by a piezoelectric layer [51]. Analogously, an epitaxial buffer layer of STO initially grown by MBE is needed for the successful epitaxial integration of the ferroelectric PZT on GaAs [52, 53]. BTO has also been successfully integrated on

GaAs using MBE and showed good ferroelectric characteristics when measured by piezoresponse force microscopy (PFM) [54].

In the past decades, most of the works on crystalline oxides thin films growth on semiconductors have been based on a layer-by-layer approach to heteroepitaxy. The main techniques used to this purpose have been MBE or PLD after adjusting the growth conditions during the deposition to avoid semiconductor surface oxidation or cationic interdiffusion at the interface. However, for future applications in industry, chemical deposition methods such as metal–organic chemical vapor deposition (MOCVD), chemical solutions and sol–gel-based processes, and atomic layer deposition (ALD) show clear advantages over MBE or PLD. These advantages are mainly due to the scalability and low cost of chemical deposition-based methods. ALD entails the sequential delivery of precursors or reagents that either adsorb to saturation coverage or undergo selective ligand reactions, which are self-limiting for the film growth [55, 56]. This growth technique can provide atomic layer control and allows the deposition of ultrathin conformal films onto very high-aspect-ratio structures.

As previously mentioned, an STO buffer layer grown by MBE is a required step for the epitaxial integration of many oxide materials. In this context, the growth of crystalline oxides on semiconductors by combining physical and chemical methods is also a matter of current research [55]. As an example, a combined MBE (to grow first a four-unit cell thick STO buffer layer) and ALD growth method to deposit crystalline oxide thins films on Si(001) including TiO_2, $BaTiO_3$, $SrTiO_3$, and $LaAlO_3$ was developed [57–60]. In addition, the deposition of ferroelectric $Pb(Zr)TiO_3$ using chemical solution spin coating on STO-buffered Si and GaAs grown by MBE was also demonstrated [61, 62].

The use of Ge or GaAs substrates makes possible to grow epitaxial perovskite oxides directly *via* ALD [63], compared to silicon substrates. In this case, a post-deposition annealing at high temperatures is required for crystallization. Recent improvements in the crystalline quality of oxides grown on Ge using ALD highlight the potentiality of this growth method as a scalable integration route of functional oxides for microelectronics technology. Indeed, epitaxial STO and Al-doped STO films up to 15 nm thick with a high degree of crystallinity were grown on the Ge(001) substrates via ALD for high-mobility Ge-based transistors [64]. ALD growth of epitaxial $SrHfO_3$ on Ge as a high-k dielectric material has also been demonstrated [65]. Likewise, high-quality epitaxial $LaLuO_3$ and $La_{2-x}Y_xO_3$ thin films were achieved on GaAs (111) by ALD, and GaAs MOS capacitors made from this epitaxial structures showed very good interface quality with small frequency dispersion and low interface trap densities [66, 67].

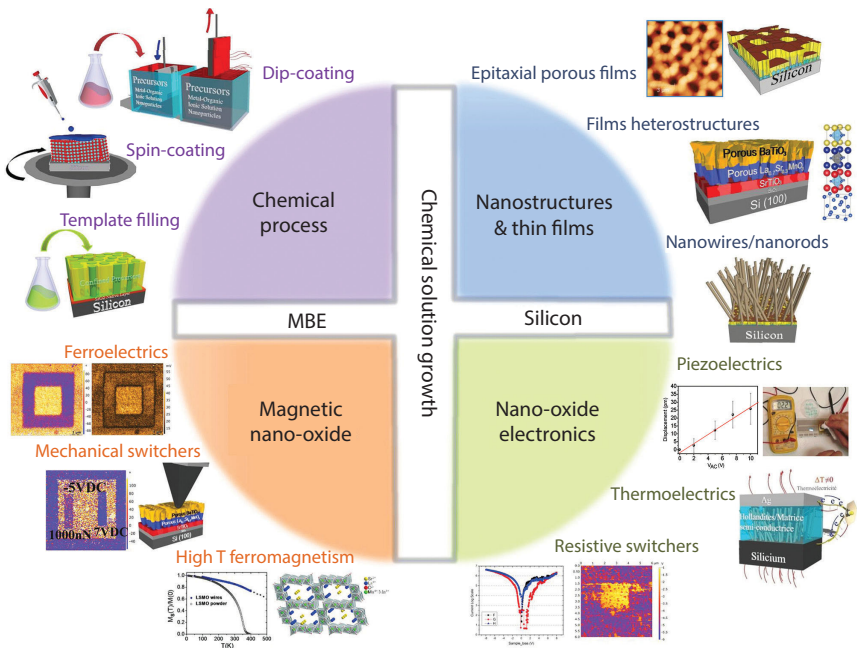

Figure 1.1 General schematic diagram representing all the processes, oxide nanomaterials integrated on silicon, and applications discussed in this book chapter.

Nevertheless, the integration of functional oxides on semiconductors entirely performed by chemical methods is still in its early stages.

In this chapter, we present recent promising strategies used to accommodate advanced oxide nanostructures on silicon substrates *via* chemical solution deposition (CSD) routes. Two different approaches are proposed, namely the growth of nanostructured oxides entirely by chemical solutions and the combination of soft chemistry and MBE. These two approaches along with relevant examples that will be further discussed in this chapter are displayed in Figure 1.1.

1.2 Integration of Epitaxial Functional Oxides Nanomaterials on Silicon Entirely Performed by Chemical Solution Strategies

Integrating functional oxides nanomaterials as active materials in devices importantly depends on the capability to incorporate crystalline metal

oxides into silicon structures. This feature represents a hard challenge issue because the matching between dissimilar (structurally, thermally, and in general chemically reactive) oxides with silicon in hybrid structures is difficult. As mentioned in the precedent section, one of the most important difficulties stems from the fact that the oxygen partial pressure and silicon temperature must be controlled to avoid the formation of an amorphous SiO_2 or silicates crystalline oxide layers at the first stage of growth, which might inhibit epitaxy [68]. In this direction, most of the precedent works on the integration of oxide materials on silicon follow the conventional MBE or PLD techniques that provide advanced control of the interfaces and growth processes [68]. These physical methods are able to develop interface engineering strategies to grow functional oxides thin films on Si and other semiconductor platforms. However, MBE and PLD methodologies are limited to the synthesis of complex oxide materials under the form of thin films. As a consequence, *top-down* approaches consisting on expensive lithography and more recently new, sophisticated and tedious electron and ion beam lithographies are needed to develop epitaxial oxide nanostructures with controllable shapes and morphologies. Additionally, controlled synthesis of epitaxial ternary and quaternary metal oxide nanostructures on silicon is challenging due to the difficulty on controlling the precursor reactions and achieving a homogeneous final stoichiometry.

As an alternative, CSD methods are very convenient since they offer a *bottom-up* strategy to produce nanostructures with large material diversity, easy setup, and good control over stoichiometry. In addition, it makes possible the use of dopants and the possibility of coating large and uniform areas, which have proved to be a highly-flexible procedure for the fabrication of electronic oxide films and nanostructures [69–75]. However, few efforts have been devoted to integrate functional oxides on semiconductors by using this technique. In a classical CSD method, the synthesis process and growth mechanism that allows to prepare epitaxial oxide nanostructures and thin films on different technological substrates is based on three different stages: (i) The synthesis of a stable and stoichiometric chemical precursor solution; (ii) the deposition of the precursor solution on a substrate either through spin coating, dip coating, or spray coating; and (iii) a thermal treatment to remove the solvent, allowing the densification and final epitaxial crystallization of oxide nanostructures and thin films. Chemical solution methods include a large variety of techniques such as sol–gel techniques, chelation, metal–organic decomposition, polymer-assisted deposition (PAD), and hydrothermal methods [68].

In this section, we present important and recent advances concerning the epitaxial growth of functional oxides nanostructures and nanostructured thin films on silicon entirely performed by chemical solution strategies. We will show that CSD methodology can be used as a new chemical strategy in which the devitrification of amorphous SiO_2 native layer on silicon permits the integration of different functional oxide nanostructures in air atmosphere. Further epitaxial stabilization of new oxide nanostructures on silicon with enhanced ferromagnetic and electric properties can then be achieved by using this novel chemical approach, supporting the validity and generality of this methodology for the fabrication of functional oxide films and nanostructures on silicon. We present the studies conducted on epitaxial growth of piezoelectric quartz nanostructures on silicon [76], as a model system, even though this growth mechanism can further be applied to the integration of other different oxide nanomaterials on silicon. Indeed, the possibility to generate epitaxial quartz films on silicon by taking advantage of the good epitaxial relation of these crystallographic structures during a catalytic devitrification process of SiO_2 native layer makes possible to extend this procedure to other functional oxide nanostructures. More specifically, using alkaline earth cations in the precursor solution is the key to promote the catalytic devitrification of amorphous SiO_2 native layer and consequently the crystallization into α-quartz during the thermal treatment. The α-quartz layer acts as template for the epitaxial growth of single-crystalline oxide nanowires of different compositions, oxide thin films and more importantly allows the direct integration on silicon substrates [77, 78]. Thus, this methodology exhibits a great potential and offers new strategies to integrate novel oxide compounds totally performed by chemical routes with unique, electric, magnetic, or optical properties.

1.2.1 Integration of Piezoelectric Quartz Thin Films on Silicon by Soft Chemistry

Quartz is one of the few materials that have an outstanding combination of properties, i.e. (i) abundant in nature, (ii) environmentally friendly, (iii) piezoelectric with high-quality factor, (iv) low solubility, (v) high hardness, and (vi) stress compensated. As a result, α-quartz is extremely used for applications in industry such as glassmaking, foundry, or hydraulic fracturing and also in a wide range of fields including microelectronics or telecommunications. Therefore, α-quartz is an important material for microelectronics industry since it is selected to fabricate oscillators and transducers that constitute any electronic device. However, to

date, α-quartz is exclusively synthesized by hydrothermal methods, which produce big crystals making impossible to decrease their size below a thickness of 10 μm [79], and for most applications, these crystals need to be bonded on Si substrates. This feature represents an important barrier for the microelectronic industry since thinner monocrystalline quartz plates are currently highly demanded to produce faster device operation, higher-frequency filtering, or transducers with lower detection levels and improved sensitivity.

In spite of the technological needs, epitaxial quartz nanostructures on silicon are not yet developed. As an alternative, chemical CSD methodology appears as a *bottom-up* approach capable to prepare quartz nanostructures by taking advantage of all the benefits of soft chemistry [80]. Nevertheless, silica has more than 11 polymorphs that make extremely difficult the crystallization of pure α-quartz phase from an amorphous SiO_2 gel. As a consequence, the synthesis of quartz using CSD requires a critical control over different parameters, such as the choice of precursors, catalyzers, thermal treatment, and humidity [81–84].

Recently, we have deciphered the mechanism behind the devitrification–crystallization process of α-quartz by studying 3D amorphous silica monoliths as a model system containing different doping levels of Sr^{2+} catalyst by *in situ* neutron thermodiffractometry [85]. Silica monoliths of specific catalyst composition were prepared by sol–gel process from alcohol/water solutions of soluble silicic acid precursors together with surfactant structure-directing-agents films. These studies showed, for the first time to our knowledge, the dynamic interaction between silica glass and Sr^{2+} catalysts and even crystalline phase changes that take place during quartz growth in real time. Particularly, these studies provided evidences that quartz formation is not driven by the presence of intermediate silicate phases and that a precise doping level of Sr^{2+} cations is needed to assist the quartz crystallization during the thermal treatment. Figure 1.2 shows the thermally activated devitrification–crystallization of amorphous silica monoliths assisted by different doping levels of Sr^{2+} catalyst with respect to Si (1%, 2%, 6%, and 12%) and monitored by neutron thermodiffractometry. Importantly, only silica monoliths containing a 6 atomic percent of Sr^{2+} catalyst produced the direct observation and synthesis of pure quartz polymorph crystallization at relative low temperature. At this Sr^{2+} concentration within the silica monoliths, pure quartz crystallization is ensured in a wide range of temperatures. Below this critical concentration (<6% Sr^{2+}), inhomogeneous and insufficient distribution of catalyst impair film devitrifications and subsequent crystallization of amorphous silica monoliths. As an example, when samples containing

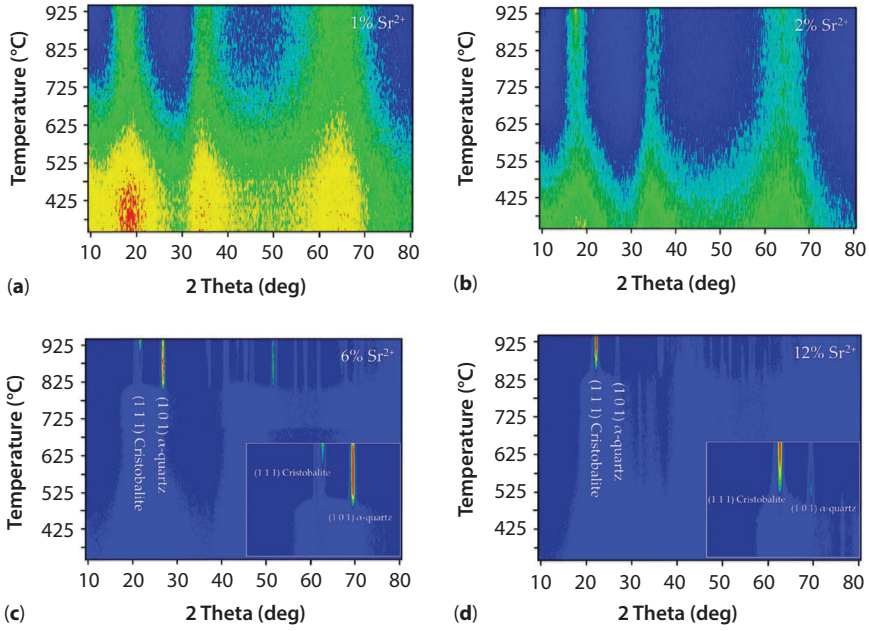

Figure 1.2 Thermally activated devitrification–crystallization of amorphous silica monoliths assisted by different doping levels of Sr^{2+} catalyst and monitored by neutron thermodiffractometry. (a) 1 atomic percent (1%) of Sr^{2+}, (b) 2 atomic percent (2%) of Sr^{2+}, and (c) 6 atomic percent (6%) of Sr^{2+}. Notice that under this amount of Sr^{2+}, amorphous silica monoliths crystallize into pure quartz polymorph at relative low temperature. (d) 12 atomic percent (12%) of Sr^{2+}. Notice that under this doping level within the silica, the crystallization of silica results in a competition between cristobalite and quartz polymorphs.

1 and 2 atomic percent of Sr^{2+} are used, amorphous patterns are observed during the neutron thermodiffractometry (Figure 1.2a and b), indicating the non-crystallization of the silica monolith. Conversely, above 6 atomic percent of Sr^{2+}, i.e. 12% Sr^{2+}, excess of the catalyst produced the crystallization of cristobalite polymorph at lower temperature, in competion with the crystallization of quartz (see Figure 1.2d).

These results demonstrated that neutron diffraction can be a useful tool for nanotechnology, although this technique needs large amounts of material to statistically prove the different processes that take place in a solid-state catalytic reaction. In this case, the authors used 3D amorphous silica monoliths as model systems to study the Sr^{2+}-mediated devitrification mechanism of silica. By taking advantage of the results obtained from neutron diffraction, it was possible to develop a new chemical route for the growth of epitaxial quartz films and nanostructures on silicon [76].

Quartz film synthesis involved a controlled dip-coating deposition on Si(100) substrates of a sol–gel solution containing partially hydrolyzed and condensed tetraethoxysilane (TEOS) quartz precursor in presence of cetrimonium bromide (CTAB). Analogously to neutron diffraction experiments, silica films were doped with 6 atomic percent of Sr^{2+}, incorporated as chloride salt, which produced the devitrification and crystallization into quartz of silica film. Importantly, strontium was homogeneously distributed along the amorphous silica film matrix and silicon interface, which is crucial to successfully crystallize silica films into quartz. Amorphous silica films were doped either by a two-step synthesis, where strontium salt is impregnated into a mesoporous silica previously prepared, or in a single-step synthesis, where this cation is directly incorporated during gelification and drying of dip-coated films through an evaporation-induced self-assembly (EISA) process [86]. Following both strategies, epitaxial quartz films were obtained after thermal treatments in air at 1000 °C during 5 h. Quartz crystallization starts at 950 °C, where the low mismatch degree between quartz and Si(100) substrates induced a preferential assembly and epitaxial growth of α-quartz crystals during heterogeneous nucleation along the silicon surface (see Figure 1.3).

X-ray diffraction (XRD) scans and transmission electron microscopy (TEM) cross-section analysis can be used to determine the good crystallinity and misorientation of epitaxial α-quartz films, as shown in Figure 1.4. Notice that quartz crystallization starts within the same temperature range observed from neutron diffraction experiments in 3D silica monoliths (Figure 1.2c and 1.4a). Inset in Figure 1.4a shows rocking curves of (100) peak at different temperatures, which confirms a complete crystallization at 1000 °C, achieving the lower full width at half-maximum (FWHM) value (3°) after 5 h of thermal treatment. Figure 1.4b confirms that only silica films with 6% of Sr^{2+} give rise to epitaxial quartz films, in agreement with the catalytic behavior of the devitrification of silica already observed from neutron diffraction. Additionally, the epitaxial relation of α-quartz films on silicon can be obtained from pole figures given by the quartz (100)||Si(100), as shown in Figure 1.4c.

1.2.2 Controllable Textures of Epitaxial Quartz Thin Films

The high versatility of CSD methodology makes possible the fabrication of epitaxial quartz with different textures on silicon. Indeed, CSD methods are very convenient since they provide a *bottom-up* strategy to engineer nanostructures with good control over the shape and morphology. An example of that is the control over the texture and porosity of epitaxial quartz thin

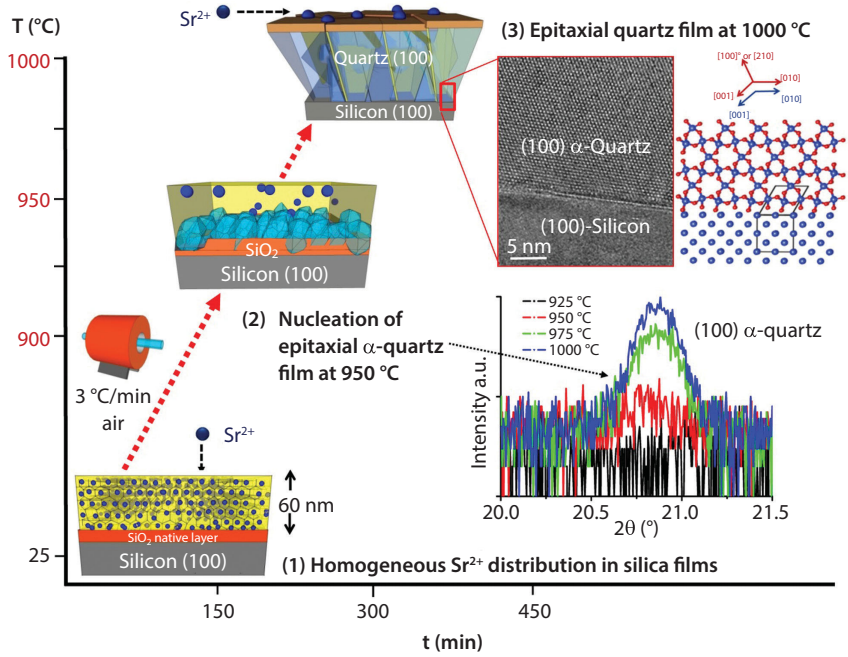

Figure 1.3 Schematics of the growth mechanism of epitaxial quartz thin films on (100) Si substrate. (1) Cross-sectional cartoon of the initial amorphous mesoporous silica film where the 6% of Sr^{2+} catalyst is homogeneously distributed along the silica matrix and silicon interface. (2) Devitrification and melting of the original amorphous mesoporous film and first crystallization above 925 °C of epitaxial α-quartz film. (3) Epitaxial quartz film formation on (100) Si substrate. After crystallization process all Sr^{2+} sinters and forms spherical amorphous nanoparticles of $SrCO_3$ that are finally fixed at the surface within quartz grain boundaries.

films. These nanostructured films can be prepared either through a single-step synthesis via a novel phase separation process or through a two-step synthesis that requires the previous preparation of a mesoporous silica film (see Figure 1.5). Evidence of these two processes is displayed in Figure 1.5, where a silica film with hexagonal close-packaged pores of 700 ± 50 nm in diameter (Figure 1.5a) yielded epitaxial α-quartz thin films that kept the initial distribution and pore size diameter (Figure 1.5b). Analogously, mesoporous quartz films were synthesized by a two-step process, where the minimum pore size to accommodate quartz crystals around the initial pore morphology is 40 nm. Below this pore size, the porosity collapses yielding the formation of dense epitaxial quartz films. This growth mechanism was among the first examples that prove the possibility of engineering

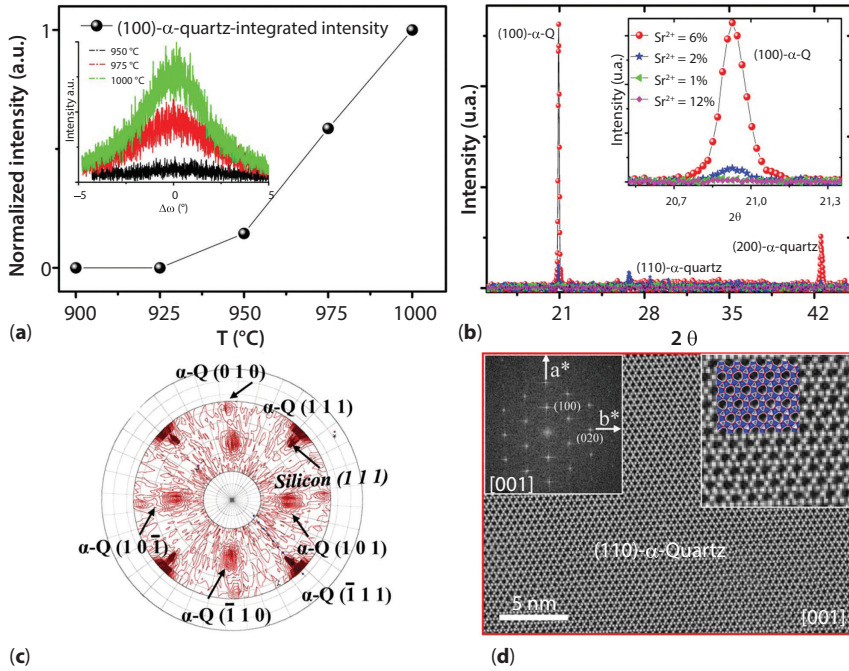

Figure 1.4 (a) Graphic that exhibits the starting crystallization temperature of epitaxial α-quartz thin films on silicon. Inset figure shows the evolution of rocking curves for samples grown at different temperatures. Notice that 1000 °C is the optimal temperature that achieves the lower FWHM value (3°), indicating low out-of-plane misorientation of nanostructured α-quartz films. (b) Devitrification–crystallization of amorphous silica films at 1000 °C assisted by different doping levels of Sr^{2+} catalyst and analyzed by XRD: 1 atomic percent (1%) of Sr^{2+} (green), 2 atomic percent (2%) of Sr^{2+} (blue), 6 atomic percent (6%) of Sr^{2+} (red), and 12 atomic percent (12%) of Sr^{2+} (pink). Notice that as shown in Figure 1.2c only samples with 6% of Sr^{2+} can achieve the crystallization of quartz polymorph and consequently the direct epitaxy on (100) silicon. (c) Pole figure of quartz films that confirms the epitaxial relationship between quartz thin film and (100) silicon substrate which is [210]Q//[100]Si. (d) HRTEM image of the α-quartz along [001] crystallographic direction that shows a high-quality crystallinity without structural and chemical defects.

the direct integration on silicon of nanostructured epitaxial functional oxides with a controlled porosity by using exclusively chemical methods.

Quartz thin films display a piezoelectric activity, as shown by PFM measurements (see Figure 1.6). The piezoelectric coefficient (d_{33}) of these films is comparable to that of the quartz bulk material (i.e. 2.3 pm/V). In addition, PFM measurements display a linear dependence between the applied AC voltage and the mean vibration amplitude, which proves a converse piezoelectric effect. In the case of nanostructured quartz films, the piezoelectric

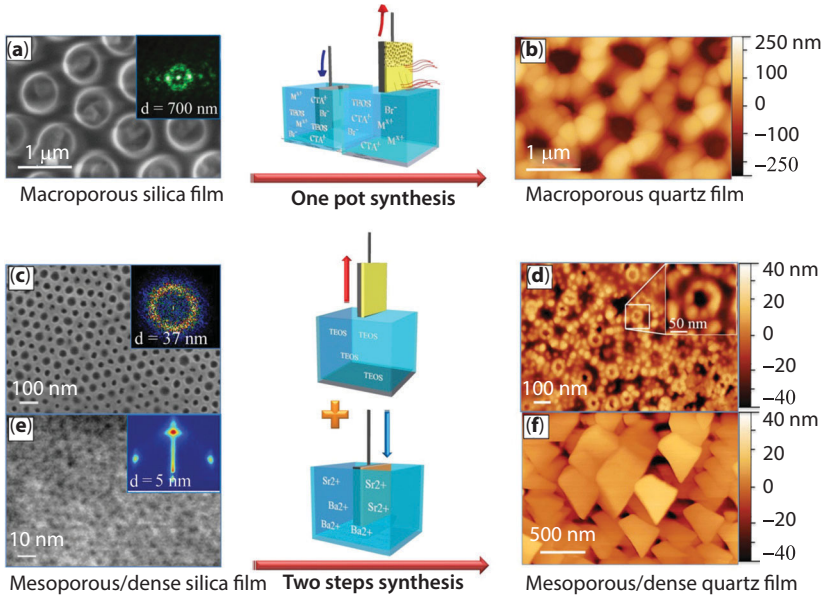

Figure 1.5 Epitaxial growth of α-quartz thin films on Si(100) with tunable textures by using sol–gel chemistry. Two different approaches can be used in order to obtain amorphous silica films with different pore sizes: one-pot synthesis which allows to prepare macropores quartz films (a and b) and two-step synthesis that can produce mesopores with an average pore of 28 nm and dense quartz films (c, d, e, and f).

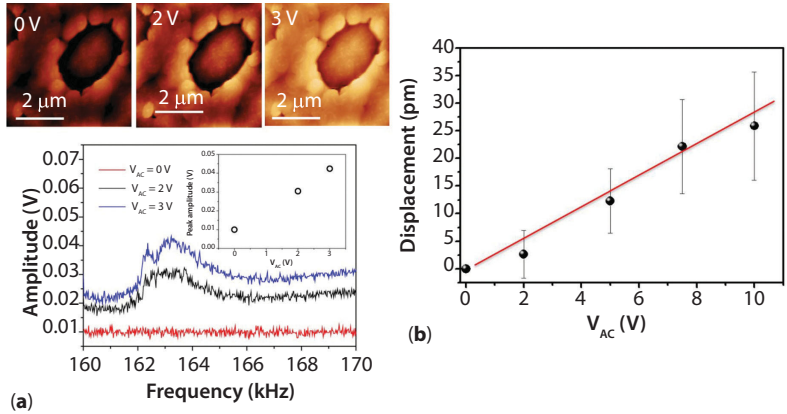

Figure 1.6 Piezoelectric measurements by PFM technique. Notice that quartz films on silicon vivrates under the applied AC voltage and this feature is detected through the deflection of the tip at a particular resonance frequency (a). The tip displacement is linear with the amplitude of the applied AC field, and the piezoelectric coefficient obtained is in the order of 2 picometers per volt, which is of comparable to the one measured in quartz bulk material.

activity is preserved (Figure 1.6a). Moreover, the PFM response obtained on the crystals surrounding the porosity and the perimeter of the pores was conserved.

This bottom-up methodology makes possible to engineer films with thickness between 150 and 750 nm, which are much thinner than those obtained by top-down technologies based on cutting and polishing of large hydrothermally grown quartz crystals. As a result, this new integration of quartz thin films has promising possibilities for many applications in the field of electromechanical devices given the higher resonance frequencies that are expected for these materials. In addition, the control of the porosity and texture of quartz thin films open up the possibility to produce more efficient devices. This is supported by the fact that porous nanostructured quartz thin films increase the specific area, thus enhancing the sensing properties of the future device. Finally, the controlled design of textured crystalline solids is highly appealing for the further integration of functional oxides onto silicon substrates.

1.2.3 Integration of Functional Oxides by Quartz Templating

Epitaxial α-quartz thin films can be used as a template to stabilize the crystallization and growth of single-crystalline octahedral molecular sieves (OMSs) of manganese oxides on silicon substrates [77]. OMS manganese oxides are 1D open-framework structures with nanometric tunnel sizes. The tunnel atomic structure is built up by edge-shared and corner-shared [MnO_6] octahedral units leading to different pore size materials. The shape of these atomic tunnel structures is expressed by the number of constituting [MnO_6] octahedral units ($n \times m$) and is characteristic of each porous manganese oxide [87]. Recently, much effort has been devoted to synthesize novel nanoscale manganese oxide OMS materials aiming at modifying their physical and chemical properties. As a result, it is possible to improve their performance as electrodes for batteries and supercapacitors and as redox catalysts [88, 89]. OMS nanowires grown on top of silicon substrates can be prepared either through a spin-coating process or through a templating synthesis that requires the previous deposition of a track-etched polymer template film on top of the silicon substrate (see Figure 1.7). On either case, a thermal treatment of the confined precursor's solutions containing alkaline earth cations will promote the confined nucleation of MnO_2 oxide nanowires seeds and the further formation of quartz crystals at the silicon interface [90, 91]. The nucleation and crystalline growth of 1D nanostructures on silicon were observed when either Sr^{2+} or Ba^{2+} cations were present in the precursor's solution. The use of supported track-etched polymer

templates that are used as nanoreactor or spin-coating synthesis will produce the homogeneous dissemination of the catalyst cations needed for the crystallization of the interfacial α-quartz layer (see Figure 1.7 (1a) and (2a)). This α-quartz film renders the necessary matching with the interface lattice for the epitaxial growth of manganate nanowires (OMS) at temperatures above 800 °C (Figure 1.7 (1c) and (2c)). The low annealing temperatures used during the crystallization process (i.e. 800 °C) will give rise to a polycrystalline *α*-quartz interface that induces different possible crystallographic orientations to the OMS nanowires. Importantly, the aspect ratios of these OMS nanowires can be modified. Samples grown by using polymer templates exhibit OMS nanowires with aspect ratios close to 50, whereas samples grown by direct spin coating exhibit a nanorod-like microstructure with aspect ratios 10 times lower, as observed in the FEG–SEM images of Figure 1.8a and b.

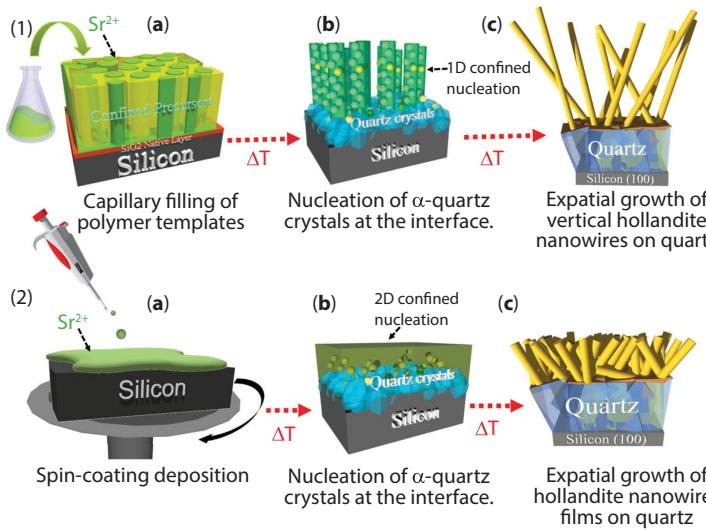

Figure 1.7 Growth mechanism and synthesis methods of both, thin-film and vertical epitaxial oxide nanowires on Si (100) substrate**.** (1a) Nanoporous polymer template deposited on a SiO_2/Si substrate filled with the chemical precursor solution containing Sr^{2+} melting agents. (1b) 1D-confined nucleation in high-aspect-ratio nanopores of oxide nanowires seeds and first devitrification and nucleation of disoriented quartz crystals at the silicon interface. (1c) α-Quartz film formation at higher temperatures (800 °C), allowing the epitaxial stabilization of oxide nanowires. (2a) Chemical precursor solution containing Sr^{2+} melting agents deposited on a SiO_2/Si substrate by using spin-coating technique. (2b) 2D-confined nucleation in thin film form of oxide nanowires seeds and first devitrification and nucleation of disoriented quartz crystals at the silicon interface. (2c) α-Quartz film formation at higher temperatures (800 °C), allowing the epitaxial stabilization of thin-film oxide nanowires.

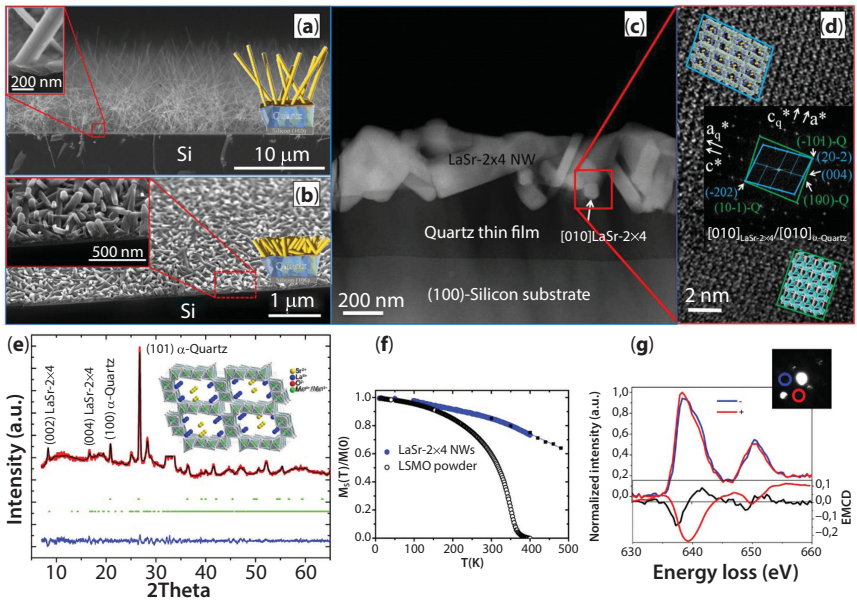

Figure 1.8 Low-magnification FEG–SEM images of both, vertical and thin film of epitaxial $SrMn_8O_{16}$ nanowires grown at 800 °C during 2 h on an α-quartz/Si substrate (a and b), respectively. Inset images and 3D schematics show an enlarged view of the $SrMn_8O_{16}$ nanowires on silicon substrate. Low-magnification HAADF image of epitaxial ferromagnetic LaSr-2 × 4 nanowires stabilized on α-quartz/Si substrate (800 °C during 5 h) (c). HRTEM image showing, the interface between quartz film and epitaxial LaSr-2 × 4 nanowires, viewed along [010]. The inset image represents the Fast Fourier Transform (FFT) of both crystallographic phases that confirm the epitaxial relation between the LaSr-2 × 4 nanowires and the α-quartz and which is given by [20-2] LaSr-2 × 4 // [-101] α-quartz. (d). Lebail fitting refinement of the XRD pattern of single-crystalline LaSr-2 × 4 nanowires on silicon substrate. Experimental records: red points; calculated: continuous black line; Bragg reflections: vertical green marks. The difference between the observed and calculated profiles is presented as a blue line. The inset image represents the proposed LaSr-2 × 4 nanowires cell model, where yellow spheres represent the Sr columns position, blue spheres the La columns position, and red and green spheres the O and Mn positions, respectively (e). Normalized magnetization versus temperature curve of LaSr-2 × 4 nanowires and $La_{0.7}Sr_{0.3}MnO_3$ powder blank samples measured at $H = 1.5$ T in an orthogonal configuration to the substrate. (f) Dichroism measurement performed by using TEM and Mn $L_{2,3}$ edges, along the two polarized configurations (+) and (−) (g).

These innovative growth methods have the possibility to modify the chemical composition and crystallographic structures of the OMS nanowires. For example, the authors synthesized a new crystallographic phase of OMS manganite nanowires namely, LaSr-2 × 4 OMS. LaSr-2 × 4 nanowires showed a new monoclinic structure with ordered arrangement of La^{3+} and Sr^{2+} cations inside the 1D channels [90, 91].

XRD and STEM analyses can be used to determine the monoclinic unit cell of LaSr-2 × 4 nanowires, which is given by the lattice parameters a = 13.8 Å, b = 5.7 Å, c = 21.8 Å, and β = 101°, with the long axis along the b crystallographic direction [90, 91]. The uniform composition of the LaSr-2 × 4 nanowires and also the epitaxial relation between NWs and α-quartz interlayer given by the (010) LaSr-2 × 4//(010) *and* [20-2] LaSr-2 × 4//[-101] α-quartz crystallographic directions is revealed by high resolution transmission electron microscopy (HRTEM) images (see Figure 1.8c and d) [77].

Superconducting quantum interference device (SQUID) magnetometer can be used to study the macroscopic magnetic properties of LaSr-2 × 4 nanowires integrated on silicon substrate [91]. Magnetic hysteresis loops measured at different temperatures between 10 and 400 K for applied fields up to 5 T showed a ferromagnetic behavior above 400 K. Figure 1.8f exhibits the temperature dependence of the magnetization, which is measured at an external applied magnetic field of 1.5 T for a polycrystalline perovskite LSMO blank sample and the monoclinic LaSr-2 × 4 nanowires, both prepared from the same chemical precursors. The magnetization of nanowires decreases more slowly with temperature, although it remains relatively high at 500 K (~40% decrease from 4 K). This suggests that the Curie temperature of the monoclinic LaSr-2 × 4 nanowires is well above 500 K, i.e. much higher than all the well-established values reported so far for any perovskite manganite compound.

The magnetism of LaSr-2 × 4 nanowires at the nanoscale has been studied using electron magnetic circular dichroism (EMCD) (see Figure 1.8g), which can be measured from TEM analyzing $L_{2,3}$ EELS absorption edges of transition metals [92]. EMCD measurements performed on a single LaSr-2 × 4 nanowire at room temperature showed that there is a significant orbital component to the magnetic moment and that this is aligned anti-parallel to the spin moment [93]. This finding suggests that Mn shells are less than half-filled and that the origin of ferromagnetism may reside in a double-exchange-like mechanism. Indeed, the spatially resolved EELS measurements confirmed the presence of mixed-valence Mn cations at different sites, as a result of the ordered arrangement of the La^{3+} and Sr^{2+} cations within the structure. However, the electronic structure of these monoclinic LaSr-2 × 4 nanowires is different from its perovskite-like counterpart and the fine structure of the O–K edge presents significant changes compared to standard manganites [94, 95]. The different arrangement of La and Sr cations in the new structure might affect the Mn–O bonds of MnO_6 octahedra. Further theoretical and experimental work is thus needed to interpret the particular features of the electronic structure of LaSr-2 × 4 monoclinic nanowires.

This synthesis method can be applied to other single-crystalline manganese-based OMS nanowires compositions such as hollandite ($Ba_{1+\delta}Mn_8O_{16}$), strontiomelane ($Sr_{1+\delta}Mn_8O_{16}$), and the quaternary oxide $(BaSr)_{1+\delta}Mn_8O_{16}$ [77].

The above results support the possibility to generate the devitrification of a silica interlayer and the further crystallization of quartz films, which might enables the integration of other functional oxide nanostructures on silicon. In the next section, we provide evidences on how this strategy can be useful for the integration of highly textured functional oxide thin films.

1.2.4 Highly Textured ZnO Thin Films

Epitaxial quartz films can be used as a new buffer layer to assist the integration of oxide nanomaterials thin films on silicon entirely performed by CSD. An example of that is shown in Figure 1.9 where a highly textured

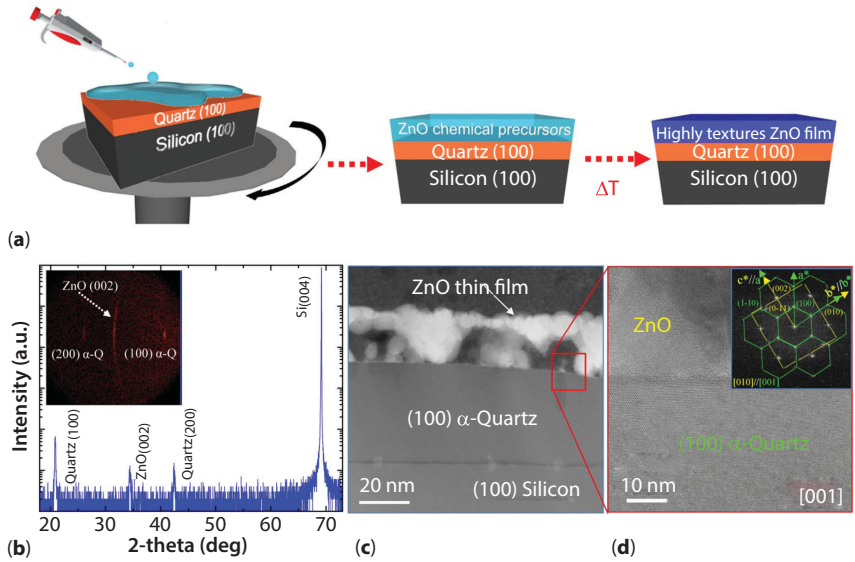

Figure 1.9 3D Schematics exhibiting the chemical deposition and growth of highly textured ZnO thin film on Si (100) substrate (a). XRD pattern of textured ZnO thin film on silicon substrate. The inset image shows the 2D XRD pattern confirming the textured growth of polycrystalline ZnO thin film (b). Low magnification HAADF image of textured polycrystalline ZnO thin films stabilized on α-quartz/Si substrate (c). Cross-sectional HRTEM image of the quartz/ZnO interface viewed along the [001] crystallographic direction of quartz phase. The inset image represents the Fast Fourier Transform (FFT) of both crystallographic phases and confirms the orientation of ZnO nanoparticles induced by the α-quartz film which is given by the following crystallographic relation [010] ZnO // [001] α-quartz (d).

polycrystalline ZnO thin film is grown on epitaxial (100)-quartz thin films. Importantly, HRTEM and XRD confirm that ZnO nanoparticles preserve an epitaxial relation with quartz films given by the [010] ZnO // [001] α-quartz (see Figure 1.9d and inset). As a result, the polycrystalline ZnO thin film is 100% oriented according to the [001] out of plane (see Figure 1.9b). This example confirms the possibility to integrate oxide heterostructures on silicon by using chemical solution methodology. In this precise example, ZnO films were prepared through a dip-coating process by using PAD, which is an aqueous chemical deposition method developed by the group of Quanxi Jia in 2004 [96]. PAD has the typical advantages of any CSD systems, therefore producing the deposition of defects-free thin films over large areas, a good control of the thickness and stoichiometry, and the growing of complex and multilayers structures. The main difference of PAD respect other chemical methods is the use of hydro-soluble polymers to coordinate cations and increase the viscosity of the water solution.

1.3 Integration of Functional Oxides by Combining Soft Chemistry and Physical Techniques

The PAD technique makes possible to obtain films with a well-controlled stoichiometry and free of cracks and other defects. As a result, PAD is among the most suitable soft chemistry techniques to be combined with physical deposition processes [97]. An example of that is the recent epitaxial growth of complex functional oxides on silicon by combining the deposition of oxide films by MBE and PAD, according to the sequence represented in Figure 1.10 [68].

More specifically, in a first step, a $SrTiO_3$ (100) film was grown by MBE on Si(100). Then, the following step consisted in the deposition of a $La_{0.7}Sr_{0.3}MnO_3$ (100) film by PAD, and the heterostructure was completed by a second MBE process to grow $BaTiO_3$. The resulting heterostructure (see Figure 1.11) was found to be epitaxial with a low mosaicity and displayed a columnar porous microstructure on the LSMO that is transferred to BTO films. This microstructure is induced by the controlled out-of-plane misorientation of the first STO film deposited by MBE. It is noteworthy that in spite of the columnar porosity of the film, the LSMO/BTO interface is remarkably sharp (see Figure 1.11c). This observation evidences the good compatibility of the PAD and MBE. The interest of combining these two techniques is even greater if one considers that the growth of good-quality LSMO on Si/STO has not been achieved by MBE

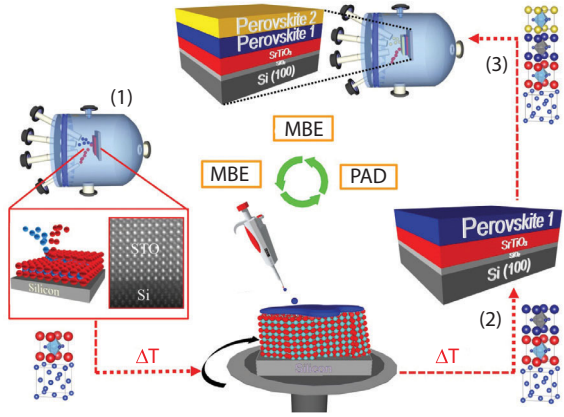

Figure 1.10 Schematic diagram that shows a new approach that combines MBE and PAD methods allowing the epitaxial growth of high-quality functional perovskite complex oxides multilayers on silicon substrate. First stage consists on the epitaxial growth of STO film on silicon by MBE. Inset shows 3D diagram and a cross-sectional HAADF–STEM image of a STO thin film epitaxially grown on silicon substrate by MBE (1). Second stage involves the use of STO/Si(100) as a large-scale pseudo-substrate which is combined with PAD chemical methodology for the integration of a new perovskite layer by spin-coating deposition technique (2). Finally, the resulting heterostructure produced by mixing MBE and PAD is combined again with MBE in order to produce the desired perovskite complex oxides multilayers on silicon substrate.

so far. As shown in the above example, introducing a PAD stage between a MBE processes can help circumventing MBE limitations.

Porous columnar BTO thin films display a ferroelectric activity, as shown by PFM measurements (see Figure 1.12). PFM images of phase and amplitude showing the ferroelectric domains previously written by electrical poling of the 50-nm-thick BTO film can be polarized (see Figure 1.12a and b, respectivelly).

1.4 Conclusions

The combination of semi-conducting substrates such as silicon with functional advanced oxide ceramics has promising applications for the microelectronic industry to develop novel and more efficient devices. The precise control of interfaces and crystallization mechanisms of silicon and metal-oxide structures at the nanoscale is still in its early stages. In this chapter, we have covered the most important and recent advances concerning the epitaxial growth of functional oxides nanostructures and nanostructured

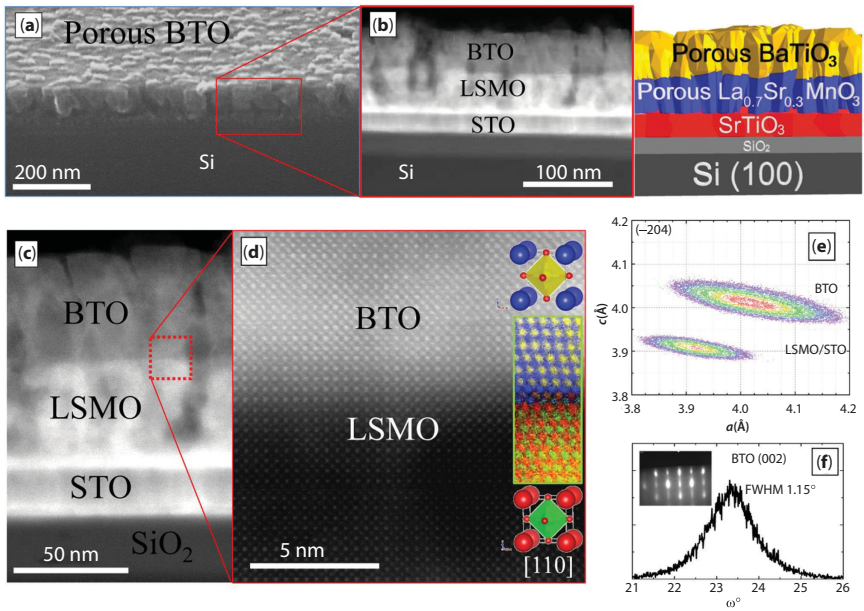

Figure 1.11 Low-magnification FEG–SEM image of a porous epitaxial BTO/LSMO/STO/Si(100) thin film grown by the combination of MBE and PAD methods. (a) Low-magnification HAADF image of a porous epitaxial BTO/LSMO/STO/Si(100) thin film (b) and (c), respectively. HRTEM image showing the interface between BTO layer grown by MBE and LSMO layer grown by PAD, viewed along the crystallographic direction [110]. Inset image shows the elemental mapping for Ti (yellow spheres), Ba (blue spheres), Mn (green spheres), and La/Sr (red spheres) indicating a high-quality and abrupt chemical interfaces between both perovskite layers (d). Reciprocal space map of a porous epitaxial BTO/LSMO/STO/Si(100) thin film (e). Rocking curve of BTO layer grown by MBE on LSMO/STO/Si(100) with a FWHM value of 1.15°. The inset shows the RHEED pattern exhibiting the epitaxial growth and high-quality surface of the BTO layer grown by MBE on the chemically synthesized LSMO film (f).

thin films on silicon as well as other technological substrates based on chemical strategies. We have presented relevant examples to show that the interplay between chemical compatibility, chemical reactivity, lattice mismatch, crystallographic structure, interface, and surface energies is crucial for the crystallographic phase stabilization and further integration of oxide nanostructures on silicon substrates. A special emphasis has been put on the synthesis of epitaxial oxide nanostructures on silicon entirely performed by chemical solution methodologies. In this chapter, we have explored the main physico-chemical principles that drive the devitrification–crystallization mechanism of α-quartz in amorphous silica monoliths by *in situ* neutron thermodiffractometry. We have shown that the doping of

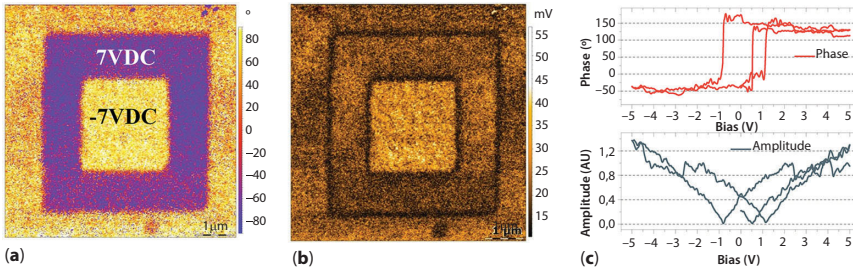

Figure 1.12 PFM analysis illustrating the electromechanical behavior of the porous columnar thick epitaxial BTO/LSMO/STO/Si(100) films. PFM phase and amplitude images of the 50-nm-thick BTO film after electrical poling (a and b), respectively. Local PFM amplitude and phase hysteresis loops measured in the same $BaTiO_3$ film, respectively (c).

silica monoliths with Sr^{2+} catalyst is the key to promote the devitrification and crystallization into α-quartz during a thermal treatment. This devitrification mechanism of silica makes possible the integration of piezoelectric quartz thin films on silicon (100) with a control over the thickness, texture, and porosity by using sol–gel chemistry. This bottom-up methodology, which produces epitaxial films with thickness between 150 and 750 nm, has promising possibilities for many applications in the field of electromechanical devices given the higher resonance frequencies that are expected for these materials. Moreover, the control of the porosity and texture of quartz thin films opens up the possibility to produce more efficient devices.

We have shown that quartz films can be used as a model system and as a novel chemical strategy in which the catalytic devitrification of the amorphous SiO_2 native layer on silicon permits the integration of different functional oxide nanostructures at air atmosphere. Consequently, α-quartz layer works as a buffer for the integration of vertical or thin-film OMS nanowires with different compositions and enhanced magnetic properties or highly textured ZnO thin films.

Another strategy presented in this chapter is based on the combination of CSD methodologies with physical methods (MBE) to obtain novel functional oxide heterostructures on silicon. We have shown that the PAD methodology can be combined with MBE to obtain epitaxial functional oxide films with a well-controlled stoichiometry and porosity. This combination of physics, chemistry, and processing allows engineering nanostructured, porous, and epitaxial crystalline thin films. As an example, we have presented the integration of ferroelectric columnar porous BTO thin films from porous LSMO layer on top of a STO/silicon buffer layer.

Altogether, *bottom-up* chemical solution-based strategies offer limitless possibilities for the integration of functional advanced oxide ceramics on silicon with unique electric, magnetic, or optical properties with interesting applications for the development of novel devices.

Acknowledgments

A.C. acknowledges the financial support from 1D-RENOX project (Cellule Energie INSIS-CNRS) and Ecole Centrale de Lyon under the BQR 2015 project. J.M.V.-F. also acknowledges MINECO for support with a PhD grant of the FPI program. We thank D. Montero and L. Picas for technical support and critical reading of the manuscript. We also thank P. Regreny, C. Botella, and J.B. Goure for technical assistance on the Nanolyon technological platform. ICMAB acknowledges MINECO (Severo Ochoa programme SEV-2015-0496, MAT2014-51778-C2-1-R) and Generalitat de Catalunya (2014SGR 753 and Xarmae). The HAADF–STEM microscopy work was conducted at the Center for Nanophase Materials Sciences, which is a DOE Office of Science User Facility. This research was supported by the European Research Council (ERC StG-2DTHERMS), Ministerio de Economía y Competitividad of Spain (MAT2013-44673-R), and EU funding Project "TIPS" Thermally Integrated Smart Photonics Systems Ref. 644453 call H2020-ICT-2014-1.

References

1. Dawber M, Rabe KM, Scott JF: Physics of thin-film ferroelectric oxides. *Reviews of Modern Physics* 77:1083–1130, 2005.
2. Ramesh R, Schlom DG: Whither oxide electronics? *MRS Bulletin* 33: 1006–1014, 2008.
3. Schlom DG, Chen L-Q, Pan X, *et al.* A thin film approach to engineering functionality into oxides. *Journal of the American Ceramic Society* 91: 2429–2454, 2008.
4. Woodhead Publishing Series in Electronic and Optical Materials, in Koster G, Huijben M, Rijnders G (eds): *Epitaxial Growth of Complex Metal Oxides*, Woodhead Publishing, 2015, pp. xiii–xvii
5. Mannhart J, Schlom DG: Oxide interfaces—an opportunity for electronics. *Science* 327:1607–1611, 2010.
6. Zubko P, Gariglio S, Gabay M, *et al.* Interface Physics in Complex Oxide Heterostructures, in Langer JS (ed): Annual Review of Condensed Matter Physics, Vol 2. Annual Review of Condensed Matter Physics, 2011, pp. 141–165.

7. Yu P, Chu Y-H, Ramesh R: Oxide interfaces: pathways to novel phenomena. *Materials Today* 15:320–327, 2012.
8. Hwang HY, Iwasa Y, Kawasaki M, *et al.* Emergent phenomena at oxide interfaces. *Nature Materials* 11:103–113, 2012.
9. Revesz P, Li J, Szabo N, *et al.* Pzt Interaction with Metal and Oxides Studied by Rutherford Backscattering Spectrometry. MRS Online Proceedings Library Archive 243, 1991.
10. McKee RA, Walker FJ, Chisholm MF: Crystalline oxides on silicon: the first five monolayers. *Physical Review Letters* 81:3014–3017, 1998.
11. Warusawithana MP, Cen C, Sleasman CR, *et al.* A ferroelectric oxide made directly on silicon. *Science* 324:367–370, 2009.
12. Lin A, Hong X, Wood V, *et al.* Epitaxial growth of $Pb(Zr_{0.2}Ti_{0.8})O_3$ on Si and its nanoscale piezoelectric properties. *Applied Physics Letters* 78:2034–2036, 2001.
13. Vaithyanathan V, Lettieri J, Tian W, *et al.* c-Axis oriented epitaxial $BaTiO_3$ films on (001) Si. *Journal of Applied Physics* 100:024108, 2006.
14. Niu F, Wessels BW: Epitaxial growth and strain relaxation of $BaTiO_3$ thin films on $SrTiO_3$ buffered (001) Si by molecular beam epitaxy. *Journal of Vacuum Science & Technology B* 25:1053–1057, 2007.
15. Largeau L, Patriarche G, Saint-Girons G, *et al.* Self-assembled Ge nanocrystals on $BaTiO_3$/$SrTiO_3$/Si(001). *Applied Physics Letters* 92:031904, 2008.
16. Niu G, Yin S, Saint-Girons G, *et al.* Epitaxy of $BaTiO_3$ thin film on Si(001) using a $SrTiO_3$ buffer layer for non-volatile memory application. *Microelectronic Engineering* 88:1232–1235, 2011.
17. Dubourdieu C, Bruley J, Arruda TM, *et al.* Switching of ferroelectric polarization in epitaxial $BaTiO_3$ films on silicon without a conducting bottom electrode. *Nature Nanotechnology* 8:748–754, 2013.
18. Posadas A, Berg M, Seo H, *et al.* Epitaxial integration of ferromagnetic correlated oxide $LaCoO_3$ with Si (100). *Applied Physics Letters* 98:053104, 2011.
19. Mechin L, Adamo C, Wu S, *et al.* Epitaxial $La_{0.7}Sr_{0.3}MnO_3$ thin films grown on $SrTiO_3$ buffered silicon substrates by reactive molecular-beam epitaxy. *Physica Status Solidi A—Applications and Materials Science* 209:1090–1095, 2012.
20. Park JW, Bogorin DF, Cen C, *et al.* Creation of a two-dimensional electron gas at an oxide interface on silicon. *Nature Communications* 1:1-6, 2010.
21. Jin EN, Kornblum L, Kumah DP, *et al.* A high density two-dimensional electron gas in an oxide heterostructure on Si (001). APL Materials 2:116109, 2014.
22. Kornblum L, Jin EN, Kumah DP, *et al.* Oxide 2D electron gases as a route for high carrier densities on (001) Si. *Applied Physics Letters* 106:201602, 2015.
23. Kornblum L, Jin EN, Shoron O, *et al.* Electronic transport of titanate heterostructures and their potential as channels on (001) Si. *Journal of Applied Physics* 118:105301, 2015.

24. Li Z, Guo X, Lu H-B, *et al.* An epitaxial ferroelectric tunnel junction on silicon. *Advanced Materials* 26:7185–7189, 2014.
25. Guo R, Wang Z, Zeng S, *et al.* Functional ferroelectric tunnel junctions on silicon. *Scientific Reports* 5:12576, 2015.
26. Laughlin RP, Currie DA, Contreras-Guererro R, *et al.* Magnetic and structural properties of $BiFeO_3$ thin films grown epitaxially on $SrTiO_3$/Si substrates. *Journal of Applied Physics* 113:17d919, 2013.
27. Wang J, Zheng H, Ma Z, *et al.* Epitaxial $BiFeO_3$ thin films on Si. *Applied Physics Letters* 85:2574–2576, 2004.
28. Zhang W, Chen A, Khatkhatay F, *et al.* Integration of self-assembled vertically aligned nanocomposite $(La_{0.7}Sr_{0.3}MnO_3)(1-x):(ZnO)(x)$ thin films on silicon substrates. *ACS Applied Materials & Interfaces* 5:3995–3999, 2013.
29. Khatkhatay F, Chen A, Lee JH, *et al.* Ferroelectric properties of vertically aligned nanostructured $BaTiO_3$-CeO_2 thin films and their integration on silicon. *ACS Applied Materials & Interfaces* 5:12541–12547, 2013.
30. Kim DH, Aimon NM, Sun XY, *et al.* Integration of self-assembled epitaxial $BiFeO_3$-$CoFe_2O_4$ multiferroic nanocomposites on silicon substrates. *Advanced Functional Materials* 24:5889–5896, 2014.
31. Hudait MK, Clavel M, Zhu Y, *et al.* Integration of $SrTiO_3$ on crystallographically oriented epitaxial germanium for low-power device applications. *ACS Applied Materials & Interfaces* 7:5471–5479, 2015.
32. Fischetti MV, Laux SE: Band structure, deformation potentials, and carrier mobility in strained Si, Ge, and SiGe alloys. *Journal of Applied Physics* 80:2234–2252, 1996.
33. Ponath P, Fredrickson K, Posadas AB, *et al.* Carrier density modulation in a germanium heterostructure by ferroelectric switching. *Nature Communications* 6:6067, 2015.
34. Le Bourdais D, Agnus G, Maroutian T, *et al.* Epitaxial manganite freestanding bridges for low power pressure sensors. *Journal of Applied Physics* 118:124509, 2015.
35. Liu S, Guillet B, Aryan A, *et al.* $La_{0.7}Sr_{0.3}MnO_3$ suspended microbridges for uncooled bolometers made using reactive ion etching of the silicon substrates. *Microelectronic Engineering* 111:101–104, 2013.
36. Fina I, Apachitei G, Preziosi D, *et al.* In-plane tunnelling field-effect transistor integrated on Silicon. *Scientific Reports* 5:14367, 2015.
37. Fork DK, Fenner DB, Connell GAN, *et al.* Epitaxial yttria-stabilized zirconia on hydrogen-terminated Si by pulsed laser deposition. *Applied Physics Letters* 57:1137–1139, 1990.
38. Wang SJ, Ong CK, You LP, *et al.* Epitaxial growth of yittria-stabilized zirconia oxide thin film on natively oxidized silicon wafer without an amorphous layer. *Semiconductor Science and Technology* 15:836–839, 2000.
39. de Coux P, Bachelet R, Gatel C, *et al.* Mechanisms of epitaxy and defects at the interface in ultrathin YSZ films on Si(001). *Crystengcomm* 14:7851–7855, 2012.

40. Bachelet R, de Coux P, Warot-Fonrose B, *et al.* $CoFe_2O_4$/buffer layer ultrathin heterostructures on Si(001). *Journal of Applied Physics* 110:086102, 2011.
41. Bachelet R, de Coux P, Warot-Fonrose B, *et al.* Flat epitaxial ferromagnetic $CoFe_2O_4$ films on buffered Si(001). *Thin Solid Films* 519:5726–5729, 2011.
42. Wakiya N, Shinozaki K, Mizutani N: Stress-induced magnetization for epitaxial spinel ferrite films through interface engineering. *Applied Physics Letters* 85:1199–1201, 2004.
43. Scigaj M, Dix N, Fina I, *et al.* Ultra-flat $BaTiO_3$ epitaxial films on Si(001) with large out-of-plane polarization. *Applied Physics Letters* 102:112905, 2013.
44. Banerjee N, Houwman EP, Koster G, *et al.* Fabrication of piezodriven, free-standing, all-oxide heteroepitaxial cantilevers on silicon. *APL Materials* 2:096103, 2014.
45. Blank DHA, Dekkers M, Rijnders G: Pulsed laser deposition in Twente: from research tool towards industrial deposition. *Journal of Physics D—Applied Physics* 47:034006, 2014.
46. Reed GT, Mashanovich G, Gardes FY, *et al.* Silicon optical modulators. *Nature Photonics* 4:518–526, 2010.
47. Joushaghani A, Jeong J, Paradis S, *et al.* Wavelength-size hybrid Si-VO_2 waveguide electroabsorption optical switches and photodetectors. *Optics Express* 23:3657–3668, 2015.
48. Bi L, Hu J, Jiang P, *et al.* Magneto-optical thin films for on-chip monolithic integration of non-reciprocal photonic devices. *Materials* 6:5094–5117, 2013.
49. Abel S, Stoeferle T, Marchiori C, *et al.* A strong electro-optically active lead-free ferroelectric integrated on silicon. *Nature Communications* 4:1671, 2013.
50. Xiong C, Pernice WHP, Ngai JH, *et al.* Active silicon integrated nanophotonics: ferroelectric $BaTiO_3$ devices. *Nano Letters* 14:1419–1425, 2014.
51. Louahadj L, Le Bourdais D, Largeau L, *et al.* Ferroelectric $Pb(Zr,Ti)O_3$ epitaxial layers on GaAs. *Applied Physics Letters* 103:212901, 2013.
52. Liang Y, Kulik J, Eschrich TC, *et al.* Hetero-epitaxy of perovskite oxides on GaAs(001) by molecular beam epitaxy. *Applied Physics Letters* 85:1217–1219, 2004.
53. Louahadj L, Bachelet R, Regreny P, *et al.* Molecular beam epitaxy of $SrTiO_3$ on GaAs(001): GaAs surface treatment and structural characterization of the oxide layer. *Thin Solid Films* 563:2–5, 2014.
54. Contreras-Guerrero R, Veazey JP, Levy J, *et al.* Properties of epitaxial $BaTiO_3$ deposited on GaAs. *Applied Physics Letters* 102:012907, 2013.
55. Leskela M, Ritala M: Atomic layer deposition (ALD): from precursors to thin film structures. *Thin Solid Films* 409:138–146, 2002.
56. George SM: Atomic layer deposition: an overview. *Chemical Reviews* 110: 111–131, 2010.
57. McDaniel MD, Posadas A, Ngo TQ, *et al.* Growth of epitaxial oxides on silicon using atomic layer deposition: crystallization and annealing of TiO_2 on $SrTiO_3$-buffered Si(001). *Journal of Vacuum Science & Technology B* 30:04e111, 2012.

58. McDaniel MD, Posadas A, Ngo TQ, *et al.* Epitaxial strontium titanate films grown by atomic layer deposition on $SrTiO_3$-buffered Si(001) substrates. *Journal of Vacuum Science & Technology A* 31:01a136, 2013.
59. Ngo TQ, Posadas AB, McDaniel MD, *et al.* Epitaxial c-axis oriented $BaTiO_3$ thin films on $SrTiO_3$-buffered Si(001) by atomic layer deposition. *Applied Physics Letters* 104:082910, 2014.
60. Ngo TQ, Posadas A, McDaniel MD, *et al.* Epitaxial growth of $LaAlO_3$ on $SrTiO_3$-buffered Si (001) substrates by atomic layer deposition. *Journal of Crystal Growth* 363:150–157, 2013.
61. Talin AA, Smith SM, Voight S, *et al.* Epitaxial $PbZr_{0.52}Ti_{0.48}O_3$ films on $SrTiO_3$/(001)Si substrates deposited by sol–gel method. *Applied Physics Letters* 81:1062–1064, 2002.
62. Gatabi J, Lyon K, Rahman S, *et al.* Functional materials integrated on III-V semiconductors. *Microelectronic Engineering* 147:117–121, 2015.
63. McDaniel MD, Ngo TQ, Hu S, *et al.* Atomic layer deposition of perovskite oxides and their epitaxial integration with Si, Ge, and other semiconductors. *Applied Physics Reviews* 2:041301, 2015.
64. McDaniel MD, Ngo TQ, Posadas A, *et al.* A chemical route to monolithic integration of crystalline oxides on semiconductors. *Advanced Materials Interfaces* 1:1400081, 2014.
65. McDaniel MD, Hu C, Lu S, *et al.* Atomic layer deposition of crystalline $SrHfO_3$ directly on Ge (001) for high-k dielectric applications. *Journal of Applied Physics* 117:054101, 2015.
66. Liu Y, Xu M, Heo J, *et al.* Heteroepitaxy of single-crystal $LaLuO_3$ on GaAs(111) A by atomic layer deposition. *Applied Physics Letters* 97:162910, 2010.
67. Wang X, Dong L, Zhang J, *et al.* Heteroepitaxy of La_2O_3 and $La_{2-x}Y_xO_3$ on GaAs (111)A by atomic layer deposition: achieving low interface trap density. *Nano Letters* 13:594–599, 2013.
68. Vila-Fungueiriño JM, Bachelet R, Saint-Girons G, *et al.* Integration of functional complex oxide nanomaterials on silicon. *Frontiers in Physics* 3:38, 2015.
69. Lange FF: Chemical solution routes to single-crystal thin films. *Science* 273:903–909, 1996.
70. Schwartz RW, Schneller T, Waser R: Chemical solution deposition of electronic oxide films. *Comptes Rendus Chimie* 7:433–461, 2004.
71. Calzada ML, Bretos I, Jimenez R, *et al.* Low-temperature processing of ferroelectric thin films compatible with silicon integrated circuit technology. *Advanced Materials* 16:1620, 2004.
72. Obradors X, Puig T, Gibert M, *et al.* Chemical solution route to self-assembled epitaxial oxide nanostructures. *Chemical Society Reviews* 43:2200–2225, 2014.
73. Schneller T, Waser R, Kosec, M, Payne, D: *Chemical Solution Deposition of Functional Oxide Thin Films* (ed 1), Springer-Verlag Wien, 2013.
74. Zabaleta J, Valencia S, Kronast F, *et al.* Photoemission electron microscopy study of sub-200 nm self-assembled $La_{0.7}Sr_{0.3}MnO_3$ epitaxial islands. *Nanoscale* 5:2990–2998, 2013.

75. Obradors X, Puig T, Ricart S, *et al.* Growth, nanostructure and vortex pinning in superconducting $YBa_2Cu_3O_7$ thin films based on trifluoroacetate solutions. *Superconductor Science and Technology* 25:123001, 2012.
76. Carretero-Genevrier A, Gich M, Picas L, *et al.* Soft-chemistry-based routes to epitaxial alpha-quartz thin films with tunable textures. *Science* 340:827–831, 2013.
77. Carretero-Genevrier A, Oro-Sole J, Gazquez J, *et al.* Direct monolithic integration of vertical single crystalline octahedral molecular sieve nanowires on silicon. *Chemistry of Materials* 26:1019–1028, 2014.
78. Carretero-Genevrier A, Puig T, Obradors X, *et al.* Ferromagnetic 1D oxide nanostructures grown from chemical solutions in confined geometries. *Chemical Society Reviews* 43:2042–2054, 2014.
79. Tadigadapa S, Mateti K: Piezoelectric MEMS sensors: state-of-the-art and perspectives. *Measurement Science and Technology* 20:092001, 2009.
80. Xia Y, Whitesides GM: Soft lithography. *Annual Review of Materials Science* 28:153–184, 1998.
81. Bruhns P, Fischer RX: Crystallization of cristobalite and tridymite in the presence of vanadium. *European Journal of Mineralogy* 12:615–624, 2000.
82. Venezia AM, La Parola V, Longo A, *et al.* Effect of alkali ions on the amorphous to crystalline phase transition of silica. *Journal of Solid State Chemistry* 161:373–378, 2001.
83. Pol VG, Gedanken A, Calderon-Moreno J: Deposition of gold nanoparticles on silica spheres: a sonochemical approach. *Chemistry of Materials* 15: 1111–1118, 2003.
84. Altamirano-Juarez DC, Carrera-Figueiras C, Garnica-Romo MG, *et al.* Effects of metals on the structure of heat-treated sol-gel SiO_2 glasses. *Journal of Physics and Chemistry of Solids* 62:1911–1917, 2001.
85. Carretero-Genevrier A: Submitted, 2016.
86. Brinker CJ, Lu YF, Sellinger A, *et al.* Evaporation-induced self-assembly: nanostructures made easy. *Advanced Materials* 11:579–585, 1999.
87. Suib SL: Porous manganese oxide octahedral molecular sieves and octahedral layered materials. *Accounts of Chemical Research* 41:479–487, 2008.
88. Ghodbane O, Pascal J-L, Favier F: Microstructural effects on charge-storage properties in MnO_2-based electrochemical supercapacitors. *ACS Applied Materials & Interfaces* 1:1130–1139, 2009.
89. Li WN, Yuan JK, Shen XF, *et al.* Hydrothermal synthesis of structure- and shape-controlled manganese oxide octahedral molecular sieve nanomaterials. *Advanced Functional Materials* 16:1247–1253, 2006.
90. Carretero-Genevrier A, Mestres N, Puig T, *et al.* Single-crystalline $La_{0.7}Sr_{0.3}MnO_3$ nanowires by polymer-template-directed chemical solution synthesis. *Advanced Materials* 20:3672–3677, 2008.
91. Carretero-Genevrier A, Gazquez J, Idrobo JC, *et al.* Single crystalline $La_{0.7}Sr_{0.3}MnO_3$ molecular sieve nanowires with high temperature ferromagnetism. *Journal of the American Chemical Society* 133:4053–4061, 2011.

92. Schattschneider P, Rubino S, Hebert C, *et al.* Detection of magnetic circular dichroism using a transmission electron microscope. *Nature* 441:486–488, 2006.
93. Gazquez J, Carretero-Genevrier A, Gich M, *et al.* Electronic and magnetic structure of LaSr-2 × 4 manganese oxide molecular sieve nanowires. *Microscopy and Microanalysis* 20:760–766, 2014.
94. Luo W, Varela M, Tao J, *et al.* Electronic and crystal-field effects in the fine structure of electron energy-loss spectra of manganites. *Physical Review B* 79:052405, 2009.
95. Varela M, Oxley MP, Luo W, *et al.* Atomic-resolution imaging of oxidation states in manganites. *Physical Review B* 79:085117, 2009.
96. Jia QX, McCleskey TM, Burrell AK, *et al.* Polymer-assisted deposition of metal-oxide films. *Nature Materials* 3:529–532, 2004.
97. Manuel Vila-Fungueirino J, Rivas-Murias B, Rodriguez-Gonzalez B, *et al.* Interface magnetic coupling in epitaxial bilayers of $La_{0.92}MnO_3/LaCoO_3$ prepared by polymer-assisted deposition. *Chemistry of Materials* 26:1480–1484, 2014.

2

Biphasic, Triphasic, and Multiphasic Calcium Orthophosphates

Sergey V. Dorozhkin

Moscow, Russia

Abstract

Due to the chemical similarity to the inorganic constituents of calcified tissues of mammals, biologically relevant calcium orthophosphates ($CaPO_4$) have been applied as artificial bioceramics suitable for reconstruction of various types of bone defects. Since none of the known individual types of $CaPO_4$ appear to be able to mimic both the composition and the properties of natural bones, various attempts have been made to overcome this problem, and a multiphasic (polyphasic) concept is one of the reasonable solutions. In general, this approach is determined by advantageous formulations consisting of homogeneous blends of two (biphasic), three (triphasic), or more (multiphasic) individual $CaPO_4$ phases possessing diverse solubility and, therefore, bioresorbability, while the optimum ratios among the phases depend on the definite applications. Therefore, all currently known multiphasic $CaPO_4$ formulations are sparingly soluble in water, and thus, after being implanted, they are gradually resorbed inside the body, releasing calcium and orthophosphate ions into the biological medium and, hence, seeding a new bone formation. They have already demonstrated a proven biocompatibility, osteoconductivity, safety, and predictability *in vitro*, *in vivo*, and in clinical trials. More recently, *in vitro* and *in vivo* studies have shown that some of them might possess osteoinductive properties. Hence, in tissue engineering, multiphasic $CaPO_4$ represents promising bioceramics to construct various scaffolds capable of carrying and/or modulating the behavior of cells. This review summarizes the available information on biphasic, triphasic, and multiphasic $CaPO_4$ formulations including their biomedical applications. New compositions have been proposed as well.

***Keywords*:** Calcium orthophosphates, hydroxyapatite, phase, biphasic, triphasic, multiphasic, polyphasic, bioceramics, bone grafts, tissue engineering.

Corresponding author: sedorozhkin@yandex.ru

Ashutosh Tiwari, Rosario A. Gerhardt and Magdalena Szutkowska (eds.) Advanced Ceramic Materials, (33–96) © 2016 Scrivener Publishing LLC

2.1 Introduction

Biologically relevant $CaPO_4$ are of the special significance for the human beings because they represent the inorganic part of major normal (bones, teeth, and deer antlers) and pathological (*i.e.*, those appearing due to various diseases) calcified tissues of mammals [1, 2]. Therefore, the majority of artificially prepared $CaPO_4$ possess remarkable biocompatibility and bioactivity. Material scientists extensively use this property to construct artificial bone grafts that are either entirely made of [3] or only surface-coated by [4] the biologically relevant $CaPO_4$. The available types of $CaPO_4$ with chemical formulae, standard abbreviations, and the solubility data are listed in Table 2.1 [3–5]. As seen from the table, the solubility values of the individual types of $CaPO_4$ are varied in a great extent.

In the mid-1980s, researchers discovered that the existing types of $CaPO_4$ could form biphasic formulations, in which the individual components could not be separated from each other [6, 7]. Currently, we know that the individual $CaPO_4$ phases in such formulations are homogeneously and intimately "mixed" at a far submicron (<1 μm) level, and therefore, they are strongly integrated with each other. Nevertheless, the presence of all individual phases is easily seen by X-ray diffraction (XRD) technique (Figure 2.1), which clearly indicates that they remain unchanged [8, 9]. However, the sharp and well-defined diffraction peaks visibly specify that the dimensions of the individual crystallites of both HA and β-TCP phases in such formulations exceed ~50 nm (otherwise, the diffraction peaks become broader). Thus, roughly speaking, the majority of the available biphasic, triphasic, and multiphasic $CaPO_4$ formulations consist of the individual phases with particle dimensions within 50–500 nm.

Concerning the properties of such multiphasic formulations, as a rule of a thumb, one can say that, in general, they are in between of those of the constituent $CaPO_4$ phases and depend on the relative amounts of the ingredients. Furthermore, by changing the ratio between more stable and more soluble types of $CaPO_4$, it is possible to adjust the major properties (such as bioactivity, bioresorbability, osteoconductivity, and osteoinductivity) of the multiphasic formulations. Therefore, multiphasic $CaPO_4$ formulations can be applied to a big variety of bone defects, including load-bearing areas, and as customized pieces, which will maintain their shape and properties over the necessary periods of time [10, 11].

The main biomedical idea on the development of multiphasic $CaPO_4$ formulations is determined by the proper balance of more stable and more soluble $CaPO_4$ phases [12, 13]. Namely, when compared to both α- and β-TCP, HA is a more stable phase under the physiological conditions

Table 2.1 Existing calcium orthophosphates and their major properties [3–5].

Ca/P molar ratio	Compound	Formula	Solubility at 25 °C, –log(K_s)	Solubility at 25 °C, g/L	pH stability range in aqueous solutions at 25 °C
0.5	Monocalcium phosphate monohydrate (MCPM)	$Ca(H_2PO_4)_2{\cdot}H_2O$	1.14	~18	0.0–2.0
0.5	Monocalcium phosphate anhydrous (MCPA or MCP)	$Ca(H_2PO_4)_2$	1.14	~17	[c]
1.0	Dicalcium phosphate dihydrate (DCPD), mineral brushite	$CaHPO_4{\cdot}2H_2O$	6.59	~0.088	2.0–6.0
1.0	Dicalcium phosphate anhydrous (DCPA or DCP), mineral monetite	$CaHPO_4$	6.90	~0.048	[c]
1.33	Octacalcium phosphate (OCP)	$Ca_8(HPO_4)_2(PO_4)_4{\cdot}5H_2O$	96.6	~0.0081	5.5–7.0
1.5	α-Tricalcium phosphate (α-TCP)	α-$Ca_3(PO_4)_2$	25.5	~0.0025	[a]
1.5	β-Tricalcium phosphate (β-TCP)	β-$Ca_3(PO_4)_2$	28.9	~0.0005	[a]
1.2–2.2	Amorphous calcium phosphates (ACP)	$Ca_xH_y(PO_4)_z{\cdot}nH_2O$, n = 3–4.5; 15–20% H_2O	[b]	[b]	~5–12 [d]

(*Continued*)

Table 2.1 Cont.

Ca/P molar ratio	Compound	Formula	Solubility at 25 °C, –log(K_s)	Solubility at 25 °C, g/L	pH stability range in aqueous solutions at 25 °C
1.5–1.67	Calcium-deficient hydroxyapatite (CDHA or Ca-def HA)[e]	$Ca_{10-x}(HPO_4)_x(PO_4)_{6-x}(OH)_{2-x}$ ($0<x<1$)	~85	~0.0094	6.5–9.5
1.67	Hydroxyapatite (HA, Hap, or OHAp)	$Ca_{10}(PO_4)_6(OH)_2$	116.8	~0.0003	9.5–12
1.67	Fluorapatite (FA or FAp)	$Ca_{10}(PO_4)_6F_2$	120.0	~0.0002	7–12
1.67	Oxyapatite (OA, OAp or OXA)[f], mineral voelckerite	$Ca_{10}(PO_4)_6O$	~69	~0.087	[a]
2.0	Tetracalcium phosphate (TTCP or TetCP), mineral hilgenstockite	$Ca_4(PO_4)_2O$	38–44	~0.0007	[a]

[a] These compounds cannot be precipitated from aqueous solutions.

[b] Cannot be measured precisely. However, the following values were found: 25.7±0.1 (pH = 7.40), 29.9±0.1 (pH = 6.00), 32.7±0.1 (pH = 5.28). The comparative extent of dissolution in acidic buffer is ACP >> α-TCP >> β-TCP > CDHA >> HA > FA.

[c] Stable at temperatures above 100 °C.

[d] Always metastable.

[e] Occasionally, it is referred to as "precipitated HA (PHA)".

[f] Existence of OA remains questionable.

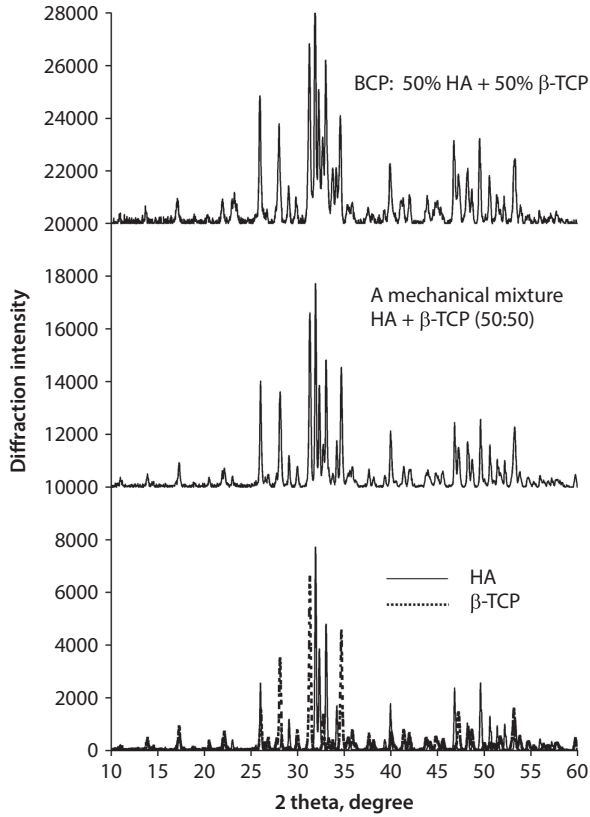

Figure 2.1 XRD patterns: bottom, the patterns of pure HA and β-TCP printed together; middle, mathematical summation of HA and β-TCP patterns; upper, biphasic calcium phosphate (BCP) consisting of 50% HA and 50% β-TCP. Reprinted from Refs [8, 9] with permission.

because it has a lower solubility (Table 2.1) and, thus, slower resorption kinetics. Therefore, due to a higher biodegradability of both α- and β-TCP components, the reactivity of biphasic formulations of HA with any type of TCP increases with the TCP/HA ratio increasing. Thus, *in vivo* bioresorbability of such biphasic formulations can be adjusted through the phase composition [14]. Similar conclusions are also valid for biphasic formulations of α- and β-TCP (in which α-TCP is a more soluble phase), as well as for triphasic (HA, α-TCP, and β-TCP) formulations, in which α-TCP appears to be the most soluble phase, while HA is the most inert phase. The biodegradable properties of biphasic (HA + β-TCP) formulations are well documented in the literature [15, 16].

The purpose of this manuscript is to review the state of the art of the knowledge on biphasic, triphasic, and multiphasic $CaPO_4$ formulations starting from the preparation techniques and ending with their biomedical applications.

2.2 General Definitions and Knowledge

Prior describing any information on multiphasic $CaPO_4$, one must define the basic terminology. Namely, according to Wikipedia, the free encyclopedia, in the physical sciences, a *phase* is a region of space, throughout which all physical and chemical properties of a material are essentially uniform. Examples of such properties include density, refraction index, chemical composition, crystal structure, *etc*. Another description is also available: a *phase* is a region of a material that is chemically uniform and physically distinct, which might be mechanically separable. Furthermore, one must note that, except of the aforementioned definitions, the term *phase* is often used as a synonym for a state of matter, such as gas, liquid, or solid. For example, in a system consisting of ice and water, solid blocks of ice represent one phase, liquid water is a second phase and humid air over the water is a third phase [17]. Since all available types of $CaPO_4$ are solids at ambient conditions, which either are thermally unstable (MCPM, MCPA, DCPD, DCPA, OCP, ACP, CDHA) or are melt at very high temperatures with a partial decomposition (α-TCP, β-TCP, HA, OA, FA, TTCP), the latter definition is not applicable to the subject of this review.

A monophasic system is one, which has just one phase. Examples include gases, gas mixtures, homogeneous solutions, and perfect monocrystals. The remaining matter of nature consists of diverse combinations of either several chemical compounds, often possessing unequal properties (so-called composites; however, that is another story), or several phases of the same chemical, in which minor compositional and/or structural variations are possible. The latter is the subject of current review. In such multiphasic systems, which, in general, can be liquid (consist of two or more immiscible liquids – not applicable to the subject of this review) and solid, the individual phases are always separated from both each other and their surroundings by phase boundaries, which may be notional or real, but which by convention delimit the finite volumes. For solids, these volumes can be as small as the regions surrounding single atoms and as big as the biggest perfect monocrystals currently available. In general, phase boundaries are related to changes in the organization of matter, such as a change from liquid to solid or a more subtle change from one crystal

structure to another. Exchanges of matter, heat, or work among the individual phases may take place across the phase boundaries. In a diagram form, the phase boundaries (or lines of equilibrium) are referred to lines on phase diagrams that mark conditions under which multiple phases can coexist at equilibrium (Figure 2.2). In a certain sense, all multiphasic systems might be related to *composites*; however, in no case, they are equal to them, since composites are made from two or more constituent materials with *significantly different* physical and/or chemical properties, while the multiphasic systems consist of individual compounds having rather similar both composition and properties. Furthermore, composites require two categories of the constituent materials: a matrix and a reinforcement, which is not the case for the multiphasic formulations. Nevertheless, in

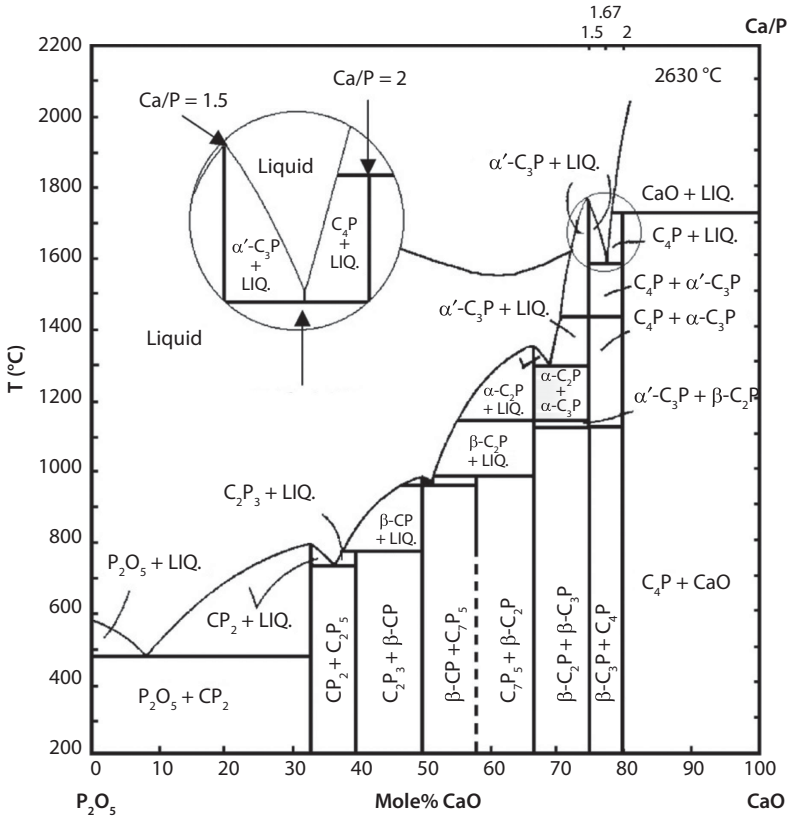

Figure 2.2 Phase diagram of the system CaO–P_2O_5 (C = CaO, P = P_2O_5) at elevated temperatures. Each line represents a phase boundary. Here, C_7P_5 means $7CaO{\cdot}5P_2O_5$; other abbreviations should be written out in the same manner. Reprinted from Refs [171, 172] with permission.

the scientific literature, the biphasic, triphasic, and multiphasic $CaPO_4$ formulations are occasionally called composites [18–28], which, with a few exceptions [29–32], is incorrect. Namely, paper by Viswanath and Ravishankar "Biphasic composite of tricalcium phosphate reinforced with hydroxyapatite whiskers" [29] undoubtedly describes composites because two categories of the constituent materials: a matrix and a reinforcement are clearly differentiated. However, studies are available, in which the real composites are called multiphasic compounds [33, 34], for example: "Our approach has focused on multiphase biomaterials that associate stem cells, bioactive factors and/or drugs with synthetic or natural scaffolds in order to replace and regenerate bone tissue in osseous or dental defects" [34, p. 17]. Clearly, it is hardly possible to mention cells as a separate phase; therefore, a more appropriate term, such as "multicomponent biomaterials", "complex biomaterials", and so on should have been used instead.

Polymorphism is another important term. In materials science, *polymorphism* is the ability of a solid material to exist in more than one form or crystal structure [35, 36]. Polymorphism can potentially be found in any crystalline material including polymers, minerals and metals, and is related to allotropy, which refers to elemental solids. When polymorphism exists due to the differences in crystal packing, it is called packing polymorphism. Polymorphism can also result from the existence of different conformers of the same molecule. This is a conformational polymorphism (not applicable to $CaPO_4$). In addition, there is a pseudo-polymorphism, in which different crystal types are the result of hydration or salvation [35, 36]. In general, polymorphs have different stabilities and may spontaneously convert from a metastable (unstable) form to the stable form at a particular temperature. They also exhibit different melting points, solubilities, and XRD patterns. Furthermore, the presence of certain impurities, as well as the preparation conditions, may stabilize certain forms and destabilize other ones. Among available types of $CaPO_4$ (Table 2.1), α- and β-modifications of TCP [37], as well as the monoclinic $P2_1/b$ and hexagonal $P6_3/m$ forms of HA [38] are two examples of a packing polymorphism, while pairs of MCPM/MCPA and DCPD/DCPA represent two examples of a pseudo-polymorphism.

2.3 Various Types of Biphasic, Triphasic, and Multiphasic $CaPO_4$

Historically, a term "biphasic calcium phosphate" (abbreviated as BCP or BCPs, if plural) appeared for the first time in 1985 in two presentations [6, 7] at the 11th Annual Meeting of the Society for Biomaterials. Nevertheless,

Nery and Lynch with co-workers [39] could use this term a bit earlier to describe bioceramics consisted of a mixture of HA and β-TCP. Based on the XRD results, those authors found that the "tricalcium phosphate" preparation material used in their early publication [40] was in fact a mixture of ~20% HA and ~80% β-TCP [41]. Both that particular material and other mixtures of β-TCP and HA were later described as BCPs. Concerning the number of individual phases, currently, only biphasic and triphasic $CaPO_4$ formulations are known; perhaps, more complicated formulations will be manufactured in future. Besides, the vast majority of currently known multiphasic $CaPO_4$ formulations consist of high-temperature phases only, such as α-TCP, β-TCP, HA and, perhaps, high-temperature ACP, OA, and TTCP. Little information on existence of multiphasic formulations, containing MCPM, MCPA, DCPD, DCPA, precipitated ACP, and OCP have been found in the literature. Perhaps, they will be produced and investigated in future. For example, formations of a CDHA-containing [42] and ACP-containing [43] biphasic formulations have been detected.

Among the possible types of multiphasic $CaPO_4$ formulations, BCPs appear to be both the simplest and best-investigated ones (one should note that in some publications abbreviation BCP means "bioactive calcium phosphate" [44] or "basic calcium phosphate" [45, 46]; such publications are not considered). In general, all types of BCP formulations could be subdivided into two major groups: those consisting of $CaPO_4$ having either the same (*e.g.*, α- and β-TCP, *i.e.*, $CaPO_4$ with a packing polymorphism) or different (*e.g.*, β-TCP and HA) Ca/P ratios. Among all currently known BCP formulations, those consisting of HA and β-TCP appear to be the senior member of the family and, therefore, the best investigated ones [10–14, 47–55]. In 1986, LeGeros [56] in USA and shortly afterwards Daculsi [14] in France initiated the basic studies on preparation of this type of BCPs and their *in vitro* properties. A similar combination of α-TCP with HA forms BCPs as well [57–65].

In 2004, the concept of BCP was extended by preparation and characterization of biphasic TCP (abbreviated as BTCP or BTCPs, if plural), consisting of α- and β-TCP phases [24, 66–72]. On the same year, triphasic formulations, consisting of HA, α-TCP, and β-TCP were prepared as well [26, 73–79].

To conclude this topic, one should stress that in multiphasic formulations the individual $CaPO_4$ phases may be present in almost unlimited proportions. Therefore, since preparation of the phase pure chemicals is extremely difficult and very expensive, strictly speaking, any actual sample of a $CaPO_4$ (even of a reagent grade quality), as well as any type of $CaPO_4$ bioceramics, in reality represents multiphasic mixtures of one or two major

phase(s) with several minor ones as admixtures; however, the subject of minor admixtures is beyond the scope of this review.

2.4 Stability

It is important to recognize that to be considered as a member of multiphasic $CaPO_4$, a candidate formulation must be stable. Otherwise, the majority of self-setting $CaPO_4$ formulations (cements, concretes, pastes, and putties), representing mixtures of two or more individual $CaPO_4$ (usually, as dry powders), such as MCPM + HA and DCPD + TTCP [80], might also be considered as biphasic, triphasic, and/or multiphasic $CaPO_4$. However, unless keeping in dry conditions, such formulations are very unstable and, in touch with moisture, they are easily and rapidly (within 5–30 min at ambient conditions) recrystallized to the single-phase products, such as DCPD or CDHA (cement setting). Just to compare, a similar transformation for β-TCP component of BCP (HA + β-TCP) into CDHA occurs during several weeks [81]. Therefore, in the scientific literature, the self-setting formulations are never associated with the subject of multiphasic $CaPO_4$. However, if either one or several component(s) of the self-setting formulations have been intentionally added in an excess from the reaction stoichiometry, formation of biphasic, triphasic, and multiphasic $CaPO_4$ bioceramics becomes plausible after setting [82, 83]. This approach might become a proper preparation technique of such formulations, especially those ones, containing thermally unstable forms of $CaPO_4$ such as MCPM, MCPA, DCPD, DCPA, precipitated ACP, OCP, and CDHA. It is important to note that the self-set $CaPO_4$ formulations might be sintered as well, and after sintering, they are transformed into multiphasic $CaPO_4$ bioceramics [84–86].

Based on both an aqueous instability of the self-setting $CaPO_4$ formulations and the stability of currently known compositions, it is possible to introduce a rule for designing of novel multiphasic $CaPO_4$. *The stable biphasic, triphasic, and multiphasic formulations might be created from individual $CaPO_4$ having either the similar or the closest Ca/P ratios*. One must stress that although this rule is an important prerequisite, in no case it is sufficient, since various single-phase (or single-component) self-setting formulations, such as α-TCP + an aqueous solution, β-TCP + an aqueous solution, DCPA + an aqueous solution, and TTCP + an aqueous solution are known [80]. Therefore, one might expect that multiphasic blends of these single-component self-setting formulations could possess the self-setting properties as well. A couple of examples of biphasic self-setting formulations of α-TCP + β-TCP + an aqueous solution have been already

described [69, 72]. Nevertheless, for want of anything better, the aforeintroduced rule currently might be used as a first approximation.

According to this rule, a polymorphic mixture of *α*- and *β*-TCP (Ca/P = 1.50 for both) forms a stable BTCP, which is confirmed by several studies [24, 66–72]. Furthermore, biphasic mixtures of HA + FA (Ca/P = 1.67 for both) are stable, which, again, is confirmed by several studies [87–91]. As mentioned above, a biphasic mixture of CDHA (Ca/P = 1.50) and *β*-TCP was found to appear when that CDHA was calcined at temperatures within 710–730 °C [42]; unfortunately, the stability of the obtained formulation was not investigated. Nevertheless, one may guess that any other case of polymorphism [*i.e.*, BCPs consisting of pairs MCPM + MCPA (Ca/P = 0.50 for both), DCPD + DCPA (Ca/P = 1.00 for both), as well as monoclinic HA + hexagonal HA should be stable (to be verified in future)]. To date, only indirect data on biphasic mixtures of monoclinic HA + hexagonal HA (they could be formed for a short period during phase transition of HA at heating) are available in the literature [92–95], in which nothing is reported on their stability in aqueous environment under ambient conditions. Similar is valid for biphasic mixtures of DCPD + DCPA (they could be formed for a short period during DCPD dehydration) [96–100] and MCPM + MCPA (they could be formed for a short period during MCPM dehydration) [101, 102]. An interesting study was performed on ultrasonic dehydration of DCPD into DCPA, followed by ultrasonic transformation of DCPA into MCPM [100]. Although biphasic mixtures of neither DCPD + DCPA, nor DCPA + MCPM were detected, their formation could have been overlooked because the authors performed measurements every 60 min. Furthermore, a thermal dehydration of biphasic mixtures of MCPM + DCPD was studied [103, 104]. Presumably, under a slow and careful heating, there might be conditions (roughly, at temperatures within 80–150 °C), at which a four-component multiphasic system MCPM + MCPA + DCPD + DCPA could be formed, similarly to the aforementioned case of CDHA + *β*-TCP preparation [42]. Unfortunately, the authors reported nothing on this point.

BCPs, consisting of $CaPO_4$ with the closest Ca/P ratios, such as HA (Ca/P = 1.67) + *β*-TCP (Ca/P = 1.50) [10–14, 47–56], or HA (Ca/P = 1.67) + *α*-TCP (Ca/P = 1.50) [57-65] are well known. Similarly, triphasic formulations, consisting of HA (Ca/P = 1.67), *α*- and *β*-TCP (Ca/P = 1.50 for both) are known as well [26, 73–79]. All these formulations are stable. Equally, biphasic combinations of HA (Ca/P = 1.67) + TTCP (Ca/P = 2.00) are stable as well; however, to the best of my findings, such formulations are prepared only by a thermal decomposition of HA during plasma spraying or at application of other high-temperature techniques. Therefore, the

biphasic combinations of HA + TTCP prepared by any type of a high-temperature technique always contain variable and hardly reproducible amounts of one or several admixture phases such as two types of TCPs, high-temperature ACP, CaO, and calcium pyrophosphate [105], which might introduce artifacts in their stability. More to the point, nothing has been ever reported on an instability of biphasic mixtures of MCPM (Ca/P = 0.50) + DCPD (Ca/P = 1.00) [103, 104]; therefore, they could be stable. Presumably, the same conclusion might be applicable to biphasic mixtures of MCPA + DCPA, MCPA + DCPD, MCPM + DCPA, as well as for DCPA (Ca/P = 1.00) + OCP (Ca/P = 1.33), and DCPD + OCP (to be verified in future). The latter formulation could have been formed during a partial re-crystallization of DCPD into OCP [106–109]. However, triphasic formulations of CDHA/OCP/β-TCP appeared to be not very stable due to a partial transformation of OCP and β-TCP into CDHA in aqueous environment [110, 111].

2.5 Preparation

Various types of $CaPO_4$ bioceramics have been long in use in medicine as bone grafts due to their chemical similarity to the mineral phase of natural bones [3]. Therefore, a variety of synthetic routes have been developed to prepare biphasic, triphasic, and multiphasic $CaPO_4$. In the case of the classical BCPs (HA + β-TCP), the most usual one consists of sintering of non-stoichiometric types of $CaPO_4$, such as ACP and CDHA, at temperatures above ~750 °C [112, 113]. Most frequently, sintering is performed at temperatures above ~1000 °C [18, 20, 42, 86, 114–117]. However, if sintering temperature approaches ~1300 °C or higher, BCP (HA + α-TCP) could be prepared [86]. This manufacturing process is simple, economic, and always results in a homogeneous distribution of the individual $CaPO_4$ phases. Various modifications of sintering, such as a two-step sintering [64, 65, 118–120] and a microwave heat processing [77, 121–130] of both ACP and CDHA are applied as well. For example, the chemical equation of a thermal decomposition of $Ca_{10-x}(HPO_4)_x(PO_4)_{6-x}(OH)_{2-x}$ (CDHA) with $x = 0.5$ looks as this:

$$2Ca_{9.5}(HPO_4)_{0.5}(PO_4)_{5.5}(OH)_{1.5} = Ca_{10}(PO_4)_6(OH)_2 + 3Ca_3(PO_4)_2 + H_2O \quad (2.1)$$

which gives rise to formation of a BCP consisting of HA and TCP. The type of BCP depends on the sintering temperatures. Namely, if the sintering temperature does not exceed ~1200 °C, BCP (HA + β-TCP) is prepared and if

it approaches ~1300 °C or higher, BCP (HA + α-TCP) is prepared. For this decomposition, a reasonable solid-state transformation mechanism based on diffusion of OH^- and Ca^{2+} ions was proposed in 2002 [8, 9]. In 2015, that mechanism was further itemized by discovering a fully separated growth of microscopic HA and β-TCP crystals, which could be adjacent, forming particles but without mutual intergrowth [131]. Synthesis conditions of precursive non-stoichiometric $CaPO_4$ were found to influence the HA/TCP ratio in resulting BCPs [132]. It is important to notice, that under the all other conditions being equal, the numerical value of the Ca/P ratio of the initial CDHA influences the grain sizes of the sintered BCP: the smaller the Ca/P ratio is, the larger the grain sizes are (Figure 2.3) [133].

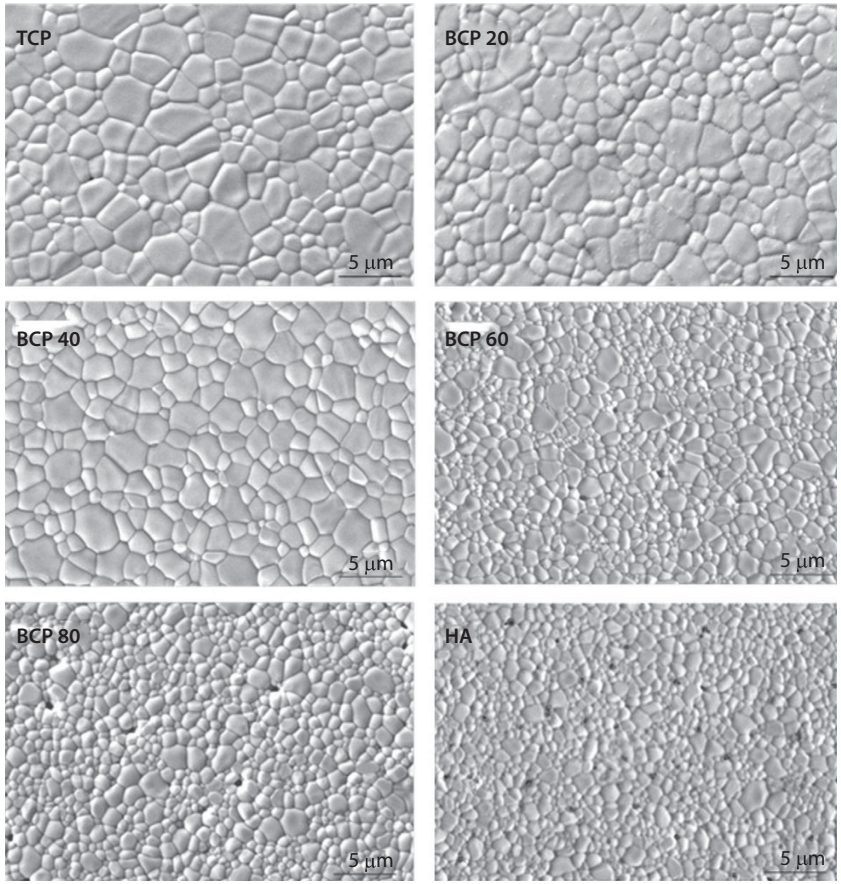

Figure 2.3 SEM images of β-TCP, HA, and BCPs with different β-TCP/HA ratios after sintering at 1130 °C. One can see that HA amount increasing results in gradual decreasing of the grain sizes. Reprinted from Ref. [133] with permission.

Another preparation approach of the classical BCPs is based on solid-state reactions among the solid reagents, performed again at elevated temperatures. The examples comprise reactions between crystals or particles of DCPD and $CaCO_3$ [134, 135], TCP and $Ca(OH)_2$ [136], MCPM and $CaCO_3$ [137–139], $NH_4H_2PO_4$ and $CaCO_3$ [140–142], $NH_4H_2PO_4$ and CaO [143], as well as among TCP, $CaCO_3$, and H_3PO_4 [144]. Presumably, at higher sintering temperatures, the same formulations would have given rise to formation of BCPs (HA + α-TCP); however, the authors of all those studies performed sintering to prepare BCPs (HA + β-TCP). Thus, to prepare multiphasic formulations, the chosen Ca- and PO_4-containing compounds should be mixed at the proportions to get the desired Ca/P ratio, followed by sintering at the desired temperatures. When milling of the initial reagents was applied, the HA/β-TCP ratio in the sintered BCPs was found to depend on the milling time [135]. Interestingly, that the Ca/P ratio of the final multiphasic formulations might be easily adjusted by addition of both soluble and thermally unstable Ca- or PO_4-containing compounds to the initial reagents. Namely, to decrease the Ca/P ratio, the necessary amount of $NH_4H_2PO_4$ solution should be added, while, to increase the Ca/P ratio, the necessary amount of $Ca(NO_3)_2$ or $Ca(CH_3COO)_2$ solution should be added to CDHA or ACP powders, or to the aforementioned mixtures of the solid reagents, followed by water evaporation, calcining, and sintering of the entire mixtures [145].

Furthermore, biphasic, triphasic, and multiphasic $CaPO_4$ formulations could be prepared by other methods, such as a flame spray pyrolysis [146], a liquid mix [147], and a sol–gel [31, 148–150] techniques; both latter processes must be followed by sintering [31, 147–150]. Besides, BCP (HA + β-TCP) might be produced by a hydrothermal treatment (carried out over a period of ~20 h at a temperature of ~300 °C and a pressure of ~35 atm) of $CaCO_3$ suspended in an aqueous solution of $NH_4H_2PO_4$ at pH of 5–6 [151]. Finally, a self-propagating high-temperature combustion synthesis might be used. In the case of combustion synthesis of solid mixtures of CaO and P_2O_5 powders, complicated combinations of various products, including traces of un-reacted CaO and P_2O_5, were often obtained [152–154]. However, a whole range of BCPs (HA + β-TCP) with a favorable control of Ca/P ratios was prepared when the raw materials comprised a colloidal solution, consisting from the reaction products among $Ca(NO_3)_2{\cdot}4H_2O$, $NH_4H_2PO_4$, citric acid (a fuel) and NH_4NO_3 (an oxidizer), followed by annealing at 1150 °C for 3 h [155]. Similarly, the combustion synthesis of the similar precursors was performed with urea or glycine as a fuel and HNO_3 as an oxidizer [156, 157]. Concerning the initial raw materials, besides the aforementioned cases of the chemically pure

compounds, multiphasic $CaPO_4$ formulations could be prepared from natural recourses, such as bovine [158–163] and cuttlefish [164] bones, corals [165], shells [143], and algae [166]. Surely, the different processing routes yield the different composition and properties of the final formulations, which is essential for biomedical applications.

A thermal decomposition of some stoichiometric $CaPO_4$, such as HA, at temperatures above ~1300 °C is one more preparation approach [167, 168]; however, this method often results in formation of complicated and poorly reproducible mixtures of various products including admixtures of high-temperature ACP, CaO, calcium pyrophosphates, *etc.* [169, 170]. Namely, transformation of HA into multiphasic $CaPO_4$ by annealing in a vacuum occurs as this: the outer part of HA is transformed into a mixture of α-TCP and TTCP, while the α-TCP phase on the surface is further converted into CaO. Besides, in the boundary phase, HA is transformed into TTCP [167]. Still other manufacturing approaches are based on investigations of the available anhydrous phase diagram $CaO–P_2O_5$ at elevated temperatures (Figure 2.2). According to this diagram, various types of calcium meta-, ortho-, pyro-, and polyphosphates and diverse combinations thereof could coexist depending on both the initial Ca/P ratio and temperature [171, 172]. Obviously, this phase diagram provides very important information for designing and development of new formulations of multiphasic calcium phosphates. Hopefully, some of them will become applicative to biomedical purposes.

BTCPs are usually prepared by calcining ACP [24, 68, 70, 71], in which the α-TCP/β-TCP ratio can be controlled by aging time and pH value during synthesis of the amorphous precursor [70]. In such systems, the α-TCP/β-TCP ratio in BTCPs was found to depend on the calcination temperature (Figure 2.4), and the optimum temperatures were between 830 and 850 °C [71]. In addition, since β-TCP is stable at temperatures 1000–1200 °C, while α-TCP is stable at temperatures >1300 °C, BTCP could be prepared by α-TCP sintering at 1000–1200 °C [72].

Triphasic $CaPO_4$ formulations, consisting of HA, α-TCP, and β-TCP, might be prepared by various techniques, for example, by a hydrothermal synthesis [76]. *In situ* preparation technique from $Ca(OH)_2$ and H_3PO_4, followed by heating was described as well [77]. According to the latter study, the preparation process of the triphasic formulations appears to be pH dependent (Figure 2.5): at pH = 6, the *in situ* mixture powders with 12 wt.% HA, 60 wt.% β-TCP, and 28 wt.% α-TCP phases were obtained, while at pH = 10 the main phases included HA (52 wt.%) and β-TCP (42 wt.%) with only a small amount of α-TCP (6 wt. %). Thus, the optimum preparation conditions of triphasic $CaPO_4$ lay within $7 < pH < 9$ [77].

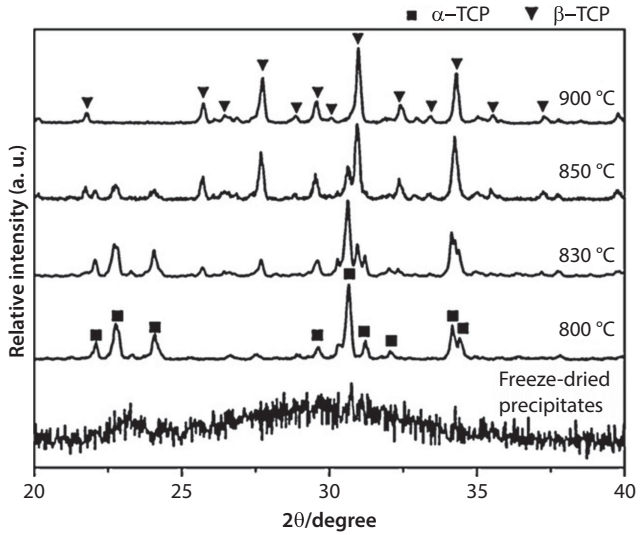

Figure 2.4 XRD patterns of the freeze-dried ACP precipitates and the calcined powders. One can see formation of biphasic formulations with variable α-TCP/β-TCP ratios at temperatures within 830–850 °C. Reprinted from Ref. [71] with permission.

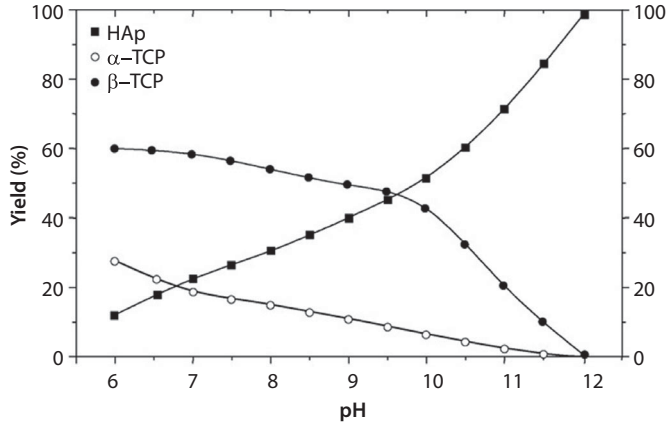

Figure 2.5 Yield of HA, α-TCP, and β-TCP depending on the pH of the starting solution. Reprinted from Ref. [77] with permission.

Furthermore, triphasic formulations might be prepared by sintering of BCPs (HA + β-TCP) at temperatures >1200 °C, when β-TCP is partly transformed into α-TCP [78, 79]; however, such formulations are converted again to biphasic ones (HA + α-TCP) at temperatures ~1400 °C [141]. In another study, a phase transition from α-TCP into β-TCP in three types

of triphasic (HA + α-TCP + β-TCP) formulations was investigated and the experimental results indicated that a sintering temperature for the complete phase transition from intermediately formed α-TCP into β-TCP (thus, triphasic formulations were transformed to BCPs) increased with HA content increasing in the formulation [26]. A rapid and an accurate phase quantification technique of multiphasic $CaPO_4$ bioceramics was developed [74].

In addition, multiphasic $CaPO_4$ might also be prepared by a mechanical mixing (blending) of the desired amounts of the individual $CaPO_4$ powders [19, 23, 28, 49, 78, 119, 173–188], or even their precursors. For example, one can mechanically mix two different types of CDHA powders, such as a CDHA with $x = 0.9$ (almost TCP) and a CDHA with $x = 0.1$ (almost HA), followed by sintering the entire mixture. In this case, the first CDHA will decompose to β-TCP with a small admixture of HA, while the second CDHA will decompose to HA with a small admixture of β-TCP, giving rise to BCP (HA + β-TCP) formation. Similarly, to achieve the same results, powders of HA and CDHA [119], as well as HA and DCPD [181] could be mixed followed by sintering. However, due to inability to get homogenous crystal distributions of the mixed phases, a mechanical mixing of either individual $CaPO_4$ or their precursors is not recommended for production of multiphasic formulations with reproducible ratios of the components. Furthermore, such type of a mechanically mixed BCP bioceramics was found to exhibit both a higher extent of dissolution [49] and an inferior sintering behavior [189] than those prepared by thermal decomposition of a single CDHA phase with the same HA/β-TCP ratio. However, when soaking in simulated body fluid (SBF), the weight gain in mechanically mixed BCP was found to be higher than that in precipitated BCP [173]. Besides, in mechanical mixtures with β-TCP, HA might become unstable at sintering, altering the final HA/β-TCP ratio in sintered BCPs [176]. More to the point, if sintering temperatures exceed ~1200 °C, α-TCP formation becomes plausible and the initial biphasic mixture of HA + β-TCP powders is transformed into triphasic (HA + β-TCP + α-TCP) ones [28, 78, 79, 141, 142]. However, this process appears to be reversible because dwelling of the triphasic formulations at ~900 °C for several hours results in α-TCP → β-TCP conversion, and, thus, transformation of the triphasic formulations into BCP (HA + β-TCP) again [78]. An unusual BCP consisting of poorly crystalline HA (PC-HA) and well crystalline β-TCP was manufactured by blending powders of PC-HA and β-TCP, followed by sintering the blends at 1150 °C for 24 h. The XRD results of the sintered blends revealed diffraction patterns of β-TCP only; however, the authors concluded that "Due to the low crystallinity of PC-HA, only the β-TCP could be detected from XRD for PC-HA/β-TCP at ratios of 70/30, 60/40 and 0/100" [180, p. 24]. Frankly speaking, the results of

that study are rather strange because it is well known that both CDHA and PC-HA are converted into the well crystalline products at sintering. Other types of blending techniques, such as a combination of gel casting with polymer sponge methods [21], have been developed as well.

Concerning multiphasic formulations containing other types of $CaPO_4$ compounds, the following preparation methods have been found. First, one should repeat the aforementioned cases of the self-setting $CaPO_4$ formulations, in which one or several components have been added in an excess from the reaction stoichiometry [82, 83]. Second, one should mention on a possibility to prepare novel types of multiphasic $CaPO_4$ formulations by incomplete thermal decomposition at moderate temperatures of non-stoichiometric $CaPO_4$, such as ACP and CDHA. In this case, ACP- or CDHA-containing formulations become available. For example, a transformation from CDHA (Ca/P = 1.50) to β-TCP was studied by a thermal decomposition [42]. The authors of that study noticed that when the CDHA was calcined at temperatures below 700 °C, it remained unchanged according to the XRD results, but when the CDHA was calcined at temperatures above 740 °C, it was transformed completely into BCP (HA + β-TCP). At intermediate temperatures of 710–730 °C, biphasic mixtures of CDHA + β-TCP were detected [42]. Unfortunately, no properties of the biphasic CDHA + β-TCP formulations were investigated.

Furthermore, biphasic whiskers consisting of OCP and CDHA were prepared by a hydrolysis of β-TCP powders in unstirred 30% H_2O_2 solutions at 90 °C for 48 h in ordinary glass media bottles [190]. Similarly, biphasic formulations of OCP and CDHA were prepared by hydrolysis of DCPD, when DCPD was soaked for 1 week in different biomineralization solutions [191, 192]. In addition, multiphasic formulations were prepared by adding an amount of concentrated NH_4OH solution into a hot (97 °C) and well-mixed solution containing dissolved MCPM, $CaCl_2$ with Ca/P = 1.67 molar ratio and a certain amount of citric acid, which after sintering were transformed into biphasic formulations of β-TCP and calcium pyrophosphate [193, 194]. According to these authors, the same experiments performed at lower temperatures resulted in precipitation of triphasic formulations of DCPA, OCP and CDHA (at 50 °C) or tetraphasic formulations of DCPD, DCPA, OCP, and CDHA (at 30–40 °C) [194]. Biphasic OCP/DCPA whiskers were manufactured as well [195].

More to the point, biphasic DCPD/CDHA formulations might be prepared by a slow hydrolysis of freshly precipitated DCPD crystals in a solution, containing NH_4HCO_3. To prepare such formulations, initially, an acidic (pH = 2.83) aqueous solution of MCPM and $CaCl_2$ (Ca/P ratio = 1.67) was prepared. Afterwards, under continuous stirring, small

portions of a 1 M NH_4HCO_3 solution were added until solution pH = 7.5. This caused DCPD precipitation, followed by its slow transformation to CDHA during aging for 1 and 2 days [196]. In addition, a biphasic OCP/DCPD formulation was prepared by a drop-wise addition of a Na_2HPO_4 solution (0.04 mol/L) into calcium acetate solution (0.04 mol/L), followed by aging for 1 h, filtration and drying at room temperature, which was further converted into ion-substituted CDHA in SBF [197].

To conclude the preparation topic, one should mention that in the presence of dopants, various types of ion-substituted multiphasic $CaPO_4$ formulations are prepared [22, 43, 57–59, 84, 131, 149, 198–228]. Depending on the nature of doping elements, in such formulations they could be present in various phases. For example, in BCPs (HA + β-TCP), F [22, 211], Cl [215], Si [222], and carbonates [220, 224] were found to enter more readily into the HA phase, Zn [199, 200] and Sr [84, 225] appeared to enter into both phases (however, the latest data revealed that increasing of Sr^{2+} addition to CDHA led to a decline in the phase content of β-TCP after sintering [226]), while Na [22, 131, 213], K [214], Mg [43, 131, 202–209], Mn [149, 216–218], and Nb [210] entered preferably into the β-TCP phase [219]. One should stress that in no case these dopants appear to be inert compounds; on the contrary, they always influenced the properties of the multiphasic $CaPO_4$ formulations. For example, addition of MgO was found to suppress a phase transition from β-TCP to α-TCP in BCPs [202].

As the final point, one should also mention that multiphasic formulations of $CaPO_4$ with both other types of calcium phosphates [229, 230] and ion-substituted types of $CaPO_4$, such as $NaCaPO_4$ [231], are also known; however, such formulations are not considered in this review.

2.6 Properties

In general, all major mechanical, physical, and chemical properties of biphasic, triphasic, and multiphasic $CaPO_4$ bioceramics are very similar to those of single-phase bioceramics prepared from the constituents (they are in between of those of the constituent phases and depend on relative amounts of the ingredients) [10, 11], while the major differences (see below) are related to the *in vivo* bioresorption behavior [232, 233]. The most important properties of both individual types of $CaPO_4$ and $CaPO_4$ bioceramics have been reviewed recently [3, 5, 80], where the interested readers are referred to. Therefore, the standard ceramic processing techniques, such as pressing [119, 187], slip casting [61, 234], gel casting [75], tape casting [178], 3D printing [144, 235], and other types of rapid

prototyping techniques [84, 85, 236–238] are also applied to produce three-dimensional objects of various dimensions and shapes from multiphasic $CaPO_4$ formulations. Porous scaffolds can be produced as well [79, 142, 144, 145, 181–185, 238–245]. In addition, BCP (HA + β-TCP) whiskers [124], spherical granules or particles [77, 125, 141, 146, 246, 247], as well as functionally graded materials (Figure 2.6) [119, 187] have been fabricated. Similarly to single-phase $CaPO_4$ bioceramics, prolonged milling of BCP results in its partial amorphization [248]. In addition, the surface of multiphasic $CaPO_4$ formulations also might be either positively or negatively polarized, which influences their interaction with proteins and cells [249], adsorption and release of bovine serum albumin [250], as well as the early stage of osteoblast-cell adhesion and proliferation [251].

Similarly to other types of $CaPO_4$ bioceramics, bone-like apatite is easily precipitated on the surface of multiphasic $CaPO_4$ from simulating solutions [252–256]. The same processes also occur *in vivo*, which results in an ability to form direct bone bonding with host bones after implantation, giving rise to a strong interface [10, 11]. Furthermore, the surface of multiphasic $CaPO_4$ is able to adsorb cells [25, 43, 178, 179, 237, 257–263], proteins [264–267], and other bioorganic molecules [267, 268]. A correlation between protein adsorption and zeta potentials on the surface was established [265]. Therefore, multiphasic $CaPO_4$ bioceramics might be used as carrier systems for bone tissue-engineering purposes. Furthermore, such bioceramics might possess both osteopromotive [269] and osteoinductive [270–281] properties, which after implantation is replaced by newly forming bones [282].

Concerning attempts to distinguish the individual phases and their distribution in multiphasic $CaPO_4$, to date little attention has been paid to this subject. The problem is that HA and two types of TCPs have either similar or almost similar chemical compositions, which strongly complicates their differentiation from each other in such formulations. Nevertheless, for BCPs prepared by a mechanical mixing of HA and β-TCP powders, both

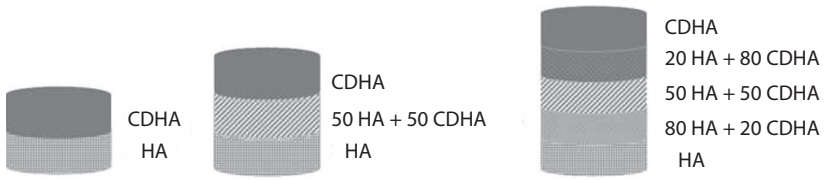

Figure 2.6 A schematic picture of uniaxially pressed $CaPO_4$ samples consisting of symmetric layers with different compositions. Sintering of such formulations will result in functionally graded multiphasic bioceramics. Reprinted from Ref. [119] with permission.

phases were differentiated by a cathodoluminescence microscopy detector attached to a scanning electron microscope [283].

2.7 Biomedical Applications

As mentioned above, the history of biomedical applications of BCPs started in 1986 [39]. Presently, although triphasic formulations are available, to the best of my knowledge, only biphasic formulations are produced commercially. The commercial BCP products of different or similar HA/β-TCP ratios are manufactured and sold in many parts of the world as bone substitute bioceramics for orthopedic, maxillofacial, and dental applications under various trade marks (Table 2.2). Similarly to other types of $CaPO_4$ bioceramics [3], the commercial BCP formulations are available in blocks, particulates (granules) and custom-designed shapes such as wedges for tibial opening osteotomy, cones for spine and knee, and inserts for vertebral cage fusion. Porous biphasic [21, 48, 49, 51, 73, 75, 85, 134, 142, 144, 145, 174, 179, 181, 182, 185, 220, 236, 238–246, 284–300] and triphasic [73, 75, 76, 79] $CaPO_4$ bioceramics have been manufactured as well. Besides, a BCP granules concept, based on three types of granulometry (submicron, round microporous 80–200 μm, and macro microporous 0.5–1 mm particles) and hydrated with water leading to formation of a putty filler for bone repair, has been applied to the development of a new generation of injectable and moldable bone substitutes [50, 51, 55, 301]. In addition, BCPs (powder or granules) might be also combined with various polymers, both natural (*e.g.*, fibrin sealant) [302–308] and synthetic (*e.g.*, hydroxylpropylmethylcellulose, poly(ε-caprolactone), polyvinyl alcohol) [34, 50, 51, 55, 279, 301, 309–316] for the development of injectable bone substitutes or $CaPO_4$ cements to improve macroporosity and greater osteoconduction. More to the point, BCP formulations might be an important constituent of various biocomposites and hybrid biomaterials [228, 298, 317–356], as well as be applied as both coatings [31, 32, 44, 88, 105, 356–363] and additives to $CaPO_4$-based cements [10, 11, 364–366]. In addition, BTCP could be used as the main component of the self-setting $CaPO_4$-based formulations [69, 72]. To improve the properties of BCP bioceramics, such as the interfacial compatibility with other components of biocomposites or biocompatibility, their surface might be modified by various chemicals [367, 368], coatings [244, 369–374], or physical treatments [249–251, 375].

Numerous studies have already revealed a superiority of the implanted BCP (HA + β-TCP) bioceramics over that of pure HA [376–380], pure β-TCP [179, 377, 381, 382], xenografts [383, 384], and autologous bone

Table 2.2 Trademarks of the commercially produced biphasic, triphasic, and multiphasic calcium orthophosphates [3].

Calcium orthophosphate	Trade name and producer (when available)
BCP (HA + β-TCP)	4Bone BCH (MIS Implants, Israel)
	AdboneBCP (Medbone Medical Devices, Portugal)
	Antartik (MedicalBiomat, France)
	Artosal (aap Implantate, Germany)
	BCP BiCalPhos (Medtronic, MN, USA)
	BioGraft (IFGL BIO CERAMICS, India)
	Biosel (Depuy Bioland, France)
	BonaGraft (Biotech One, Taiwan)
	BoneCeramic (Straumann, Switzerland)
	BoneSave (Stryker Orthopaedics, NJ, USA)
	BoneSigma BCP (SigmaGraft, CA, USA)
	BONITmatrix (DOT, Germany)
	Calcicoat (Zimmer, IN, USA)
	Calciresorb (Ceraver, France)
	Calc-i-oss crystal (Degradable Solutions, Switzerland)
	CellCeram (Scaffdex, Finland)
	Ceraform (Teknimed, France)
	Ceratite (NGK Spark Plug, Japan)
	Cross.Bone (Biotech Dental, France)
	CuriOs (Progentix Orthobiology BV, Netherlands)
	Eurocer (FH Orthopedics, France)
	GENESIS-BCP (DIO Corporation, Korea)
	GenPhos HA TCP (Baumer, Brazil)
	Graftys BCP (Graftys, France)
	Hatric (Arthrex, Naples, FL, USA)

Table 2.2 Cont.

Calcium orthophosphate	Trade name and producer (when available)
	Indost (Polystom, Russia)
	Kainos (Signus, Germany)
	MasterGraft (Medtronic Sofamor Danek, TN, USA)
	MBCP (Biomatlante, France)
	NT-BCP (OssGen, Korea)
	OrthoCer HA TCP (Baumer, Brazil)
	OpteMX (Exactech, FL, USA)
	OSPROLIFE HA-βTCP (Eurocoating, Italy)
	OsSatura BCP (Integra Orthobiologics, CA, USA)
	Ossceram nano (bredent medical, Germany)
	OsteoFlux (VIVOS-Dental, Switzerland)
	OSTEON (GENOSS, Korea)
	Osteosynt (Einco, Brazil)
	Ostilit (Stryker Orthopaedics, NJ, USA)
	ReproBone (Ceramisys, UK)
	SBS (Expanscience, France)
	Scaffdex (Scaffdex Oy, Finland)
	SigmaOs BCP (SigmaGraft, CA, USA)
	SinboneHT (Purzer Pharmaceutical, Taiwan)
	Synergy (unknown producer)
	TCH (Kasios, France)
	Triosite (Zimmer, IN, USA)
	Tribone (Stryker, Europe)
	Without trade name (Cam Bioceramics, Netherlands)
	Without trade name (CaP Biomaterials, WI, USA)
	Without trade name (Himed, NY, USA)

(*Continued*)

Table 2.2 Cont.

Calcium orthophosphate	Trade name and producer (when available)
	Without trade name (MedicalGroup, France)
	Without trade name (SigmaGraft, CA, USA)
	Without trade name (Xpand Biotechnology, Netherlands)
BCP (HA + α-TCP)	Skelite (Millennium Biologix, ON, Canada)
BCP (HA + β-TCP)/ collagen	Allograft (Zimmer, IN, USA)
	Collagraft (Zimmer, IN, USA)
	Cross.Bone Matrix (Biotech Dental, France)
	MasterGraft (Medtronic Sofamor Danek, TN, USA)
	without trade name (MedicalGroup, France)
BCP (HA + β-TCP)/ polymer	In'Oss (Biomatlante, France)
	Hydros (Biomatlante, France)
BCP (HA + TTCP)	OSPROLIFE HA-TTCP (Eurocoating, Italy)
BCP/fibrin	TricOS (Baxter BioScience, France)
BCP/silicon	FlexHA (Xomed, FL, USA)
FA + BCP (HA + β-TCP)	FtAP (Polystom, Russia)

grafts [385, 386], but not pure α-TCP cement [387] on bone formation. However, a superiority of the implanted BCP was not always the case [388–392]. Namely, the differences in vital bone formation appeared to be not significant ($n = 9$ patients, paired t-test) between bilateral sinuses treated with the BCP and those treated with an anorganic bovine bone matrix (Bio-Oss®) [388]. Similar conclusion was also made for a comparison between BCP and bioglass [389], between BCP and β-TCP [390], as well as between BCP and deproteinised bovine bone mineral [391]. However, the latter could also depend on the implantation time. For example, the following histologic and histomorphometric results have been obtained after implantation of HA, BCP, β-TCP samples, and autogenous bone chips at healing periods of 2, 4, 8, and 24 weeks: "2 weeks: more bone formation in defects filled with autograft than with the three CaP materials ($P < 0.05$).

4 weeks: bone formation differed significantly ($P < 0.05$) between all four materials (autograft > TCP > HA/TCP > HA). 8 weeks: more bone formation in defects with autograft and TCP than with HA/TCP ($P < 0.05$), and HA/TCP had more bone formation than HA ($P < 0.05$). 24 weeks: no difference in bone formation between the groups" [393, abstract]. Concerning attempts to find the optimum balance of the two phases in BCPs, the results obtained by various researchers appear to be different. For example, among BCPs having different HA/β-TCP ratios, the one containing 20% of HA and 80% of β-TCP was found to be the best [174, 377, 384]. Rather, similar results for the optimum ratio of 15% of HA and 85% of β-TCP [394], 25% of HA and 75% of β-TCP [178, 233], and 30% of HA and 70% of β-TCP [359] were obtained in other studies. However, in still other studies, formulations containing 5% of HA and 95% of β-TCP [395], 50% of HA and 50% of β-TCP [177, 385], and 60% of HA and 40% of β-TCP [396] or 100% HA [124, 397] were found to encourage cell proliferation to the maximum extent. Furthermore, improved cell–material interactions were observed as the percentage of HA content in BCPs was increased [251]. On the other hand, a study is available, in which the authors found that higher β-TCP ratios had beneficial effects during the early phase of cell proliferation and differentiation, whereas higher HA ratios performed better in the later stages [398]. Thus, the relationship between the cellular activity and the percentage of β-TCP in BCPs appears to be complicated. Presumably, this inconsistency might be explained by the presence of various admixtures in BCP samples, used by various researchers, as well as unmentioned differences in preparation, crystallinity, porosity, and surface topography of the samples. For example, the particle sizes (212–300, 106–212, 45–106, and <45 μm) of the implanted BCP was found to influence its osteoinductivity; the effect was explained by different degree of macroporosity, which influenced the body fluid infiltration, cell/tissue ingrowth, and angiogenesis [399]. To make things even more complicated, one must stress that an inflammatory response occasionally was initiated by implanted BCPs [400–403].

Potential biomedical applications of multiphasic $CaPO_4$ are various and resemble those for other types of $CaPO_4$ bioceramics [3]. However, the majority of the *in vivo* applications are still limited to the experimental trials performed with BCPs in artificially created bone defects and/or cavities of animals. Namely, they were successfully tested in orthopedic and trauma surgery [404–410], in periapical surgery [411], to repair diaphyseal [412], femur [413] and calvarial [414, 415] bone defects, nasal septum [416, 417], vertebral laminae [418], acetabulum [419], femoral [123, 302, 420], mandibular [384, 421], dental bony [422] and metaphyseal [423] defects, middle

ear cavities [424], tibial valgisation osteotomy [425], cervical spondylosis [426], malar [427] and sinus [388, 428–432] augmentations, orbital reconstruction [345], as well as for other purposes [269, 433–439]. For example, in critical-size bone defects created in rabbit femora, an application of BCP (65% HA + 35% β-TCP) alone was found to lead to major bone mass gain, corresponding to a minimum of 4-fold the volume of applied bioceramics [408]. In a recent study, 66 patients received BCP as bone substitutes in orthopedic surgeries. Most of the patients who presented cavitary defects or bone losses due to prosthesis placement or revision, osteotomies or arthrodesis showed good results and some of them excellent results, while patients with segmental defects equal or larger than 3 cm in length were classified as moderate results [409]. An example of a bone defect reconstruction with BCP is shown in Figure 2.7. A similar positive effect on bone fracture healing was found when implanted BCP grafts were irradiated at every other day during two weeks with infrared laser light [440]. These effects might be used for tissue-engineering purposes. Besides, a biological performance of BCP bioceramics could be improved by cold plasma [441]. Various biocomposites and hybrid biomaterials based on multiphasic $CaPO_4$ are widely used in medicine as well [279, 442–445].

To extend the healing properties and for tissue-engineering applications, multiphasic $CaPO_4$ formulations might be loaded by drugs [125, 353, 446–450], proteins [54, 235, 295, 313, 343, 352, 424, 451–454],

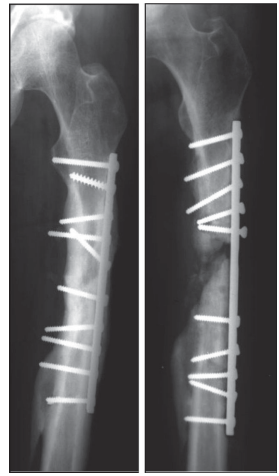

Figure 2.7 Reconstruction of a femoral bone defect with BCP. X-ray images of a femur before (a) and after (b) reconstruction with the BCP and stabilized with internal fixation system, after trauma. Reprinted from Ref. [409] with permission.

growth factors [318, 350, 352, 455], peptides [456], blood or plasma clots [457–459], bone marrow [285, 460], and other biomedically important compounds [302–307, 461–463], as well as seeded by cells [43, 235, 374, 464–470]. Furthermore, additional application of a hyperbaric oxygen therapy was found to result in a large reduction in fibrous tissue and an increase in its replacement with marrow [471]. Additional details on the biomedical applications of BCP (HA + β-TCP) are well described in the literature [10, 11].

2.8 Conclusions

In general, the multiphasic concept for $CaPO_4$ bioceramics has the advantage of a controlled bioactivity by manipulation of the more soluble/less soluble ratio owing to the preferential dissolution of the more soluble $CaPO_4$ components. However, biphasic and triphasic formulations are currently available only, and in the majority cases, they contain HA and β-TCP. They are produced by various techniques, mainly by thermal decomposition of CDHA and ACP. The available formulations are sparingly soluble and, after being implanted, they are gradually dissolved in the body releasing calcium and orthophosphate ions into the biological medium and, thus, seeding new bone formation. Presumably, more complicated formulations including other types of calcium phosphates (Figure 2.2) will be manufactured in future. Hopefully, some of them will be suitable for biomedical purposes.

Similarly to other types of bioactive materials, the implants manufactured from multiphasic $CaPO_4$ have the ability to form a layer of carbonate apatite on their surface by partial dissolution followed by precipitation [472], which provides a chemical bonding between the implants and newly forming bones. Furthermore, multiphasic $CaPO_4$ appears to be osteoconductive, but they can be made osteoinductive by appropriate geometry, specifically, macroporosity, and microporosity [270, 271, 284]. Namely, the proper associating of an appropriate microporosity (pore diameter <10 μm) and an interconnecting macroporosity (pore diameter >100 μm) with the BCP (HA + β-TCP) chemical concept has already resulted in high osteogenicity and osteoinductive properties. Presently, such BCP bioceramics is recommended for use as an alternative or additive to autogenous bone for orthopedic and dental applications [10, 11]. Furthermore, such formulations can also be used as scaffolds [473] for tissue engineering using stem cells, delivery system for drugs, antibiotics and hormones, as well as carriers for growth factors.

References

1. Lowenstam, H.A., Weiner, S. *On biomineralization*. Oxford University Press, New York, USA, 324, 1989.
2. Ruys, A.J. (Ed.) *Biomimetic biomaterials: structure and applications*. Woodhead Publishing, Cambridge, UK, 344, 2013.
3. Dorozhkin, S.V. Calcium orthophosphate bioceramics. *Ceram. Int.* 41, 13913–13966, 2015.
4. Dorozhkin, S.V. Calcium orthophosphate deposits: preparation, properties and biomedical applications. *Mater. Sci. Eng. C* 55, 272–326, 2015.
5. Dorozhkin, S.V. Calcium orthophosphates: occurrence, properties, biomineralization, pathological calcification and biomimetic applications. *Biomatter* 1, 121–164, 2011.
6. Anuta, D.A., Richardson, D. Biphasic hydroxyapatite/beta-tricalcium phosphate granules bound in polymerized methyl methacrylate: bone substitute studies. *Transactions of the Annual Meeting of the Society for Biomaterials in conjunction with the Interna* 8, 62, 1985.
7. Moore, D.C., Chapman, M.W., Manske, D.J. Evaluation of a new biphasic calcium phosphate ceramic for use in grafting long bone diaphyseal defects. *Transactions of the Annual Meeting of the Society for Biomaterials in conjunction with the Interna* 8, 160, 1985.
8. Dorozhkina, E.I., Dorozhkin, S.V. Mechanism of the solid-state transformation of a calcium-deficient hydroxyapatite (CDHA) into biphasic calcium phosphate (BCP) at elevated temperatures. *Chem. Mater.* 14, 4267–4272, 2002.
9. Dorozhkin, S.V. Mechanism of solid-state conversion of non-stoichiometric hydroxyapatite to diphase calcium phosphate. *Russ. Chem. Bull. (Int. Ed.)* 52, 2369–2375, 2003.
10. Daculsi, G., Jegoux, F., Layrolle, P. The micro macroporous biphasic calcium phosphate concept for bone reconstruction and tissue engineering. In: Basu, B., Katti, D.S., Kumar, A. Eds. *Advanced biomaterials: fundamentals processing and applications*. Wiley-American Ceramic Society; pp. 101–142, 2009.
11. Daculsi, G., Baroth, S., LeGeros, R.Z. 20 years of biphasic calcium phosphate bioceramics development and applications. In: Narayan, R., Colombo, P., Singh, D., Salem, J. Eds. *Advances in bioceramics and porous ceramics II*. Wiley-American Ceramic Society; pp. 45–58, 2010.
12. Daculsi, G. Biphasic calcium phosphate concept applied to artificial bone, implant coating and injectable bone substitute. *Biomaterials* 19, 1473–1478, 1998.
13. Lobo, S.E., Arinzeh, T.L. Biphasic calcium phosphate ceramics for bone regeneration and tissue engineering applications. *Materials* 3, 815–826, 2010.

14. Daculsi, G., LeGeros, R.Z., Nery, E., Lynch, K., Kerebel, B. Transformation of biphasic calcium phosphate ceramics *in vivo*: ultrastructural and physicochemical characterization. *J. Biomed. Mater. Res.* 23, 883–894, 1989.
15. Soueidan, A., Gan, O.I., Bouler, J.M., Gouin, F., Daculsi, G. Biodegradation of synthetic biphasic calcium phosphate and biological calcified substratum by cells of hemopoietic origin. *Cells Mater.* 5, 31–44, 1995.
16. Benahmed, M., Bouler, J.M., Heymann, D., Gan, O., Daculsi, G. Biodegradation of synthetic biphasic calcium phosphate by human monocytes *in vitro*: a morphological study. *Biomaterials* 17, 2173–2178, 1996.
17. http://en.wikipedia.org/wiki/Phase_(matter) – accessed in October 2015.
18. Kivrak N., Taş, A.C. Synthesis of calcium hydroxyapatite–tricalcium phosphate (HA–TCP) composite bioceramic powders and their sintering behavior. *J. Am. Ceram. Soc.* 81, 2245–2252, 1998.
19. Yasuda, H.Y., Mahara, S., Nishiyama, T., Umakoshi, Y. Preparation of hydroxyapatite/*α*-tricalcium phosphate composites by colloidal process. *Sci. Tech. Adv. Mater.* 3, 29–33, 2002.
20. Kwon, S.H., Jun, Y.K., Hong, S.H., Kim, H.E. Synthesis and dissolution behavior of *β*-TCP and HA/*β*-TCP composite powders. *J. Eur. Ceram. Soc.* 23, 1039–1045, 2003.
21. Ramay, H.R.R., Zhang, M. Biphasic calcium phosphate nanocomposite porous scaffolds for load-bearing bone tissue engineering. *Biomaterials* 25, 5171–5180, 2004.
22. Kannan, S., Ferreira, J.M.F. Synthesis and thermal stability HAP and *β*-TCP composites with co-substituted sodium, magnesium and fluorine. *Chem. Mater.* 18, 198–203, 2006.
23. Ruseska, G., Fidancevska, E., Bossert, J. Mechanical and thermal-expansion characteristics of $Ca_{10}(PO_4)_6(OH)_2$-$Ca_3(PO_4)_2$ composites. *Sci. Sintering* 38, 245–253, 2006.
24. Li, Y., Li, D., Weng, W. *In vitro* dissolution behavior of biphasic tricalcium phosphate composite powders composed of *α*-tricalcium phosphate and *β*-tricalcium phosphate. *Key Eng. Mater.* 2008, 368–372, 1206–1208.
25. Guha, A.K., Singh, S., Kumaresan, R., Nayar, S., Sinha, A. Mesenchymal cell response to nanosized biphasic calcium phosphate composites. *Colloids Surf. B* 73, 146–151, 2009.
26. Huang, Y., Huang, W., Sun, L., Wang, Q., He, A., Han, C.C. Phase transition from *α*-TCP into *β*-TCP in TCP/HA composites. *Int. J. Appl. Ceram. Technol.* 7, 184–188, 2010.
27. Mehdikhani, B., Mirhadi, B. Densification and hardness behaviour of nanocrystalline hydroxyapatite/*β*-tricalcium phosphate composite powders. *J. Biomim. Biomater. Tissue Eng.* 14, 81–91, 2012.
28. Izawa, T., Kobayashi, S., Murakoshi, T. Pulse electric current sintering of hydroxyapatite/*β*-tricalcium phosphate composites. *Adv. Composite Mater.* 2015, (early view).

29. Viswanath, B., Ravishankar, N. Biphasic composite of tricalcium phosphate reinforced with hydroxyapatite whiskers. *Mater. Res. Soc. Symp. Proc.* 898, 80–85, 2005.
30. Liu, T., Yang, D.A., Di, L. Preparation of β-TCP/HAP composite bioceramics. *Key Eng. Mater.* 336–338, 1642–1645, 2007.
31. Cheng, K., Zhang, S., Weng, W.J. Sol-gel prepared β-TCP/FHA biphasic coatings. *Thin Solid Films* 515, 135–140, 2006.
32. Cheng, K., Zhang, S., Weng, W., Khor, K.A., Miao, S., Wang, Y. The adhesion strength and residual stress of colloidal-sol gel derived β-tricalcium-phosphate/fluoridated-hydroxyapatite biphasic coatings. *Thin Solid Films* 516, 3251–3255, 2008.
33. Daculsi, G., Chappard, D., Aguado, E., Legeay, G., Layrolle, P., Weiss, P. Multiphasic biomaterials: a concept for bone substitutes developed in the "Pays de la Loire". *Key Eng. Mater.* 361–363, -17-1, 2008.
34. Daculsi, G., Uzel, A.P., Weiss, P., Goyenvalle, E., Aguado, E. Developments in injectable multiphasic biomaterials. The performance of microporous biphasic calcium phosphate granules and hydrogels. *J. Mater. Sci. Mater. Med.* 21, 855–861, 2010.
35. Bernstein, J. *Polymorphism in molecular crystals*. Oxford University Press, New York, USA. 424 p, 2002.
36. Bernstein, J. *Polymorphism – a perspective*. *Cryst. Growth Des*. 11, 632–650, 2011.
37. Kamitakahara, M., Ohtsuki, C., Miyazaki, T. Behavior of ceramic biomaterials derived from tricalcium phosphate in physiological condition. *J. Biomater. Appl.* 23, 197–212, 2008.
38. Ma, G., Liu, X.Y. Hydroxyapatite: hexagonal or monoclinic? *Cryst. Growth Des.* 9, 2991–2994, 2009.
39. Ellinger, R.F., Nery, E.B., Lynch, K.L. Histological assessment of periodontal osseous defects following implantation of hydroxyapatite and biphasic calcium phosphate ceramics: a case report. *Int. J. Periodont. Restor. Dent.* 3, 22–33, 1986.
40. Nery, E.B., Lynch, K.L., Hirthe, W.M., Mueller, K.H. Bioceramic implants in surgically produced infrabony defects. *J. Periodontol.* 46, 328–347, 1975.
41. LeGeros, R.Z. Calcium phosphate materials in restorative dentistry: a review. *Adv. Dent. Res.* 2, 164–183, 1988.
42. Gibson, I.R., Rehman, I., Best, S.M., Bonfield, W. Characterization of the transformation from calcium-deficient apatite to β-tricalcium phosphate. *J. Mater. Sci. Mater. Med.* 11, 799–804, 2000.
43. Singh, S.S., Roy, A., Lee, B.E., Banerjee, I., Kumta, P.N. MC3T3-E1 proliferation and differentiation on biphasic mixtures of Mg substituted β-tricalcium phosphate and amorphous calcium phosphate. *Mater. Sci. Eng. C* 45, 589–598, 2015.
44. Yang, X., Lu, X., Zhang, Q., Zhang, X., Gu, Z., Chen, J. BCP coatings on pure titanium plates by CD method. *Mater. Sci. Eng. C* 27, 781–786, 2007.

45. Molloy, E.S., Morgan, M.P., McDonnell, B., O'Byrne, J., McCarthy, G.M. BCP crystals increase prostacyclin production and upregulate the prostacyclin receptor in OA synovial fibroblasts: potential effects on mPGES1 and MMP-13. *Osteoarthr. Cartilage* 15, 414–420, 2007.
46. Rosenthal, A.K., Ryan, L.M. Nonpharmacologic and pharmacologic management of CPP crystal arthritis and BCP arthropathy and periarticular syndromes. *Rheum. Dis. Clin. N. Am.* 40, 343–356, 2014.
47. Lecomte, A., Gautier, H., Bouler, J.M., Gouyette, A., Pegon, Y., Daculsi, G., Merle, C. Biphasic calcium phosphate: a comparative study of interconnected porosity in two ceramics. *J. Biomed. Mater. Res. B Appl. Biomater.* 84B, 1–6, 2008.
48. Tancret, F., Bouler, J.M., Chamousset, J., Minois, L.M. Modelling the mechanical properties of microporous and macroporous biphasic calcium phosphate bioceramics. *J. Eur. Ceram. Soc.* 26, 3647–3656, 2006.
49. Bouler, J.M., Trecant, M., Delecrin, J., Royer, J., Passuti, N., Daculsi, G. Macroporous biphasic calcium phosphate ceramics: influence of five synthesis parameters on compressive strength. *J. Biomed. Mater. Res.* 32, 603–609, 1996.
50. Daculsi, G., Weiss, P., Bouler, J.M., Gauthier, O., Millot, F., Aguado, E. Biphasic calcium phosphate/hydrosoluble polymer composites: a new concept for bone and dental substitution biomaterials. *Bone* 25, Suppl. 2, 59 S–61 S, 1999.
51. Gauthier, O., Goyenvalle, E., Bouler, J.M., Guicheux, J., Pilet, P., Weiss, P., Daculsi, G. Macroporous biphasic calcium phosphate ceramics versus injectable bone substitute: a comparative study 3 and 8 weeks after implantation in rabbit bone. *J. Mater. Sci. Mater. Med.* 12, 385–390, 2001.
52. LeGeros, R.Z., Lin, S., Rohanizadeh, R., Mijares, D., LeGeros, J.P. Biphasic calcium phosphate bioceramics: preparation, properties and applications. *J. Mater. Sci. Mater. Med.* 14, 201–209, 2003.
53. Daculsi, G., Laboux, O., Malard, O., Weiss, P. Current state of the art of biphasic calcium phosphate bioceramics. *J. Mater. Sci. Mater. Med.* 14, 195–200, 2003.
54. Alam, I., Asahina, I., Ohmamiuda, K., Enomoto, S. Comparative study of biphasic calcium phosphate ceramics impregnated with rhBMP-2 as bone substitutes. *J. Biomed. Mater. Res.* 54, 129–138, 2001.
55. Daculsi, G. Biphasic calcium phosphate granules concept for injectable and mouldable bone substitute. *Adv. Sci. Technol.* 49, 9–13, 2006.
56. LeGeros, R.Z. Variability of HAP/β-TCP ratios in sintered apatites. *J. Dent. Res.* 65, 292, 1986.
57. Langstaff, S.D., Sayer, M., Smith, T.J.N., Pugh, S.M., Hesp, S.A.M., Thompson, W.T. Resorbable bioceramics based on stabilized calcium phosphates. Part I: Rational design, sample preparation and material characterization. *Biomaterials* 20, 1727–1741, 1999.
58. Langstaff, S.D., Sayer, M., Smith, T.J.N., Pugh, S.M. Resorbable bioceramics based on stabilized calcium phosphates. Part II: Evaluation of biological response. *Biomaterials* 22, 135–150, 2001.

59. Reid, J.W., Pietak, A.M., Sayer, M., Dunfield, D., Smith, T.J.N. Phase formation and evolution in the silicon substituted tricalcium phosphate/apatite system. *Biomaterials* 26, 2887–2897, 2005.
60. Pan, L., Li, Y., Weng, W., Cheng, K., Song, C., Du, P., Zhao, G., Shen, G., Wang, J., Han, G. Preparation of submicron biphasic α-TCP/HA powders. *Key Eng. Mater.* 309–311, 219–222, 2006.
61. Kui, C. Slip casting derived α-TCP/HA biphasic ceramics. *Key Eng. Mater.* 330–332, 51–54, 2007.
62. Sanchez-Sálcedo, S., Arcos, D., Vallet-Regí, M. Upgrading calcium phosphate scaffolds for tissue engineering applications. *Key Eng. Mater.* 377, 19–42, 2008.
63. Li, Y., Kong, F., Weng, W. Preparation and characterization of novel biphasic calcium phosphate powders (α-TCP/HA) derived from carbonated amorphous calcium phosphates. *J. Biomed. Mater. Res. B Appl. Biomater.* 89B, 508–517, 2009.
64. Chu, K.T., Ou, S.F., Chen, S.Y., Chiou, S.Y., Chou, H.H., Ou, K.L. Research of phase transformation induced biodegradable properties on hydroxyapatite and tricalcium phosphate based bioceramic. *Ceram. Int.* 39, 1455–1462, 2013.
65. Chan, Y.H., Chang, Y.S., Shen, Y.D., Yang, T.S., Ou, S.F., Hsu, Y.J., Huang, M.S., Ou, K.L. Comparative *in vitro* osteoinductivity study of HA and α-TCP/HA bicalcium phosphate. *Int. J. Appl. Ceram. Technol.* 12, 192–198, 2015.
66. Oishi, M., Ohtsuki, C., Kitamura, M., Kamitakahara, M., Ogata, S., Miyazaki, T., Tanihara, M. Fabrication and chemical durability of porous bodies consisting of biphasic tricalcium phosphates. *Phosphorus Res. Bull.* 17, 95–100, 2004.
67. Kamitakahara, M., Ohtsuki, C., Oishi, M., Ogata, S., Miyazaki, T., Tanihara, M. Preparation of porous biphasic tricalcium phosphate and its *in vivo* behavior. *Key Eng. Mater.* 284–286, 281–284, 2005.
68. Wang, R., Weng, W., Deng, X., Cheng, K., Liu, X., Du, P., Shen, G., Han, G. Dissolution behavior of submicron biphasic tricalcium phosphate powders. *Key Eng. Mater.* 309–311, 223–226, 2006.
69. Jian, P., Jiemo, T., Limin, D., Chen, W., Qingfeng, Z. Self-setting biphase porous calcium phosphate cement. *Key Eng. Mater.* 336–338, 1615–1617, 2007.
70. Li, Y., Weng, W., Tam, K.C. Novel highly biodegradable biphasic tricalcium phosphates composed of α-tricalcium phosphate and β-tricalcium phosphate. *Acta Biomater.* 3, 251–254, 2007.
71. Zou, C., Cheng K., Weng, W., Song, C., Du, P., Shen, G., Han, G. Characterization and dissolution–reprecipitation behavior of biphasic tricalcium phosphate powders. *J. Alloy Compd.* 509, 6852–6858, 2011.
72. Sariibrahimoglu, K., Wolke, J.G.C., Leeuwenburgh, S.C.G., Yubao, L., Jansen, J.A. Injectable biphasic calcium phosphate cements as a potential bone substitute. *J. Biomed. Mater. Res. B Appl. Biomater.* 102B, 415–422, 2014.
73. Albuquerque, J.S.V., Nogueira, R.E.F.Q., Pinheiro da Silva, T.D., Lima, D.O., Prado da Silva, M.H. Porous triphasic calcium phosphate bioceramics. *Key Eng. Mater.* 254–256, 1021–1024, 2004.

74. Reid, J.W., Hendry, J.A. Rapid, accurate phase quantification of multiphase calcium phosphate materials using Rietveld refinement. *J. Appl. Crystallogr.* 39, 536–543, 2006.
75. Mendonça, F., Louro, L.H.L., de Campos, J.B., da Silva, M.H.P. Porous biphasic and triphasic bioceramics scaffolds produced by gelcasting. *Key Eng. Mater.* 361–363, 27–30, 2008.
76. Vani, R., Girija, E.K., Elayaraja, K., Prakash Parthiban, S., Kesavamoorthy, R., Kalkura, S.N. Hydrothermal synthesis of porous triphasic hydroxyapatite/(α and β) tricalcium phosphate. *J. Mater. Sci. Mater. Med.* 20, S43–S48, 2009.
77. Lee, B.T., Youn, M.H., Paul, R.K., Lee, K.H., Song, H.Y. *In situ* synthesis of spherical BCP nanopowders by microwave assisted process. *Mater. Chem. Phys.* 104, 249–253, 2007.
78. Brown, O., McAfee, M., Clarke, S., Buchanan, F. Sintering of biphasic calcium phosphates. *J. Mater. Sci. Mater. Med.* 21, 2271–2279, 2010.
79. Ahn, M.K., Moon, Y.W., Koh, Y.H., Kim, H.E. Production of highly porous triphasic calcium phosphate scaffolds with excellent *in vitro* bioactivity using vacuum-assisted foaming of ceramic suspension (VFC) technique. *Ceram. Int.* 39, 5879–5885, 2013.
80. Dorozhkin, S.V. Self-setting calcium orthophosphate formulations. *J. Funct. Biomater*. 4, 209–311, 2013.
81. Kohri, M., Miki, K., Waite, D.E., Nakajima, H., Okabe, T. *In vitro* stability of biphasic calcium phosphate ceramics. *Biomaterials* 14, 299–304, 1993.
82. Ko, C.L., Chen, J.C., Hung, C.C., Wang, J.C., Tien, Y.C., Chen, W.C. Biphasic products of dicalcium phosphate-rich cement with injectability and nondispersibility. *Mater. Sci. Eng. C* 39, 40–46, 2014.
83. Ko, C.L., Chen, J.C., Tien, Y.C., Hung, C.C., Wang, J.C., Chen, W.C. Osteoregenerative capacities of dicalcium phosphate-rich calcium phosphate bone cement. *J. Biomed. Mater. Res. A* 103, 203–210, 2015.
84. Guo, D., Xu, K., Liu, Y. Physicochemical properties and cytotoxicities of Sr-containing biphasic calcium phosphate bone scaffolds. *J. Mater. Sci. Mater. Med.* 21, 1927–1936, 2010.
85. Guo, D., Xu, K., Han, Y. The *in situ* synthesis of biphasic calcium phosphate scaffolds with controllable compositions, structures, and adjustable properties. *J. Biomed. Mater. Res. A* 88A, 43–52, 2009.
86. Stulajterova, R., Medvecky, L., Giretova, M., Sopcak, T. Structural and phase characterization of bioceramics prepared from tetracalcium phosphate–monetite cement and *in vitro* osteoblast response. *J. Mater. Sci. Mater. Med.* 26, article 183, 2015.
87. Gross, K.A., Bhadang, K.A. Sintered hydroxyfluorapatites. Part III: Sintering and resultant mechanical properties of sintered blends of hydroxyapatite and fluorapatite. *Biomaterials* 25, 1395–1405, 2004.
88. Bhadang, K.A., Gross, K.A. Influence of fluorapatite on the properties of thermally sprayed hydroxyapatite coatings. *Biomaterials* 25, 4935–4945, 2004.

89. Barinov, S.M., Shvorneva, L.I., Ferro, D., Fadeeva, I.V., Tumanov, S.V. Solid solution formation at the sintering of hydroxyapatite-fluorapatite ceramics. *Sci. Technol. Adv. Mater.* 5, 537–541, 2004.
90. Bhadang, K.A., Gross, K.A. Mechanical property development in isothermally sintered mechanical blends of hydroxyapatite and fluorapatite. *J. Aust. Ceram. Soc.* 41, 56–67, 2005.
91. Tredwin, C.J., Young, A.M., Abou Neel, E.A., Georgiou, G., Knowles, J.C. Hydroxyapatite, fluor-hydroxyapatite and fluorapatite produced via the sol-gel method: Dissolution behaviour and biological properties after crystallization. *J. Mater. Sci. Mater. Med.* 25, 47–53, 2014.
92. van Rees, H.B., Mengeot, M., Kostiner, E. Monoclinic-hexagonal transition in hydroxyapatite and deuterohydroxyapatite single crystals. *Mater. Res. Bull.* 8, 1307–1309, 1973.
93. Takahashi, H., Yashima, M., Kakihana, M., Yoshimura, M. A differential scanning calorimeter study of the monoclinic ($P2_1/b$) ↔ hexagonal ($P6_3/m$) reversible phase transition in hydroxyapatite. *Thermochim. Acta* 371, 53–56, 2001.
94. Hochrein, O., Kniep, R., Zahn, D. Atomistic simulation study of the order/disorder (monoclinic to hexagonal) phase transition of hydroxyapatite. *Chem. Mater.* 17, 1978–1981, 2005.
95. Slepko, A., Demkov, A.A. Hydroxyapatite: vibrational spectra and monoclinic to hexagonal phase transition. *J. Appl. Phys.* 2015, 117, 074701.
96. Mulley, V.J., Cavendish, C.D. A thermogravimetric method for the analysis of mixtures of brushite and monetite. *Analyst* 95, 304–307, 1970.
97. Dosen, A., Giese, R.F. Thermal decomposition of brushite, $CaHPO_4{\cdot}2H_2O$ to monetite $CaHPO_4$ and the formation of an amorphous phase. *Am. Mineral.* 96, 368–373, 2011.
98. Kaushal, A.M., Vangala, V.R., Suryanarayanan, R. Unusual effect of water vapor pressure on dehydration of dibasic calcium phosphate dihydrate. *J. Pharm. Sci.* 100, 1456–1466, 2011.
99. Tamimi, F., Nihouannen, D.L., Eimar, H., Sheikh, Z., Komarova, S., Barralet, J. The effect of autoclaving on the physical and biological properties of dicalcium phosphate dihydrate bioceramics: brushite *vs*. monetite. *Acta Biomater.* 8, 3161–3169, 2012.
100. Sánchez-Enríquez, J., Reyes-Gasga, J. Obtaining $Ca(H_2PO_4)_2{\cdot}H_2O$, monocalcium phosphate monohydrate, via monetite from brushite by using sonication. *Ultrason. Sonochem.* 20, 948–954, 2013.
101. Pyldme, M., Tynsuaadu, K., Paulik, F., Paulik, J., Arnold, M. Dehydrations of $Ca(H_2PO_4)_2{\cdot}H_2O$ and $Mg(H_2PO_4)_2{\cdot}2H_2O$ and their reactions with KCl, examined with simultaneous TG, DTG, DTA and EGA. *J. Thermal Anal.* 17, 479–488, 1979.
102. Aldabergenov, M.K., Balakaeva, G.T. The mechanism of dehydration of $Ca(H_2PO_4)_2{\cdot}H_2O$. *Russ. J. Phys. Chem.* 72, 1391–1393, 1998.
103. Vaimakis, T.C., Pomonis, P.J., Sdoukos, A.T. A detailed study of the condensation of the $Ca(H_2PO4)_2{\cdot}H_2O$–$CaHPO_4{\cdot}2H_2O$ system under thermal treatment. *Thermochim. Acta* 168, 103–113, 1990.

104. Vaimakis, T.C., Pomonis, P.J., Sdoukos, A.T. The kinetics of the thermal dehydration of the system $Ca(H_2PO_4)_2{\cdot}H_2O$–$CaHPO_4{\cdot}2H_2O$. *Thermochim. Acta* 173, 101–115, 1990.
105. Kim, H., Camata, R.P., Vohra, Y.K., Lacefield, W.R. Control of phase composition in hydroxyapatite/tetracalcium phosphate biphasic thin coatings for biomedical applications. *J. Mater. Sci. Mater. Med.* 16, 961–966, 2005.
106. Perez, L., Shyu, L.J., Nancollas, G.H. The phase transformation of calcium phosphate dihydrate into octacalcium phosphate in aqueous suspensions. *Colloids Surf.* 38, 295–304, 1989.
107. Zhang, J., Ebrahimpour, A., Nancollas, G.H. Dual constant composition studies of phase transformation of dicalcium phosphate dihydrate into octacalcium phosphate. *J. Coll. Interf. Sci.* 152, 132–140, 1992.
108. Mandel, S., Taş, A.C. Brushite ($CaHPO_4{\cdot}2H_2O$) to octacalcium phosphate ($Ca_8(HPO_4)_2(PO_4)_4{\cdot}5H_2O$) transformation in DMEM solutions at 36.5 °C. *Mater. Sci. Eng. C* 30, 245–254, 2010.
109. Temizel, N., Girisken, G., Taş, A.C. Accelerated transformation of brushite to octacalcium phosphate in new biomineralization media between 36.5 °C and 80 °C. *Mater. Sci. Eng. C* 31, 1136–1143, 2011.
110. Morejón-Alonso, L., Carrodeguas, R.G., García-Menocal, J.A.D., Pérez, J.A.A., Manent, S.M. Effect of sterilization on the properties of CDHA-OCP-β-TCP biomaterial. *Mater. Res.* 10, 15–20, 2007.
111. Morejón-Alonso, L., Carrodeguas, R.G., García-Menocal, J.A.D. Transformations in CDHA/OCP/β-TCP scaffold during ageing in simulated body fluid at 36.5 °C. *J. Biomed. Mater. Res. B Appl. Biomater.* 84B, 386–393, 2008.
112. Caroline Victoria, E., Gnanam, F.D. Synthesis and characterisation of biphasic calcium phosphate. *Trends Biomater. Artif. Organs.* 16, 12–14, 2002.
113. Nawawi, N.A., Singh, R., Hamdi, M., Young, T.C., Purbolaksono, J., Sopyan, I., Toulouei, R. Synthesis and properties of biphasic calcium phosphate prepared by different methods. *Adv. Mater. Res.* 970, 20–25, 2014.
114. Lin, S., LeGeros, R.Z., Rohanizadeh, R., Mijares, D., LeGeros, J.P. Biphasic calcium phosphate (BCP) bioceramics: preparation and properties. *Key Eng. Mater.* 240–242, 473–476, 2004.
115. Petrov, O.E., Dyulgerova, E., Petrov, L., Popova, R. Characterization of calcium phosphate phases obtained during the preparation of sintered biphase Ca-P ceramics. *Mater. Lett*. 48, 162–167, 2001.
116. Maciejewski, M., Brunner, T.J., Loher, S.F., Stark, W.J., Baiker, A. Phase transitions in amorphous calcium phosphates with different Ca/P ratios. *Thermochim. Acta* 468, 75–80, 2008.
117. Zyman, Z.Z., Tkachenko, M.V., Polevodin, D.V. Preparation and characterization of biphasic calcium phosphate ceramics of desired composition. *J. Mater. Sci. Mater. Med.* 19, 2819–2825, 2008.
118. Lukić, M., Stojanović, Z., Škapin, S.D., Maček-Kržmanc, M., Mitrić, M., Marković, S., Uskoković, D. Dense fine-grained biphasic calcium phosphate

(BCP) bioceramics designed by two-step sintering. *J. Eur. Ceram. Soc.* 31, 19–27, 2011.
119. Marković, S., Lukić, M.J., Škapin, S.D., Stojanović, B., Uskoković, D. Designing, fabrication and characterization of nanostructured functionally graded HAp/BCP ceramics. *Ceram. Int.* 41, 2654–2667, 2015.
120. Zhou, C., Xie, P., Chen, Y., Fan, Y., Tan, Y., Zhang, X. Synthesis, sintering and characterization of porous nano-structured CaP bioceramics prepared by a two-step sintering method. *Ceram. Int.* 41, 4696–4705, 2015.
121. Manjubala, I., Sivakimar, M. *In situ* synthesis of biphasic calcium phosphate ceramics using microwave irradiation. *Mater. Chem. Phys.* 71, 272–278, 2001.
122. Ji, J., Ran, J., Gou, L., Wang, F., Sun, L. Microwave plasma sintering and *in vitro* study of porous HA/*β*-TCP biphasic bioceramics. *Key Eng. Mater.* 280–283, 1519–1524, 2005.
123. Manjubala, I., Sastry, T.P., Kumar, R.V. Bone in-growth induced by biphasic calcium phosphate ceramic in femoral defect of dogs. *J. Biomater. Appl.* 19, 341–360, 2005.
124. Jalota, S., Bhaduri, S.B., Taş, A.C. *In vitro* testing of calcium phosphate (HA, TCP, and biphasic HA-TCP) whiskers. *J. Biomed. Mater. Res. A* 78A, 481–490, 2006.
125. Victor, S.P., Kumar T.S.S. BCP ceramic microspheres as drug delivery carriers: synthesis, characterisation and doxycycline release. *J. Mater. Sci. Mater. Med.* 19, 283–290, 2008.
126. Rameshbabu, N., Rao, K.P. Microwave synthesis, characterization and *in-vitro* evaluation of nanostructured biphasic calcium phosphates. *Cur. Appl. Phys.* 9, S29–S31, 2009.
127. Farzadi, A., Solati-Hashjin, M., Tahmasebi-Birgani, Z., Aminian, A. Microwave-assisted synthesis and characterization of biphasic calcium phosphate nanopowders. *Ceram. Trans.* 218, 59–65, 2010.
128. Veljović, D., Palcevskis, E., Dindune, A., Putić, S., Balać, I., Petrović, R., Janaćković, D. Microwave sintering improves the mechanical properties of biphasic calcium phosphates from hydroxyapatite microspheres produced from hydrothermal processing. *J. Mater. Sci.* 45, 3175–3183, 2010.
129. Veljović, D., Zalite, I., Palcevskis, E., Smiciklas, I., Petrović, R., Janaćković, D. Microwave sintering of fine grained HAP and HAP/TCP bioceramics. *Ceram. Int.* 36, 595–603, 2010.
130. Wagner, D.E, Jones, A.D., Zhou, H., Bhaduri, S.B. Cytocompatibility evaluation of microwave sintered biphasic calcium phosphate scaffolds synthesized using pH control. *Mater. Sci. Eng. C* 33, 1710–1719, 2013.
131. Miramond, T., Rouillon, T., Daculsi, G. Biphasic calcium phosphate: preferential ionic substitutions and crystallographic relationships at grain boundaries. *Key Eng. Mater.* 631, 73–77, 2015.
132. Marchi, J., Greil, P., Bressiani, J.C., Bressiani, A., Müller, F. Influence of synthesis conditions on the characteristics of biphasic calcium phosphate powders. *Int. J. Appl. Ceram. Technol.* 6, 60–71, 2009.

133. Descamps, M., Boilet, L., Moreau, G., Tricoteaux, A., Lu, J., Leriche, A., Lardot, V., Cambier, F. Processing and properties of biphasic calcium phosphates bioceramics obtained by pressureless sintering and hot isostatic pressing. *J. Eur. Ceram. Soc.* 33, 1263–1270, 2013.
134. Yang, X., Wang, Z. Synthesis of biphasic ceramics of hydroxyapatite and *β*-tricalcium phosphate with controlled phase content and porosity. *J. Mater. Chem.* 8, 2233–2237, 1998.
135. Tadjiev, T.R., Sungsu, C., Sukyoung, K. Mechano-chemical synthesis of biphasic calcium phosphates with the various ratio of HA and *β*-TCP. *Key Eng. Mater.* 330–332, 7–10, 2007.
136. Rao, R.R., Roopa, H.N., Kannan, T.S. Solid state synthesis and thermal stability of HAP and HAP – *β*-TCP composite ceramic powders. *J. Mater. Sci. Mater. Med.* 8, 511–518, 1997.
137. Hsu, C.K. A study on thermal behavior of uncalcined $Ca(H_2PO_4)_2 \cdot H_2O$ and $CaCO_3$ mixtures. *Thermochim. Acta*, 392–393, 157–161, 2002.
138. Hsu, C.K. The preparation of biphasic porous calcium phosphate by the mixture of $Ca(H_2PO_4)_2 \cdot H_2O$ and $CaCO_3$. *Mater. Chem. Phys.* 80, 409–420, 2003.
139. Jaw, K.S. Preparation of a biphasic calcium phosphate from $Ca(H_2PO_4)_2 \cdot H_2O$ and $CaCO_3$. *J. Therm. Anal. Calorim.* 83, 145–149, 2006.
140. Webler, G.D., Zapata, M.J.M., Agra, L.C., Barreto, E., Silva, A.O.S., Hickmann, J.M., Fonseca, E.J.S. Characterization and evaluation of cytotoxicity of biphasic calcium phosphate synthesized by a solid state reaction route. *Cur. Appl. Phys.* 14, 876–880, 2014.
141. Kim, D.H., Chun, H.H., Lee, J.D., Yoon, S.Y. Evaluation of phase transformation behavior in biphasic calcium phosphate with controlled spherical micro-granule architecture. *Ceram. Int.* 40, 5145–5155, 2014.
142. Kim, D.H., Kim, K.L., Chun, H.H., Kim, T.W., Park, H.C., Yoon, S.Y. *In vitro* biodegradable and mechanical performance of biphasic calcium phosphate porous scaffolds with unidirectional macro-pore structure. *Ceram. Int.* 40, 8293–8300, 2014.
143. Alqap, A.S.F., Sopyan, I., Zubir, S.A. Concentration effect of aqueous synthesis on biphasic hydroxyapatite – *β*-tricalcium phosphate composition. *Adv. Mater. Res.* 93–94, 405–408, 2010.
144. Castilho, M., Moseke, C., Ewald, A., Gbureck, U., Groll, J., Pires, I., Teßmar, J., Vorndran, E. Direct 3D powder printing of biphasic calcium phosphate scaffolds for substitution of complex bone defects. *Biofabrication* 6, 015006, 2014.
145. Fujiwara, K., Okada, M., Takeda, S., Matsumoto, N. A novel strategy for preparing nanoporous biphasic calcium phosphate of controlled composition via a modified nanoparticle-assembly method. *Mater. Sci. Eng. C* 35, 259–266, 2014.
146. Cho, J.S., Ko, Y.N., Koo, H.Y., Kang, Y.C. Synthesis of nano-sized biphasic calcium phosphate ceramics with spherical shape by flame spray pyrolysis. *J. Mater. Sci. Mater. Med.* 21, 1143–1149, 2010.

147. Peña, J., Vallet-Regí, M. Hydroxyapatite, tricalcium phosphate and biphasic materials prepared by a liquid mix technique. *J. Eur. Ceram. Soc.* 23, 1687–1696, 2003.
148. Chen, J., Wang, Y., Chen, X., Li, R., Chen, L., Wen, H., Zhang, Q. A simple sol-gel technique for synthesis of nanostructured hydroxyapatite, tricalcium phosphate and biphasic powders. *Mater. Lett*. 65, 1923–1926, 2011.
149. Sopyan, I., Natasha, A.N. Preparation of nanostructured manganese-doped biphasic calcium phosphate powders via sol-gel method. *Ionics* 15, 735–741, 2009.
150. Nazemi, Z., Nazarpak, M.H., Mehdikhani-Nahrkhalaji, M., Staji, H., Kalani, M.M. Synthesis, characterisation and antibacterial effects of sol-gel derived biphasic calcium phosphate nanopowders. *Micro Nano Lett*. 9, 403–406, 2014.
151. Schopper, C., Ziya-Ghazvini, F., Goriwoda, W., Moser, D., Wanschitz, F., Spassova, E., Lagogiannis, G., Auterith, A., Ewers, R. HA/TCP compounding of a porous CaP biomaterial improves bone formation and scaffold degradation – a long-term histological study. *J. Biomed. Mater. Res. B Appl. Biomater.* 74B, 458–467, 2005.
152. Castillo, M., Ayers, R.A., Zhang, X., Schowengerdt, F., Moore, J.J. Combustion synthesis of porous glasses and ceramics for bone repair. *Biomed. Sci. Instrum.* 37, 469–474, 2001.
153. Ayers, R., Nielsen-Preiss, S., Ferguson, V., Guglielmo, G., Moore, J.J., Kleebe, H.J. Osteoblast-like cell mineralization induced by multiphasic calcium phosphate ceramic. *Mater. Sci. Eng. C* 26, 1333–1337, 2006.
154. Ayers, R., Hannigan, N., Vollmer, N., Unuvar, C. Combustion synthesis of heterogeneous calcium phosphate bioceramics from calcium oxide and phosphate precursors. *Int. J. Self-Propag. High-Temp. Synth.* 20, 6–14, 2011.
155. Zhao, J., Zhao, J., Chen, J.H., Wang, X.H., Han, Z., Li, Y. Rietveld refinement of hydroxyapatite, tricalcium phosphate and biphasic materials prepared by solution combustion method. *Ceram. Int.* 40, 3379–3388, 2014.
156. Ghosh, S.K., Nandi, S.K., Kundu, B., Datta, S., De, D.K., Roy, S.K., Basu, D. *In vivo* response of porous hydroxyapatite and *β*-tricalcium phosphate prepared by aqueous solution combustion method and comparison with bioglass scaffolds. *J. Biomed. Mater. Res. B Appl. Biomater.* 86B, 217–227, 2008.
157. Aghayan, M.A., Rodríguez, M.A. Influence of fuels and combustion aids on solution combustion synthesis of bi-phasic calcium phosphates (BCP). *Mater. Sci. Eng. C* 32, 2464–2468, 2012.
158. Lin, F.H., Liao, C.J., Chen, K.S., Sun, J.S. Preparation of a biphasic porous bioceramic by heating bovine cancellous bone with $Na_4P_2O_7{\cdot}10H_2O$ addition. *Biomaterials* 20, 475–484, 1999.
159. Lin, F.H., Liao, C.J., Chen, K.S., Sun, J.S., Lin, C.Y. Preparation of *β*-TCP/HAP biphasic ceramics with natural bone structure by heating bovine cancellous bone with the addition of $(NH_4)_2HPO_4$. *J. Biomed. Mater. Res.* 51, 157–163, 2000.

160. Tavangarian, F., Emadi, R., Esfahani, S.I.R. A novel method to synthesis of β-TCP/HA biphasic nanocrystalline powder by using bovine bone. *Int. J. Modern Phys. B* 24, 3365–3372, 2010.
161. Emadi, R., Esfahani, S.I.R., Tavangarian, F. A novel, low temperature method for the preparation of β-TCP/HAP biphasic nanostructured ceramic scaffold from natural cancellous bone. *Mater. Lett*. 64, 993–996, 2010.
162. Jin, H.B., Guo, C.B., Mao, K.Y., Dorozhkin, S., Agathopoulos, S. Preparation of porous biphasic β-TCP/HA bioceramics with a natural trabecular structure from calcined cancellous bovine bone. *J. Ceram. Soc. Jpn*. 118, 52–56, 2010.
163. Lee, N.H., Hwang, K.H., Lee, J.K. Fabrication of biphasic calcium phosphate bioceramics from the recycling of bone ash. *Adv. Mater. Res*. 610–613, 2328–2331, 2013.
164. Sarin, P., Lee, S.J., Apostolov, Z.D., Kriven, W.M. Porous biphasic calcium phosphate scaffolds from cuttlefish bone. *J. Am. Ceram. Soc*. 94, 2362–2370, 2011.
165. Babu, N.R., Rao, K.P., Kumar, T.S.S. Effect of coralline derived biphasic calcium phosphate shot blasting on titanium surfaces. *T. Indian I. Metals* 57, 85–89, 2004.
166. Spassova, E., Gintenreiter, S., Halwax, E., Moser, D., Schopper, C., Ewers, R. Chemistry, ultrastructure and porosity of monophasic and biphasic bone forming materials derived from marine algae. *Materialwiss. Werkst.* 38, 1027–1034, 2007.
167. Nakano, T., Kaibara, K., Umakoshi, Y., Imazato, S., Ogata, K., Ehara, A., Ebisu, S., Okazaki, M. Change in microstructure and solubility improvement of HAp ceramics by heat-treatment in a vacuum. *Mater. Transact.* 43, 3105–3111, 2002.
168. Kiba, W., Imazato, S., Takahashi, Y., Yoshioka, S., Ebisu, S., Nakano, T. Efficacy of polyphasic calcium phosphates as a direct pulp capping material. *J. Dent.* 38, 828–837, 2010.
169. Weng, J., Liu, X., Zhang, X., Ma, Z., Ji, X., Zyman, Z.Z. Further studies on the plasma-sprayed amorphous phase in hydroxyapatite coatings and its deamorphization. *Biomaterials* 14, 578–582, 1993.
170. Gross, K.A., Berndt, C.C., Herman, H. Amorphous phase formation in plasma-sprayed hydroxyapatite coatings. *J. Biomed. Mater. Res.* 39, 407–414, 1998.
171. Kreidler, E.R., Hummel, F.A. Phase relationships in the system SrO–P_2O_5 and the influence of water vapor on the formation of $Sr_4P_2O_9$. *Inorg. Chem.* 6, 884–891, 1967.
172. Carayon, M.T., Lacout, J.L. Study of the Ca/P atomic ratio of the amorphous phase in plasma-sprayed hydroxyapatite coatings. *J. Solid State Chem*. 172, 339–350, 2003.
173. Yang, D.J., Tadjiev, T.R., Kim, J.W., You, C.K., Choi, S.K., Park, K.B., Ryoo, K.H., Kim, S. Comparative study of the degradation behavior of mechanically mixed and chemically precipitated biphasic calcium phosphates. *Key Eng. Mater.* 309–311, 227–230, 2006.

174. Zhang, Y., Yokogawa, Y., Kameyama, T. Bimodal porous bi-phasic calcium phosphate ceramics and its dissolution in SBF solution. *Key Eng. Mater.* 330–332, 91–94, 2007.
175. Zhang, Y., Yokogawa, Y., Kameyama, T. Preparation of biphasic calcium phosphate porous ceramics prepared from fine powders with different particle size and its dissolution behavior in simulated body fluid. *Key Eng. Mater.* 336–338, 1688–1691, 2007.
176. Nilen, R.W.N., Richter, P.W. The thermal stability of hydroxyapatite in biphasic calcium phosphate ceramics. *J. Mater. Sci. Mater. Med.* 19, 1693–1702, 2008.
177. Kong, Y.M., Kim, H.E., Kim, H.W. Phase conversion of tricalcium phosphate into Ca-deficient apatite during sintering of hydroxyapatite–tricalcium phosphate biphasic ceramics. *J. Biomed. Mater. Res. B Appl. Biomater.* 84B, 334–339, 2008.
178. Tanimoto, Y., Shibata, Y., Murakami, A., Miyazaki, T., Nishiyama, N. Effect of varying HAP/TCP ratios in tape-cast biphasic calcium phosphate ceramics on response *in vitro*. *J. Hard Tissue Biol*. 18, 71–76, 2009.
179. Wongwitwichot, P., Kaewsrichan, J., Chua, K.H., Ruszymah, B.H.I. Comparison of TCP and TCP/HA hybrid scaffolds for osteoconductive activity. *Open Biomed. Eng. J*. 4, 279–285, 2010.
180. Hung, C.L., Yang, J.C., Chang, W.J., Hu, C.Y., Lin, Y.H., Huang, C.H., Chen, C.C., Lee, S.Y., Teng, N.C. *In vivo* graft performance of an improved bone substitute composed of poor crystalline hydroxyapatite based biphasic calcium phosphate. *Dent. Mater. J*. 30, 21–28, 2011.
181. Bizari, D., Moztarzadeh, F., Rabiee, M., Tahriri, M., Banafatizadeh, F., Ansari, A., Khoshroo, K. Development of biphasic hydroxyapatite/dicalcium phosphate dihydrate (DCPD) bone graft using polyurethane foam template: *in vitro* and *in vivo* study. *Adv. Appl. Ceram*. 110, 417–425, 2011.
182. Ebrahimi, M., Pripatnanont, P., Monmaturapoj, N., Suttapreyasri, S. Fabrication and characterization of novel nano hydroxyapatite/β-tricalcium phosphate scaffolds in three different composition ratios. *J. Biomed. Mater. Res. A* 100A, 2260–2268, 2012.
183. Yang, D.H., Park, H.N., Bae, M.S., Lee, J.B., Heo, D.N., Lee, W.J., Park, Y.M., Cho, Y.H., Kim, D.S., Kwon, I.K. Evaluation of GENESIS-BCP™ scaffold composed of hydroxyapatite and β-tricalcium phosphate on bone formation. *Macromol. Res*. 20, 627–633, 2012.
184. Gao, C., Yang, B., Hu, H., Liu, J., Shuai, C., Peng, S. Enhanced sintering ability of biphasic calcium phosphate by polymers used for bone scaffold fabrication. *Mater. Sci. Eng. C* 33, 3802–3810, 2013.
185. Zhang, Y., Ai, J., Wang, D., Hong, Z., Li, W., Yokogawa, Y. Dissolution properties of different compositions of biphasic calcium phosphate bimodal porous ceramics following immersion in simulated body fluid solution. *Ceram. Int.* 39, 6751–6762, 2013.
186. Kreethawate, L., Tong-On, S., Siriarchavatana, P., Larpkiattaworn, S. Microstructure and properties of TCP/HA composite materials. *Key Eng. Mater.* 608, 259–263, 2014.

187. Gasik, M., Keski-Honkola, A., Bilotsky, Y., Friman, M. Development and optimization of hydroxyapatite–β-TCP functionally gradated biomaterial. *J. Mech. Behav. Biomed. Mater*. 30, 266–273, 2014.
188. Yetmez, M. Sintering behavior and mechanical properties of biphasic calcium phosphate ceramics. *Adv. Mater. Sci. Eng*. 2014, 871749, 2014.
189. Jun, Y.K., Hong, S.H., Kong, Y.M. Effect of co-precipitation on the low-temperature sintering of biphasic calcium phosphate. *J. Am. Ceram. Soc*. 89, 2295–2297, 2006.
190. Tas, A.C. Formation of calcium phosphate whiskers in hydrogen peroxide (H_2O_2) solutions at 90 °C. *J. Am. Ceram. Soc*. 90, 2358–2362, 2007.
191. Miller, M.A., Kendall, M.R., Jain, M.K., Larson, P.R., Madden, A.S., Tas, A.C. Testing of brushite ($CaHPO_4 \cdot 2H_2O$) in synthetic biomineralization solutions and *in situ* crystallization of brushite micro-granules. *J. Am. Ceram. Soc*. 95, 2178–2188, 2012.
192. Miller, M.A., Kendall, M.R., Jain, M.K., Larson, P.R., Madden, A.S., Tas, A.C. Maturation of brushite ($CaHPO_4 \cdot 2H_2O$) and *in situ* crystallization of brushite micro-granules. *Ceram. Eng. Sci. Proc*. 34, 77–91, 2014.
193. Mitsionis, A.I., Vaimakis, T.C., Trapalis, C.C. The effect of citric acid on the sintering of calcium phosphate bioceramics. *Ceram. Int.* 36, 623–634, 2010.
194. Mitsionis, A.I., Vaimakis, T.C. A calorimetric study of the temperature effect on calcium phosphate precipitation. *J. Therm. Anal. Calorim.* 99, 785–789, 2010.
195. Nouri-Felekori, M., Mesgar, A.S.M., Mohammadi, Z. Development of composite scaffolds in the system of gelatin – calcium phosphate whiskers/fibrous spherulites for bone tissue engineering. *Ceram. Int.* 41, 6013–6019, 2015.
196. Aslanidou, M., Vaimakis, T., Mitsionis, A., Trapalis, C. A novel approach on the preparation of biphasic calcium phosphate bioceramics under physiological conditions. The effect of the starting material. *Ceram. Int.* 39, 539–546, 2013.
197. Rau, J.V., Fosca, M., Komlev, V.S., Fadeeva, I.V., Albertini, V.R., Barinov, S.M. *In situ* time-resolved studies of octacalcium phosphate and dicalcium phosphate dihydrate in simulated body fluid: cooperative interactions and nanoapatite crystal growth. *Cryst. Growth Des*. 10, 3824–3834, 2010.
198. Sogo, Y., Sakurai, T., Onuma, K., Ito, A. The most appropriate (Ca+Zn)/P molar ratio to minimize the zinc content of ZnTCP/HAP ceramic used in the promotion of bone formation. *J. Biomed. Mater. Res.* 62, 457–463, 2002.
199. Costa, A.M., Soares, G.A., Calixto, R., Rossi, A.M. Preparation and properties of zinc containing biphasic calcium phosphate bioceramics. *Key Eng. Mater.* 254–256, 119–122, 2004.
200. Gunawan, Sopyan, I., Mel, M., Suryanto, Investigations of the effects of initial Zn concentration and sintering conditions on the phase behavior and mechanical properties of Zn-doped BCP. *Adv. Environ. Biol.* 8, Spec. Iss., 680–685, 2014.
201. Manjubala, I., Kumar, T.S.S. Preparation of biphasic calcium phosphate doped with magnesium fluoride for osteoporotic applications. *J. Mater. Sci. Lett*. 20, 1225–1227, 2001.

202. Ryu, H.S., Hong, K.S., Lee, J.K., Kim, D.J., Lee, J.H., Chang, B.S., Lee, D.H., Lee, C.K., Chung, S.S. Magnesia-doped HA/β-TCP ceramics and evaluation of their biocompatibility. *Biomaterials* 25, 393–401, 2004.
203. Kannan, S., Lemos, I.A.F., Rocha, J.H.G., Ferreira, J.M.F. Synthesis and characterization of magnesium substituted biphasic mixtures of controlled hydroxyapatite/β-tricalcium phosphate ratios. *J. Solid State Chem*. 178, 3190–3196, 2005.
204. Ryu, H.S., Hong, K.S., Lee, J.K., Kim, D.J. Variations of structure and composition in magnesium incorporated hydroxyapatite/β-calcium phosphate. *J. Mater. Res*. 21, 428–436, 2006.
205. Kannan, S., Goetz-Neunhoeffer, F., Neubauer, J., Rebelo, A.H.S., Valério, P., Ferreira, J.M.F. Rietveld structure and *in vitro* analysis on the influence of magnesium in biphasic (hydroxyapatite and β-tricalcium phosphate) mixtures. *J. Biomed. Mater. Res. B Appl. Biomater.* 90B, 404–411, 2009.
206. Gomes, S., Renaudin, G., Jallot, E., Nedelec, J.M. Structural characterization and biological fluid interaction of sol-gel-derived Mg-substituted biphasic calcium phosphate ceramics. *ACS Appl. Mater. Interf.* 1, 505–513, 2009.
207. Kim, T.W., Lee, H.S., Kim, D.H., Jin, H.H., Hwang, K.H., Lee, J.K., Park, H.C., Yoon, S.Y. *In situ* synthesis of magnesium-substituted biphasic calcium phosphate and *in vitro* biodegradation. *Mater. Res. Bull*. 47, 2506–2512, 2012.
208. Kumar, P.N., Mishra, S.K., Kannan, S. Probing the limit of magnesium uptake by β-tricalcium phosphate in biphasic mixtures formed from calcium deficient apatites. *J. Solid State Chem*. 231, 13–19, 2015.
209. Webler, G.D., Correia, A.C.C., Barreto, E., Fonseca, E.J.S. Mg-doped biphasic calcium phosphate by a solid state reaction route: characterization and evaluation of cytotoxicity. *Mater. Chem. Phys.* 162, 177–181, 2015.
210. Tamai, M., Isama, K., Nakaoka, R., Tsuchiya, T. Synthesis of a novel β-tricalcium phosphate/hydroxyapatite biphasic calcium phosphate containing niobium ions and evaluation of its osteogenic properties. *J. Artif. Organs* 10, 22–28, 2007.
211. Kannan, S., Ventura, J.M.G., Ferreira, J.M.F. *In situ* formation and characterization of fluorine-substituted biphasic calcium phosphate ceramics of varied F-HAP/β-TCP ratios. *Chem. Mater.* 17, 3065–3068, 2005.
212. Kannan, S., Rocha, J.H.G., Ferreira, J.M.F. Synthesis of hydroxy-chloroapatites solid solutions. *Mater. Lett*. 60, 864–868, 2006.
213. Kannan, S., Ventura, J.M.G., Lemos, A.F., Barba, A., Ferreira, J.M.F. Effect of sodium addition on the preparation of hydroxyapatites and biphasic ceramics. *Ceram. Int.* 34, 7–13, 2008.
214. Kannan, S., Ventura, J.M.G., Ferreira, J.M.F. Synthesis and thermal stability of potassium substituted hydroxyapatites and hydroxyapatite/β-tricalciumphosphate mixtures. *Ceram. Int.* 33, 1489–1494, 2007.

215. Kannan, S., Rebelo, A., Lemos, A.F., Barba, A., Ferreira, J.M.F. Synthesis and mechanical behaviour of chlorapatite and chlorapatite/β-TCP composites. *J. Eur. Ceram. Soc.* 27, 2287–2294, 2007.
216. Mayer, I., Cuisinier, F.J.G., Popov, I., Schleich, Y., Gdalya, S., Burghaus, O., Reinen, D. Phase relation between β-tricalcium phosphate and hydroxyapatite with manganese (II): structural and spectroscopic properties. *Eur. J. Inorg. Chem*. 7, 1460–1465, 2006.
217. Sopyan, I., Nawawi, N.A., Shah, Q.H. Dense manganese doped biphasic calcium phosphate for load bearing bone implants. *Adv. Mater. Res*. 93–94, 393–396, 2010.
218. Sopyan, I., Ramesh, S., Nawawi, N.A., Tampieri, A., Sprio, S. Effects of manganese doping on properties of sol-gel derived biphasic calcium phosphate ceramics. *Ceram. Int.* 37, 3703–3715, 2011.
219. Kannan, S., Goetz-Neunhoeffer, F., Neubauer, J., Ferreira, J.M.F. Ionic substitution in biphasic hydroxyapatite and β-tricalcium phosphate mixtures: structural analysis by Rietveld refinement. *J. Am. Ceram. Soc*. 91, 1–12, 2008.
220. Li, B., Chen, X., Guo, B., Wang, X., Fan, H., Zhang, X. Fabrication and cellular biocompatibility of porous carbonated biphasic calcium phosphate ceramics with a nanostructure. *Acta Biomater.* 5, 134–143, 2009.
221. Wang, H., Yu, J., Li, J., Cheng, X., Huang, Z. The room temperature photoluminescence properties of Eu^{3+}-doped bi-phase calcium phosphate under visible light. *J. Mater. Sci*. 45, 1237–1241, 2010.
222. Gomes, S., Renaudin, G., Mesbah, A., Jallot, E., Bonhomme, C., Babonneau, F., Nedelec, J.M. Thorough analysis of silicon substitution in biphasic calcium phosphate bioceramics: a multi-technique study. *Acta Biomater.* 6, 3264–3274, 2010.
223. Kanchana, P., Sekar, C. Influence of strontium on the synthesis and surface properties of biphasic calcium phosphate (BCP) bioceramics. *J. Appl. Biomater. Biomech*. 8, 153–158, 2010.
224. Kannan, S., Vieira, S.I., Olhero, S.M., Torres, P.M.C., Pina, S., da Cruz e Silva, O.A.B., Ferreira, J.M.F. Synthesis, mechanical and biological characterization of ionic doped carbonated hydroxyapatite/β-tricalcium phosphate mixtures. *Acta Biomater.* 7, 1835–1843, 2011.
225. Kim, H.W., Koh, Y.H., Kong, Y.M., Kang, J.G., Kim, H.E. Strontium substituted calcium phosphate biphasic ceramics obtained by a powder precipitation method. *J. Mater. Sci. Mater. Med.* 15, 1129–1134, 2004.
226. Kumar, P.N., Mishra, S.K., Kiran, R.U., Kannan, S. Preferential occupancy of strontium in the hydroxyapatite lattice in biphasic mixtures formed from non-stoichiometric calcium apatites. *Dalton Transact*. 44, 8284–8292, 2015.
227. Radovanović, Ž., Jokić, B., Veljović, D., Dimitrijević, S., Kojić, V., Petrović, R., Janaćković, D. Antimicrobial activity and biocompatibility of Ag^{+}- and Cu^{2+}-doped biphasic hydroxyapatite/α-tricalcium phosphate obtained from hydrothermally synthesized Ag^{+}- and Cu^{2+}-doped hydroxyapatite. *Appl. Surf. Sci*. 307, 513–519, 2014.

228. Baradaran, S., Moghaddam, E., Nasiri-Tabrizi, B., Basirun, W.J., Mehrali, M., Sookhakian, M., Hamdi, M., Alias, Y. Characterization of nickel-doped biphasic calcium phosphate/graphene nanoplatelet composites for biomedical application. *Mater. Sci. Eng. C* 49, 656–668, 2015.
229. Takahashi, K., van den Beucken, J.J.J.P., Wolke, J.G.C., Hayakawa, T., Nishiyama, N., Jansen, J.A. Characterization and *in vitro* evaluation of biphasic calcium pyrophosphate-tricalciumphosphate radio frequency magnetron sputter coatings. *J. Biomed. Mater. Res. A* 84A, 682–690, 2008.
230. Chen, G., Li, W., Zhao, B., Sun, K. A novel biphasic bone scaffold: β-calcium phosphate and amorphous calcium polyphosphate. *J. Am. Ceram. Soc*. 92, 945–948, 2009.
231. Yang, Y.W., Mao, T.Q., Gao, Z., Hou, R., Su, X.D., Hu, X.G., Cheng, X.B. Biocompatibility of ostrich multiphasic calcium phosphate ceramic scaffold. *Chinese J. Clin. Rehabil*. 8, 2626–2627, 2004.
232. Yamada, S., Heymann, D., Bouler, J.M., Daculsi, G. Osteoclastic resorption of biphasic calcium phosphate ceramic *in vitro*. *J. Biomed. Mater. Res.* 37, 346–352, 1997.
233. Yamada, S., Heymann, D., Bouler, J.M., Daculsi, G. Osteoclastic resorption of calcium phosphate ceramics with different hydroxyapatite/β-tricalcium phosphate ratios. *Biomaterials* 18, 1037–1041, 1997.
234. Newe, C., Cunningham, E., Buchanan, F., Walker, G., Prendergast, P., Lennon, A., Dunne, N.J. Static and dynamic degradation of sintered calcium phosphate ceramics. *Key Eng. Mater.* 493–494, 861–865, 2012.
235. Strobel, L., Rath, S., Maier, A., Beier, J., Arkudas, A., Greil, P., Horch, R., Kneser, U. Induction of bone formation in biphasic calcium phosphate scaffolds by bone morphogenetic protein-2 and primary osteoblasts. *J. Tissue Eng. Regen. Med*. 8, 176–185, 2014.
236. Schumacher, M., Deisinger, U., Ziegler, G., Detsch, R. Indirect rapid prototyping of biphasic calcium phosphate scaffolds as bone substitutes: influence of phase composition, macroporosity and pore geometry on mechanical properties. *J. Mater. Sci. Mater. Med.* 21, 3119–3127, 2010.
237. Schumacher, M., Uhl, F., Detsch, R., Deisinger, U., Ziegler, G. Static and dynamic cultivation of bone marrow stromal cells on biphasic calcium phosphate scaffolds derived from an indirect rapid prototyping technique. *J. Mater. Sci. Mater. Med.* 21, 3039–3048, 2010.
238. Jo, I.H., Ahn, M.K., Moon, Y.W., Koh, Y.H., Kim, H.E. Novel rapid direct deposition of ceramic paste for porous biphasic calcium phosphate (BCP) scaffolds with tightly controlled 3-D macrochannels. *Ceram. Int.* 40, 11079–11084, 2014.
239. Ahn, M.K., Shin, K.H., Moon, Y.W., Koh, Y.H., Choi, W.Y., Kim, H.E. Highly porous biphasic calcium phosphate (BCP) ceramics with large interconnected pores by freezing vigorously foamed BCP suspensions under reduced pressure. *J. Am. Ceram. Soc*. 94, 4154–4156, 2011.

240. Baradararan, S., Hamdi, M., Metselaar, I.H. Biphasic calcium phosphate (BCP) macroporous scaffold with different ratios of HA/*β*-TCP by combination of gel casting and polymer sponge methods. *Adv. Appl. Ceram*. 111, 367–373, 2012.
241. Ahn, M.K., Moon, Y.W., Koh, Y.H., Kim, H.E. Use of glycerol as a cryoprotectant in vacuum-assisted foaming of ceramic suspension technique for improving compressive strength of porous biphasic calcium phosphate ceramics. *J. Am. Ceram. Soc*. 95, 3360–3362, 2012.
242. Nie, L., Chen, D., Yang, Q., Zou, P., Feng, S., Hu, H., Suo, J. Hydroxyapatite/poly-L-lactide nanocomposites coating improves the adherence and proliferation of human bone mesenchymal stem cells on porous biphasic calcium phosphate scaffolds. *Mater. Lett*. 92, 25–28, 2013.
243. Qader, S.T.A., Rahman, I.A., Ismail, H., Kannan, T.P., Mahmood, Z. A simple pathway in preparation of controlled porosity of biphasic calcium phosphate scaffold for dentin regeneration. *Ceram. Int.* 39, 2375–2381, 2013.
244. Kim, W.S., Nath, S.D., Bae, J.S., Padalhin, A., Kim, B., Song, M.J., Min, Y.K. *In vitro* and *in vivo* evaluation of composite scaffold of BCP, bioglass and gelatin for bone tissue engineering. *Korean J. Mater. Res*. 24, 310–318, 2014.
245. Lee, M.H., You, C., Kim, K.H. Combined effect of a microporous layer and type I collagen coating on a biphasic calcium phosphate scaffold for bone tissue engineering. *Materials* 8, 1150–1161, 2015.
246. Tuyen, D.V., Lee, B.T. Formation and characterization of porous spherical biphasic calcium phosphate (BCP) granules using PCL. *Ceram. Int.* 37, 2043–2049, 2011.
247. Sarkar, S.K., Tuyen, D.V., Lee, B.T. Evaluation of formation process of spherical porous biphasic calcium phosphate (BCP) granules by slurry dripping method. *Met. Mater. Int*. 18, 717–721, 2012.
248. Ilieva, R., Dyulgerova, E., Petrov, O., Aleksandrova, R., Titorenkova, R. Effects of high energy dry milling on biphase calcium phosphates. *Adv. Appl. Ceram*. 112, 219–226, 2013.
249. Wolf-Brandstetter, C., Hempel, U., Clyens, S., Gandhi, A.A., Korostynska, O., Oswald, S., Tofail, S.A., Theilgaard, N., Wiesmann, H.P., Scharnweber, D. The impact of heat treatment on interactions of contact-poled biphasic calcium phosphates with proteins and cells. *Acta Biomater.* 8, 3468–3477, 2012.
250. Tarafder, S., Banerjee, S., Bandyopadhyay, A., Bose, S. Electrically polarized biphasic calcium phosphates: adsorption and release of bovine serum albumin. *Langmuir* 26, 16625–16629, 2010.
251. Tarafder, S., Bodhak, S., Bandyopadhyay, A., Bose, S. Effect of electrical polarization and composition of biphasic calcium phosphates on early stage osteoblast interactions. *J. Biomed. Mater. Res. B Appl. Biomater.* 97B, 306–314, 2011.
252. Bouler, J.M., Daculsi, G. *In vitro* carbonated apatite precipitation on biphasic calcium phosphate pellets presenting various HA/*β*-TCP ratios. *Key Eng. Mater.* 192–195, 119–122, 2001.

253. Leng, Y., Chen, J., Qu, S. TEM study of calcium phosphate precipitation on HA/TCP ceramics. *Biomaterials* 24, 2125–2131, 2003.
254. Duan, Y.R., Zhang, Z.R., Wang, C.Y., Chen, J.Y., Zhang, X.D. Dynamic study of calcium phosphate formation on porous HA/TCP ceramics. *J. Mater. Sci. Mater. Med.* 15, 1205–1211, 2004.
255. Deng, C., Wang, Y., Wu, Y., Wang, X., Chen, X., Zheng, H., Chen, J., Zhang, X. Apatite formation on porous HA/TCP in animals' serums *in vitro*. *Key Eng. Mater.* 330–332, 955–958, 2007.
256. Deng, C., Wang, Y., Chen, J., Zheng, H., Chen, H., Zhang, D., Zhang, X. Growth of apatite in bovine serums on porous HA/TCP ceramics. *Key Eng. Mater.* 368–372, 1184–1186, 2008.
257. Toquet, J., Rohanizadeh, R., Guicheux, J., Couillaud, S., Passuti, N., Daculsi, G., Heymann, D. Osteogenic potential *in vitro* of human bone marrow cells cultured on macroporous biphasic calcium phosphate ceramic. *J. Biomed. Mater. Res.* 44, 98–108, 1999.
258. Silva, S.N., Pereira, M.M., Goes, A.M., Leite, M.F. Effect of biphasic calcium phosphate on human macrophage functions *in vitro*. *J. Biomed. Mater. Res. A* 65A, 475–481, 2003.
259. Rochet, N., Loubat, A., Laugier, J.P., Hofman, P., Bouler, J.M., Daculsi, G., Carle, G.F., Rossi, B. Modification of gene expression induced in human osteogenic and osteosarcoma cells by culture on a biphasic calcium phosphate bone substitute. *Bone* 32, 602–610, 2003.
260. de Kok, I.J., Peter, S.J., Archambault, M., van den Bos, C., Kadiyala, S., Aukhil, I., Cooper, L.F. Investigation of allogeneic mesenchymal stem cell-based alveolar bone formation: preliminary findings. *Clin. Oral Implants Res.* 14, 481–489, 2003.
261. Holtorf, H.L., Sheffield, T.L., Ambrose, C.G., Jansen, J.A., Mikos, A.G. Flow perfusion culture of marrow stromal cells seeded on porous biphasic calcium phosphate ceramics. *Ann. Biomed. Eng.* 33, 1238–1248, 2005.
262. Eslaminejad, M.B., Jafarian, M., Khojasteh, A., Abbas, F.M., Dehghan, M.M., Hassanizadeh, R. *In vivo* bone formation by canine mesenchymal stem cells loaded onto HA/TCP scaffolds: qualitative and quantitative analysis. *Yakhteh Med. J.* 10, 205–212, 2008.
263. Lobo, S.E., Glickman, R., da Silva, W.N., Arinzeh, T.L., Kerkis, I. Response of stem cells from different origins to biphasic calcium phosphate bioceramics. *Cell Tissue Res.* 361, 477–495, 2015.
264. Oda, S., Kinoshita, A., Higuchi, T., Shizuya, T., Ishikawa, I. Ectopic bone formation by biphasic calcium phosphate (BCP) combined with recombinant human bone morphogenetic protein-2 (rhBMP-2). *J. Med. Dent. Sci.* 44, 53–62, 1997.
265. Zhu, X., Fan, H., Li, D., Xiao, Y., Zhang, X. Protein adsorption and zeta potentials of a biphasic calcium phosphate ceramic under various conditions. *J. Biomed. Mater. Res. B Appl. Biomater.* 82B, 65–73, 2007.
266. Kim, J.I., Yun, J.H., Chae, G.J., Jung, S.W., Kim, C.S., Cho, K.S. rhBMP-2 using biphasic calcium phosphate block as a carrier induces new bone

formation in a rat subcutaneous tissue. *J. Korean Acad. Periodontol.* 38, 355–362, 2008.
267. Zhu, X.D., Fan, H.S., Xiao, Y.M., Li, D.X., Zhang, H.J., Luxbacher, T., Zhang, X.D. Effect of surface structure on protein adsorption to biphasic calcium-phosphate ceramics *in vitro* and *in vivo*. *Acta Biomater.* 5, 1311–1318, 2009.
268. Banerjee, S.S., Bandyopadhyay, A., Bose, S. Biphasic resorbable calcium phosphate ceramic for bone implants and local alendronate delivery. *Adv. Eng. Mater*. 12, B148–B155, 2010.
269. Miramond, T., Aguado, E., Goyenvalle, E., Moreau, F., Borget, P., Daculsi, G. Osteopromotion of biphasic calcium phosphate granules in critical size defects after osteonecrosis induced by focal heating insults. *IRBM* 34, 337–341, 2013.
270. Daculsi, G., Layrolle, P. Osteoinductive properties of micro macroporous biphasic calcium phosphate bioceramics. *Key Eng. Mater.* 254–256, 1005–1008, 2004.
271. Shin, H.I., Kim, K.H., Kang, I.K., Oh, K.S. Successful osteoinduction by cell-macroporous biphasic HA-TCP ceramic matrix. *Key Eng. Mater.* 288–289, 245–248, 2005.
272. le Nihouannen, D., Daculsi, G., Saffarzadeh, A., Gauthier, O., Delplace, S., Pilet, P., Layrolle, P. Ectopic bone formation by microporous calcium phosphate ceramic particles in sheep muscles. *Bone* 36, 1086–1093, 2005.
273. Ye, F., Lu, X., Wang, J. A long-term evaluation of osteoinductive HA/β-TCP ceramics *in vivo*: 4.5 years study in pigs. *J. Mater. Sci. Mater. Med.* 18, 2173–2178, 2007.
274. Fellah, B.H., Gauthier, O., Weiss, P., Chappard, D., Layrolle, P. Comparison of osteoinduction by autologous bone and biphasic calcium phosphate ceramic in goats. *Key Eng. Mater.* 330–332, 1063–1066, 2007.
275. Schwarz, F., Herten, M., Ferrari, D., Wieland, M., Schmitz, L., Engelhardt, E., Becker, J. Guided bone regeneration at dehiscence-type defects using biphasic hydroxyapatite + beta tricalcium phosphate (Bone Ceramic®) or a collagen-coated natural bone mineral (BioOss Collagen®): an immunohistochemical study in dogs. *Int. J. Oral Maxillofac. Surg.* 36, 1198–1206, 2007.
276. Ripamonti, U., Richter, P.W., Nilen, R.W.N., Renton, L. The induction of bone formation by smart biphasic hydroxyapatite tricalcium phosphate biomimetic matrices in the non-human primate *Papio ursinus*. *J. Cell. Mol. Med.* 12, 2609–2621, 2008.
277. Sun, L., Wu, L., Bao, C., Fu, C., Wang, X., Yao, J., Zhang, X., van Blitterswijk, C.A. Gene expressions of Collagen type I, ALP and BMP-4 in osteo-inductive BCP implants show similar pattern to that of natural healing bones. *Mater. Sci. Eng. C* 29, 1829–1834, 2009.
278. Roldán, J.C., Detsch, R., Schaefer, S., Chang, E., Kelantan, M., Waiss, W., Reichert, T.E., Gurtner, G.C., Deisinger, U. Bone formation and degradation of a highly porous biphasic calcium phosphate ceramic in presence of BMP-7, VEGF and mesenchymal stem cells in an ectopic mouse model. *J. Craniomaxillofac. Surg.* 38, 423–430, 2010.

279. Barbieri, D., Yuan, H., de Groot, F., Walsh, W.R., de Bruijn, J.D. Influence of different polymeric gels on the ectopic bone forming ability of an osteoinductive biphasic calcium phosphate ceramic. *Acta Biomater.* 7, 2007–2014, 2011.
280. Li, B., Liao, X., Zheng, L., Zhu, X., Wang, Z., Fan, H., Zhang, X. Effect of nanostructure on osteoinduction of porous biphasic calcium phosphate ceramics. *Acta Biomater.* 8, 3794–3804, 2012.
281. Miramond, T., Corre, P., Borget, P., Moreau, F., Guicheux, J., Daculsi, G., Weiss, P. Osteoinduction of biphasic calcium phosphate scaffolds in a nude mouse model. *J. Biomater. Appl.* 29, 595–604, 2014.
282. Hashimoto-Uoshima, M., Ishikawa, I., Kinoshita, A., Weng, H.T., Oda, S. Clinical and histologic observation of replacement of biphasic calcium phosphate by bone tissue in monkeys. *Int. J. Periodont. Rest. Dent.* 15, 205–213, 1995.
283. Diggs, A.B., Halloran, J.W., Hollister, S.J. Cathodoluminescence as a method of microstructure characterization of biphasic ceramics composed of hydroxyapatite and β-tricalcium phosphate. *Key Eng. Mater.* 284–286, 333–336, 2005.
284. LeGeros, R.Z. Calcium phosphate-based osteoinductive materials. *Chem. Rev.* 108, 4742–4753, 2008.
285. Grundel, R.E., Chapman, M.W., Yee, T., Moore, D.C. Autogeneic bone marrow and porous biphasic calcium phosphate ceramic for segmental bone defects in the canine ulna. *Clin. Orthop. Rel. Res*. 266, 244–258, 1991.
286. Passuti, N., Delécrin, J., Daculsi, G. Experimental data regarding macroporous biphasic calcium phosphate ceramics. *Eur. J. Orthop. Surg. Traumatol.* 7, 79–84, 1997.
287. Gauthier, O., Bouler, J.M., Aguado, E., Pilet, P., Daculsi, G. Macroporous biphasic calcium phosphate ceramics: influence of macropore diameter and macroporosity percentage on bone ingrowth. *Biomaterials* 19, 133–139, 1998.
288. Gauthier, O., Bouler, J.M., Aguado, E., LeGeros, R.Z., Pilet, P., Daculsi, G. Elaboration conditions influence, physicochemical properties and *in vivo* bioactivity of macroporous biphasic calcium phosphate ceramics. *J. Mater. Sci. Mater. Med.* 10, 199–204, 1999.
289. Li, S., de Wijn, J.R., Li, J., Layrolle, P., de Groot, K. Macroporous biphasic calcium phosphate scaffold with high permeability/porosity ratio. *Tissue Eng.* 9, 535–548, 2003.
290. Teixeira, C.C., Nemelivsky, Y., Karkia, C., LeGeros, R.Z. Biphasic calcium phosphate: a scaffold for growth plate chondrocyte maturation. *Tissue Eng.* 12, 2283–2289, 2006.
291. Chung, R.J., Hsieh, M.F., Huang, K.C., Chou, F.I., Perng, L.H. Preparation of porous HA/beta-TCP biphasic bioceramic using a molten salt process. *Key Eng. Mater.* 309–311, 1075–1078, 2006.

292. Rabiee, S.M., Mortazavi, S.M.J., Moztarzadeh, F., Sharifi, D., Sharifi, Sh., Solati-Hashjin, M., Salimi-Kenari, H., Bizari, D. Mechanical behavior of a new biphasic calcium phosphate bone graft. *Biotechnol. Bioprocess Eng*. 13, 204–209, 2008.
293. Macchetta, A., Turner, I.G., Bowen, C.R. Fabrication of HA/TCP scaffolds with a graded and porous structure using a camphene-based freeze-casting method. *Acta Biomater.* 5, 1319–1327, 2009.
294. Sánchez-Salcedo, S., Balas, F., Izquierdo-Barba, I., Vallet-Regí, M. *In vitro* structural changes in porous HA/*β*-TCP scaffolds in simulated body fluid. *Acta Biomater.* 5, 2738–2751, 2009.
295. lan Levengood, S.K., Polak, S.J., Poellmann, M.J., Hoelzle, D.J., Maki, A.J., Clark, S.G., Wheeler, M.B., Wagoner Johnson, A.J. The effect of BMP-2 on micro- and macroscale osteointegration of biphasic calcium phosphate scaffolds with multiscale porosity. *Acta Biomater.* 6, 3283–3291, 2010.
296. le Ray, A.M., Gautier, H., Bouler, J.M., Weiss, P., Merle, C. A new technological procedure using sucrose as porogen compound to manufacture porous biphasic calcium phosphate ceramics of appropriate micro- and macrostructure. *Ceram. Int.* 36, 93–101, 2010.
297. Pecqueux, F., Tancret, F., Payraudeau, N., Bouler, J.M. Influence of microporosity and macroporosity on the mechanical properties of biphasic calcium phosphate bioceramics: modelling and experiment. *J. Eur. Ceram. Soc.* 30, 819–829, 2010.
298. Peroglio, M., Gremillard, L., Gauthier, C., Chazeau, L., Verrier, S., Alini, M., Chevalier, J. Mechanical properties and cytocompatibility of poly(ε-caprolactone)-infiltrated biphasic calcium phosphate scaffolds with bimodal pore distribution. *Acta Biomater.* 6, 4369–4379, 2010.
299. Roohani-Esfahani, S.I., Nouri-Khorasani, S., Lu, Z., Appleyard, R., Zreiqat, H. The influence hydroxyapatite nanoparticle shape and size on the properties of biphasic calcium phosphate scaffolds coated with hydroxyapatite–PCL composites. *Biomaterials* 31, 5498–5509, 2010.
300. Calvo-Guirado, J.L., Delgado-Ruíz, R.A., Ramírez-Fernández, M.P., Maté-Sánchez, J.E., Ortiz-Ruiz, A., Marcus, A. Histomorphometric and mineral degradation study of Ossceram®: a novel biphasic B-tricalcium phosphate, in critical size defects in rabbits. *Clin. Oral Implants Res*. 23, 667–675, 2012.
301. Baroth, S., Bourges, X., Goyenvalle, E., Aguado, E., Daculsi, G. Injectable biphasic calcium phosphate bioceramic: the HYDROS® concept. *Bio-Med. Mater. Eng*. 19, 71–76, 2009.
302. le Guehennec, L., Goyenvalle, E., Aguado, E., Pilet, P., Bagot D'Arc, M., Bilban, M., Spaethe, R., Daculsi, G. MBCP® biphasic calcium phosphate granules and tissucol® fibrin sealant in rabbit femoral defects: the effect of fibrin on bone ingrowth. *J. Mater. Sci. Mater. Med.* 16, 29–35, 2005.
303. Jegoux, F., Goyenvalle, E., Bagot D'Arc, M., Aguado, E., Daculsi, G. *In vivo* biological performance of composites combining micro-macroporous biphasic

calcium phosphate granules and fibrin sealant. *Arch. Orthop. Trauma Surg.* 125, 153–159, 2005.
304. Bluteau, G., Pilet, P., Bourges, X., Bilban, M., Spaethe, R., Daculsi, G., Guicheux, J. The modulation of gene expression in osteoblasts by thrombin coated on biphasic calcium phosphate ceramic. *Biomaterials* 27, 2934–2943, 2006.
305. le Nihouannen, D., Saffarzadeh, A., Gauthier, O., Moreau, F., Pilet, P., Spaethe, R., Layrolle, P., Daculsi, G. Bone tissue formation in sheep muscles induced by a biphasic calcium phosphate ceramic and fibrin glue composite. *J. Mater. Sci. Mater. Med.* 19, 667–675, 2008.
306. Goyenvalle, E., Aguado, E., Pilet, P., Daculsi, G. Biofunctionality of MBCP ceramic granules (TricOs™) plus fibrin sealant (Tisseel®) versus MBCP ceramic granules as a filler of large periprosthetic bone defects: an investigative ovine study. *J. Mater. Sci. Mater. Med.* 21, 1949–1958, 2010.
307. Reppenhagen, S., Reichert, J.C., Rackwitz, L., Rudert, M., Raab, P., Daculsi, G., Nöth, U. Biphasic bone substitute and fibrin sealant for treatment of benign bone tumours and tumour-like lesions. *Int. Orthop*. 36, 139–148, 2012.
308. Franco-Vidal, V., Daculsi, G., Bagot D'Arc, M., Sterkers, O., Smail, M., Robier, A., Bordure, P., Claros, P., Paiva, A., Darrouzet, V., Anthoine, E., Bebear, J.P. Tolerance and osteointegration of TricOs™/MBCP® in association with fibrin sealant in mastoid obliteration after canal wall-down technique for cholesteatoma. *Acta Oto-Laryngol.* 134, 358–365, 2014.
309. Daculsi, G., Khairoun, I., LeGeros, R.Z., Moreau, F., Pilet, P., Bourges, X., Weiss, P., Gauthier, O. Bone ingrowth at the expense of a novel macroporous calcium phosphate cement. *Key Eng. Mater.* 330–332, 811–814, 2007.
310. Dupraz, A., Nguyen, T.P., Richard, M., Daculsi, G., Passuti, N. Influence of a cellulosic ether carrier on the structure of biphasic calcium phosphate ceramic particles in an injectable composite material. *Biomaterials* 20, 663–673, 1999.
311. Iooss, P., le Ray, A.M., Grimandi, G., Daculsi, G., Merle, C. A new injectable bone substitute combining poly(ε-caprolactone) microparticles with biphasic calcium phosphate granules. *Biomaterials* 22, 2785–2794, 2001.
312. Trojani, C., Boukhechba, F., Scimeca, J.C., Vandenbos, F., Michiels, J.F., Daculsi, G., Boileau, P., Weiss, P., Carle, G.F., Rochet, N. Ectopic bone formation using an injectable biphasic calcium phosphate/Si-HPMC hydrogel composite loaded with undifferentiated bone marrow stromal cells. *Biomaterials* 27, 3256–3264, 2006.
313. Zhou, A.J., Peel, S.A., Clokie, C.M. An evaluation of hydroxyapatite and biphasic calcium phosphate in combination with Pluronic F127 and BMP on bone repair. *J. Craniofac. Surg.* 18, 1264–1275, 2007; correction: 19, 871, 2008.
314. Bao, T.Q., Franco, R.A., Lee, B.T. Preparation and characterization of novel poly(ε-caprolactone)/biphasic calcium phosphate hybrid composite microspheres. *J. Biomed. Mater. Res. B Appl. Biomater.* 98B, 272–279, 2011.
315. Struillou, X., Rakic, M., Badran, Z., Macquigneau, L., Colombeix, C., Pilet, P., Verner, C.b, Gauthier, O., Weiss, P., Soueidan, A. The association of hydrogel and biphasic calcium phosphate in the treatment of dehiscence-type

peri-implant defects: an experimental study in dogs. *J. Mater. Sci. Mater. Med.* 24, 2749–2760, 2013.
316. Seyedlar, R.M., Nodehi, A., Atai, M., Imani, M. Gelation behavior of *in situ* forming gels based on HPMC and biphasic calcium phosphate nanoparticles. *Carbohyd. Polym*. 99, 257–263, 2014.
317. Bleach, N.C., Nazhat, S.N., Tanner, K.E., Kellomäki, M., Törmälä, P. Effect of filler content on mechanical and dynamic mechanical properties of particulate biphasic calcium phosphate-polylactide composites. *Biomaterials* 23, 1579–1585, 2002.
318. Sun, J.S., Lin, F.H., Wang, Y.J., Huang, Y.C., Chueh, S.C., Hsu, F.Y. Collagen-hydroxyapatite/tricalcium phosphate microspheres as a delivery system for recombinant human transforming growth factor-β1. *Artif. Organs* 27, 605–612, 2003.
319. Yang, C.R., Wang, Y.J., Chen, X.F., Zhao, N.R. Biomimetic fabrication of BCP/COL/HCA scaffolds for bone tissue engineering. *Mater. Lett*. 59, 3635–3640, 2005.
320. Radić, M., Ignjatović, N., Nedić, Z., Mitrić, M., Miličević, D., Uskoković, D. Synthesis and characterization of biphasic calcium phosphate/poly-(DL-lactide-*co*-glycolide) biocomposite. *Mater. Sci. Forum* 494, 537–542, 2005.
321. Ignjatović, N., Ninkov, P., Ajduković, Z., Konstantinović, V., Uskoković, D. Biphasic calcium phosphate/poly-(DL-lactide-*co*-glycolide) biocomposite as filler and blocks for reparation of bone tissue. *Mater. Sci. Forum* 494, 519–524, 2005.
322. Li, J., Habibovic, P., Yuan, H., van den Doel, M., Wilson, C.E., de Wijn, J.R., van Blitterswijk, C.A., de Groot, K. Biological performance in goats of a porous titanium alloy–biphasic calcium phosphate composite. *Biomaterials* 28, 4209–4218, 2007.
323. Ignjatovic, N., Ninkov, P., Ajdukovic, Z., Vasiljevic-Radovic, D., Uskokovic, D. Biphasic calcium phosphate coated with poly-D,L-lactide-*co*-glycolide biomaterial as a bone substitute. *J. Eur. Ceram. Soc.* 27, 1589–1594, 2007.
324. Oudadesse, H., Derrien, A.C., Mami, M., Martin, S., Cathelineau, G., Yahia, L. Aluminosilicates and biphasic HA-TCP composites: studies of properties for bony filling. *Biomed. Mater.* 2, S59–S64, 2007.
325. Urkmez, A.S., Jamison, R.D. The addition of biphasic calcium phosphate to porous chitosan scaffolds enhances bone tissue development *in vitro*. *J. Biomed. Mater. Res. A* 81A, 624–633, 2007.
326. Urkmez, A.S., Clark, S.G., Wheeler, M.B., Goldwasser, M.S., Jamison, R.D. Evaluation of chitosan/biphasic calcium phosphate scaffolds for maxillofacial bone tissue engineering. *Macromol. Symp.* 269, 100–105, 2008.
327. Lee, B.T., Quang, D.V., Youn, M.H., Song, H.Y. Fabrication of biphasic calcium phosphates/polycaprolactone composites by melt infiltration process. *J. Mater. Sci. Mater. Med.* 19, 2223–2229, 2008.
328. Wu, T.X., Yang, W.Z., Li, Y.D., Zhang, H.J., Chen, L.H., Zhou, D.L., Yin, G.F. Biocompatibility of biphasic calcium phosphate/poly L-lactic acid composite material. *J. Clin. Rehabil. Tissue Eng. Res.* 13, 4025–4028, 2009.

329. Shen, J., Li, Y., Zuo, Y., Zou, Q., Cheng, L., Zhang, L., Gong, M., Gao, S. Characterization and cytocompatibility of biphasic calcium phosphate/polyamide 6 scaffolds for bone regeneration. *J. Biomed. Mater. Res. B Appl. Biomater.* 95B, 330–338, 2010.
330. Bakhtiari, L., Rezaie, H.R., Hosseinalipour, S.M., Shokrgozar, M.A. Investigation of biphasic calcium phosphate/gelatin nanocomposite scaffolds as a bone tissue engineering. *Ceram. Int.* 36, 2421–2426, 2010.
331. Bakhtiari, L., Rezai, H.R., Hosseinalipour, S.M., Shokrgozar, M.A. Preparation of porous biphasic calcium phosphate-gelatin nanocomposite for bone tissue engineering. *J. Nano Res.* 11, 67–72, 2010.
332. Yang, W., Yin, G., Zhou, D., Gu, J., Li, Y. *In vitro* characteristics of surface-modified biphasic calcium phosphate/poly(L-lactide) biocomposite. *Adv. Eng. Mater*. 12, B128–B132, 2010.
333. Zhang, M.Y., Ye, C., Erasquin, U.J., Huynh, T., Cai, C., Cheng, G.J. Laser engineered multilayer coating of biphasic calcium phosphate/titanium nanocomposite on metal substrates. *ACS Appl. Mater. Interf*. 3, 339–350, 2011.
334. Puértolas, J.A., Vadillo, J.L., Sánchez-Salcedo, S., Nieto, A., Gómez-Barrena, E., Vallet-Regí, M. Compression behaviour of biphasic calcium phosphate and biphasic calcium phosphate–agarose scaffolds for bone regeneration. *Acta Biomater.* 7, 841–847, 2011.
335. Lee, J.H., Lee, Y.B., Rim, N.G., Jo, S.Y., Lim, Y.M., Shin, H. Development and characterization of nanofibrous poly(lactic-*co*-glycolic acid)/biphasic calcium phosphate composite scaffolds for enhanced osteogenic differentiation. *Macromol. Res*. 19, 172–179, 2011.
336. Kim, M., Franco, R.A., Lee, B.T. Synthesis of functional gradient BCP/ZrO_2 bone substitutes using ZrO_2 and BCP nanopowders. *J. Eur. Ceram. Soc.* 31, 1541–1548, 2011.
337. He, H., Yu, J., Cao, J., E, L., Wang, D., Zhang, H., Liu, H. Biocompatibility and osteogenic capacity of periodontal ligament stem cells on nHAC/PLA and HA/TCP scaffolds. *J. Biomater. Sci. Polym. Ed.* 22, 179–194, 2011.
338. Nie, L., Chen, D., Suo, J., Zou, P., Feng, S., Yang, Q., Yang, S., Ye, S. Physicochemical characterization and biocompatibility *in vitro* of biphasic calcium phosphate/polyvinyl alcohol scaffolds prepared by freeze-drying method for bone tissue engineering applications. *Colloids Surf. B* 100, 169–176, 2012.
339. Gunawan, Sopyan, I., Nurfaezah, S., Ammar, M. Development of triphasic calcium phosphate-carbon nanotubes (HA/TCP-CNT) composite: a preliminary study. *Key Eng. Mater.* 531–532, 258–261, 2013.
340. Silva, E.S., da Freitas, D.G., da Silva, S.N. Processing and characterization of a composite of hyaluronic acid (HA) and microspheres biphasic calcium phosphate (BCP) for dermal repair. *Key Eng. Mater.* 529–530, 421–425, 2013.
341. Chen, J.P., Tsai, M.J., Liao, H.T. Incorporation of biphasic calcium phosphate microparticles in injectable thermoresponsive hydrogel modulates bone cell proliferation and differentiation. *Colloids Surf. B* 110, 120–129, 2013.
342. Zhao, Y., Sun, K.N., Wang, W.L., Wang, Y.X., Sun, X.L., Liang, Y.J., Sun, X.N., Chui, P.F. Microstructure and anisotropic mechanical properties of graphene

nanoplatelet toughened biphasic calcium phosphate composite. *Ceram. Int.* 39, 7627–7634, 2013.

343. Bölükbaşı, N., Yeniyol, S., Tekkesin, M.S., Altunatmaz, K. The use of platelet-rich fibrin in combination with biphasic calcium phosphate in the treatment of bone defects: a histologic and histomorphometric study. *Curr. Ther. Res. Clin. Exp.* 75, 15–21, 2013.
344. Monmaturapoj, N., Thepsuwan, W., Hobang, N., Mai-Ngam, K. Influences of reinforcing agents on properties of biphasic calcium phosphate ceramics. *Adv. Appl. Ceram*. 112, 389–396, 2013.
345. van Leeuwen, A.C., Yuan, H., Passanisi, G., van der Meer, J.W., de Bruijn, J.D., van Kooten, T.G., Grijpma, D.W., Bos, R.R. Poly(trimethylene carbonate) and biphasic calcium phosphate composites for orbital floor reconstruction: a feasibility study in sheep. *Eur. Cell. Mater.* 27, 81–96, 2014; discussion 96–97.
346. Kwak, K.A., Jyoti, A.M., Song, H.Y. *In vitro* and *in vivo* studies of three dimensional porous composites of biphasic calcium phosphate/poly ε-caprolactone: effect of bio-functionalization for bone tissue engineering. *Appl. Surf. Sci*. 301, 307–314, 2014.
347. Badr-Mohammadi, M.R., Hesaraki, S., Zamanian, A. Mechanical properties and in vitro cellular behavior of zinc-containing nano-bioactive glass doped biphasic calcium phosphate bone substitutes. *J. Mater. Sci. Mater. Med.* 25, 185–197, 2014.
348. Kim, B.R., Nguyen, T.B.L., Min, Y.K., Lee, B.T. *In vitro* and *in vivo* studies of BMP-2-loaded PCL-gelatin-BCP electrospun scaffolds. *Tissue Eng. A* 20, 3279–3289, 2014.
349. Shin, Y.M., Jo, S.Y., Park, J.S., Gwon, H.J., Jeong, S.I., Lim, Y.M. Synergistic effect of dual-functionalized fibrous scaffold with BCP and RGD containing peptide for improved osteogenic differentiation. *Macromol. Biosci.* 14, 1190–1198, 2014.
350. Amirian, J., Linh, N.T.B., Min, Y.K., Lee, B.T. The effect of BMP-2 and VEGF loading of gelatin-pectin-BCP scaffolds to enhance osteoblast proliferation. *J. Appl. Polym. Sci.* 132, 41241, 2015.
351. Kumar, B.S., Muthukumar, T., Deepachitra, R., Charumathy, R.K., Hemalatha, T., Sastry, T.P. *In-vitro* evaluation of biphasic calcium phosphate/casein incorporated with *Myristica fragrans* for bone tissue engineering. *Ceram. Int.* 41, 1725–1734, 2015.
352. Amirian, J., Linh, N.T., Min, Y.K., Lee, B.T. Bone formation of a porous gelatin-pectin-biphasic calcium phosphate composite in presence of BMP-2 and VEGF. *Int. J. Biol. Macromol.* 76, 10–24, 2015.
353. Upho, N., Tangtrakulwanich, B., Pripatnanont, P., Thitiwongsawet, P., Ingviya, N. Development of novel PHBV/PCL and BCP composite for musculoskeletal infection: an *in vitro* vancomycin release and anti-MRSA effect. *J. Pharm. Innov.* 10, 211–221, 2015.
354. Jeong, J.O., Jeong, S.I., Shin, Y.M., Park, J.S., Gwon, H.J., An, S.J., Huh, J.B., Shin, H., Lim, Y.M. Development of acrylic acid grafted polycaprolactone (PCL)/biphasic calcium phosphate (BCP) nanofibers for bone tissue engineering using gamma-irradiation. *Polymer (Korea)* 39, 418–425, 2015.

355. Lee, E.U., Kim, D.J., Lim, H.C., Lee, J.S., Jung, U.W., Choi, S.H. Comparative evaluation of biphasic calcium phosphate and biphasic calcium phosphate collagen composite on osteoconductive potency in rabbit calvarial defect. *Biomater. Res.* 19, 1–7, 2015.
356. Seyfoori, A., Mirdamadi, S., Seyedraoufi, Z.S., Khavandi, A., Aliofkhazraei, M. Synthesis of biphasic calcium phosphate containing nanostructured films by micro arc oxidation on magnesium alloy. *Mater. Chem. Phys.* 142, 87–94, 2013.
357. Lee, T.M., Wang, B.C., Yang, Y.C., Chang, E., Yang, C.Y. Comparison of plasma-sprayed hydroxyapatite coatings and hydroxyapatite/tricalcium phosphate composite coatings: *in vivo* study. *J. Biomed. Mater. Res.* 5, 360–367, 2001.
358. Stewart, M., Welter, J.F., Goldberg, V.M. Effect of hydroxyapatite/tricalcium-phosphate coating on osseointegration of plasma-sprayed titanium alloy implants. *J. Biomed. Mater. Res. A* 69A, 1–10, 2004.
359. Hahn, B.D., Park, D.S., Choi, J.J., Ryu, J., Yoon, W.H., Lee, B.K., Kim, H.E. Effect of the HA/β-TCP ratio on the biological performance of calcium phosphate ceramic coatings fabricated by a room-temperature powder spray in vacuum. *J. Am. Ceram. Soc*. 92, 793–799, 2009.
360. Benhayoune, H., Drevet, R., Fauré, J., Potiron, S., Gloriant, T., Oudadesse, H., Laurent-Maquin, D. Elaboration of monophasic and biphasic calcium phosphate coatings on Ti6Al4 V substrate by pulsed electrodeposition current. *Adv. Eng. Mater*. 12, B192–B199, 2010.
361. Abudalazez, A.M.A., Kasim, S.R., Ariffin, A.B., Ahmad, Z.A. Effect of temperature on BCP ceramics coating on 316L stainless steel using electrophoretic technique. *Adv. Mater. Res*. 501, 66–70, 2012.
362. Abudalazez, A.M.A., Kasim, S.R., Ariffin, A.B., Ahmad, Z.A. Electrophoretic deposition of biphasic calcium phosphate (BCP) coatings on 316L stainless steel at room temperature. *Adv. Mater. Res*. 501, 169–175, 2012.
363. Elayaraja, K., Chandra, V.S., Joshy, M.I.A., Suganthi, R.V., Asokan, K., Kalkura, S.N. Nanocrystalline biphasic resorbable calcium phosphate (HAp/β-TCP) thin film prepared by electron beam evaporation technique. *Appl. Surf. Sci*. 274, 203–209, 2013.
364. Daculsi, G., LeGeros, R., Durand, M., Borget, P., Baroth, S., Goyenvalle, E., Aguado, E., Jegoux, F. Injectable apatitic calcium phosphate cements and microporous biphasic calcium phosphate granules complex for bone repair. *J. Australian Ceram. Soc*. 46, 1–5, 2010.
365. Khairoun, I., LeGeros, R.Z., Daculsi, G., Bouler, J.M., Guicheux, J., Gauthier, O. Macroporous resorbable and injectable calcium phosphate – based cements (MCPC) for bone repair augmentation regeneration and osteoporosis treatment. Eur. Patent 1 761 472 B1 2011.
366. Srakaew, N.L.O., Rattanachan, S.T. The pH-dependent properties of the biphasic calcium phosphate for bone cements. *J. Biomim. Biomater. Biomed. Eng.* 21, 3–16, 2014.
367. Yang, W.Z., Zhou, D.L., Yin, G.F., Li, G.D. Surface modification of biphasic calcium phosphate bioceramic powders. *Appl. Surf. Sci*. 255, 477–479, 2008.

368. Zhu, Z.L., Yu, H.Y., Zeng, Q., He, H.W. Characterization and biocompatibility of fluoridated biphasic calcium phosphate ceramics. *Appl. Surf. Sci.* 255, 552–554, 2008.
369. Katić, M.H.M., Babić, M.M. Sol-gel derived biphasic calcium phosphate ceramics on nitinol for medical applications. *Int. J. Electrochem. Sci.* 8, 1394–1408, 2013.
370. Abudalazez, A.M.A., Shah, R.K., Ariffin, A.B., Zainal, A.A. Preparation and characterization of biphasic calcium phosphate coatings on 316l stainless steel fabricated by electrophoretic deposition. *Adv. Mater. Res*. 620, 373–377, 2013.
371. Kwak, K.A., Kim, Y.H., Kim, M., Lee, B.T., Song, H.Y. Bio-functionalization of polycaprolactone infiltrated BCP scaffold with silicon and fibronectin enhances osteoblast activity *in vitro*. *Appl. Surf. Sci*. 279, 13–22, 2013.
372. Hu, J., Zhou, Y., Huang, L., Liu, J., Lu, H. Effect of nano-hydroxyapatite coating on the osteoinductivity of porous biphasic calcium phosphate ceramics. *BMC Musculoskelet. Disord.* 15, article 114, 2014.
373. Nie, L., Chen, D., Fu, J., Yang, S., Hou, R., Suo, J. Macroporous biphasic calcium phosphate scaffolds reinforced by poly-L-lactic acid/hydroxyapatite nanocomposite coatings for bone regeneration. *Biochem. Eng. J*. 98, 29–37, 2015.
374. Hu, J., Yang, Z., Zhou, Y., Liu, Y., Li, K., Lu, H. Porous biphasic calcium phosphate ceramics coated with nano-hydroxyapatite and seeded with mesenchymal stem cells for reconstruction of radius segmental defects in rabbits. *J. Mater. Sci. Mater. Med.* 26, article 257, 2015.
375. Choi, Y.R., Kwon, J.S., Song, D.H., Choi, E.H., Lee, Y.K., Kim, K.N., Kim, K.M. Surface modification of biphasic calcium phosphate scaffolds by non-thermal atmospheric pressure nitrogen and air plasma treatment for improving osteoblast attachment and proliferation. *Thin Solid Films* 547, 235–240, 2013.
376. Piattelli, A., Scarano, A., Mangano, C. Clinical and histologic aspects of biphasic calcium phosphate ceramic (BCP) used in connection with implant placement. *Biomaterials* 17, 1767–1770, 1996.
377. Arinzeh, T.L., Tran, T., Mcalary, J., Daculsi, G. A comparative study of biphasic calcium phosphate ceramics for human mesenchymal stem-cell-induced bone formation. *Biomaterials* 26, 3631–3638, 2005.
378. Yuan, H., van Blitterswijk, C.A., de Groot, K., de Bruijn, J.D. A comparison of bone formation in biphasic calcium phosphate (BCP) and hydroxyapatite (HA) implanted in muscle and bone of dogs at different time periods. *J. Biomed. Mater. Res. A* 78A, 139–147, 2006.
379. Yuan, H., van Blitterswijk, C.A., de Groot, K., de Bruijn, J.D. Cross-species comparison of ectopic bone formation in biphasic calcium phosphate (BCP) and hydroxyapatite (HA) scaffolds. *Tissue Eng*. 12, 1607–1615, 2006.
380. Balçik, C., Tokdemir, T., Senköylü, A., Koç, N., Timuçin, M., Akin, S., Korkusuz, P., Korkusuz, F. Early weight bearing of porous HA/TCP (60/40)

ceramics *in vivo*: a longitudinal study in a segmental bone defect model of rabbit. *Acta Biomater.* 3, 985–996, 2007.
381. Kurashina, K., Kurita, H., Wu, Q., Ohtsuka, A., Kobayashi, H. Ectopic osteogenesis with biphasic ceramics of hydroxyapatite and tricalcium phosphate in rabbits. *Biomaterials* 23, 407–412, 2002.
382. Zhang, L., Hanagata, N., Maeda, M., Minowa, T., Ikoma, T., Fan, H., Zhang, X. Porous hydroxyapatite and biphasic calcium phosphate ceramics promote ectopic osteoblast differentiation from mesenchymal stem cells. *Sci. Technol. Adv. Mater.* 10, 025003 (9 pages), 2009.
383. Jafarian, M., Eslaminejad, M.B., Khojasteh, A., Abbas, F.M., Dehghan, M.M., Hassanizadeh, R., Houshmand, B. Marrow-derived mesenchymal stem cells-directed bone regeneration in the dog mandible: a comparison between biphasic calcium phosphate and natural bone mineral. *Oral Surg. Oral Med. Oral Pathol. Oral Radiol. Endod*. 105, e14–e24, 2008.
384. Jensen, S.S., Bornstein, M.M., Dard, M., Bosshardt, D.D., Buser, D. Comparative study of biphasic calcium phosphates with different HA/TCP ratios in mandibular bone defects. A long-term histomorphometric study in minipigs. *J. Biomed. Mater. Res. B Appl. Biomater.* 90B, 171–181, 2009.
385. Fellah, B.H., Gauthier, O., Weiss, P., Chappard, D., Layrolle, P. Osteogenicity of biphasic calcium phosphate ceramics and bone autograft in a goat model. *Biomaterials* 29, 1177–1188, 2008.
386. de Lange, G.L., Overman, J.R., Farré-Guasch, E., Korstjens, C.M., Hartman, B., Langenbach, G.E.J., van Duin, M.A., Klein-Nulend, J. A histomorphometric and micro-computed tomography study of bone regeneration in the maxillary sinus comparing biphasic calcium phosphate and deproteinized cancellous bovine bone in a human split-mouth model. *Oral Surg. Oral Med. Oral Pathol. Oral Radiol.* 117, 8–22, 2014.
387. Grandi, G., Heitz, C., dos Santos, L.A., Silva, M.L., Filho, M.S., Pagnocelli, R.M., Silva, D.N. Comparative histomorphometric analysis between α-Tcp cement and β-Tcp/Ha granules in the bone repair of rat calvaria. *Mater. Res.* 14, 11–16, 2011.
388. Froum, S.J., Wallace, S.S., Cho, S.C., Elian, N., Tarnow, D.P. Histomorphometric comparison of a biphasic bone ceramic to anorganic bovine bone for sinus augmentation: 6- to 8-month postsurgical assessment of vital bone formation. A pilot study. *Int. J. Periodontics Restorative Dent*. 28, 273–281, 2008.
389. Pandit, N., Gupta, R., Gupta, S. A comparative evaluation of biphasic calcium phosphate material and bioglass in the treatment of periodontal osseous defects: a clinical and radiological study. *J. Contemp. Dent. Pract*. 11, 025–032, 2010.
390. Kunert-Keil, C., Scholz, F., Gedrange, T., Gredes, T. Comparative study of biphasic calcium phosphate with beta-tricalcium phosphate in rat cranial defects – a molecular-biological and histological study. *Ann. Anat*. 199, 79–84, 2015.

391. Chakar, C., Soffer, E., Cohen, N., Petite, H., Naaman, N., Anagnostou, F. Vertical bone regeneration with deproteinised bovine bone mineral or biphasic calcium phosphate in the rabbit calvarium: effect of autologous platelet lysate. *J. Mater. Sci. Mater. Med.* 26, article 23, 2015.
392. Miron, R.J., Sculean, A., Shuang, Y., Bosshardt, D.D., Gruber, R., Buser, D., Chandad, F., Zhang, Y. Osteoinductive potential of a novel biphasic calcium phosphate bone graft in comparison with autographs, xenografts, and DFDBA. *Clin. Oral Implants Res*. 27, 668–675, 2016.
393. Jensen, S.S., Yeo, A., Dard, M., Hunziker, E., Schenk, R., Buser, D. Evaluation of a novel biphasic calcium phosphate in standardized bone defects: a histologic and histomorphometric study in the mandibles of minipigs. *Clin. Oral Implants Res*. 18, 752–760, 2007.
394. Nery, E.B., LeGeros, R.Z., Lynch, K.L., Lee, K. Tissue response to biphasic calcium phosphate ceramic with different ratios of HA/β-TCP in periodontal osseous defects. *J. Periodontol*. 63, 729–735, 1992.
395. Shiwaku, Y., Neff, L., Nagano, K., Takeyama, K.I., de Bruijn, J., Dard, M., Gori, F., Baron, R. The crosstalk between osteoclasts and osteoblasts is dependent upon the composition and structure of biphasic calcium phosphates. *PLoS One* 10, article number e0132903, 2015.
396. Cho, J.S., Chung, C.P., Rhee, S.H. Bioactivity and osteoconductivity of biphasic calcium phosphates. *Bioceram. Dev. Appl*. 2011, 1, Article ID D101129, 3 pages.
397. Suzuki, T., Hukkanen, M., Ohashi, R., Yokogawa, Y., Nishizawa, K., Nagata, F., Buttery, L., Polak, J. Growth and adhesion of osteoblast-like cells derived from neonatal rat calvaria on calcium phosphate ceramics. *J. Biosci. Bioeng*. 89, 18–26, 2000.
398. Ebrahimi, M, Pripatnanont, P., Suttapreyasri, S., Monmaturapoj, N. *In vitro* biocompatibility analysis of novel nano-biphasic calcium phosphate scaffolds in different composition ratios. *J. Biomed. Mater. Res. B Appl. Biomater.* 102B, 52–61, 2014.
399. Wang, L., Barbieri, D., Zhou, H., de Bruijn, J.D., Bao, C., Yuan, H. Effect of particle size on osteoinductive potential of microstructured biphasic calcium phosphate ceramic. *J. Biomed. Mater. Res. A* 103A, 1919–1929, 2015.
400. Malard, O., Bouler, J.M., Guicheux, J., Heymann, D., Pilet, P., Coquard, C., Daculsi, G. Influence of biphasic calcium phosphate granulometry on bone ingrowth, ceramic resorption, and inflammatory reactions: preliminary *in vitro* and *in vivo* study. *J. Biomed. Mater. Res.* 46, 103–111, 1999.
401. Curran, J.M., Gallagher, J.A., Hunt, J.A. The inflammatory potential of biphasic calcium phosphate granules in osteoblast/macrophage co-culture. *Biomaterials* 26, 5313–5320, 2005.
402. Fellah, B.H., Josselin, N., Chappard, D., Weiss, P., Layrolle, P. Inflammatory reaction in rats muscle after implantation of biphasic calcium phosphate micro particles. *J. Mater. Sci. Mater. Med.* 18, 287–294, 2007.

403. Fellah, B.H., Delorme, B., Sohier, J., Magne, D., Hardouin, P., Layrolle, P. Macrophage and osteoblast responses to biphasic calcium phosphate microparticles. *J. Biomed. Mater. Res. A* 93A, 1588–1595, 2010.
404. Daculsi, G., Passuti, N., Martin, S., Deudon, C., LeGeros, R.Z., Raher, S. Macroporous biphasic calcium phosphate ceramic for long bone surgery in human and dogs: clinical and histological study. *J. Biomed. Mater. Res.* 24, 379–396, 1990.
405. Schwartz, C., Liss, P., Jacquemaire, B., Lecestre, P., Frayssinet, P. Biphasic synthetic bone substitute use in orthopaedic and trauma surgery: clinical, radiological and histological results. *J. Mater. Sci. Mater. Med.* 10, 821–825, 1999.
406. Bodde, E.W.H., Wolke, J.G.C., Kowalski, R.S.Z., Jansen, J.A. Bone regeneration of porous β-tricalcium phosphate (Conduit™ TCP) and of biphasic calcium phosphate ceramic (Biosel®) in trabecular defects in sheep. *J. Biomed. Mater. Res. A* 82A, 711–722, 2007.
407. Ozalay, M., Sahin, O., Akpinar, S., Ozkoc, G., Cinar, M., Cesur, N. Remodeling potentials of biphasic calcium phosphate granules in open wedge high tibial osteotomy. *Arch. Orthop. Trauma Surg*. 129, 747–752, 2009.
408. Lobo, S.E., Wykrota, F.H., Oliveira, A.C., Kerkis, I., Mahecha, G.B., Alves, H.J. Quantification of bone mass gain in response to the application of biphasic bioceramics and platelet concentrate in critical-size bone defects. *J. Mater. Sci. Mater. Med.* 20, 1137–1147, 2009.
409. Garrido, C.A., Lobo, S.E., Turíbio, F.M., LeGeros, R.Z. Biphasic calcium phosphate bioceramics for orthopaedic reconstructions: clinical outcomes. *Int. J. Biomater*. 2011, 129727 (9 pages), 2011.
410. Petronis, S., Petronis, J., Zalite, V., Locs, J., Skagers, A., Pilmane, M. New biphasic calcium phosphate in orthopedic surgery: first clinical results. *IFMBE Proc*. 38 IFMBE, 174–177, 2013.
411. Suneelkumar, C., Datta, K., Srinivasan, M.R., Kumar, S.T. Biphasic calcium phosphate in periapical surgery. *J. Conserv. Dent*. 11, 92–96, 2008.
412. Moore, D.C., Chapman, M.W., Manske, D. The evaluation of a biphasic calcium phosphate ceramic for use in grafting long-bone diaphyseal defects. *J. Orthop. Res*. 5, 356–365, 1987.
413. Soares, L.G.P., Marques, A.M.C., Guarda, M.G., Aciole, J.M.S., dos Santos, J.N. Pinheiro, A.L.B. Influence of the λ780 nm laser light on the repair of surgical bone defects grafted or not with biphasic synthetic micro-granular hydroxylapatite + beta-calcium triphosphate. *J. Photoch. Photobio. B* 131, 16–23, 2014.
414. Park, J.W., Kim, E.S., Jang, J.H., Suh, J.Y., Park, K.B., Hanawa, T. Healing of rabbit calvarial bone defects using biphasic calcium phosphate ceramics made of submicron-sized grains with a hierarchical pore structure. *Clin. Oral Implants Res*. 21, 268–276, 2010.
415. de C. Silva, L.G.R., Kim, S.H., Luczyszyn, S.M., Papalexiou, V., Giovanini, A., Almeida, L.E., Tramontina, V.A. Histological and immunohistochemical evaluation of biphasic calcium phosphate and a mineral trioxide aggregate

for bone healing in rat calvaria. *Int. J. Oral Maxillofac. Surg.* 44, 535–542, 2015.
416. de Gabory, L., Bareille, R., Stoll, D., Bordenave, L., Fricain, J.C. Biphasic calcium phosphate to repair nasal septum: the first *in vitro* and *in vivo* study. *Acta Biomater.* 6, 909–919, 2010.
417. de Gabory, L., Delmond, S., Deminiere, C., Stoll, D., Bordenave, L., Fricain, J.C. Assessment of biphasic calcium phosphate to repair nasal septum defects in sheep. *Plast. Reconstr. Surg.* 127, 107–116, 2011.
418. Wang, J., Chen, W., Li, Y., Fan, S., Weng, J., Zhang, X. Biological evaluation of biphasic calcium phosphate ceramic vertebral laminae. *Biomaterials* 19, 1387–1392, 1998.
419. Bolder, S.B., Verdonschot, N., Schreurs, B.W., Buma, P. Acetabular defect reconstruction with impacted morsellized bone grafts or TCP/HA particles. A study on the mechanical stability of cemented cups in an artificial acetabulum model. *Biomaterials* 23, 659–666, 2002.
420. Nich, C., Bizot, P., Nizard, R., Sedel, L. Femoral reconstruction with macroporous biphasic calcium phosphate ceramic in revision hip replacement. *Key Eng. Mater.* 240–242, 853–856, 2003.
421. Zwetyenga, N., Catros, S., Emparanza, A., Deminiere, C., Siberchicot, F., Fricain, J.C. Mandibular reconstruction using induced membranes with autologous cancellous bone graft and HA-βTCP: animal model study and preliminary results in patients. *Int. J. Oral Maxillofac. Surg.* 38, 1289–1297, 2009.
422. Huang, M.S., Wu, H.D., Teng, N.C., Peng, B.Y., Wu, J.Y., Chang, W.J., Yang, J.C., Chen, C.C., Lee, S.Y. *In vivo* evaluation of poorly crystalline hydroxyapatite-based biphasic calcium phosphate bone substitutes for treating dental bony defects. *J. Dent. Sci.* 5, 100–108, 2010.
423. Sunil, P., Goel, S.C., Rastogi, A., Aryya, N.C. Incorporation and biodegradation of hydroxyapatite–tricalcium phosphate implanted in large metaphyseal defects – an animal study. *Indian J. Exp. Biol.* 46, 836–841, 2008.
424. Kim, S.E., Yun, Y.P., Song, H.R., Choi, K.H., Kim, B.H., Lee, E.K., Song, J.J. Bone formation of middle ear cavity using biphasic calcium phosphate lyophilized with *Escherichia coli*-derived recombinant human bone morphogenetic protein 2 using animal model. *Int. J. Pediatr. Otorhinolaryngol.* 77, 1430–1433, 2013.
425. Rouvillain, J.L., Lavallé, F., Pascal-Mousselard, H., Catonné, Y., Daculsi, G. Clinical, radiological and histological evaluation of biphasic calcium phosphate bioceramic wedges filling medial high tibial valgisation osteotomies. *Knee* 16, 392–397, 2009.
426. Cho, D.Y., Lee, W.Y., Sheu, P.C., Chen, C.C. Cage containing a biphasic calcium phosphate ceramic (Triosite) for the treatment of cervical spondylosis. *Surg. Neurol.* 63, 497–503, 2005; discussion 503–504.
427. Grybauskas, S., Locs, J., Salma, I., Salms, G., Berzina-Cimdina, L. Volumetric analysis of implanted biphasic calcium phosphate/collagen composite by

three-dimensional cone beam computed tomography head model superimposition. *J. Craniomaxillofac. Surg.* 43, 167–174, 2015.
428. Artzi, Z., Weinreb, M., Carmeli, G., Lev-Dor, R., Dard, M., Nemcovsky, C.E. Histomorphometric assessment of bone formation in sinus augmentation utilizing a combination of autogenous and hydroxyapatite/biphasic tricalcium phosphate graft materials: at 6 and 9 months in humans. *Clin. Oral Implants Res.* 19, 686–692, 2008.
429. Lee, J.H., Jung, U.W., Kim, C.S., Choi, S.H., Cho, K.S. Histologic and clinical evaluation for maxillary sinus augmentation using macroporous biphasic calcium phosphate in human. *Clin. Oral Implants Res*. 19, 767–771, 2008.
430. Friedmann, A., Dard, M., Kleber, B.M., Bernimoulin, J.P., Bosshardt, D.D. Ridge augmentation and maxillary sinus grafting with a biphasic calcium phosphate: histologic and histomorphometric observations. *Clin. Oral Implants Res*. 20, 708–714, 2009.
431. Lindgren, C., Hallman, M., Sennerby, L., Sammons, R. Back-scattered electron imaging and elemental analysis of retrieved bone tissue following sinus augmentation with deproteinized bovine bone or biphasic calcium phosphate. *Clin. Oral Implants Res*. 21, 924–930, 2010.
432. Seong, K.C., Cho, K.S., Daculsi, C., Seris, E., Daculsi, G. Eight-year clinical follow-up of sinus grafts with micro-macroporous biphasic calcium phosphate granules. *Key Eng. Mater.* 587, 321–324, 2014.
433. Nery, E.B., Lee, K.K., Czajkowski, S., Dooner, J.J., Duggan, M., Ellinger, R.F., Henkin, J.M., Hines, R., Miller, M., Olson, J.W. A Veterans Administration Cooperative Study of biphasic calcium phosphate ceramic in periodontal osseous defects. *J. Periodontol.* 61, 737–744, 1990.
434. Daculsi, G., Corlieu, P., Bagot D'Arc, M., Gersdorff, M. Macroporous biphasic calcium phosphate efficiency in mastoid cavity obliteration: experimental and clinical findings. *Ann. Otol. Rhinol. Laryngol.* 101, 669–674, 1992.
435. Toth, J.M., An, H.S., Lim, T.H., Ran, Y., Weiss, N.G., Lundberg, W.R., Xu, R.M., Lynch, K.L. Evaluation of porous biphasic calcium phosphate ceramics for anterior cervical interbody fusion in a caprine model. *Spine* 20, 2203–2210, 1995.
436. Shi, H., Ma, J., Zhao, N., Chen, Y., Liao, Y. Periodontal regeneration in experimentally-induced alveolar bone dehiscence by an improved porous biphasic calcium phosphate ceramic in beagle dogs. *J. Mater. Sci. Mater. Med.* 19, 3515–3524, 2008.
437. Wang, Y., Ni, M., Tang, P.F., Li, G. Novel application of HA-TCP biomaterials in distraction osteogenesis shortened the lengthening time and promoted bone consolidation. *J. Orthop. Res*. 27, 477–482, 2009.
438. Wang, L., Shi, H., Chen, Y., Xue, J., Chen, Y., Liao, Y. Healing of acute alveolar bone dehiscence following treatment with porous biphasic calcium phosphate in beagle dogs. *Clin. Oral Invest*. 15, 983–991, 2011.
439. Chen, L., Liu, H.L., Gu, Y., Feng, Y., Yang, H.L. Lumbar interbody fusion with porous biphasic calcium phosphate enhanced by recombinant bone

morphogenetic protein-2/silk fibroin sustained-released microsphere: an experimental study on sheep model. *J. Mater. Sci. Mater. Med*. 26, article 126, 2015.

440. de Carvalho, F.B., Aciole, G.T.S., Aciolea, J.M.S., Silveira, Jr., L., dos Santos, J.N., Pinheiro, A.L.B. Assessment of bone healing on tibial fractures treated with wire osteosynthesis associated or not with infrared laser light and biphasic ceramic bone graft (HATCP) and guided bone regeneration (GBR): Raman spectroscopy study. *Proc. SPIE* 7887, 78870 T, 2011.
441. Su, B., Su, J., Ran, J., Su, B. Biological performance of dental biphasic calcium phosphate ceramics modified by cold plasma. *Key Eng. Mater.* 368–372, 1264–1267, 2008.
442. Grimes, J.S., Bocklage, T.J., Pitcher, J.D. Collagen and biphasic calcium phosphate bone graft in large osseous defects. *Orthopedics* 29, 145–148, 2006.
443. Zorica, A., Nenad, I., Dragan, P., Dragan, U. Substitution of osteoporotic alveolar bone by biphasic calcium phosphate/poly-DL-lactide-*co*-glycolide biomaterials. *J. Biomater. Appl.* 21, 317–328, 2007.
444. Im, G.I., Ahn, J.H., Kim, S.Y., Choi, B.S., Lee, S.W. A hyaluronate-atelocollagen/*β*-tricalcium phosphate-hydroxyapatite biphasic scaffold for the repair of osteochondral defects: a porcine study. *Tissue Eng. A* 16, 1189–1200, 2010.
445. Struillou, X., Boutigny, H., Badran, Z., Fellah, B.H., Gauthier, O., Sourice, S., Pilet, P., Rouillon, T., Layrolle, P., Weiss, P., Soueidan, A. Treatment of periodontal defects in dogs using an injectable composite hydrogel/biphasic calcium phosphate. *J. Mater. Sci. Mater. Med.* 22, 1707–1717, 2011.
446. Gautier, H., Merle, C., Auget, J.L., Daculsi, G. Isostatic compression, a new process for incorporating vancomycin into biphasic calcium phosphate: comparison with a classical method. *Biomaterials* 21, 243–249, 2000.
447. Sunder, M., Babu, N.R., Victor, S.P., Kumar, K.R., Kumar, T.S.S. Biphasic calcium phosphates for antibiotic release. *Trends Biomaterials Artif. Organs* 18, 213–218, 2005.
448. Laurent, F., Bignon, A., Goldnadel, J., Chevalier, J., Fantozzi, G., Viguier, E., Roger, T., Boivin, G., Hartmann, D. A new concept of gentamicin loaded HAP/TCP bone substitute for prophylactic action: *in vitro* release validation. *J. Mater. Sci. Mater. Med.* 19, 947–951, 2008.
449. Viguier, E., Bignon, A., Laurent, F., Goehrig, D., Boivin, G., Chevalier, J. A new concept of gentamicin loaded HAP/TCP bone substitute for prophylactic action: *in vivo* pharmacokinetic study. *J. Mater. Sci. Mater. Med.* 22, 879–886, 2011.
450. Kim, S.E., Yun, Y.P., Lee, D.W., Kang, E.Y., Jeong, W.J., Lee, B. , Jeong, M.S., Kim, H.J., Park, K., Song, H.R. Alendronate-eluting biphasic calcium phosphate (BCP) scaffolds stimulate osteogenic differentiation. *BioMed Res. Int.* 320713, 2015.
451. Schopper, C., Moser, D., Spassova, E., Goriwoda, W., Lagogiannis, G., Hoering, B., Ewers, R., Redl, H. Bone regeneration using a naturally grown

HA/TCP carrier loaded with rhBMP-2 is independent of barrier-membrane effects. *J. Biomed. Mater. Res. A* 85A, 954–963, 2008.
452. Kim, J.W., Choi, K.H., Yun, J.H., Ui-Won, J., Kim, C.S., Choi, S.H., Cho, K.S. Bone formation of block and particulated biphasic calcium phosphate lyophilized with *Escherichia coli*-derived recombinant human bone morphogenetic protein 2 in rat calvarial defects. *Oral Surg. Oral Med. Oral Pathol. Oral Radiol. Endod*. 112, 298–306, 2011.
453. Jang, J.W., Yun, J.H., Lee, K.I., Jang, J.W., Jung, U.W., Kim, C.S., Choi, S.H., Cho, K.S. Osteoinductive activity of biphasic calcium phosphate with different rhBMP-2 doses in rats. *Oral Surg. Oral Med. Oral Pathol. Oral Radiol. Endod*. 113, 480–487, 2012.
454. Park, J.C., So, S.S., Jung, I.H., Yun, J.H., Choi, S.H., Cho, K.S., Kim, C.S. Induction of bone formation by *Escherichia coli*-expressed recombinant human bone morphogenetic protein-2 using block-type macroporous biphasic calcium phosphate in orthotopic and ectopic rat models. *J. Periodontal. Res.* 46, 682–690, 2011.
455. Schwarz, F., Sager, M., Ferrari, D., Mihatovic, I., Becker, J. Influence of recombinant human platelet-derived growth factor on lateral ridge augmentation using biphasic calcium phosphate and guided bone regeneration: a histomorphometric study in dogs. *J. Periodontol.* 80, 1315–1323, 2009.
456. Gaebler, A., Schaefer, T., Fischer, K., Scharnweber, D., Mauth, C., Schwenzer, B. Peptide linkers for the immobilization of bioactive molecules on biphasic calcium phosphate via a modular immobilization system. *Acta Biomater.* 9, 4899–4905, 2013.
457. Balaguer, T., Boukhechba, F., Clavé, A., Bouvet-Gerbettaz, S., Trojani, C., Michiels, J.F., Laugier, J.P., Bouler, J.M., Carle, G.F., Scimeca, J.C., Rochet, N. Biphasic calcium phosphate microparticles for bone formation: benefits of combination with blood clot. *Tissue Eng. A* 16, 3495–3505, 2010.
458. Mouline, C.C., Quincey, D., Laugier, J.P., Carle, G.F., Bouler, J.M., Rochet, N., Scimeca, J.C. Osteoclastic differentiation of mouse and human monocytes in a plasma clot/biphasic calcium phosphate microparticles composite. *Eur. Cell Mater*. 20, 379–391, 2010; discussion 391–392.
459. Paul, A.J., Momier, D., Boukhechba, F., Michiels, J.F., Lagadec, P., Rochet, N. Effect of G-CSF on the osteoinductive property of a BCP/blood clot composite. *J. Biomed. Mater. Res. A* 103A, 2830–2838, 2015.
460. Castellani, C., Zanoni, G., Tangl, S., van Griensven, M., Redl, H. Biphasic calcium phosphate ceramics in small bone defects: potential influence of carrier substances and bone marrow on bone regeneration. *Clin. Oral Implants Res*. 20, 1367–1374, 2009.
461. Ignjatovic, N., Ajdukovic, Z., Uskokovic, D. New biocomposite [biphasic calcium phosphate/poly-DL-lactide-*co*-glycolide/biostimulative agent] filler for reconstruction of bone tissue changed by osteoporosis. *J. Mater. Sci. Mater. Med.* 16, 621–626, 2005.
462. Sculean, A., Windisch, P., Szendröi-Kiss, D., Horváth, A., Rosta, P., Becker, J., Gera, I., Schwarz, F. Clinical and histologic evaluation of an enamel matrix

derivative combined with a biphasic calcium phosphate for the treatment of human intrabony periodontal defects. *J. Periodontol.* 79, 1991–1999, 2008.

463. Son, S.R., Sarkar, S.K., Linh, N.T.B., Padalhin, A.R., Kim, B.R., Jung, H.I., Lee, B.T. Platelet-rich plasma encapsulation in hyaluronic acid/gelatin-BCP hydrogel for growth factor delivery in BCP sponge scaffold for bone regeneration. *J. Biomater. Appl.* 29, 988–1002, 2015.
464. Livingston, T.L., Gordon, S., Archambault, M., Kadiyala, S., Mcintosh, K., Smith, A., Peter, S.J. Mesenchymal stem cells combined with biphasic calcium phosphate ceramics promote bone regeneration. *J. Mater. Sci. Mater. Med.* 14, 211–218, 2003.
465. Wang, J., Qiu, Y., Xia, C.L., Tang, X.B., Hu, Y. Enriched bone marrow mesenchymal stem cells combined with HA/TCP for spine fusion. *J. Clin. Rehabil. Tissue Eng. Res*. 11, 5536–5539, 2007.
466. Ng, A.M.H., Tan, K.K., Phang, M.Y., Aziyati, O., Tan, G.H., Isa, M.R., Aminuddin, B.S., Naseem, M., Fauziah, O., Ruszymah, B.H.I. Differential osteogenic activity of osteoprogenitor cells on HA and TCP/HA scaffold of tissue engineered bone. *J. Biomed. Mater. Res. A* 85A, 301–312, 2008.
467. Zhang, W., Walboomers, X.F., van Osch, G.J.V.M., van den Dolder, J., Jansen, J.A. Hard tissue formation in a porous HA/TCP ceramic scaffold loaded with stromal cells derived from dental pulp and bone marrow. *Tissue Eng. A* 14, 285–294, 2008.
468. Wang, T., Tian, W.D., Li, S.W., Liao, Y.M. Biphasic calcium phosphate nanocomposite loaded with bone marrow stromal cells for repair of critical cranial defect in rats. *J. Clin. Rehabil. Tissue Eng. Res*. 12, 2606–2610, 2008.
469. Gamblin, A.L., Brennan, M.A., Renaud, A., Yagita, H., Lézot, F., Heymann, D., Trichet, V., Layrolle, P. Bone tissue formation with human mesenchymal stem cells and biphasic calcium phosphate ceramics: the local implication of osteoclasts and macrophages. *Biomaterials* 35, 9660–9667, 2014.
470. Brennan, M.A., Renaud, A., Amiaud, J., Rojewski, M.T., Schrezenmeier, H., Heymann, D., Trichet, V., Layrolle, P. Pre-clinical studies of bone regeneration with human bone marrow stromal cells and biphasic calcium phosphate. *Stem Cell Res. Therapy* 5, article 428, 2014.
471. Jan, A., Sándor, G.K., Brkovic, B.B., Peel, S., Kim, Y.D., Xiao, W.Z., Evans, A.W., Clokie, C.M. Effect of hyperbaric oxygen on demineralized bone matrix and biphasic calcium phosphate bone substitutes. *Oral Surg. Oral Med. Oral Pathol. Oral Radiol. Endod.* 109, 59–66, 2010.
472. Rohanizadeh, R., Padrines, M., Bouler, J.M., Couchourel, D., Fortun, Y., Daculsi, G. Apatite precipitation after incubation of biphasic calcium-phosphate ceramic in various solutions: influence of seed species and proteins. *J. Biomed. Mater. Res.* 42, 530–539, 1998.
473. Kim, K.L., Ok, K.M., Kim, D.H., Park, H.C., Yoon, S.Y. Fabrication and characterization of biphasic calcium phosphate scaffolds with an unidirectional macropore structure using tertiary-butyl alcohol-based freeze-gel casting method. *J. Korean Ceram. Soc*. 50, 263–268, 2013.

3

An Energy Efficient Processing Route for Advance Ceramic Composites Using Microwaves

Satnam Singh*, Dheeraj Gupta and Vivek Jain

Department of Mechanical Engineering, Thapar University, Patiala, India

Abstract

The recent development in advanced ceramic materials has revolutionized the technologies in various industries such as aerospace engineering, surface engineering, and structural components. These materials have proved their worth in cutthroat engineering and technological advancement era. Conventional processing methods for ceramic composites are getting obsolete due to limitations in processing of variety of materials and higher energy consumptions. Sustainability of any processing method depends upon the lower-energy requirements, lower processing times, better properties of processed material, and eco-friendly characteristics. Earlier developments in the microwave material processing were reported in heating of foodstuffs, processing of rubbers, plastics, drying of wood, and enhancing chemical reactions that require lower temperatures. These developments paved the path for higher-temperature applications including processing of various ceramics, glasses, and metallic powders. The sintering process of ceramics with microwave energy proved all the beneficial characteristics and allowed enhanced diffusion rates with higher product density, which allowed commercialization of this process. However, the processing of metallic materials with microwaves is a challenging task due to opaque characteristics of metals, which tends to reflect them. These challenges were recently overcome, and microwaves were successfully employed for bulk metallic processing using hybrid heating concepts. Present work focuses on the applications of efficient microwave processing in manufacturing sectors such as development of cermets/composite claddings on bulk steel surfaces, joining of various bulk metals, and casting of metal–ceramic composites. These processes exhibit lower defects in the processed material owing

**Corresponding author*: satnam.singh@thapar.edu

Ashutosh Tiwari, Rosario A. Gerhardt and Magdalena Szutkowska (eds.) Advanced Ceramic Materials, (97–144) © 2016 Scrivener Publishing LLC

to the uniform heating provided by microwaves. In near future, microwave material processing will be developed and employed at large scale for various industrial applications.

***Keywords*:** Microwaves, heating, cermets, composites, casting, cladding, joining, microstructure, microhardness, defects

3.1 Introduction

The advanced applications of ceramic-based materials in the field of aerospace, nuclear, automobile, mechanical, thermal, etc. allowed ceramic composites as substitute for the conventional monolithic metals [1–5]. The unique characteristics of metal–ceramic composite materials in terms of higher working temperatures, higher thermal stability, higher wear, and corrosion resistance allowed enhanced application in cutthroat engineering applications [6–8]. The lack of ductility and aggregation further allowed metal–ceramic composites to grow over sintered pure ceramics materials. There is huge demand from the industry to develop materials having high structure–property [9, 10] correlations, as it is well known that the properties and performance of materials directly depends upon the microstructures of the materials. To enhance physical and mechanical properties of materials, finer microstructures are essential. This is the area where microwave heating technology is found to be profitable and helps in the mitigation of defects like porosity, cracking, microstructure dislocations, etc. and suppression of these defects allows refinement in properties [11–13]. In the past few decades, microwave oven has become one of the important electrical appliances in kitchen, which allowed faster food heating and processing. The benefits of higher cooking rates coupled with lower-energy consumptions over conventional cooking methods allowed tremendous growth in microwave oven R&D industries. Although widespread utilization of microwaves in cooking food has been utilized since discovery of ovens, processing of materials through microwave energy is relatively new development. In processing of materials via microwaves, the developments in processing of metals and metallic powders are relatively challenging and are of current interest. These materials, including metal matrix composites, ceramics and cermets, require high temperatures for processing and are exigent for researchers.

James Clerk Maxwell predicted the existence of microwaves in the year 1865 in the electromagnetic spectrum by using Maxwell's equations. Microwaves frequency ranges from 0.3 to 300 GHz with corresponding wavelengths of 1 m to 1 mm in air [14–16]. The effects of heating by

microwaves were accidently discovered by P.L. Spencer who filed the patent [17] on heating foodstuffs using microwaves in 1945. Initially, microwaves were utilized for communication systems including broadcasting and radar; however, with the discovery of heating effects, microwaves were used for material processing [18–20]. The most common frequencies used for industrial and heating applications are 0.915 and 2.45 GHz. The most of domestic microwave ovens works on 2.45 GHz frequency; however, higher-frequency microwave furnaces ranging from 1 to 18 GHz have been developed for material processing [21–23]. Microwave heating offers certain advantages which allowed progressive fruitful developments in the field of materials processing science. This chapter focuses on the recent developments and processes utilized in the field of processing metal–ceramic composite materials by using novel microwave heating techniques.

3.2 Historical Developments in Materials Processing by Microwaves

The initial heating through microwaves were focused on low-temperature applications such as heating of foodstuffs, curing of resins, moisture removal from woods, drying of materials, etc. [19, 23, 24]. These earlier developments in microwave heating were also characterized by lower-energy consumptions and rapid-heating process. These characteristics of microwave heating process attracted many researchers, and novel field of microwave sintering was evolved and explored. Sintering of many microwave coupled materials and ceramics were successfully achieved by researchers and now it is well-established route for sintering of variety of materials [25–27]. The developments taking place in the field of microwave materials processing in chronological order are shown in Figure 3.1.

It can be seen that earlier developments (from 1950 to 1970) were focused on processing of microwave coupled materials which require lower processing temperatures (less than 500 °C) and were good absorber of microwaves. Main focus was on cooking, drying, chemical reactions, polymers, synthesis of chemicals, etc. After these developments, the area shifted from drying and synthesis toward sintering of materials which required temperatures in the range of 450–1000 °C. Till that time, it was believed that metals cannot be processed by this technique as metals and metallic materials possess lower skin depth due to which microwaves are not absorbed within the material. This causes reflection of microwave radiations that creates plasma formations, which can deteriorate the wave guides of microwave applicator. But in year 1999, it was reported that metals in the form of powders can be

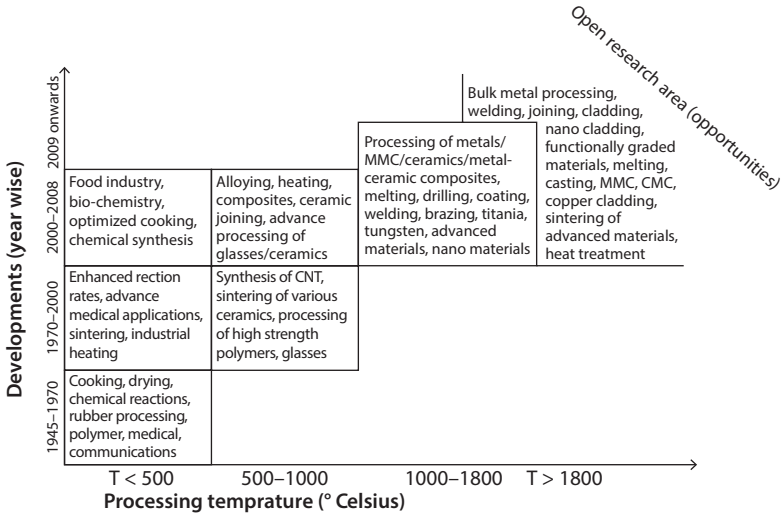

Figure 3.1 Developments in microwave material processing.

processed via microwaves and the sintering of metallic powder was successfully reported by Roy *et al.* [28]. This allowed extensive research (from the year 1999) in the processing of various metallic powders, metal–ceramic composites, and metal matrix composites by microwave sintering process which requires temperature greater than 1000 °C. Microwave sintering of metallic/metal-based powders draw intensive efforts from the researchers due to the output product quality achieved by microwave heating. During sintering of ceramics, authors reported improvement in product quality in terms of refinement of microstructures and improved mechanical properties [29–31]. However, engineering ceramics, with some exceptions of carbides, are difficult to process and heat at room temperatures owing to low loss tangents [32]. To resolve this issue, a new heating effect called "microwave effect" was researched and proved by many researchers. It was stressed that there exists a critical temperature value at which ceramic materials undergoes phase changes that transited properties into higher loss tangent [33–35]. At this temperature, the microwaves directly couple with ceramics to enhance the heating rates as shown in Figure 3.2, and this effect is termed as microwave effect.

This microwave effect is often characterized by rapid heating rates coupled with rising loss tangents that causes volumetrically heating throughout the ceramic load, but due to deprived thermal conductivities of ceramics, regions of excessive microwave effects produced hot spots [36] within the material. At these spots, uncontrollable microwave heating

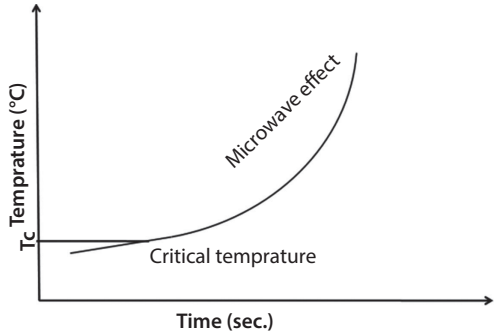

Figure 3.2 Effect of critical temperature on temperature rise (microwave effect).

causes irreversible damages, and these are termed as "thermal runaways". However, no satisfactory explanations have been given regarding microwave effect because results presented by various researchers are specific material dependent and cannot be applied to other. To reduce the hot spot defects and for improving the thermal conductivities, ceramic matrix composites (CMCs) were successfully processed by addition of metallic particles such as tungsten, aluminum, and copper [37–40].

Overall results of microwave sintering process revealed enhanced densification of processed products, improved sinterability in lower processing times, lower defects due to uniform thermal gradients, and better product properties [41–45].

Further, authors tried to process and sinter ceramic materials of lower dielectric loss by adding suitable microwave couplers such as carbides and carbon nano tubes and were successful [46–48]. These positive results of successful sintering of various ceramics allowed researchers to concentrate on processing of metallic powders, CMCs, and MMCs using microwave energy.

3.3 Introduction to Microwave Heating Process

In conventional heating technology, heat energy is initially available at the outer surfaces, and it further propagates from the surface of material to the core by conduction, convection, and radiation. In contract, microwave heating occurs by the direct absorption of radiations within the material with inverse profile, i.e. from inner surfaces to outer surfaces. In comparison to the conventional heating where heat is transferred due to temperature differences, whereas in microwave heating, electromagnetic radiations interacts

at molecular levels by getting absorbed and conversion of energy takes place within the volume of material. Due to energy deposit within the material, heat generation is volumetrically in the load, and it consequently makes heating process faster with higher heating rates. Moreover, microwave interaction occurs simultaneously in the volume of material, which allows rapid heating throughout the volume instantly and reduces thermal gradients. In microwave heating of materials heat is generated at molecular levels which subsequently allow heating of whole volume with lower gradients and this generated heat transfer from depth of material and causes inverse profile of heating. Under the controlled parameters, microwave processing allows product development in shorter times, with pollution-free environment, using lower energy and space, coupled with higher densification, uniform grains formation thus enhancing the required mechanical properties [49–52].

The devastating increase in the processing of materials by microwave energy is the brighter side of this novel technology, but on the other side, it is also true that all the known engineering materials cannot be processed directly by microwave radiations [34, 49, 56]. This is due to the fact that different materials possess different properties and based on properties microwave absorption behavior changes. Though it is noteworthy that researchers are continuously working in broadening the area of microwave materials processing, starting from heating of foodstuffs to development of microwave manufacturing processes involving metallic materials [53–55]. Processes such as microwave cladding process [56–58], microwave joining of bulk metals [56, 59–61], and microwave casting of metals [62] are recently targeted by researchers. These efforts boosts the researchers to further explore this fascinating field which is full of uncertainties, yet yields fruitful results in the field of materials processing. Before understanding the basic principles of heating involved by microwaves, it is essential to throw some light on microwave–materials interactions and issues in effective coupling of materials with microwaves.

3.3.1 Microwave–materials Interaction Theory

The efficient heating of materials by microwave energy depends upon number of factors; however, dependency of materials physical properties is one of the major factors. It distinguishes the materials into two main categories of microwave absorber and non-absorber materials. These physical properties decide the interactions of microwaves with the exposed material. Further, the variations of magnetic field strength (**H**) and electrical field strength (**E**) within the material volume allow variations in absorbing characteristics of materials. Depending upon the absorption behavior of

microwaves components in materials, materials are categorized into three main groups as shown in Figure 3.3.

Group 1: Materials which allows microwaves to pass through them without causing any changes in the **E** and **H** fields, hence causes zero absorption of microwave energy. These materials are known as transparent material. In some cases, little bit heating may occur but maximum amount of microwave exposure passes without causing effective heating due to negligible loss tangents and higher skin depths. Typical examples of microwave transparent materials are quartz, Teflon, thin plastic sheets, etc.

Group 2: Materials which are good absorber of microwaves owing to high dielectric losses and allows absorption of radiations (also called lossy insulators). These materials can convert the microwaves into heat even at low frequencies and temperatures and are called microwave absorber materials and examples of such materials include water, silicon carbide, carbon fibers, etc. In some cases, transparent materials can be heated by addition of some filler materials which increases the dielectric properties of the materials and are termed as mixed absorber materials. The best example of these materials includes multiphase materials in which one phase acts as transparent or opaque but other phase allows microwave absorption. This can

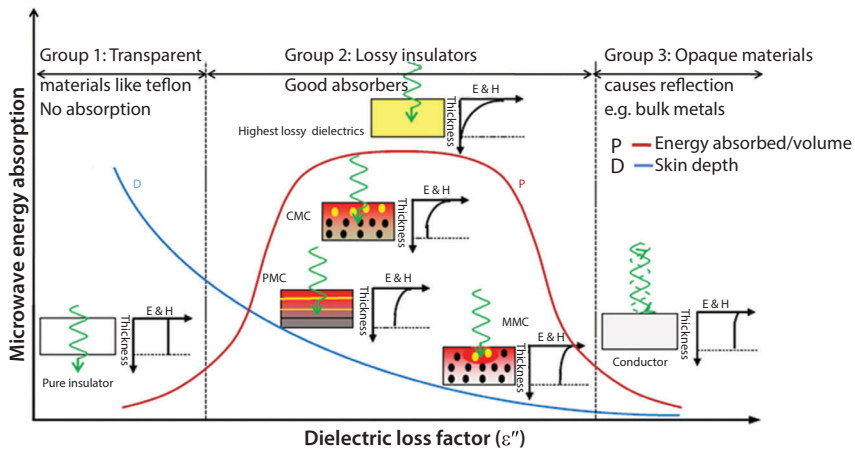

Figure 3.3 Microwave–material interactions for various materials [119] © [Elsevier]. Reproduced by permission of Elsevier. Permission to reuse must be obtained from the rights holder.

be seen in MMC, CMC, and PMC containing fillers of CNT, carbon black, copper, silver, and alloys which can modify the dielectric properties.

Group 3: Some materials act opaque to microwaves, i.e. they reflect back the radiations from the surfaces owing to lower skin depths. Though in some cases surface heating may take place, maximum radiations are rebounded. These materials are known as opaque, and bulk metals are one of the best examples.

3.3.2 Microwave Heating Mechanisms

Microwave heating applicators consist of three main parts: source, transmission lines, and applicator [14]. The microwave source (vacuum tubes, magnetrons, klystrons, etc.) generates the electromagnetic radiations, which are transferred to the applicator heating area through transmission lines. Depending upon the load (material to be heated), either microwaves are directly absorbed or reflected by material kept in the cavity. The theoretical analysis of microwave heating can be analyzed and governed by using appropriate boundary conditions to the Maxwell equations (Equation 3.1) [14, 63–66] shown below:

$$\nabla \times E = \frac{\partial B}{\partial t}, \qquad \nabla . B = 0$$
$$\nabla \times B = \frac{\partial D}{\partial t} + I, \quad \nabla . D = \rho \tag{3.1}$$

Where:
E = Electric field vector
H = Magnetic field vector
D = Electric flux density vector
B = Magnetic flux density vector
I = Current density vector
ρ = Charge density

The Maxwell equations can be solved with the suitable boundary conditions for obtaining the analytical/numerical results of electric field and magnetic field distributions within the microwave applicator. It allows determining the placement of load for efficient heating inside the applicator. Depending upon the type of applicator, i.e. single mode or multimode, the favorable sites where the highest required fields accumulates, can be found for the given type of material.

The properties of microwave absorber materials which are highly responsible for the absorption of microwaves within the material are loss tangent and complex relative permittivity represented by Equations 3.2 and 3.3 [14, 49, 56, 59].

$$\tan\delta = \frac{\varepsilon''}{\varepsilon'} \tag{3.2}$$

$$\varepsilon = \varepsilon_0(\in -j\in'') = \varepsilon_0 \in'(1 - j\tan\delta) \tag{3.3}$$

Where:

ε = Electric constant in medium
ε_0 = Electrical permittivity in space
$\in'$ = Electrical permittivity in medium (real part called dielectric constant)
$\in''$ = Dielectric loss factor (imaginary part)
δ = Dielectric loss tangent
j = Electrical polarizability

Here, term $(\in' - j\in'')$ is complex permittivity of a non-magnetic material and defines the level of heat to be generated within the material via microwaves interaction with material. The dielectric loss factor represents the ability of heated materials to dissipate microwave energy. Further, these dielectric interactions of materials with microwaves are described with two important parameters, i.e. power dissipation (P) and depth of penetration (D). The effective heating and uniformity of heating depend on these factors and are reported in detailed by many authors. However, the important parameter which allows coupling of materials with microwaves is skin depth associated with materials. It is represented by Equation 3.4 [67–69], which is a function of some physical variables of the materials like electrical resistivity and magnetic permeability.

$$\delta = \sqrt{\frac{\rho}{\pi f \mu_o \mu_r}} \tag{3.4}$$

Where,

δ = Skin depth (μm)
ρ = Resistivity ($\mu\Omega$-cm)
μ = Magnetic permeability = $\mu_r\mu_o$ (H/m)
μ_o = Absolute permeability (H/m)
μ_r = Relative permeability

If the skin depth associated with material is comparable to material thickness, then effective heating occurs by absorption of microwaves; however, if skin depth is low then microwaves will be reflected from surfaces of load as in case of bulk metals. Figure 3.4a–c represents the effect of skin depth on material processing, which shows heating occurs when skin depths are equivalent to material dimensions.

At room temperatures, some ceramics and all metallic powders exhibit lower values of skin depths, and this problem accounts for non-processing characteristics of such materials via microwave route. Researchers are continuously working on this problem, and as stated earlier, it was found that by achieving a certain critical temperatures, the skin depth of materials can be altered by altering the physical properties. This produces microwave effect and efficient heating can be expected by microwaves. It is very burdensome to calculate the powder absorbed in the various materials due to the complex heating phenomenon involved, and further variation of electric and magnetic field within the exposed load, with varying temperatures at varying time intervals allows more complexities. However, to estimate the power absorbed within the load under microwave exposure, energy balance empirical relation is used as shown in Equation 3.5 [70].

$$\Sigma mC\Delta T = 2\pi f \varepsilon_0 \varepsilon'' E_{rms}^2 Vt \tag{3.5}$$

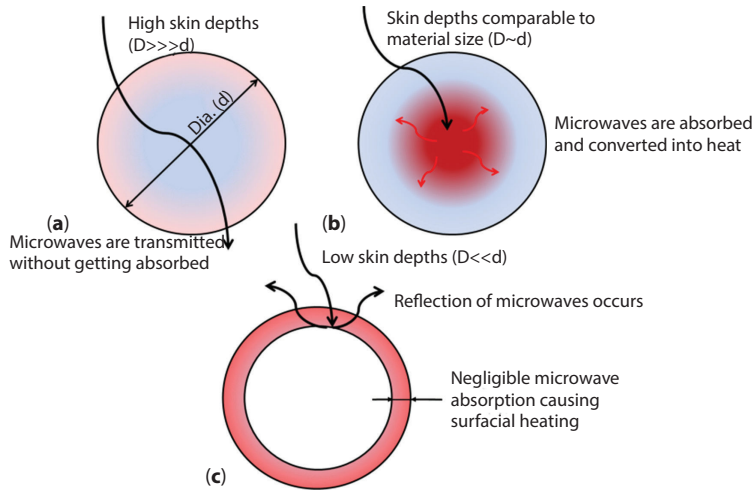

Figure 3.4 Effect of skin depth on microwave absorption for materials having (a) high skin depths, (b) skin depth comparable to material size, and (c) low skin depths.

It has been reported in the literature [71] that lower skin depth associated with individual metallic/ceramic powders (Cobalt metal powder = 2.5 μm and for WC powder = 4.7 μm) can further be varied by lowering the particle sizes by preparing powder green compacts. It was reported that the penetration depth of WC–Co green parts with mean powder particle size of 1 μm can reach up to 7.5 cm, and this value is sufficient for processing compacts under lower frequency of 2.45 GHz. These further variations of size effects on effective coupling of microwaves with materials are important and complicate the heating process.

The basic heating governing equations briefed about parameters required for efficient heating by microwave energy. But the various phenomena which occur within the material that allows heating of material are discussed by many authors in details [72–74]. Depending upon the type of material, i.e. magnetic/non-magnetic, the various heat generating processes involved in microwave heating includes, frictional heating due to continuous changes in dipole orientations, position and movement of dipoles, free electrons, domain wall movements, and electron spin. For processing of non-magnetic materials such as Al, Cu, Ceramics, and water, the phenomena of dipolar loss and conduction loss are predominant. In case of magnetic materials such as Fe, Ni, steel powder, and W, the phenomena of hysteresis losses, Eddy current losses, and Residual losses (domain wall resonance and electron spin) are predominant. Further, heating by microwaves can be directly or indirectly used in many applications, and these methods of heating are discussed in the next section.

3.4 Heating Methods by Microwaves

Microwaves are directly or indirectly used in many industrial applications; however, with the passage of time, newer technology are emerging which is collaborating with microwave heating in field of materials processing. Heating methods are divided into four categories and are shown in Figure 3.5a–d.

3.4.1 Direct Microwave Heating

The materials which are microwave absorber (lossy insulator) are usually processed directly by microwaves. These materials directly couple with microwaves, absorb them, and convert into heat energy as shown in Figure 3.5a. Typical examples are water, foodstuffs, some ceramics, etc. Though heating can occur at rapid rates, uniformity in heating is a critical

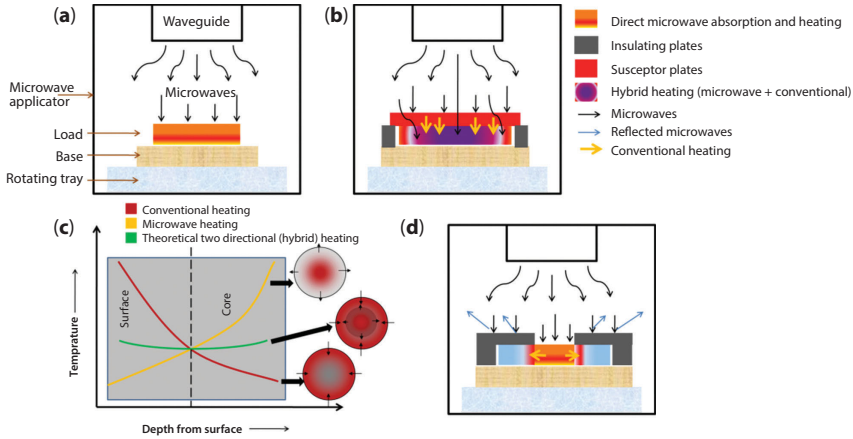

Figure 3.5 (a) Direct microwave heating, (b) MHH, (c) effect of MHH on temperature profile, and (d) selective microwave heating.

issue. Selection of higher processing times can seriously damage the materials by producing hot spots. Authors have reported many issues while exposing materials (such as SiO_2, ZrO_2, and alumina) directly to microwaves, and these include thermal instabilities, non-uniform heating, and cracking.

3.4.2 Microwave Hybrid Heating

There are some materials which cannot be exposed to microwaves directly such as metallic powders and bulk metals. If these materials are exposed directly, then due to reflection of microwaves within the microwave cavity can produce plasma formations. To overcome these problems and to process materials which cannot be exposed to radiations directly, the techniques of hybrid heating or microwave hybrid heating (MHH) were developed [75–78]. Using this technique, materials are processed under suscepting environment by using suitable susceptor, which are good absorber of microwaves. Initially, susceptor gets heated by absorbing microwaves and transfer heats to the metallic/non coupled powders via conventional modes of heat transfer. On reaching the critical states, the powder starts coupling with microwaves directly [33, 34], whereas conventional heating still continues from susceptor. A suitable separator material is also required which performs the function of separating susceptor material from processed materials and also acts as a heat transfer media from susceptor to load. Schematic representation of MHH is shown in

Figure 3.5b. Recently, a lot of work has been carried out on MHH of metallic powders [79–81], where MHH was used due lower skin depth associated with powders. To efficiently process the metallic powders, MHH was utilized successfully and results were encouraging in the field of material processing. Earlier, this technique was successfully used in sintering of materials and was termed as two-directional heating or bi-directional heating. It was reported that this technique allows in lowering the thermal gradients within the processing load and also allows higher heating rates coupled with uniformity. Figure 3.5c shows the comparison between conventional heating, direct microwave heating, and uniformity achieved in MHH process due to two-directional heating, which lowers the varying thermal gradients and flattens the temperature profile throughout the volume of processed materials [49, 82].

3.4.3 Selective Heating

This type of heating is a part of direct heating method where heating is to be carried out at a selection location of load placed in the microwave applicator. The best example of selective heating is in the case of joining of materials, where microwave radiations are allowed to fall on joint regions, and other parts are kept away from exposure by using masking materials. The schematic of selective heating is shown in Figure 3.5d. It is highly effective when heating is to be carried out at particular locations, and researchers have used technique for localized doping/heating of materials [83–85].

3.4.4 Microwave-assisted Processing of Materials

In recent years, microwaves have been efficiently coupled with other technologies such that microwave processing assists in the other material processing techniques to increase the efficiency. A lot of work has been reported on the microwave-assisted plasma technique for manufacturing of carbon fibers [86–90]. Presently, microwave-assisted technologies are used in many industrial applications, and lot of literature is available on these processing routes [91–95]. Nowadays, researchers are working on combined laser-assisted microwave processing in the field of material processing, and this area allows the integrity of other processes with efficient microwave heating process [96]. Research on microwave plasma-assisted CVD has been utilized in processing of many materials [97–99]. These developments enhance the importance of microwaves in many industrial applications.

3.5 Advantages/Limitations of Microwave Material Processing

All the developed technologies have certain advantages and anomalies associated with it. The novel technologies of microwave processing have extensively widened the area and are used in many industrial applications and material processing methods. The favorable characteristics of microwave processing are shown in Figure 3.6, which shows volumetric heating characteristics, rapid heating, selective heating, economical processing, and environmental-friendly characteristics. The various advantages of microwave materials processing are listed below.

3.5.1 Highly Energy Efficient Processing Method

Microwave processing of materials is considered to be highly efficient method, and this is due to the fact that microwaves are directly absorbed within the materials and are transferred into heat energy rapidly. The economies of microwave heating have been reported in almost every manuscript which focuses on heating by microwave radiations. It has been reported that microwave heating consumes 10–100 times less energy than conventional methods, and also it takes 100–200 times less processing times [100].

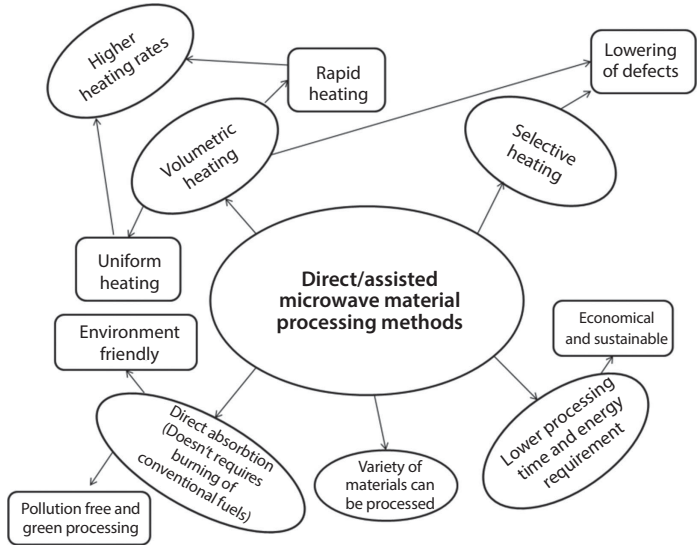

Figure 3.6 Favorable characteristics of microwave material processing.

The energy savings in microwave processing are due to the lower power required for achieving high temperatures as heat is generated within materials in this process, whereas heat transfer takes place in conventional heating processes. Further, lower power required is coupled with lower processing times due to rapid heating, and this allows microwave heating process as efficient. In one of the project reports available online [101] on the sintering behavior of titanium, it was reported that microwave process produced heat with 50 °C/min rate, which was 12.5 times faster than conventional heating rate. Figure 3.7 shows the comparison of microwave and conventional sintering, which clearly indicates the energy savings due to lower power consumption and lower time taken to process the materials, which is due to higher heating rates associated with microwaves.

The work carried out on sintering time of various steels by Panda *et al.* [102] revealed that microwave processing was faster and reduced the processing times by a factor of 10 as shown in Figure 3.8.

The power consumption and heating time comparison for conventional sintering and microwave sintering of W–Fe–Ni alloy was reported by Upadhyaya *et al.* [103] and results are presented in Figure 3.9.

The results clearly revealed the time savings by factor of 7 and power savings by a factor of 4 were observed in microwave processing. Similar results were obtained for melting of aluminum metal by Chandrasekaran *et al.* [104], and it was reported that microwave melting time was reduced 2.5 times the time taken by conventional melting process. Comparative results of melting time are shown in Figure 3.10.

These researches supported the microwave processing efficiency in terms of lower power consumptions and reduced processing timings.

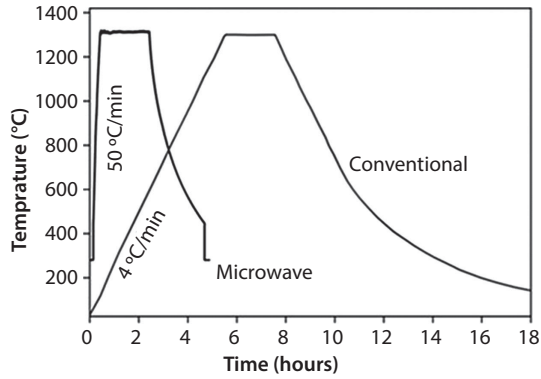

Figure 3.7 Comparison of sintering time for microwave and conventional heating of titanium [101].

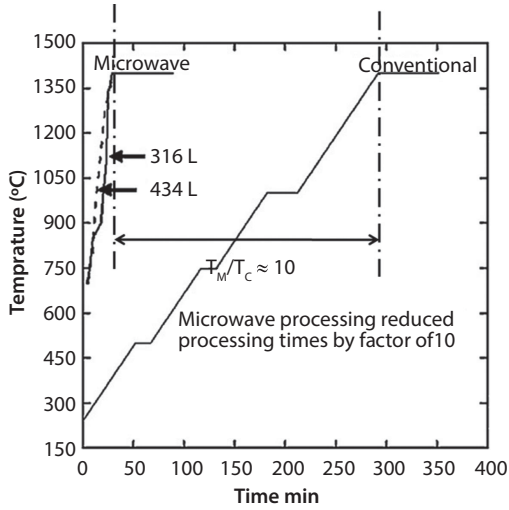

Figure 3.8 Processing time curve for conventional and microwave heating of stainless steels [102]. © [Elsevier]. Reproduced by permission of Elsevier. Permission to reuse must be obtained from the rights holder.

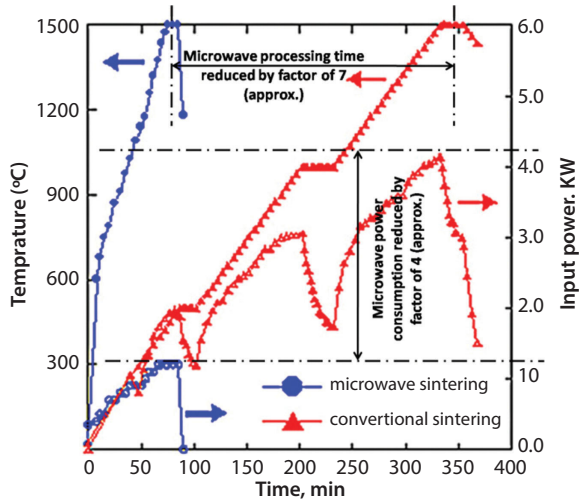

Figure 3.9 Temperature and power curves for microwave and conventional heating of W–Fe–Ni alloy [103]. © [Elsevier]. Reproduced by permission of Elsevier. Permission to reuse must be obtained from the rights holder.

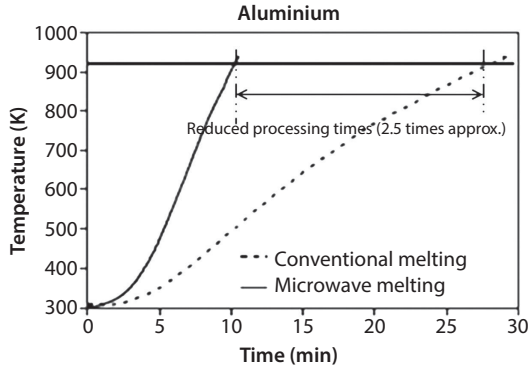

Figure 3.10 Comparison of microwave and conventional heating on melting of aluminum [104]. © [Elsevier]. Reproduced by permission of Elsevier. Permission to reuse must be obtained from the rights holder.

3.5.2 Better Quality of Processed Materials

Literatures on microwave processing of materials have revealed many favorable characteristics on the quality of product produced. The advantageous role of microwaves in product quality includes:

- Higher densification of processed materials.
- Lower defect formations in terms of cracks, porosity, and dislocations in the microstructures.
- Uniform grain growths and lowering the coursing of grains due to volumetric heating and rapid heating, which allows lower thermal gradients within the processed materials.
- Lower processing temperatures for sintering of materials due to heat generations within the materials, which allows lower chances of overheating the materials.

The work carried out by Mondal *et al.* [105] showed that in sintering of W–Cu composites, the density improved by 12.82% by microwave heating in comparison to conventional heating process as shown in Figure 3.11.

It was reported that density reached ~100% by microwave processing, and this resulted in the improvement of properties of W–Cu alloys sintered by microwave. This could be attributed to the volumetric heating and higher heating rates associated with microwave process. The work of Pian *et al.* [106] reported on the rapid densification of ceramic rollers of SiC by

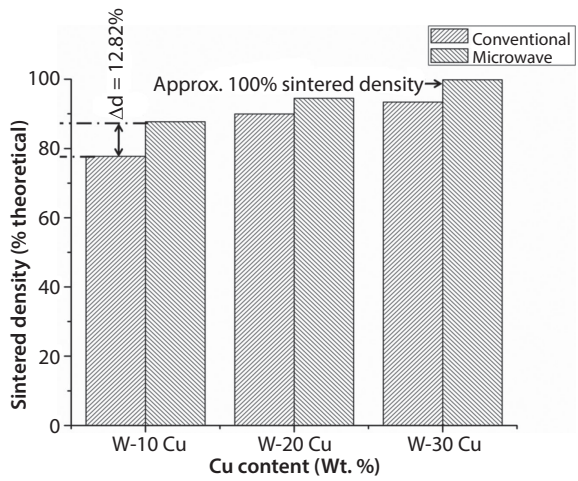

Figure 3.11 Effect of heating modes on sintered density of W–Cu alloys [105].

microwave sintering process (2.45 GHz frequency radiations), and authors reported that microwave sintering temperature was 400 °C less than the conventional sintering temperature. Yu *et al.* [107] reported that in sintering of ceramics by microwaves, very short cycle time was observed and impurity phases were eliminated in comparison to conventional heating. Results also revealed higher densification and more uniform grain growth in microwave-processed samples. Such results encourages researchers to further explore the possibilities of microwave material processing technologies such that processed products are cost effective and with enhanced properties.

3.5.3 Cleaner Energy Processing

Microwave energy is directly absorbed by materials and gets converted into heat, thus does not create any pollution. Microwave processing is green processing, and researchers have reported that heating through electromagnetic energy is environmentally friendly [108–112]. In comparison to conventional welding method where lot of fumes and dangerous gases are produced, microwave joining process is safe, non-polluting, and spatter free.

3.5.4 Compact Processing Unit

Microwave processing unit is compact in size, which requires less floor area and is not expensive in contrast to other advanced material processing equipments such as laser. As discussed earlier, microwave heating

equipment consists of three main parts, i.e. generator, transmission wave guides, and applicator area. Though microwave processing of material is highly dependent on applicator area, which restricts the size of specimen to be processed and for large load, bigger applicators are required such as in industrial heating systems.

In spite of having remarkable advantages in material processing industry, microwave processing possesses some limitations, and these are discussed under:

3.5.5 Restriction in Processing of All Varieties of Materials

The chief limitation regarding microwave material processing is that all the materials cannot be processed [49, 56]. All the microwave transparent and opaque materials possess limitations to microwave processing and cannot be processed directly. Coupling of materials with microwaves is an important issue, which has to tackle before processing of materials with microwave energy.

3.5.6 Restrictions in Processing of Complex Shapes

Microwaves can be efficiently used in processing of simpler shapes such as sintering of rectangular or cylindrical shapes. But sintering of complex shape is a big challenge as electric and magnetic fields vary at various locations, and this causes non uniformity in heating. A lot of efforts are required to process complex structures with microwaves, and this requires the simulation studies before actual processing so that effects can be studied for varying cross sections. However, some studies on development of complex shape [113] using microwaves are available, but still it has to be explored for development of 3D complex shapes.

3.5.7 Non-uniformity in Heating

Though microwave heating is considered to be uniform as volumetric heating occurs throughout the materials, in some cases, authors [114–117] have reported non-uniform heating which can lead to irreversible effects of hot spots within the processed materials. Further variations of electromagnetic field at various locations add to the non-uniformity heating.

3.5.8 Human Safety Issues

Though microwave material processing is considered to be safe, if radiations leaks from the applicator, then it is of serious concern. It was reported

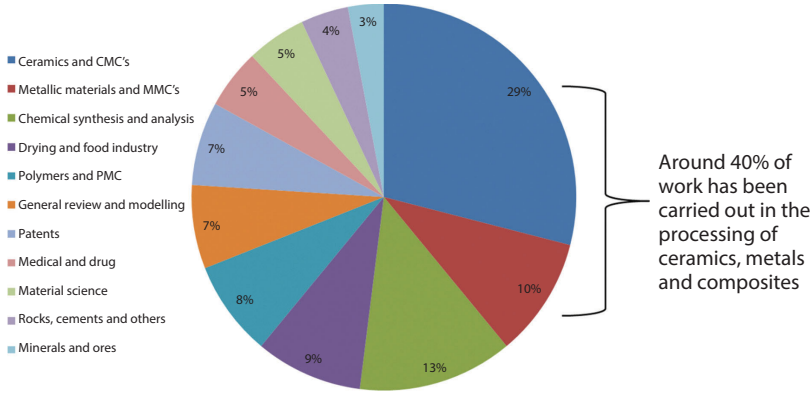

Figure 3.12 Fields of microwave material processing [119] © [Elsevier]. Reproduced by permission of Elsevier. Permission to reuse must be obtained from the rights holder.

[49, 118] that microwave energy can be hazardous if comes in direct contact to the body because human body allows high absorption rates of microwave energy. This can cause irreversible heating of tissues, and these effects are well used in biomedical applications for treatment of cancer cells.

To summarize the developments in this novel field of material processing by microwaves, Mishra and Sharma [119] in their review manuscript reported the percentage of literature available on various materials processed by microwaves. Figure 3.12 shows the published literature on microwave processing, and results shows that about 10% of work is published on metal processing and MMC, whereas 29% of work has been reported on ceramics processing and CMCs. This shows that still a lot of scope is left in MMC material processing via microwave energy.

3.6 Application of Microwave Heating in Composite Processing

As discussed earlier, the composite materials are considered as a backbone of many industries [120–121]. Numerous metal–ceramic composites are used as advanced materials in various fields of science and technology. However, the cost involved in processing of these composites and degree of isotropic nature obtained by the processing methods are of primary concern. Authors [14, 28, 49, 50, 56, 58, 60, 100] have already reported that microwave processing is novel in terms of huge savings involved with the processing method, and also properties of processed composites are far better than the conventionally processed methods.

Table 3.1 Comparison of alloys/composite properties processed conventionally and microwave heating.

S. No.	Alloy/ composites	Parameter	Processing mode		Conclusion
			Conventional	Microwave	
1	W–Ni–Fe [103]	Tensile Strength (MPa)	642 ± 23	805 ± 14	Better mechanical properties, refine microstructures, lower processing time, and power consumption in microwave processing
		Elongation (%)	3.5 ± 0.8	11.2 ± 1.1	
		Avg. W Grain Size (μm)	17.3 ± 0.8	9.4 ± 0.5	
		Processing Time (min)	~350	~80	
2	W–30Cu [105]	Sintered Density (% Theoretical)	~92	~99.98	Better microstructure, properties, and six times lower power consumption in microwave heating
		Sintering Time	~480	~80	
		Avg. Grain Size (nm)	499 ± 75	302 ± 63	
		Electrical Conductivity (%IACS)	40.0 ± 0.3	43.1 ± 0.7	
		Hardness (HV_5)	258 ± 8	322 ± 9	

(*Continued*)

Table 3.1 Cont.

S. No.	Alloy/ composites	Parameter	Processing mode		Conclusion
			Conventional	Microwave	
3	Al–Mg–Si–Cu [135]	Processing Time (min)	T	58% lower than T	Lower processing time which restricted the formation of intermetallics in microwave processing
		XRD Analysis	Formation of intermetallics	Absence of intermetallics due to insufficient time for diffusion	
4	WC/Co [45]	Soaking Time (min)	100	12	Lower processing time and better corrosion properties of microwave sintered samples
		Rockwell A hardness (GPa)	175.5	177.6	
		Corrosion Loss (in HNO_3, 48 h, wt%)	1.16	0.20	
5	434L Stainless Steels [102]	Processing Time (min)	~350	90% reduction in processing times (~40–50)	Microwave processing allowed lower times and higher density
		Densification Parameter	0.61	0.63	

Table 3.1 shows the effect of microwave and conventional heating on properties of various alloys and compares the times required for both methods of processing. It is clearly observed that microwave heating supports the grain refinement and enhancement of properties with lot of energy and time savings. This section of chapter will be focused on the recent developments in metal–ceramic composites/MMC processed by microwave energy route.

3.6.1 Recent Review of Work Carried Out in MMC/CMC/Alloys/Ceramic Processing by Microwaves

To include the latest work from material scientists, we are reporting the most recent work (from 2010 to till date) in the field of MMC/Alloy processing using the microwaves. This work will be selected on the basis of novelty and applications of developed composite materials. However, the basics for the metallic powder processing/metallic alloys processing by microwaves were provided by Roy *et al.* [122].

The work on TiN-reinforced aluminum MMC was carried out by Venkateswarlu *et al.* [123] by microwave sintering process. Authors utilized the concept of hybrid heating by using SiC as susceptor to sinter the Al–TiN composites under inert environment of argon. It was reported that the presence of TiN particles at grain boundaries of MMC plays a significant role in improving the densification and hardness values. The dry sliding wear results revealed improvement in wear resistance of the composites which was due to the presence of TiN particles. Further, the wear results of microwave sintered samples were superior to the Al–TiN samples made by hot-pressing technique. Comparative evaluation of microwave and conventional heating on sintering of 90W–7Ni–3Cu alloy was carried out by Mondal *et al.* [124]. It was reported that microwave sintering required about 75% less processing time in comparison to conventional method, and microwave sintering yields better physical and mechanical properties in terms of densification parameter, microstructures and hardness. The growing applications of copper (being highly conductive) in electrical contacts [125] attracted researchers toward copper matrix composites fabrications and properties enhancement in the past few years. The work carried by Rajkumar and Aravindan [126] on microwave sintered copper–TiC–graphite hybrid composites revealed that microstructures revealed uniform dispersion of reinforcements in the copper matrix and due to volumetric and rapid heating in microwave processing, no cracks were visible in the sintered composite specimens. The Indian patent [127] filed by Srinath *et al.* in year 2009 sparked the work on joining of bulk metallic

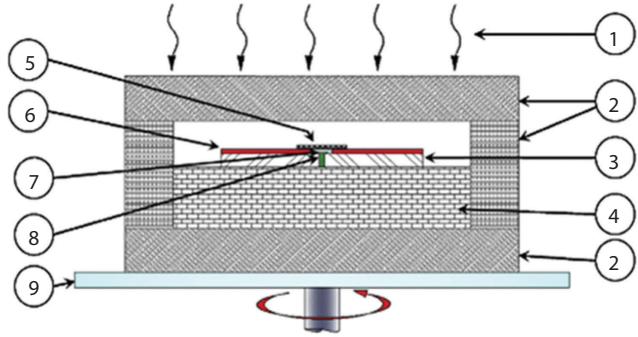

1. Microwave radiation 2. Alumina insulation 3. Base metal 4. Refractory base 5. Susceptor 6. Masking material 7. Separator 8. Nickel based powder 9. Turn table.

Figure 3.13 Schematic principle for developments of joints through microwave [131]. © [Elsevier]. Reproduced by permission of Elsevier. Permission to reuse must be obtained from the rights holder.

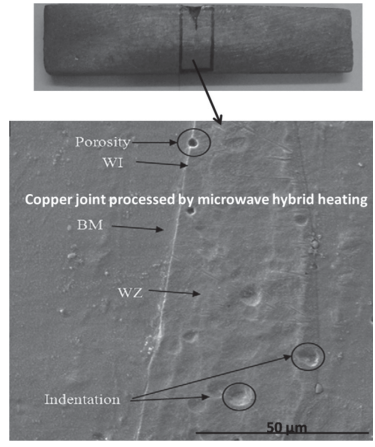

Figure 3.14 Copper joint produced by microwave heating [129]. © [Elsevier]. Reproduced by permission of Elsevier. Permission to reuse must be obtained from the rights holder.

parts using MHH technique. Authors [128–132] further explored the joining of bulk steels and copper using microwaves. The schematic principle of microwave joining and some results on joints produced by MHH are shown in Figures 3.13–3.16.

Gupta and Sharma [133] in year 2010 have diversified the domain of microwave materials processing by patenting a novel process for surface engineering known as microwave cladding. The authors claimed the microwave cladding of tungsten-based composite powder on an austenitic

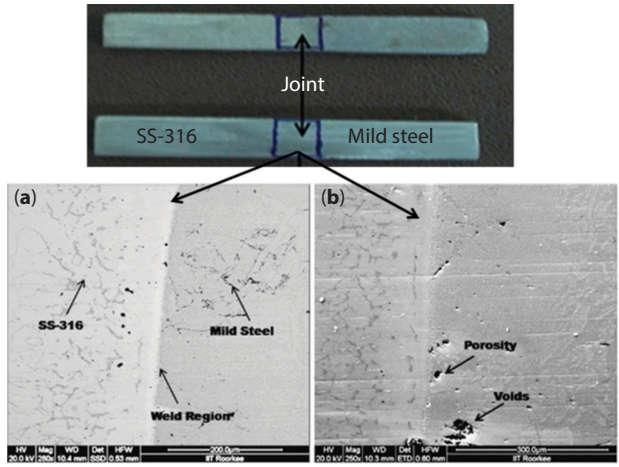

Figure 3.15 (a and b) SEM images of dissimilar joints of SS-316 and mild steel produced by MHH [128]. © [Elsevier]. Reproduced by permission of Elsevier. Permission to reuse must be obtained from the rights holder.

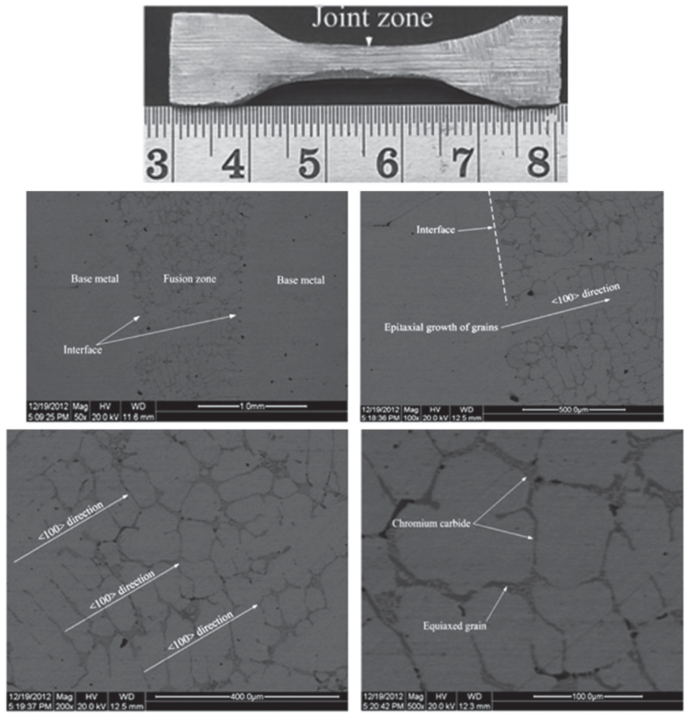

Figure 3.16 Development of stainless steel (SS) joints by MHH [130]. © [Elsevier]. Reproduced by permission of Elsevier. Permission to reuse must be obtained from the rights holder.

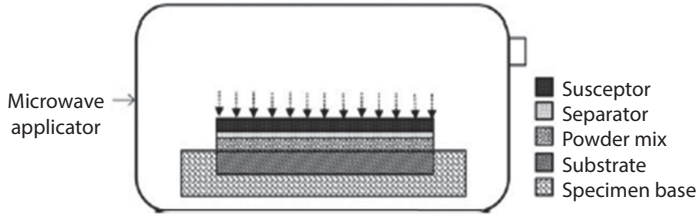

Figure 3.17 Schematic principle of MHH for development of claddings on bulk substrate [138]. © [Elsevier]. Reproduced by permission of Elsevier. Permission to reuse must be obtained from the rights holder.

stainless steel substrate was developed in short time of 120 s. Clads were developed in the household microwave oven working on 2.45 GHz frequency and power level of 900 W. A schematic representation of microwave cladding process is shown in Figure 3.17.

Gupta *et al.* [134] further developed composite cladding of EWAC + 20%$Cr_{23}C_6$ on the austenitic stainless steel SS316 substrate by using MHH. The developed claddings were characterized by relevant techniques of FE-SEM, energy dispersive X-ray spectroscopy, XRD, and measurement of Vicker's microhardness. The results of X-ray diffraction patterns of the clad are shown in Figure 3.18a, which showed the presence of chromium carbide, nickel–chromium, and nickel iron phases that contributed toward the enhancement of microhardness. The microwave developed clads were formed having 500 μm thickness without any visible interfacial cracks. The microstructure of clads revealed by the back-scattered electron image of clad cross section showed reinforced chromium carbide ($Cr_{23}C_6$) particles are embedded in the Ni-based matrix and are uniformly distributed as shown in Figure 3.18b. The developed clads exhibit higher microhardness than the substrate material, and results are shown in Figure 3.18c.

The results of the present research highlighted that these claddings would be effectively used in wear-resistance applications. Padmavathi *et al.* [135] reported the effect of microwave and conventional heating on sintering behavior and properties of Al–Mg–Si–Cu alloy. It was reported that microwaves coupled effectively with the alloy compacts and resulted in ~58% reduction in processing with higher heating rates. However, it was reported that rapid heating rate resulted in inhomogeneous microstructure of sintered compacts and XRD analysis revealed the absence of intermetallics due to insufficient time for diffusion in microwave heating. Gupta and Sharma [136] developed a composite cladding (WC10Co2Ni) on mild steel substrate by microwave irradiation and investigated the sliding wear performance of the developed clad. It was reported that cladding

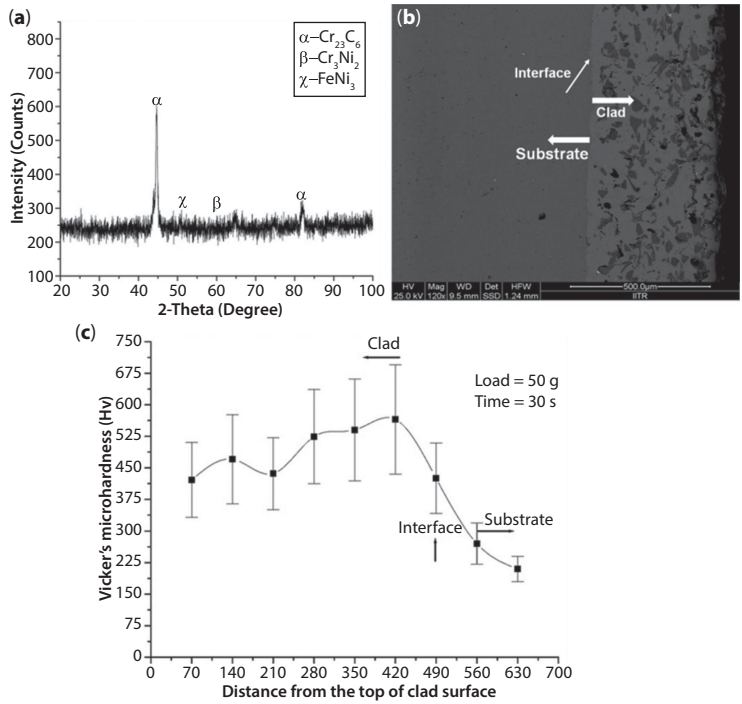

Figure 3.18 (a) XRD spectrum of composite clad, (b) typical SEM image showing microstructure of composite clad, and (c) microhardness profile along the cross section of clad [134]. © [Elsevier]. Reproduced by permission of Elsevier. Permission to reuse must be obtained from the rights holder.

with metallurgical bonding was obtained in a very short time of microwave exposure (360 s), and authors claimed that very less porosity (0.89%) was observed. The clad microstructure revealed that within soft metallic matrix hard carbide phases were uniformly distributed with 'skeleton'-like structure. The developed clads exhibit an average microhardness of 1064 ± 99 HV and was due to the formation of hard phases during microwave processing. It was shown that microwave-processed clad showed 84 times higher wear resistance than substrate material. Further, cladding research is going on by using this novel heating technique, and many authors [137–139] have reported valuable results in this fascinating field. Vennerberg [140] investigated the production of copper–carbon nanotube composites by using a novel microwave-assisted carbothermic processing route. It was reported that this new fabrication technique for processing carbon nanotube-reinforced metal matrix composites eliminates many limitations associated with traditional methods while requiring lower

time and energy. A research on development of WC–8Co composites via microwave sintering was carried out by Bao *et al.* [141]. It was reported that properties of the alloy can be improved with lower processing cycles using microwaves. Bian *et al.* [142] reported the research on alumina–titania composite ceramic processing by microwaves and conventional pressure less sintering. It was again found that in processing of nanostructured composite powders, microwave processing exhibits shorter sintering time coupled with higher densification and enhanced properties in comparison to conventional sintering. Microwaves were further used for development of functionally graded materials (FGM) such as development of W/Cu FGM using microwave sintering process by Liu *et al.* [143] for fusion reactor applications. It was reported that the five-layered W/Cu FGM (W30% + Cu70%/W50% + Cu50%/W70% + Cu30%/W 90% + Cu10%/W100%, volume fraction) was fabricated by a microwave sintering method within 30 min of processing. Results of characterizations showed that the graded structure was retained even when the microwave sintering temperature was as high as 1300 °C (well above the melting temperature of Cu), and the fine microstructure of W in each layer was maintained due to the short sintering time associated with the process. The work carried by Demirskyi *et al.* [144] compared the grain growth and properties of titanium nitride sintering by microwave as well as conventional route. It was reported that fully dense materials with a submicron grain size of 170 nm using microwave sintering and around 240 nm using conventional sintering were achieved. The overall improvement of the mechanical properties such as increase in hardness (from 18 to 20 GPa) and fracture toughness (from 2.9 to 3.4 MPa $m^{1/2}$) was observed in case of microwave sintering, and this was due to the grains refinement. Jerby *et al.* [145] utilized the microwaves for development of additive manufacturing (AM) of 3D structures by stepwise consolidation of metal powders. Metal layers were developed by localized heating using microwaves. The experimental observations and numerical results of this research suggested that the enhanced electric field between adjacent metallic particles excites the electric discharges (micro-plasmas) which in turn initiate the magnetic heating process. Results of the experiments lead to the development of localized microwave heating (LMH) technique for stepwise formation of metal structures, as a low-cost substitute for laser-based technologies for rapid prototyping (RP) and AM systems. This research can open wide area in the field of AM by localized heating. Further, the problem of getting complex shapes by microwave heating can be attempted based on this research. Figure 3.19a and b shows the conceptualization process of LMH.

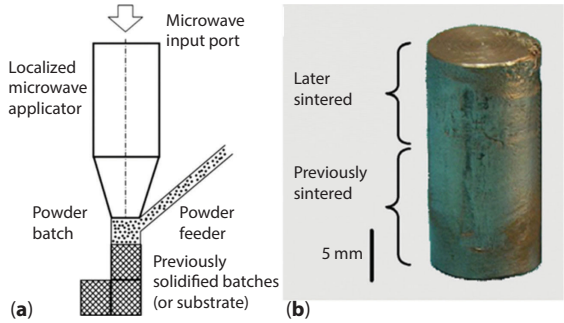

Figure 3.19 Schematic of LMH and (b) part produced by LMH [145]. © [Elsevier]. Reproduced by permission of Elsevier. Permission to reuse must be obtained from the rights holder.

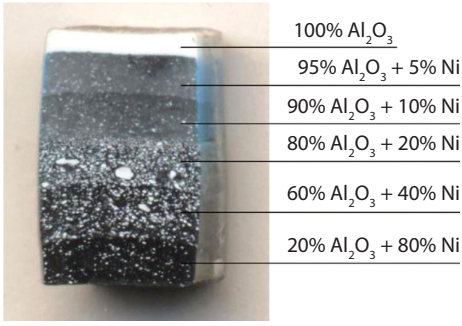

Figure 3.20 FGM developed by microwave heating [148]. © [Elsevier]. Reproduced by permission of Elsevier. Permission to reuse must be obtained from the rights holder.

Thuault *et al.* [146] investigated the processing of reaction bonded B_4C–SiC composites in a single-mode microwave cavity. It was reported that pore-free B_4C–SiC composite was successfully produced which consists of a mixture of B_4C and polygonal shaped β-SiC within a residual silicon matrix. Further, it was observed that average hardness was constant throughout the sample thickness, and this was due to the homogeneity of microstructures. In year 2014, Li *et al.* [147] studied the interactions of metal–ceramic systems in microwave sintering. The results revealed that there are some special mixed-interaction mechanisms during sintering, which may promote the sintering process during the microwave heating of metal–ceramic materials. Some particular sintering phenomena that were different from the microwave sintering of pure metal materials were observed, such as fast interface bonding and particle swallowing.

This helped in understanding the mechanisms involved in the improvement of the microstructure characteristics of metal–ceramic materials in microwave sintering. Bykov *et al.* [148] carried out the sintering of bulk Ni–Al_2O_3 FGM through microwave heating. Figure 3.20 shows the developed FGM and characterization results revealed that samples have flat boundaries between layers, and microstructures are free from cracks and delamination.

In addition to metal–ceramic graded transitions, metal–ceramic–metal-graded insulator structures have been fabricated. The work carried by Porada *et al.* [149] reported the AM of ceramic composites by laser-assisted microwave plasma processing (LAMPP) method. According to authors, LAMPP is a versatile new process for manufacturing of ceramic coatings on top of other materials substrates including metals/composites/ceramics, etc. As compared to laser or electron beam processing of ceramics, LAMPP can avoid the evaporation of the ceramic. It was stressed that processing can be done at different pressure levels in different atmosphere, including ambient pressure, air, nitrogen, or argon. In this process of LAMPP, the depth and size of the heat-affected zone depend upon the microwave power absorbed in the plasma, while the smoothness of the heat-affected zone can be adjusted by the laser beam scan parameters. Authors reported that using this process sintering and melting of ceramics on top of different substrates is possible, which will yield crack-free dense coatings. Zafar and Sharma [150] processed the micrometric (MM) and nanometric (NM) cladding of WC–12Co on SS304 substrate using microwave energy. Authors studied the detailed microstructures and tribological behavior (erosion and abrasive wear). It was reported that the microstructures of the microwave-processed MM WC–12Co clads show skeleton structured carbides, whereas the NM WC–12Co exhibited uniformly distributed clusters of nano-carbides in the matrix. It was found that the average Vickers's microhardness of the NM clad (1564 ± 53 HV) was ~1.37 times the microhardness of the MM clad (1138 ± 90 HV). Results of wear revealed that NM clads possess higher wear resistant and were highly effective in controlling the material loss due to higher carbide volume fraction and decreased mean free path of the binder in nanostructured clads.

In year 2014–2015, various authors [151–155] have again reported the similar findings on the material processing by microwave route which mainly includes lower-energy consumptions, higher heating rates, quality product with reduced defects, and cleaner processing technology. However, researchers are looking for newer routes in this field and are mainly focusing on melting of metals through microwave energy. To utilize the applications of microwaves in manufacturing industries, casting and melting

are the sectors which require attention from the processing engineers. Development of manufacturing processes via microwave efficient route is a novel field and should be researched on with practical implementations. As per the literature review, maximum of the work carried out is in the field of sintering of materials. Some of the literature available on melting of materials is reported in the next section.

3.6.2 Microwave Melting/Casting of Metals/Metal Matrix Composites

Some results are reported on melting of metals and development of MMC by melting using microwave energy. In year 2001, Moore *et al.* [156] filed an US patent on "Method and apparatus for melting metals". It was reported that a method and apparatus for melting metals was developed using microwave energy as the primary source of heat. The metal or mixtures of metals are placed within a ceramic crucible which directly couples, at least partially, with the microwaves. The crucible is encased in a ceramic casket for insulation and placed within a microwave chamber which may be evacuated and refilled to exclude oxygen. After microwave exposure and melting, the crucible may be removed for pouring molten metal. It was further reported that apparent coupling of the microwaves with softened or molten metal produces high temperatures with great energy savings.

Agrawal [157] reported the sintering and melting of some metallic materials using 2.45 GHz microwaves. It was reported that some bulk metals have been melted in a microwave field by using some special insulation packages with susceptor. Figure 3.21 shows some of the sintered/melted bulk metals reported by the author.

Recently (2015), we have filed an Indian patent [158] on development of metal–ceramic composites castings by using domestic microwave applicator working on 2.45 GHz. Castings of nickel-based powder (EWAC-EN1004 make: L&T) was reinforced with 10% wt of ceramic (silicon carbide, alumina, and WC10Co2Ni) were developed by pre-placing the composite powder in graphite cavity. Cavity containing the premixed powder was irradiated with microwaves under suscepting environment. Figure 3.22a and b shows the schematic and actual processing metal–ceramic castings in domestic microwave applicator. It was found that the average processing time for developing casting of 50mm×10mm×6mm dimensions was 24 min.

Developed metal–ceramic castings are shown in Figure 3.23.

It was observed that with addition of carbide reinforcements, the processing time was lowered to 18 min, which was due to the direct microwave absorption. It was found that EWAC+10% SiC, EWAC+10%Al_2O_3,

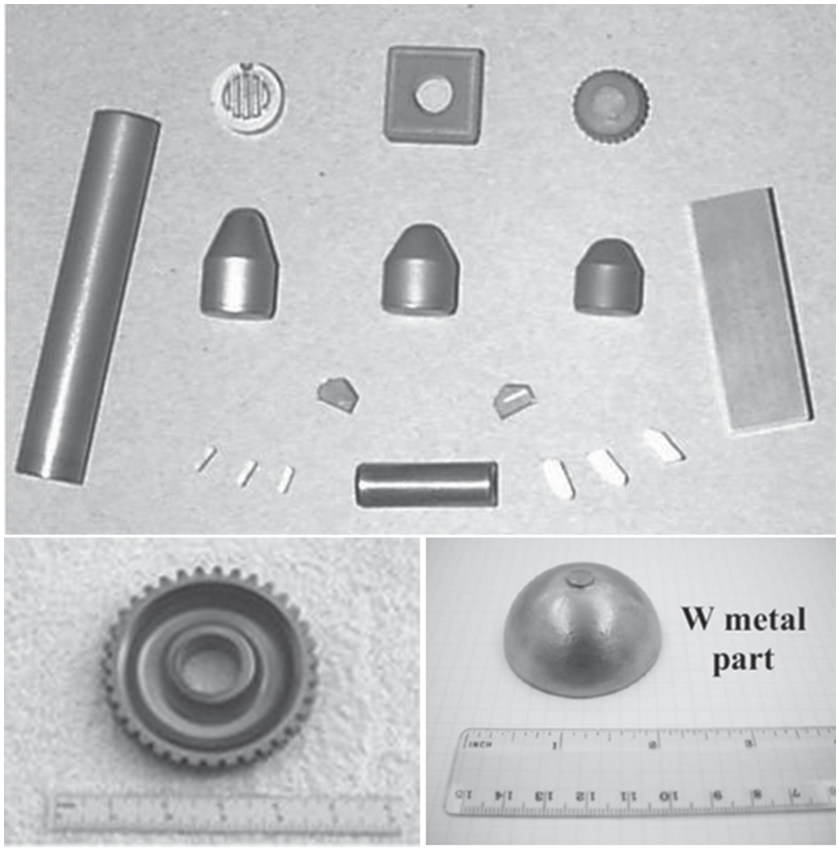

Figure 3.21 Various metallic parts sintered by microwaves [157].

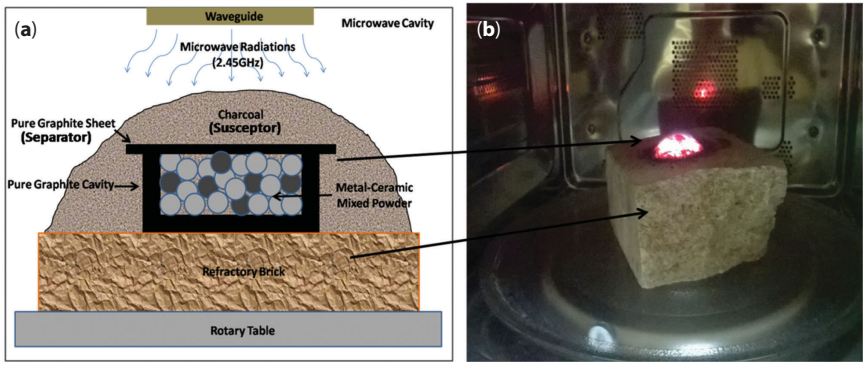

Figure 3.22 (a) Schematic setup for development of composites via MHH and (b) actual processing of composites.

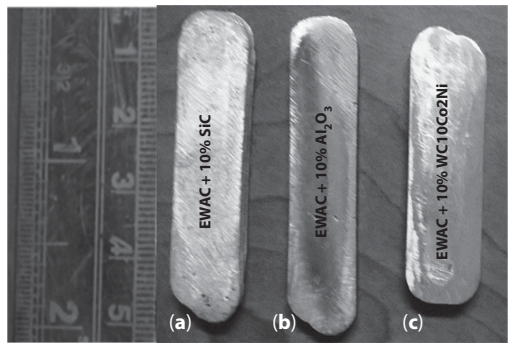

Figure 3.23 Metal–ceramic composites developed by MHH.

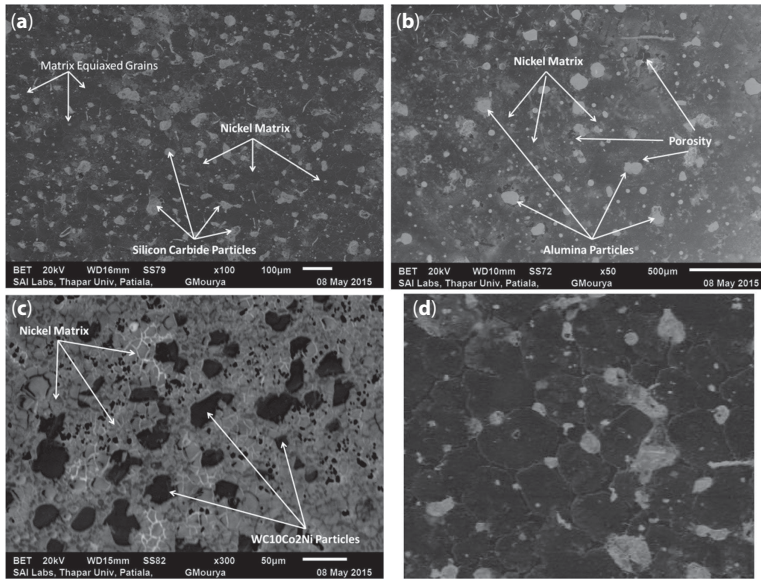

Figure 3.24 Typical back electron scattered images showing microstructures of (a) EWAC+10%SiC, (b) EWAC+10% Al_2O_3, (c) EWAC+10%WC10Co2Ni metal ceramic composites, and (d) magnified image showing the equiaxed grains.

and EWAC+10%WC10Co2Ni composites were processed by complete melting and fusion of nickel-based metal. Microstructures of developed composites revealed uniformity in dispersion of reinforcements in the cellular structured matrix. Figure 3.24a–d shows the developed composites and their microstructures.

Castings were free from major defects such as blow holes and cracks, but minor porosity was observed in the microstructures. It was claimed that:

- An efficient method of casting for metal–ceramic composites, which requires high temperatures for processing, was developed by this process. The process consists of following steps: irradiation of metal–ceramic powders in a pure graphite cavity in the susceptor environment for melting and followed by atmospheric cooling.
- Graphite cavity and susceptor initially heat up by direct microwave radiations, and this developed heat is subsequently allowed to pass conventionally from all the directions of cavity to the placed composite powder.
- The temperature initially rises through conventional heating till it reaches critical value at which metal powders starts interacting with microwaves.
- Castings were obtained at optimized parameters in the domestic microwave by using principles of MHH.

Authors have emphasized that this work will further be targeted while considering the casting sector of manufacturing industries, where microwaves can be utilized efficiently in melting and casting of smaller parts.

Table 3.2 summarizes the important mile stones in processing of bulk/metallic/composite materials by microwave energy.

3.7 Future Prospectives

The demand of sustainable greener technologies for processing of advanced materials is the current topic of interest among the researchers. The future of microwave material processing depends upon the industrial applications associated with these processes such that efficient heating by microwaves can be utilized commercially. The future opportunities in this field include to upper hand the limitations associated with the processing of materials via microwaves and these limitations has already been mentioned above. One of the emerging areas in microwave processing is development of advanced materials through microwave energy, and this includes processing of metal–ceramic composites, melting and alloying of elements for developing advance materials. Review of literature has demonstrated the opportunities of microwaves in material processing and further, clubbing of processes such as laser and microwaves, increases the efficiency and quality of processed product. Some developments in the field of micromachining using microwaves have been explored such as drilling [159–161]

Table 3.2 Summary of the developments in metallic/composite materials by microwave energy.

S. No.	Material processed and year	Conclusion
1	Fe, Ni, W, Co, Sn, Fe–Cu–C, Fe–Ni–C sintering (1998–2001) [28, 122]	First literature on sintering of metallic powders using microwave energy. Authors reported that modulus of rupture (MR) and densities of microwave-processed samples were better than the conventional samples. A huge saving in sintering times and energy for processing metal parts was reported.
2	Al, Mg, lead-free solder sintering using hybrid heating [29]	Authors reported successful sintering of metals using MHH technique. This allowed higher superior combination of tensile properties obtained from the microwave-assisted two-directionally sintering.
3	Austenitic (316L) and ferritic (434L) stainless steel sintering (2006) [102]	Authors successfully processed SS powders and reported the advantages of microwave sintering in terms of better microstructures obtained, lower power required, lower sintering times, and enhanced properties.
4	Austenitic stainless steel composites (2007) [39]	Authors successfully sintered 316L SS and 316L SS reinforced with yttrium aluminum garnet (YAG) using conventional and microwave sintering. It was reported that the 316L–5YAG composites consolidated in microwave furnace at 1400 °C yields the highest corrosion resistance. This was due to the fact that 316L–5YAG compacts show a maximum sintered density via microwave route and further uniform distribution of YAG was found in microwave sintering.

(*Continued*)

Table 3.2 Cont.

S. No.	Material processed and year	Conclusion
5	Joining of bulk steels and copper (2009, 2011, 2012, 2014) [127–132]	Authors reported a novel technique of joining bulk metals using MHH techniques. Joints obtained by this route shows lower defects, better microstructures, and lower heating effects due to selective heating involved.
6	Metallic/Cermet/ Composite Claddings on bulk metallic steels (2010–2016) [58, 133–134, 136–139, 150–151]	Another interesting area of microwave cladding was patented by Gupta and Sharma in year 2010. This research led to some interesting results which showed potential in surface engineering applications. Further, authors moved from micron sizes to submicron and nanocladdings.
7	Melting of bulk metals (2011) [104]	Author reported the melting of tin, lead, aluminum, and copper using susceptor. It was reported that in comparison to conventional melting microwave melting was twice fast and economical.
8	Melting and casting of Ni-based metal ceramic composites by MHH (2015) [158]	Singh *et al.* filed an Indian patent on development of metal–ceramic composite casting by MHH technique. It was reported that castings were obtained with complete melting and microstructures revealed equiaxed grains with uniform dispersion of reinforcements

of materials. However, all the advanced techniques in this field of microwaves are emerging, and these developments still require some time before getting established as matured methods of processing. Further, the precision and repeatability of the processes is a major issue which has to be addressed in achieving the sustainability of microwave-based processing methods.

3.8 Conclusion

The potential of microwave material processing has been accepted worldwide, and in recent time, lot of research is carried out in this novel field. The earlier developments which were based on low-temperature applications have been transformed to material processing methods at high temperatures. After the extensive use of microwave heating for sintering of materials, it has gained the popularity, and now this technology has been well established and commercialized for many materials. However, the developments in processing of metals and metallic-based powder have been started, but yet major breakthrough has to be achieved which can allow commercialization of microwaves in manufacturing sectors. Microwave heating used in the joining of bulk metallic materials and cladding on bulk metals allowed researchers to explore this technology, but availability of limited literature and understanding of the phenomena in microwaves–material interactions, the use of microwaves remained limited to few materials. The advantageous characteristics of microwave material processing should be further improved and optimized for processing of advanced materials. This will demand better understanding of microwave/materials behavior during interaction. Developments in the casting of metallic materials will further look at the possibilities of processing advanced metal matrix composites. The present work has enlightened the basics of microwave processing of engineering materials with the advantages and limitations of the processes. Special emphasis on processing of advanced materials via microwave route has been discussed, and future potential in this very novel field of materials processing has been discussed. The vast opportunities of using microwaves in various field of material processing by using pioneering engineered approaches will broaden the scopes for manufacturing-based industries.

References

1. Rodriguez-Suarez, T., Bartolome, J.F., Moya, J.S., Mechanical and tribological properties of ceramic/metal composites: A review of phenomena spanning from the nanometer to the micrometer length scale. *J. Eur. Ceram. Soc.*, 32, 3887, 2012.
2. Manocha, L.M., Prasad, G., Manocha, S., Carbon-ceramic composites for friction applications. *Mech. Adv. Mater. Struct.*, 21, 172, 2014.
3. Zhou, M., Lin, T., Huang, F., Zhong, Y., Wang, Z., Tang, Y., Bi, H., Wan, D., Lin, J., Highly conductive porous graphene/ceramic composites for heat transfer and thermal energy storage. *Adv. Funct. Mater.,* 23, 2263, 2013.

4. Singh, J., Chauhan, A., Overview of wear performance of aluminium matrix composites reinforced with ceramic materials under the influence of controllable variables. *Ceram. Int.*, 42, 56, 2016.
5. Cao, X.Q., Vassen, R., Stoever, D., Ceramic materials for thermal barrier coatings. *J. Eur. Ceram. Soc.*, 24, 1, 2004.
6. Wang, Y., Liu, Z., Tribological properties of high temperature self-lubrication metal ceramics with an interpenetrating network. *Wear* 265, 1720, 2008.
7. Standke, G., Müller, T., Neubrand, A., Weise, J., Göpfert, M., Cost-efficient metal–ceramic composites—novel foam-preforms, casting processes and characterisation. *Adv. Eng. Mater.*, 12, 189, 2010.
8. Prakash, A., Rajasankar, J., Iyer, N.R., Anandavalli, N., Biswas, S.K., Mukhopadhyay, A.K., Prediction of behavior of ceramic/metal composite panels under two consecutive ballistic impacts. *Int. J. Comput. Methods Eng. Sci. Mech*., 15, 192, 2014.
9. Silva, A.A.M., dos Santos, J.F., Strohaecker, T.R., Reguly, A., Study of structure/property relationships of diffusion bonded Ti_6Al_4V + 10 wt-%TiC particulate composite. *Sci. Technol. Weld. Join.,* 10, 413, 2005.
10. Wang, J., Shen, Y., Structure–Property–functionality relationships in bimetal composites. *JOM*, 64, 1190, 2012.
11. Lin, W., Moon, K.-S., Zhang, S., Ding, Y., Shang, J., Chen, M., Wong, C., Microwave makes carbon nanotubes less defective. *ACS Nano,* 4, 1716, 2010.
12. Das, S., Mukhopadhyay, A.K., Datta, S., Basu, D., Microwave sintering of titania. *Trans. Indian Ceram. Soc.,* 64, 143, 2005.
13. De, A., Ahmad, I., Whitney, E.D., Clark, D.E., Microstructural uniformity and homogeneity in alumina sintered by microwave (hybrid) heating at 2.45 GHz. *Trans. Indian Ceram. Soc.,* 54, 156, 1995.
14. Thostenson, E.T., Chou, T.-W., Microwave processing: fundamentals and applications. *Compos. A Appl. Sci. Manuf.,* 30, 1055, 1999.
15. Agrawal, D., Microwave sintering of ceramics, composites and metallic materials, and melting of glasses. *Trans. Indian Ceram. Soc*., 65, 129, 2006.
16. Feher, L., Thumm, M., Industrial higher frequency microwave processing of composite materials, in: *Advances in Microwave and Radio Frequency Processing SE - 74*, Willert-Porada, M. (Ed.), pp. 681–686, Springer Berlin Heidelberg, 2006.
17. P.L Spencer, Method of treating foodstuffs, US patent 2495429 A, assigned to Raytheon Mfg Co., 1945.
18. Rao, K.J., Vaidhyanathan, B., Ganguli, M., Ramakrishnan, P.A., Synthesis of inorganic solids using microwaves. *Chem. Mater.,* 11, 882, 1999.
19. Jones, D.A., Lelyveld, T.P., Mavrofidis, S.D., Kingman, S.W., Miles, N.J., Microwave heating applications in environmental engineering—a review. *Resour. Conserv. Recycl.*, 34, 75, 2002.
20. Buchelnikov, V.D., Louzguine-Luzgin, D.V., Xie, G., Li, S., Yoshikawa, N., Sato, M., Anzulevich, A.P., Bychkov, I.V., Inoue, A., Heating of metallic

powders by microwaves: experiment and theory. *J. Appl. Phys.,* 104, 113505, 2008.
21. Bykov, Y., Eremeev, A., Glyavin, M., Kholoptsev, V., Luchinin, A., Plotnikov, I., Denisov, G., Bogdashev, A., Kalynova, G., Semenov, V., Zharova, N., 24-84-GHz gyrotron systems for technological microwave applications. *Plasma Sci. IEEE Trans.,* 32, 67, 2004.
22. Kumar, N., Singh, U., Singh, T.P., Sinha, A.K., A review on the applications of high power, high frequency microwave source: gyrotron. *J. Fusion Energy*, 30, 257, 2011.
23. Ku, H.S., Siu, F., Siores, E., Ball, J.A.R., Variable frequency microwave (VFM) processing facilities and application in processing thermoplastic matrix composites. *J. Mater. Process. Technol.*, 139, 291, 2003.
24. Das, S., Mukhopadhyay, A.K., Datta, S., Basu, D., Prospects of microwave processing: an overview. *Bull. Mater. Sci.,* 31, 943, 2008.
25. Croquesel, J., Bouvard, D., Chaix, J.-M., Carry, C.P., Saunier, S., Development of an instrumented and automated single mode cavity for ceramic microwave sintering: application to an alpha pure alumina powder. *Mater. Des.,* 88, 98, 2015.
26. Babaghorbani, P., Gupta, M., Enhancing the mechanical response of a lead-free solder using an energy-efficient microwave sintering route. *J. Electron. Mater.,* 37, 860, 2008.
27. Xu, J.L., Bao, L.Z., Liu, A.H., Jin, X.J., Tong, Y.X., Luo, J.M., Zhong, Z.C., Zheng, Y.F., Microstructure, mechanical properties and superelasticity of biomedical porous NiTi alloy prepared by microwave sintering. *Mater. Sci. Eng. C,* 46, 387, 2015.
28. Roy, R., Agrawal, D., Cheng, J., Gedevanishvili, S., Full sintering of powdered-metal bodies in a microwave field. *Nature,* 399, 668, 1999.
29. Gupta, M., Wong, W.L.E., Enhancing overall mechanical performance of metallic materials using two-directional microwave assisted rapid sintering. *Scr. Mater.*, 52, 479, 2005.
30. Wong, W.L.E., Karthik, S., Gupta, M., Development of hybrid Mg/Al_2O_3 composites with improved properties using microwave assisted rapid sintering route. *J. Mater. Sci.,* 40, 3395, 2005.
31. Yan, Y., Liu, L., Ning, C., Yang, Y., Xia, C., Zou, Y., Liu, S., Wang, X., Liu, K., Liu, X., Liu, G., Improved electrical properties of SiO_2-added $BaTiO_3$ ceramics by microwave sintering. *Mater. Lett.,* 165, 135, http://dx.doi.org/10.1016/j.matlet.2015.11.015, 2015.
32. Ahmed, A., Siores, E., Microwave joining of 48% alumina–32% zirconia–20% silica ceramics. *J. Mater. Process. Technol.,* 118, 88, 2001.
33. Spotz, M.S., Skamser, D.J., Johnson, D.L., Thermal stability of ceramic materials in microwave heating. *J. Am. Ceram. Soc.,* 78, 1041, 1995.
34. Clark, D.E., Folz, D.C., West, J.K., Processing materials with microwave energy. *Mater. Sci. Eng. A,* 287, 153, 2000.

35. Aravindan, S., Krishnamurthy, R., Joining of ceramic composites by microwave heating. *Mater. Lett.,* 38, 245, 1999.
36. Kriegsmann, G.A., Hot spot formation in microwave heated ceramic fibres. *IMA J. Appl. Math.,* 59, 123, 1997.
37. Veronesi, P., Leonelli, C., Pellacani, G.C., Boccaccini, A.R., Unique microstructure of glass-metal composites obtained by microwave assisted heat-treatments. *J. Therm. Anal. Calorim.,* 72, 1141, 2003.
38. Menendez, J.A., Arenillas, A., Fidalgo, B., Fernandez, Y., Zubizarreta, L., Calvo, E.G., Bermudez, J.M., Microwave heating processes involving carbon materials. *Fuel Process. Technol.,* 91, 1, 2010.
39. Padmavathi, C., Panda, S.S., Agarwal, D., Upadhyaya, A., Effect of microstructural characteristics on corrosion behaviour of microwave sintered stainless steel composites. *Mater. Sci. Technol. IRON STEEL Technol.,* 5, 517, 2006.
40. Minay, E.J., Boccaccini, A.R., Veronesi, P., Cannillo, V., Leonelli, C., Processing of novel glass matrix composites by microwave heating. *J. Mater. Process. Technol.,* 155–156, 1749, 2004.
41. Huang, Z., Gotoh, M., Hirose, Y., Improving sinterability of ceramics using hybrid microwave heating. *J. Mater. Process. Technol.,* 209, 2446, 2009.
42. Fang, Y., Cheng, J., Roy, R., Roy, D.M., Agrawal, D.K., Enhancing densification of zirconia-containing ceramic-matrix composites by microwave processing. *J. Mater. Sci.,* 32, 4925, 1997.
43. Kimrey, H.D., Kiggans, J.O., Janney, M.A., Beatty, R.L., Microwave sintering of zirconia-toughened alumina composites. *MRS Online Proc. Libr. Arch.,* 189, 243, 1990.
44. Jiao, Z., Shikazono, N., Kasagi, N., Comparison of ultra-fast microwave sintering and conventional thermal sintering in manufacturing of anode support solid oxide fuel cell. *J. Power Sources* 195, 8019, 2010.
45. Breval, E., Cheng, J.P., Agrawal, D.K., Gigl, P., Dennis, M., Roy, R., Papworth, A.J., Comparison between microwave and conventional sintering of WC/Co composites. *Mater. Sci. Eng. A,* 391, 285, 2005.
46. Meek, T.T., Blake, R.D., Petrovic, J.J., Microwave Sintering of Al_2O_3 and Al2O3-SiC whisker composites, in: *11th Annual Conference on Composites and Advanced Ceramic Materials: Ceramic Engineering and Science Proceedings*, 8, pp. 861–871, Wiley Online Library, 1987.
47. Panneerselvam, M., Agrawal, A., Rao, K.J., Microwave sintering of $MoSi_2$–SiC composites. *Mater. Sci. Eng. A,* 356, 267, 2003.
48. Thakur, S.K., Kwee, G.T., Gupta, M., Development and characterization of magnesium composites containing nano-sized silicon carbide and carbon nanotubes as hybrid reinforcements. *J. Mater. Sci.,* 42, 10040, 2007.
49. Singh, S., Gupta, D., Jain, V., Sharma, A.K., Microwave processing of materials and applications in manufacturing industries: a review. *Mater. Manuf. Process.,* 30, 1, 2015.

50. Agrawal, D., Latest global developments in microwave materials processing. *Mater. Res. Innov.,* 14, 3, 2010.
51. Sharma, A.K., Aravindhan, S., Krishnamurthy, R., Microwave glazing of alumina–titania ceramic composite coatings. *Mater. Lett.,* 50, 295, 2001.
52. Menezes, R.R., Souto, P.M., Kiminami, R.H.G.A., Microwave hybrid fast sintering of porcelain bodies. *J. Mater. Process. Technol.,* 190, 223, 2007.
53. Mishra, P., Upadhyaya, A., Sethi, G., Modeling of microwave heating of particulate metals. *Metall. Mater. Trans. B,* 37, 839, 2006.
54. Luo, J., Hunyar, C., Feher, L., Link, G., Thumm, M., Pozzo, P., Theory and experiments of electromagnetic loss mechanism for microwave heating of powdered metals. *Appl. Phys. Lett.,* 84, 576, 2004.
55. Huang, X., Hwang, J.Y., Method for direct metal making by microwave energy, US patent 6277168 B1, assigned to Xiaodi Huang and Jiann-Yang Hwang, 2001.
56. Singh, S., Gupta, D., Jain, V., Recent applications of microwaves in materials joining and surface coatings. *Proc. Inst. Mech. Eng. B J. Eng. Manuf.,* 230, 603, 2015.
57. Pathania, A., Singh, S., Gupta, D., Jain, V., Development and analysis of tribological behavior of microwave processed EWAC + 20% WC10Co2Ni composite cladding on mild steel substrate. *J. Manuf. Process.,* 20, 79, 2015.
58. Zafar, S., Sharma, A.K., Development and characterisations of WC–12Co microwave clad. *Mater. Charact.,* 96, 241, 2014.
59. Zafar, S., Sharma, A.K., On friction and wear behavior of WC-12Co microwave clad. *Tribol. Trans.,* 58, 584, 2015.
60. Bansal, A., Sharma, A.K., Das, S., Metallurgical and mechanical characterization of mild steel-mild steel joint formed by microwave hybrid heating process. *Sadhana,* 38, 679, 2013.
61. Bansal, A., Sharma, A., Kumar, P., Das, S., Structure–property correlations in microwave joining of Inconel 718. *JOM*, 67, 2087, 2015.
62. Bist, V., Sharma, A.K., Kumar, P., Development and microstructural characterisations of the lead casting using microwave technology. *i-Manager's J. Mech. Eng.*, 4, 6, 2014.
63. Zhu, J., Kuznetsov, A. V, Sandeep, K.P., Mathematical modeling of continuous flow microwave heating of liquids (effects of dielectric properties and design parameters). *Int. J. Therm. Sci.,* 46, 328, 2007.
64. Geedipalli, S.S.R., Rakesh, V., Datta, A.K., Modeling the heating uniformity contributed by a rotating turntable in microwave ovens. *J. Food Eng.,* 82, 359, 2007.
65. Hill, J.M., Marchant, T.R., Modelling microwave heating. *Appl. Math. Model.,* 20, 3, 1996.
66. Yoshikawa, N., Fundamentals and applications of microwave heating of metals. *J. Microw. Power Electromagn.,* 44, 4, 2010.
67. Sueyoshi, H., Kakiuchi, S., Microwave heating of thin Au film. *Mater. Trans.,* 48, 531, 2007.

68. Santos, T., Valente, M.A., Monteiro, J., Sousa, J., Costa, L.C., Electromagnetic and thermal history during microwave heating. *Appl. Therm. Eng.,* 31, 3255, 2011.
69. Zohm, H., Kasper, E., Mehringer, P., Müller, G.A., Thermal processing of silicon wafers with microwave co-heating. *Microelectron. Eng.,* 54, 247, 2000.
70. Saltiel, C., Datta, A.K., Heat and mass transfer in microwave processing. *Adv. Heat Transf.,* 33, 1, 1999.
71. Bao, R., Yi, J.-H., Peng, Y.-D., Li, F.-X., Li, S., Li, S.-Y., Skin effect of WC–8 wt% Co alloy by microwave sintering. *Rare Met.,* 2015.
72. Torres, F., Jecko, B., Complete FDTD analysis of microwave heating processes in frequency-dependent and temperature-dependent media. *Microw. Theory Tech. IEEE Trans.,* 45, 108, 1997.
73. Pozar, D.M., *Microwave engineering*, John Wiley & Sons, 2009.
74. Metaxas, A C and Meredith, R.J., *Industrial microwave heating*, IET, 1983.
75. De, A., Ahmad, I., Whitney, E.D., Clark, D.E., Microstructural uniformity and homogeneity in alumina sintered by microwave (hybrid) heating at 2.45 GHz. *Trans. Indian Ceram. Soc.*, 54, 156, 1995.
76. Danko, G.A., Silberglitt, R., Colombo, P., Pippel, E., Woltersdorf, J., Comparison of microwave hybrid and conventional heating of preceramic polymers to form silicon carbide and silicon oxycarbide ceramics. *J. Am. Ceram. Soc.,* 83, 1617, 2000.
77. Zhao, C., Vleugels, J., Groffils, C., Luypaert, P.J., Van der Biest, O., Hybrid sintering with a tubular susceptor in a cylindrical single-mode microwave furnace. *Acta Mater.,* 48, 3795, 2000.
78. Gupta, D., Sharma, A.K., The Minerals, M.& M.S. (TMS), Development of Copper Coating on Austenitic Stainless Steel through Microwave Hybrid Heating, in: *Supplemental Proceedings*. John Wiley & Sons, Inc., pp. 263–270, 2011.
79. Gedevanishvili, S., Agrawal, D., Roy, R., Microwave combustion synthesis and sintering of intermetallics and alloys. *J. Mater. Sci. Lett.,* 18, 665, 1999.
80. Vaidhyanathan, B., Agrawal, D.K., Roy, R., Novel synthesis of nitride powders by microwave-assisted combustion. *J. Mater. Res.,* 15, 974, 2000.
81. Tun, K.S., Gupta, M., Effect of heating rate during hybrid microwave sintering on the tensile properties of magnesium and Mg/Y 2 O 3 nanocomposite. *J. Alloys Compd.,* 466, 140, 2008.
82. Wang, J., Binner, J., Vaidhyanathan, B., Joomun, N., Kilner, J., Dimitrakis, G., Cross, T.E., Evidence for the microwave effect during hybrid sintering. *J. Am. Ceram. Soc.,* 89, 1977, 2006.
83. Livshits, P., Dikhtyar, V., Inberg, A., Shahadi, A., Jerby, E., Local doping of silicon by a point-contact microwave applicator. *Microelectron. Eng.,* 88, 2831, 2011.
84. Jerby, E., Meir, Y., Salzberg, A., Aharoni, E., Levy, A., Torralba, J.P., Cavallini, B., Incremental metal-powder solidification by localized microwave-heating and its potential for additive manufacturing. *Addit. Manuf.,* 6, 53, 2015.

85. Nagao, D., Fukushima, J., Hayashi, Y., Takizawa, H., Synthesis of homologous compounds $Fe_2O_3(ZnO)_m$ (m = 6, 8, 34) by various selective microwave heating conditions. *Ceram. Int.,* 41, 14021, 2015.
86. Windischmann, H., Epps, G.F., Cong, Y., Collins, R.W., Intrinsic stress in diamond films prepared by microwave plasma CVD. *J. Appl. Phys.,* 69, 2231, 1991.
87. Chen, Y., Bagnall, D.M., Koh, H., Park, K., Hiraga, K., Zhu, Z., Yao, T., Plasma assisted molecular beam epitaxy of ZnO on c-plane sapphire: growth and characterization. *J. Appl. Phys.,* 84, 3912, 1998.
88. Pauleau, Y., Thiery, F., Latrasse, L., Dub, S.N., Characteristics of copper/carbon and nickel/carbon composite films produced by microwave plasma-assisted deposition techniques from argon–methane gas mixtures. *Surf. Coatings Technol.,* 188, 484, 2004.
89. Pauleau, Y., Thiery, F., Uglov, V. V, Anishchik, V.M., Kuleshov, A.K., Samtsov, M.P., Tribological properties of copper/carbon films formed by microwave plasma-assisted deposition techniques. *Surf. Coatings Technol.,* 180, 102, 2004.
90. GavinaWhittaker, A., Microwave-assisted solid-state reactions involving metal powders. *J. Chem. Soc. Dalt. Trans.,* 2751, 1992.
91. Kalita, G., Wakita, K., Umeno, M., Low temperature growth of graphene film by microwave assisted surface wave plasma CVD for transparent electrode application. *RSC Adv.,* 2, 2815, 2012.
92. Zong, L., Zhou, S., Sgriccia, N., Hawley, M.C., Kempel, L.C., A review of microwave-assisted polymer chemistry (MAPC). *J. Microw. Power Electromagn. energy Publ. Int. Microw. Power Inst.*, 38, 49, 2002.
93. Kobashi, K., Nishimura, K., Kawate, Y., Horiuchi, T., Synthesis of diamonds by use of microwave plasma chemical-vapor deposition: morphology and growth of diamond films. *Phys. Rev. B*, 38, 4067, 1988.
94. Duan, X., Zhang, M., Mujumdar, A.S., Wang, R., Trends in microwave-assisted freeze drying of foods. *Dry. Technol.,* 28, 444, 2010.
95. Liu, Y., Baudelet, M., Richardson, M., Elemental analysis by microwave-assisted laser-induced breakdown spectroscopy: Evaluation on ceramics. *J. Anal. At. Spectrom.,* 25, 1316, 2010.
96. Jerby, E., Meir, Y., Salzberg, A., Levy, A., Rubio, R., Planta, X., Cavallini, B., Stepwise consolidation of metal powder by localized microwaves for additive manufacturing of 3D structures, in: *1*4th International Conference on Microwave and High Frequency Heating, *AMPERE-2013*, pp. 345–348, UK, 2013.
97. Glasnov, T.N., Kappe, C.O., Microwave-assisted synthesis under continuous-flow conditions. *Macromol. Rapid Commun.,* 28, 395, 2007.
98. Hozumi, A., Takai, O., Preparation of ultra water-repellent films by microwave plasma-enhanced CVD. *Thin Solid Films*, 303, 222, 1997.
99. Füner, M., Wild, C., Koidl, P., Novel microwave plasma reactor for diamond synthesis. *Appl. Phys. Lett.,* 72, 1149, 1998.
100. Siores, E., Do Rego, D., Microwave applications in materials joining. *J. Mater. Process. Technol.,* 48, 619, 1995.

101. Qian, M, Project:5- Low Cost Powder Metallurgy of Titanium, http://www.arclightmetals.org.au/archive/content/research/phase02-2/p2-2projectA5.htm, 2010.
102. Panda, S.S., Singh, V., Upadhyaya, A., Agrawal, D., Sintering response of austenitic (316L) and ferritic (434L) stainless steel consolidated in conventional and microwave furnaces. *Scr. Mater.,* 54, 2179, 2006.
103. Upadhyaya, A., Tiwari, S.K., Mishra, P,. Microwave sintering of W–Ni–Fe alloy. *Scr. Mater*., 56, 5, 2007.
104. Chandrasekaran, S., Basak, T., Ramanathan, S., Experimental and theoretical investigation on microwave melting of metals. *J. Mater. Process. Technol.,* 211, 482, 2011.
105. Mondal, A.; Upadhyaya, A.; Agrawal, D. Effect of heating mode and copper content on the densification of W-Cu alloys. *Indian J. Mater. Sci.,* 2013, 1, 2013.
106. Pian, X., Shao, G., Fan, B., Chen, H., Wang, C., Zhang, R., Rapid densification of SiC ceramic rollers by microwave sintering. *Adv. Appl. Ceram.,* 114, 28, 2014.
107. Yu, J., Shen, C., Qiu, T., Effect of microwave sintering on the microstructure and dielectric properties of $0.92MgAl_2O_4–0.08(Ca_{0.8}Sr_{0.2})TiO_3$ ceramics. *J. Mater. Sci. Mater. Electron.,* 26, 2737, 2015.
108. Leonelli, C., Mason, T.J., Microwave and ultrasonic processing: now a realistic option for industry. *Chem. Eng. Process. Process Intensif.,* 49, 885, 2010.
109. Yu, H., Xu, Z., Fan, Z., Zhao, Z., Li, C., Mechanical property and microstructure of aluminum alloy-steel tubes joint by magnetic pulse welding. *Mater. Sci. Eng. A.*, 561, 259, 2013.
110. Zhang, P., Yin, S., Sato, T., Synthesis of high-activity TiO_2 photocatalyst via environmentally friendly and novel microwave assisted hydrothermal process. *Appl. Catal. B Environ.*, 89, 118, 2009.
111. Fu, Z., Liao, H., Xiong, D., Zhang, Z., Jiang, Y., Yin, D., A highly-efficient and environmental-friendly method for the preparation of Mn(III)–aalen complexes encapsulated HMS by using microwave irradiation. *Microporous Mesoporous Mater.,* 106, 298, 2007.
112. Farhat, A., Ginies, C., Romdhane, M., Chemat, F., Eco-friendly and cleaner process for isolation of essential oil using microwave energy: Experimental and theoretical study. *J. Chromatogr., A* 1216, 5077, 2009.
113. Thuault, A., Savary, E., Bazin, J., Marinel, S., Microwave sintering of large size pieces with complex shape. *J. Mater. Process. Technol.,* 214, 470, 2014.
114. Manickavasagan, A., Jayas, D.S., White, N.D.G., Non-uniformity of surface temperatures of grain after microwave treatment in an industrial microwave dryer. *Dry. Technol.,* 24, 1559, 2006.
115. Li, Z.Y., Wang, R.F., Kudra, T., Uniformity issue in microwave drying. *Dry. Technol.,* 29, 652, 2011.
116. Vilayannur, R.S., Puri, V.M., Anantheswaran, R.C., Size and shape effect on nonuniformity of temperature and moisture distributions in microwave heated food materials: part II experimental validation. *J. Food Process Eng.,* 21, 235, 1998.

117. Vadivambal, R., Jayas, D.S., Non-uniform temperature distribution during microwave heating of food materials—a review. *Food Bioprocess Technol.,* 3, 161, 2010.
118. Kim, J., Mun, S.C., Ko, H.-U., Kim, K.-B., Khondoker, M.A.H., Zhai, L., Review of microwave assisted manufacturing technologies. *Int. J. Precis. Eng. Manuf.*, 13, 2263, 2012.
119. Mishra, R.R., Sharma, A.K., Microwave–material interaction phenomena: heating mechanisms, challenges and opportunities in material processing. *Compos. A Appl. Sci. Manuf.,* 81, 78, 2016.
120. Huang, L., Chen, D., Ding, Y., Feng, S., Wang, Z.L., Liu, M., Nickel–cobalt hydroxide nanosheets coated on NiCo2O4 nanowires grown on carbon fiber paper for high-performance pseudocapacitors. *Nano Lett.,* 13, 3135, 2013.
121. Nicole, L., Laberty-Robert, C., Rozes, L., Sanchez, C., Hybrid materials science: a promised land for the integrative design of multifunctional materials. *Nanoscale*, 6, 6267, 2014.
122. Al-Oqla, F.M., Sapuan, S.M., Natural fiber reinforced polymer composites in industrial applications: feasibility of date palm fibers for sustainable automotive industry. *J. Clean. Prod.,* 66, 347, 2014.
123. Venkateswarlu, K., Saurabh, S., Rajinikanth, V., Sahu, R.K., Ray, A.K., Synthesis of TiN reinforced aluminium metal matrix composites through microwave sintering. *J. Mater. Eng. Perform.,* 19, 231, 2010.
124. Mondal, A., Upadhyaya, A., Agrawal, D., Microwave and conventional sintering of 90W–7Ni–3Cu alloys with premixed and prealloyed binder phase. *Mater. Sci. Eng. A*, 527, 6870, 2010.
125. Bares, J.A., Argibay, N., Mauntler, N., Dudder, G.J., Perry, S.S., Bourne, G.R., Sawyer, W.G., 2009. High current density copper-on-copper sliding electrical contacts at low sliding velocities. *Wear, 267*, 417, 2009.
126. Rajkumar, K., Aravindan, S., Tribological performance of microwave sintered copper–TiC–graphite hybrid composites. *Tribol. Int.*, 44, 347, 2011.
127. Sharma, A.K., Srinath, M.S., Pradeep, K., Microwave joining of metallic materials, Indian patent, 1994/Del/2009, 2009.
128. Srinath, M.S., Sharma, A.K., Kumar, P., Investigation on microstructural and mechanical properties of microwave processed dissimilar joints. *J. Manuf. Process. 13.,* 141, 2011.
129. Srinath, M.S., Sharma, A.K., Kumar, P., A new approach to joining of bulk copper using microwave energy. *Mater. Des.*, 32, 2685, 2011.
130. Bansal, A., Sharma, A. K., Kumar, P., Das, S. Characterization of bulk stainless steel joints developed through microwave hybrid heating. *Mater. Charact.,* 91, 34, 2014.
131. Bansal, A., Sharma, A.K., Kumar, P., Das, S., Joining of mild steel plates using microwave energy, in: Advanced Materials Research. *Trans Tech Publ., pp.*, 465, 2012.

132. Gupta, P., Kumar, S., Investigation of stainless steel joint fabricated through microwave energy. *Mater. Manuf. Process.,* 29, 910, 2014.
133. D Gupta, A.K Sharma., A method of cladding/coating of metallic and non-metallic powders on metallic substrate by microwave irradiation, Indian patent 527/Del/2010, 2010.
134. Gupta, D., Bhovi, P.M., Sharma, A.K., Dutta, S., Development and characterization of microwave composite cladding. *J. Manuf. Process*., 14, 243, 2012.
135. Padmavathi, C., Upadhyaya, A., Agrawal, D., Effect of microwave and conventional heating on sintering behavior and properties of Al–Mg–Si–Cu alloy. *Mater. Chem. Phys.*, 130, 449, 2011.
136. Gupta, D., Sharma, A.K., Investigation on sliding wear performance of $WC_{10}Co_2Ni$ cladding developed through microwave irradiation. *Wear,* 271, 1642, 2011.
137. Gupta, D., Sharma, a. K., Copper coating on austenitic stainless steel using microwave hybrid heating. *Proc. Inst. Mech. Eng. E J. Process Mech. Eng.*, 226, 132, 2011.
138. Sharma, A.K., Gupta, D., On microstructure and flexural strength of metal–ceramic composite cladding developed through microwave heating. *Appl. Surf. Sci*., 258, 5583, 2012.
139. Gupta, D., Sharma, A.K., Microwave cladding: a new approach in surface engineering. *J. Manuf. Process.*, 16, 176, 2014.
140. Vennerberg, D., Quirino, R., Kessler, M.R., A novel microwave-assisted carbothermic route for the production of copper-carbon nanotube metal matrix composites directly from copper oxide. *Adv. Eng. Mater.,* 15, 366, 2013.
141. Bao, R., Yi, J., Zhang, H., Peng, Y., A research on WC–8Co preparation by microwave sintering. *Int. J. Refract. Met. Hard Mater.* 32, 16, 2012.
142. Bian, H., Yang, Y., Wang, Y., Tian, W., Jiang, H., Hu, Z., Yu, W., Alumina–titania ceramics prepared by microwave sintering and conventional pressure-less sintering. *J. Alloys Compd.*, 525, 63, 2012.
143. Liu, R., Hao, T., Wang, K., Zhang, T., Wang, X.P., Liu, C.S., Fang, Q.F., Microwave sintering of W/Cu functionally graded materials. *J. Nucl. Mater.* 431, 196, 2012.
144. Demirskyi, D., Agrawal, D., Ragulya, A., Comparisons of grain size-density trajectory during microwave and conventional sintering of titanium nitride. *J. Alloys Compd.*, 581, 498, 2013.
145. Jerby, E., Meir, Y., Salzberg, A., Aharoni, E., Levy, A., Torralba, J.P., Cavallini, B., Incremental metal-powder solidification by localized microwave-heating and its potential for additive manufacturing. *Addit. Manuf*., 6, 53, 2015.
146. Thuault, A., Marinel, S., Savary, E., Heuguet, R., Saunier, S., Goeuriot, D., Agrawal, D., Processing of reaction-bonded B4C–SiC composites in a single-mode microwave cavity. *Ceram. Int.*, 39, 1215, 2013.

147. Li, Y.C., Xu, F., Hu, X.F., Kang, D., Xiao, T.Q., Wu, X.P., In situ investigation on the mixed-interaction mechanisms in the metal–ceramic system's microwave sintering. *Acta Mater.*, 66, 293, 2014.
148. Bykov, Y. V., Egorov, S.V., Eremeev, a. G., Holoptsev, V.V., Plotnikov, I.V., Rybakov, K.I., Semenov, V.E., Sorokin, A. A., Temperature profile optimization for microwave sintering of bulk Ni–Al_2O_3 functionally graded materials. *J. Mater. Process. Technol.,* 214, 210, 2014.
149. Willert-Porada, M.A., Rosin, A., Pontiller, P., Richter, C., Boeckler, J., 2015. Additive manufacturing of ceramic composites by laser assisted microwave plasma processing, LAMPP. *Microw. Symp. (IMS), IEEE MTT-S Int.,* 2015.
150. Zafar, S., Sharma, A.K., Abrasive and erosive wear behaviour of nanometric WC–12Co microwave clads. *Wear*, 346, 29, 2016.
151. Zafar, S., Sharma, A.K., On friction and wear behavior of WC-12Co microwave clad. *Tribol. Trans.,* 58, 584, 2015.
152. Kaushal, S., Sirohi, V., Gupta, D., Bhowmick, H., Singh, S., Processing and characterization of composite cladding through microwave heating on martensitic steel. *Proc. Inst. Mech. Eng. L J. Mater. Des. Appl.,* 2015.
153. Zhao, Z., Chen, F., Wang, M., Zheng, H., Synthesis of chromium carbide nanopowders via a microwave heating method. *Int. J. Refract. Met. Hard Mater.,* 51, 212, 2015.
154. Youn, D.H., Jang, J.-W., Kim, J.Y., Jang, J.S., Choi, S.H., Lee, J.S., Fabrication of graphene-based electrode in less than a minute through hybrid microwave annealing. *Sci. Rep.,* 4, 5492, 2014.
155. El-Khatib, E.M., Ali, N.F., Ramadan, M.A., Environmentally friendly dyeing of silk fabrics using microwave heating. *Int. J. Curr. Microbiol. Appl. Sci*., 3, 757, 2014.
156. Moore, A.F., Schechter, D.E., Morrow, M.S., 2006. Method and apparatus for melting metals. US7011136 B2
157. Agrawal, D., 12–Microwave sintering of metal powders, in: *Woodhead Publishing Series in Metals and Surface Engineering*, Chang, I., Zhao, Y.B.T.-A. P.M. (Eds.), p. 361, Woodhead Publishing, 2013.
158. Singh, S., Gupta, D., Jain, V., Kumar, R., A method for metal ceramic composite casting through microwave energy, Indian patent, 2051/DEL/2015, 2015.
159. Lautre, N.K., Sharma, A.K., Kumar, P., Das, S., A photoelasticity approach for characterization of defects in microwave drilling of soda lime glass. *J. Mater. Process. Technol.,* 225, 151, 2015.
160. Sharma, A.K., Das, S., Kumar, P., On crack control strategy in near-field microwave drilling of soda lime glass using precursors. *J. Therm. Sci. Eng. Appl.,* 7, 41001, 2015.
161. Meir, Y., Jerby, E., Localized rapid heating by low-power solid-state microwave drill. *Microw. Theory Tech. IEEE Trans.,* 60, 2665, 2012.

Part 2

CERAMIC COMPOSITES: FUNDAMENTAL AND FRONTIERS

Ashutosh Tiwari, Rosario A. Gerhardt and Magdalena Szutkowska (eds.) Advanced Ceramic Materials, (145–146) © 2016 Scrivener Publishing LLC

4

Continuous Fiber-reinforced Ceramic Matrix Composites

Rebecca Gottlieb[1], Shannon Poges[1], Chris Monteleone[2] and Steven L. Suib[1–3]*

[1]Department of Chemistry, Unit 3060, University of Connecticut, Storrs, USA
[2]Institute of Materials Science, University of Connecticut, Storrs, USA
[3]Department of Chemical and Biomolecular Engineering, University of Connecticut, Storrs, USA

Abstract

Nano-ceramics are traditionally used in smaller-scale electronics application, but other more recent uses include larger strength-providing materials like those in aircraft engines and aerospace technology. Ceramics have recently become an ideal candidate for applications that require high temperature, high chemical resistivity, oxidation resistance, and high thermal conductivity; however, these applications are limited by the inherent brittle nature of ceramics. One step in overcoming this issue is through the use of ceramic matrix composites (CMCs), including fiber-reinforced CMCs. These systems are made up of three components, each made of nano-ceramic materials. The inner reinforcing fiber, typically fabricated from polymer-derived ceramics, is composed of amorphous to nano-crystalline ceramic and provides strength and durability for the composite. The fiber is then coated with an interphase, typically applied through chemical vapor deposition. This interphase allows for energy-absorbing mechanisms in the composite including crack deflection and fiber pullout. The final component of the composite is the matrix or the bulk material. This nano-ceramic material is also produced using chemical vapor deposition and provides the bulk material and strength of the composite. This review gives an overview of continuous fiber-reinforced CMCs made with chemical vapor-deposited nano-ceramics. Despite this non-traditional application of nano-ceramics, these materials exhibit incredibly desirable characteristics for use in high-temperature and high-strength applications like those in the aircraft and engine industries.

***Keywords*:** Ceramics, composites, fibers

**Corresponding author*: steven.suib@uconn.edu

Ashutosh Tiwari, Rosario A. Gerhardt and Magdalena Szutkowska (eds.) Advanced Ceramic Materials, (147–200) © 2016 Scrivener Publishing LLC

4.1 Introduction

The need for materials withstanding high temperatures has increased significantly within the past century and with the development of powerful vehicle components and engines. Ceramic matrix composites (CMCs) are systems designed to combine the excellent strength and high-temperature properties of ceramics with the durability of advanced composites. These CMCs use a three-part system of ceramics to provide the hardness, heat and oxidation resistance, low density, low thermal expansion coefficient, and refractory properties of ceramics while combating the inherent brittle nature of these materials through a multi-component composite.

Materials capable of operating at elevated temperatures are fundamentally necessary for the function of components in power generation, aerospace, and aircraft technologies. These components and engines are able to function with more power and efficiency as the operational temperature is increased, and development of new high-temperature materials is constant to keep up with these systems. Historically, high-temperature materials have been used in advanced engineering since the invention of the steam turbine in the 1880s. Steel alloys, tungsten filament lamps, nickel-chromium alloys, and the production of petrol chemicals all lead to the development of today's high-temperature materials. Within the last 50 years, carbon fibers, titanium alloys, thermal barrier coatings, alumina, nickel super alloys, and CMCs have provided significant advancement in high-temperature materials, going above 1000 °C for operational temperatures [1].

Use of nickel alloys in high-temperature application like aircraft and aerospace engines has been conventional since the mid-1900s. These alloys, initially designed with nickel and chromium, were developed to improve both oxidation and corrosion resistance and also proved to have considerable strength and showed excellent properties for use in engine turbines. Alloys like the Brightray™ series and Inconel™ metals incorporated nickel, chromium, iron, silicon, and aluminum and varying concentrations and were the industry standard for exhaust manifolds in aircraft engines [2]. Nickel super-alloys like Nimonic® as well as other manufacturers used elements like aluminum, tantalum, and titanium for precipitation strengthening, molybdenum, tantalum, tungsten, and rhenium for solid solution strengthening, boron, carbon, zirconium, and hafnium for grain growth inhibition and strengthening, and aluminum and chromium for surface oxidation and corrosion protection [3]. Continued research through the 1990s provided materials like CMSX-4®, which can operate as

high as 1050 °C in engine turbine blades [4]. These alloys provide excellent strength and durability in these applications, however, are still limited by their operational temperature.

Titanium alloys also showed excellent high-temperature properties, with titanium aluminides melting at 1460 °C while still maintaining strength at temperatures above 1100 °C. These properties were considered in the development of both titanium and aluminum metal matrix composites (MMCs).

Reinforcing materials composed of silicon carbide as well as boron and aluminum metal provided structure and strength for these composites. Composite systems were fabricated using chemical vapor deposition of silicon carbide onto tungsten or carbon core wires, followed by application of the metal matrix through hot pressing. Though these materials were strong and durable with a strongly bound interphase, ultimately the mismatch in thermal expansion coefficient was the downfall in these composite systems. At elevated temperatures, during the heat-up and cool-down processes, damage occurred where the fiber met the matrix, and the composites performed poorly in heat cycling tests [5]. These composites were also denser than CMCs, which was an additional deterrent from using these systems in typical aircraft and aerospace applications.

CMCs were designed to overcome the failures seen in these alloys and MMCs. The inherently high melting temperatures, low reactivities, and low thermal expansion coefficients of ceramics meant longer lifetimes of machines which were exposed to high temperatures and multiple heating cycles. These advantages allowed for the continued development of CMCs and everntually their incorporation into aircraft. The potential for future use in both military and commercial aircrafts remains high with the continued research and development of these materials.

4.2 Parts of a CMC

CMCs are made up of three different parts (Figure 4.1), designed to be a system with optimum durability and strength from these separate components. These systems are typically either oxide CMCs, made out of oxide ceramics, or non-oxide, composed of non-oxygen-containing ceramic materials. Both oxide and non-oxide CMCs are designed for use in high-temperature applications, and are able to withstand extreme heat and oxidizing environments. Oxides typically operate at lower temperatures and can be used with or without an interphase component.

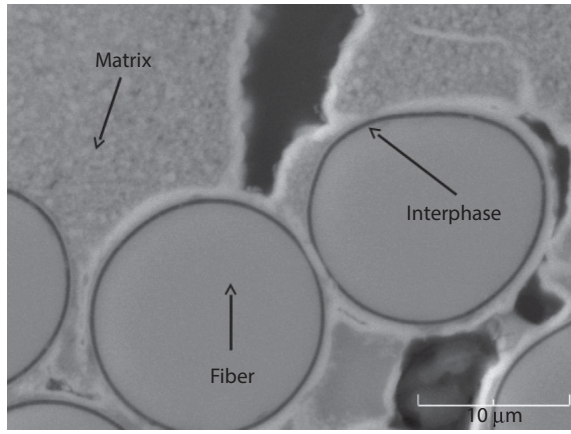

Figure 4.1 Cross-sectional micrograph of CMC.

Non-oxides, materials like silicon carbide, are designed to operate at very high temperatures (>1400 °C) due to the natural very high melting points of these ceramics and inherent oxidation resistance [6]. These materials are used with an interphase as part of the three-part composite system. As technologies advance, new materials are incorporated into these systems, taking advantage of the refractory properties of ceramics like borides, as well as additional dopants used in all three parts of the CMC system. As new materials are produced, these studies will continue as a part of the effort to design an incredibly high-temperature, durable composite system.

4.2.1 Fibers

Fibers provide strength and structure for the ceramic composite. These fibers exist in CMCs as unidirectional tow and as both two-dimensional (2D) and three-dimensional (3D) woven fabrics in continuous fiber-reinforced CMCs (CF-CMCs). Fibers can also be used in short, chopped, multi-directional fiber whiskers in these composites. The fibers are designed to have very small diameters in the range of 10–20 microns, allowing for increased flexibility [7]. Young's moduli of these fibers are relatively high when the fibers are designed with these small diameters, due to the relationship of cross-sectional area in Young's modulus equation, defined in Equation 4.1 below [8]:

$$E \equiv \frac{\text{tensile stress}}{\text{extensional strain}} = \frac{\sigma}{\varepsilon} = \frac{F/A_0}{\Delta L/L_0} = \frac{FL_0}{A_0 \Delta L} \tag{4.1}$$

These fibers are designed to produce exceptional strength, durability, and refractory properties for high-temperature applications. Fibers in CMCs typically exist as either non-oxide or oxide ceramics. Oxide fibers include ceramics like silicon dioxide, alumina, boria, and zirconia in varying combinations [9], while non-oxides are typically composed of silicon carbide, silicon nitride, and carbon, as well as additives like boron, titanium, and zirconium. These materials all have low densities and high melting points, making them excellent ceramics for these composites. Fibers are typically fabricated using methods different than those used in bulk ceramic production. Hot-pressing and sintering do not allow for the fine diameters required for these advanced fibers, and production is generally limited to spinning the fiber from a liquid, organic precursor, or through chemical vapor deposition of these ceramics on an existing fiber substrate. Spun fibers are cured through irradiation or through sintering, producing small diameter, uniform continuous fiber filaments. These filaments are combined to produce unidirectional fiber tow, which can be used in CMCs, or can be woven into complex shapes and patterns for fabrics in composite systems [10].

Fibers provide structure and reinforcement in the composite system. The inherent stiffness of the ceramic provides strength and durability for the CMC, while the high modulus and high tenacity provide added mechanical durability, despite the brittle nature of bulk ceramics. The ceramics used in these fibers are typically designed to be amorphous to micro-crystalline, which allows for more flexibility and less rigidity in the reinforcement system [11]. Advanced ceramic materials, as well as the use of grain growth inhibitors and newly developed pre-ceramic polymers, will lead to continued research on these fiber systems, increasing the strength and durability in future materials.

4.2.2 Interphase

The interphase in a CMC is essential to the energy-absorbing mechanisms exhibited in these systems which differentiate them from bulk ceramic monoliths. Bulk ceramics have very low fracture toughness and low tolerance to crack propagation. These properties make bulk ceramics susceptible to catastrophic failure resulting from even a small crack in the material. These same properties apply in a CMC without an interphase. The interphase provides a weak interfacial bond to the fiber and the matrix, allowing for slipping and energy dispersion of the mechanical stresses experienced in the composite.

Composition of interphases in CMC typically relies in the layered molecular structure of materials like hexagonal boron nitride and graphitic

carbon. These materials both have hexagonal-layered structures, with the in-plane atoms strongly and covalently bound, while the layers are held together by weak van der Waals' forces. This structure allows for slipping of the layers, providing a solid-state lubricant as the interphase. Boron nitride is quite thermally stable, decomposing at 1000 °C in air and 2800 °C under inert atmosphere; however, it is very susceptible to moisture damage [12]. A protective layer of non-oxide ceramic is typically applied over a boron nitride interphase during the fabrication process to prevent moisture damage in the coating. Carbon interphase has much lower thermal stability, decomposing in air at around 500 °C [13], however, can also be coated with a non-oxide ceramic as a means of oxidation protection. Non-oxide interphases are in the process of being developed, and candidate materials include calcium oxides and phosphates [14]. Interphases are typically applied using chemical vapor deposition, in which the reaction or decomposition of gaseous precursors produce a uniform, thin coating on a fiber or fabric.

Mechanical stresses applied to a ceramic typically result in a crack which can propagate through the bulk material, resulting in mechanical failure of the material. In a CMC, the interphase allows for several energy absorbing mechanisms, including crack deflection, fiber bridging, and fiber pullout. All of these mechanisms allow for the energy of the mechanical stress applied to disperse across the perimeter of the fiber and through the matrix, rather than transferring directly though the CMC. The weakly bound interphase provides a pathway for energy dispersion without a crack propagating directly through the fibers. Instead, the crack travels a more complicated path, allowing for energy dispersion and absorption in the composite system. These mechanisms are what contribute to the strength and durability of three-part CMC systems [15].

4.2.3 Matrix

The matrix is the bulk ceramic material in a CMC. Matrices are designed to be extremely thermally stable, with a similar thermal expansion coefficient to the fiber and a low density. The matrix provides both protection for the fiber and interphase as well as a means for which energy from mechanical stresses can disperse through the composite.

The coefficient of thermal expansion (CTE) plays a very important role in selection of a matrix material. Large differences in CTE between the fiber and the matrix can result in stresses, cracking, and composite damage when the CMC is both heated and cooled. Low thermal expansion in materials like C–C and SiC–SiC composites result in reduced expansion

and contraction during heating cycles, making both carbon and silicon carbide excellent matrix materials in non-oxide CMCs. In a scenario where the CTE of the matrix was higher than that of the fiber, the matrix expands, gripping to the fiber upon cooling and resulting in a strong bond between the fiber and matrix. Energy-absorbing mechanisms like fiber pullout and crack deflection would then not occur, resulting in a brittle composite and ultimate failure of the system. In the opposite case scenario where the CTE of the fiber was greater than that of the matrix, complete fiber debonding may occur upon cooling, providing no reinforcement in the CMC and resulting in failure of the composite. Fiber and matrix CTE match allows for expansion and contraction at similar rates in both components, preventing damage and composite failure [16].

The matrix in non-oxide systems is also designed to provide oxidation resistance to prevent damage to both the interphase and fiber. Materials like silicon carbide and silicon nitride have incredibly high melting points and good mechanical properties, even at high temperatures. Silicon carbide provides oxidation resistance at temperatures up to 1480 °C. The outermost layer of silicon carbide forms an oxide scale of silica, protecting the bulk material from further oxidation. At even higher temperatures above 1700 °C, the silica layer becomes molten and flows to fill microcracks formed in the matrix. This unique property makes silicon carbide an excellent candidate for non-oxide matrices. Silicon nitride has similar high-temperature properties; however, the overall operating temperature is slightly less than that of silicon carbide.

Oxide matrix materials include ceramics like alumina, mullite, silica, and zirconia. These matrices are stable to lower temperatures than typical oxide matrices, but sinter easily for ease of production and provide inherent oxidation resistance. These oxide matrix materials are limited by their higher thermal expansion coefficients as well as the loss of high strength and toughness at elevated temperatures [17]. Oxide matrices are used exclusively with oxide fibers in the production of oxide CMCs.

Matrices, both oxide and non-oxide, are applied using a variety of techniques. The hot-pressing method of ceramic matrix application is limited by the very high melting point of these ceramics; however, it does produce a matrix with low porosity and excellent uniformity. Oxide matrices can also be applied using a sol–gel method, where materials like silica and alumina are fabricated using tetraethylorthosilicate [18] sol–gel and aluminum tri-*sec*-butoxide [19] sol–gel, respectively. Matrices produced by sol–gel methods require multiple cycles of heated curing, followed by reimpregnation to achieve a fully densified matrix. Both oxide and non-oxide matrices can be applied using chemical vapor infiltration (CVI), in which

the fiber (which may or may not be coated with an interphase) is exposed to gaseous precursor, resulting in the deposition of a uniform, fully infiltrated coating. Matrices produced by CVI exhibit relatively low porosity and the deposition rate and thickness can easily be controlled. Silicon carbide, silicon nitride, carbon, and boron nitride matrices are typically deposited using CVI, required significantly lower temperatures than hot pressing of these materials. This method also allows for matrix application to a variety of complex 3D shapes with ease. Recent development in polymer synthesis has also lead to the design and development of unique pre-ceramic polymers for use as a matrix material. These polymers are a viscous liquid at room temperature, and dip-coating methods are used to coat the fiber substrate. These polymers are then cured and pyrolyzed, producing ceramics like silicon carbide and silicon nitride [20]. This polymer impregnation and pyrolysis (PIP) method also requires multiple cycles of impregnation to achieve a fully densified composite. PIP processing can be used on complex 3D composites and is relatively cost effective as compared to other matrix application methods.

4.3 Modern Uses of CMCs

Applications for CMCs typically exist where high temperature resistance and strength are a necessity. These systems have excellent properties for use in aircraft and aerospace technologies including engine and brake components and tiles and exterior panels. These lightweight, durable, and refractory systems provide the hardness, toughness, and lightweight nature needed for these types of aircraft. CMCs have shown promise in engine turbine blades, surpassing the operational temperatures of conventional nickel alloys and allowing for engines to be designed to have more power and run at these extreme temperatures over 1400 °C. Ceramic composite systems also have applications for multiple uses in military applications like personal armors and panels in tanks and armored warfare vehicles, providing excellent strength and properties in ballistics. CMCs have also been designed for the automotive industry, including passenger vehicles, in both brake pads, rotors, and clutch components [21]. These composites have excellent wear resistance and provide toughness and durability, while maintaining low density. Added weight in any type of vehicle is a disadvantage, and the natural low densities of ceramics make these systems ideal candidates where weight of the operating system is a factor. CMCs have also shown excellent properties in biological applications. These systems can be used in bone scaffolding and tissue regeneration as well as implants and cements in dental science. Ceramics like silicon carbide and

hydroxyapatite have excellent biocompatibility, allowing the body's natural tissue growth mechanisms to occur over these materials. The strength of CMCs allows for use of these materials in places in the body which undergo high stresses and strains, like bone grafts and dental implants. Finally, other applications for these CMCs are being designed to take advantage of some of the other properties of ceramics, including electrical conductivity. Circuit breakers, microelectronics [22], and structural electronic packages have been designed out of CMCs, incorporating strength and durability, as well as the electrical conductivity needed in these applications.

4.4 History

CMC systems have a wide variety of applications in systems that require high-temperature and high-strength components. CMCs have desirable properties that make them ideal substitutes for metals and super-alloys, which are limited by melting points and oxidation at elevated temperatures. Ceramics also have much lower densities, making them ideal candidate materials in applications in which weight of the components is a factor. Over the last century, development of composite materials was driven by the need for stronger, more durable, and more lightweight materials. The primary goal of this research was to develop and fabricate materials for military applications. Components for military ground vehicles, aircraft, helicopters, rockets, and armors required the strength and durability provided by CMCs while maintaining a lower weight than available metals.

The study of these types of composite materials began in the 1940s with the advancement of glass fibers for use in aircraft components like wings and nosecones. Previously, these pieces were made of single solid pieces of metal or riveted metal panels. Designers proposed the use of ceramic materials, but it was quickly discovered that solid ceramic and glass components were fatally brittle. These pieces cracked easily and their brittle nature resulted in catastrophic failure of the components. Research showed that the theoretical high strengths were not occurring in these materials due to flaws in the bulk structure, beginning with small cracks. The strengths varied greatly from different identical parts because of innate faults in the material structure. A proposed solution was to use glass fibers as a filler for the bulk material in an attempt to minimize these faults in the system. These new systems provided strengths greater than that of the original material because the fibers prevented crack propagation throughout the matrix.

This "fiberglass" was designed to contain glass fiber whiskers in a polymer resin, providing strength, flexibility, and low density for aircraft

components. Glass fibers for use in these and other composite applications were designed by Owens, and by 1935, manufacture of the fiber for mass production began when the company merged with Owens-Corning fibers. Polymers used in these composite systems included Pittsburgh Plate Glass's allyl polyester resin (1940) and Marco Chemical Company's fiberglass laminate (1942). The US Navy implemented fiberglass electrical terminal boards that year, and by 1944 boats containing glass fiber-reinforced polymers were used in the Allied invasion of Normandy. These materials were used in aircraft components at both the Wright-Patterson Air Force Base and Republic Aviation Corporation in the 1940s.

The use of these composite systems continued throughout the 1950s, advancing to use both fiberglass–epoxy combinations as well as asbestos fiber and phenolic resin composites. These materials were used for helicopter blades, body components for Chevrolet Corvettes, and circuit boards. With the advancement of aircraft and the desire for space exploration, engineers began to research new composite systems like MMCs for materials capable of standing up to the extreme conditions required for space travel. These MMCs comprised a ceramic fiber, fiber whisker, or particle surrounded by a durable, lightweight metal. Initial systems used carbon and boron fibers, and by the 1960s, both of these materials were undergoing extensive research for use in composites. Graphite fibers were designed and manufactured from both Rayon (Texaco) and polyacrylonitrile (A. Shindo); however, these fibers reacted readily with magnesium and aluminum matrices, resulting in failure of these initial systems. To combat this issue, air-stable coatings were produced on these fibers to allow for fabrication of graphite magnesium and graphite aluminum composites. Boron fibers were also being studied due to their increased strength as compared to carbon, however, had several major shortcomings, making them difficult for mass production and advanced usage. Boron fibers were created through deposition on a thin tungsten wire, limiting manufacture and adding additional cost. These boron fibers also had reactivity issues at elevated temperatures with the metal matrix and coatings to prevent this had to be developed to prevent these reactions.

With the decline of the Space Race in the early 1970s, new applications had to be found for the existing composite technology. These advanced materials, specifically carbon fibers, were used in sports applications, including bicycles, golf clubs, and tennis rackets, allowing for durable products with lighter weights than those composed of metals (Figure 4.2).

Application also began to shift toward computer components and electrical parts like capacitors, resistors, and transformers. MMCs were

Figure 4.2 Photograph of a bicycle composed of carbon fiber composite.

still studied for their use in aerospace applications and were advanced to withstand the thermal cycling involved with these applications. These systems required high strength and refractory properties as well as low thermal expansion coefficients which reduced damage caused by expansion and contraction from these temperature cycles. By the 1980s, silicon carbide fibers were produced commercially and were used alongside aluminum, producing a composite with a CTE lower than that of the metal alone.

With the advancement of silicon carbide pre-ceramic polymers and fiber production of Yajima's Nicalon® fibers, new systems superior to MMCs were produced with ceramic matrices. These CMCs were able to provide strength and temperature resistance, without the extreme brittle nature of typical monolithic ceramics. CF-CMCs were designed with solid-state lubricating interphases between the fibers and matrices, which greatly added to the fracture toughness of the material. The weak interfacial bond between the fiber and matrix causes some of the the energy from cracks to be absorbed, thereby slowing crack propagation. The toughening mechanisms that result from this are known as fiber pullout/pushout, crack deflection, and crack bridging. SiC–SiC composites provided excellent strength, temperature resistance, and durability for advanced aircraft and aerospace applications. Carbon–carbon composites were also designed for brake components on these vehicles, providing excellent strength, toughness, and temperature resilience.

Advanced applications of composite systems have continued into the new millennium with the development of hybrid systems for applications

varying from biological to military to electronic components. Biological hybrid systems combine CMCs with organic, biologically active molecules, providing strength and structure for dental and bone implants. In these systems, ceramics like hydroxyapatite are designed into composite systems to provide bone scaffolding for human graft materials with considerable strength and similarity to autograft bone. Hybrid composites have also been designed for cements and electronic components, combining the desirable properties of a variety materials tailored to specific applications. These types of systems will continue to advance with additional research and the need for new materials and unique material applications [23].

4.5 Ceramic Fibers

Ceramic fibers are composed of amorphous, nano-crystalline, and/or crystalline non-metallic inorganic solids. These fibers are characterized by their refractory properties and are chosen for a CMC based on their ability to withstand extreme conditions while exemplifying energy-absorbing mechanisms including fiber pullout and crack deflection. The two broad classifications of ceramic fibers are oxide and non-oxide. Ceramic fibers for CMCs are traditionally grouped into tows, which are fabricated to typically contain between 300 and 800 ceramic fibers in the 10–20 μm diameter range (Figure 4.3a). Tows are then woven into either 2D or 3D fabric for use in CF-CMCs (Figure 4.3b) [24]. These fabrics are characterized by the warp and weave that the tows have been woven into. The warp is the direction in which the fiber has the most strength and comprises the majority of the tows in the fabric. The weave, or the support tows, are woven around the warp tows as filler in the fabric. When fabricating a CF-CMC, warp and weave are manipulated to optimize strength in the x and y planes, providing extra reinforcement in the CMC [25].

4.5.1 Oxide Fibers

Oxide fibers are ideal for CMCs that are exposed to oxidizing environments above 1300 °C. They require metal oxides with high melting points and stable crystal structures [26]. The largest manufacturer of oxide fibers is 3M Corporation in St. Paul, MN [27]. 3M has created a mature line of oxide fibers called the Nextel™ series, including 312, 440, 550, 610, 650, and 720. The 610 (alumina), 650 (yittria, zirconia, alumina), and 720 (mullite–alumina) fibers are used in high-temperature applications due

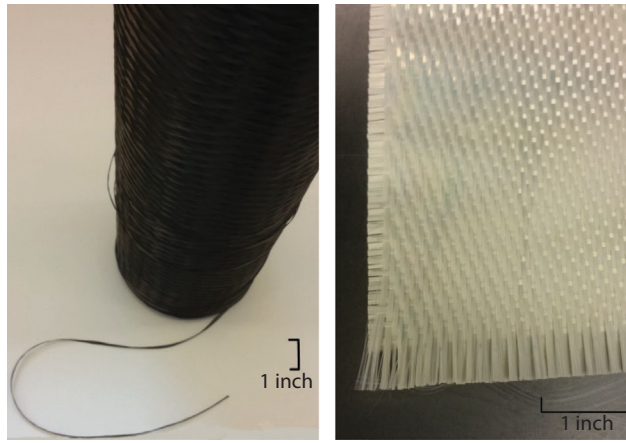

Figure 4.3 (a) Toray® T-300 Carbon tow. (b) 3MNextel™ 610 woven fabric.

to their thermal stability. The 550 fibers, primarily comprising γ-alumina, are limited to slightly lower-temperature applications due to the crystallization point of a-alumina, at which the ceramic undergoes a contractive phase change. Nextel 312 and 440 are used in CMCs for low-temperature applications because they consist of a glassy amorphous boria phase which limits the creep properties of the fibers [27].

4.5.1.1 Alumina Fibers

The most popular metal oxide used in the production of oxide fibers is *α*-alumina. *α*-Alumina is the most stable crystalline form of alumina. Alumina (Al_2O_3) fiber production typically starts with sol–gel synthesis. These sol–gels are viscous aqueous solutions of aluminum salts paired with inorganic/organic ligands [28]. The gel fiber is pulled from solution via spinning, dried, and heat treated to produce *α*-alumina. During the heat treatment process from about 500 °C to 1000 °C, the alumina precursor gel transitions into 10–100 nm grains of mixed phased alumina. The *α*-alumina phase begins forming around 1100 °C and forms micron-sized larger grains, causing the ceramic fiber to be porous and extremely brittle [26]. The conditions used to heat the fibers are strictly controlled due to the large volume change and resulting porosity created by the residual compounds [29]. These factors, along with the inherent high creep of alumina at high temperatures, result in the requirement of grain growth inhibitors to stabilize the grains and prevent porosity.

4.5.1.2 Stabilized Alumina Fibers

Despite these grain growth and high-temperature creep shortcomings, there are several α-alumina fibers still available for CF-CMCs. The 3M fiber Nextel 610 is composed of 99% α-Al_2O_3 as well as 1% SiO_2 and Fe_2O_3 for stabilization. Compared with the other 3M oxide fibers of 10–12 μM diameter, the Nextel 610 alumina fiber has moderate strength (1.9 GPa) and superior Young's modulus of 370 GPa as shown in Table 4.1 [27]. Yttria and zirconia are used to suppress grain growth and to stabilize the fiber as observed in Nextel 650 fibers. These fibers exhibit an increase in strength to 2.5 GPa. Nextel 650 differs from Nextel 610 in the manufacturing process through the addition of zirconium acetate and yttrium chloride, which are mixed in with the alumina precursors before the fiber-spinning process [30]. Increased strength in pure α-alumina fibers is also achieved when single crystal orientation lies along the c-axis. This orientation is very challenging to fabricate, and the only fiber commercially available currently is Saphikon, Inc. Sapphire 100% alumina fiber [6]. Single grain alumina fibers are grown from molten alumina which is very costly and slow. This fiber is typically drawn from a laser-heated alumina rod and has a modulus of 435 GPa as well as a much larger diameter of 70–250 μM. The larger diameter and rigidity hinder the ability for the fiber to be woven, and therefore typical use of these fibers is in the optical materials industry [6].

4.5.1.3 Alumina Silicate Fibers

Alumina–silica fibers are used in a wide range of industries depending on the thermal properties resulting from the ratio of Al_2O_3 to SiO_2. Small amounts of silica (5 wt%) allows the alumina to sinter slowly in the transitional forms of alumina while controlling the nucleation and retarding the growth of α-Al_2O_3 up to 1300 °C [31]. When larger amounts (~20 wt%) of silica are introduced to the fiber composition, gamma-alumina grains are formed surrounded by amorphous silica. Once these fibers are heated above 1100 °C, mullite is formed thus restricting the growth of α-alumina. 3M's Nextel 310, 440, 550, and 720 alumina silicate fibers are the industry standard in oxide composites. The only Nextel™ fibers rated for high-temperature application (<1000 °C) are the 610 and 720 fibers, while the remaining alumina silicate fibers are more applicable for thermal insulation (>1000 °C). Nextel 720 has improved creep resistance over 610 due to the inherent creep resistance present in mullite and elongation of the alumina grains. Nextel 720 is manufactured via

Table 4.1 Various fiber types, manufacturer, trade mark name, composition, strength, and modulus.

Fiber type	Manufacturer	Trade mark	Composition (wt%)	Strength (GPa)	Young's modulus (GPa)
OXIDE	3M	Nextel 312	62% Al_2O_3	1.7	152
			24% SiO_2		
			14% B_2O_3		
		Nextel 440	70% Y-Al_2O_3	2.1	190
			28% SiO_2		
			2% B_2O_3		
		Nextel 550	73% Y-Al_2O_3	2.1	193
			27 % SiO_2		
		Nextel 610	99% a-Al_2O_3	1.9	370
			0.2%-0.3% SiO_2		
			0.4%-0.7% Fe_2O_3		
		Nextel 650	89% a-Al_2O_3	2.5	360
			10% ZrO_2		
			1% Y_2O_3		
		Nextel 720	85% a-Al_2O_3	2.1	260
			15% SiO_2		

(*Continued*)

Table 4.1 Cont.

Fiber type	Manufacturer	Trade mark	Composition (wt%)	Strength (GPa)	Young's modulus (GPa)
	Saphikon inc.	Sapphire	100% a-Al_2O_3	2.2	435
	ICI	Saffil	95% a-Al_2O_3	2	300
			5% SiO_2		
NON-OXIDE	Nippon Carbon	Nicalon NLM 202	56.6% Si	3	200
			31.7% C		
			11.7% O		
		Hi-Nicalon	62.4% Si	2.6	270
			37.1% C		
			0.5% O		
		Hi-Nicalon Type S	68.9% Si	2.6	380
			30.9% C		
			0.2% O		
	Ube Industries	Tyranno LOX-M	54.0% Si	3.3	180
			31.6% C		
			12.4% O		
			2.0% Ti		
		Tyranno LOX-E	54.8% Si	2.5	200
			37.5% C		

			5.8% O		
			1.9% Ti		
		Tyranno SA	99.99% SiC	2.4	380
			<1% Al		
			<1% C + O		
	Dow Corning	Sylramic	96% SiC	4.7	400
			3.0% TiB2		
			1.0% B4C		
			0.3% O		
CARBON (PAN)	Toray	T300	93% C	3.34	230
			<50 ppm Na + K		
		T1000	95% C	7.06	294
			<50 ppm Na + K		
		M55J	>99% C	3.92	540
			<50 ppm Na + K		
CARBON (PITCH)	Cytec	Thornel P25	>97% C	1.56	159
		Thornel P120	>99% C	2.4	830

Data are those given by the manufacturers. Adapted from [26].

a sol–gel synthesis containing silica and alumina precursors for the bulk of the fiber as well as iron oxide compounds to induce crystallization of the alumina [27].

4.5.1.4 Other Oxide Fibers

Other polycrystalline oxide fibers are currently under experimental development. These fibers aim to eliminate creep in the alumina grains while maintaining strength. Yttrium aluminum garnet (YAG) fibers appear to be the most promising thus far. Alumina–YAG eutectic fibers with fine diameter have been produced with virtually no creep and are currently under commercial development to improve tensile strength [32]. Other variations of oxide fibers under development include zirconia (ZrO_2) and various lanthanide oxide fibers [33].

4.5.2 Non-oxide Fibers (SiC)

Silicon carbide (SiC) fibers were developed in the early 1970s for high-temperature applications (>1200 °C) where mechanical stability, chemical stability, and creep resistance would be preserved for long-term use [34]. These fibers have high tensile strength (>2 GPa) and Young's moduli at 200 GPa or greater regardless of synthesis method [26]. The largest manufactures of SiC fibers are Nippon Carbon, Ube Industries, and Dow Corning [35–37]. These fiber manufacturers are summarized in Table 4.1 with the various chemical compositions and strengths of their respective fibers. The common denominator for all of these fibers is each synthesis begins with an organosilicon polymer. These polymers are primarily composed of Si–C bonds with various ligands containing but not limited to carbon, hydrogen, and oxygen. Polycarbosilane (PCS) and its derivatives are used to create these fibers, which are spun from the bulk polymer melt [38]. Once the fiber is spun, the polymer is cross-linked to prevent softening. There are various ways to both cross-link and pyrolyze the polymer into SiC, each of which highlights different properties from the material [39].

4.5.2.1 Oxidation

Oxidative cross-linking of melt-spun PCS fibers into SiC ceramic fibers is performed in air to 200 °C [26]. The polymer chains are bound via Si–O–Si or Si–O–C linkages with oxygen scavenged from air. A slow heat cure to SiC-based ceramic is then performed to 1200 °C. The first major transition in the polymer is the out gassing of carbon oxides, alkyls and hydrogen

up to 900 °C. This changes the stoichiometry of silicon and carbon in the ceramic, decreasing the free carbon concentration and producing a near stoichiometric SiC ceramic. After pyrolysis at 1200 °C, the ceramic SiC still contains oxygen (12 wt%) and an excess of carbon raising the atomic ratio of C:Si to 1.3. This excess of contaminants causes the fibers to be described as "SiC-based fibers" and not stoichiometric SiC fibers [40]. Nippon Carbon manufactures their NL-200 Nicalon® fiber by this method. The introduction of oxygen to these fibers reduced the SiC-like properties, resulting in creep above 900 °C and a Young's modulus of only 200 GPa, about half that of pure SiC. The Si–C–O phase created upon introduction of oxygen to the cure represents about 40 wt% of the ceramic. Free carbon particles represent 5 wt% with the remaining mass as β-SiC. Above 1200 °C, the fiber degrades as the Si–C–O phase decomposes, resulting in strength loss in the fiber. Ube Industries produced a fiber with reduced strength loss at high temperatures using oxidation curing through synthesis using a polytitanocarbosilane (PTC) precursor which produces a ceramic of SiC and TiC [41]. While the fiber was stabilized by the TiC in terms of reduced grain growth at high temperatures, the oxygen contamination was even greater (13 wt%) than that of Nicalon and therefore there was little to no improvement in these Tyranno LOX-M fibers.

4.5.2.2 Irradiation

The use of a 2 MeV electron beam in inert atmosphere to cure the polymer fibers was introduced in order to reduce oxygen contamination in the fibers. This cure process uses Si and C radical sites recombining to crosslink the polymer. The fibers are pyrolyzed up to 1400 °C, resulting in a decrease in the oxygen content (reduced to 0.5 wt%); however, the C to Si ratio was raised to 1.39 in the Nippon Carbon Hi-Nicalon fiber. With the improved oxygen reducing cure the creep rates were reduced and not observed until over 1100 °C. Ube Industries also produced another PTC precursor fiber using the irradiation method. The Tyranno LOX-E fibers inevitably contain higher oxygen contamination (5 wt%) than Hi-Nicalon due to the addition of titanium alkoxides in the PTC polymer [42, 43].

4.5.2.3 Sintering

Stoichiometric SiC fibers are produced through the addition of sintering aids to pre-ceramic polymers from which fibers are spun initially cured via oxidation or irradiation. Nippon Carbon markets Hi-Nicalon Type S from a PCS polymer precursor which undergoes initial curing through

irradiation methods. The fiber is then pyrolyzed in a hydrogen rich atmosphere up to 1500 °C to reduce the excess carbon content found in its predecessor Hi-Nicalon fiber [44]. While these Nippon fibers exhibit no detectable chemical sintering aids, the heat treatment in the reducing atmosphere aids the sintering process. Ube Industries produced Tyranno SA fiber cured through oxidation and then through pyrolysis to 1800 °C, during which the excess carbon and oxygen are lost as volatile species [45]. The fiber strength is maintained due to the addition of aluminum acetylacetonate as a sintering aid in the PCS polymer. No detectable aluminum compounds are observed after sintering, and grains of about 200 nm SiC are detected. Finally, Dow Corning manufactures Sylramic™ through the oxidation of PTC doped with boron as a sintering aid [46]. These fibers are pyrolyzed to 1600 °C, during which TiB_2 is formed to stabilize and prevent grain growth in the SiC grains. These three fibers all are still below Young's modulus of stoichiometric SiC due to an excess of free carbon in between grains.

4.5.3 Carbon Fibers

Carbon fibers are a popular choice for ceramic reinforcement due to large strength to weight ratios. On the atomic level (<0.5 nm), carbon fibers are composed of hexagonally arranged carbon atoms in an imperfect graphene sheet. On the meso scale (1–50 nm), the graphene sheets are arranged in a turbostratic structure. Turbostratic indicates the random rotational alignment between sheets with maintained long-range order within each respective sheet. Finally, on the micron scale, the cross sections of these fibers show radial-folded and onion-like structures of the turbostratic graphene sheets [47].

Carbon fibers exhibit vastly different mechanical properties based on how they are synthesized. Carbon fiber precursors are categorized into two main groups: polyacrylonitrile (PAN) and pitch [48]. Both precursors undergo fiber formation, stabilization, and carbonization in order to produce strong carbon fibers. PAN is composed of acrylonitrile coupled with monomers and copolymers which enhance oxidative stabilization during the cure to a thermally stable hexagonal structure. PAN fibers are valued for high strength and moderate modulus as shown in Table 4.1. They can also be heat treated to increase modulus, but through this method the overall strength is decreased. Pitch fibers have a wide variety of strength and modulus properties based on the source of the mesophase pitch precursor (MPP). These pitch precursors are obtained from the thermal

polymerization of petroleum-based pitches and are received as liquid crystalline material [48]. There are a few other ways to synthesize carbon fibers including the use of rayon precursors or chemical vapor deposition of silane precursors onto wire filaments. These two methods are not used commercially and are most popular in research settings with limited applications to date.

4.5.3.1 Polyacrylonitrile

The strongest PAN fibers are wet spun from the bulk polymer dissolved in solvent and heated to 300 °C for a stiff, thermally stable fiber [49]. From there, the fibers undergo carbonization up to 1500 °C in inert atmosphere, after which they are composed of mainly turbostratic carbon with some nitrogen impurities. PAN fibers can be heat treated to upwards of 1800 °C to remove the nitrogen; however, this treatment decreases the fiber strength because of the formation of flaws in the overall structure [48]. PAN-based carbon fibers were originally developed for military aircraft applications, which quickly spread into commercial aircraft applications, sporting goods, infrastructure, and medical devices. The top manufacturer of PAN carbon fibers is Toray® with their T (ex. T300) and M (ex. M55J) categories [50].

4.5.3.2 Pitch

High-performance pitch fibers are melt spun from thermally polymerized aromatic petroleum by-product or coal-tar-based pitches [51]. Low molecular weights are maintained through solvent extraction in order to spin the fibers below 300 °C, reducing the cost of equipment. Fiber stabilization occurs in the presence of oxygen up to 600 °C in order to slowly remove hydrogen impurities and cross-link molecules, increasing molecular weights [47]. These initial heat treatments also involve careful manipulation of the Boudouard reaction in order to remove free carbon in the fiber. From there, the fibers undergo carbonization via heat treatment to upwards of 1600 °C. The resulting aromatics are self-organizing and provide strength to the fiber by orienting crystallites along the axis of the fiber during heat treatment. This strict crystal orientation along with pitch rheology is significant to the strength and modulus of the fibers [52]. Heat treatments are used to densify and further customize these properties, which are precisely controlled for application specifications. For example, as heat treatment temperature increases, the modulus of the resulting fiber increases up to the theoretical modulus of 1 TPa (graphene)

[47]. Pitch fibers have high thermal conductivity due to the dense, oriented nature of the crystallites. High-performance pitch-based carbon fibers are used in aerospace applications as well as in biomedical and automotive applications. One of the more popular pitch-based carbon fibers is Cytec Engineered Materials line of Thornel® fibers [53].

4.6 Interface/Interphase

The objective in fabrication of CF-CMCs is to allow the fibers to reinforce the matrix material and create damage tolerant composites. The interface boundary is a critical part of this goal. When a dense matrix is physically stressed, cracks form and spider throughout the CMC. In order for the CF-CMC to truly be continuous, the fiber is bound to the matrix. When a crack in the matrix reaches the bound fiber deflection around the fiber or going straight through the effected fiber can occur. Catastrophic failure can occur if the fiber is cracked and the strength of the CF-CMC plummets as a result of this crack propagation. It is critical to reduce brittleness and promote crack deflection around the fiber/matrix interface. Interphase materials surround the fiber, providing a new interface route for the crack to follow. This is required if the interface between just the fiber and matrix material are bound too tightly to promote the deflection on their own. A bonus property of an interphase or interface material is the ability to protect the fiber from aggressive environments both upon fabrication and long-term use [54].

A fiber interface is characterized as being a single surface where two phases touch. Interfaces require weak fiber/matrix interactions that are easily debonded. An interphase (interface material) is required when the natural interface between the fiber and the matrix does not exhibit these properties. Interface materials are deposited in between the fiber and the matrix. This deposition can be performed with a variety of syntheses including sol–gel liquid phase and physical vapor deposition techniques [55]. The deposited material works by creating two new interfaces, one between the fiber and the interface material and the other between the interface material and the matrix as depicted in Figure 4.4a. Interface promoted crack deflection is depicted in Figure 4.4b where the crack grows through the matrix and is deflected around the fiber via the easier route of debonding the fiber from the interface material. Duplex interface materials are useful when it is difficult to find one interphase that will easily debond to both the matrix and the fiber. In a duplex interphase system,

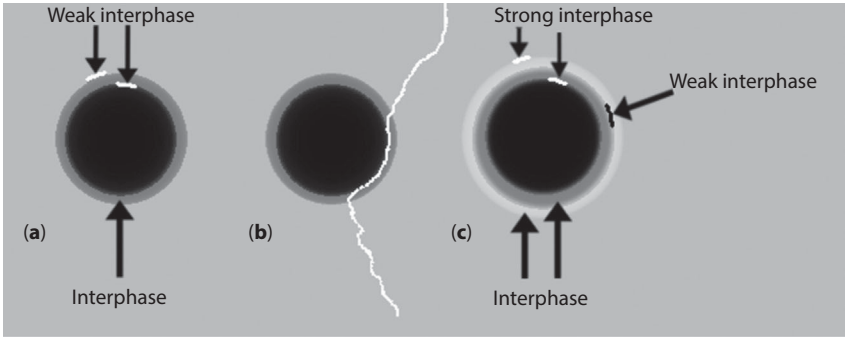

Figure 4.4 (a) A fiber (black) coated in an interphase (dark grey) surrounded by a matrix (grey). White lines indicate where the weak debonding interface lies. (b) A crack (white) traveling through the matrix (grey) into the interface material (dark grey) and deflecting around the fiber (black). (c) Duplex interphase system composed of a fiber (black), interphase 1 (dark grey), interphase 2 (light grey), and a matrix (grey). Interphase 1 bonds strong to the fiber and weak to interphase 2. Interphase 2 bonds weak to interphase 1 and strong to the matrix. The weak interface is where debonding will occur.

as long as the two interphases are weakly bound to each other it is not a problem for the interphases to be strongly bound to the fiber and/or matrix because there is at least one route for debonding. This concept is shown in Figure 4.4c. Interface material layers can bond to the fiber/matrix either chemically or mechanically. Mechanical bonding occurs when high-temperature matrix material shrinks significantly upon cooling and grips the interface tightly. This mechanical bonding can be enhanced based on interface surface morphology providing more points at which the matrix can fill in. A rough surface is bound more tightly than a smooth surface via mechanical bonding. Chemical bonding at the interface provides stronger bonding than mechanical bonds. This occurs when there is a chemical reaction between the two materials fusing them together with chemical bonds [54].

4.6.1 Requirements

One of the more difficult components of fabricating a CF-CMC is finding an interface material that will properly provide the energy absorbing mechanisms such as crack deflection and fiber pullout. These crucial mechanisms will be described in detail in the energy-absorbing mechanisms section of this chapter. The first requirement for an ideal interface material is relatively low interfacial opening strength (σ_i). Opening strength is the

amount of stress needed to detach the interface material from the material it is bonded to. The material that the interphase material is bound to can be the fiber, second interphase, or matrix. Interfacial opening strength must be below the strength of the material it is forming an interface with (σ_m). When $\sigma_i < \sigma_m$, it allows the crack to take the path of least resistance around the interface by separating the two materials, as opposed to continuing the crack through the stronger material. On a similar note, elastic moduli of the two materials forming the interface must be taken into consideration [56]. The elastic modulus of the interphase (E_i) must be below that of the material (E_m) it forms an interface with. An ideal ratio of E_m/E_i is between 1 and 100. There is a master curve derived from elastic moduli and the ratio of opening strength components depicted in the work by Pompidou as well as a more in depth discussion of these properties [57].

The CTE is an important parameter that is considered when choosing to use an interphase. The CTE describes the change in length, typically in the micron range, of a material per original length and degree temperature change [58]. CTE can represent the extent in which a material expands when heated, which is an important factor in high-temperature materials. This measurement is typically depicted with the units (μm/m/K or 10^{-6}/K) and examples can be seen in Table 4.2. Keeping two materials with an interface within 50% CTE of one another is good practice to avoid incompatibility and failure upon heating. For example, if a SiC fiber (CTE = ~3.9) [35] is coated in BN (CTE = 2.5) [59] as an interphase, then these two materials should not be susceptible to separation at high temperatures.

Examples are as follows.

4.6.2 Non-oxide

There are a variety of types of interphases used today in CF-CMCs. The goal of each interphase is a low shear strength achieved by a layered crystal

Table 4.2 Interphase materials with their respective modulus, strength, and CTE values [5, 59–64].

Interphase material	Young's Modulus (GPa)	Strength (Mpa)	CTE ($\times 10^{-6}$/K)
Boron Nitride	24	115	2.5
Pyrolytic Carbon	30	151	2
Silicon Carbide	280	124–266	4
Lanthanum Phosphate	110	137	10

structure. Optimal thickness reported in the literature for interphase coatings are 0.1–1 μm [65]. Oxide interphases are currently undergoing development for use with fully dense oxide/oxide CMCs. Development of non-oxide interphases began development in the 1980s and are now well characterized and used for many applications in CF-CMCs. The most widely used of these non-oxide interphases are boron nitride (BN), pyrolytic carbon (PyC), and silicon carbide (SiC). Boron nitride interphase can be deposited via CVD gaseous precursors including but not limited to, boron triflouride, boron trichloride, ammonia, nitrogen, and hydrogen. The hexagonal graphene-like planes of BN account for the solid-state lubricant properties in the material that promote slipping between the fiber and matrix. CVD-deposited BN interphases can also have a turbostratic structure that maintains these hexagonal planes but differ from graphene like orientation with slight rotations out of alignment in between sheets. BN interphases are aimed toward long-term high-temperature applications. BN shows less degradation at high temperature (1200 °C) than PyC interphase on SiC fiber in air [66]. For this reason, PyC interphases are generally used for low-temperature applications in less oxidizing environments. Since BN and PyC have the ideal layered crystal structures, they are widely used on their own as interphases. To compensate for other materials lacking this orientation, the layered effect has been moved to the microstructure level where alternating layers of materials are forming artificial debonding interfaces $(X–Y)_n$ [65]. This duplex interface system allows the incorporation of oxidative resistant materials such as SiC to be incorporated providing protection to coatings like PyC. PyC/SiC interphases show improved oxidation resistance and long-term use at higher temperatures over PyC alone [67].

4.6.3 Oxide

Oxide composites, having controlled porosity in the matrix phase, are traditionally made without interphases since cracks can be deflected around matrix pores. Overall, however, these CF-CMCs are not as strong as fully dense non-oxide composites, potentially due to the high porosity. In the development of a fully dense oxide/oxide CMC, an interphase is needed. Since oxide materials with desirable high-temperature application properties lack a stacked plane structure (which is seen in boron nitride and graphite interphases), there are a few approaches that need to be implemented in order to produce a good interphase. First, the duplex interphase coatings can be applied to provide a slippage plane. Second, the polarization of oxygen bonds with high-valence cations can be manipulated to induce

low adhesion at the interface. This phenomenon is observed in interface materials such as vanadates, phosphates, and niobates generally paired with rare earth metals [68]. There are many options for oxide interphases that fit these criteria, and they are actively being filtered based on ease of synthesis and long-term compatibility with other oxide CMC materials.

4.7 Matrix Materials

The matrix is the phase of the composite that binds the reinforcement together. It surrounds the fibers and may be directly bonded to an interphase layer if one is present. The matrix gives the composite rigidity and is responsible for the transfer of stress throughout the material. Without reinforcement, a ceramic matrix would be brittle. Low-density matrix materials are typically used to achieve a lightweight composite. The material should be chosen in conjunction with the fiber and interphase materials. If the composite is to be used in conditions of widely varying temperatures, then the coefficients of thermal expansion (CTE) must be compatible between all three materials. The effects of CTE mismatch are discussed in detail by Hull and Clyne [69]. In summary, the components of a CMC can become debonded or even crack if each of their CTEs is not in agreement. Another important factor is the strength of the bond between the matrix and fiber, which is controlled by choosing an interphase.. The bond should be neither too strong nor too weak in order to effectively toughen the composite. This is discussed in detail in the section on energy-absorbing mechanisms. It is also important to consider the composite's environment of use when selecting the matrix material. As previously mentioned, the CTE should be considered in conditions of widely varying temperatures. The material should also be inert to any other materials it comes in contact with during use. For example, a common concern in the aerospace industry is the resistance to oxidation when exposed to air at high temperatures. Lastly, the matrix strength should be well above any and all expected loads during typical use.

4.7.1 Carbon

Carbon is a material of great importance in many fields of study. Carbon is naturally and synthetically formed as many different allotropes, the most commonly discussed ones being graphite, diamond, and nanotubes. Each allotrope has its own set of chemical, physical, and mechanical properties,

but they are all recognized for their high strength and stability. Graphene, the 2D network of covalently bound carbon that makes up graphite, is considered the strongest material ever tested. Single-layer, defect-free graphene has been measured to be over 200 times stronger than steel [70, 71]. The carbon–carbon covalent bond is so stable that graphene can withstand temperatures of at least 2600 K (2327 °C) [72]. Not only can graphene handle these temperatures, but it can also dissipate heat at least five times better than copper [73, 74].

Due to its superior physical and mechanical properties, carbon-based composites were originally developed for use in defense applications. There was a need for lightweight and thermally stable materials to be used on rocket nozzles and missiles in the 1960s. Carbon fiber was fabricated from an organic polymer precursor and used to reinforce a carbon matrix. Since then, carbon/carbon composites have been used in many more applications and have been improved upon [75].

A number of precursors, mostly polymers, are used to make carbon matrices. When choosing a precursor, it is important to consider the resulting density of the carbon. Factors that influence this are ceramic yield, shrinkage during pyrolysis, concentration (in solvent), and degree of polymerization. The ceramic yield is the mass of carbon produced as a percent of the mass of the precursor used. A high-concentration polymer (low solvent content) will have a high ceramic yield because there will be less material to be removed from the polymer during heating and the final mass will be closer to the initial mass. This also results in less shrinkage and porosity because as solvent is driven off, the polymer will either constrict or leave open volume. However, some solvent may be desirable in order to maintain a low viscosity and properly infiltrate the fiber. A precursor with a high degree of polymerization will also result in a high ceramic yield and therefore less shrinkage and porosity. During polymerization reactions, gaseous byproducts and low-molecular-weight oligomers may form and evaporate with the solvent. If the precursor already has a high degree of polymerization, then less gaseous byproduct will form, minimizing shrinkage and porosity the same way a high concentration does. In order to prevent damage to the composite during manufacturing, porosity should remain below 10% and ceramic yield should remain above 84% [75]. Of course, other factors are also considered when selecting precursors, such as difficulty to process, cost, and shelf life.

Polymer precursors for carbon matrices can be either thermosetting resins or thermoplastics. Commonly used thermosets include phenolics, isocyanates, polyimides, and polyarylacetylene, as well as others. Phenolics were the first to be used due to their low cost and ease of processing. Some

can achieve ceramic yields up to 74%. Isocyanates also have relatively high ceramic yields and exhibit very little shrinkage during pyrolysis. Polyimides and polyarylacetylene are the most advanced thermosetting precursors, achieving ceramic yields above 84%. The processing of these materials includes just one pyrolysis step, so they save processing time and money. Unfortunately, they tend to be high-cost materials [75].

Thermoplastics may also be used, but they come with some disadvantages that need to be accommodated for. Pitches are the typical thermoplastic precursor, but they cannot achieve high ceramic yields unless high pressures are used or they are developed as mesophase pitches. In addition, thermoplastics will melt at high-enough temperatures, so they must be oxidized or vulcanized in order to induce cross-linking and make a more stable precursor. The benefit of these precursors is that they produce a more graphitic carbon, while thermosets produce a glassy carbon. Carbon matrices with high degrees of graphitization are desirable when high thermal conductivities are needed. If higher matrix strengths are needed, however, glassy carbon from thermosetting resins may be preferred [75].

Carbon matrices can also be formed from gas-phase reactions. In a process called CVI, gaseous hydrocarbons are passed over fiber reinforcement at high temperatures where they decompose into carbon and deposit on the surface. Over time, a fully densified carbon matrix is deposited around the fiber. Hydrocarbons with high carbon-to-hydrogen ratios are used to maximize carbon deposition and minimize byproduct formation.

Carbon matrix composites have very low shear strengths compared to their tensile and compressive strengths. In one case, a carbon/carbon composite showed a tensile strength of 250 MPa and a shear strength of 20 MPa. Compressive strengths of these systems are on the order of 200 MPa [75]. This may be explained by the bonding within the graphite structure. Graphite may be made up of the impressively strong layers of carbon atoms known as graphene, but van der Waals' forces connecting these layers are relatively weak. This allows the layers to slide over each other easily. When shear stresses are applied to a composite containing a graphite matrix, failure can easily occur due to the weakly bonded graphene layers. This effect also causes composites with carbon matrices to have weak tensile strengths in the direction perpendicular to the fibers [76].

Graphene also lends its thermal properties to graphite matrix materials. In the plane of graphene layers, the thermal conductivity of graphite is very high. Perpendicular to this plane, however, the material demonstrates thermally insulating properties. Since monolithic graphite does not contain perfectly aligned graphene layers, its thermal conductivity will reflect that of both graphene orientations—about half of the thermal conductivity of

copper. If the matrix is made up of glassy carbon, the thermal conductivity will be much lower. Hence, graphitic carbon is used in high-temperature applications such as brakes, re-entry shields, and rocket nozzles. In these applications, it remains stable at the high temperatures and effectively dissipates heat away from the other components of the object [75].

Carbon displays stability up to very high temperatures but has one drawback which limits its use in high-temperature applications: oxidation. If carbon is exposed to air at high temperatures, oxidization will readily occur and its mechanical properties will drastically decline. Fortunately, there are a number of ways in which carbon matrix composites can be protected from oxidation. In the case of carbon brakes, the design can be such that exposure to air is minimized [75]. More commonly, coatings can be applied to the composite to block oxygen from making contact with its surface. Silica and alumina have both been used due to their high oxidation resistance and low oxygen permeability. Non-oxide coatings such as hafnium diboride, silicon nitride, and silicon carbide have also been used. These materials form protective oxide layers at high temperatures, effectively blocking the composite from oxygen exposure. Another method of oxidation protection is by using additives in the matrix which oxygen will preferentially react with. For example, boron and boron carbide powders act as oxygen scavengers and form boron oxide. Boron oxide is a glass former that melts at 450 °C and subsequently fills in previously formed cracks. The glass then provides additional oxidation resistance [76].

Carbon matrices are most often used with carbon fibers. In applications that require good thermal stability and high rates of heat dissipation, graphite is the superior material. Composites made of both graphite fibers and a graphite matrix can achieve these thermal properties, as long is sufficient oxidation protection is applied [75].

4.7.2 Silicon Carbide

Carbon is an excellent matrix material in many applications; however, its sensitivity to oxidation limits its high-temperature uses, even with oxidation protection. The use of silicon carbide (SiC) as a matrix material produces composites of similar strengths and thermal properties as compared to carbon matrix composites, but with superior oxidation resistance. At elevated temperatures in oxygen-containing environments, SiC will form a protective layer of silica on the surface, preventing further oxidation of the matrix or fiber. SiC may be used with carbon or on its own. Just like carbon, SiC is stable at high temperatures (up to 2300 °C) and can maintain its high strengths. A disadvantage of SiC is susceptibility to degradation when exposed to water

at temperatures above 1000 °C. Silica and gaseous $SiOH_4$ are formed, causing loss of material and significantly decreased strengths [77].

There are a number of ways in which SiC or SiC–C matrices are manufactured, including CVI, polymer impregnation pyrolysis (PIP), and melt infiltration (MI). Each of the processes, which are discussed in detail later, use different types of precursors. In the gas phase, the precursor methyltrichlorosilane (MTS) is decomposed at high temperatures with hydrogen using CVI. The SiC forms on the surface of the fiber and builds up to a fully densified matrix. The SiC produced is in the β phase and has a fine-grained structure, which allows for superior mechanical properties. The other methods of forming SiC matrices involve infiltration of the fibers with liquid precursors. With the PIP method, silicon-based pre-ceramic polymers are used and pyrolyzed to SiC. Examples include polymethylsilane, allylhydridopolycarbosilane, polyvinylsilazane, and various other PCSs and polysilazanes. PCSs tend to be the more expensive class of pre-ceramic polymers, so their applications are more limited. These materials are manufactured by proprietary means by companies such as Starfire® Systems and KiON Defense Technologies. Different precursors have different ceramic yields, but unlike carbon precursors, this will not impact the ultimate porosity of the composite. Multiple impregnation steps are taken to fully densify the composite, so pre-ceramic polymers with different ceramic yields will take different amounts of impregnation steps [77]. Table 4.3 lists different pre-ceramic polymers with their ceramic yields.

The process of MI is much different from CVI and PIP. Where the previous two methods lead to the direct production of a SiC matrix composite, MI starts with a carbon/carbon composite and uses molten silicon to make the SiC matrix. A porous carbon/carbon composite is formed from precursors listed in the previous section and liquid silicon is infiltrated into the pores to react with the carbon matrix, forming SiC. The final product can either be a carbon/SiC or carbon/carbon–SiC composite, depending on the extent of infiltration. A disadvantage of this method is that the molten silicon will also react with the carbon fiber, resulting in degradation of the composite. To prevent this, interface coatings must be applied to the fibers before the composite is made. For example, thin films of silicon carbide, silicon nitride, or boron nitride can be coated on the fibers to effectively prevent contact with the molten silicon [77]. Alternatively, the same process can be performed on SiC/carbon composites to produce SiC/SiC or SiC/carbon–SiC composites. By using SiC fibers, the problem of fiber degradation is completely avoided since molten silicon will not react with SiC.

Table 4.3 Ceramic yields of various SiC-forming pre-ceramic polymers.

Polymer	Type	Company	Ceramic yield (%)	Pyrolysis temperature (°C)	Reference
StarPCS™ SMP-10	PCS	Starfire Systems	72–78	1000	[78]
StarPCS™ SMP-500	PCS	Starfire Systems	65–70	1000	[79]
StarPCS™ SMP-730	PCS	Starfire Systems	65–70	1000	[80]
StarPCS™ SMP-800	PCS	Starfire Systems	60–65	1000	[81]
StarPCS™ SMP-877	PCS	Starfire Systems	58–62	1000	[82]
Ceraset® Polysilazane 20	Polysilazane	KDT	73	1400	[83]
Ceraset® Polyureasilazane	Polysilazane	KDT	71	1400	[84]
Ceraset® DI-200	Polysilazane	KDT	91–92	1400	[85]

4.7.3 Oxides

The final class of matrix materials that will be discussed is the family of oxides. These are materials like alumina, silica, silicon carboxide, aluminosilicate, yttria-stabilized zirconia, etc. The primary reason for using oxide ceramics is to achieve the highest possible amount of oxidation resistance. These materials are already fully oxidized and therefore cannot oxidize further at high temperatures when exposed to oxygen. By the same reasoning, these matrices are most often used with oxide fibers to make oxide/oxide composites. When used in place of carbon- and silicon carbide-based composites, these materials show potential to significantly extend the lifetimes of parts used in aerospace and other high-temperature applications. In addition, the processes to develop these matrices are much simpler and less expensive than the processes to develop carbon and silicon carbide matrices.

Most oxide/oxide composites do not include an interface coating between the fiber and matrix. This is because the toughness of an oxide/oxide composite is provided through a different source: pores in the matrix. Most oxide materials are naturally porous due to the methods in which they are manufactured. In the previously discussed matrix systems, cracks are stopped when they reach the fiber/matrix interface and interface coatings allow for energy-absorbing mechanisms. In porous oxide matrices, cracks are stopped because the process of propagating through a pore requires more energy than propagating through a solid material [86]. This effectively prevents fiber fracture and eliminates the need for an interface coating. Since the pores are beneficial to the toughness of the composite, there is also no need for multiple densification cycles. With non-oxide CMCs, it can take weeks or months to make a finished product between applying interface coatings and achieving a fully densified matrix. These steps also dramatically increase the cost of manufacturing. Oxide/oxide composites can be made in a matter of days and at a fraction of the cost [87].

There are also certain disadvantages associated with oxide matrices. They tend to result in lower strengths of the overall composite. Without an interface coating, the fiber and matrix will bond strongly. This is especially true if the matrix and fiber are composed the same material because grains will be able to merge at the interface at elevated temperatures [88]. Upon loading, pores in the matrix will dissipate the energy of cracks up to a certain value of stress: the ultimate tensile strength. When that stress value is reached, fiber fracture will begin. Due to the strong fiber/matrix bond, the cracks in the fibers will propagate through the surrounding matrix

and into neighboring fibers. Because of this phenomenon, the strength of the composite is dominated by the strengths of the weakest fibers. For composite systems in which the matrices are not strongly bound to the fibers, the strength of the composite is dominated by the average strength of the fibers. An important factor in optimizing the toughness of an oxide/oxide composite is the pore volume distribution. Pores are more effective at preventing crack propagation if they are evenly distributed and closed off. Matrix cracks formed during the manufacturing process, which are considered a form of porosity, actually make it easier for other cracks to propagate [86].

Oxide/oxide composites have been developed with interphase coatings in attempts to maximize the amount of energy-absorbing mechanisms. This has been done with carbon interface coatings, which are intentionally oxidized out after applying the oxide matrix. This creates a gap between the fiber and matrix, preventing fiber cracks from propagating to neighboring fibers [88]. Oxide interface coatings have also been produced, such as monazite ($LaPO_4$) and scheelite ($CaWO_4$). Both have been shown to prevent crack propagation and extend the lifetimes of oxide/oxide composites [86]. Weakly bound interphase coatings, combined with the energy absorption of matrix pores, have given oxide/oxide composites the potential to be the class of CMCs with the highest amount of toughness. Unfortunately, this makes the fabrication procedure more complicated and would add to the cost of an oxide/oxide part.

The precursors typically used in the fabrication of oxide matrices are powder slurries of the oxide material. These are made by mixing the oxide powder in water and adding other materials such as binders, dispersants, and plasticizers in small quantities. Oxide powders should have particle sizes small enough to properly allow for infiltration between fibers [86]. Alternatively, liquid metal-alkoxide precursors can be used, often in the form of sol–gels. These form polymeric networks upon removal of solvent, which must be pyrolyzed to form the metal oxide matrix. These typically have low ceramic yields and therefore high amounts of shrinkage during pyrolysis, so they are best used as final densification steps [88].

4.8 Matrix Fabrication Techniques

Various methods of applying matrices to fibers have been developed. Most of the methods discussed here were mentioned in the previous chapter on matrix materials, so now they will be discussed in more detail. Not every

process can be used to make all types of matrices. Each one has its own benefits and disadvantages, making them useful for certain applications.

4.8.1 Polymer Impregnation and Pyrolysis

This manufacturing technique is an advanced method for making high-density (and low-porosity) CMCs. PIP can be used to make composites with carbon, silicon carbide, or oxide matrices. The precursors used are pre-ceramic polymers, which were discussed in the previous chapter. For carbon matrices, the polymers are carbon based, and for silicon carbide matrices, the polymers are silicon based. For oxide matrices, the precursors are metal alkoxides, which polymerize upon the removal of solvent. When PIP of oxide matrices is done, it is often called sol–gel processing, because the precursor begins as a liquid alkoxides sol and solidifies into a gel. The basis of this process involves heat treating these polymers under inert atmospheres to induce pyrolysis and form a ceramic matrix.

The first step is typically to apply an interphase coating to the fiber. Though not always necessary, interphase coatings usually increase the toughness and lifetimes of composites. Next, the fiber is impregnated with the pre-ceramic polymer to make a continuous fiber-reinforced polymer (CFRP) preform. This can be done by multiple methods. In the wet filament winding method, fiber is drawn through a polymer bath and wrapped around a mold. The shape of the mold is roughly the shape of the final CMC part. The benefit of this method is that it minimizes the porosity that forms during the impregnation step [89]. In vacuum infiltration, the polymer is poured over the fiber and placed in a vacuum chamber. Under vacuum, air will be pulled out of the fiber, causing polymer to be pulled in. Vibration of the vacuum chamber may be used to assist in the removal of air bubbles [86]. Another method, resin transfer molding, injects the polymer into the fiber using a pumping system. However, this method is known to leave a relatively high amount of porosity in the CFRP [90]. In the final method of polymer impregnation discussed here, pressure infiltration, polymer is poured over the fiber and placed in a pressure chamber. High pressures force the polymer between fibers [86]. In all methods, carbon or silicon carbide powder may be loaded into the pre-ceramic polymer in order to achieve a higher ceramic yield.

The next step is solidification of the preform to form a green body composite. The purpose here is to remove all solvent from the polymer. Again, there are multiple methods of doing this involving heat and/or pressure, which should all be done in non-oxidizing environments. Temperatures should not be high enough to induce pyrolysis, which typically begins around 800 °C for

most of the pre-ceramic polymers discussed. First, the preform can simply be heated to remove solvent. This is known as pressure-less sintering. This may be done simultaneously with any of the above impregnation methods. Another option is warm-pressing, in which the preform is placed between plates under high pressures and warm temperatures. This method achieves high densities because it prevents the preform from expanding [86].

Next, the green body composite is pyrolyzed under inert atmosphere. This includes vacuum or inert gas. This step requires high temperatures to break down the polymer into either carbon or silicon carbide. During pyrolysis, gaseous byproducts form as they are driven from the polymer structure. After this step, the polymer becomes ceramic material and the green body turns into a CMC. Slow heating rates and higher temperatures (up to 1600 °C) will lead to denser, more crystalline composites. However, composites are typically left relatively porous after this initial pyrolysis. This is a result of the high amount of mass loss from evaporated solvent and the removal of gaseous byproducts during pyrolysis. To achieve denser composites, the process steps are repeated for multiple cycles. In the subsequent re-impregnations, powder fillers should not be used unless their particle size is in the nanometer range. This ensures that matrix pores can be properly filled. The amount of re-impregnations necessary for full densification depends on the ceramic yield of the polymer, with higher yields leading fewer re-impregnations [77].

In the case of carbon matrices, a final heat treatment step is necessary to maximize the amount of graphitic carbon. This is performed at temperatures between 1700 °C and 3000 °C. A high degree of graphitization is necessary for applications that require high thermal and/or electrical conductivities. Such graphitization also defines the mechanical properties since graphite and vitreous carbon do not behave similarly with applied loads [75].

Due to the number of steps required and the nature of the precursor materials, PIP is an expensive and time-consuming process. It can take weeks to months to finish a composite, depending on the size and complexity of the part. For this reason, PIP composites are typically used in high-performance applications [77]. The full PIP process is summarized in the flow chart in Figure 4.5.

4.8.2 Chemical Vapor Infiltration

The method of CVI is performed in the gas phase at high temperatures. CVI can be used to fabricate carbon (pyrolytic, or PyC), silicon carbide (β-SiC), and sometimes oxide matrices. CVI involves the deposition of solid materials onto fiber substrates from the thermal decomposition or

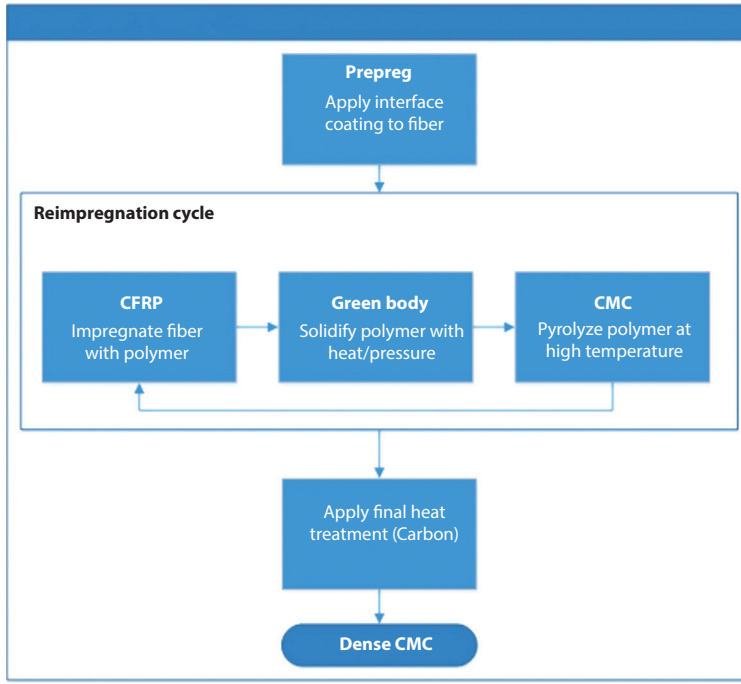

Figure 4.5 PIP process.

chemical reactions of gas precursors. CVI can be performed a number of ways based on the temperature and pressure parameters. Each method may result in different pore sizes and distributions. Ideally, CVI will form a matrix of 0% porosity; however, that is not practical due to the formation of closed porosity before full densification. CVI may be used as the main matrix forming step or as a final densification step following other matrix forming methods. Typical temperatures are in the range of 800–1200 °C depending on the gaseous precursors used [75].

In isothermal CVI, the temperature and pressure (<100 mbar) are kept constant. Pores are commonly sealed off, so the composite is removed from the reactor and machined multiple times during infiltration. This is time consuming but can accommodate multiple parts and achieve a high density. Thermal gradient CVI uses inductive heating. This first heats the fiber to begin deposition, and then the high-temperature region moves outward as the matrix is deposited. In pressure gradient CVI, the entire reactor is heated and the precursor gas is forced through the fiber with a pressure gradient. As the deposition profile advances, the pressure gradient shifts, similar to the thermal gradient method previously described.

This method is only able to infiltrate one object at a time. In the final CVI method, rapid CVI, the fiber is immersed in a hydrocarbon liquid inside of a sealed reactor. The fiber is inductively heated, causing the liquid to boil and decompose to carbon on the fiber. Of course, this can only be used to make carbon matrices [75].

CVI has the capability of producing very pure and fine-grained matrices, allowing for optimal mechanical properties. Processing times can be weeks to months depending on the type of CVI used and the size/complexity of the part. CVI temperatures are typically lower than those used in the pyrolysis and heat treatment steps of PIP [77].

4.8.3 Melt Infiltration

MI for matrix formation is different and requires the fabrication of a carbon matrix composite. The composite can be made either by PIP or CVI as previously described. Molten silicon is then infiltrated into the composite and reacts with the carbon matrix to form silicon carbide. Depending on the extent of molten silicon infiltration, the matrix can be fully reacted to silicon carbide or partially reacted to form a carbon-silicon carbide matrix. This method is able to achieve composites of high thermal conductivities. This method is optimal for applications requiring the dissipation of heat [77].

MI can be used in conjunction with CVI of silicon carbide to produce a fully densified composite. Before molten silicon is applied to a carbon/carbon composite, there are two major types of pores: small pores between individual fiber filaments and larger pores between bundles of fibers. CVI can be used to fill the small pores with silicon carbide. However, it would likely seal off larger pores before being able to fully infiltrate them. Molten silicon can then be used to infiltrate these larger pores with silicon carbide [91].

A disadvantage of this method arises with the use of carbon fibers and carbon interphase coatings. The molten silicon reacts with the fibers and coatings if they are not protected, leading to decreased composite strength. Other interphase coatings can be used to protect the fiber, such as silicon carbide, but this can lead to thermal expansion mismatch at the interface. A solution has been proposed to use fiber with a carbon inner coating and a silicon carbide outer coating. The molten silicon will not be able to diffuse past the silicon carbide layer, leaving the carbon fibers and coating intact [91].

The silicon infiltration is performed at 1650 °C to allow for the full melting of the silicon. The infiltration can be done by capillary forces alone to distribute the melt, rather than injection or high pressures. This is possible due to the low viscosity of liquid silicon, high wettability of carbon with silicon, and high surface tension. To prevent oxidation, the process

is performed under vacuum. Multiple infiltrations are necessary to fully convert the matrix to silicon carbide. The volume of the new silicon carbide matrix will be greater than the original carbon matrix, allowing the pores to be filled by expansion. This method is likely to leave behind some unreacted silicon and carbon [77].

4.8.4 Slurry Infiltration

Matrix formation by slurry infiltration is primarily used to form oxide matrices. The precursors are ceramic oxide powders dispersed in a liquid solvent, usually water. The ceramic oxide powder is the same material that the matrix will be made up of, since there will be no reactions during processing. Additives such as binders, dispersants, and plasticizers are used in small quantities to modify the slurry. The powder particle size should be controlled based on the fiber diameter to allow for efficient infiltration. This process is similar to PIP process in many aspects, except that it does not involve a pyrolysis step [86].

The first step to make a composite by slurry infiltration is to impregnate the fiber with the slurry. This can be done by various methods, including pressure infiltration and vacuum infiltration, which have been described in the PIP section. Another, less common method is known as freeze forming. It first involves impregnation of the fibers by either of the previous two methods. Then the slurry is frozen, resulting in the separation of the solvent and powder. The solvent freezes in a dendritic fashion, pushing the powder between fibers in a well-dispersed manner. The frozen solvent is then removed by freeze drying, leaving behind pores. The green body can be sintered to maximize the density; however, pores will still be present. The benefit of this method is that cracks are not formed in the process [86].

A fairly new method of fiber impregnation is based on electrophoretic deposition (EPD). In this method, the oxide particles in the slurry are charged between two electrodes and they attract to one electrode, which the fibers are fastened to. The advantages of EPD are shorter processing times and more control over the infiltration of the fiber. This process is described in detail by Stoll *et al.* [92].

After infiltration, the matrix needs to be solidified if it has not already been done (as is the case in freeze forming). This can be done by pressureless sintering or hot pressing, which have both been described in the PIP section. Temperatures above 1000 °C should be applied for full solidification and crystallization [86].

4.8.5 Metal Oxidation

The metal oxidation method is similar to MI, which also starts with an oxide/oxide composite made by other means, then continues with infiltration of the pores with a melt. The difference is that metals (usually aluminum) are used instead of silicon, and the metal is oxidized after infiltration. The first step is to coat all but one side of the oxide/oxide composite with a barrier material. The open side of the composite is held in contact with the molten metal, allowing capillary forces to pull it through the porous structure. After the pores are filled, the metal is oxidized to match the matrix of the original oxide/oxide composite. Expansion of the metal to a metal oxide increases the density of the material [86]. Unfortunately, this method leaves residual aluminum metal and can damage the fibers [88].

4.9 Toughness of CMCs

The property of CMCs that designates them as advanced materials is their unparalleled toughness, or ability to resist the propagation of cracks before catastrophic failure. Monolithic (non-reinforced) ceramic materials are known for high strengths and high temperature stability. However, if a crack forms in a ceramic material then propagation through the entire object can happen. With the addition of fiber reinforcement through the ceramic matrix, cracks can be stopped at the interface between the two materials. This effect is shown in Figure 4.6.

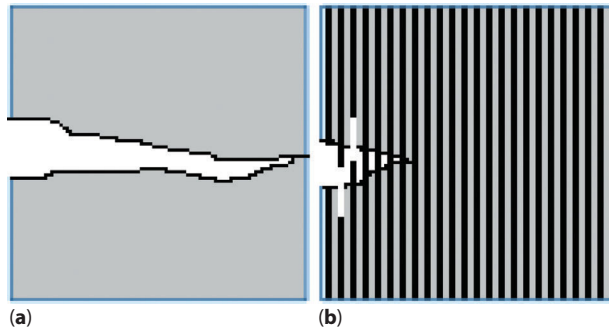

Figure 4.6 (a) Monolithic ceramic showing full crack propagation. (b) Ceramic matrix composite showing the disruption of crack propagation at the fiber–matrix interface.

4.9.1 Fiber/Matrix Interface

The area between fibers is filled with dense ceramic matrix, which acts the same as a monolithic material. Cracks can travel through the matrix relatively easily, and it is not until the crack reaches the fiber/matrix interface that cracking can be stopped. However, if the fiber and matrix are strongly bound, then stresses are easily transferred from matrix to fiber and the object will act like a monolithic material. There needs to be a weak bond at the interface to allow for energy absorbing mechanisms. Weak bonds are achieved through application of a thin film coating at the interface, separating the other two phases. Interphase coatings are discussed in detail in previous chapters. If successful, cracks will travel through a minimal amount of the fibers.

4.9.2 Modes of Failure

Considering a composite in which the fibers are unidirectional, there are three major modes of failure. This includes axial tensile failure, transverse tensile failure, and shear failure, as shown in Figure 4.7.

When the stress is parallel to the direction of the fiber, the load will be distributed between the fiber and the matrix. The matrix, being the weaker of the two components will break first. The load on the matrix is gradually transferred to the fiber until the fiber carries the entire load. Ultimately, the composite will fail when the tensile strength of the fiber is reached. This demonstrates the importance of protecting the fiber from degradation during processing, as it is the component that contributes the most strength to the composite. When the stress is perpendicular to the fiber direction, the strength of the composite is dominated by the matrix, which is relatively weak. The composite will fail at low stresses because once the matrix cracks

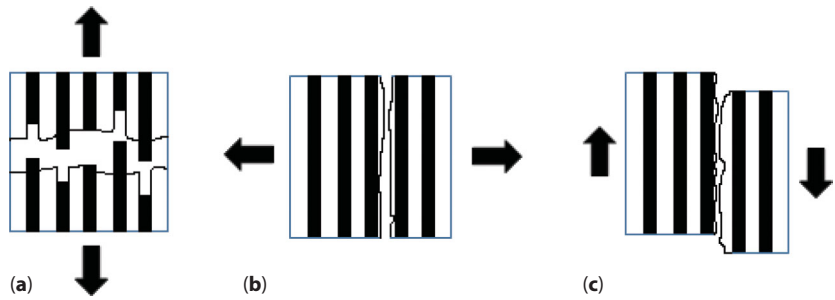

Figure 4.7 (a) Axial tensile failure, (b) transverse tensile failure, and (c) shear failure.

there is nothing preventing crack propagation parallel to the fibers. Under shear stress, the composite will fail similarly to conditions of transverse tensile stress. Due to the weak interfacial bonding, the matrix is likely to separate from the fiber and fail at relatively low stress values. Shear failure can also occur in the direction perpendicular to the fibers, however, this is not a common mode of failure. Also uncommon is failure due to compressive loads. In this situation, fibers tend to buckle, putting them under flexural loads. Fracture occurs in the same manner as tensile failure [69].

4.9.3 Energy-Absorbing Mechanisms

The reason for the high toughness observed in CMCs is due to processes that occur at the fiber–matrix interface resulting in the deflection of cracks. The more of these energy-absorbing mechanisms that a crack encounters, the more likely the crack can be stopped.

Despite being undesirable, fiber fracture is one type of energy absorbing mechanism. A specific amount of energy is required to break through a fiber, so as a crack passes through fibers cracking will be slowed down. The same can be said for matrix fracture [69].

When a crack reaches an interface, debonding can occur between the fiber and the matrix (Figure 4.8a). This can be attributed to the weak bond strength caused by the interphase coating. Some of the energy of the crack is transferred to travel along the interface, leaving the original crack with less energy than it initially had. Debonding can occur either between the fiber and the interface or between the matrix and the interface, depending on which is more weakly bonded [69].

The most significant sources of energy absorption are fiber pullout (Figure 4.8b) and pushout. Once debonding occurs, it is possible for the fiber to be pulled or pushed from its original location as a crack widens. The frictional sliding caused from this motion absorbs energy and assists in slowing the crack. This effect is greater for rough surfaces on the fiber and matrix. Other factors that affect this are the contact pressure and the distance of pulling or pushing [69].

Another crack deflection mechanism exists in the case of porous matrix composites. When applying oxide matrices, it is nearly impossible to achieve densities beyond 10–15% porosity. Therefore, pores are controlled to add to the toughness of the composite [86]. As a crack approaches a pore, the energy of the crack is distributed around the surface of the pore. The stress required to propagate depends on the curvature and radius of the pore. If the pore is spherical, then the required stress is greater and energy is absorbed. If the pore is elongated with a small radius at its tip

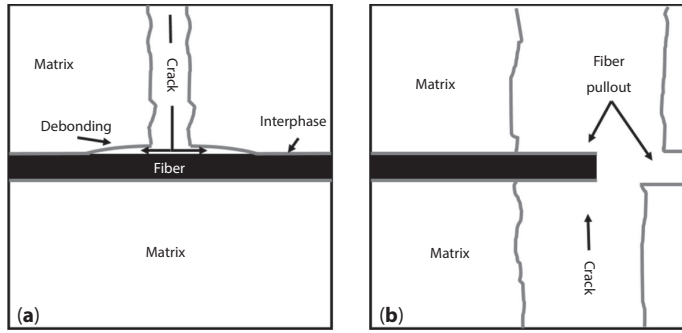

Figure 4.8 Schematic representation of (a) fiber-matrix debonding and (b) fiber pullout.

then the crack is more likely to propagate through [93]. This describes the importance of evenly distributed, small, closed-off pores.

4.9.4 Stress Testing of Composites

It is possible to measure the amount of energy absorbed due to debonding and frictional sliding. Single fibers can be pulled from their matrix, while the stress required to do so is recorded. A chart with this data can show three things: stress to cause debonding, stress to propagate the debonding, and stress from fiber pullout. Similarly, the fibers can also be pushed [69].

More common are tests on bulk composites. These mainly include tensile and flexural strength testing. In tensile testing, composite strips are pulled apart and the stress at which the composite breaks is the tensile strength. In flexure testing, composite strips are bent and the stress at which the composite breaks is the flexural strength. These properties are used to compare the effect of energy absorbing mechanisms between different composites.

The image below is a cross section of a composite displaying some of the mentioned energy absorbing mechanisms (Figure 4.9).

4.10 Applications

As previously described, CMCs have ideal properties for applications in turbine engines. The use of ceramic components in turbine engines allows for higher operating temperatures and more power from these engines. Typical engine components are fabricated from nickel-based super-alloys and are limited by the temperatures at which the metals deform, as well as material oxidation at these elevated temperatures. Ceramics can surpass the operational temperatures of these nickel-based alloys, which end

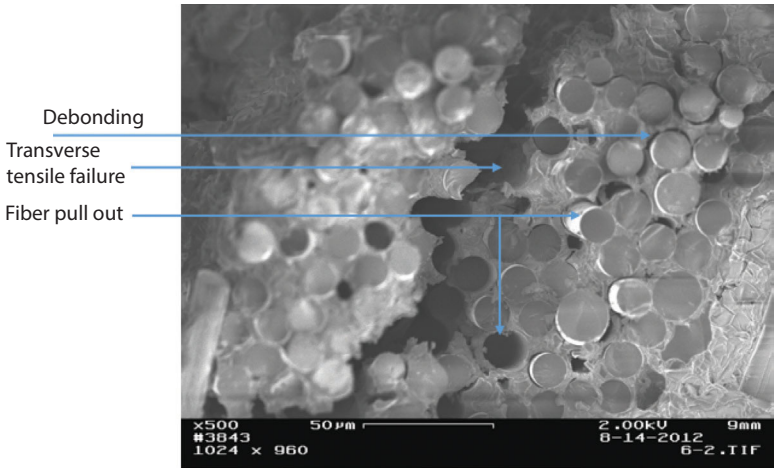

Figure 4.9 SEM micrograph of a composite cross section showing energy absorbing mechanisms such as debonding and fiber pullout.

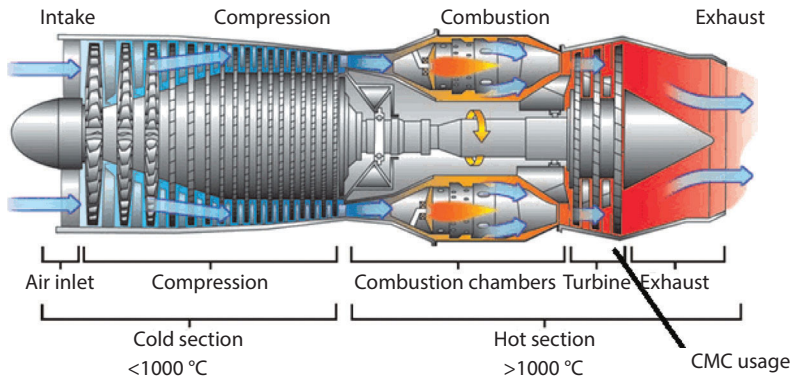

Figure 4.10 Diagram of cold and hot sections of an aircraft engine. Adapted from The Federal Aviation Administration, Tikalon, LLC [96].

at 1100 °C, and can provide structure and oxidation resistance at 1300 °C and higher [94] Ceramics in these applications, specifically CMCs, allow for higher operational temperatures, reduced weight due to the low density of ceramics, and improved wear resistance [95]. There is also significant chemical and oxidation resistance in materials like silicon carbide and silicon nitride. These materials can withstand the extreme heat and oxidizing conditions in the hot section of the combustion engine, and recent advancements have made the fabrication, manufacture, and usage of CMCs in engine components a reality (Figure 4.10).

Non-rotating turbine blades composed of CMC systems have shown success in CFM International's LEAP engine, which will be used in the Airbus 320neo, Boeing 737 MAX, and the COMAC (CHINA) C919 aircrafts. In February 2015, GE Aviation developed and tested the first rotating set of CMC turbine blades with great success. These blades, manufactured for use in a F414 turbofan, underwent 500 cycle tests, proving the durability, temperature, and oxidation resistance anticipated from this system, while still weighing about one-third less than conventional metal components. An added benefit of this system was also that the lighter blades resulted in less centrifugal force in the rotating blades, providing opportunity for smaller and thinner disks, bearings, and other engine parts. These new systems, like the Adaptive Versatile Engine Technology (ADVENT, produced by GE) boast a 25% fuel consumption reduction, 30+% improvement in vehicle range, and 10% higher maximum thrust. The F414 cycle engine can withstand temperatures several hundred degrees higher than traditional nickel-based alloys present in comparable aircraft engines and does not need traditional air-cooling, resulting in increased efficiency thought both aerodynamics and fuel consumption [97]. Further research to implement these CMCs into both military and commercial aircraft will continue to develop with the recent successful tests of CM-inclusive turbine engines.

4.10.1 Brakes and Friction

Properties that make CMCs excellent candidate materials for aircraft and aerospace engine applications also make them ideal for advanced friction and braking systems. Carbon–carbon CMCs as well as carbon/carbon–SiC CMCs have been designed and manufactured for use in vehicle brake parts for both passenger cars, as well as aircrafts. These composites have excellent thermal conductivity, high strength and hardness, high thermal stability, and chemical and oxidation resistance required for brake parts including pads and rotors. Composite systems were designed based on melt-infiltrated silicon systems through the use of molten silicon in a carbon preform, which is converted to silicon carbide. Capillary action pulls the silicon into the carbon form, producing composites with low overall porosity. The carbon forms, either fibers, sponges, or other porous forms, are typically highly graphitized and coated with a layer to protect the carbon from damage from molten silicon. These composites can operate at temperatures in the range of 1600 °C, and have excellent durability in these applications. Brake pads were designed with carbon fiber oriented parallel to the friction surface, optimizing wear conditions for long-term usage [98].

These brakes showed excellent properties as compared to carbon–carbon components produced with CVI and to grey cast iron systems. These brakes provide stable coefficients of friction, high wear stability, low density, and relatively low overall cost as compared to commercially available brake components. The concentration of silicon carbide in these systems can be tailored to control some of these properties, providing higher thermal conductivity, but decreasing the tolerance for damage in the brake. Non-homogeneous systems containing higher SiC concentrations at the surface of the brake and lower SiC concentrations at the center of the part are being designed to combat these problems, with the consideration of CTE. A braking system with a CTE mismatch would result in microcracking and structural stability issues when the part is exposed to elevated temperatures and is a significant consideration in design and development of these components. Studies in the tribological behavior of these brakes are being studied extensively to determine the effect of these properties on the durability and wear of the brakes.

Ceramic brake and other friction components are currently already in use in some high-end passenger vehicles, including Porsche. The brake rotors and pads are composed of composite ceramic systems, available as the Porsche Ceramic Composite Brake (PCCB) as well as in the clutch component in these vehicles as the Porsche Ceramic Composite Clutch (PCCC), both in the Porsche Carrera GT [99]. The PCCC boasts a weight reduction of over 50% from the 7.6 kg conventional clutch in a Porsche 911 turbo. This composite clutch is fabricated of a carbon fiber-based ceramic, treated through 1700 °C silicization process, producing a silicon carbide matrix. This smaller, lighter, and stronger clutch provides the car the ability for increased speeds and the material durability for demanding conditions expected from a powerful sports car.

4.10.2 Biomedical Applications

The biomedical field shows potential for the structural and mechanical benefits of CMC systems. These ceramics have shown to range between biocompatible to bioactive in tissue, bone, and dental applications. The low density and ability to tailor the porosity in these systems allow for great potential for use in bone scaffolding, soft tissue, and cartilage regeneration as well as dental implants, scaffolds, and cements. Materials like silicon carbide, carbon, graphite, and carbon nanotubes, and hydroxyapatite have shown excellent properties in both strengths and biocompatibilities in both animal and preliminary human trials [100]. These structures allow for natural tissue and bone growth to occur around the composite material, providing scaffolding

for tissue regeneration. Several variations of materials have been researched extensively for their properties and strengths in these biological applications.

Caron nanotubes have also shown success as reinforcement material in biological applications. These structures allow for significant load-bearing properties as well as biocompatibility for a variety of uses in the body [101]. These carbon nanotubes, both single-walled (SWCNT) and multi-walled (MWCNT), have been used in composite systems including metal matrices [102], ceramic matrices [103], and polymer-derived matrices like SiC, SiN, quartz, and aluminum. These carbon nanotubes have a low density, high tensile [104], and compressive strengths [105], and excellent biocompatibility, making them ideal for use in CMCs for biological purposes. Carbon nanotube-reinforced composites show promise for scaffolding for bone and tissue regeneration, structural material for bone cement, and substitutes for soft tissue or cartilage [106]. Ceramics show excellent biocompatibility as compared to metals and polymers, but again are limited but their brittle nature and low fracture toughness. Composites designed with carbon nanotubes add strength as well as biocompatible physical properties into these systems. PCSs have been used in fabrication of these composites as well as hydroxyapatite [107] intended for both bone and dental usage. MWCNT and PCS composites were fabricated using Spark Plasma Sintering, and implantation into femurs of rats showed newly formed bone tissues after 1–4 weeks [108].

CMC systems have also been of significant interest in dental applications. Ceramics have been used for several decades in restorative and cosmetic dentistry, but new developments in composite systems have opened doors for use of these materials as scaffolding for natural tissue regeneration and advanced dental implants. Computer-aided design and computer-aided manufacturing have allowed for fabrication of these composites specific to each patient and dental application [109]. Composite systems composed of resin-based CMCs have shown promising results with biocompatibility and long-term durability [110]. These composite systems are composed of a variety of different ceramic materials, including hydroxyapatite, magnesium aluminate spinel, yttria–zirconia/alumina, and calcium and magnesium oxides. Whisker-based composites as well as particle-based composites have been designed to control density, porosity, and composition for optimal results [111]. These types of materials are continuously being researched for long-term use in both dental and bone applications and show promise for advanced medical applications.

Low-temperature applications of CMCs also include electronics and circuitry, providing a durable, conductive packaging structure for microelectronics and semiconductor chips. Composites fabricated from aluminum

nitride, silicon carbide, and titanium diboride, as well as glass–ceramic composites provide packaging structure for these microelectronic systems. These packaging components are used for interconnecting, powering, cooling, and protecting of semiconductors in electronics, serving as conductive media, heat sinks, and durable structures. The high thermal conductivity and low thermal expansion coefficients made these materials ideal candidates for these advanced electronic applications [112].

CMCs are also of considerable value in military application, showing incredible strength in armors, both for combat vehicles and for personal protection. CMCs exhibit high strengths, durability, and low weights as compared to metals traditionally used in armors. Fibers like Kevlar® have traditionally provided protection in personal armors like combat helmets, ballistics vests, and protective gloves and face masks [113], as well as in military vehicles as floor and side panel protection [114]. These fibers, though strong and durable, are limited by their overall strengths and do little to protect against armor piercing projectiles like those used in modern combat. New composite systems using ceramics like silicon carbide, titanium diboride, tungsten carbide, and alumina use CF-CMCs to provide the strength needed against these types of weapons. Composites can be fabricated into panels for armored vehicles to be employed in both ground and air combat, as well as in naval applications. These CMCs are also incorporated into personal armors like helmets, vests, leg and arm protection, and in footwear. These systems are designed to withstand impact from projectiles and explosions though the dissipation of energy through the composite. They also provide surface area for the protection from these projectiles, which shatter upon impact. These CMCs are designed in complex, 3D shapes needed for personal armors and in combat vehicles, while providing low-density protection in warfare [115].

Acknowledgments

We acknowledge the use of the UCONN FEI Center of Excellence in Microscopy for some of this work.

References

1. E. Bullock, R. Brunetaud, J. F. Conde, S. R. Keown and S. F. Pugh, *Research and Development of High Temperature Materials for Industry*, Springer Netherlands, pp. 51–58, 2012.

2. R. A. Higgins, *Materials for Engineers and Technicians*, Taylor & Francis, 2006.
3. C. T. Sims, *A History of Superalloy Metallurgy for Superalloy Metallurgists*, General Electric Company, pp. 399–418, 1982.
4. A. Sengupta, S. K. Putatunda, L. Bartosiewicz, J. Hangas, P. J. Nailos, M. Peputapeck and F. E. Alberts, *Journal of Materials Engineering and Performance,* Vol. 3, pp. 73–81, 1994.
5. F. C. Campbell, *Structural Composite Materials*, ASM International, pp. 575–580, 2010.
6. J. B. Wachtman, *18th Annual Conference on Composites and Advanced Ceramic Materials—A: Ceramic Engineering and Science Proceedings, Volume 15*, Wiley, 2009.
7. J. W. S. Hearle, *High-performance Fibers*, Woodhead Publishing Ltd, 2001.
8. A. Alavudeen, N. Venkateshwaran and J. T. W. Jappes, *A Textbook of Engineering Materials and Metallurgy*, Laxmi Publications Pvt Limited, p. 291, 2006.
9. D. V. Grashchenkov, Y. A. Balinova and E. V. Tinyakova, *Glass and Ceramics,* Vol. 69, pp. 130–133, 2012.
10. B. Clauß, *Fibers for Ceramic Matrix Composites*, *Ceramic Matrix Composites*, Wiley-VCH Verlag GmbH & Co. KGaA, pp. 1–20, 2008.
11. K. S. Mazdiyasni, *Fiber Reinforced Ceramic Composites: Materials, Processing, and Technology*, Noyes Publications, pp. 2–6, 1990.
12. R. T. Paine and C. K. Narula, *Chemical Reviews,* Vol. 90, pp. 73–91, 1990.
13. A. A. Balandin, *Nature Materials,* Vol. 10, pp. 569–581, 2011.
14. M. Parlier, M. H. Ritti and A. Jankowiak, Potential and Perspectives for Oxide/Oxide Composites, *Journal of Aerospace Lab,* Vol. 3, pp. 1–12, 2011.
15. A. G. Evans and D. B. Marshall, *Acta Metallurgica,* Vol. 37, pp. 2567–2583, 1989.
16. P. K. Mallick, *Fiber-Reinforced Composites: Materials, Manufacturing, and Design, Third Edition*, CRC Press, 2007.
17. E. Mouchon and P. Colomban, *Composites,* Vol. 26, pp. 175–182, 1995.
18. A. M. Buckley and M. Greenblatt, *Journal of Chemical Education,* Vol. 71, p. 599, 1994.
19. M. Nguefack, A. F. Popa, S. Rossignol and C. Kappenstein, *Physical Chemistry Chemical Physics,* Vol. 5, pp. 4279–4289, 2003.
20. N. P. Bansal, *Handbook of Ceramic Composites*, Kluwer Academic Publishers, 2006.
21. A. Mortensen, *Concise Encyclopedia of Composite Materials*, Elsevier Science, pp. 1–31, 2006.
22. R. Alias, "24—Multilayer glass–ceramic composites for microelectronics: processing and properties", *Advances in Ceramic Matrix Composites*, Woodhead Publishing, pp. 587–610, 2014.
23. T. Palucka and B. Bensaude-Vincent, *Materials Research, Composites Overview,* The Dibner Institute for the History of Science and Technology [Online] October 19, 2002, http://authors.library.caltech.edu/5456/1/hrst

.mit.edu/hrs/materials/public/composites/Composites_Overview.htm (accessed Jun 8, 2016).
24. Bunsell, A. R., Oxide Fibers, In *Handbook of Ceramic Composites*, Bansal, N. P., Ed., Springer Science+Business Media, Inc., New York, pp. 3–32, 2005.
25. K. S. Anoush Poursartip, *Proceedings of the Tenth International Conference on Composite Materials: Characterization and ceramic matrix composites*, Woodhead Publishing, 1995.
26. M.-H. B. Anthony and R. Bunsell, *Ceramic Fibres*, Woodhead Publishing Ltd, 2001.
27. 3M. *Nextel Ceramic Textiles Technical Notebook*. http://www.3m.com/market/industrial/ceramics/misc/tech_notebook.html (2015).
28. T. Maki and S. Sakka, *Journal of Non-Crystalline Solids,* Vol. 100, pp. 303–308, 1988.
29. J. Chandradass and M. Balasubramanian, *Journal of Materials Processing Technology,* Vol. 173, pp. 275–280, 2006.
30. D. M. Wilson, D. C. Lueneburg and S. L. Lieder, "High Temperature Properties of Nextel 610 and Alumina-Based Nanocomposite Fibers", *Proceedings of the 17th Annual Conference on Composites and Advanced Ceramic Materials: Ceramic Engineering and Science Proceedings*, John Wiley & Sons, Inc., pp. 609–621, 2008.
31. J. D. Birchall, *Transactions and Journal of the British Ceramic Society,* Vol. 82, pp. 143–145, 1983.
32. M. Shojaie-Bahaabad, E. Taheri-Nassaj and R. Naghizadeh, *Ceramics International,* Vol. 34, pp. 1893–1902, 2008.
33. Zircar Zirconia, Inc. *Zircar Zirconia, Inc. Technical Documents*. https://zircarzirconia.com/technical-documents/ (2015).
34. K. O. Seishi Yajima, Josaburo Hayashi, Mamoru Omori, *Journal of the American Ceramic Society,* Vol. 59, pp. 324–327, 1976.
35. COI Ceramics. *Sylramic SiC Fibers*. http://www.coiceramics.com/sylramicfiber.html
36. Nippon Carbon Co. Ltd. *Silicon Carbide Continuous Fibers*. http://www.carbon.co.jp/english/products/silicon_carbide/
37. UBE Industries, Ltd. *Chemicals: Continuous Inorganic Fiber Tyranno Fiber*. http://www.ube-ind.co.jp/english/products/chemical/chemical_19.htm
38. D. C. Deleeuw, J. Lipowitz and P. P. Lu, *Preparation of Substantially Crystalline Silicon Carbide Fibers from Polycarbosilane*, U.S. Patent 5,071,600, Dec 10, 1991.
39. N. P. Bansal and J. Lamon, *Ceramic Matrix Composites: Materials, Modeling and Technology*, Wiley, pp. 1–54, 2014.
40. P. Le Coustumer, M. Monthioux and A. Oberlin, *Journal of the European Ceramic Society,* Vol. 11, pp. 95–103, 1993.
41. T. Yamamura, T. Ishikawa, M. Shibuya, T. Hisayuki and K. Okamura, *Journal of Materials Science,* Vol. 23, pp. 2589–2594, 1988.
42. K. Kumagawa, H. Yamaoka, M. Shibuya and T. Yamamura, "Thermal Stability and Chemical Corrosion Resistance of Newly Developed Continuous

Si-Zr-C-O Tyranno Fiber", *Proceedings of the 21st Annual Conference on Composites, Advanced Ceramics, Materials, and Structures—A: Ceramic Engineering and Science Proceedings*, John Wiley & Sons, Inc., pp. 113–118, 2008.
43. M. Takeda, Y. Imai, H. Ichikawa, T. Ishikawa, T. Seguchi and K. Okamura, "Properties of the Low Oxygen Content SiC Fiber on High Temperature Heat Treatment", *Proceedings of the 15th Annual Conference on Composites and Advanced Ceramic Materials: Ceramic Engineering and Science Proceedings*, John Wiley & Sons, Inc., pp. 1007–1018, 2008.
44. H. Ichikawa, K. Okamura and T. Sequchi, *Oxygen-free Ceramic Fibers from Organosilicon Precursors and E-beam Curing*, Medium: X; Size: pp. 65–74, 1995.
45. T. Ishikawa, S. Kajii, T. Hisayuki and Y. Kohtoku, "New Type of SIC-Sintered Fiber and Its Composite Material", *22nd Annual Conference on Composites, Advanced Ceramics, Materials, and Structures: A: Ceramic Engineering and Science Proceedings*, John Wiley & Sons, Inc., pp. 283–290, 2008.
46. J. Lipowitz, J. A. Rabe, A. Zangvil and Y. Xu, "Structure and Properties of Sylramic™ Silicon Carbide Fiber—A Polycrystalline, Stoichiometric β-Sic Composition", *Proceedings of the 21st Annual Conference on Composites, Advanced Ceramics, Materials, and Structures—A: Ceramic Engineering and Science Proceedings*, John Wiley & Sons, Inc., pp. 147–157, 2008.
47. J. G. Lavin, "Carbon Fibers", *High-performance Fibers*, Woodhead Publishing Ltd, pp. 156–190, 2001.
48. L. H. Peebles, *Carbon Fibres: Formation, Structure and Properties*, CRC Press, 1994.
49. M. Guigon, A. Oberlin and G. Desarmot, *Fibre Science and Technology,* Vol. 20, pp. 55–72, 1984.
50. Toray Carbon Fibers America, Inc. *TORAYCA Carbon Fiber Products*. http://www.toraycfa.com/index.htm (2015).
51. D. D. Edie and M. G. Dunham, *Carbon,* Vol. 27, pp. 647–655, 1989.
52. G. M. Pennock, G. H. Taylor and J. D. F. Gerald, *Carbon,* Vol. 31, pp. 591–609, 1993.
53. Cytec. *Thornel*. https://www.cytec.com/businesses/aerospace-materials/brands/thornel (2015).
54. J. Lamon, "Influene of Interfaces and Interphases on the Mechanical Behavior of Fiber-Reinforced Ceramic Matrix Composites", *Ceramic Matrix Composites: Materials, Modeling and Technology*, Wiley, pp. 40–64, 2014.
55. B. Pukánszky, *European Polymer Journal,* Vol. 41, pp. 645–662, 2005.
56. D. O. Swenson and C. A. Rau, Jr., *International Journal of Fracture Mechanics,* Vol. 6, pp. 357–365, 1970.
57. S. Pompidou and J. Lamon, *Composites Science and Technology,* Vol. 67, pp. 2052–2060, 2007.
58. *ASM Ready Reference: Thermal Properties of Metals*, 2002.
59. "Boron Nitride (BN) Linear Thermal Expansion, Temperature Dependence of Lattice Parameters", *Group IV Elements, IV-IV and III-V Compounds. Part A—Lattice Properties*, Springer Berlin Heidelberg, pp. 1–6, 2001.

60. "Ceramic Matrix Composites: Microstructure, Properties and Applications", *Ceramic Matrix Composites: Microstructure, Properties and Applications*, Woodhead Publishing Limited, pp. 339–341, 2006.
61. J. L. Bobet and J. Lamon, *Acta Metallurgica et Materialia,* Vol. 43, pp. 2241–2253, 1995.
62. Dow Corning. *CVD Silicon Carbide*. http://www.dow.com/assets/attachments/business/gt/advanced_ceramics/cvd_silicon_carbide/tds/cvd_silicon_carbide.pdf (2015).
63. F. Heurtevent, *Matériaux multicouches nanoséquencés (PyC/SiC)n: application en tant qu'interphases dans les composites thermostructuraux,* Ph.D, p. 193, 1996.
64. A. Lipp, K. A. Schwetz and K. Hunold, *Journal of the European Ceramic Society,* Vol. 5, pp. 3–9, 1989.
65. R. Naslain, *Composites Science and Technology,* Vol. 64, pp. 155–170, 2004.
66. G. N. Morscher, *Journal of the American Ceramic Society,* Vol. 80, pp. 2029–2042, 1997.
67. R. R. Naslain, *Composites Part A: Applied Science and Manufacturing,* Vol. 29, pp. 1145–1155, 1998.
68. M. H. Lewis, A. Tye, E. G. Butler and P. A. Doleman, *Journal of the European Ceramic Society,* Vol. 20, pp. 639–644, 2000.
69. D. Hull and T. Clyne, *An Introduction to Composite Materials*, Cambridge University Press, 326 pages, 1996.
70. C. Lee, X. Wei, J. W. Kysar and J. Hone, *Science,* Vol. 321, pp. 385–388, 2008.
71. J. Shackelford, W. Alexander and J. Park, "CRC Materials Science and Engineering Handbook", *2E*, pp. 387–388, 1994.
72. K. Kim, W. Regan, B. Geng, B. Alemán, B. Kessler, F. Wang, M. Crommie and A. Zettl, *Physica Status Solidi (RRL)-Rapid Research Letters,* Vol. 4, pp. 302–304, 2010.
73. A. A. Balandin, *Nature Materials,* Vol. 10, pp. 569–581, 2011.
74. R. Powell, C. Y. Ho and P. E. Liley, *Thermal Conductivity of Selected Materials*, No. NSRDS-NBS-8, National Standard Reference Data Series, 1966.
75. H. Hatta, R. Weiss and P. David, "Carbon/Carbons and Their Industrial Applications", *Ceramic Matrix Composites: Materials, Modeling and Technology*, John Wiley & Sons, pp. 87–146, 2014.
76. J. Sheehan, K. Buesking and B. Sullivan, *Annual Review of Materials Science,* Vol. 24, pp. 19–44, 1994.
77. B. Heidenreich, "C/SiC and C/C-SiC Composites", *Ceramic Matrix Composites: Materials, Modeling and Technology*, John Wiley & Sons, pp. 147–216, 2014.
78. *Joint Committee for Powder Diffraction Standards, Powder Diffraction File No. 01-087-0712, JCPDS International Center for Diffraction Data, Swarthmore, PA (1991).*
79. N. C. H. a. C. N. J. Wagner, *Acta Crystallographica,* Vol. 20, p. 2, 1966.
80. A. P. Abbott and K. J. McKenzie, *Physical Chemistry Chemical Physics,* Vol. 8, pp. 4265–4279, 2006.

81. C. B. Roberts, *Aluminum Plating Corrosion Resistance,* US Patent US3969555A, 1976.
82. X. Shen, X. Nie, H. Hu and J. Tjong, *Surface and Coatings Technology,* Vol. 207, pp. 96–101, 2012.
83. L. K. Keefer and G. Lunn, *Chemical Reviews,* Vol. 89, pp. 459–502, 1989.
84. C. Suryanarayana, *Progress in Materials Science,* Vol. 46, pp. 1–184, 2001.
85. A. Korchef, Y. Champion and N. Njah, *Journal of Alloys and Compounds,* Vol. 427, pp. 176–182, 2007.
86. K. A. Keller, G. Jefferson and R. J. Kerans, "Oxide-Oxide Composites", *Ceramic Matrix Composites: Materials, Modeling and Technology*, John Wiley & Sons, pp. 236–272, 2014.
87. E. Volkmann, K. Tushtev, D. Koch, C. Wilhelmi, J. Göring and K. Rezwan, *Composites Part A: Applied Science and Manufacturing,* Vol. 68, pp. 19–28, 2015.
88. M. Parlier and M. Ritti, *Aerospace Science and Technology,* Vol. 7, pp. 211–221, 2003.
89. A. Banerjee, L. Sun, S. Mantell and D. Cohen, *Composites Part A: Applied Science and Manufacturing,* Vol. 29, pp. 251–263, 1998.
90. M. K. Kang, W. I. Lee and H. T. Hahn, *Composites Science and Technology,* Vol. 60, pp. 2427–2434, 2000.
91. Y. Xu, L. Cheng and L. Zhang, *Carbon,* Vol. 37, pp. 1179–1187, 1999.
92. E. Stoll, P. Mahr, H.-G. Krüger, H. Kern, B. Thomas and A. Boccaccini, *Journal of the European Ceramic Society,* Vol. 26, pp. 1567–1576, 2006.
93. W. D. Callister and D. G. Retwisch, *Materials Science and Engineering: An Introduction 9E*, John Wiley & Sons, 962 pages, 2014.
94. K. L. Luthra, *Emerging Applications and Challenges in using Ceramics at General Electric,* 2011 Ceramic Leadership Summit, Baltimore, MD, August 2, 2011; The American Ceramic Society, Westerville, OH, 2011.
95. H. E. Helma, L. C. Lindgren, P. E. Heitman and S. R. Thrasher, *Ceramic Applications in Turbine Engines*, Noyes Publications, 1986.
96. Handbook, Airplane Flying, US Department of Transportation Federal Aviation Administration, 1999 Annual Report, 2004.
97. G. E. Aviation, *GE Successfully Tests World's First Rotating Ceramic Matrix Composite Material for Next-Gen Combat Engine,* http://www.geaviation.com/press/military/military_20150210.html (accessed Jun 8, 2016).
98. W. Krenkel and F. Berndt, *International Conference on Recent Advances in Composite Materials,* Vol. 412, pp. 177–181, 2005.
99. C. Becker, *Little, Strong, Black,* Cristophorus, Vol. 306, pp. 40–42, Feb 2004.
100. M. Kutz, *Standard Handbook of Biomedical Engineering and Design*, McGraw-Hill, 2003.
101. X. Li, L. Wang, Y. Fan, Q. Feng and F.-z. Cui, *Biocompatibility and Toxicity of Nanoparticles and Nanotubes,* Vol. 2012, p. 19, 2012.
102. W. X. Chen, J. P. Tu, L. Y. Wang, H. Y. Gan, Z. D. Xu and X. B. Zhang, *Carbon,* Vol. 41, pp. 215–222, 2003.

103. Z. Xia, L. Riester, W. A. Curtin, H. Li, B. W. Sheldon, J. Liang, B. Chang and J. M. Xu, *Acta Materialia,* Vol. 52, pp. 931–944, 2004.
104. S. G. Prolongo, M. Burón, M. R. Gude, R. Chaos-Morán, M. Campo and A. Ureña, *Directions in Damage and Durability of Composite Materials, with regular papers,* Vol. 68, pp. 2722–2730, 2008.
105. N. Yu, Z. H. Zhang and S. Y. He, *Advances in Microstructure-based Modeling and Characterization of Deformation Microstructures Held at the TMS Annual Meeting 2007, Orlando, Florida,* Vol. 494, pp. 380–384, 2008.
106. W. Wang, Y. Zhu, S. Liao and J. Li, *Carbon Nanotubes Reinforced Composites for Biomedical Applications,* Vol. 2014, p. 14, 2014.
107. T. D. Stewart, J. L. Tipper, G. Insley, R. M. Streicher, E. Ingham and J. Fisher, *Journal of Biomedical Materials Research Part B: Applied Biomaterials,* Vol. 66B, pp. 567–573, 2003.
108. W. Wang, F. Watari, M. Omori, S. Liao, Y. Zhu, A. Yokoyama, M. Uo, H. Kimura and A. Ohkubo, *Journal of Biomedical Materials Research Part B: Applied Biomaterials,* Vol. 82B, pp. 223–230, 2007.
109. L. Yin and R. Stoll, "26—Ceramics in restorative dentistry", *Advances in Ceramic Matrix Composites*, Woodhead Publishing, pp. 624–655, 2014.
110. H. Mirmohammadi, "27—Resin-based ceramic matrix composite materials in dentistry", *Advances in Ceramic Matrix Composites*, Woodhead Publishing, pp. 656–677, 2014.
111. F. Krumeich, M. Wörle, R. Nesper, M. Höland, C. Ritzberger, F. Rothbrust, J. Chevalier, V. M. Rheinberger and W. Höland, *Journal of the American Ceramic Society,* Vol. 97, pp. 1602–1609, 2014.
112. R. R. Tummala, *Journal of the American Ceramic Society,* Vol. 74, pp. 895–908, 1991.
113. Dupont Industries. *Kevlar Military Personal Protection Equipment Body Armor*. http://www.dupont.com/products-and-services/personal-protective-equipment/body-armor.html (2015).
114. A. S. Miguel, *Composite Floor Armor for Military Tanks and the Like,* US Patent US4404889, 1983.
115. T. E. Strasser and S. D. Atmur, *Fiber Reinforced Ceramic Matrix Composite Armor,* US Patent US6314858, 2001.

5

Yytria- and Magnesia-doped Alumina Ceramic Reinforced with Multi-walled Carbon Nanotubes

Iftikhar Ahmad[1] and Yanqiu Zhu[2]*

[1]Center of Excellence for Research in Engineering Materials, Advanced Manufacturing Institute, King Saud University, Riyadh , Kingdom of Saudi Arabia
[2]College of Engineering, Mathematics and Physical Sciences, University of Exeter, United Kingdom

Abstract

Carbon nanotubes (CNTs) are commonly referred to as the ultimate reinforcement for ceramic materials with the main purpose to enhance both the mechanical and functional properties of the structural ceramics. Several ceramics have shown reasonable improvements in toughness and other mechanical properties after incorporating CNTs; however, the exciting properties of the CNTs failed to be fully transferred to the nanocomposites due to hitches in obtaining uniform distribution of the CNTs and high densification and flaw-free microstructures in the final nanocomposites; thus, new design philosophies are in demand. This chapter describes new concept of the doping of multiwalled carbon nanotubes (MWCNTs)-reinforced alumina (Al_2O_3) nanocomposites with yytria (Y_2O_3) and magnesia (MgO). These dopants have indeed refined the grain size and contributed to attaining near theoretical densities of the nanocomposites without any adverse effect on the structure and morphology of the MWCNTs. Thus, allowed MWCNTs to utilize their intrinsic traits for converting brittle Al_2O_3 ceramic into tough and hard material suitable for several structural applications.

***Keyword*:** Al_2O_3, CNT composite, microstructure modification, doping

**Corresponding author*: y.zhu@exeter.ac.uk

Ashutosh Tiwari, Rosario A. Gerhardt and Magdalena Szutkowska (eds.) Advanced Ceramic Materials, (201–230) © 2016 Scrivener Publishing LLC

5.1 Introduction

Since their discovery, carbon nanotubes (CNTs) are considered as a potential reinforcement for ceramic materials with the main purpose to enhance both the mechanical and functional properties [1]. Although significant improvements in toughness and strengths of the CNT-reinforced ceramics have been claimed in the past few years, marginal improvements have also been reported at the same time [2]. Debates remained on issues related to the CNT quality, agglomeration, densification, CNT-ceramic interfacial connections, and even mechanical testing protocols; however, little attention was given toward the microstructural modification of the overall matrix [3, 4]. Among many structural ceramics, alumina (Al_2O_3) has broad applications in conventional engineering industries [5]. However, its promising mechanical behavior could not be utilized for load-bearing components, such as bullet-proof armors, aircraft engine parts, and space engineering, due to its extreme brittleness [6]. In this context, both single- (SWCNTs) and multi-walled CNTs (MWCNTs) were attempted to enhance the toughness of monolithic Al_2O_3, but the tendency of CNTs to segregate at grain boundaries hindered the matrix grain from coalescing during sintering; thus, it is quite a challenging task to obtain a fully dense structure, even using pressure-assisted sintering, and the residual porosity led to poor mechanical performance for the resulting nanocomposites [7, 8]. Existing literature indicates that the microstructural modification of pure Al_2O_3- and Al_2O_3-based composites using rare-earth metal/transitional oxides, such as magnesia (MgO), cerium oxide (Ce_2O_3), lithia (Li_2O), and yttria (Y_2O_3) is an effective practice [9–12]. Dopants altered the microstructure by refining the grain size, contributed to the consolidation during sintering for achieving higher density and forming new phases in the microstructure, thus resulting in improved mechanical strength. CNTs as the second phase hamper the densification process, and dopants, however, have indeed facilitated to improve the densification of MWCNT/Al_2O_3 nanocomposites by lowering the sintering temperatures. MgO and Y_2O_3 have also been utilized in MWCNT/Al_2O_3 nanocomposites and their presence tuned the microstructure (fracture mode, grain size, morphology of the crack developments under load, etc.) and improved the mechanical properties (fracture toughness, flexural strength, and hardness) which will be discussed in this chapter.

5.2 Dispersions and Stability of MWCNTs

Uniformly distributing MWCNTs (morphology and structure is shown in Figure 5.1a) within the Al_2O_3 matrix is a challenging issue for the

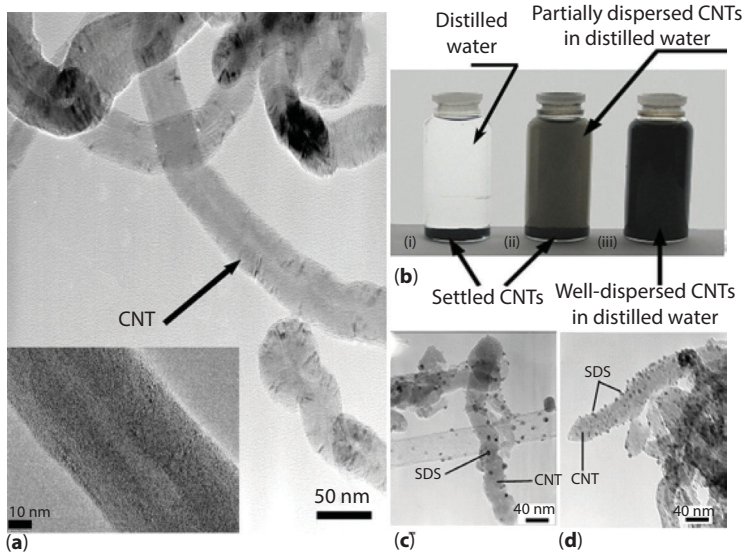

Figure 5.1 (a) TEM image of a MWCNT; (b) MWCNTs in an aqueous suspension, (i) agglomerated MWCNTs, (ii) partially suspended MWCNTs, and (iii) homogenously suspended MWCNTs; and (c and d) TEM images of SDS around MWCNTs.

fabrication of mechanically strong ceramic-based nanocomposites. Underline reason for severe MWCNT agglomeration is probably the high aspect ratio, metallic impurities and tube–tube van der Waals' interactions [13, 14]. Several dispersion processes based on mechanical and chemical routes have been attempted; however, homogenous dispersion up to 2wt% MWCNTs could merely be attained [15]. Wet water-based colloidal chemistry route is attractive due to its simple and environmental-friendly advantages for dispersing MWCNTs homogenously into the Al_2O_3 matrix. In the colloidal dispersion process, high-frequency ultrasonication and surfactant (SDS) are efficiently contributed to obtain good distribution of the MWCNTs within the parent Al_2O_3 matrix; thus, this will be the main focus of this discussion, rather than other processes [16].

Using the environmental water-based colloidal process, a uniform suspension of the MWCNT into distilled water was attained in a three-stage process (Figure 5.1b). Hydrophobic nature always restrict MWCNTs suspending into distilled water due to poor wetting characteristics and difference in density, as shown in Figure 5.1b(i). However, the addition of a small quantity of surfactant (SDS) decreased the surface tension facilitated of water, thereby the dispersion capability; thus, a partially excellent dispersion of MWCNTs could be attained, as displayed in Figure 5.1b(ii). It is believed that proper adsorption of the surfactant on the MWCNT's surface

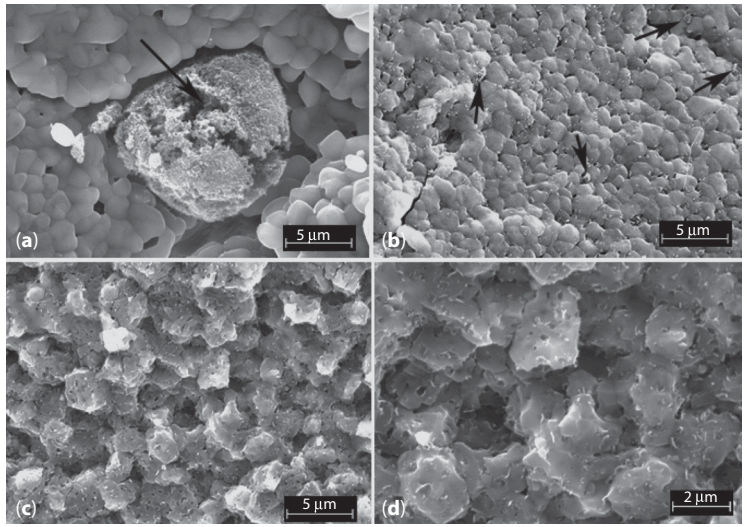

Figure 5.2 Fractured surface SEM images of MWCNT/Al_2O_3 nanocomposites. (a) MWCNT gluts (black arrows), (b) partially dispersed MWCNTs and well-dispersed MWCNTs at (c) low and (d) high magnifications.

and the uniform suspension of MWCNTs in water were achieved, as exhibited in Figure 5.1b(iii).

Molecular modeling has shown the aliphatic dodecyl groups to partially wrap around the MWCNT (see Figure 5.1c and d), while ionized sulfate group sticks out in the water to provide hydrophilicity. The negative charges of the ionized sulfate group cause repulsion among the MWCNTs [15, 16]. Furthermore, the dispersion of MWCNTs in the Al_2O_3 matrix was also confirmed by examining the fractured nanocomposite samples under SEM, and homogenous dispersion (Figure 5.2) was successfully achieved [16]. Whereas the nanocomposites prepared without the SDS addition showed severe MWCNT agglomerations (Figure 5.2a), and huge MWCNT glut is clearly visible, and finally individually well-dispersed MWCNT was obtained (see Figure 5.2d).

During homogenous MWCNT dispersion process, the hydrophobic tails of the SDS surfactant particles are attached to the hydrophobic MWCNTs and the MWCNT surfaces were covered by positively charged surfactant molecules [16]. This phenomenon physically creates an envelope around MWCNTs and increased the magnitude of steric hindrance between the MWCNTs and counteracted the van der Waals interaction among them. Moreover, the sulfonic group in the surfactant (SDS) also altered the wetting behavior by making MWCNT hydrophilic, and in this

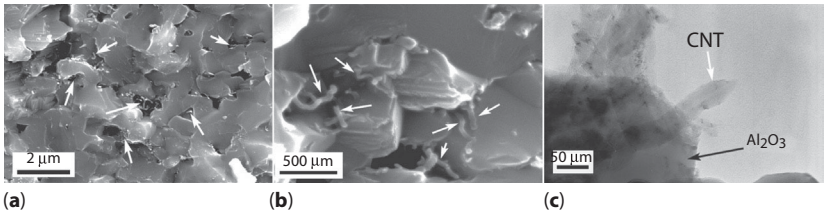

Figure 5.3 SEM fractured surface images of the nanocomposites showing well-dispersed MWCNTs (white arrows) within Al_2O_3 grains at (a) low and (b) high magnifications; and (c) TEM image of a MWCNT (white arrow) retrieved from the sintered nanocomposites, exhibiting its structural and morphological stability.

way helped disperse MWCNTs into the ceramic matrix [17]. Figure 5.3 also provides interesting features, other than MWCNT distribution, regarding the physical and structural stability of the MWCNTs, which negates doubts about their degradation during processes involving higher temperature and/or pressures [18, 19]. Fibrous-like tubular morphology with curly features (Figure 5.3a and b) was seen under SEM on fractured surfaces of the nanocomposite, which depict the retention of the promising high elastic strain characteristics, predicted for the MWCNTs [20]. Furthermore, Figure 5.3c shows the TEM microstructure of a chemically etched nanocomposite sample where firm attachment of tube-like structure of the MWCNT (white arrow) with the Al_2O_3 matrix (black arrow) is clearly visible. Such observations made during electron microscope studies corroborate with that the MWCNTs are both mechanically and thermally stable, maintaining their tubular morphology and nanoscale features even under elevated temperatures and high-pressure sintering environments. These findings, therefore, are well in-line with the inferences drawn from molecular dynamics simulation study for estimating physical, mechanical, structural, and thermal stability of the MWCNTs [19].

5.3 Influence of Yttria (Y_2O_3) Doping on MWCNT/Al_2O_3 Nanocomposites

5.3.1 Densification and Microstructure Development

The homogenous dispersion of MWCNT within the Al_2O_3 matrix is certainly beneficial for improving the mechanical performance; however, these individually dispersed MWCNTs conversely influence the densification process by wrapping around the growing Al_2O_3 grain boundaries.

Thus, MWCNTs hindered the matrix grains coalescence and prevented them from sealing off the voids. This phenomenon influences the final densities of the sintered MWCNT/Al_2O_3 nanocomposites and produces nanocomposites always less dense than monolithic Al_2O_3, the influence of MWCNT addition on the densification is clearly visible in Figure 5.4 [21–23].

The polished and thermally etched surfaces of the Y_2O_3 dopant-free nanocomposites revealed several flaws/porous features inside the matrix grains (black arrows in Figure 5.5b) upon examination under SEM at high magnification. These undesirable microstructural defects are believed to generate during consolidification process when pores were detached from the grain boundary during boundary movement and ultimately trapped inside the grains, thus contributing to the decreased nanocomposite densities [24].

The Y_2O_3 additions into Al_2O_3-based nanocomposites, as a dopant, certainly altered the grain boundary chemistry, lattice structure, and surface diffusivity of the matrix grains, thus improved the sintering ability arising from the control of grain boundary structure and pore mobility, leading to higher densities [25].

It is shown in Figure 5.4 that the Y_2O_3 doping facilitated Al_2O_3/MWCNT nanocomposites to attain near theoretical densities (99%), and the fractured surface studies further confirmed the elimination of grain porosities

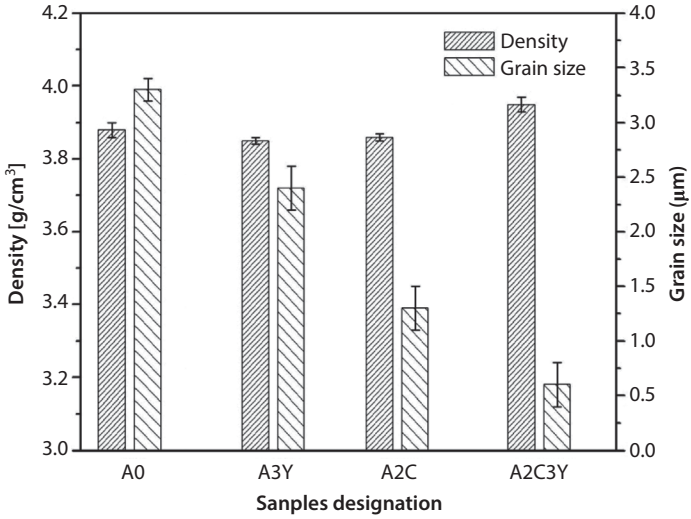

Figure 5.4 Densities and grain size of monolithic Al_2O_3 and MWCNT/Al_2O_3 nanocomposite samples with/without Y_2O_3 doping.

due to Y_2O_3 doping, in both monolithic Al_2O_3 (Figure 5.5c) and Al_2O_3/CNT nanocomposites (Figure 5.5d). Indeed, Y_2O_3 has improved the sintering of Al_2O_3/CNT nanocomposites by managing the mass transport of the Al_2O_3 matrix grains through Al and O ions diffusion control, and secondly obstructed the pores detachment from the grain boundaries during the migration, thereby prevented them trapping inside the matrix grains. As a result, the pores finally shifted to grain junctions during sintering final stage [26]. These results indicate that the contribution of Y_2O_3 lies in eliminating the porosity from the matrix grains and sealing the gaps at

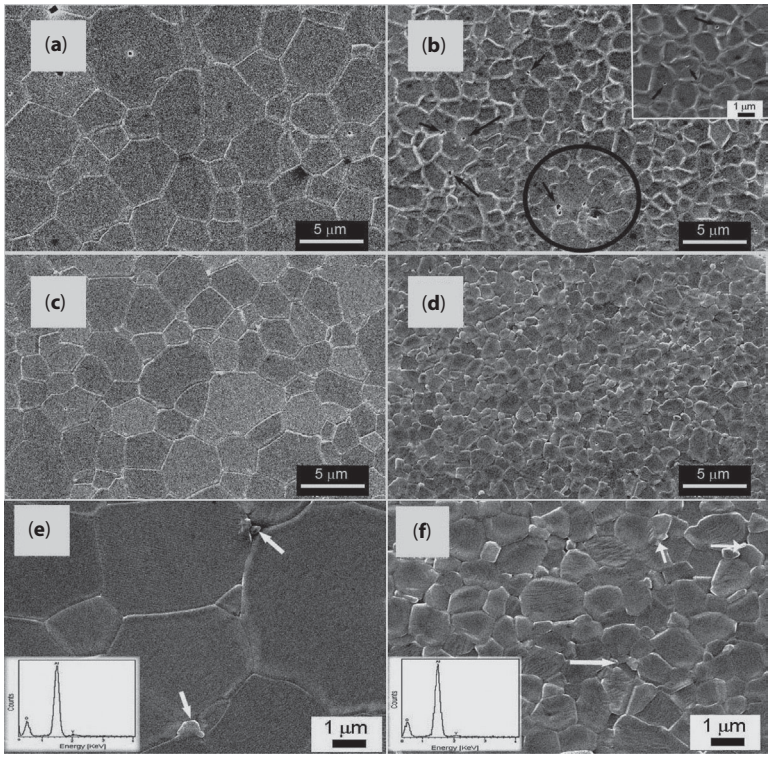

Figure 5.5 SEM images of polished and thermally etched (a) monolithic Al_2O_3-coarse Al_2O_3 grains; (b) Y_2O_3-free nanocomposites, showing heterogeneous fine and coarse (black circle) grained microstructure with residual flaws/pores (black arrows) in inset; (c) Y_2O_3-doped Al_2O_3 showing equiaxed grains; (d) Y_2O_3-doped nanocomposites exhibit flaw-free, fine-grained, and dense microstructure; (e) Y_2O_3-doped Al_2O_3 showing submicron $Y_3Al_5O_{12}$ precipitates (white arrow) at grain junctions with EDS analysis of the same precipitates in the inset; and (f) Y_2O_3-doped nanocomposite showing $Y_3Al_5O_{12}$ precipitates (white arrow) within matrix grains, at high magnification with EDS analysis of precipitate particle in the inset.

the triple-grain junctions by segregating in the form of YAG particulates; therefore, dense MWCNT/Al_2O_3 nanocomposites could be produced. In the Y_2O_3–Al_2O_3 phase system, Y_2O_3 can be soluble up to 6–10 ppm, and the excessive amount of Y_2O_3, if present in the system, was segregated at the junctions of Al_2O_3 matrix grains and formed another phase [27]. In the polished and thermally etched samples of the doped Al_2O_3 [(Figure 5.5e) and MWCNT/Al_2O_3 nanocomposites (Figure 5.5f)], the particulate precipitates of another phase at the Al_2O_3 grain junctions (indicated by white arrows) were seen under SEM, and the chemical composition of these particulate were detected as yttrium (Y) and oxygen (O) in both the doped Al_2O_3 and the dopant-free nanocomposites (insets of Figure 5.5e and f). Moreover, the X-ray diffraction patterns of all the samples (Figure 5.6) were indexed for crystalline α-Al_2O_3 (JCPDS No. 01-078-2426) for the matrix phase, and $Y_3Al_5O_{12}$ (YAG) (JCPDS card no. 01-072-1853) which must be corresponding to the precipitates. No characteristic peaks associated with the MWCNTs were observed in all nanocomposite samples, which is probably due to their low contents and possible overlap of the strongest (002) peak of MWCNTs (JCPDS No. 01-075-1621, included in Figure 5.6 as a reference) with the (012) peak of Al_2O_3.

It is widely suggested that the high aspect ratio and fibrous morphology facilitated MWCNTs to interact with wide areas of Al_2O_3 matrix grain

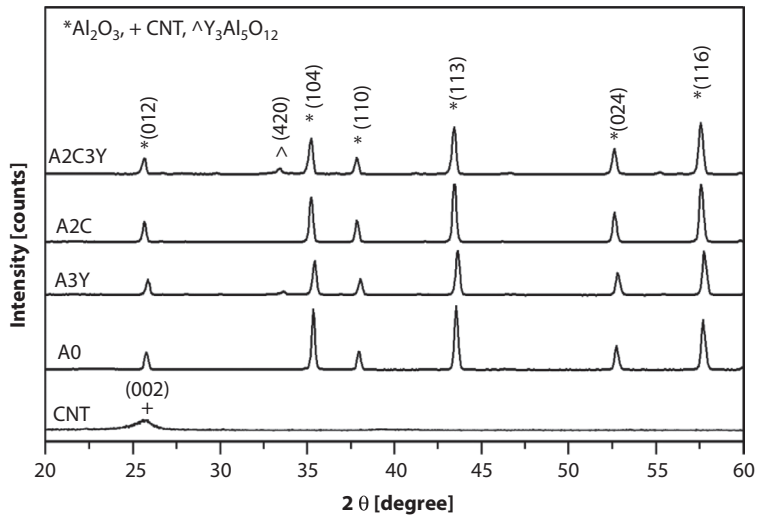

Figure 5.6 XRD patterns of powdered MWCNT and sintered samples of Al_2O_3 and Al_2O_3–CNT nanocomposites containing 0 ppm (A0, A2C) and 300 ppm (A3Y, A2C3Y) Y_2O_3, respectively.

boundaries and hampered their growth during sintering; thus, Al_2O_3/CNT nanocomposite revealed 50% reduction, as graphically (Figure 5.4) and structurally (Figure 5.5a and b) represented. Although wet chemistry method has now being considered as one of the most efficiently dispersion techniques to disperse the MWCNT homogenously into the matrix, discrete fine and coarse grain areas were also detected in the microstructure of dopant-free nanocomposites (highlighted by black circle in Figure 5.5b). Such structural irregularities are probably due to the hitches in obtaining even distribution of MWCNTs throughout the Al_2O_3 matrix [27]. This phenomenon corroborates that MWCNTs may not be available at some Al_2O_3 grain boundaries to act as a pinning agent, and the grain obstacle role of the MWCNT does not seem to be prevalent in the entire microstructure of the nanocomposites.

An interesting change in the same nanocomposites after Y_2O_3 doping was seen, as the microstructure became more homogenous and fine in grain sizes (Figure 5.5d). High-magnification SEM image (Figure 5.5f) details are helpful in understanding the exact role of the dopant in the microstructural improvements. Bimodal grain size distribution representing relatively smaller YAG grains around large matrix grains and defect-free prominent matrix grain surfaces in Y_2O_3-doped nanocomposites, elucidating the excellent thermal stability of Al_2O_3, were particularly notable in the polished/thermally etched doped nanocomposite, as shown in Figure 5.5f. The distribution of the MWCNTs into the Al_2O_3 matrix is based on physical/mechanical phenomenon, whereas the YAG precipitates are thermodynamically formed from Y_2O_3–Al_2O_3 solid solution through a phase-transformation process; therefore, their presence and thorough distributions in the overall microstructure are rational [25]. These YAG particulates offer the advantages such as (i) they filled the voids existed at grain junctions for an enhanced densification and (ii) simultaneously provided additional pinning sites in those regions of microstructures where there were no CNT presence, as marked in Figure 5.5b with black circle. Adding on, the numerical simulation supports that the small particles are more effective than larger ones in pinning the grain in the polycrystalline materials [29]. In fact, YAG precipitates exhibited submicron dimensions around matrix grains (Figure 5.5f). Based on these results, it can be deduced that, compared with pure Al_2O_3, the preliminary 50% grain size reduction in the dopant-free MWCNT/Al_2O_3 nanocomposites is merely due to CNT's grain pinning effect, whilst the further ~30% grain refinement is the effect of Y_2O_3 on the nanocomposites. In short, the Y_2O_3 showed influences in several ways on enhancing the quality of CNT-reinforced Al_2O_3, such as (i) the elimination of porosity and other sintering defects, (ii) the substitution of

the grain junction voids with submicron YAGs for enhanced densities, and (iii) the provision of more grain pinning sites to suppress the matrix grain coarsening through Zener pinning phenomenon [27]. The combined role of these phenomena eventually led the Y_2O_3-doped MWCNT/Al_2O_3 nanocomposites to near theoretical densities and much finer microstructures, compared with the pure Al_2O_3.

5.3.2 Mechanical Performance and Toughening Mechanism

The weak grain bonding, large grain sizes, residual flaws, and intergranular fracture mode are generally attributed to the low fracture toughness/strength of the monolithic Al_2O_3 [30–33]. Numerous individually dispersed MWCNTs owning strong bonding with the Al_2O_3 matrix in Figure 5.7 have led the K_{IC} value of the dopant-free nanocomposites to 30% higher, against the reference monolithic Al_2O_3 (indicated in Table 5.1). It means that the MWCNTs have somehow transferred their strong and flexible feature to the matrix [10, 34].

Toughening mechanism associated with the MWCNTs such as bridging the cracked gaps (Figure 5.7a, black circles and Figure 5.7b, black arrow) indeed resisted in pull-out (Figure 5.7, white arrows), and thereby strengthened the composites and led to higher fracture toughness. It is a fact that the transgranular fracture mode (Figure 5.8b) is operated when the grain boundary attained the fracture strength near the matrix grain, and similar fracture behavior was observed in Al_2O_3–CNT nanocomposites; however, the presence of residual defects in the microstructure of nanocomposites explained the deprived fracture resistance [34]. The sensitivity of residual flaws in ceramics can be gauged by an empirical square root relationship

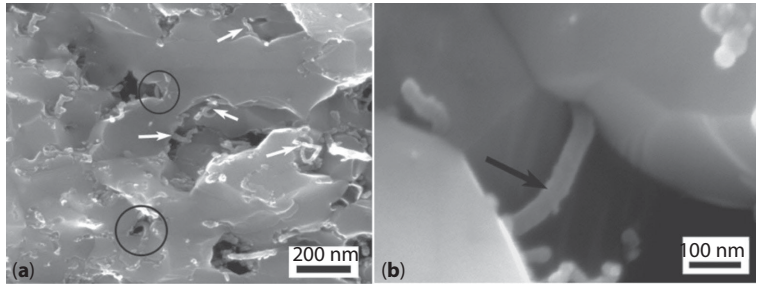

Figure 5.7 SEM images. (a) The fractured surface of MWCNT/Al_2O_3 nanocomposites, exhibiting MWCNT across the flaws (black circles), MWCNT pull-out (white arrows) and (b) MWCNT bridging the crack surfaces (black arrow).

Table 5.1 Mechanical properties of Y_2O_3-doped MWCNT/Al_2O_3 nanocomposites.

Sample designation	Matrix material	CNT contents (wt%)	Y_2O_3 contents (ppm)	Vickers' hardness (*HV*) GPa	Flexural strength (σy) MPa	Fracture toughness (K_{IC}) MPa $m^{1/2}$
A0	Al_2O_3	–	0	16.0 ± 0.3	340± 21	3.2 ± 0.1
A3Y	Al_2O_3	–	300	16.5 ± 0.2	359 ± 22	3.2 ± 0.3
A2C	Al_2O_3	2	0	18.2 ± 0.2	367 ± 18	4.3 ± 0.3
A2C3Y	Al_2O_3	2	300	19.4 ± 0.2	442 ± 15	5.0 ± 0.1

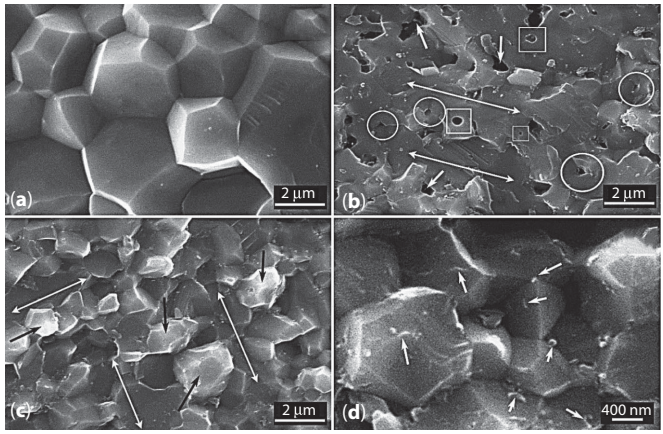

Figure 5.8 SEM images of fractured surface: (a) monolithic Al_2O_3-large grains with intergranular fracture; (b) Y_2O_3-free nanocomposites showing residual porosity (white square), sharp flaws at matrix grain junctions (white circle), MWCNTs within flaw cavity (short white arrow), transgranular fracture (double-headed long white arrows); (c) mixed mode fracture in doped MWCNT/Al_2O_3 nanocomposites transgranular (double-headed long white arrows), intergranular (short black arrows); and (d) high-magnification SEM image of doped nanocomposites showing MWCNT (short white arrows) at individual matrix grains.

($\sigma_F \infty l^{-0.5}$) which describes the fracture strength (σ_F) dependency on the flaw (c), where (c) is calculated with the grain size (l) [35–36].

Based on the microstructure, it is anticipated that the flaw morphology and their high population could affect the amounts of stress required to start a crack. For example, sharp flaws marked as white circles in Figure 5.8b are logically more susceptible to stress concentration than blunt ones as spotted by white squares in Figure 5.8b.

It has been postulated that the failure in MWCNT/Al_2O_3 nanocomposites may have started after piling a large amount of stresses around these exiting flaws and the fracture occurs upon tensile loading, instantaneously at the flaw's edge, rather than through intergranular, which normally occurs along weakly bonded grains. Although the MWCNTs are present inside these flaws (pointed with white arrows in Figure 5.8b), it seems they could not efficiently reinforce the matrix; thus, the failure started at much lower loads than expected. The transgranular fracture behavior in the nanocomposites depicts the strong matrix grains/MWCNT bonding, and the straight indent crack propagation profile confirms the existence of such a failure mechanism in the dopant-free nanocomposites (see Figure 5.9c). It can thus be concluded that the failure in MWCNT/Al_2O_3 nanocomposite follow transgranular fracture mode, leading to the higher

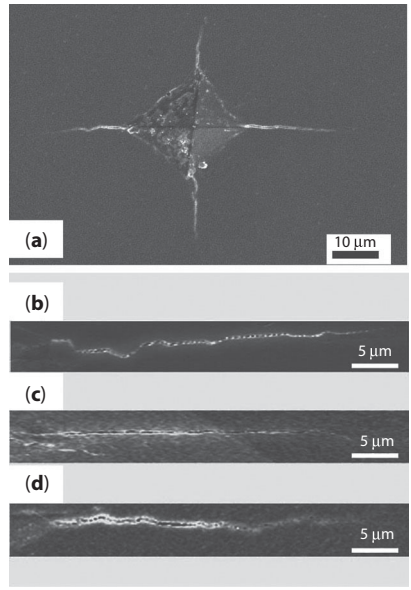

Figure 5.9 SEM images of (a) Vickers' hardness indent at 9.8 N used for fracture toughness assessment and indent crack profile of (b) monolithic Al_2O_3, (c) dopant-free nanocomposites and (d) Y_2O_3-doped MWCNT/Al_2O_3 nanocomposites.

fracture toughness, rather than the mixed inter- and transgranular mode, as proposed by other [37]. These details corroborate that the residual flaws suppressed the MWCNT's strengthening role and hurdled the final nanocomposites from attaining maximum toughness and strength. This shows that the elimination of such defects is imperative.

The addition of 300 ppm Y_2O_3 into the same MWCNT/Al_2O_3 nanocomposite improved the K_{CI} by 40%, 15% and flexural strength (σ_f) by 20%, 17% than monolithic Al_2O_3 and dopants-free nanocomposite, respectively, as summarized in Table 5.1. The role of Y_2O_3 into the nanocomposite was studied by fractographic comparison, as demonstrated in Figure 5.8b, and clear distinctive fracture mode changes from transgranular in the dopant-free nanocomposites to a mixed inter-transgranular (see Figure 5.8c) in doped nanocomposites are evident along with the absence of flaws and other microstructural defects. As already discussed that the Y_2O_3 improved the density and segregated at the grain boundaries of the matrix and formed the YAG phase preferably at Al_2O_3 grain junctions in the doped nanocomposites. New microstructural design thus offers two benefits of the elimination of the residual flaws and the reduction of the grain size in one go. The domination of mixed fracture mode in Y_2O_3-doped MWCNT/

Al_2O_3 nanocomposite could be due to the good contact between the YAG phase and Al_2O_3, hence a smooth transfer of dislocations (generated upon loading) from the matrix grains to bi-grain junctions through the YAG phase instead of piling up at triple-grain junctions [38]. The Y^{3+} ions segregation on the weak Al_2O_3–Al_2O_3 grain boundaries, an intergranular fracture mode was expected in the doped nanocomposites, otherwise a mixed inter- and transgranular fracture mode, as shown in Figure 5.6c, was produced [39]. Therefore, a mixed indent crack profile in the doped nanocomposite (Figure 5.9d), which is neither zigzag nor straight, indicates the complexity of the fracture modes.

The fractured surfaces of the doped nanocomposites were also studied at high magnification using SEM, and the obtained information showed that fewer MWCNT were present within individual matrix grains, and the composite underwent an intergranular fracture, as marked as white arrows in Figure 5.8d. Thereby, it can be deduced that in these regions MWCNTs are present in very small amount and do not effectively reinforce the matrix grains, leading to the intergranular fracture. This kind of fracture may be associated with the lacking MWCNTs at individual grain level and with the weak matrix grain boundaries due to dopant segregation. Furthermore, the fine-grained microstructure in Y_2O_3-doped nanocomposites contributed to increase the critical strain-energy release rate, by providing more crack deflections during the intergranular fracture [39]. In this way, the mixed (inter- and transgranular) fracture modes with the support of fine grains and flaw-free microstructure led the doped nanocomposites to a higher mechanical performance.

Generally, the grain boundaries and reinforcing constituents are considered as pinning points in the matrix microstructures, as they impede the dislocation movements across their respective microstructures by hindering the onset of plasticity, thus making the fine-grained ceramics-based composites harder [40, 41]. Therefore, high hardness in both dopant-free (18.2 GPa) and doped (19.4 GPa) nanocomposites was recorded, compared with the hardness of the monolithic Al_2O_3 (16.0 GPa). Adding on, the renowned Hall–Petch equation (Eq. 5.4) could also be used to assess the hardness of ceramics [42].

$$H = H_R + Kd^{-1/2} \tag{5.1}$$

where H is the measured hardness by Vickers' indentation, H_R is the reference hardness, K is the proportionality constant, and d the mean grain size. The relationship between hardness and grain sizes is evident from Eq. 5.1. It can be deduced that the 12% higher hardness for the dopant-free

nanocomposites against monolithic Al_2O_3 is most probably due to the 50% finer grains and good CNT–matrix bonding [10, 34]. The role of Y_2O_3 doping in the microstructure tuning in nanocomposite granted extra advantages such as (i) minimizing the stress concentration sites (removal of residual flaws/pores), (ii) extra grain boundaries (grains refinement), (iii) additional crack resistance through the mixed mode fracture mechanism (fracture-mode alteration), and all these resisted deformations, and consequently led it to mechanically strong material.

5.4 Magnesia (MgO)-Tuned MWCNT/Al_2O_3 Nanocomposites

5.4.1 Role of MgO on the Densification and Microstructural Features

MgO is another well-known dopant used to efficiently control abnormal grain growth, pore mobility, and O_2 loss from Al_2O_3 during pressure less (PL) sintering. It alters the boundary chemistry, lattice structure, and surface diffusivities and led Al_2O_3 to the highest possible density and much finer microstructures [43]. Study showed that small additions of (300 and 600 ppm) MgO additions had consolidated the PL-sintered unreinforced Al_2O_3 to higher density.

Tubular morphology, high aspect ratio, and high thermal/chemical stability allowed MWCNTs to check the material migration during densification, thus prevented the Al_2O_3 grains integration and adversely affecting the densification of nanocomposites upon sintering under pressure-free condition. Therefore, a relative lower density is always achieved after PL sintering the nanocomposites and even with MgO doping, at both levels, barely contributed toward the density improvement, as shown in Figure 5.10a. The reason behind the poor densification can be understood by investigating the low-magnification SEM fractographs of the PL-sintered nanocomposites and heterogeneous microstructure along with isolated dense patches separated by microcracks, spotted as white arrows in Figure 5.11b, is evident, whereas no such microstructural irregularities are present in monolithic Al_2O_3 samples (see Figure 5.11a). It seems that the MWCNTs are the potential source of scanty densification of PL-sintered nanocomposites.

The appearance of defected microstructures may be associated to two potential reasons: (i) gases (Al_2O and CO) are generated during elevated temperatures (~1600 °C) carbothermal reduction of Al_2O_3 by MWCNTs

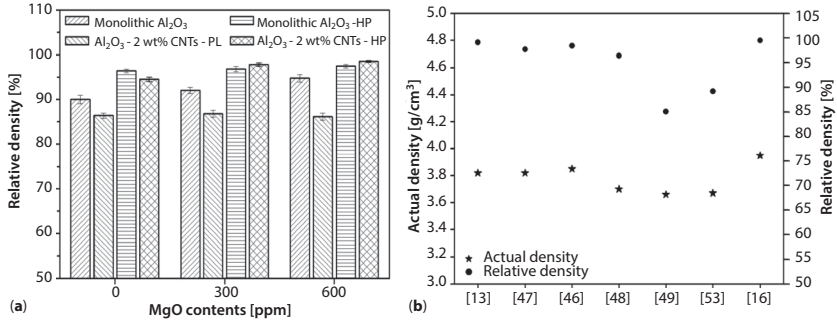

Figure 5.10 (a) Densities of the monolithic Al_2O_3 and nanocomposites samples as the function of MgO concentrations, sintered under pressures and pressure-free conditions, and (b) comparison of the density of MgO-doped nanocomposites with previous reports.

and these gases gradually generated pressure inside the nanocomposite, thus could produce microcracks while escaping during subsequent cooling, and (ii) being an effective grain refining agent, MWCNTs hindered the Al_2O_3 grain expansion during PL sintering through segregating at grain boundaries, as well as restricted grain coalesce, thus giving rise to porous or heterogeneous microstructures of the nanocomposites [44]. In contrast, the constant application of external pressures during HP sintering integrated with both pure Al_2O_3 (Figure 5.11c) and nanocomposite (Figure 5.11d) into firm, dense, and homogenous microstructure, keeping negligible microstructural flaws with high relative densities, which are higher than their respective PL-sintered counterparts, as shown in Figure 5.10a.

It is evident that the existence of high pressure during whole sintering process assisted in simultaneously eliminated the shrinkage-induced microcracks or microcracks/void formation due to release of gases generated during sintering, thus consequently consolidating the nanocomposites to higher densities by dominating over the hurdles arising from MWCNTs. Furthermore, MgO doping by 300 or 600 ppm into nanocomposites of the same composition further raised the relative densities of the HP-sintered samples higher than to their MgO-free nanocomposite counterparts, as shown in Figure 5.10a. This increase in the density value suggests that MgO doping has probably altered the sintering behavior of Al_2O_3 in the nanocomposites during HP sintering. Lower density of Al_2O_3-based composites is associated with the diminution of O_2 from Al_2O_3 during high-temperature sintering which is generally greater than 1600 °C [45]. However, dopants like MgO influence mass transport of the Al_2O_3 matrix grains by controlling diffusion of Al^{3+} and O^{2-} ions as well as improve thermal stability of Al_2O_3, thus resulting in nanocomposites with higher

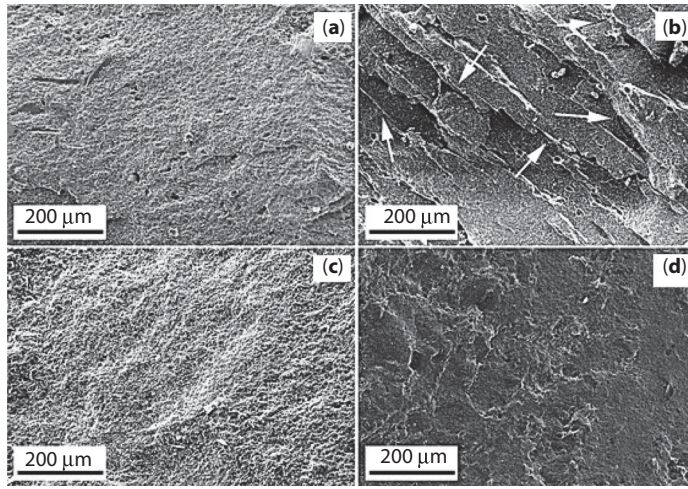

Figure 5.11 Low-magnification images SEM fractured surfaces details the samples sintered without external pressures, 600 ppm MgO-doped (a) monolithic Al_2O_3, (b) nanocomposite, microcracks clearly visible (white arrows) and HP-sintered MgO-free (c) monolithic Al_2O_3, (d)nanocomposite, exhibiting well-integrated flaws-free homogenous microstructure.

densities [30]. The significance of MgO doping in MWCNT/Al_2O_3 nanocomposites is also evident from graphical comparison of the density results with previous reports in Figure 5.10b. For example, Ahmad *et al.* [13] and Wie *et al.* [46] could obtain respective density values of 3.82 and 3.85 g/cm^3 for nanocomposites after HP sintering, whereas Yamamoto *et al.* [47], sintered nanocomposites to a density of 3.82 g/cm^3 using SPS. Similarly, Ghobadi *et al.* [48], Ueda *et al.* [49], and Bakhsh *et al.* [50] reported low densities of 3.70, 3.66, and 3.67 g/cm^3, respectively, for PL-sintered nanocomposites with the same composition. HP-sintered nanocomposite doped with 600 ppm MgO demonstrated a density of 3.95 g/cm^3, which is close to theoretical density (99.6%). These details confirm the collective importance of the external pressures and MgO, as dopant, during elevated temperature sintering regimes in order to achieve advanced structures and properties in the MWCNT-reinforced Al_2O_3 nanocomposites.

5.4.2 Effect of MgO on the Grain Size and Fracture Behavior

The influence of MgO on the grain size of monolithic Al_2O_3 was studied, and significant reduction upon tuning with 300 and 600 ppm MgO was reported against monolithic Al_2O_3, as shown in Figure 5.12. Furthermore,

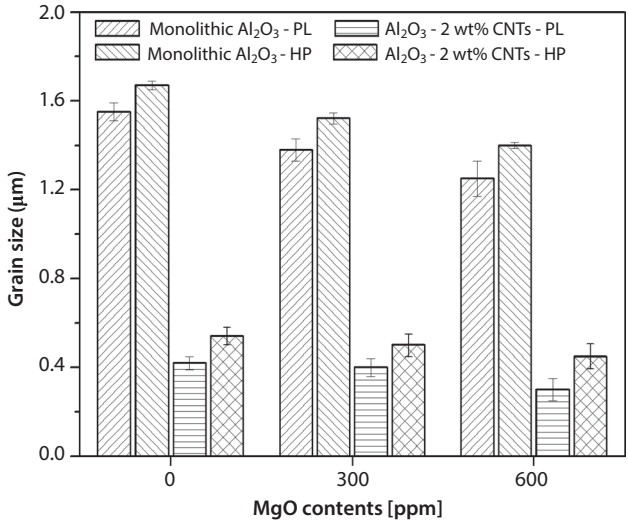

Figure 5.12 Influence of the MgO contents on the grain size of the monolithic Al_2O_3 and nanocomposites consolidated by PL sintering and HP sintering.

untuned Al_2O_3 demonstrated uneven grain growth (Figure 5.13a), whereas finer and more uniform grain (Figure 5.13b and c) structure was produced after adding MgO. It has been well understood that the MWCNTs always act as grain refining agent; therefore, PL-sintered MgO-free MWCNT/Al_2O_3 nanocomposite exhibited 70% finer grain morphology as compared with pure Al_2O_3 (Figure 5.13d). PL-sintered nanocomposites tuned with 300 and 600 ppm MgO showed a further drop in the grain size by 5 and 28%, respectively, as shown in Figure 5.6e and f.

It is quite possible that the MWCNTs are absent at some Al_2O_3 grain boundaries for pinning the grains because fewer reported that MWCNTs could be distributed evenly only up to very low levels of 2 wt% [12]. It may be deduced that the grain refinement in the tuned nanocomposites is likely due to the precipitates of magnesium–aluminate–spinel phase ($MgAl_2O_4$) that are present throughout the microstructure. These precipitates are generally formed thermodynamically from MgO–Al_2O_3 system through phase-transformation process [43].

X-ray diffraction technique was used on the densified and MgO-tuned nanocomposites (Figure 5.14a), and the result showed the presence of diffraction peaks characteristic of the $MgAl_2O_4$ phase according to the JCPDS card no. 01-073-1959. The elemental constituents of the same samples were further confirmed by EDS analysis (Figure 5.14c) spotted on the areas marked by white arrows in the thermally etched micrograph in

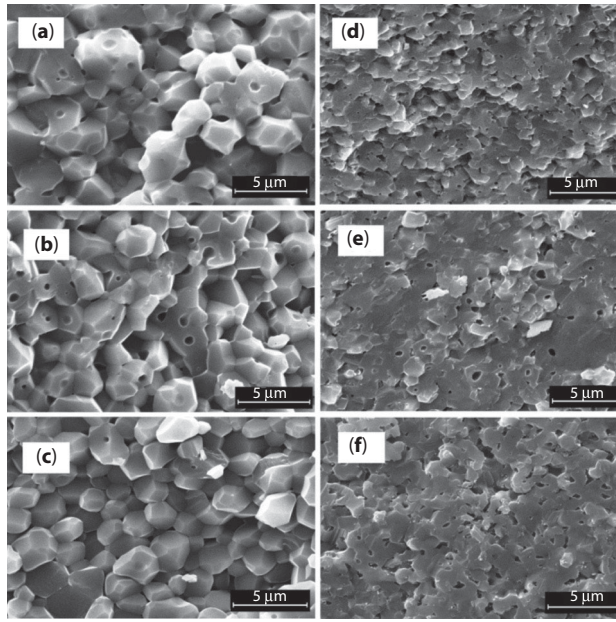

Figure 5.13 Fractured surfaces SEM images of the samples underwent PL sintering, (a) untuned Al_2O_3, (b) 300 ppm MgO-tuned Al_2O_3, (c) 600 ppm MgO-tuned Al_2O_3, (d) untuned nanocomposite, (e) 300 ppm MgO-tuned nanocomposite, and (f) 600 ppm MgO-tuned nanocomposite.

Figure 5.14b of the MgO-tuned sample. It is believed that these submicron size precipitates have effectively pinned the grains of the tuned nanocomposites, leading to fine microstructures.

HP-sintered samples demonstrated interesting microstructural features (Figure 5.15) and both the pure Al_2O_3 and nanocomposites exhibited somewhat bigger grain sizes than similar PL-sintered samples, respectively. This large grain development with homogenous size after pressure-assisted sintering may probably be due to the reduced extent of drag forces on boundary movement, because the application of external pressure during sintering certainly increased the rate of consolidification, thus causing reduction of drag forces during the sintering process. The excessively high sintering temperature, used to densify the samples, in the presence of applied external pressure led to unfavorable grain growth as suggested in earlier study [39]. Microstructural features obtained from the study of samples under SEM are presented in Figure 5.15. These features helped to identify the exact role of MgO addition in the nanocomposites, because nanocomposite samples without MgO addition showed several structural

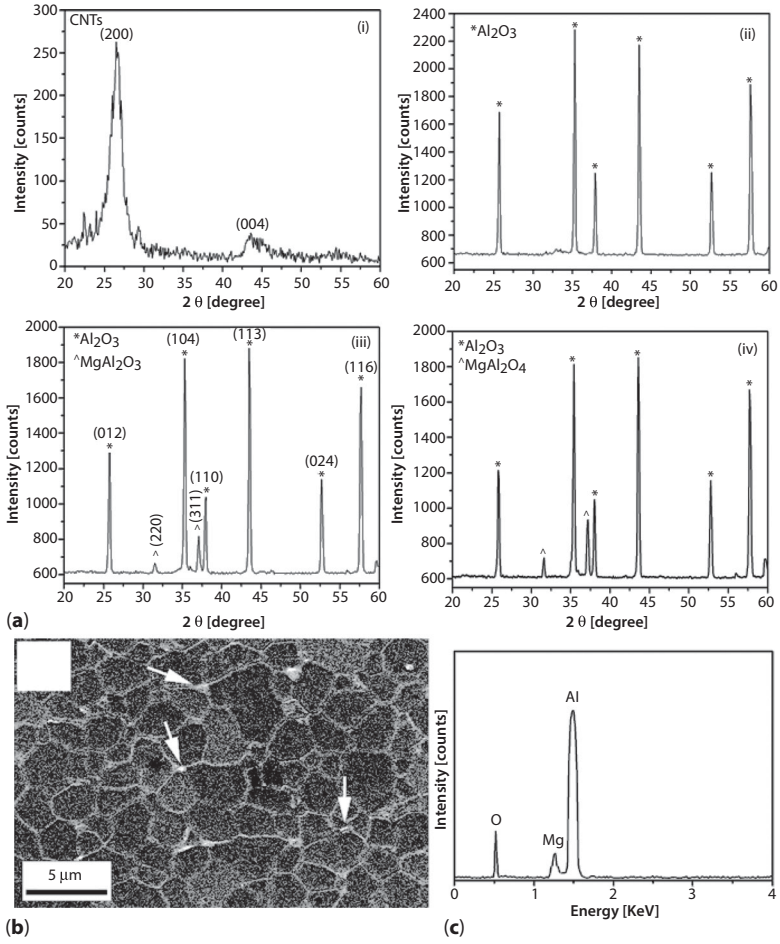

Figure 5.14 (a) XRD patterns of (i) pristine MWCNT, (ii) monolithic Al_2O_3, (iii) 300 ppm MgO-tuned Al_2O_3, (iv) 600 ppm MgO-tuned nanocomposite, (b) SEM micrograph of thermally etched 600 ppm MgO-tuned Al_2O_3 showing precipitates of $MgAl_2O_4$ at Al_2O_3 grain boundaries (white arrows), and (c) chemical composition of the same precipitates confirming the elements of sample constituents.

microscale flaws (larger in dimensions and thicker in population as indicated with white arrows in Figure 5.15d).

However, MgO addition at either level (300 or 600 ppm) changed the microstructures (Figure 5.15e and f), and a significant drop in the density of structural defects is evident. Thus, it is concluded that the MgO has played a significant role in changing the sintering mechanism to produce far better and more homogenous microstructures in nanocomposites, by

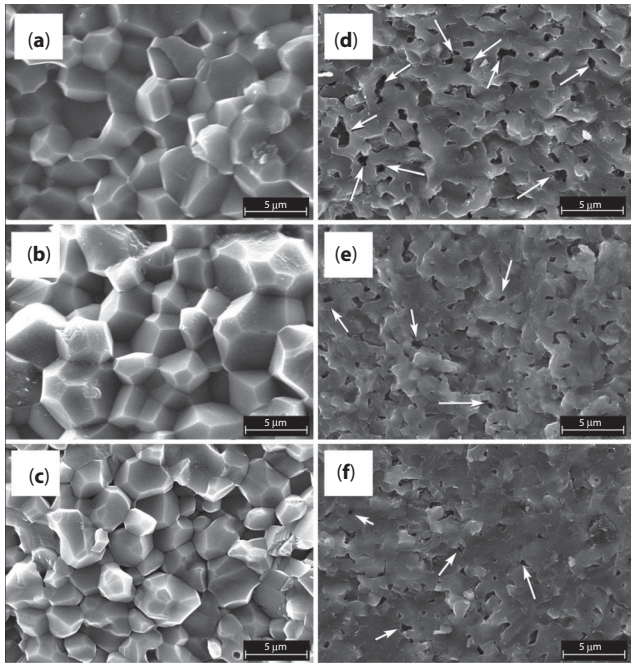

Figure 5.15 Fractured surfaces SEM images of the HP-sintered monolithic Al_2O_3 tuned with MgO contents (a) 0 ppm, (b) 300 ppm, and (c) 600 ppm and nanocomposites tuned with MgO (d) 0 ppm, (e) 300 ppm, and (f) 600 ppm contents.

somehow offsetting the apparent disadvantages of MWCNT addition, and finally led to higher densities in comparison with MgO-free nanocomposites. This discussion advocates that the MgO has efficiently tuned the structure in the nanocomposites and enhanced the extent of interaction between MWCNT and the Al_2O_3 matrix for exhibiting crack bridging and/or pull-out toughening mechanisms [2, 3, 7, 13].

5.4.3 Mechanical Response of MgO-Doped MWCNT/Al_2O_3 Nanocomposite

As discussed in the last section, MWCNTs showed unfavorable effects on important sintering mechanisms of material diffusion and porosity elimination, despite their even dispersion as second phase, thus resulting in nanocomposites with poor densification, weak MWCNT/matrix interface, and reduced hardness [51]. Hardness measurements showed 5% drop in hardness in nanocomposite (16.2 GPa) from that of monolithic Al_2O_3 (17.1 GPa) sintered under similar PL-sintering conditions without any

MgO tuning. As opposed to MgO-free samples (Figure 5.16), PL-sintered monolithic Al_2O_3 (17.6 GPa) and nanocomposites (18.4 GPa) showed superior hardness after tuning with 300 ppm MgO, whereas further addition of MgO content (600 ppm) barely influenced the hardness values (18.5 GPa). After tuning with 300 ppm MgO, the nanocomposites attained 12% higher hardness that could be due to lower sintering temperature during PL sintering and having allowed the MWCNT to stick tightly with the Al_2O_3 grains so that the proposed strengthening mechanisms could efficiently be performed [2, 3, 7]. Another reason of higher hardness in MgO-doped nanocomposites could be the fine-grained microstructures, as shown in Figure 5.15.

Grain boundaries are potential pinning sites in the matrix microstructures of ceramic nanocomposites, thus act as stopper for dislocation movement across their respective microstructures by obstructing the onset of plasticity, so it can be deduced that the fine-grained microstructure, as appeared in ceramic nanocomposites, owns higher hardness value [20]. In Figure 5.16, it is further illustrated that the unturned and MgO-tuned HP-sintered nanocomposites (300 and 600 ppm) attained higher hardness levels by 15, 12, and 14%, respectively, against their PL-sintered nanocomposite counterparts. These hardness results suggest that the existence of pressure during high-temperature sintering process is essentially vital for improving the interaction amongst the reinforcing MWCNTs and the

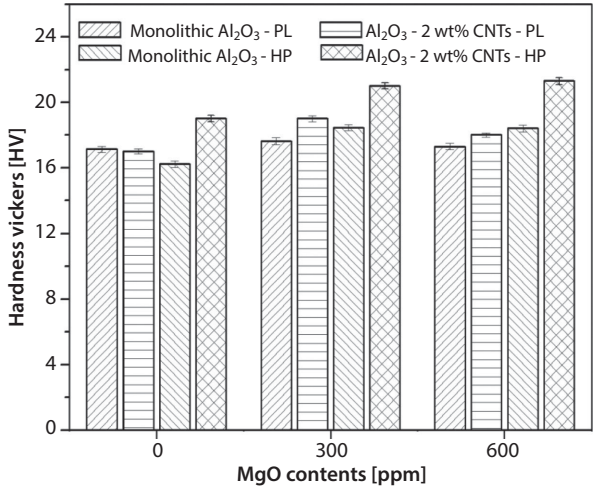

Figure 5.16 Hardness Vickers' profile of the monolithic Al_2O_3 and nanocomposites tuned with various (300 and 600 ppm) MgO contents and sintered with and without external pressures.

Al_2O_3 matrix, which is highly desirable for good matrix/reinforcement cohesion [15, 51]. Moreover, the external application of pressure during HP sintering can (i) enhance the MWCNT/Al_2O_3 adhesion, (ii) improve the consolidation through elimination of microstructural defects, while at the same time, MgO addition controls the sintering mechanisms, thereby increasing hardness in the doped nanocomposites.

Lower K_{IC} and σ_f in the Al_2O_3 ceramic are mainly due to the presence of structural defects like flaws, porosity, weak grain bonding, large grain size, and brittle intergranular fracture mechanism [12]. The HP-sintered monolithic Al_2O_3 samples with or without MgO also exhibited poor toughness as shown in Table 5.2, which are in good agreement with previous reports [2, 3, 15]. However, after the addition of 2 wt% MWCNT, the MgO-free nanocomposites obtained a reasonable 22% hike in the K_{IC} values and 12% increase in σ_f values against monolithic Al_2O_3, as shown in Table 5.2. In earlier studies on MWCNT/Al_2O_3 nanocomposites, it has been suggested that the unique nanoscale features of the CNTs and theirs firm attachments with the Al_2O_3 matrix at interfaces facilitate MWCNTs to perform efficient load sharing between the MWCNT and the Al_2O_3 matrix through proposed matrix grains sharing and crack bridging toughening mechanisms [2, 4, 7, 11, 15]. Adding on, the transgranular fracture mode in the nanocomposites further confirms that the Al_2O_3 boundaries are somehow obtained certain level of strengthen due to CNT reinforcement (Figure 5.8b); otherwise, intergranular fracture mode should occur, as normally appear in monolithic Al_2O_3 shown in Figure 5.8a. Detailed study of the fractured surface of nanocomposite provides interesting details depicting the contribution of the MWCNT toward strengthening the Al_2O_3 matrix grains because transgranular fracture dominates only when strength of the grain boundary is close to that of the matrix grain [52]. This proposes that firmly bonded MWCNTs have surely facilitated the Al_2O_3 matrix to propagate the fracture through the grains other than travelling through grain boundaries, as happened in the case of monolithic Al_2O_3. The nanocomposites tuned with 600 ppm MgO showed improvements in K_{IC} (5.1 MPa.m$^{1/2}$) and σ_f (435 MPa) values, respectively, that are 37 and 22% higher than those for monolithic Al_2O_3, *i.e.* K_{IC} = 3.2 MPa.m$^{1/2}$ and σ_f = 340 MPa). Figure 5.14e and f shows the domination of transgranular fracture mode in nanocomposite containing either MgO levels. Although mechanical superiority in ceramics composites is produced after microstructural refining, the presence of elongated porous features in the MgO-free nanocomposite fractograph, depicted as white arrows in Figure 5.14d, had surely shortened the advantage of grain refinement, thus poor mechanical response, as shown in Table 5.2. This suggests that the MgO tuning hardly influenced the failure

Table 5.2 Chemical compositions, densities, and mechanical properties of the HP-sintered monolithic Al_2O_3 and nanocomposites with and without MgO tuning.

Matrix material	MgO contents (ppm)	MWCNT contents (wt%)	Measured density g/cm^3	Flexural strength (σy) MPa	Fracture toughness (K_{IC}) MPa.m$^{1/2}$
Al_2O_3	–	–	3.88 ± 0.01	340 ± 21	3.2 ± 0.1
Al_2O_3	300	–	3.90 ± 0.02	346 ± 18	3.1 ± 0.2
Al_2O_3	600	–	3.92 ± 0.01	355 ± 26	3.2 ± 0.1
Al_2O_3	–	2	3.82 ± 0.02	390 ± 10	4.1 ± 0.3
Al_2O_3	300	2	3.93 ± 0.01	410 ± 22	4.8 ± 0.2
Al_2O_3	600	2	3.95 ± 0.01	435 ± 10	5.1 ± 0.3

behavior of the nanocomposites, but it improved the mechanical properties probably by means of microstructural alteration.

The fractographs of the nanocomposites tuned with MgO helped in unveiling the role of MgO in enhancing the mechanical strength and toughness. Plenty of structural defects can be seen in the fractograph of MgO-free nanocomposite (see Figure 5.15d); however, a significant flaws reduction can be noticed in the nanocomposites tuned with MgO, as shown in Figure 5.15e and f. In ceramic nanocomposites, microstructural defects are the leading cause behind the meager fracture resistance, because the fracture strength depends on the presence of flaws [35, 36]. Moreover, higher residual defects (pores/flaws) density lowered the stress levels required for crack initiation, and similar defects were found in the nanocomposite fractograph without MgO, as shown in Figure 5.15d. From fractured surfaces features, the failure in the MgO-free nanocomposites can be predicted, as it may have started in the flaws vicinities in terms of stress concentration and lowered the fracture toughness values. As the MgO improves the density of nanocomposite by improving densification and segregated as $MgAl_2O_4$ phase at Al_2O_3 grain junctions in the tuned nanocomposites, thus offering two benefits (elimination of residual flaws and grain refinement). The apparent drop in structural defects density certainly confirmed the minimizing the number of stress concentration sites. The fine-grained structure is also beneficial to the increased critical strain-energy release rate which provides more crack deflections during the course of failure. The net contribution is superior mechanical properties of the nanocomposites than

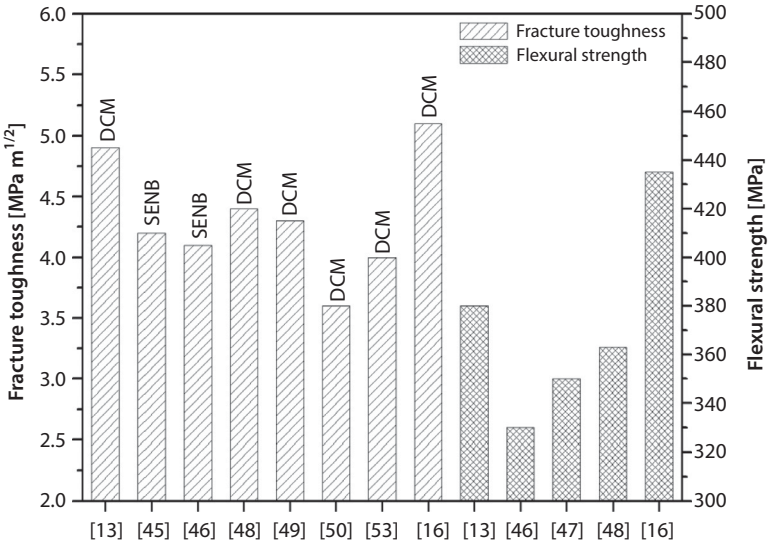

Figure 5.17 Comparison of the (a) K_{IC} and (b) σ_f values obtained in the present study with previous reports.

pure Al_2O_3 in terms of increases in toughness, flexibility and hardness by 37, 22, and 20%, respectively. The comparison of K_{IC} and σ_f results obtained from MgO-tuned nanocomposites with values extracted from the previous studies on Al_2O_3 nanocomposites containing ~2 wt% MWCNTs and a clear difference can be recognized in Figure 5.17 [46–51]. This enhancement in mechanical properties (K_{IC}, σ_f) recorded in nanocomposites containing MgO is presumably due to the cumulative effect of uniform MWCNT dispersion procedure and MgO incorporation in small amounts. It is a fact that even MWCNT dispersion at concentration levels greater than 2 wt% into Al_2O_3 matrix is challenging, and previous studies merely relied on the surfactant characteristics to ameliorate the MWCNT distribution issue [46]. Indeed, the addition of MgO incorporation altered the sintering characteristics of the nanocomposites, so as to limit the densification hurdles generated by CNTs besides fine-grained structure with minimum level of unwanted microstructural defects. The superior mechanical properties, therefore, can be attributed to the microstructure modification in the MgO-doped MWCNT/Al_2O_3 nanocomposites.

5.5 Conclusions

In short, both Y_2O_3 and MgO have contributed to the improved microstructure and mechanical properties of 2 wt% MWCNT/Al_2O_3 nanocomposites.

Uniform MWCNT dispersion within the Al_2O_3 matrix was successfully achieved through optimization of surfactant-assisted and wet chemistry route. A small amount of Y_2O_3 addition into the Al_2O_3 matrix refined the overall microstructure of the 2 wt% MWCNT/Al_2O_3 nanocomposites and improved their key mechanical properties. The Y_2O_3 doping resulted in a near theoretical density of >99 %, which is attributed to the improved sinterability and the removal of residual flaws/pores within the matrix. An 80% reduction in the grain size in the doped MWCNT/Al_2O_3 nanocomposites than the pure Al_2O_3 was due to the grain boundary pinning associated with both the MWCNT and submicron YAG ($Y_3Al_5O_{12}$) participate particulates. Furthermore, the Y_2O_3 doping also contributed to the fracture mode transformation from the transgranular in dopant-free nanocomposites to a mixed inter/trans-granular fracture mode in the doped nanocomposites. The fracture toughness, flexural strength, and hardness values for Y_2O_3-doped MWCNT/Al_2O_3 nanocomposites showed a respective percentage increase by 40, 20, and 18 than the pure Al_2O_3 samples, while an improvement of 15, 17, and 6%, respectively, was achieved than the dopant-free nanocomposites. Similarly, 2 wt% MWCNT/Al_2O_3 nanocomposites were doped with 300 and 600 ppm contents of MgO and fabricated via PL and HP techniques. PL sintering with and without any MgO addition could not consolidate nanocomposites to well-integrated microstructures with marginal differences in densities and hardness values when compared with MgO-free nanocomposite samples. HP sintering and MgO addition had combined effects on the reduction in the residual pores/flaws density and dimensions through modification of the sintering mechanism, thus consolidating the nanocomposites to near-theoretical densities (~99.6%) with well-integrated microstructures. HP-sintered nanocomposites tuned with MgO (0, 300, and 600 ppm) demonstrated higher hardness levels by 15, 12, and 14%, respectively, when compared with their PL-sintered nanocomposite counterparts. Moreover, MgO additions led to further improvement on hardness (10 and 11%), flexural strength (5 and 10%), and fracture toughness (15 and 20%). Finally, an overall enhancement of 37, 22, and 20% in fracture toughness, flexural strength, and hardness, respectively, was obtained in the HPed nanocomposites containing 600 ppm MgO, against the monolithic Al_2O_3.

Acknowledgments

IA gratefully acknowledges the technical support of the University of Nottingham, UK and financial support of the Center of Excellence for

Research in Engineering Materials (CEREM), Advanced Manufacturing Institute, King Saud University, Saudi Arabia.

References

1. Gadd, G.E., Blackford, M.S., Moricca, N., Evans, P.J., Smith, A.M., Hua, Q., The world's smallest gas cylinders, *Science*, 277, 933–936, 1997.
2. Zapata-Solvas, E., Gómez-García, D., Domínguez-Rodríguez, A., Towards physical properties tailoring of carbon nanotubes-reinforced ceramic matrix composites, *J. Eur. Ceram. Soc.*, 32, 3001–3020, 2012.
3. Cho, J., Boccaccini, A.R., Shaffer, M.S.P., Ceramic matrix composites containing carbon nanotubes, *J. Mater. Sci.*, 44, 1934–1951, 2009.
4. Kasperski, A., Weibel, A., Estourne's, C., Laurent, C., Peigney, A., Multi-walled carbon nanotube–Al_2O_3 composites: covalent or non-covalent functionalization for mechanical reinforcement, *Scr. Mater*., 75, 46–49, 2014.
5. Osayande, L., Okoli, I., Fracture toughness enhancement for alumina system: review, *Int. J. App. Ceram. Technol.*, 5, 313–323, 2008.
6. Ohnabe, H., Masaki, S., Sasa, T., Potential application of ceramics matrix composites to aeroengine components, *Composites*, A30, 489–496, 1999.
7. Ahmad, I., Yazdani, B., Zhu, Y.Q., Recent advances on carbon nanotubes and graphene reinforced ceramics nanocomposites, *Nanomaterials*, 5, 90–114, 2015.
8. Ahmad, I., Dar, M.A., Structure and properties of Y_2O_3-doped Al_2O_3–MWCNT nanocomposites prepared by PL-sintering and hot-pressing, *J. Mater. Eng. Perform.* 23, 2110–2119, 2014.
9. Rani, D.A., Yoshizawa, Y., Hirao, K., Yamushi, Y., Effect of rare-earth dopants on mechanical properties of Al_2O_3, *J. Am. Ceram. Soc.*, 87, 289, 2004.
10. Lartigue, S., Carry, C., Priester, L., Grain boundaries in high temperature deformation of yttria and magnesia Co-doped Al_2O_3, *J. Phys. Colloq.*, 51, 985–990, 1990.
11. Kosmac, K., Wallance, S., Claussen, N., Influence of MgO addition on the microstructure and mechanical properties of Al_2O_3–ZrO_2 composite, *Comm. Am. Ceram. Soc.*, 66–67, 1982.
12. Ahmad, I., Islam, M., Almajid, A.A., Yazdani, B., Zhu, Y.Q., Investigation of yttria-doped Al_2O_3 nanocomposites reinforced by multi-walled carbon nanotubes, *Ceram. Int.,* 40, 9327–9335, 2014.
13. Ahmad, I., Kennedy, A., Zhu, Y.Q., Carbon nanotubes reinforced alumina nanocomposites: mechanical properties and interfacial investigations, *Comp. Sci. Tech.*, 70, 1199–1206, 2010.
14. Inam, F., Pijis, T., Reece, M.J., The production of advanced fine-grained alumina by carbon nanotubes addition, *J. Eur. Ceram. Soc.*, 31, 2853–2859, 2011.
15. Ahmad, I., Cao, H., Chen, H., Zhao, H., Kennedy, A., Zhu, Y.Q., Carbon nanotube toughened aluminium oxide nanocomposites, *J. Eur. Ceram. Soc.*, 30, 865–873, 2009.

16. Ahmad, I., Mohammad I., Zhu, Y., Magnesia tuned multi-walled carbon nanotubes-reinforced alumina nanocomposites, *Mater. Charact.,* 99, 210–219, 2015.
17. Sun, J., Gao, L., Reinforcement of Al_2O_3 matrix with multi-walled MWCNT, *Ceram. Int.*, 31, 893–896, 2005.
18. Inam, F., Yan, H., Reece, M.J., Peijs, T., Structural and chemical stability of multiwall carbon nanotubes in sintered ceramic nanocomposite, *Adv. Appl. Ceram.*,109, 240–247, 2010.
19. Liew, K.M., Wong, C.H., He, X.Q., Tan, M.J., Thermal stability of single and multi-walled carbon nanotubes, *Phys. Rev.*, B71, 075424, 2005.
20. Yu, M.F., Lourie, O., Dyer, M.J., Moloni, K., Kelly, T.F., Ruoff, R.S., *Science*, 287, 637, 2000.
21. Fan, J., Zhao, D., Song, J., Preparation and microstructure of multi-walled carbon nanotubes toughened Al_2O_3 composite, *J. Am. Ceram. Soc.*, 89, 750–753, 2006.
22. Lartigue-Korineka, S., Carryb, C., Priestera, L., Multiscale aspects of the influence of yttrium on microstructure, sintering and creep of alumina, *J. Eur. Ceram. Soc.* 22, 1525–1541, 2002.
23. Coble, R. L., Diffusion models for hot pressing with surface energy and pressure effects as driving forces, *J. Appl. Phys.*, 41, 4798–4808, 1970.
24. Powers, J. D., Glaeser, A. M., Grain boundary migration in ceramics, *Inter. Sci.*, 6, 23–39, 1998.
25. Kumar, C. P. S., Baron, B., Hampshire, S., Effect of dopants on densification, microstructure and mechanical properties of alumina–silicon nanocomposites ceramics prepared by pressure less sintering, *J. Eur. Ceram. Soc.*, 24, 3317–3326, 2004.
26. Fang, J., Thompson, A. M., Harmer, M. P., Chan, H. M., Effect of yttrium and lanthanum on the final-stage sintering behavior of ultrahigh-purity alumina, *J. Am. Ceram. Soc.*, 80, 2005–2012, 1997.
27. Cawley, J. D., Halloran, J. W., Dopant distribution in nominally yttrium-doped sapphire. *J. Am. Ceram. Soc.*, 69, 195–196, 1986.
28. Zhan, G., Kuntz, J., Wan, J., Mukherjee, K., Single-walled carbon nanotubes as attractive toughing agent in alumina based nanocomposites, *Nat. Mater.*, 2, 38–42, 2003.
29. Danan, F., Chen, L. Q., Chen, S. P., Numerical simulation of Zener pinning with growing second-phase particles, *J. Am. Ceram. Soc*., 81, 526–532, 1998.
30. Ahmad, I., Kennedy, A., Zhu, Y. Q., Wear resistance properties of multi-walled carbon nanotubes reinforced Al_2O_3 nanocomposite, *Wear*, 269, 71–78, 2010.
31. Inam, F., Reece, M. J., Electrically conductive alumina–carbon nanotubes prepared by spark plasma sintering, *J. Eur. Ceram. Soc*., 30, 153–157, 2010.
32. Wang, J., Lim, S. Y., Ng, S. C., Gan, L. M., Chew, C. H., Dramatic effect of a small amount of MgO addition on the sintering of Al_2O_3–5 vol.% SiC nanocomposite, *Mater. Lett*., 33, 273–277, 1998.

33. Jeong, Y. K., Nakahira, A., Niihara, K., Effects of additives on microstructure and properties of alumina–silicon carbide nanocomposites, *J. Am. Ceram. Soc*., 82, 3609–3612, 1999.
34. Kim, B. N., Wakayama, S., Kawahara, M., Characterization of 2-dimensional crack propagation behaviour simulation and analysis, *Int. J. Fract*., 75, 247–259, 1996.
35. Griffith, A. A., *Trans. R. Soc. London* 221, 163, 1920.
36. Chantikul, P., Bennison, S. J., Lawn, B. R., Role of grain size in the strength and R-curve performance of alumina, *J. Am. Ceram. Soc*., 73, 2419, 1990.
37. Sarkar, S., Das, P.K., Microstructure and physicomechanical properties of pressure-less sintered multi-walled carbon nanotube/alumina nanocomposites, *Ceram. Int*., 38, 423–432, 2012.
38. Nakagawa, T., Sakaguchi, I., Ikuhara, Y., Yttrium doping effect on oxygen grain boundary diffusion in α-Al_2O_3, *Acta. Mater*., 55, 6627–6633, 2007.
39. Deng, Z. Y., Ohiji, T., Fracture-mode change in alumina–silicon carbide composites doped with rare-earth impurities, *J. Am. Ceram. Soc*., 86, 1789–1792, 2003.
40. Callister, W.D., *Materials Science and Engineering; An Introduction*. 5th ed, New York, John Wiley & Sons, 2000.
41. Schaffer, J., Saxena, A., Antolovich, S. D., Sanders, T. H., Warner, S. B., *The Science and Design of Engineering Materials*, Chicago, 1995.
42. Hall, E. O., The deformation and ageing of mild steel: III discussion of results, *Proc. Phys. Soc*., 69, 747–753, 1951.
43. Kosmac, K., Wallance, S., Claussen, N., Influence of MgO addition on the microstructure and mechanical properties of Al_2O_3-ZrO_2 composite, *Comm. Amer. Ceram. Soc*., 66–67, 1982.
44. Sarkar, S., Das, P. K., Microstructure and physico-mechanical properties of pressure-less sintered multi-walled carbon nanotubes/alumina nanocomposites, *Ceram. Int*., 38, 423–432, 2012.
45. Satoshi, K., Matsudaira, T., Masashi, W., Mass-transfer mechanism of alumina ceramics under oxygen potential gradients at high temperatures, *Mater. Trans*., 50, 1023–1031, 2009.
46. Wie, T., Fan, Z., Wie, F., A new structure for multi-walled carbon nanotubes reinforced alumina nanocomposite with high strength and toughness, *Mater. Lett*., 62, 641–644, 2008.
47. Yamamoto G., Omori M., Hashida T., Kimura H., A novel structure for carbon nanotube reinforced alumina composites with improved mechanical properties, *Nanotechnology*, 19, 315708, 2008.
48. Ghobadi, H., Ali, N., Ebadzade, T., Sadeghian, Z., Barzegar-Bafrooei, H., Improving CNT distribution and mechanical properties of MWCNT reinforced alumina matrix, *Mater. Sci. Eng. A*, 617, 110–114, 2014.
49. Ueda, N., Yamakami, T., Yamaguchi, T., Taruta, S., Influence of CNF content on microstructure and fracture toughness of CNF/alumina composites, *J. Ceram. Soc. Jpn*, 122, 292–299, 2014.

50. Bakhsh, N., Khalid, F.A., Hakeem, A.S., Effect of sintering temperature on densification and mechanical properties of pressure less sintered CNT–alumina nanocomposites, *Mater. Sci. Eng.*, 60, 012059, 2014.
51. Sarkar, S., Das, P.K., Processing and properties of carbon nanotube/alumina nanocomposites: a review, *Rev. Adv. Mater. Sci.*, 37, 53–82, 2014.
52. Sheldon, B.W., Curtin W.A., Nanoceramic composites: tough to test, *Nat. Mater.*, 3, 505–506, 2004.
53. He, C.N., Tian, F., Liu, S.J., A carbon nanotube/alumina network structure for fabricating alumina matrix composites, *J. Alloys Compd.*, 478, 816–819, 2009.

6

Oxidation-induced Crack Healing in MAX Phase Containing Ceramic Composites

Guoping Bei[1,2]* and Peter Greil[1]

[1]Ceramic and Glass Group (ww3), Department of Materials Science, Friedrich-Alexander University Erlangen-Nürnberg, Erlangen, Germany
[2]Department of Materials Science and Engineering, 3ME, Delft University of Technology, Delft, The Netherlands

Abstract

Crack healing in MAX phase-based ceramics is mainly attributed to the reaction of M and A metal with oxygen penetrating into the crack. The intrinsic healing mechanisms of Al-contained MAX phases are due to formation of adhesive Al_2O_3 phase in the crack gaps, while Sn-contained MAX phases are ascribed to formation of major TiO_2 and SnO_2 in the bigger crack gaps and metallic Sn formation in the smaller secondary cracks. The oxides as well as metallic phase filling the crack may restore the integrity of MAX phase ceramic components. The mechanical strength and the electrical conductivity of the MAX phase ceramics can be fully restored after the healing process. The remarkable healing abilities of those MAX phases make them promising repair fillers for those ceramics with poor healing ability. Al_2O_3 mixed with $Ti_2Al_{0.5}Sn_{0.5}C$ MAX phase was selected as a model to demonstrate the healing efficiency. The fracture strength of 20 vol.% repair filler composites containing artificial indent cracks recovered fully to the level of the virgin material upon isothermal annealing in air atmosphere after 48 h at 700 °C and 0.5 h at 900 °C. The evolution of the crack-filling microstructure was explored by X-ray powder diffraction and transmission electron microscopy analyses.

***Keywords*:** Crack healing, MAX phases, oxidation, solid solution, strength recovery

**Corresponding author*: g.bei@tudelft.nl

Ashutosh Tiwari, Rosario A. Gerhardt and Magdalena Szutkowska (eds.) Advanced Ceramic Materials, (231–260) © 2016 Scrivener Publishing LLC

6.1 History of Crack Healing in Ceramics

Advanced engineering and functional ceramics are sensitive to crack damage resulting from machining, overloading, creep fatigue, or friction. Once cracks are formed within a ceramic component, its integrity significantly compromised. Besides improving the toughness of ceramics, the concept of healing of structural defects (cracks and pores) is an emerging approach to improve the performance and reliability of ceramic components [1–3].

Engineering ceramics that are able to heal cracks (often denoted as self-repair or self-healing materials) are inspired by geological systems in which pressure solution and frictional healing triggers fault zone strengthening [4] as well as by biological systems in which damage triggers an autonomic healing response [5]. The history of research on crack healing in ceramics can be traced back to the 1960s [6] comprising single crystal systems [7], polycrystalline materials [8] as well as amorphous glasses [9, 10]. Most work was related to repair of surface cracks introduced by thermal shocking, indenting, impacting, cleaving, inscribing, or stressing of a precrack [11]. The main crack-healing mechanisms can be categorized into sintering and crack bonding by oxidation [3]. Crack healing in ceramics via sintering (e.g. UO_2 [12, 13], Al_2O_3 [14, 15], ZnO [16], MgO [17]) requires temperatures which exceed 0.7–0.9 times the melting temperature. The activation energy corresponds to values typical for surface and grain boundary dominated diffusion, while the rate of crack healing is equivalent to that of grain growth [12]. Compare to sintering, oxidation-induced crack healing [18–22] usually occurs at much lower healing temperatures.

Oxidation-induced crack healing in oxide ceramics can be realized by adding sacrificial particles that upon exposure to ambient air at high temperatures form an oxide product filling the crack gap. For example, in SiC-containing ceramics, SiO_2 is formed associated with a large volume expansion and combined with a low viscosity facilitates filling of the crack space [18–22]; see Figure 6.1. It has been demonstrated that ceramics with more than 10 vol.% SiC particles or whiskers exhibit efficient crack-healing ability giving rise to a pronounced strength recovery and reliability as well as reduction of manufacturing costs [23–25]. Oxidation in air as well as viscous flow was successfully demonstrated to trigger healing reaction in ceramic matrix [26] and in glass matrix [27] fiber composites even at relatively low temperatures of 500–600 °C. Very large surface cracks (>2 mm) prepared on alumina with a borosilicate glass could be healed at 1500 °C. The strength of the healed sample was even stronger than the mother material, which was attributed to thermal expansion mismatch-induced compressive surface stress [28]. In addition to healing temperature and

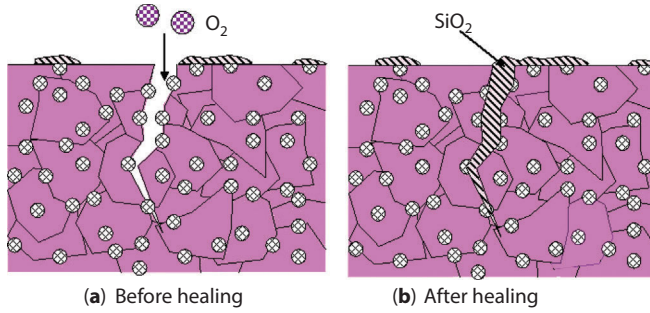

Figure 6.1 Schematic image of oxidation-induced crack-healing mechanism [3].

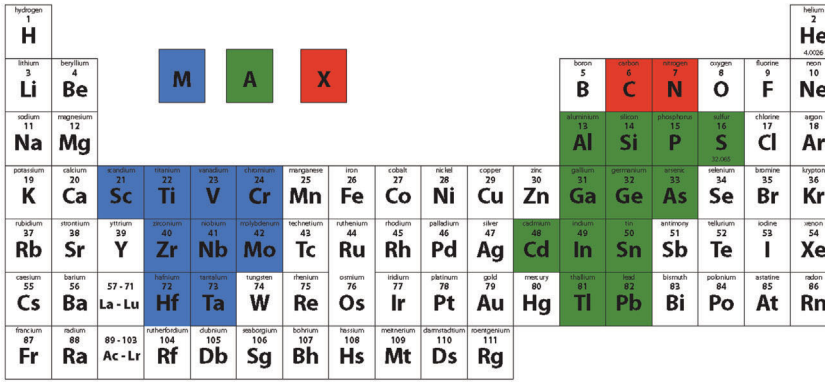

Figure 6.2 Location of the elements of $M_{n+1}AX_n$ in the periodic table [31].

time, critical thresholds for oxygen partial pressure [23] as well as constant and cyclic loading stress were reported to control the recovery of strength.

6.2 High-temperature Crack Healing in MAX Phases

6.2.1 MAX Phases

MAX phases form a group of nanolaminated ternary carbides and nitrides with the general formula $M_{n+1}AX_n$ ($n = 1–6$), where M denotes an early transition metal, A is an A-group element (from IIIA to VIA) and X is either C or N [29, 30]; cf. Figure 6.2. These ternary MAX phases are characterized by hexagonal symmetry ($P6_3/mmc$) with a unit cell composed of MX slabs separated by planar layers of the A element; see Figure 6.3. Since the M–A bonds are weaker than the M–X bonds, the MAX phases are able to combine both merits of metal and ceramic materials such as

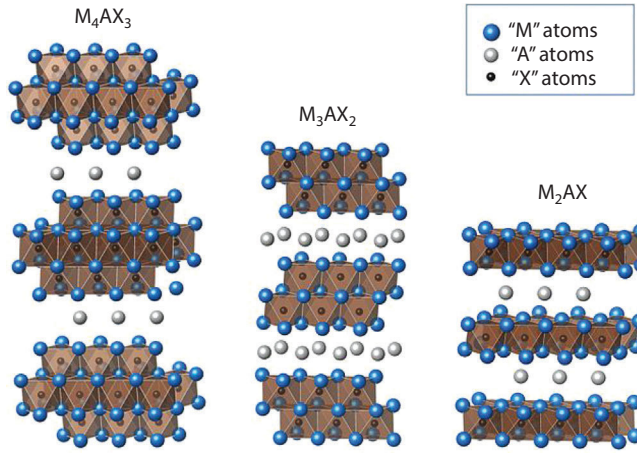

Figure 6.3 Unit cells of MAX phase (http://en.wikipedia.org/wiki/MXenes).

high thermal and electrical conductivities, excellent machinability, and oxidation resistance [29].

MAX phases containing Al such as Ti_3AlC_2, Ti_2AlC, and Cr_2AlC exhibit excellent oxidation resistance due to formation of an adhesive and protective Al_2O_3 scale on the surface [32–40]. The oxidation reaction is dominated by preferred oxidation of the Al [31]. The lower cohesive bonding energy E_B as well as migration energy E_M of the *A* element compared to that of the *M* element [41] is beneficial for the preferential oxidation of *A* element. The substitution of the *A* element Al by Sn, which exhibits a lower cohesive bonding energy and migration energy (i.e. for Ti_2SnC the values are E_B = 8.1 eV and E_m = 0.66 eV, whereas the values for Ti_2AlC are E_B=10.4 eV, E_m = 0.82 eV [41]), promotes oxidation at lower temperatures [1]. Hence, Al-containing MAX phase ceramics with low melting metals like Sn, In, or Pb that partially occupy the A position might be of great interest to trigger oxidation-induced crack-healing reaction at significantly lower temperatures [1].

6.2.2 Crack Healing in Al-contained MAX Phases

6.2.2.1 Ti_3AlC_2

Oxidation-induced crack healing in Ti_3AlC_2 was first reported in 2008 [42]. Ti_3AlC_2 containing an artificial crack with a length of 7 mm and an opening of 2–5 μm was annealed in air at 1100 °C for 2 h. The crack was completely filled with α-Al_2O_3 and a minor fraction of rutile (TiO_2). Due to the differences in Al and Ti bonding, Al was assumed to diffuse faster than Ti in the lamellar grains [43]. Al has higher affinity with oxygen than Ti and C because

the Gibbs free energy for the reaction of Al with oxygen to form Al_2O_3 is more negative than to form TiO_2 [32]. Moreover, Al diffuses faster than Ti in the lamellar grains due to the differences in Al and Ti bonding [43]. High-resolution transmission electron microscopy (HRTEM) demonstrated that no amorphous phase was formed at the Al_2O_3–Ti_3AlC_2 interface [34]. The orientation relationships at the interface were identified as $(0001)_{Al_2O_3}$–$(0001)_{Ti_3AlC_2}$ and $[1210]_{Al_2O_3}$–$[1120]_{Ti_3AlC_2}$ or $[11\,00]_{Al_2O_3}$–$[1120]_{Ti_3AlC_2}$, which means Al_2O_3 scale is likely to grow epitaxially. Furthermore, the small mismatch between the coefficient thermal expansion of Al_2O_3 [33] and Ti_3AlC_2 [44] will result small thermal stresses. The presence of TiO_2 in the oxidation layer, however, is supposed to trigger spallation failure in Ti_3AlC_2 and correspondingly causes loss of the strength recovery.

6.2.2.2 *Ti_2AlC*

In the Ti_2AlC MAX phase [45–47], the Al concentration is higher than in Ti_3AlC_2. After healing at 1200 °C for 2 h, the crack opening was almost fully filled with α-Al_2O_3 and very less rutile-TiO_2 phase; see Figure 6.4.

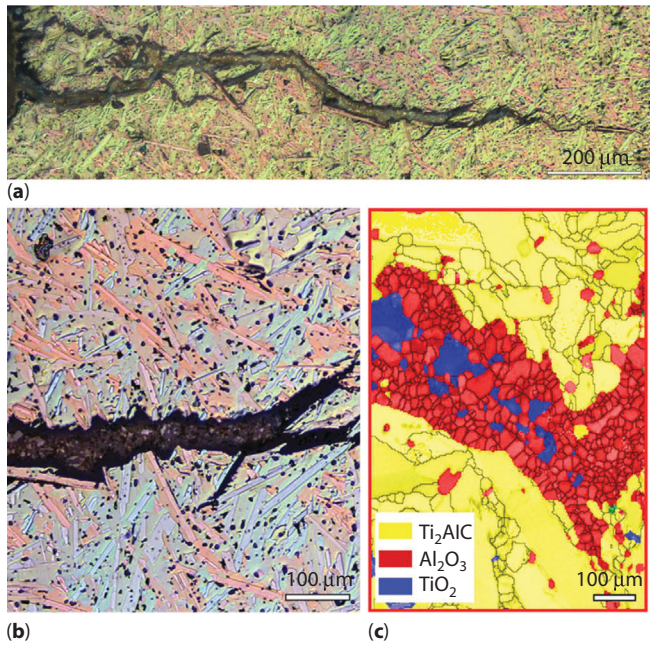

Figure 6.4 Low- and high-magnification images showing the completely filled crack in the Ti_2AlC sample after eigth fracture and then annealing at 1200 °C for 100 h. (a) Optical overview image of the healed crack. (b) An enlarged optical image taken from (a). (c) Detailed micrograph of the healed-damage zone obtained with scanning electron microscopy using EBSD [46].

More attractively, the Ti_2AlC ceramic is capable of repeatedly repairing damage events [46]. Three-point bending tests were applied on the virgin, pre-damaged, and healed samples [46], see Figure 6.5a. After healing at 1200 °C for 2 h in air, the indents were completely filled by oxide reaction products and the microcracks disappeared completely; see Figure 6.5b. The fracture path of the healed Ti_2AlC samples did not coincide with the induced indent fracture path but was found to have propagated always some distance away from it; see Figure 6.5b. This observation suggests that the healed zone is stronger than the original material. The flexural strength of the healed material recovered or even slightly exceeded the initial strength; see Figure 6.5c.

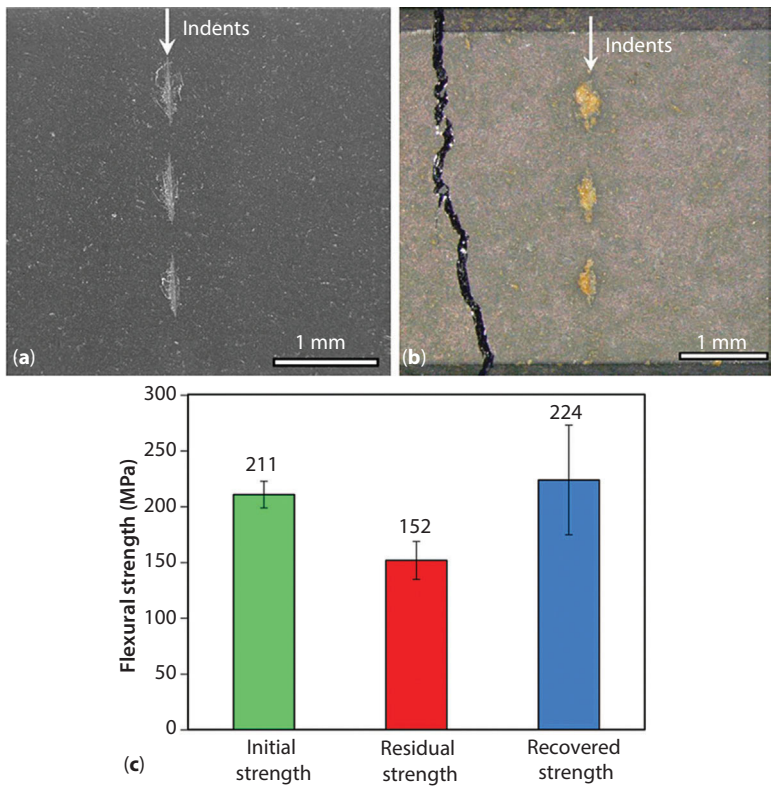

Figure 6.5 Strength recovery of Ti_2AlC specimens after crack healing at 1200 °C for 2 h in air. (a) Optical image of the 3 Knoop indents at the center of long sample to create crack damage. (b) Optical image of the healed sample after flexural strength testing. (c) Flexural strength of the virginal Ti_2AlC, after creating crack damage and after crack healing, respectively [46].

In many practical applications, a single healing event of a crack will not be sufficient. During service, crack damage of a component can happen multiple times, even at the same location. The multiple re-cracking–healing process was successfully demonstrated for Ti_2AlC ceramics [46] (Figure 6.6). First, artificial cracks with a length longer than 1 mm were

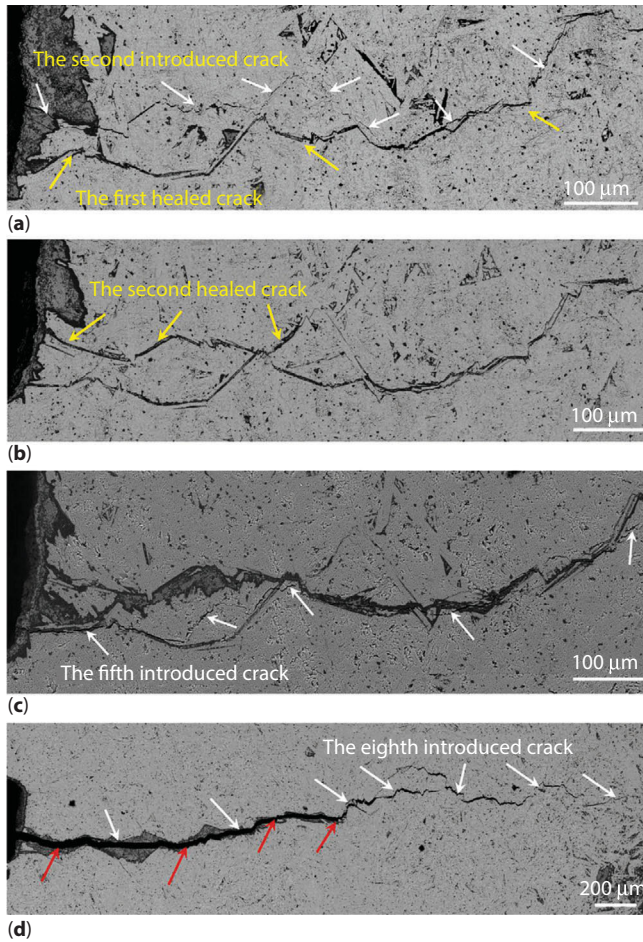

Figure 6.6 Black-scattered scanning electron micrographs of fracture and crack healing of Ti_2AlC samples. (a) Crack path after one cycle of healing and subsequent fracture. The yellow arrows indicate the crack completely filled, and the white arrows indicate the new introduced crack. Note that the subsequent crack almost deflects around the healed zone of the first crack. (b) After two cycles of healing, the second crack was completely filled again. (c) Crack path after four cycles of healing, and subsequent fracture. (d) Crack path after seven cycles of healing, and subsequent fracture. The red arrows indicate the location of remnant crack parts [46].

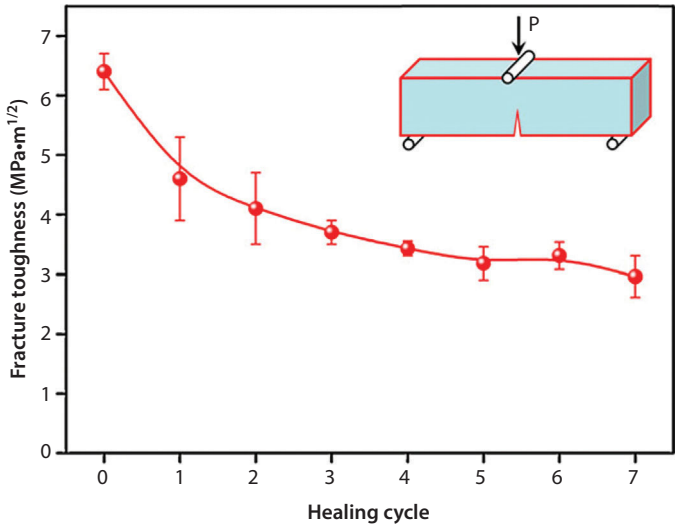

Figure 6.7 Fracture toughness of Ti_2AlC as a function of the number of fracture and healing cycles [46].

completely healed after annealing in air at 1200 °C for 2 h; see Figure 6.6a. Up to the fourth fracture and healing cycle, the reproduced crack was still fully filled but became wider upon repeatable crack healing; see Figure 6.6b–d. After the sixth cycle of healing, however, the newly produced crack in the region close to the notch could not be fully healed and remained open; see Figure 6.6d. Figure 6.7 shows the change of fracture toughness recovery of the Ti_2AlC composite as a function of the number of healing cycles. The fracture toughness (K_{IC}) decreased from 6.4 MPa $m^{1/2}$ of the virginal Ti_2AlC to about 3 MPa $m^{1/2}$ after 7 healing cycles. The drop in fracture toughness is the result of the lower fracture toughness of the reaction products (K_{IC}: Al_2O_3 = 3–4 MPa $m^{1/2}$ [48], TiO_2 = 2–4 MPa $m^{1/2}$ [49]; Al_2O_3/TiO_2 composite = 4–5 MPa $m^{1/2}$) [50].

6.2.2.3 Cr_2AlC

Cr_2AlC MAX phase demonstrated excellent crack-healing ability [40]. The crack-healing mechanism of Cr_2AlC is similar to that of Ti_3AlC_2 and Ti_2AlC MAX phases, respectively. After the healing treatment, the crack opening was filled with Al_2O_3 as well as with minor fractions of $(Cr, Al)_2O_3$ solid solution; see Figure 6.8. Compared to Ti_2AlC, the oxidation kinetics of Cr_2AlC were found to be much slower when the temperature was below 1200 °C; see Figure 6.9.

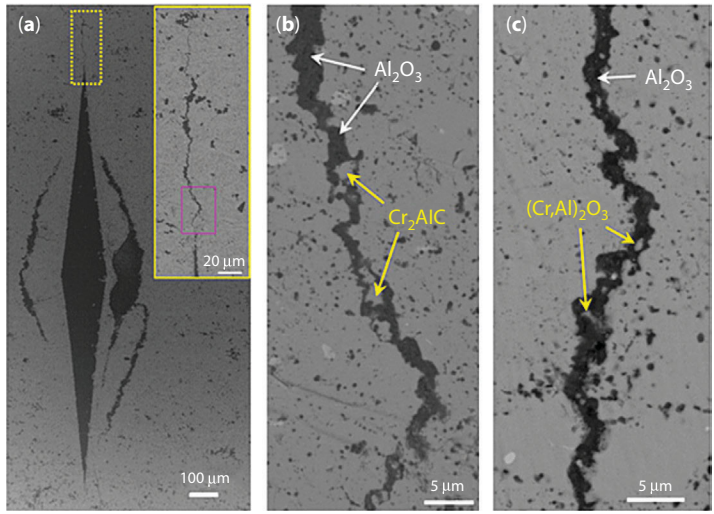

Figure 6.8 Back-scattered electron images of the polished Cr_2AlC samples after healing at 1100 °C for (a–b) 4 h and (c) 100 h. (a) Low-magnification image of the healed zones around indentation on the polished surface. The inset is an enlarged image taken from the marked area in (a). (b) An enlarged image taken from the marked area in the inset in (a). (c) An enlarged image showing a 100 h healed crack [40].

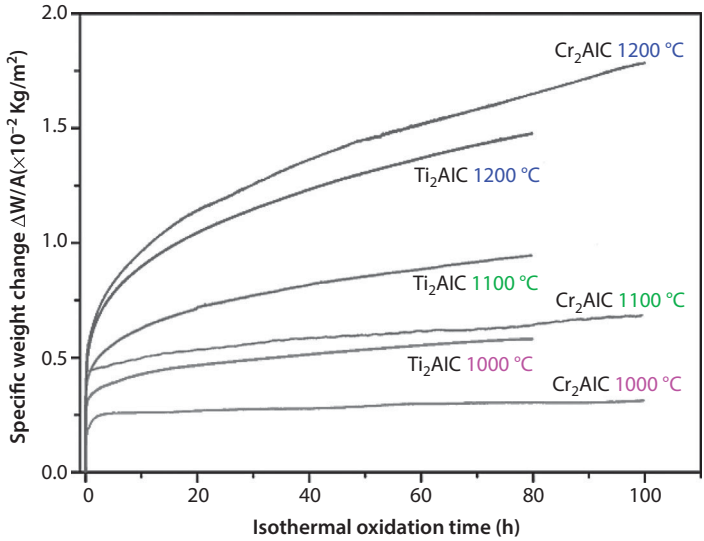

Figure 6.9 Oxidation behavior of Ti_2AlC and Cr_2AlC ceramic at 900–1200 °C in synthetic air [40].

The strength recovery of Cr_2AlC depends not only on the healing temperature and time but on the crack size as well; see Figure 6.10. When the crack length was smaller than 0.5 mm, the strength could be fully restored or even higher than the virgin strength after healing at 1100 °C for 4 h; see Figure 6.10a. However, if the crack was longer than 0.5 mm, the strength could not be recovered even prolonged healing time up to 100 h at 1100 °C;

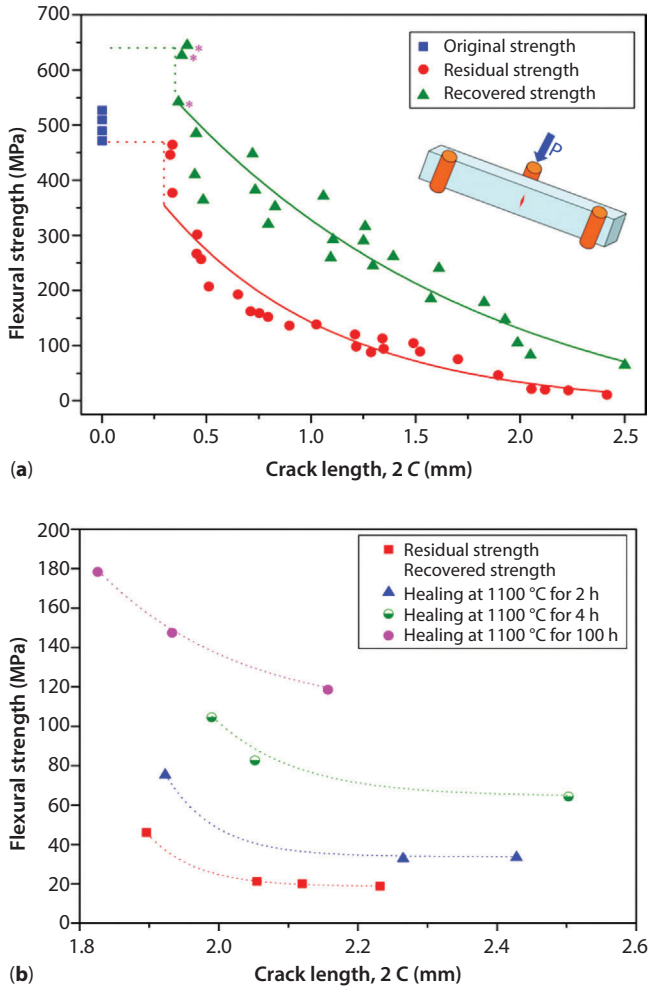

Figure 6.10 Strength recovery of Cr_2AlC after healing at 1100 °C for 4 h in air, (a) residual flexural strength and recovered flexural strength as a function of crack length. Data marked with asterisks mean that samples fractured outside the crack-healed zones. (b) Recovered flexural strength as a function of crack length and for different healing time [40].

see Figure 6.10b. This may be due to the residual pores, which were attributed to the evaporation of Cr_2O_3.

In summary, Al containing MAX phases exhibit excellent crack-healing ability at elevated temperatures. The recovery of strength was attributed to the formation of adhesive Al_2O_3 filling of the crack gap.

6.3 Lower-temperature Crack Healing in MAX Phase-based Ceramics

Although some MAX phase ceramics can heal millimeter-size cracks in a short period of time, yet oxidation-induced crack healing still requires elevated temperatures exceeding 1000 °C. Since a low cohesion as well as migration energy of the A element [41] may favor mobilization and oxidation reaction Ti_2AC with the element on the A site being a metal element of low melting temperature (A = Ga, Cd, Sn, In, and Pb) might be of interest in order to lower the healing temperature of MAX phases.

6.3.1 Oxidation Behavior of $Ti_2Al_{(1-x)}Sn_xC$ MAX Phase Solid-solution Powders

Substituting Al by Sn on the A sites causes the 211 type MAX phase $Ti_2Al_{(1-x)}Sn_xC$ solid-solution lattice (space group $P6_3/mmc$) to expand along the *a* axis ($a = 3.06$ Å for $x = 0$ to $a = 3.16$ Å for $x = 1$), whereas *c* remains almost constant (13.68 Å) [51]. A linear reduction of *c/a* ratio with increasing *x* is consistent with the formation of an ideal solid solution following Vegard's law [52]; see Figure 6.11a. The unit cell of Ti_2AC can be considered being constituted of edge-shared $[Ti_6C]$ octahedrons forming the slabs and $[Ti_6A]$ trigonal prisms are forming the A-element layers [29]. Figure 6.11b shows the variation of the mean Ti–A and Ti–C atomic distances with increasing *x*, where a monotonically increase of the Ti–A distance with higher substitution degree of Al by Sn with modest changes in Ti–C bonding length can be observed [51].

Ab initio calculations of the Al–Sn substitution predict a reduction of the cohesive energy of 21.7%, which is supposed to contribute to a reduction of the thermal stability as well as to enhanced disintegration of the Sn content in MAX phases at lower temperatures when compared to the Al [41]. Furthermore, calculated vacancy formation energy on A-element site as well as migration energy in the case of defect-controlled diffusion of A element along basal (0001) planes shows a preferential migration and vacancy formation in Ti_2SnC. Overall $Ti_2Al_{(1-x)}Sn_xC$ MAX phase solid

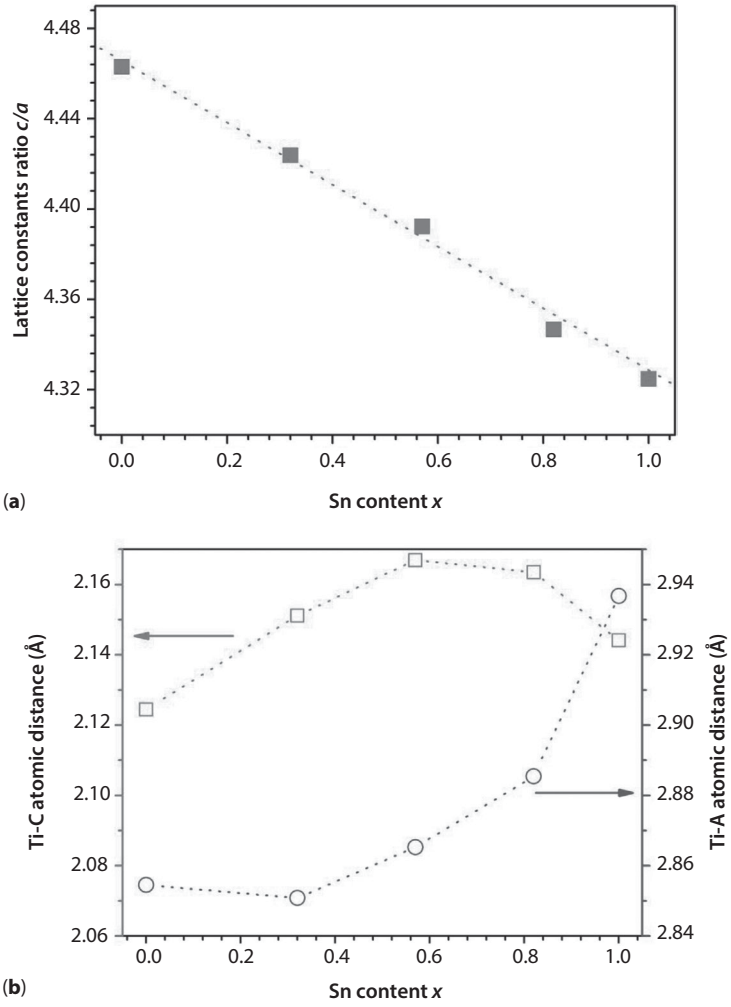

Figure 6.11 (a) Lattice parameters ratio c_0/a_0 and (b) mean Ti–A and Ti–C atomic distances as a function of Sn content in $Ti_2Al_{(1-x)}Sn_xC$ solid solution [51].

solution may be favorable to promote crack healing at lower temperatures due to the weakened bonds of Sn on the A sites.

The oxidation behavior of $Ti_2Al_{(1-x)}Sn_xC$ solid-solution powder was investigated by differential thermal analysis (DTA) [51]; see Figure 6.12a. The three exothermic peaks at approximately 600, 820, and 900 °C (Ti_2AlC) are supposed to be controlled by selective oxidation and phase transformation reactions due to crystalline TiO_2 formation above 600 °C. Both anatase (space group $I4_1/amd$) and rutile (space group $P4_2/mmm$) were detected to

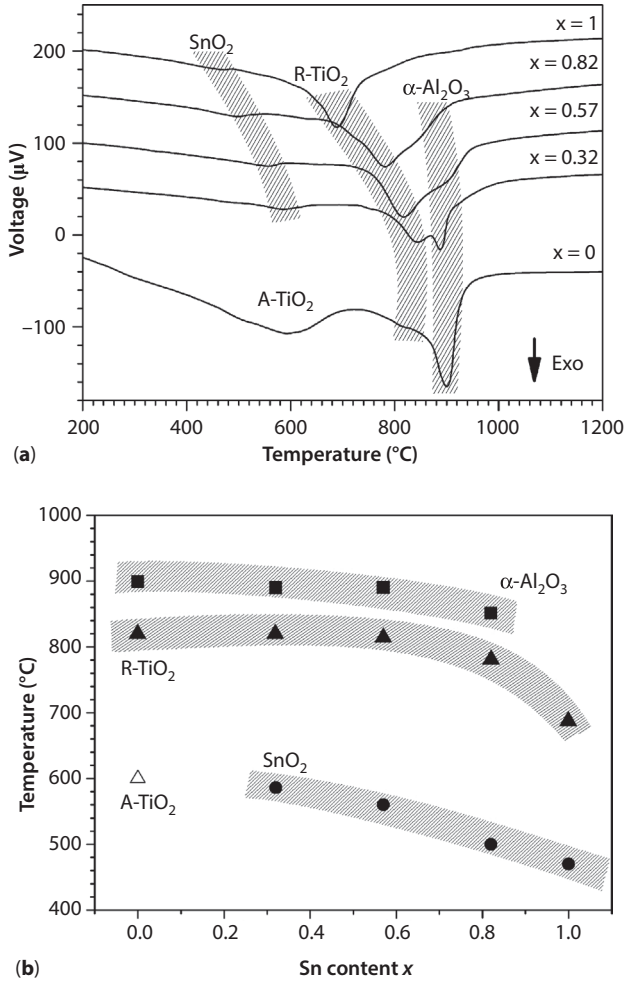

Figure 6.12 (a) DTA spectra of $Ti_2Al_{(1-x)}Sn_xC$ solid-solution powder heated in air atmosphere with a constant heating rate of 5 °C/min. (b) Characteristic temperatures of oxide reaction product formation derived from DTA, TG, and XRD measurements [51].

coexist below 820 °C. Hence, the exothermic reaction at this point triggers a complete transformation of anatase to rutile. Beyond 900 °C, crystalline a-Al_2O_3 formation can be detected. The temperatures of oxidation reaction for TiO_2 formation as well as the transformation from anatase to rutile investigated on the Ti_2AlC powder specimen are in good agreement with reported values for bulk Ti_2AlC [35]. Substituting Al with Sn in $Ti_2Al_{(1-x)}Sn_xC$ triggers a pronounced shift of the initial oxidation at 600 °C to lower

temperatures. From X-ray powder diffraction (XRD) analyses the formation of rutile instead of anatase as well as tetragonal SnO_2 (cassiterite, space group $P4_2/mnm$) was indicated. Figure 6.12b summarizes the reaction temperatures of Ti and Al elements (Al and Sn) derived from DTA. As a result of the Sn content increase in the solid solution, the initial formation of SnO_2 observed at high Sn contents ($x > 0.5$) reaches a minimum reaction temperature of 460 °C for $x = 1$, e.g. Ti_2SnC.

6.3.2 Oxidation-induced Crack Healing in Thermal-shocked Ti_2SnC MAX Phase

Artificial crack patterns were generated in Ti_2SnC by thermal shock quenching at 525–725 °C [53]. The damaged Ti_2SnC was annealed in air at 700 and 800 °C for 1 h. Each quench followed by heat treatment is referred to as one cycle of healing. Multiple healing involved up to four cycles of quenching followed by subsequent healing applying the same temperature, time, and atmosphere conditions.

After quenching–healing cycling, the composition of crack-filling phases was found to depend strongly on the crack opening and oxygen partial pressure. In the wider cracks or cracks near the sample surface, the cracks were mainly filled with a mixture of TiO_2 or SnO_2 as identified by X-ray microanalysis due to the higher oxygen partial pressure. TiO_2 covered the crack opposite faces, whereas SnO_2 distributed preferentially in the center of the crack gap; see Figure 6.13a. At low oxygen potential far from the surface or in secondary cracks with small crack opening, elemental Sn was detected; see Figure 6.13b and c. After the first quenching–healing cycling, all cracks were almost healed. However, increasing the number quenching–healing cycles up to four, some bigger cracks were not be able to be healed anymore.

The crack-healing reactions are strongly depending on the oxidation behavior of Ti_2SnC [51, 54, 55]. At temperatures below 800 °C, destabilization of the MAX phase crystal lattice tends to release Sn leaving a distorted $Ti_2Sn_{1-x}C$ phase. At higher temperatures, TiO_2 formation seems to dominate due to the lower-standard Gibbs free energy of TiO_2 formation (ΔG_f(800 °C) = −750 kJ/mol) compared to that of SnO_2 (ΔG_f(800 °C) = −358 kJ/mol). If the oxygen potential is high enough ($p_{O_2} > 10^{-16}$ Pa at 1000 °C [56]), SnO_2 may be formed as observed in large cracks at least near to the surface. In contrast, the secondary cracks with small crack opening, or the cracks located at the interior of the sample with low oxygen potential; however, elemental Sn may be left. The high mobility of Sn in Ti_2SnC as a consequence of its low migration energy of

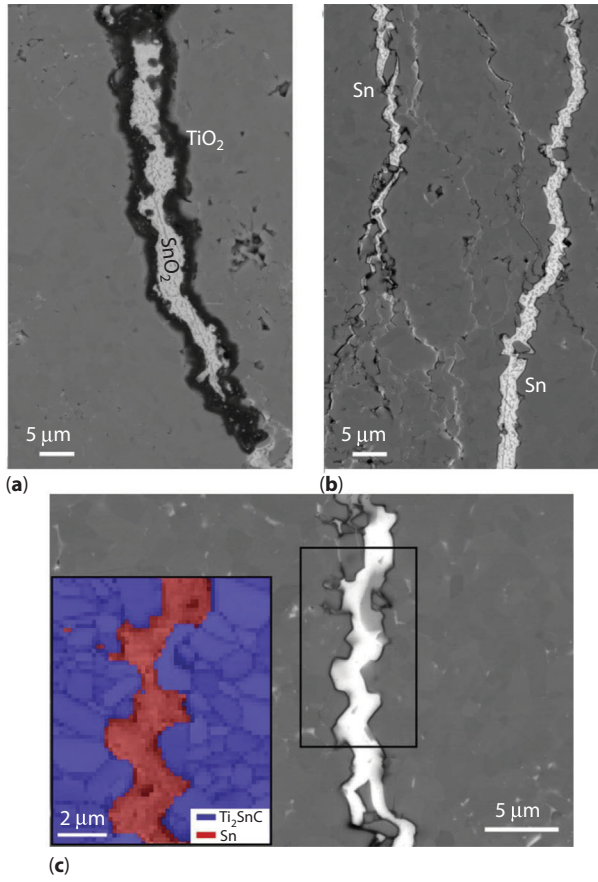

Figure 6.13 Cross-sectional BSE-SEM images of healed zones after 4 cycles of healing at 800 °C. (a) Larger crack opening filled by the mixture of TiO_2 and SnO_2, (b) thinner cracks filled with Sn, and (c) EBSD micrograph of metallic Sn distribution in a small crack area [53].

0.66 eV [41] as well as fluid flow transport above its low melting point of 232 °C seems to favor transport of Sn even into small cracks and micro-cracks with narrow crack opening; see Figure 6.14. Since MAX phases combine the merits of the metal and ceramic properties, they can be used not only as structural ceramics but also as functional ceramics. Hence, in addition to the mechanical strength recovery, it is interesting to investigate the recovery of electrical conductivity after the healing process. One cycle of quenching at different temperatures results in a decrease in the residual flexural strength and electrical conductivity; see Figure 6.15. For example, after quenching at 700 °C, the residual flexural strength decreased from

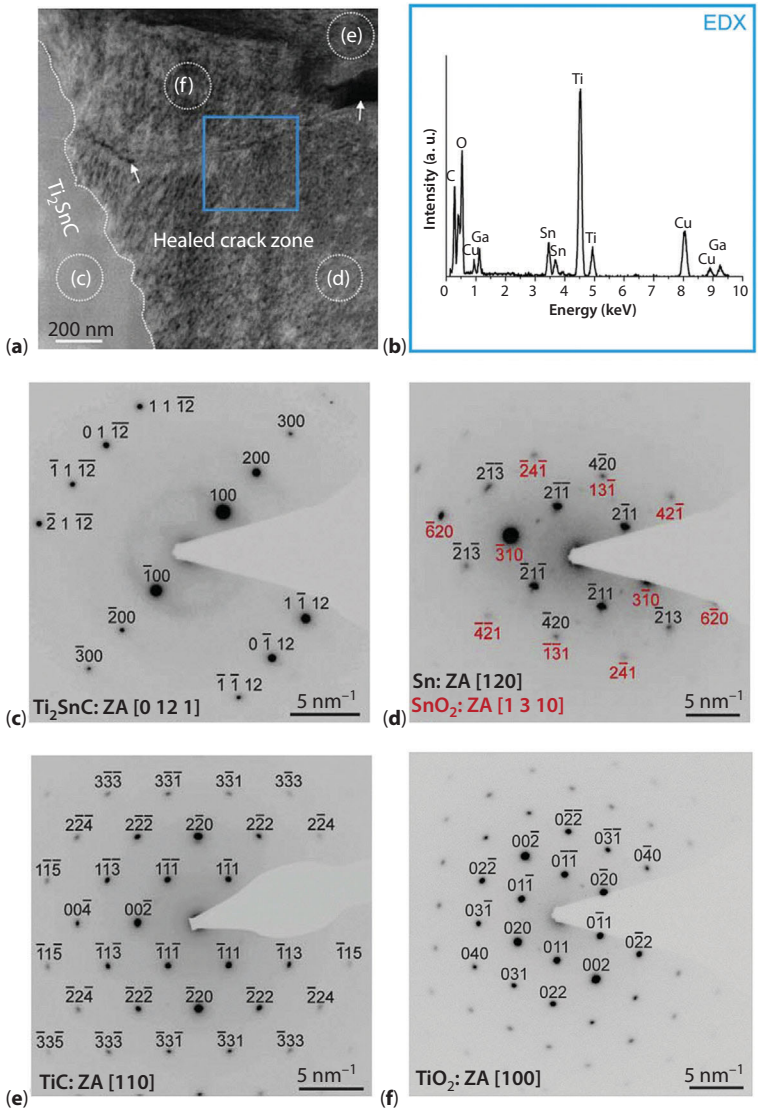

Figure 6.14 TEM analysis of the healed $T_{i2}SnC$ sample. (a) Representative HAADF-STEM image showing the healed zone in a major crack. The dotted line in (a) indicates the boundary between the Ti_2SnC and the healed crack zone; (b) is an EDX spectrum of the area marked with the blue square in (a). (c–f) are SAED patterns of the regions marked with the dotted circles and letters (c–f) in (a). (c) The [0 1 2 1] ZA of hexagonal Ti_2SnC, (d) the [1 2 0] ZA of tetragonal Sn and the [1 3 1 0] ZA of tetragonal SnO_2, (e) the [0 0 1] ZA of cubic TiC, and (f) the [1 0 0] of tetragonal TiO_2 [53].

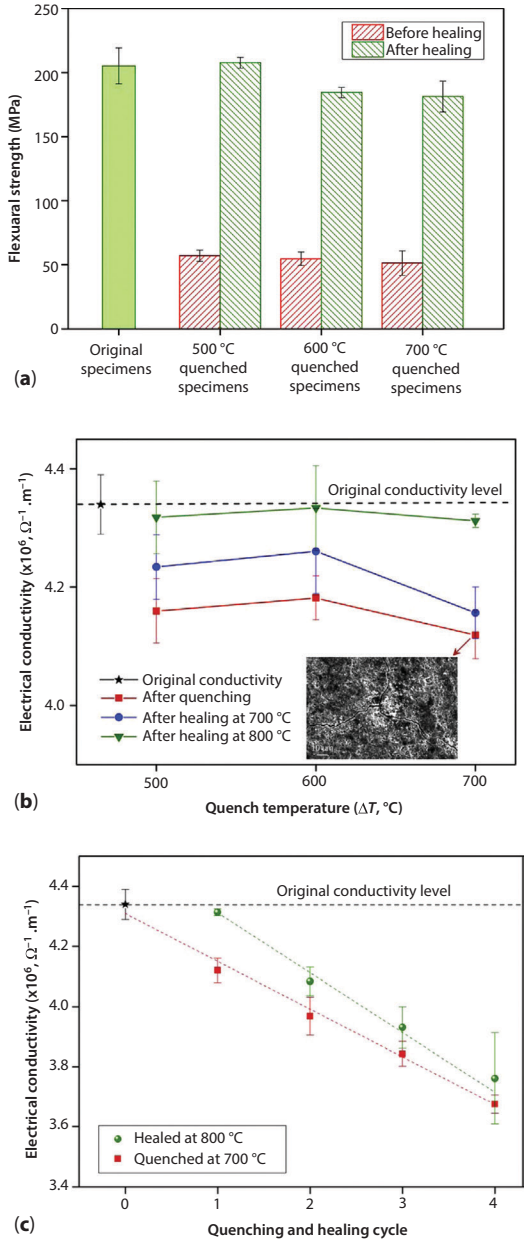

Figure 6.15 Strength recovery and electrical conductivity recovery after healing process. (a) Flexural strengths of quenched samples before and after healing at 800 °C for 1 h. (b) Recovered electrical conductivity as a function of quenching and healing temperature. (c) Electrical conductivity as a function of quenching and healing cycle. In each cycle, samples were quenched at 700 °C in water and then healed at 800 °C for 1 h in air [53].

205 MPa to about 50 MPa; see Figure 6.15a. Also, the electrical conductivity decreased from 4.36×10^6 to $4.04\times10^6\,\Omega^{-1}m^{-1}$; see Figure 6.15b. Thus, a loss occurred of 76% in flexural strength and 7% in electrical conductivity. After healing at 800 °C for 1 h in air, both the flexural strength and the electrical conductivity recovered. The electrical conductivity also recovers after multiple healing cycles; see Figure 6.15c. The recovered electrical conductivity after one quenching and healing cycle attains a value close to the original value of $4.34 \times 10^6\,\Omega^{-1}m^{-1}$. However, with an increasing number of quenching and healing cycles both the values for the damaged and the recovered Ti_2SnC materials are reduced and the healing effect becomes less pronounced.

The thermal expansion coefficients of TiO_2 (7×10^{-6}/K along *a*-axis direction and 9.4×10^{-6}/K along *c*-axis direction) [57] were smaller than of Ti_2SnC (10×10^{-6}/K) [59]. The mismatch of thermal expansion between the matrix and the crack-filling phase may cause generation of compressive stresses in the vicinity of a healed crack, which is expected to increase the resistance against crack growth and hence promotes an effective strength recovery. The release of liquid metallic Sn (coefficient of thermal expansion 22×10^{-6}/K [60]) should result in the formation of tensile matrix stresses, which however, may be relaxed by melt flow. Since healing of large cracks will dominate the strength recovery, no detrimental effect on the mechanical properties is assumed by the presence of Sn in small secondary cracks. However, the presence of metallic Sn in the healed cracks should play a key role in recovery of the electrical conductivity. Both SnO_2 and rutile-TiO_2 are semiconductors with electrical conductivities of $1.82 \times 10^{-6}\,\Omega^{-1}m^{-1}$ [61] and $10^{-8}\,\Omega^{-1}m^{-1}$[62], respectively, which is much lower than $4.34 \times 10^6\,\Omega^{-1}m^{-1}$ of Ti_2SnC. Hence, a crack filled with TiO_2 and SnO_2 may act as a barrier for electron transport in Ti_2SnC giving rise to limited recovery of the conductivity upon healing. Due to the high electrical conductivity of Sn metal, the healed crack exhibits a low resistance to electron transport explaining the recovery of the electrical conductivity after healing in air.

In summary, Ti_2SnC ceramic exhibits excellent crack-healing capability at a lower temperature of 800 °C. The microstructure evolution of the healed crack is dependent on the crack opening and the oxygen partial pressure. In large cracks near the surface, a high oxygen potential triggers the formation of TiO_2 and SnO_2 filling the crack space. Limitation of oxygen transport in small secondary cracks gives rise to a low oxygen potential and metallic Sn remains. Both flexural strength and electrical conductivity could be recovered almost to the values of the virgin material after healing in air at 800 °C for 1 h.

6.3.3 Crack Healing in $Ti_2Al_{0.5}Sn_{0.5}C$–Al_2O_3 Composites

Crack healing in monolithic Al_2O_3 is a diffusive crack-healing process, and crack closure is attributed to grain growth and sintering as the dominating mechanisms [3]. The healing temperature is almost equal the sintering temperature (above 1400 °C) to attain remarkable strength recovery [15]. Accelerated healing ability is observed in Al_2O_3 ceramics mixed with SiC repair fillers, which trigger oxidation crack healing at temperatures below 1400 °C [63, 64]. However, to obtain a good healing efficiency, a high temperature above 1200 °C and a volume fraction of 15–20% repair filler is required [63]. Hence, it is attractive to use $Ti_2Al_{(1-x)}Sn_xC$ as repair filler for Al_2O_3 matrix since then oxidation-induced crack healing is already triggered at temperatures below 1000 °C. Al_2O_3 mixed with 5–20 vol.% $Ti_2Al_{0.5}Sn_{0.5}C$ powder was prepared by pressure-less sintering [65]. Artificial cracks of 280–320 μm in length and 0.4 μm in width were created by indentation; see Figure 6.16a and b. The specimens were annealed in air at 700, 900, and 1100 °C with a maximum healing period up to 96 h. Cracks were fully healed in Al_2O_3 composites loaded with 10 vol.% $Ti_2Al_{0.5}Sn_{0.5}C$ after annealing at 900 °C for 3 h; see Figure 6.16c and d. The crack gap was filled mainly by TiO_2 and some SnO_2 as confirmed by X-ray diffraction and X-ray microanalysis. A gradient in the phase composition was observed in the crack gap; see Figure 6.16e. TiO_2 (rutile) was identified as the major crystalline reaction product filling the crack gap. Near the surface SnO_2 (cassiterite) was observed; however, at large distance from the surface, metallic Sn was detected; see Figure 6.16e.

The crack filling in the $Ti_2Al_{0.5}Sn_{0.5}C$–Al_2O_3 composites was controlled by oxidation of $Ti_2Al_{0.5}Sn_{0.5}C$ giving rise for a volume increase due to the reaction of oxygen and outward diffused cations of Ti^{4+}, Al^{3+}, and Sn^{4+}. Although the migration energy along the (0001) basal plane in the MAX crystal structure of Sn (63 kJ/mol) is even lower than that of Al (80 kJ/mol) [41], the Gibbs energy of formation of SnO_2 (–372.6 kJ/mol at 700 °C) is much less negative compared to that of TiO_2 (–767.4 kJ/mol) and Al_2O_3 (–913.6 kJ/mol), which suggests that the initial oxidation reaction will be governed by oxidation of Al and Ti [66] leaving deintercalated metallic Sn at least at low oxygen concentration. SnO_2 may be formed only near the surface when the local oxygen partial pressure exceeds a critical threshold (i.e. $pO_2 > 10^{-16}$ Pa at 1000 °C) [56].

The degree of the strength recovery, $\sigma_{heal}/\sigma_{virgin}$, is defined as the ratio of the flexural strength measured on the virgin composites and after thermal healing treatment. If no healing occurred, e.g. at room temperature, σ_{heal} is equivalent to the strength of the indented specimens σ_{indent}. For the

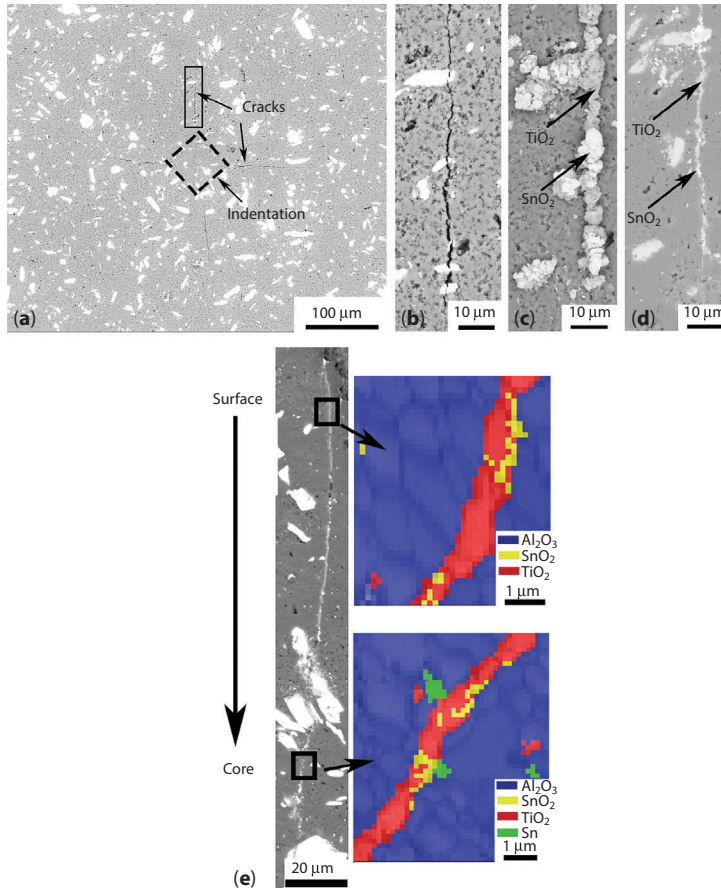

Figure 6.16 The morphologies of cracks generated on Al_2O_3 composite mixed with 10 vol.% $Ti_2Al_{0.5}Sn_{0.5}C$ repair filler before and after healing. (a) Cracks generation by Vickers' indentation with a load of 100 N, (b) enlarged SEM image of cracks in the black rectangle in (a), and (c) a crack healed at 900 °C for 3 h. (d) a polished surface of (c), (e) EBSD analysis of crack filling near to the surface and at large distance from the surface [65].

case of full recovery of strength, $\sigma_{heal}/\sigma_{virgin} \rightarrow 1$. Higher values than 1 indicate a healed strength of the Al_2O_3 composite even higher than the virgin strength due to healing of initial manufacturing defects.

The flexural strength of the virgin samples (σ_{virgin} = 393 ± 28 MPa) of the repair filler free alumina was reduced to 282 ± 27 MPa of the composite, which correlates with the reduction of fractional sintered density; see Figure 6.17. After crack formation by indentation, the strength of the composites (σ_{indent}) fell to about 45% of the virgin strength with flexural strength ranging from 150–160 MPa. Upon thermal treatment at temperatures

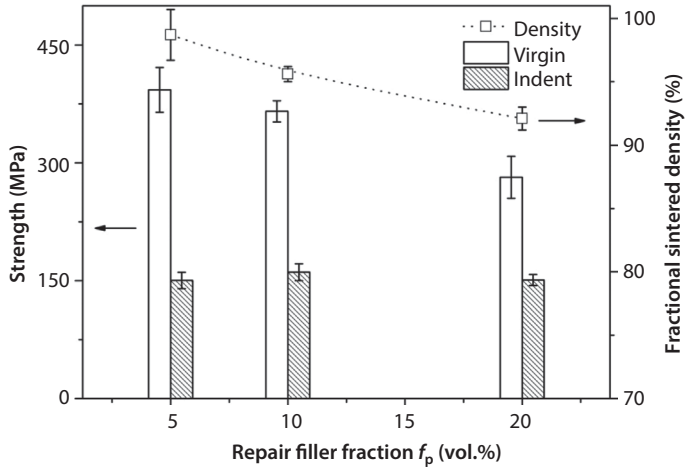

Figure 6.17 The virgin strength, residual strength, and sintered density of $Ti_2Al_{0.5}Sn_{0.5}C$–Al_2O_3 composite as a function of repair filler content [65].

above 700 °C in air, a pronounced recovery of strength compared to the values of the indented specimens was observed, see Figure 6.18. While Al_2O_3 composite mixed with the lowest repair filler fraction ϕ_{MAX} of 5 vol.% could not attain full-strength recovery at 700 °C even after a long healing period of 96 h and specimens mixed with 20 vol.% almost recovered after 48 h. At 1100 °C, accelerated healing gave rise for full recovery after 1 h (ϕ_{MAX} = 5 vol.%) and 0.02 h (ϕ_{MAX} = 20 vol.%), respectively.

The time dependence of the recovery of fractional strength ($\sigma_{heal}(t)/\sigma_{virgin}$) of brittle ceramic composites may be related to an effective crack size regression $x(t)$ which describes reduction of the crack size during healing treatment, hence:

$$\left(\frac{\sigma_{heal}(t)}{\sigma_{virgin}}\right)^2 = \frac{c_{virgin}}{c_{heal}(t)} = \frac{c_{virgin}}{c_{indent} - x(t)} \tag{6.1}$$

c_{virgin} and c_{indent} denote the crack sizes prior and after indentation, respectively. The crack size after healing treatment $c_{heal}(t)$ corresponds to the difference between the indentation crack length c_{indent} minus the growth length of effective healing zone $x(t)$. The time dependent crack size regression $x(t)$ for the case of oxidation-induced crack healing was studied for a number of ceramic material systems including MAX phases ceramics as well as metal particle-dispersed ceramic matrix composites, which reported on cubic, quadratic, and linear dependence of regression length x on t [1]. For the case that the oxidation-induced crack size regression is governed by

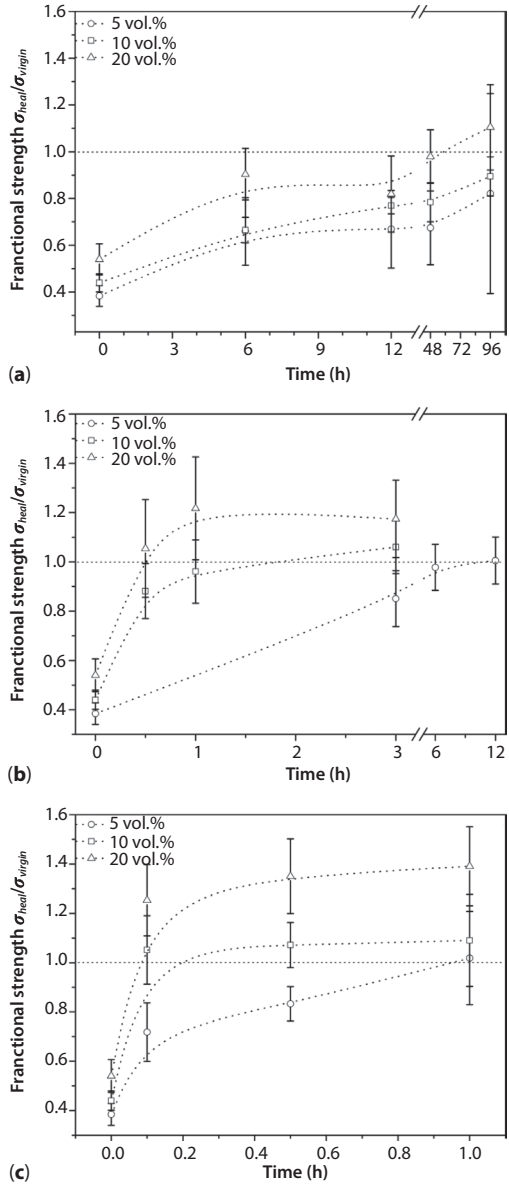

Figure 6.18 Strength recovery ($\sigma_{heal}/\sigma_{virgin}$) as function of the repair filler content and annealing time at (a) 700 °C, (b) 900 °C, and (c) 1100 °C, respectively [65].

oxygen transport from the surface with oxygen partial pressure p_0 to the reaction site at the MAX phase particle interface with reduced local oxygen partial pressure p_{if}, the relation derived for oxidation-induced healing [23] can be extended to express $x(t)$ as a function of temperature T, oxygen partial pressure p_i and MAX filler volume fraction ϕ_{MAX}, thus:

$$x(t) = \left[D_O^{eff} \exp\left(-\frac{E_a}{RT} \right) \ln\left(\frac{p_{if}}{p_0} \right)^q \phi_{MAX}^m t \right]^n \tag{6.2}$$

D_0^{eff} denotes the effective diffusivity for surface, grain boundary, or vapor diffusion, respectively; R is the gas constant; and E_a is the activation energy of the relevant transportation mechanism. For the case of equal indent crack length (and hence similar ratio of the oxygen partial pressures at the crack interface and at the surface p_{if}/p_0), regression analyses of the logarithmic plot of the experimental strength recovery data

$$\log\left[\left(\frac{\sigma_{virgin}}{\sigma_{indent}} \right)^2 - \left(\frac{\sigma_{virgin}}{\sigma_{heal}} \right)^2 \right] \propto -\frac{nE_a}{RT} + mn \log \phi_{MAX} + n \log t \tag{6.3}$$

yield values of n, m, and E_a as listed in Table 6.1. Mean n values at temperatures below 900 °C are close to 0.5, whereas at 1100 °C it is about

Table 6.1 Crack-healing kinetic parameters of $Ti_2Al_{0.5}Sn_{0.5}C$–Al_2O_3 composites [65].

Temperature (°C)		700			900			1100	
Filler loading	0.05	0.1	0.2	0.05	0.1	0.2	0.05	0.1	0.2
N	0.31	0.45	0.49	0.44	0.34	0.46	0.61	0.64	0.68
Temperature (°C)		700			900			1100	
Healing time (h)	6	48	96	0.5	1	3	0.1	0.5	1
M	2.54	2.59	2.63	2.45	2.47	2.45	1.60	1.60	1.60
Healing time (h)		1			6				
Filler loading	0.05	0.1	0.2	0.05	0.1	0.2			
E_a (kJ/mol)	30.3	21.8	24.0	12.6	12.0	13.0			

0.65 which are in the same range as reported for the oxidation kinetics of Ti_2AlC ($n \approx 1/3$) [47], the oxidation of metallic particles dispersed in Al_2O_3 matrix composites ($n \approx 1/2$) [67], and the high- temperature oxidation of ZrO_2 composites dispersed with Ni particles ($n \approx 1$) [68]. Filler loading volume fraction f_{MAX} is supposed to have a strong impact on the healing kinetics as indicated by values of m ranging from 2.5 (700 and 900 °C) and 1.6 (1100 °C). Compared to the activation energies reported for the oxidation of MAX phase ceramics (Cr_2AlC $E_a \approx 300$ kJ/mol [39], $Ti_3(Al,Si)C_2$ $E_a \approx 151.7$ kJ/mol [69]) and oxidation-induced crack healing of a variety of ceramics and ceramic composites (Si_3N_4 $E_a \approx 130–150$ kJ/mol [22], and SiC repair filler-loaded Si_3N_4 $E_a \approx 280$ kJ/mol, Al_2O_3 $E_a \approx 330$ J/mol, $Al_6Si_2O_{13}$ $E_a \approx 410$ kJ/mol, respectively [70]) the values of apparent E_a derived from our experimental data are an order of magnitude smaller. While crack-healing kinetics of A-element Al- and Si-containing MAX phases is governed by the formation of Al_2O_3- and SiO_2-based oxidation reaction products characterized by apparent activation energies of 151.7 kJ/mol[69], significant lower E_a of 180 and 86 kJ/mol were reported on the decomposition of sintered Ti_3SiC_2, and Ti_2AlC [71], respectively. Even lower activation energy (−72 kJ/mol) of Ti_3AlC_2 was attributed to the release of lower-order Ti_2AlC and TiC from the crystal structure via spontaneous deintercalation [71]. The low migration energy of Sn ($E_m \approx 64$ kJ/mol) [41] may facilitate deintercalation in $Ti_2(Al,Sn)C$ upon partial oxidation at low oxygen partial pressure. As confirmed by X-ray diffraction and X-ray microanalyses, elemental Sn was found partially filling the crack gap. Transport of oxygen through elemental Sn melt filling the crack gap is characterized by an activation energy of 6.3 kJ/mol at 700 °C.

Figure 6.19 shows the healing time and temperature relation of the Al_2O_3 composites mixed with MAX phase ($Ti_2Al_{0.5}Sn_{0.5}C$, TASC) repair filler. The data were referenced to a healing time period t_{heal} at which more than 80% of initial strength was recovered by isothermal annealing at the healing temperature T_{heal}. For comparison kinetic data of Al_2O_3 [15], Al_2O_3 mixed with 15 vol.% of SiC platelets [64] as well as 20 vol.% of SiC whiskers [63] are displayed. While crack healing by sintering requires elevated (sintering) temperatures exceeding 1600 °C, oxidation-induced healing may be achieved at significantly lower temperatures. Compared to alumina composites mixed with SiC repair fillers [1], cracks can be healed at lower temperature within shorter time by applying $Ti_2Al_{0.5}Sn_{0.5}C$ as repair filler.

In summary, Al_2O_3 ceramic composite loaded with $Ti_2Al_{0.5}Sn_{0.5}C$ MAX phase triggers oxidation crack healing at moderate temperatures <1000 °C. Compared to SiC repair filler ceramic composites, the MAX phase

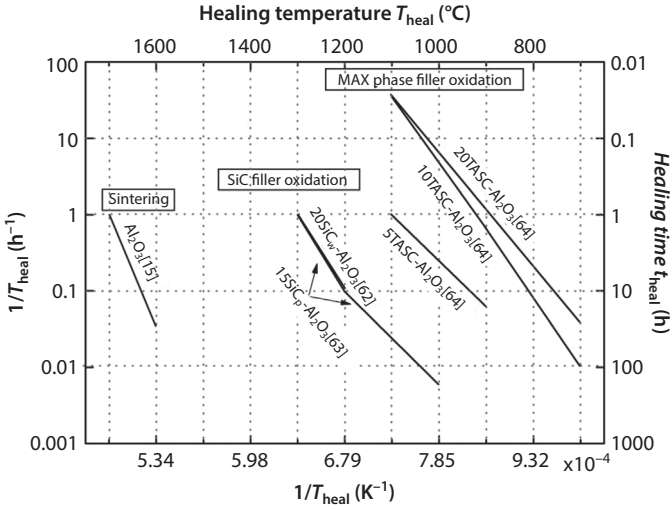

Figure 6.19 Summary of crack-healing dependence on temperature and time measured on the MAX phase alumina composites [65].

composites are distinguished by accelerated crack-healing ability, which is attributed to the accelerated oxidation reaction of $Ti_2Al_{0.5}Sn_{0.5}C$ particles. The oxidation reaction of $Ti_2Al_{0.5}Sn_{0.5}C$ particles located near a surface crack results in filling of the crack gap with the oxidation products TiO_2, Al_2O_3, and SnO_2. Inside the crack, however, where oxygen concentration is supposed to be lower than on the surface, preferential oxidation of Al and Ti may give rise for an oxygen concentration below a threshold necessary for oxidizing Sn to form SnO_2.

6.4 Conclusions

MAX phase ceramics are distinguished by a high crack-healing capability when exposed to air atmosphere. Al-containing MAX phases such as Ti_3AlC_2, Ti_2AlC, and Cr_2AlC can heal larger cracks up to millimeters at temperature above 1100 °C. Full-strength recovery can be realized when the crack gap is filled Al_2O_3 and minor fractions of M-metal oxide. Furthermore, the multiple healing ability of MAX phases makes them potential ceramics with durable applications in very harsh environments.

Lower healing temperatures are observed for Ti_2SnC. After healing at 800 °C, thermal shock-induced cracks were completely filled with mainly TiO_2 and SnO_2 (high oxygen potential) and TiO_2 and metallic Sn (low

oxygen potential). Both the flexural strength and electrical conductivity could be restored efficiently. The presence of high-mobility Sn in smaller cracks may redistribute residual stresses in the healed zone and play an important role in recovery of the electrical conductivity.

Adding $Ti_2Al_{0.5}Sn_{0.5}C$ MAX phase to an Al_2O_3 matrix was demonstrated to trigger accelerated oxidation-induced crack healing at temperature as low as 700 °C. The fracture strength of 20 vol.% repair filler composites containing artificial indent cracks recovered fully to the level of the virgin material upon isothermal annealing in air after 48 h at 700 °C and 0.5 h at 900 °C. Two different oxidation reaction regimes were identified to govern the crack filling: near the surface SnO_2, TiO_2, and Al_2O_3 were formed, whereas cracks at the interior Al_2O_3, TiO_2, and metallic Sn were detected. The presence of metallic Sn may open a novel approach for enhancement of crack-healing and mechanical property recovery of ceramic composites.

Acknowledgments

The authors would like to thank Dr Wim Sloof and Prof. S. Van der Zwaag from TU-Delft for their valuable discussions and refinement of manuscript. Financial support from DFG grant no. GR 961/33-1 is gratefully acknowledged.

References

1. Greil P., Generic principles of crack-healing ceramics. *J. Ad. Ceram*., 1, 249, 2012.
2. Van der Zwaag S., *Self healing materials an alternative approach to 20 centuries of materials science*, pp:309–321, Springer, 2007.
3. Ghosh S.K., *Self-healing materials: fundamentals, design strategies and applications*, pp:183–217, Wiley-VCH, 2009.
4. Yasuhara H., Marone C., Elsworth D., Fault zone restrengthening and frictional healing: The role of pressure solution. *J. Geophys. Res*., 110, 1, 2005.
5. Feng Q.L., Cui F.Z., Pu G., Wang R.Z., Li H.D., Crystal orientation, toughening mechanisms and a mimic of nacre. *Mater. Sci. Eng. C*, 11, 19, 2000.
6. Heuer A.H., Roberts J.P., The influence of annealing on the strength of corundum. *Proc. Brit. Ceram. Soc.*, 6, 17, 1966.
7. Yen C.F., Coble R.L., Spheroidization of tubular voids in Al_2O_3 crystals at high temperatures. *J. Am. Ceram. Soc.*, 55, 507, 1972.
8. Evans A.G., Charles E.A., Strength recovery by diffusive crack healing. *Acta Mater.*, 25, 919, 1977.

9. Wiederhorn S.M., Townsend P.R., Crack healing in glass. *J. Am. Ceram. Soc.*, 53, 486, 1970.
10. Ackler H.D., Healing of Lithographically introduced cracks in glass and glass-containing ceramics. *J. Am. Ceram. Soc.*, 81, 3093, 1998.
11. Wang Z., Li Y.Z., Harmer M.P., Chou Y.T., Thermal healing of laser-induced internal cracks in lithium fluoride crystals. *J. Am. Ceram. Soc.*, 75, 1596, 1992.
12. Roberts J.T.A., Wrona B.J., Crack healing in UO_2. *J. Am. Ceram. Soc.*, 56, 297, 1973.
13. Bandyopadhyay G., Roberts J.T.A., Crack healing and strength recovery in UO_2. *J. Am. Ceram. Soc.*, 59, 415, 1976.
14. Lange F.F., Radford K.D., Healing of surface cracks in polycrystalline Al_2O_3. *J. Am. Ceram. Soc.*, 53, 420, 1970.
15. Gupta T.K., Crack healing and strengthening of thermally shocked alumina. *J. Am. Ceram. Soc.*, 59, 259, 1976.
16. Lange F.F., Gupta T.K., Crack healing by heat treatment. *J. Am. Ceram. Soc.*, 53, 54, 1970.
17. Gupta T.K., Crack Healing in Thermally Shocked MgO. *J. Am. Ceram. Soc.*, 58, 143, 1975.
18. Lange F.F., Healing of Surface cracks in SiC by oxidation. *J. Am. Ceram. Soc.*, 53, 290, 1970.
19. Korouš J., Chu M.C., Nakatani M., Ando K., Crack healing behavior of silicon carbide ceramics. *J. Am. Ceram. Soc.*, 83, 2788, 2000.
20. Ando K., Takahashi K., Nakayama S., Saito S., Crack-healing behavior of Si_3N_4/SiC ceramics under cyclic stress and resultant fatigue strength at the healing temperature. *J. Am. Ceram. Soc.*, 85, 2268, 2002.
21. Takahashi K., Kim B.S., Chu M.C., Sato S., Ando K., Crack-healing behavior and static fatigue strength of Si_3N_4/SiC ceramics held under stress at temperature (800, 900, 1000 °C). *J. Eur. Ceram. Soc.*, 23, 1971, 2003.
22. Houjou K., Ando K., Liu S.P., Sato S., Crack-healing and oxidation behavior of silicon nitride ceramics. *J. Eur. Ceram. Soc.*, 24, 2329, 2004.
23. Osada T., Nakao W., Takahashi K., Ando K., Kinetics of self-crack-healing of alumina/Silicon carbide composite including oxygen partial pressure effect. *J. Am. Ceram. Soc.*, 92, 864, 2009.
24. Jung Y.-S., Nakao W., Takahashi K., Ando K., Saito S., Crack healing of machining cracks introduced by wheel grinding and resultant high-temperature mechanical properties in a Si_3N_4/SiC composite. *J. Am. Ceram. Soc.*, 92, 167, 2009.
25. Harrer W., Danzer R., Morrell R., Influence of surface defects on the biaxial strength of a silicon nitride ceramic – increase of strength by crack healing. *J. Eur. Ceram. Soc.*, 32, 27, 2012.
26. Quemard L., Rebillat F., Guette A., Tawil H., Louchet-Pouillerie C., Self-healing mechanisms of a SiC fiber reinforced multi-layered ceramic matrix composite in high pressure steam environments. *J. Eur. Ceram. Soc.*, 27, 2085, 2007.

27. Boccaccini A.R., Ponton C.B., Chawla K.K., Development and healing of matrix microcracks in fibre reinforced glass matrix composites: assessment by internal friction. *Mate. Sci. Eng. A*, 241, 141, 1998.
28. Chu M.-C., Cho S.-J., Yoon K.-J., Park H.-M., Crack repairing in alumina by penetrating glass. *J. Am. Ceram. Soc.*, 88, 491, 2005.
29. Barsoum M.W., The $M_{N+1}AX_N$ phases: a new class of solids thermodynamically stable nanolaminates. *Prog. Solid State Chem.*, 28, 201, 2000.
30. Sun Z.M., Progress in research and development on MAX phases: a family of layered ternary compounds. *Inter. Mater. Rev.*, 56, 143, 2011.
31. Farle A.-S., Kwakernaak C., van der Zwaag S., Sloof W.G., A conceptual study into the potential of $M_{n+1}AX_n$-phase ceramics for self-healing of crack damage. *J. Eur. Ceram. Soc.*, 35, 37, 2015.
32. Tallman D.J., Anasori B., Barsoum M.W., A critical review of the oxidation of Ti_2AlC, Ti_3AlC_2 and Cr_2AlC in air. *Mater. Res. Lett.*, 1, 115, 2013.
33. Wang X.H., Zhou Y.C., Oxidation behavior of Ti_3AlC_2 at 1000–1400 °C in air. *Corros. Sci.*, 45, 891, 2003.
34. Lin Z.J., Zhuo M.J., Zhou Y.C., Li M.S., Wang J.Y., Interfacial microstructure of Ti_3AlC_2 and Al_2O_3 oxide scale. *Scripta Mater.*, 54, 1815, 2006.
35. Song G.M., Pei Y.T., Sloof W.G., Li S.B., De Hosson J.T.M., van der Zwaag S., Early stages of oxidation of Ti_3AlC_2 ceramics. *Mater. Chem. Phys.*, 112, 762, 2008.
36. Wang X.H., Zhou Y.C., High-temperature oxidation behavior of Ti_2AlC in air. Oxid. Met., 59, 303, 2003.
37. Cui B., Jayaseelan D.D., Lee W.E., Microstructural evolution during high-temperature oxidation of Ti_2AlC ceramics. *Acta Mater.*, 59, 4116, 2011.
38. Rao J.C., Pei Y.T., Yang H.J., Song G.M., Li S.B., De Hosson J.T.M., TEM study of the initial oxide scales of Ti_2AlC. *Acta Mater.*, 59, 5216, 2011.
39. Lin Z.J., Li M.S., Wang J.Y., Zhou Y.C., High-temperature oxidation and hot corrosion of Cr_2AlC. *Acta Mater.*, 55, 6182, 2007.
40. Li S., Xiao L., Song G., Wu X., Sloof W.G., Van Der Zwaag S., Oxidation and crack healing behavior of a fine-grained Cr_2AlC ceramic. *J. Am. Ceram. Soc.*, 96, 892, 2013.
41. [41]Liu B., Wang J.Y., Zhang J., Li F.Z., Zhou Y.C., Theoretical investigation of A -element atom diffusion in Ti_2AC (A = Sn, Ga, Cd, In, and Pb). *Appl. Phys. Lett.*, 94, 181906, 2009.
42. Song G.M., Pei Y.T., Sloof W.G., Li S.B., De Hosson J.T.M., van der Zwaag S., Oxidation-induced crack healing in Ti_3AlC_2 ceramics. *Scripta Mater.*, 58, 13, 2008.
43. Wang X.H., Zhou Y.C., Stability and Selective Oxidation of Aluminum in Nano-Laminate Ti_3AlC_2 upon Heating in Argon. *Chem. Mater.*, 15, 3716, 2003.
44. Tzenov N.V., Barsoum M.W., Synthesis and characterization of Ti_3AlC_2. *J. Am. Ceram. Soc.*, 83, 825, 2000.
45. Yang H.J., Pei Y.T., Rao J.C., De Hosson J.T.M., Li S.B., Song G.M., High temperature healing of Ti_2AlC: on the origin of inhomogeneous oxide scale. *Scripta Mater.*, 65, 135, 2011.

46. Li S., Song G., Kwakernaak K., van der Zwaag S., Sloof W.G., Multiple crack healing of a Ti_2AlC ceramic. *J. Eur. Ceram. Soc.*, 32, 1813, 2012.
47. Yang H.J., Pei Y.T., Rao J.C., De Hosson J.T.M., Self-healing performance of Ti_2AlC ceramic. *J. Mater. Chem.*, 22, 8304, 2012.
48. Anstis G.R., Chantikul P., Lawn B.R., Marshall D.B., A critical evaluation of indentation techniques for measuring fracture toughness: I, Direct crack measurements. *J. Am. Ceram. Soc.*, 64, 533, 1981.
49. Kim H.-C., Park H.-K., Shon I.-J., Ko I.-Y., Fabrication of ultra-fine TiO_2 ceramics by a high-frequency induction heated sintering method. *J. Ceram. Proc. Res.*, 7, 327, 2006.
50. Wang C.-J., Huang C.-Y., Effect of TiO_2 addition on the sintering behavior, hardness and fracture toughness of an ultrafine alumina. *Mater. Sci. Eng. A*, 492, 306, 2008.
51. Bei G., Pedimonte B.J., Fey T., Greil P., Oxidation behavior of MAX phase $Ti_2Al_{(1-x)}Sn_xC$ solid solution. *J. Am. Ceram. Soc.*, 96, 1359, 2013.
52. Jacob K.T., Raj S., Rannesh L., Vegard's law: A fundamental relation or an approximation? *Inter. J. Mater. Res.*, 98, 776, 2007.
53. Li S., Bei G., Chen X., Zhang L., Zhou Y., Mačković M., Spiecker E., Greil P., Crack healing induced electrical and mechanical properties recovery in a Ti_2SnC ceramic. *J. Eur. Ceram. Soc.*, 36, 25, 2016.
54. Dong H.Y., Yan C.K., Chen S.Q., Zhou Y.C., Solid-liquid reaction synthesis and thermal stability of Ti_2SnC powders. *J. Mate. Chem.*, 11, 1402, 2001.
55. Zhou Y.C., Dong H.Y., Wang X.H., High-temperature oxidation behavior of a polycrystalline Ti_2SnC ceramic. *Oxid. Met.*, 61, 365, 2004.
56. Dean J.A., *Lange's handbook of chemistry 14th Edition*. pp:841–1009, McGraw-Hill, 1992.
57. Hummer D.R., Heaney P.J., Post J.E., Thermal expansion of anatase and rutile between 300 and 575 K using synchrotron powder X-ray diffraction. *Powder Diffr.*, 22, 352, 2007.
58. Batzill M., Diebold U., The surface and materials science of tin oxide. *Prog. Surf. Sci.*, 79, 47, 2005.
59. El-Raghy T., Chakraborty S., Barsoum M.W., Synthesis and characterization of Hf_2PbC, Zr_2PbC and M_2SnC (M = Ti, Hf, Nb or Zr). *J. Eur. Ceram. Soc.*, 20, 2619, 2000.
60. Ho C.-Y., Taylor R.E., *Thermal expansion of solids*. pp:135–153, ASM International, 1998.
61. Yakuphanoglu F., Electrical conductivity, seebeck coefficient and optical properties of SnO_2 film deposited on ITO by dip coating. *J. Alloy. Compd.*, 470, 55, 2009.
62. Kishi Y., Ogura K., Kamata K., Saitoh H., Uematsu K., High strength, electrically conductive pore-free TiO_2 ceramics made by hot isostatic pressing. *J. Mater. Res.*, 12, 1056, 1997.
63. Ando K., Kim B.S., Chu M.C., Saito S., Takahashi K., Crack-healing and mechanical behaviour of Al_2O_3/SiC composites at elevated temperature. *Fatigue Fract. Eng. Mater. Struct.*, 27, 533, 2004.

64. Chlup Z., Flasar P., Kotoji A., Dlouhy I., Fracture behaviour of Al_2O_3/SiC nanocomposite ceramics after crack healing treatment. *J. Eur. Ceram. Soc.*, 28, 1073, 2008.
65. Bei G.P., Pedimonte B.J., Pezoldt M., Ast J., Fey T., Goeken M., Greil P., Crack healing in $Ti_2Al_{0.5}Sn_{0.5}C$–Al_2O_3 composites. *J. Am. Ceram. Soc.*, 98, 1604, 2015.
66. Li A., Hu C., Li M., Zhou Y., Joining of Ti–Al–C ceramics by oxidation at low oxygen partial pressure. *J. Eur. Ceram. Soc.*, 29, 2619, 2009.
67. Nanko M., High-temperature oxidation of ceramic matrix composites dispersed with metallic particles. *Sci. Tech. Adv. Mater.*, 6, 129, 2005.
68. Nanko M., Yoshimura M., Maruyama T., High temperature oxidation of Y_2O_3 partially-stabilized ZrO_2 composites dispersed with Ni particles. *Mater. Trans.*, 44, 736, 2003.
69. Zhang H.B., Zhou Y.C., Bao Y.W., Li M.S., Improving the oxidation resistance of Ti_3SiC_2 by forming a $Ti_3Si_{0.9}Al_{0.1}C_2$ solid solution. *Acta Mater.*, 52, 3631, 2004.
70. Takahashi K., Ando K., Nakao W., Crack-healing ability of structural ceramics and methodology to guarantee the reliability of ceramic components. In: *Advances in Ceramics: Characterization, Raw Materials, Processing, Properties, Degradation and Healing*, edited by C. Sikalidis. pp:351–370, InTech., Rijeka, 2011.
71. Pang W.K., Low I.M., Connor B.H.O., Studer A.J., Peterson V.K., Sun Z.M., Palmquist J.P., Comparison of thermal stability in MAX 211 and 312 phases. *J. Phys.Conf. Ser.*, 251, 012025, 2010.

7

SWCNTs versus MWCNTs as Reinforcement Agents in Zirconia- and Alumina-based Nanocomposites: Which One to Use

M.H. Bocanegra-Bernal[1]*, C. Dominguez-Rios[1], A. Garcia-Reyes[2], A. Aguilar-Elguezabal[1] and J. Echeberria[3]

[1]Centro de Investigaciòn en Materiales Avanzados, CIMAV S.C., Laboratorio Nacional de Nanotecnologìa, Chihuahua, Mexico
[2]Interceramic, Departamento de Investigación y Desarrollo, Chihuahua, Mexico
[3]CEIT and TECNUN (University of Navarra), San Sebastian, Spain

Abstract

The recent advances reported in the field of carbon nanotubes (CNTs) as reinforcement agents in zirconia- and alumina-based nanocomposites are summarized. Although the full potential of CNTs has yet to be reached, the extraordinary and exceptional mechanical, electrical, and thermal properties that CNT displays as well as the current state of research make it a perfect candidate for the design and creation of new strong and tough nanocomposite systems. When the interest is to combine CNTs with zirconia and/or alumina to form composites, it is very important and essential to develop different processing methods leading to obtain homogeneous dispersion of the CNTs into the ceramic matrices. In this context, here we compare the effect on mechanical properties using single-walled carbon nanotube (SWCNT) or multi-walled carbon nanotube (MWCNT) as reinforcement agents in zirconia- and alumina-based ceramic nanocomposites densified under different sintering techniques analyzing the influence of sintering on the dispersion of the CNTs within the ceramic host matrix to clarify whether or not an actual improvement has been achieved in terms of fracture toughness and hardness adopting a composite microstructure instead of monolithic one. In addition, we discuss the levels of reinforcement that have actually been achieved in order to obtain high functional properties for high-end applications.

**Corresponding author*: miguel.bocanegra@cimav.edu.mx

Ashutosh Tiwari, Rosario A. Gerhardt and Magdalena Szutkowska (eds.) Advanced Ceramic Materials, (261–298) © 2016 Scrivener Publishing LLC

Keywords: Alumina, zirconia, carbon nanotubes, fracture toughness, hardness, reinforcement agent, indentation fracture

7.1 Introduction

Nowadays, carbon nanotubes (commonly abridged as CNTs) emerge as potentially attractive materials as reinforcing agents in diverse composites, particularly in ceramic–matrix composites [1] offering a tremendous opportunity for the development of fundamental new material systems [2].

Although the discovery of hollow and nanometer tubes composed of graphitic carbon has been attributed to Sumio Iijima [3], clear images of approximately 50 nm diameter tubes made of carbon were reported by Radushkevich and Lukyanovich [4] and subsequently, Oberlin *et al.* [5] showed hollow carbon fibers with nanometer-scale diameters using a vapor-growth technique and at the 14th Biennial Conference of Carbon at Penn State University [6], Abrahamson *et al.* [7] published evidence of CNTs. CNTs are considered to have excellent properties originating from their unique one-dimensional character where a combination of outstanding mechanical (elastic modulus ~1.28 TPa, tensile strength ~30 GPa), thermal (conductivity > 2000 W/mK), and electrical (conductivity > 1.5×10^4 S/m) leads to suitable reinforcing materials for different systems [8].

On the other hand, CNTs are structures of nanometric dimension built up entirely by atoms of carbon, and they can have a ratio of length to diameter up to 10,000:1 and can be visualized as a graphene sheet that has been rolled into a tube with hemispherical caps at both ends [9, 10] where the walls of the tubes are hexagonal carbon. Although in some cases the scientific literature has reported significant improvement of mechanical properties, the results obtained with alumina and other ceramics systems as zirconia-based ceramics reinforced with CNTs remain controversial and the wide-scattered and highly debatable results can arise from different testing techniques used. However, many researchers have reported mechanical properties of CNTs that exceed those of any previously existing materials [11].

Different kinds of CNTs can be used as reinforcement agent into ceramic–matrix composites such as single-, double-, single-double-, and multi-walled CNTs (SWCNTs, DWCNTs, SDWCNTs, and MWCNTs, respectively), which in turn could also produce different microstructure owing to their difference in parameters as aspect ratio, defect proportion, mechanical properties, and tendency to gather into bundles [12]. Nevertheless, the two main types of CNTs used as reinforcement in ceramic systems are

SWCNTs consisting of a single graphite sheet seamlessly wrapped into a cylindrical tube (Figure 7.1a) [13, 14] and MWCNTs that comprise an array of such nanotubes that are concentrically nested like rings of a tree trunk (Figure 7.1b) [13, 14].

From the experimental point of view, the tubes are generally less perfect than the idealized versions in the scientific literature and shown in Figure 7.1 and, as pointed out, may be multi-walled or single walled. Commonly, SWCNT can have diameters typically ranging from ~0.8 nm with the smallest diameter reported to date of 0.4 nm to > 3 nm and with lengths reaching several micrometers and sometimes some tens of micrometers, giving therefore very high aspect ratios (1000–10,000). On the other side, MWCNTs tend to have diameters in the range 1.7 to at least 100 nm and lengths from a few tens of nanometers to several micrometers [15]. High-resolution transmission electron microscopy (HRTEM) micrographs of SWCNTs, SDWCNTs, and MWCNTs are shown in Figure 7.2a, b, and c, respectively. Inset in each figure shows in detail different diameters as well as the distribution of the number of walls. It is noteworthy the multilayered structure in Figure 7.2c exhibiting a high crystallinity and some surface roughness. In Figure 7.2c, the nanostructure of MWCNTs where the individual layers making up the concentric tubes is clearly evident.

As mentioned above, in spite of different kinds of CNTs available to reinforce ceramic matrices, there has been much documented research attempting to incorporate both SWCNTs and MWCNTs in brittle ceramics

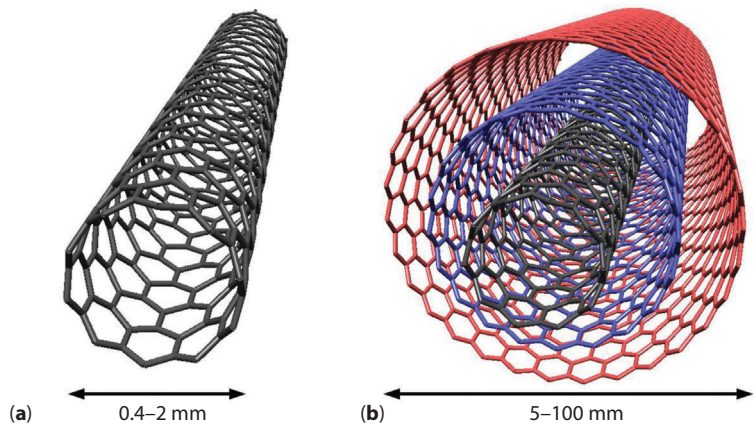

Figure 7.1 (a) SWCNT and (b) MWCNT. (From Ben Cornwell-Mott, Effect of perfectly aligned CNTs under cohesive crack bridging in adhesive joints. A project submitted in conformity with the requirements for the degree of Master of Engineering Graduate Department of Mechanical and Industrial Engineering University of Toronto, 2010 [13]).

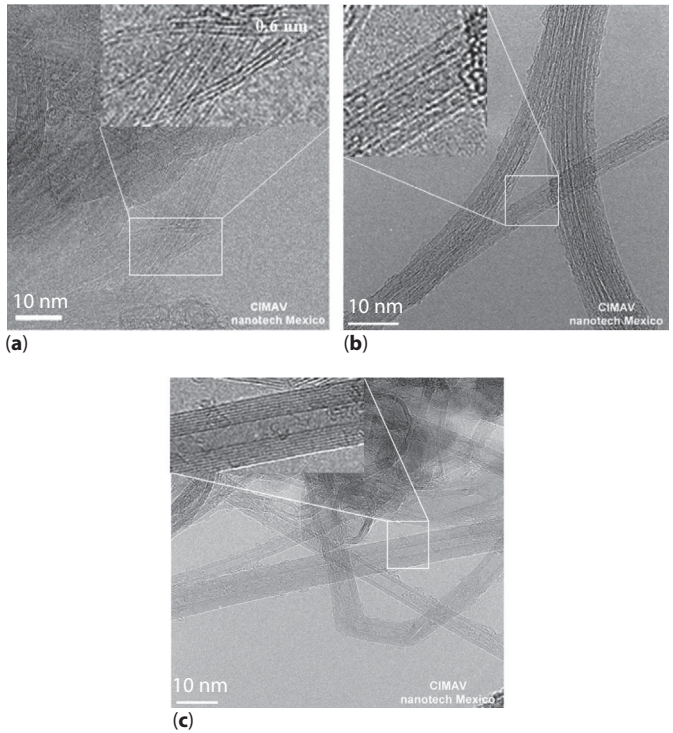

Figure 7.2 HRTEM micrographs of SWCNTs (a), SDWCNTs (b), and MWCNTs (c). Note in each inset the distribution of the number of walls.

in order to convert them into tough, strong, electric, and thermal conductive materials [16, 17]. A survey of the scientific literature indicates that 88% of the reported cases used the readily available and economically feasible MWCNTs as reinforcement agent in comparison to SWCNTs. Likewise, nearly 40% adopted a wet oxidation process to purify the CNTs to remove unwanted impurities including carbon nanoparticles, amorphous carbon coating layers as well as metallic catalyst residues. About 33% of the reports attempted pristine CNTs, whilst the other tried oxidation through annealing [16, 18]. Regardless of this, the problems with homogeneous distribution of CNTs and related problems with reproducible preparation of ceramic composites with improved mechanical properties can be considered as a chief obstacle.

Both the nature of CNTs and the processing conditions must be considered. The great variety of available CNTs, which undoubtedly differ significantly due to the conditions of their preparation, and subsequent treatment along with poor dispersion, which plays a major role in defining

the mechanical properties, could be the main problem. In fact, different types of CNTs [produced by many methods such as arc discharge in the absence or presence of metal, laser vaporization of a metal–graphite composite target, carbon monoxide disproportionation or catalytic metal particles (Fe, Co, Ni, Cu) [1]] can exhibit various levels of mechanical strength, density, affinity to the ceramic matrix owing to differences in their tubular structure, numbers and crystallinity of rolled graphene sheets, number and nature of surface defects, and surface chemistry, just to name only the most important ones [19–21], which could also produce different microstructures and final mechanical properties when the ceramic composites are prepared by different processing routes such as conventional sintering, sintering + post-hot isostatic pressing (HIP), hot pressing (HP), and recently spark plasma sintering (SPS) [22]. The industrial application of the CNTs requires the development of techniques for large-scale production of defect-free nanotubes, considering that a cost-effective method has yet to be discovered [23].

In spite of that the role of CNTs in the sintering of ceramic matrix composites is not completely clarified in the literature, many interesting works have been carried out with the aim to improve their mechanical properties. Indeed, Zhan *et al.* [24] prepared 100% dense Al_2O_3 + 10 vol.% SWCNTs at 1150 °C during 3 min by means of SPS resulting in a fracture toughness of 9.7 MPa $m^{1/2}$ being nearly three times that of nanocrystalline alumina (3.5 MPa $m^{1/2}$), but the results have not been reproduced up to now. In fact, these results were refuted by Wang *et al.* [25] who reported that CNT–alumina composites are highly contact damage resistant and also showed that a more reliable single edge V-notched beam test, could reveal no enhanced toughening, refuting therefore the claims of high toughness by Zhan *et al.* [24]. Other composites prepared by HP mixture of MWCNTs and nano-SiC powders were reported by Ma *et al.* [26] being the dispersion of the MWCNTs very poor. However, an increase in both the bending strength and fracture toughness when the CNTs content is around of 10 vol.% was observed. On the other hand, Siegel *et al.* [27] reported that the fracture toughness of 10 vol.% MWCNTs alumina hot-pressed composites is increased by 24% (to 4.2 MPa $m^{1/2}$) over that the pure alumina. The above mentioned are only a few examples where both SWCNTs and MWCNTs have been used as reinforcement agent.

In the manufacture of CNTs-reinforced alumina- and zirconia-based ceramics, the achieving near full density preserving the CNTs after exposure at high temperatures is a fundamental requirement and another important challenge in ceramic matrix composite technology considering that the mechanical properties are strongly affected by the density [16].

It is well known that CNTs hinder the ceramic grains coalescence by existing at the grain boundaries, which tends to lead to poorly densified microstructures [28]. In this context, nowadays pressure-assisted sintering processes are being used to counter this problem. A recent study [16] reports that approximately 76% nanocomposites were consolidated by pressure-assisted sintering processes, in which SPS and HP have a share of 50% and 26%, respectively. Till now, the alumina and zirconia ceramics are the most important ones developed in these years. For being characterized with excellent chemical and physical properties such as high hardness, high strength, high chemical and wear resistance, etc., zirconia ceramics is stepping to replace the alumina ceramics in many fields. Zirconia ceramics are widely applied in machinery, electronic, petroleum, chemical, aviation, textile, precious apparatus, and organic engineering. In this context and in view of the vast applications of the Al_2O_3, ZrO_2 and the combination of them in industry, lots of studies have been done to improve their fracture toughness by CNT additions. Therefore, the authors consider that this review paper will serve as an important guideline to the best choice of CNTs as reinforcing agents that can improve the mechanical properties of the different ceramic systems. Likewise, in this review paper, we will explore briefly the influence of the different kind of CNTs (SWCNTs and MWCNTs) on the mechanical properties of CNTs-reinforced alumina and/or zirconia ceramic composites following different processing routes.

7.2 Single-walled Carbon Nanotubes

SWCNTs are structurally unique materials that exhibit excellent mechanical, electrical, thermal, and optical properties, and they offer potential promise for a number of novel applications [29]. Although much progress has been made, it is widely recognized that the bottleneck toward applications is the purity and dispersion of SWCNTs [30]. Methods such as laser ablation, arc discharge methods, and chemical vapor deposition (CVD) are commonly [31] used to produce SWCNTs. In general, the morphologies of the carbon nanostructures and the SWCNTs can differ notably with respect to the experimental conditions. Likewise, different theories have been proposed for the growth mechanism, some from the vapor phase and others from a condensed phase, with growth taking place either at the tip or the root [32]. Early fabrication relied on a modified version of arc-discharge generators used for fullerene synthesis [33, 34]. Nevertheless, while high-quality SWCNTs can be produced, some defects are always present which in turn could significantly affect the physical, chemical, and mechanical

properties of the CNTs. However, the availability of pristine and isolated SWCNTs is scarce for researchers. As consequence of their great flexibility and high surface energy, SWCNTs tend to aggregate into large bundles containing huge numbers of both metallic and semi-conducting SWCNTs in a random mixture affecting negatively the mechanical properties of SWCNT-reinforced ceramics inasmuch as the bundle properties are generally inferior to those of isolated SWCNTs. Therefore, the properties and applicability of SWCNTs may also change dramatically depending on whether single SWCNT or SWCNT ropes are involved. In the field of ceramics reinforced with CNTs, the separation of SWCNTs is extremely difficult, making this issue a serious hurdle in the way of real applications [35]. As pointed out by Liang and Chen [36], one of the main barriers to the extensive application of SWCNTs is that their growth processes lead to the production of a mixture of diameter and chirality distributions. Their structure, purity, and physical orientation for specific applications can be greatly optimized by changing synthesis technique, temperature, pressure, catalyst, electric field, and carbon resources.

According to Baughman *et al*. [14], all currently known synthesis methods for SWCNTs result in major concentrations of impurities. Carbon-coated metal catalyst contaminates the nanotubes of the HiPco route, and both carbon-coated metal catalyst and, typically, ~60% forms of carbon other than nanotubes are formed in the carbon-arc route [37]. Regrettably, these impurities are typically removed by acid treatment, which introduces other impurities, degrading nanotube length and perfection, and adds to nanotube an additional cost. On the other side, an additional problem during acid treatment is that the usual synthetic routes result in mixtures of various semiconducting and metallic nanotubes being the metallic SWCNTs selectively destroyed by electrical heating so that only the semiconducting nanotubes needed for nanotube field-effect transistors (NTFETs) survive [38]. A more detailed description concerning to the methods used to produce CNTs (SWCNTs and MWCNTs), and its purification as well as routes to disperse them is found in reference [23].

For an effective reinforcement of alumina- and zirconia-based ceramics with CNTs, four requirements must be identified as follows: (i) large aspect ratio (30–10,000), (ii) good and homogeneous dispersion of the reinforcing CNTs into the ceramic matrix, (iii) alignment, and (iv) interfacial stress transfer [35]. On the other side, it is of paramount importance to avoid damage to the CNTs during processing at high temperatures [39]. Being the dispersion of CNTs (both SWCNTs and MWCNTs) a great challenge, the effects of a poor dispersion can be detrimental to improve the mechanical properties [40]. Undoubtedly, the most important requirement

for a CNT-reinforced ceramic composite is that external stresses applied to the composite as a whole are efficiently transferred to the nanotubes, allowing them to take a disproportionate share of the load [35]. With the purpose to obtain an "ideal" ceramic composite, it is of paramount importance the connectivity with the matrix and uniform distribution within the matrix for stronger and tougher CNT/ceramic composites [41]. When the ceramic is reinforced with SWCNTs, it is important to know that the diameters of these SWCNTs fall in the nanometer regime and can be hundreds of micrometers long. SWCNTs are narrower in diameter than the thinnest line that can be obtained in electron beam lithography. Moreover, SWCNTs are stable up to ~750 °C in air (however, they are usually damaged before this temperature is reached due to oxidation mechanisms) and are stable up to ≈1500–1800 °C under inert atmosphere, beyond which they transform into regular, polyaromatic solids (phases built with stacked graphenes instead of single graphenes) [42], they are also highly flexible and attain their original shape after buckling and bending and have low density of about one-sixth of the density of steel [43]. The physical and chemical behaviors of a SWCNT are therefore related to its unique structural features [44], meanwhile the final cost of CNTs can be related to the production method. Therefore, it is very important to consider that the CVD seems to be promising as it requires less expensive raw materials and utilizes the flowing gas as the carbon source, and less purification techniques are required. However, this technique requires more studies in terms of increasing yield and purity level [45].

According to the statement by Fraunhofer Institute for Material and Beam Technology IWS [46], SWCNTs are surely the CNTs variant with the most interesting combination of physical properties. They show world records in mechanical, electrical, and thermal properties. For most of the time, there was no guarantee for a sufficient availability of this outstanding material. In the meantime, however, increasingly larger quantities of SWCNTs have entered the market, which enable the development of attractive applications. Therefore, the worldwide fascination in connection with CNTs as such may finally become reality with SWCNTs. Some characteristics of SWCNTs [47] and a comparison of mechanical properties of SWCNTs with stainless steel and Kevlar [48] are given in Tables 7.1 and 7.2, respectively. Taking into account the characteristics and properties mentioned in these tables, as well as different mechanical properties collected in the scientific literature, SWCNTs have led to commercial products such as strengthened, lightweight carbon composite sports equipment, owing to their unique size-related properties.

Apart from other potential applications such as hydrogen storage medias [49], nanoelectronic devices [50], energy storage devices [51],

Table 7.1 Some characteristics of SWCNTs (from Ref. [47]).

- Single layer of grapheme.
- Catalyst is required for synthesis.
- Bulk synthesis is difficult as it requires proper control over growth and atmospheric condition.
- Purity is poor.
- A chance of defect is more during functionalization.
- Less accumulation in the body.
- Characterization and evaluation are easy.
- It can be easily twisted and is more pliable.

Table 7.2 Comparison of mechanical properties (from Ref. [48]).

Material	Young's modulus (TPa)	Tensile strength (GPa)	Elongation at break (%)
SWCNT	~1 (from 1 to 5)	13–53[E]	16
Amchair SWCNT	0.94[T]	126.2[T]	23.1
Zigzag SWCNT	0.94[T]	94.5[T]	15.6–17.5
Chiral SWCNT	0.92		
Stainless steel	~0.2	~0.65–1	15–50
Kevlar[T]	~0.25	29.6	

[E]Experimental observation.
[T]Theoretical prediction.

transistor [52], and sensors [53–56], the SWCNTs as attractive reinforcement agents in alumina- and zirconia-based nanocomposites are being nowadays proposed to improve the mechanical properties of nanocrystalline ceramics to develop nanometer-scale composite materials [24]. In reason of this, CNTs have become an attractive and interesting research area in the field of nanotechnology.

7.3 Multi-walled Carbon Nanotubes

According to Eatemadi *et al.* [47], "Multi-walled carbon nanotubes can be formed in two structural models: Russian Doll model and Parchment model. When a carbon nanotube contains another nanotube inside it and the outer nanotube has a greater diameter than thinner nanotube, it

is called the Russian Doll model. On other hand, when a single grapheme sheet is wrapped around itself manifold times, the same as a rolled up scroll of paper, it is called the Parchment model. MWCNTs and SWCNTs have similar properties. Because of the multilayer nature of MWCNTs, the outer walls can not only shield the inner carbon nanotubes from chemical interactions with outside substances but also present high tensile strength properties, which do not exist in SWCNTs".

When Iijima [3] reported the structural morphology of MWCNTs by use of a HRTEM and electron diffraction, these were produced at extremely high temperatures (near 3500 °C) by use of an arc discharge between graphite electrodes [3]. However, today MWCNTs are produced industrially at much lower temperatures (near 700–950 °C) via CVD process developed by Oberlin and coworkers in the 1970s [5]. Currently, hundreds of tons of MWCNTs are produced each year and in far greater numbers than SWCNTs [57, 58]. Nevertheless very often, SWCNTs or MWCNTs are found together in bundles where the intertube interaction may be strong. Although SWCNTs possess better properties than MWCNTs [9], but the relative simplicity in preparation of MWCNTs and ease in its isolation and purification makes it more economical for most applications including dispersing in ceramic matrix.

MWCNTs [59] are produced with the use of pure graphite arc with an inner diameter 1–3 nm and outer diameter approximately 10 nm. Considering that catalyst is not used in this process, there is no need for a heavy acidic purification. Therefore, MWCNTs can be formed with a less number of defects. Different methods commonly used to synthesize are: (i) synthesis in liquid nitrogen [60] generating arc discharge in liquid nitrogen where low pressure and expensive inert gas are not needed (yield is about 70% of reaction product) and (ii) magnetic field synthesis [61] which forms MWCNTs defect free and having high purity due to the extremely pure graphite rods (purity > 99.999%) used as electrodes. Highly pure MWCNTs (purity > 95%) are obtained without further purification, which disorders walls of MWCNTs, (iii) plasma rotating arc discharge [62] where at the rotation speed of 5000 rpm, a yield of 60% can be obtained at a temperature 1025 °C without the use of a catalyst. However, the yield can be increased up to 90% after purification if the rotation speed is increased and the temperature is enlarged.

Building MWCNTs is a little bit more complex since it involves the various ways graphenes can be displayed and mutually arranged within filamentary morphology [63]. Likewise, their diffraction patterns are difficult to differentiate from those of anisotropic polyaromatic solids. The easiest MWCNT to imagine is the concentric type (*c*-MWCNT), in which

SWCNTs with regularly increasing diameters are coaxially arranged (according to a Russian-doll model mentioned above) into a multi-walled nanotube (see Figure 3.5 in Ref. [63]). Such nanotubes are generally formed either by the electric arc technique (without the need for a catalyst), by catalyst-enhanced thermal cracking of gaseous hydrocarbons as well as by CO disproportionation. There can be any number of walls (or coaxial tubes), from two upwards.

MWCNTs are usually hydrophobic, so they are not readily dispersed in water. Method such as sonication can be useful, but without the addition of a surfactant (which must be considered along with the intrinsic properties of the MWCNTs) could result difficult. Organic solvents (e.g. toluene, chloroform, acetone, methanol, and ethanol) are commonly used, but no accepted standard method of dispersion in solvent exists to our knowledge [58]. It is very important to point out that the defects present in the MWCNTs are extremely important in determining the physiochemical properties of crystals and nanostructures. In particular, defects could affect the morphology and functionality of the MWCNTs. Certainly, a challenge for the future will be the use of defects to design new types of MWCNTs such as helicoidal or hemitoroidal tubules, which will possess some specificity for sensing molecules or anchoring specific polymer chains. CNTs with different tubule morphologies have their own special properties and potential applications. Many different shapes such as straight, waved, coiled, and branched are predicted, observed, and target synthesized as reported by Zhang and Li [64]. MWCNTs in different shapes will have significant impact on the mechanical properties in CNTs-reinforced ceramic composites when they can be efficiently produced ensuring uniform properties in large quantities. Important details concerning process carried out for purification, dispersion, and sintering techniques in Al_2O_3 and ZrO_2 ceramic matrix composites reinforced with CNTs are collected in Table 7.3 [16].

On the other hand, Table 7.4 gives some general characteristics of MWCNTs [47], which are commonly used as reinforcement agents in ceramic matrices.

In summary, SWCNTs have better properties than MWCNTs, but the experience has proved that its dispersion is more difficult to obtain composite materials. Nevertheless, MWCNTs have a higher tensile strength than SWCNTs despite that theoretical analysis predicts that ideal SWCNTs should possess extremely high tensile strength [77, 78]. On the other hand, direct tensile loading tests of SWCNT [79] and MWCNT [78] have been performed by Yu *et al.* Young's modulus obtained under specific conditions ranges from 320 to 1470 GPa (mean: 1002 GPa) for SWCNT and from 270 to 950 GPa for MWCNT suggesting that Young's modulus was

Table 7.3 Processing details of different CNTs-reinforced Al_2O_3 and ZrO_2 ceramics nanocomposites.

Reference	Matrix	CNT types	Purification methods	Dispersion procedures	Sintering techniques
[41]	Al_2O_3	MW	Oxidation at 500 °C for 90 min	UT of CNTs in ethanol.	SPS at 1500 °C for 10 min under 50 MPa
[65]	Al_2O_3	MW	AT (H_2SO_4 + HNO_3)	UT of CNTs into water and SDS then incubation for 2 weeks.	HP at 1600 °C, 60 min , 40 MPa
[66]	Al_2O_3	MW	AT (H_2SO_4 + HNO_3) for 3 h.	24 h BM Al_2O_3 powder and 30 min UT of CNTs in water and then BM of CNTs/Al_2O_3 mixture.	PLS at 1500–1600 °C, 120–240 min, Ar
[67]	Al_2O_3	MW	P	UT of CNTs for 1 h in alcohol.	CIP at 150 MPa and PLS at 1500 °C, and 1700 °C with 2 h
[68]	Al_2O_3	MW	AT (heating in 65%HNO_3 at 80 °C for 8 h)	BM and Surfactant (Darvan C–N).	PLS at 1500 °C for 2 h using Ar
[69]	Al_2O_3	MW	–	DG (CVD at 750 °C for 15 min for direct CNTs growth on Al_2O_3 nanoparticles)	SPS at 1150 °C for 10 min under 100 MPa

[70]	Al_2O_3+ZrO_2	MW SW	P	UT of CNTs in ethanol.	SPS at 1520 °C under 80 MPa
[71]	Al_2O_3	MW	P	35 h UT in water.	SPS at 1300 °C, 20 min, 90 MPa
[72]	Al_2O_3	MW	AT	UT of CNTs and Al_2O_3 in water followed by 2 h and BM of MW CNTs/Al_2O_3.	PLS at 1600 °C, 15 min, Ar
[73]	Al_2O_3	MW	AT (HNO_3 for 30 min)	5 h BM of CNTs and 1 h UT of CNTs. 5 h BM of CNTs/Al_2O_3 in ethanol.	PLS at 1550 °C, Ar
[74]	Al_2O_3	MW	AT (H_2SO_4 + HNO_3 in 3:1 for 7 h)	Surfactant (SDS) using combination of UT and 24 h BM.	HP at 1550 °C for 1 h under 30 MPa using Ar gas.
[75]	Al_2O_3+ZrO_2	MW	AT (heating in 65%HNO3 at 80 °C for 8 h)	2 min UT of CNTs with surfactant (SDS)and 24 BM then freezing with liquid N_2	HP at 1500 °C for 2 h under 30 MPa in Ar atmosphere
[76]	Al_2O_3	SW	AT (H_2SO_4 + HNO_3)	UT for 24 h.	SPS at 1300 °C for 5 min under 75 MPa.

SW, single wall; MW, multi-wall; CNTs, carbon nanotubes; UT, ultrasonication; BM, ball milling; HP, hot pressing; SPS, spark plasma sintering; PLS, pressureless sintering; SDS, sodium dodecyle sulfate; CIP, cold isostatic pressing; P, pristine; MS, magnetic stirring.

Adapted from Ref. [16] with permission.

Table 7.4 Some general characteristics of MWCNTs (from Ref. 47).

• Multiple layer of grapheme.
• Can be produced without catalyst.
• Bulk synthesis is easy.
• Purity is high.
• A chance of defect is less but once occurred it is difficult to improve.
• More accumulation en the body.
• It has very complex structure.
• It cannot be easily twisted.

approximately the same. Therefore and as can be seen from Table 7.3, it is evident that higher percentage of the reported cases used as reinforcement available and economically feasible MWCNTs in comparison to SWCNTs.

7.4 The Effects of CNTs Types on the Mechanical Properties of Al_2O_3- and ZrO_2-based Ceramics

During the last decade and due to the increased interest to develop advanced ceramic composites with improved mechanical and physical properties by incorporating CNTs, high-performance ceramic matrix structural composites have been developed aiming to take advantage from these CNTs [80, 81]. Aluminum oxide or alumina (Al_2O_3), as one of the most common groups of advanced ceramics, has a great potential due to its hardness as well as good chemical and thermal stabilities but regrettably has low fracture toughness, which is an intrinsic characteristic of ceramic materials. Considering that the properties of the alumina can be improved, this important ceramic would be expected to have applications such as cutting tools, dies, dental implants and chemical and electrical insulators, among others. On the other hand, zirconia (ZrO_2) [82], zirconia-toughened alumina (ZTA) and alumina-toughened zirconia (ATZ) [83] ceramics have received significant scientific and technological attention due to their high melting point, excellent room temperature strength, toughness, and wear resistance [84]. These have improved fracture toughness and strength values owing to a stress-induced tetragonal to monoclinic zirconia phase transformation [8]. For the preparation of CNT-ceramic nanocomposite powders, there are three main methods: (i) mechanical milling, which involves long processing times that could damage the nanotubes, being wet-milling preferred, despite often requires

the addition of organic additives to stabilize both the nanotubes and the ceramic powder; (ii) *in situ* synthesis of the matrix on preformed nanotubes, which can lead to a good adhesion between the nanotubes and the ceramic, but can be rather complex to implement; and (iii) *in situ* synthesis of the nanotubes within the ceramic powder using procedures closely related to those described for the production techniques for CNTs [63]. On the other side, the densification of the nanocomposite powders is made difficult by the detrimental influence of the different kinds of nanotubes. The most common method is HP where most of the works [1, 15] report that increasing the nanotube content inhibits the densification of the material. For example, it has been shown that for a series of CNT–$MgAl_2O_4$ composites [85] a low CNTs content (<9 vol.%) favors the rearrangement of the grains, which is the first shrinkage step, probably due to a lubricating role which facilitates the sliding at grain contacts or grain boundaries. Conversely, for higher contents, CNTs form a too rigid web-like structure, therefore inhibiting the rearrangement process and in the second sintering step, at higher temperatures, CNTs inhibit the shrinkage, all the more when their content is increased above 5.0 vol.% only, leading to decreasing densifications. The SPS technique has been reported as an efficient method to achieve the total densification of CNT oxide at comparatively lower temperatures with substantial shorter holding time. However, the successful densification by SPS at a lower temperature than for HP supposes that matrix grains are non-agglomerated and with size in the range few tens of nanometers. The influence of the nanotube dispersion onto mechanical properties, in particular on toughness, has been controversial.

When either SWCNTs or MWCNTs are used as reinforcement agents in alumina- and zirconia-based nanocomposites, dispersion is the great challenge in the processing nanotube composites [86]. This behavior is due to the fact that CNTs have a great surface area exceeding in most of the cases 1000 $m^2\ g^{-1}$ (capped) or 2200 $m^2\ g^{-1}$ (uncapped) surpassing the value of 400–1000 $m^2\ g^{-1}$ for HiPco samples. Microstructurally the agglomeration state produced by inhomogeneous dispersion is extremely undesirable, especially in ceramic matrices which lead to formation of clusters owing to van der Waals' (vdW) forces [87] and concentration of reinforcement at certain point and this could lead to worsening of overall mechanical properties [86]. Meanwhile, with a good dispersion, each nanotube is loaded individually over a maximum interfacial area and therefore, can contribute directly to toughening mechanisms [87]. SWCNTs tend to cluster into ropes while MWCNTs produced by CVD are often tangled together like spaghetti [88, 89].

Knowing that CNTs are insoluble in water and organic solvents, a surfactant is commonly added to disperse them, and with the use of sonication, a homogeneous and stable suspension could be obtained. In addition to this, it is very important to stress that CNTs are not the simple, straight pipes they are being represented. Regardless of the kind of CNTs, they can be curved, wrap around each other and are never evenly aligned, dispersed and distributed throughout a matrix, despite all efforts to make them that way [90, 91]. Additionally, a sonication process is very necessary as a source of external mechanical energy which helps the particles to overcome the attractive can der Waals forces. Sonication is a commonly used method for separating CNT aggregates in solution because it quickly disperses CNT without the need for any chemical modification [90, 91]. Despite being the most commonly used method of dispersion in ceramic–matrix composites to date, many researchers still observed CNT aggregates after sonication in aqueous solution [92, 93]. Figure 7.3 illustrates examples of typical microstructure of agglomerated SWCNTs (Figure 7.3a) and MWCNTs (Figure 7.3b) reinforced ZTA ceramic nanocomposite.

It is clear from Figure 7.3 that the dispersion of SWCNTs by sonication (Figure 7.3a) [65] would require longer times in order to break apart the vdW physical bonds which make the SWCNTs agglomerate into bundles in comparison to the dispersion of MWCNTs (Figure 7.3b). In this context, the CNTs may even act as a source of microcracks, leading to premature failure. Undoubtedly, high CNTs contents (10 vol.% in Figure 7.3) favor agglomeration not only because the ceramic particles come into contact more often, but also because there can be a shortage of matrix material to 'wet out' the large surface area of the filler. The mechanical properties of MWCNTs- and/or SWCNTs-reinforced ceramic matrix composites have been investigated in different studies. However, the exact role of CNTs is

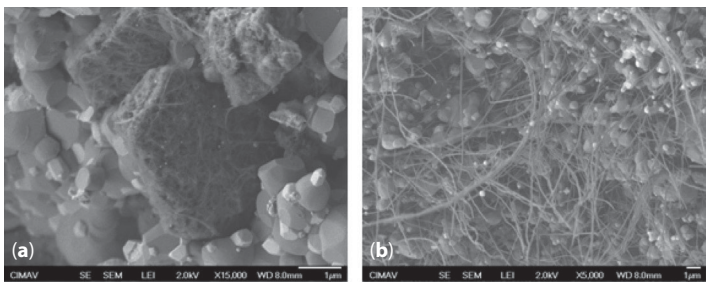

Figure 7.3 SEM image of fracture surface of a ZTA composite [94] sintered at 1520 °C, 1 h showing SWCNT bundles (a) and MWCNT tangles (b) after sonication in aqueous solution.

unclear, and controversial results have been reported. It is of paramount importance therefore to investigate and underscore the tremendous importance of nanotube position within the microstructure and the resulting effects on the mechanical properties of alumina- and/or zirconia-based ceramics [8].

Several parameters must be considered when evaluating the hardness of CNT-reinforced ceramic composites. The most reported cases in the scientific literature are related to the decrease of microhardness with the addition of CNTs and these are most often related to the presence of residual porosity, which increases with the CNT content. This issue is also aggravated by uneven dispersion of the CNTs in the matrix, the presence of porous bundles of nanotubes, which act as defects with no load-bearing capacity, and poor cohesion between CNTs and the matrix [15, 95]. As a result of this, Aguilar-Elguezabal and Bocanegra-Bernal [96] reported a decrease of hardness from 17 GPa in monolithic alumina to 12.5 GPa with the addition of a mixture of MWCNTs and SWCNTs due to the poor cohesion between matrix grains and CNTs weakened by the positioning of CNTs in intergranular regions in the microstructure. A decreasing in hardness was also observed by Ahmad *et al.* [97] in Al_2O_3 with additions of 2 and 5 wt% MWCNTs and Echeberría *et al.* [70] in ATZ composites sintered by means of SPS adding as reinforcement 0.1 and 0.01 wt% of SWCNTs and MWCNTs. Other works report monotonous decrease of Vickers' hardness with increasing volume fraction of CNTs, sometimes with small positive deviation from the trend at 1 vol.% of MWCNTs [75], suggesting a weak interfacial bonding between the MWCNTs and the alumina matrix grains. In general, decrease of hardness in the nanocomposites with increasing CNT content is usually attributed to several factors such as presence of soft phases at the alumina grain boundaries (hardness of MWNTs in the radial direction is 6–10 GPa [20]), very poor adherence between the CNTs and the ceramic matrix grains, the lubricating nature of the CNTs as well as poor dispersion of CNTs in the ceramic matrix, which counteract the influence of microstructure refinement due to the pinning effect of the CNTs at grain boundaries [19]. Generally, a degradation of CNTs during sintering treatment has been observed suggesting therefore a responsible parameter to decreasing hardness and fracture toughness mainly [98].

Taking into account the variety of results reported in the literature related to the performance of MWCNTs and SWCNTs as reinforcement of this kind of ceramic composites, it could be very interesting to know the optimal percentage of CNTs to improve the mechanical properties. Undoubtedly, this percentage will depend on variables such as dispersion method, nature of matrix, surface charges of particles, and particle size

distribution as well as kinds and dimensions of CNTs [94]. On the base of this, it is very venturous to determine which will be the optimum vol.% or wt% CNTs content to reach excellent mechanical properties mentioning that each specific ceramic composite could have different composition. For example, the hardness improvement reached by Sakar and Das [67] was undoubtedly higher than reported by Mo *et al.* [99], Ahmad *et al.* [100], and Zhang *et al.* [66]. This improvement in hardness values can be due to a good dispersion at low additions of CNTs (low CNTs content are more easily dispersible). However, when the addition of CNTs was increased up to 5 wt%, the hardness was suppressed approximately 7%. Higher concentrations of CNTs in the ceramic matrix can also affect the elimination of pores and mass transportation through bulk diffusion, parameters of paramount importance to reach full density during sintering according to pointed out by Jinpeng *et al.* [101]. It seems to be that the adequate dispersion of CNTs in the alumina or zirconia matrix can be the common problem to achieve high mechanical properties values.

It is believed that there is an absolute lack of information about the behavior of ZTA nanocomposites when they are reinforced with CNTs. In applications such as load bearing orthopedic joints, where the hardness is very important, ZTA could have some drawbacks. For example, the introduction of ZrO_2 into the hard alumina matrix results in a decrease in hardness of the ceramic being very attractive to explore the behavior of these ceramic composites reinforced with different kinds of CNTs to obtain a ceramic composite as hard as alumina, toughened by phase transformation, or toughened and reinforced by the presence of CNTs [102]. The breakthrough in the application of ceramics in the field of arthroplasty can be the ZTA/CNTs nanocomposites [63]. To attempt the manufacturing of ZTA composites with competent mechanical properties Echeberría *et al.* [103] reported that the hardness can be increased up to ~17% after HIP treatment (1475 °C 1 h at 150 MPa) in ZTA (Al_2O_3 + 0.025% MgO + 13% TZ-3Y + 2% $ZrO_{2(m)}$) composites with MWCNTs content of 0.01 wt% in comparison to the "as sintered" pressureless sintered composites free of CNTs and ~9% compared to monolithic Al_2O_3 free of HIP. Doubtless and as was mentioned above, a lower amount of CNTs favors the dispersion and therefore, the increasing in mechanical properties.

In recent investigations [94], ZTA composites were reinforced with both SWCNTs and MWCNTs to analyze the effect of these CNTs on the hardness. An increasing of hardness (~6%) with additions as low as 0.01 wt% SWCNTs for ZTA pressureless sintered at 1520 °C during 1 h in air using a graphite bed powder was observed. However and considering the experimental error, the measured Vickers hardness remains approximately

constant for pure ZTA and CNTs-reinforced ZTA composites. On the other hand, when 0.01 wt% of SWCNTs or MWCNTs are added to pure Al_2O_3, a drop in hardness is observed (~15% referenced to monolithic alumina). An example where the measured hardness is practically the same when SWCNTs or MWCNTs are added into the matrix of ZTA composites sintered by SPS at 1475 °C is shown in Figure 7.4. It is clear that Vickers' indentation size was similar in both samples indicating that the amount of CNTs added does not contribute to improve the hardness of the ZTA composites.

The interaction between the ceramic phases (in this case alumina and zirconia), the CNTs surface charges of particles and particle size distribution as well as diameters and lengths of CNTs, could be parameters that affect the mechanical properties [94] even a good dispersion of CNTs can be reached. This suggests that for a same ceramic matrix and CNTs content, the mechanical properties can be different considering the processing route followed in the consolidation of the composite. Regarding that hardness no consensus has been reached by several authors [24, 86, 99, 104], it is speculated that the variations found in the hardness values and other mechanical properties in different studies are the result of a wide processing routes of the composites. Therefore, regardless of the processing methods, ceramic matrix and CNTs used in different investigations, there are works that have reported no effect, for example An and Lim [105] and Ahmad and Pan [106], or improved hardness by the incorporation of CNTs according to reported by Chan *et al.* [107], Peigney *et al.* [12], and Burghard *et al.* [108]. Meanwhile, the improvements obtained by some authors have been marginal but unfortunately, no comments were presented explaining in detail the interfacial interactions between hard ceramic particles and the CNTs [63].

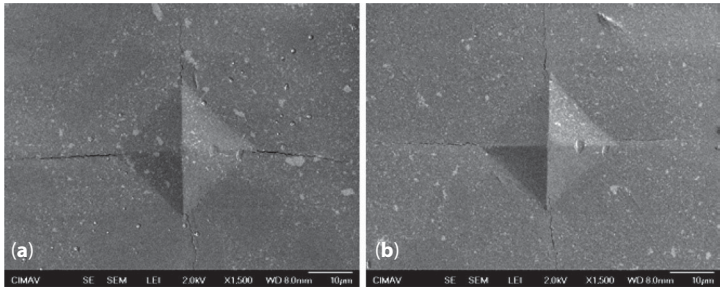

Figure 7.4 ZTA composites sintered by means of SPS at 1475 °C with additions of 0.01 wt% MWCNTs (a) and 0.01 wt% SWCNTs.

As mentioned previously, the addition of CNTs into the ceramic matrices affects positively or negatively the hardness. A very similar behavior occurs with the fracture toughness. Now, it is well known that Al_2O_3 and ZrO_2 ceramics have received significant scientific and technological attention for different applications due to their excellent room temperature strength, toughness, and wear resistance combined with a moderate hardness [83]. Nevertheless, the brittleness of these oxide ceramics and its combination has limited, no doubt, their potential use in structural and functional applications [109]. Despite these great difficulties, attempts have been made using different kinds of CNTs to devise ways of controlling the microstructure of ceramics to improve their fracture toughness [23, 110, 111] where the toughening behavior observed for most of the CNT-reinforced ceramic matrix is mainly linked to CNT crack bridging, CNT dispersion, and crack deflection [112, 113]. In the open literature, many reports related to the fracture toughness of ceramic nanocomposites with additions of different volume content of both SWCNTs and MWCNTs and consolidated by means of different sintering techniques have been published. However, it is observed in these investigations that a poor dispersion of CNTs within the alumina, zirconia, and combination of them could create weak regions where cracks can be originated, leading therefore, to decreasing of fracture toughness.

Since investigation reported by Zhan *et al.* [24], many attempts have been made to use CNTs as a toughening agent as reported [35, 40, 41]. Likewise, the most investigations focused on alumina-based composites, using either SWCNTs or MWCNTs, but conclusive demonstration of toughening has not been full achieved [114]. According to Galusek and Galusková [19], the results have been generally (but not unambiguously) disappointing for the composites containing MWCNTs and in other cases SWCNTs, where most authors observed only a marginal increase, or even a decrease of fracture toughness in comparison to monolithic alumina [104, 115]. However, significant improvement of fracture toughness in MWCNT–alumina composites, similar to that achieved by Zhan [24] has also been revealed [100, 116]. Contrary to the results of Zhan [24], several authors report no toughening effect in the Al_2O_3 nanocomposites with 10 vol.% of SWCNTs, which were as brittle as the monolithic alumina [95]. Despite the some controversial and contradictories results, most authors involved in this theme believe SWCNTs to be more efficient toughening agents than MWCNTs. It is very important to point out that this is sometimes explained by the fact that MWCNTs exhibit easy sliding between individual graphene sheets in a "sword and sheath" manner, with small ability to carry or transfer loads [9, 19]. Moreover, the MWCNTs have much lower bending strength and stiffness than the SWCNTs, which

makes them less efficient reinforcement aids [117]. This appreciation has been reported by Aguilar and Bocanegra [96] where fracture toughness values of 2.85 ± 0.42 and 3.0 ± 0.21 MPa.m$^{1/2}$ were obtained in Al_2O_3 reinforced with 0.1 wt% of SWCNTs and MWCNTs, respectively.

Different features of Al_2O_3 reinforced with 0.1 wt% of SWCNTs and MWCNTs can be seen in Figure 7.5a and b (from investigation Ref. [96]), respectively, corresponding to fracture surfaces. In Figure 7.5a, SWCNTs formed large bundles or agglomerates and long-torn MWCNTs (Figure 7.5b) located intergranularly (marked with dotted arrow), footprints on the grains after pullout of the CNT and pullout of MWCNTs are clearly observed. A detailed analysis of the fracture surface in Figure 7.5b revealed that some MWCNTs were deformed elastically until failure in a "sword in a sheath" mode (an axial fracture mechanism) where the outer nanotube fractures followed by pullout of the interior walls. This sword-in-sheath breaking mechanism is a common failure mechanism for MWCNTs loaded in this way [25], which is not present in SWCNTs. Commonly with MWCNTs, the diameter of the pullout MWCNT drastically slenderized toward their tip.

For fractured nanotubes [96], a critical force is required to pull the fractured wall ends through the outer wall(s). In reason of this, a uniformly applied force exercised on the outer MWCNT wall leads to both stick–slip behavior and an increase in the pullout force for fractured nanotubes [118]. Failure of nanotubes by this fracture mechanism suggests good interfacial stress transfer [119]. On the other hand, marginal improvement, or even deterioration, of flexural strength of CNT-reinforced nanocomposites is usually associated with the failure to achieve required dispersion of the CNTs and problems with densification, which result in the presence of residual porosity where both residual pores and residual bundles

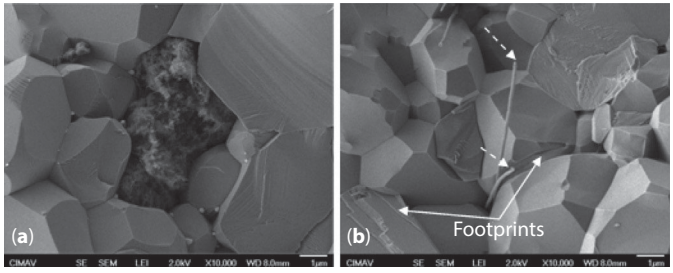

Figure 7.5 SEM fracture surfaces of Al_2O_3 ceramics with additions of 0.1 wt% SWCNTs (a) and MWCNTs (b) pressureless sintered at 1520 °C during 1 h. Arrow marks explained in text [96].

of agglomerated nanotubes act as strength defining defects and origins of fracture [19, 75]. From the point of view of improving the mechanical properties of alumina ceramics, an interesting option is represented by the so-called hybrid microstructure design, i.e., preparation of complex Al_2O_3–ZrO_2–CNT microstructures [94,106]. The addition of as little as 0.01 wt% of MWCNTs to conventionally sintered ZTA ceramics is reported to result in an increase of fracture toughness, with the MWCNT acting as an efficient toughening agent. Similar results observed in ZTA ceramics reinforced by the addition of up to 2 vol.% of MWCNT are attributed to synergy effect of transformation toughening with small contribution of crack bridging and CNT pullout [75]. With the purpose to employ the excellent elastic properties of CNTs and to achieve toughening in alumina and zirconia ceramic matrix composites, parameters such as a homogeneous dispersion and de-agglomeration of CNTs added into the matrix, a sintering process to a high density with the residual porosity eliminated, a strong interfacial bonding between CNTs and the matrix as well as the preservation of the CNTs at high temperatures must be taken into account [19, 120]. More recently, Bocanegra-Bernal *et al.* [21] reported the poor fracture toughness obtained with pure alumina reinforced with SDWCNTs, SWCNTs, and MWCNTs and the authors ask whether is it justifiable the effort to reinforce alumina and other ceramic composites with CNTs? Considering that although there are reports showing significant improvement on mechanical properties of alumina and other ceramics systems reinforced with CNTs, an inappropriate choice of CNTs or treatment then impairs the mechanical properties of the composites [19]. An important collection of a variety of mechanical properties of CNTs-reinforced alumina and zirconia-based ceramics is given in Table 7.5 from recent review by Ahmad *et al.* [16] with the addition of other research works [8, 70, 94, 96].

It is observed from Table 7.5 an inconsistency in the different results emphasizing that the observed discrepancies are consequence of the CNT dispersion methods as well as sintering process employed and techniques adopted for the characterization. Likewise and taking into account the wide availability of MWCNTs, the majority of the research works have been carried out using as reinforcement agents MWCNTs. The variety in mechanical properties could also be influenced by the toughening mechanisms imparted by the CNTs which can be different for each specific ceramic composite suggesting therefore that existing microscale mechanisms may not be fully applicable to all CNTs-ceramic systems [16].

Table 7.5 Properties of different CNTs-reinforced ceramics.

Reference	Matrix	CNTs contents	Relative density (%)	Hardness (GPa)	Flexural strength (MPa)	Fracture toughness (MPa $m^{1/2}$)
[41]	Al_2O_3	0	95.6	17.3	500	4.4
		0.5 wt% MWCNTs	99.2	16.8	685	5.9
		1 wt% MWCNTs	98.9	15.9	650	5.7
[109]	Al_2O_3	0	–	–	–	3.3
		3 wt% SWCNTs	–	–	–	7.9
[18]	Al_2O_3	0	97.7	–	326	3.08
		6 wt% MWCNTs	95.4	–	314	5.55
[65]	Al_2O_3	0	99.8	16	356	3.5
		2 wt% MWCNTs	99.5	18	402	6.8
		5 wt% MWCNTs	99.1	–	423	5.7
[67]	Al_2O_3	0	99.5	17.5	222	3.92
		0.15 vol.% MWCNTs	98.4	21.4	242	5.27
[68]	Al_2O_3	0	–	16.9	–	5.5
		1 vol.% MWCNTs	–	13.5	–	6.0
[121]	Al_2O_3	0	–	–	395	4.41
		20 vol.% MWCNTs	–	–	403	4.62
[122]	Al_2O_3	0	–	–	–	3
		1 wt% MWCNTs	–	–	–	5

(*Continued*)

Table 7.5 Cont.

Reference	Matrix	CNTs contents	Relative density (%)	Hardness (GPa)	Flexural strength (MPa)	Fracture toughness (MPa $m^{1/2}$)
[123]	Al_2O_3	0	–	15.71	–	3.24
		5 wt% MWCNTs	–	0.72	–	4.14
[124]	Al_2O_3	0	–	18.2	–	4.5
		2.5 wt% MWCNTs	–	15.75	–	11.4
[125]	Al_2O_3	0	99.9	22.9	–	3.54
		10 vol.% MWCNTs	97.4	11	–	2.76
[94]*	Al_2O_3+12 wt% ZrO_2	0	–	16.12	–	3.32
		0.01 wt% SWCNTs	–	17.10	–	3.25
[70]**	Al_2O_3+12 wt% ZrO_2	0.1 wt% MWCNTs	–	21.65	–	8.17
		0.1 wt% SWCNTs	–	20.27	–	6.04
[70]**	Al_2O_3+12 wt% ZrO_2	0.01 wt% MWCNTs	–	20.51	–	4.52
		0.01 wt% SWCNTs	–	20.31	–	7.66
[96]*	Al_2O_3	0.1 wt% MWCNTs	–	16.66	–	3.00
		0.1 wt% SWCNTs	–	15.55	–	2.85
[8]**	Al_2O_3+90% vol. ZrO_2	0.5 wt% MWCNTs	–	19.61	453	4.92
		2.0 wt% MWCNTs	–	17.03	356	4.31
[8]**	Al_2O_3	0	–	19.38	302	2.82

*Pressureless sintering, **SPS, MWCNTs, SWCNTs.
Adapted from Ref. [16] with permission.

7.5 Why SWCNTs? or Why MWCNTs?

From a variety of results obtained in CNTs-reinforced ceramics and although SWCNTs possess better properties than MWCNTs, the relative simplicity in preparation of MWCNTs and ease in its isolation and purification make it more economical for most applications including a homogeneous dispersion in ceramic matrix at low CNT concentrations (<2 wt%) to attain some improvement in mechanical properties [9]. SWCNTs are surely the CNTs variant with the most interesting combination of physical properties and a wide range of potential applications. They show world records in mechanical, electrical, and thermal properties. For most of the time, there was no guarantee for a sufficient availability of this outstanding material. In the meantime, however, increasingly larger quantities of SWCNTs have entered the market, which enable the development of attractive applications [46]. However, the dispersion of SWCNTs is more difficult, and this issue remains the bane to achieve a homogeneous distribution of the CNTs into the ceramic matrix and therefore, to obtain a ceramic composite with improved mechanical properties.

Unfortunately, SWCNTs are always held together in rope form due to their extremely small dimension and vdW attraction, thus their strength can neither be exploited nor measured due to facile inter-SWCNT sliding under load. However, according to Estili and Kawasaki [116] if several SWCNTs are concentrically nested in a confined space, the sliding issue can be resolved and the SWCNTs may share the applied tensile load to realize nanometer-scale materials remarkably stronger than the individual SWCNTs. However, MWCNTs suffer from extremely weak vdW-based interwall shear resistance (ISR) [126] allowing only the defective outermost wall to receive and carry the load [78]. A strong ISR could be created throughout the MWCNT structure but regrettably the appropriate technology to address this challenge is absent, which leads to a fundamental lack of knowledge about the resultant mechanical responses. A strategy to engineer strong ISR deeply in radial direction and uniformly along the entire length of the MWCNT in an almost nondestructive way (preserving the in-wall integrity) was implemented and investigated the tensile failure load and failure mechanism [116]. In reason of the aforementioned and with continuously decreasing cost of CNTs as result of the ability to synthesize in high yield by different techniques, the efforts to incorporate them in the a variety of ceramic systems is likely to accelerate [127]. Nevertheless, the final price of MWCNTs is still lower than that of SWCNTs.

Indeed, it is important to take in mind that the mechanical, electrical, and thermal properties of CNTs depend strongly on their structure and

considering that they are grown at very high temperatures (3000–4000 °C), the CNTs produced by arc discharge have a structure close to ideal because contain far less defects than CNTs produced by any other method. In reason of that, they are nowadays the best choice for every application where high performance is essential. Generally speaking, the advantage of MWCNTs over SWCNTs is that their outer surface can be functionalized without affecting the inner layers, thereby preserving the mechanical properties of the whole structure. The suitable choice of CNTs as reinforcement in alumina and zirconia-based ceramics along with the dispersion method and sintering process is of paramount importance in order to obtain ceramic composites taking advantage of the ability of CNTs to induce toughening mechanisms such as crack bridging and CNTs pullout in combination with crack deflection reaching in most cases important improvement in mechanical properties. Therefore, parameters of interest including optical properties, size (inner diameter, outer diameter, length, and number of shells), purity, type of defects, topology, and surface area [58] of the different types of CNTs that will be used are very important for designing new MWCNT-based materials with the desired final properties in order to obtain optimum performance. However, in spite of good choice of CNTs, the final mechanical properties as well as the distribution of CNTs within the microstructure of the ceramic composite can reveal surprising features. As example, Bocanegra-Bernal *et al.* [21] in a recent paper reported detrimental fracture toughness values in pure alumina with additions of different kinds of CNTs due to the poor dispersion of CNTs which leads to a variety of microstructural features as consequence of inhomogeneous distribution of the CNTs into the alumina matrix as can be seen in Figure 7.6 as well as other characteristics of the used CNTs.

From Figure 7.6, it is evident the variety of effects which can have the different types of CNTs on the microstructural evolution in the ceramic matrix composite during the sintering which in turn produce some final controversial results for the mechanical properties (hardness, fracture toughness, and flexural strength mainly) of these ceramic composites in accordance with Table 7.5.

It is important to note that Figure 7.6a–d corresponds to different kinds of MWCNTs but due to its characteristics such as outer diameter, inner diameter, length, specific surface area, and purity, among others, could produce diverse microstructural behavior resulting in different fracture modes. On the other hand, when the alumina is reinforced with SDWCNTs (Figure 7.6e) and MWCNTs (Figure 7.6f), the fracture surface and the distribution and location of the CNTs is completely different to the shown in the microstructures in Figure 7.6a–d. Judging from fracture surfaces in Figure 7.6a–f, we

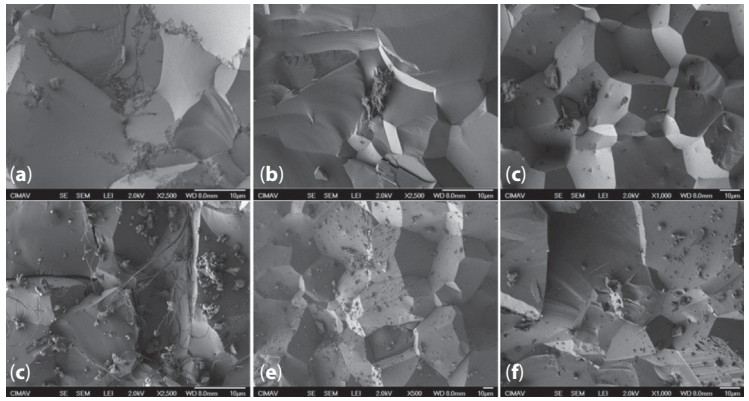

Figure 7.6 SEM fracture surfaces of pure Al_2O_3 reinforced with MWCNTs: MW1 (a), MW2 (b), MW3 (c), MW CIMAV (d), SDWCNT (SD) (e), and SWCNTs (SW) (f). Characteristics of these CNTs can be shown in Table S1 in Supplementary information Ref. [21].

would think that CNTs with large specific surface area and lower aspect ratio would lead to a degradation of the strengthening because the CNTs could be embedded within the grains and have little effect on strengthening due to its short length and therefore, inefficient connection between grains (for example, Figure 7.6e and f) affecting negatively an improvement in the fracture toughness during fracture process [65]. In this context, we considerer that a priori knowledge to distinguish MWCNTs from SWCNTs and SDWCNTs should be required in order to tailoring possible resulting microstructure and mechanical properties of ceramic systems under different dispersion and sintering processes commonly used such as shown in Table 7.3. It is also speculated that there will be a feasible correlation between the final grain size, surface area and aspect ratio of CNTs to obtain an effective reinforcement for achieving superior mechanical performance with high fracture toughness values. We conclude that is very difficult to choose the type of CNTs to be used as reinforcement agents considering that la interaction between ceramic matrix and the specific CNTs (SWCNTS or MWCNTs) can be different for each ceramic composite.

7.6 Conclusions

The exceptional mechanical and physical properties of CNTs along with their low density make this new form of carbon an excellent candidate to be added in composite as reinforcement agents. However, during last 10 years,

the processing routes, microstructural characteristics as well as mechanical and functional properties of CNTs have received an intensive study. It is noteworthy that although in several cases the scientific community has reported significant improvement of mechanical properties (mainly hardness, fracture toughness, and flexural strength), the results obtained with Al_2O_3, ZrO_2, and a combination of both as well as other ceramics systems reinforced with both SWCNTs and MWCNTs remain controversial and can arise from different dispersion techniques, sintering processes, and testing techniques used for their characterization. In accordance to some published reports, CNTs-reinforced ceramics show only a marginal increasing in mechanical properties meanwhile a decreasing of the fracture toughness from 8% to 40% over monolithic Al_2O_3 was reported with the addition of CNTs [21]. Even if some problems of reinforcing MWCNTs into alumina-based ceramics have been partially solved; the addition of SWCNTs or alternatively SDWCNTs still carries serious questions and a full understanding about thermo-mechanical behavior of these ceramic nanocomposites reinforced with both SWCNTs and MWCNTs, requires a wide knowledge of the elastic and fracture properties of CNTs as well as of interactions at the nanotube/matrix interface. However, in alumina, ZTA, and zirconia ceramics reinforced with CNTs (pure zirconia is rarely reinforced with CNTs and the literature related with this theme is scarce) where the fracture toughness was increased, the mechanisms associated with toughening behavior in reinforced composites have been exhibited: crack deflection, crack bridging, and CNT pullout. However, there are still many problems to overcome before the full potential of CNTs containing ceramic composites can be realized.

The difficulty to choose between a CNT and another to obtain a ceramic composite with improved mechanical properties leads to explore in depth how to control the interface between the CNTs and the ceramic matrix in order to understand the mechanical performance considering that in a CNT-reinforced ceramic material, interface behavior is expected to be significantly different from conventional carbon fibers because of the unique chemical bonding inherent in CNTs. For example, even using the same contents (vol.% or wt%) and the same type of CNTs into the ceramic matrix of two different kinds of alumina, the expected values of fracture toughness, and/or hardness may differ from each other favorably or unfavorably, particularly for higher fractions of CNTs. Generally speaking and taking into account the pros and cons of the different types of CNTs, it is very difficult to speculate what could be the optimal amount and type of CNTs to be added to ceramics based on alumina, zirconia, or combination of them with the purpose to reach higher fracture toughness. In spite of that SWCNTs are more commonly used in order to improve the mechanical

properties for the case of alumina-based ceramics, the investigations have shown that high-quality MWCNTs could exhibit very easy interwall sliding, with inner graphitic walls able to be extracted from outer walls in a 'sword-and-sheath' mechanism at low applied forces improving in some cases, the mechanical properties compared to SWCNTs [23]. Judging by the results reported by the scientific literature, the homogeneous dispersion of CNTs into the ceramic matrices is the main issue to be solved being essential to develop efficient and economical processing methods that enable homogeneous dispersion of different types of CNTs in the appropriate matrices. Indeed, it is demonstrated that the variety of results on mechanical properties can be attributed in great measure to the dispersion. Further research on these approaches will almost certainly lead to better materials such as those based in alumina and zirconia. As a final remark, it is important to point out that selection of kind of CNTs as reinforcement additive for a specific ceramic must be selected after experimental trials since prediction of results from characteristics of raw materials (kind of CNTs even knowing its diameter, length and agglomeration state, and ceramic powders) is not an option, considering that dispersion of CNTs is not an easily controllable and reproducible process and final properties will depend of the way of CNTs dispersion on ceramic matrix.

Acknowledgments

The authors wish to thank Wilber Antúnez and Cesar Leyva for SEM and TEM assistance, respectively.

References

1. Peigney, A., Laurent, Ch., Flahaut, E., Rousset, A., Carbon nanotubes in novel ceramic matrix nanocomposites. *Ceram. Int.* 26, 677, 2000.
2. Mao, D., Improving mechanical properties of nanocomposites using carbon nanotubes. *The Society for the Advancement of Material and Process Engineering (SAMPE)*, paper 2009, Baltimore MD-May 18–21 2009.
3. Iijima, S., Helical microtubules of graphitic carbon. *Nature* 354, 56, 1991.
4. Radushkevich, L.V., Lukyanovich, V.M., Carbon structure formed under thermal decomposition of carbon monoxide on iron. *Sov. J. Phys. Chem.* 26, 88, 1952.
5. Oberlin, A., Endo, M., Koyana, T., Filamentous growth of carbon through benzene decomposition. *J. Cryst. Growth* 32, 335, 1976.

6. Extended abstracts and program/14th Biennial Conference on Carbon: June 25–29, 1979, the Pennsylvania State University, University Park, Pennsylvania
7. Abrahamson, J., Wiles, P.G., Rhoades, B.L., Structure of Carbon Fibres Found on Carbon Arc Anodes. 14th Biennial Conference on Carbon June 25–29, 1979; Penn. State Univ., University Park, Penn., USA. 254-5. (republished in *Carbon* 37, 1873, 1999)
8. Akin, I., Investigation of the microstructure, mechanical properties and cell viability of zirconia toughened alumina composites reinforced with carbon nanotubes. *J. Ceram. Soc. Jpn*. 123, 405, 2015.
9. Samal, S.S., Bal, S., Carbon nanotube reinforced ceramic matrix composites—a review. *J. Miner. Mater. Charact. Eng.* 7, 355, 2008.
10. Mazzuccoa, D., Squizzatoa, D., Mantovania, S., Canonicob, P., Nanotoughened carbon fibers composite materials. SAATI Group (SEAL S.p.A.), a partner of Nanoledge, 2009.
11. Thostenson, E.T., Ren, Z., Chou, T-W., Advances in the science and technology of carbon nanotubes and their composites: a review. *Compos. Sci. Technol*. 61, 1899, 2001.
12. Peigney, A., Legorreta García, F., Estournes, C., Weibel, A., Laurent, Ch., Toughening and hardening in double-walled carbon nanotube/nanostructured magnesia composites. *Carbon* 48, 1952, 2010.
13. Cornwell-Mott, B., Effect of perfectly aligned CNTs under cohesive crack bridging in adhesive joints. Master Thesis, Department of Mechanical and Industrial Engineering University of Toronto, 2010.
14. Baughman, R.H., Zakhidov, A., de Heer, W.A., Carbon nanotubes-the route toward applications. *Science* 297, 787, 2002.
15. Laurent, C., Peigney, A., Dumortier, O., Rousset, A., Carbon nanotubes-Fe-alumina nanocomposites. Part II: Microstructure and mechanical properties of the hot-pressed composites. *J. Eur. Ceram. Soc*. 18, 2005, 1998.
16. Ahmad, I., Yazdani, B., Zhu, Y., Recent advances on carbon nanotubes and grapheme reinforced ceramic nanocomposites. *Nanomaterials* 5, 90, 2015.
17. Padture, N.P., Multifunctional composites of ceramics and single-walled carbon nanotubes. *Adv. Mater.* 21, 1767, 2009.
18. Fan, Y., Wang, L., Li, J., Sun, S., Chen, F., Chen, L., Jiang, W., Preparation and electrical properties of grapheme nanosheet/Al_2O_3 composites. *Carbon* 48, 1743, 2010.
19. Galusek, D., Galuskova, D., Alumina matrix composites with non-oxide nanoparticle addition and enhanced functionalities. *Nanomaterials* 5, 115, 2015.
20. Hayashi, T., Endo, M., Carbon nanotubes as structural material and their application in composites. *Compos. B* 42, 2151, 2011.
21. Bocanegra-Bernal, M.H., Dominguez-Rios, C., Echeberria, J., Reyes-Rojas, A., Garcia-Reyes, A., Aguilar-Elguezabal, A., Spark plasma sintering of multi-, single/double- and single-walled carbon nanotube-reinforced alumina composites: is it justifiable the effort to reinforce them? *Ceram. Int*. 42, 2054, 2016.

22. Duszova, A., Dusza, J., Tomasek, K., Blugan, G., Keubler, J., Microstructure and properties of carbon nanotube/zirconia composite. *J. Eur. Ceram. Soc*. 28, 1023, 2008.
23. Bocanegra-Bernal, M.H., Aguilar-Elguézabal, A., Echeberria, J., Carbon nanotubes (CNTs) and mechanical properties of Al_2O_3 and zirconia toughened alumina (ZTA) composites reinforced by them: a review. *Recent Res. Devel. Mat. Sci*. 9, 45, 2012.
24. Zhan, G.D., Kuntz, J.D., Wan, J., Mukherjee, A.K., Single-wall carbon nanotubes as attractive toughening agents in alumina-based composites. *Nat. Mater.* 2, 38, 2003.
25. Wang, X., Padture, N.P., Tanaka, H., Contact-damage-resistant ceramic/single-wall carbon nanotubes and ceramic/graphite composites. *Nat. Mater*. 3, 539, 2004.
26. Ma, R.Z., Wu, J., Wei, B.Q., Liang, J., Wu, D.H., Processing and properties of carbon nanotube/nano-SiC ceramic. *J. Mater. Sci*. 33, 5243, 1998.
27. Siegel, R.W., Chang, S.K., Ash, B.J., Stone, J., Ajayan, P.M., Doremus, R.W., Schadler, L.S., Mechanical behaviour of polymer and ceramic matrix nanocomposites. *Scr. Mater*. 44, 2061, 2001.
28. Sugai, T., Yoshida, H., Shimada, T., Okazaki, T., Shinohara, H., New synthesis of high-quality double-walled carbon nanotubes by high-temperature pulsed arc discharge. *Nano Lett*. 3, 769, 2003.
29. Wang, H., Zhou, W., Ho, D.L, Winey, K.I., Fischer, J.E., Glinka, C.J., Hobbie, E.K., Dispersing single-walled carbon nanotubes with surfactants: a small angle neutron scattering study. *Nano Lett*. 9, 1789, 2004.
30. Islam, M.F., Rojas, E., Bergey, D.M., Johnson, A.T., Yodh, A.G., High weight fraction surfactant solubilization of single-wall carbon nanotubes in water. *Nano Lett*. 3, 269, 2003.
31. Thess, A., Lee, R., Nikolaev, P., Dai, H., Petit, P., Robert, J., Xu, Ch., Hee, Lee., Kim, S.G., Rinzler, A.G., Colbert, D.T., Scuseria, G.E., Tomanek, D., Fischer, J.E., Smalley, R.E., Crystalline ropes of metallic carbon nanotubes. *Science* 273, 483, 1996.
32. Fan, X., Buczko, R., Puretzky, A.A., Geohegan, D.B., Howe, J.Y., Pantelides, S.T., Pennycook, S,J., Nucleation of single-walled carbon nanotubes. *Phys. Rev. Lett*. 90, 145501-1, 2003.
33. Bethune, D.S., Kiang, C.H., Devries, M.S., Gorman, G., Savoy, R., Vazquez, J., Cobalt-catalyzed growth of carbon nanotubes with single atomic-layer walls. *Nature* 363, 605, 1993.
34. Iijima, S., Ichihashi, T., Single-shell carbon nanotubes of 1-nm diameter. *Nature* 363, 603, 1993.
35. Coleman, J.N., Khan, U., Blau, W.J., Gun'ko, Y.K., Small but strong: a review of the mechanical properties of carbon nanotube–polymer composites. *Carbon* 44, 1624, 2006.
36. Liang, F., Chen, B., A review on biomedical applications of single-walled carbon nanotubes. *Curr. Med. Chem.* 17, 10, 2010.

37. Ding, R.G., Lu, G.Q., Yan, Z.F., Wilson, M.A., Recent advances in the preparation and utilization of carbon nanotubes for hydrogen storage. *Nanosci. Nanotechnol*. 1, 7, 2001.
38. Collins, P.G., Arnold, M.S., Avouris, Ph., Engineering carbon nanotubes and nanotube circuits using electrical breakdown. *Science* 292, 706, 2001.
39. Mukhopadhyay, A., Chu, B.T.T., Green, M.L.H., Todd, R.I., Understanding the mechanical reinforcement of uniformly dispersed multiwalled carbon nanotubes in alumino-borosilicate glass ceramic. *Acta Mater.* 58, 2685, 2010.
40. Manchado, M.A.L., Valentini, L., Biagiotti, J., Kenny, J.M., Thermal and mechanical properties of single-walled carbon nanotubes-polypropylene composites prepared by melt processing. *Carbon* 43, 1499, 2005.
41. Yamamoto, G., Omori, M., Hashida, T., Kimura, H., A novel structure for carbon nanotube reinforced alumina composites with improved mechanical properties. Nanotechnology 19, 315708, 2008.
42. Méténier, K., Bonnamy, S., Béguin, F., Journet, C., Bernier, P., de la Chapelle, L.M., Chauvet, O., Lefrant, S., Coalescence of single walled nanotubes and formation of multi-walled carbon nanotubes under high temperature treatments. *Carbon* 40, 1765, 2002.
43. [43]Michael, F., De Volder, L., Tawfick, S.H., Baughman, R.H., Hart, A.J., Carbon nanotubes: present and future commercial applications. *Science* 339, 535, 2013.
44. Collins, P.G., Avouris, P., Nanotubes for electronics. *Sci. Am*. 283, 38, 2000.
45. Abdalla, S., Al-Marzouki, F., Al-Ghamdi, A.A., Abdel-Daiem, A., Different technical applications of carbon nanotubes. *Nanoscale Res. Lett.* 10, 358, 2015.
46. Fraunhofer Institute for Material and Beam Technology IWS. Single-wall carbon nanotubes SWCNT. High-quality carbon nanotubes and their applications. Technical brochure. http://www.iws.fraunhofer.de/content/dam/iws/en/documents/publications/product_sheets/500-3_swcnt_en.pdf. 2014.
47. Eatemadi, A., Daraee, H., Karimkhanloo, H., Kouhi, M., Zarghami, N., Akbarzadeh, A., Abasi, M., Hanifehpour, Y., Joo, S.W., Carbon nanotubes: properties, synthesis, purification, and medical applications. *Nanoscale Res. Lett*. 9, 393, 2014.
48. Carbon nanotube. (2008, April 24). In Wikipedia, The Free Encyclopedia. April 28, 2008, from http://en.wikipedia.org/w/index.php?title= Carbon_nanotube&oldid=207910667
49. Terrones, M., Science and technology of the twenty-first century: synthesis, properties, and applications of carbon nanotubes. *Annu. Rev. Mater. Res*. 33, 419, 2003.
50. Feldman, A.K., Steigerwald, M.L., Guo, X., Nuckolls, C., Molecular electronic devices based on single-walled carbon nanotube electrodes. *Acc. Chem. Res.* 41, 1731, 2008.
51. Umeyama, T., Imahori, H., Carbon nanotube-modified electrodes for solar energy conversion. *Energy Environ. Sci.* 1, 120, 2008.
52. Qu, L., Du, F., Da, L., Preferential syntheses of semiconducting vertically aligned single-walled carbon nanotubes for direct use in FETs. *Nano Lett*. 8, 2682, 2008.

53. Agüí, L., Yáñez-Sedeño, P., Pingarrón, J.M., Role of carbon nanotubes in electroanalytical chemistry. *Anal. Chim. Acta* 622, 11, 2008.
54. Vairavapandian, D., Vichchulada, P., Lay, M.D., Preparation and modification of carbon nanotubes: review of recent advances and applications in catalysis and sensing. *Anal. Chim. Acta* 626, 119, 2008.
55. Yan, J., Zhou, H., Yu, P., Su, L., Mao, L., Rational functionalization of carbon nanotubes leading to electrochemical devices with striking applications. *Adv. Mater*. 20, 2899, 2008.
56. Star, A., Kauffman, D.R., Carbon nanotube gas and vapor sensors. *Angew. Chem. Int. Ed*. 47, 6550, 2008.
57. Eklund, P., Ajayan, P., Blackmon, R., Hart, A.J., Kong, J., Pradhan, B., Rao, A., Rinzler A., WTEC international assessment of research and development of carbon nanotube manufacturing and applications. Technical Report. World Technology Evaluation Center, Inc., 2007.
58. Lehman, J.H., Terrones, M., Mansfield, E., Hurst, K.E., Meunier, V., Evaluating the characteristics of multiwall carbon nanotubes. *Carbon* 49, 2581, 2011.
59. Hirlekar, R., Yamagar, M., Garse, H., Vij, M., Kadam, V., Carbon nanotubes and its applications: a review. *Asian J. Pharm. Clin. Res*. 2, 17, 2009.
60. Wang, H., Chhowalla, M., Sano, N., Jia, S., Amaratunga, G.A.J., Large-scale synthesis of single-walled carbon nanohorn by submerged arc. Institute of Physics Publishing, *Nanotechnology* 15, 546, 2004.
61. Anazawa, K., Shimotanim K., Manabe, C., Watanabe, H., Shimizu, M., High-purity carbon nanotube synthesis method by an arc discharging in magnetic field. *App. Phys. Lett*. 81, 739, 2002.
62. Lee, S.J., Baik, H.K., Yoo, J-E., Han, J.H., Large scale synthesis of carbon nanotubes by plasma rotating arc discharge technique. *Diamond Relat. Mater*. 11, 914, 2002.
63. Bhushan, B., Introduction to carbon nanotubes, Chapter 3. In: Bhushan B, editor. Springer Handbook of Nanotechnology. Springer; 2007, pp. 47–118.
64. Zhang, M., Li, J., Carbon nanotube in different shapes. *Mater. Today* 12, 12, 2009.
65. Ahmad, I., Kennedy, A., Zhu, Y.Q., Carbon nanotubes reinforced Al_2O_3 nanocomposites: mechanical properties and interfacial investigations. *J. Comput. Sci. Technol*. 70, 1199, 2010.
66. Zhang, S.C., William, G., Hilmas, G.E., Edward, J.Y., Pressureless sintering of carbon nanotube-Al_2O_3 composites. *J. Eur. Ceram. Soc*. 30, 1373, 2010.
67. Sarkar, S., Das, P.K., Microstructure and physic-mechanical properties of pressure-less sintered multi-walled carbon nanotubes/Al_2O_3 nanocomposites. *Ceram. Int*. 38, 423, 2012.
68. Michalek, M., Lkova, M., Sedla, J., Galusek, D., Al_2O_3/MWCNTs composites by aqueous slip casting and pressureless sintering. *Ceram. Int*. L39, 6543, 2013.
69. Kumari, L., Zhang, T., Du, G.H., Li, W.Z., Wang, Q.W., Datye, A., Wu, K.H., Synthesis, microstructure and electrical conductivity of carbon nanotube–alumina nanocomposites. *Ceram. Int*. 35, 1775, 2009.

70. Echeberria, J., Rodríguez, N., Vleugels, J., Vanmeensel, K., Reyes-Rojas, A., Garcia-Reyes, A., Domínguez-Rios, C., Aguilar-Elguézabal, A., Bocanegra-Bernal MH., Hard and tough carbon nanotube-reinforced zirconia-toughened Al_2O_3 composites prepared by spark plasma sintering. *Carbon* 50, 706, 2012.
71. Kim, S.W., Chung, W.S., Sohn, K.S., Son, C.Y., Lee, C., Improvement of flexure strength and fracture toughness in alumina matrix composites reinforced with carbon nanotubes. *Mater. Sci. Eng. A* 517, 293, 2009.
72. Bakhsh, N., Khalid, F.A., Hakeem, A.S., Effect of sintering temperature on densification and mechanical properties of pressureless sintered CNT–Al_2O_3 nanocomposites. *Mater. Sci. Eng.* 60, 012059, 2014.
73. Li, T., Improving the antistatic ability of polypropylene fibers by inner antistatic agent filled with carbon nanotubes. *Comput. Sci. Tech*. 64, 2089, 2004.
74. Hanzel, O., Sedlácek, J., Sajgalík, P., New approach for distribution of carbon nanotubes in Al_2O_3 matrix. *J. Eur. Ceram. Soc.* 34, 1845, 2014.
75. Michalek, M., lkova, M., Sedla, J., Galusek, D., Mechanical properties and electrical conductivity of Al_2O_3/MWCNT and Al_2O_3/zirconia/MWCNT composites. *Ceram. Int.* 40, 1289, 2014.
76. Poyato, R., Gallardo-López, A., Gutiérrez-Mora, F., Morales-Rodríguez, A., Muñoz, A., Domínguez-Rodríguez, A., Effect of high SWNT content on the room temperature mechanical properties of fully dense 3YTZP/SWNT composites. *J. Eur. Ceram. Soc.* 34, 1571, 2014.
77. Yakobson, B.I., In Fullerenes-Recent Advances in the Chemistry and Physics of Fullerenes and Related Materials, pp. 549–560, R.S. Ruoff and K.M. Kadish, Eds. (Electrochemical Society, Pennington, NJ, 1997.
78. Yu, M.F., Lourie, O., Dyer, M.J., Moloni, K., Kelly, T.F., Ruoff, R.S., Strength and breaking mechanism of multiwalled carbon nanotubes under tensile load. *Science* 287, 637, 2000.
79. Yu, M.F., Files, B.S., Arepalli, S., Ruoff, R.S., Tensile loading of ropes of single wall carbon nanotubes and their mechanical properties. *Phys. Rev. Lett*. 84, 5552, 2000.
80. Guimaraes, F.A.T., Silva, K.L., Trombini, V., Pierri, J.J., Rodrigues, J.A., Tomasi, R., Pallone, E.M.J.A., Correlation between microstructure and mechanical properties of Al_2O_3/ZrO_2 nanocomposites. *Ceram. Int*. 35, 741, 2009.
81. Duszová, A., Dusza, J., Tomásek, K., Blugan, G., Kuebler, J., Microstructure and properties of carbon nanotube/zirconia composite. *J. Eur. Ceram. Soc*. 28, 1023, 2008.
82. Zhu, Y-F., Shi, L., Liang, J., Hui, D., Lau, K-T., Synthesis of zirconia nanoparticles on carbon nanotubes and their potential for enhancing the fracture toughness of alumina ceramics. *Compos. B* 39, 1136, 2008.
83. Sarkar, D., Adak, S., Mitra, N.K., Preparation and characterization of an Al_2O_3-ZrO_2 nanocomposite, Part I: Powder synthesis and transformation behaviour during fracture. *Compos. A* 38, 124, 2007.

84. Kerkwijk, B., Winnbst, L., Mulder, E.J., Verweij, H., Processing of homogeneous zirconia-toughened alumina ceramics with high dry-sliding wear resistance. *J. Am. Ceram. Soc.* 82, 2087, 1999.
85. Peigney, A., Rul, S., Lefevre-Schlick, F., Laurent, C., Densification during hot-pressing of carbon nanotube metal-ceramic composites. *J. Eur. Ceram. Soc*. 27, 2183, 2007.
86. Cho, J., Boccaccini, A.R., Shaffer, M.S.P., Ceramic matrix composites containing carbon nanotubes. *J. Mater. Sci.* 44, 1934, 2009.
87. Bakshi, S.R., Lahiri, D., Agarwal, A., Carbon nanotube reinforced metal matrix composites—a review. *Int. Mater. Rev*. 55, 41, 2010.
88. Thostenson, E.T., Li, Ch., Chou, T-W., Nanocomposites in context. *Compos. Sci. Technol*. 65, 491, 2005.
89. Robertson, D.H., Brenner, D.W., Mintmire, J.W., Energetics of nanoscale graphitic tubules. *Phys. Rev. B* 45, 12592, 1992.
90. Krishnan, A., Dujardin, E., Ebbesen, T.W., Yianilos, P.N., Treacy, M.M.J., Young's modulus of single-walled nanotubes. *Phys. Rev. B* 58, 14013, 1998.
91. Meguid, S.A., Wernik, J.M., Cheng, Z.Q., Atomistic-based continuum representation of the effective properties of nano-reinforced epoxies. *Int. J. Solids Struct*. 47, 1723, 2010.
92. Smart, S.K., Cassady, A.L., Lu, G.Q., Martin, D.J., The biocompatibility of carbon nanotubes. *Carbon* 44, 1034, 2006.
93. Hilding, J., Grulke, E.A., Zhang, Z.G., Lockwood, F., Dispersion of carbon nanotubes in liquids. *J. Dispers. Sci. Technol*. 24, 1, 2003.
94. Bocanegra-Bernal, M.H., Echeberria, J., Ollo, J., Garcia-Reyes, A., Domínguez-Rios, C., Reyes-Rojas, A., Aguilar-Elguezabal, A., A comparison of the effects of multi-wall and single-wall carbon nanotube additions on the properties of zirconia toughened alumina composites. *Carbon* 49, 1599, 2011.
95. Inam, F., Peijs, T., Reece, M.J., The production of advanced fine-grained alumina by carbon nanotube addition. *J. Eur. Ceram. Soc.* 31, 2853, 2011.
96. Aguilar-Elguézabal, A., Bocanegra-Bernal, M.H., Fracture behaviour of α-Al_2O_3 ceramics reinforced with a mixture of single-wall and multi-wall carbon nanotubes. *Compos. B* 60, 463, 2014.
97. Ahmad, I., Unwin, M., Cao, H., Chen, H., Zhao, H., Kennedy, A., Zhu, Y.Q., Multi-walled carbon nanotubes reinforced Al_2O_3 nanocomposites: Mechanical properties and interfacial investigations. *Compos. Sci. Technol*. 70, 1199, 2010.
98. Jiang, D., Thomson, K., Kuntz, J.D., Agerb, J.W., Mukherjee, A.K., Effect of sintering temperature on a single-wall carbon nanotube-toughened alumina-based nanocomposite. *Scr. Mater.* 56, 959, 2007.
99. Mo, Ch.B., Cha, S.I., Kim, K.T., Lee, K.H., Hong, S.H., Fabrication of carbon nanotube reinforced alumina matrix nanocomposite by sol-gel process. *Mater. Sci. Eng. A* 385, 124, 2005.
100. Ahmad, I., Cao, H., Chen, H., Zhao, H., Kennedy, A., Zhu, Y.Q., Carbon nanotube toughened aluminium oxide nanocomposite. *J. Eur. Ceram. Soc.* 30, 865, 2010.

101. Jinpeng, F., Zhao, D., Song, J., Preparation and microstructure of multi-walled carbon nanotubes toughened Al_2O_3 composites. *J. Am. Ceram. Soc.* 89, 750, 2006.
102. Piconi, C., Maccauro, G., Muratori, F., Brach Del Prever, E., Alumina and zirconia ceramics in joint replacements. *J. Appl. Biomater. Biomech*. 1, 19, 2003.
103. Echeberria, J., Ollo, J., Bocanegra-Bernalm M.H., Garcia-Reyes, A., Domínguez-Rios, C., Aguilar-Elguezabal, A., Reyes-Rojas, A., Sinter and hot isostatic pressing (HIP) of multi-wall carbon nanotubes (MWCNTs) reinforced ZTA nanocomposite: Microstructure and fracture toughness. *Int. J. Refract. Met. H.* 28, 399, 2009.
104. Sun, J., Gao, L., Jin, X.H., Reinforcement of alumina matrix with multi-walled carbon nanotubes. *Ceram. Int*. 31, 893, 2005.
105. An, J.W., Lim, D.S., Effect of carbon nanotube additions on the microstructure of hot-pressed alumina. *J. Ceram. Process. Res*. 3, 201, 2002.
106. Ahmad, K., Pan, W., Hybrid composites: a new route towards tougher alumina ceramics. *Compos. Sci. Technol*. 68, 1321, 2008.
107. Chan, S.I., Kim, K.T., Lee, K.H., Mo, Ch.B., Hong, S.H., Strengthening and toughening of carbon nanotube reinforced alumina nanocomposite fabricated by molecular level mixing process. *Scr. Mater.* 53, 793, 2005.
108. Burghard, Z., Schon, D., Garstel, P., Bill, J., Aldinger, F., Polymer-derived Si-C-N ceramics reinforced by single-wall carbon nanotubes. *Int. J. Mater. Res*. 97, 1667, 2006.
109. Zhan, G-D., Mukherjee, A.K., Processing and characterizations of nanoceramic composites with interesting structural and functional properties. *Rev. Adv. Mater. Sci*. 10, 185, 2005.
110. Balani, K., Bakshi, S.R., Chen, Y., Laha, T., Agarwal, A., A role of powder treatment and carbon nanotube dispersion in the fracture toughening of plasma-sprayed aluminium oxide–carbon nanotube nanocomposite. *J. Nanosci. Nanotechnol*. 7, 3553, 2007.
111. Curtin, W.A., Sheldon, B.W., CNT-reinforced ceramics and metals. *Mater. Today* 7, 44, 2004.
112. Bai, J.B., Vignes, J-L., Fournier, T., Michel, D., A novel method for preparing preforms of porous Alumina and carbon nanotubes by CVD. *Adv. Eng. Mater.* 4, 701, 2002.
113. Xia, Z., Riester, L., Curtin, W.A., Li, H., Sheldon, B.W., Liang, J., Chang, B., Xu, J.M., Direct observation of toughening mechanisms in carbon nanotube ceramic matrix composites. *Acta Mater.* 52, 931, 2004.
114. Fu, Y.Q., Gu, Y.W., Du, H.J., SiC whisker toughened Al_2O_3-(Ti, W)C ceramic matrix composites. *Scr. Mater.* 44, 111, 2001.
115. Cha, S.I., Kim, K.T., Lee, K.H., Mo, C.B., Hong, S.H., Strengthening and toughening of carbon nanotube reinforced alumina nanocomposite fabricated by molecular level mixing process. *Scr. Mater*. 53, 793, 2005.
116. Estili, M., Kawasaki, A., Engineering strong intergraphene shear resistance in multi-walled carbon nanotubes and dramatic tensile improvements. *Adv. Mater.* 22, 607, 2010.

117. Wong, E.W., Sheehan, P.E., Liebert, C.M., Nanobeam mechanics: elasticity, strength, and toughness of nanorods and nanotubes. *Science* 277, 1971, 1997.
118. Xia, Z., Curtin, W.A., Pullout forced and friction in multiwall carbon nanotubes. *Phys. Rev. B* 69, 233408-1, 2004.
119. Estili, M., Kawasaki, A., Sakamoto, H., Mekuchi, Y., Kuno, M., Tsukada, T., The homogeneous dispersion of surfactantless, slightly disordered, crystalline, multiwalled carbon nanotubes in α-alumina ceramics for structural reinforcement. *Acta Mater*. 56, 4070, 2008.
120. Fu, Z.Y., Huang, L.W., Zhang, J.Y., Todd, R., Ultra-fast densification of CNTs reinforced alumina based on combustion reaction and quick pressing. *Sci. China Technol. Sci*. 55, 484, 2012.
121. Estili, M., Kawasaki, A., Sakka, Y., Highly concentrated 3D macrostructure of individual carbon nanotubes in a ceramic environment. *Adv. Mater.* 24, 4322, 2012.
122. Martinlli, J.R., Sene, F.F., Electrical resistivity of ceramic-metal composite materials: application in crucibles for induction furnaces. *Ceram. Int*. 26, 325, 2000.
123. Puchy, V., Hvizdos, P., Dusza, J., Kovac, F., Inam, F., Reece, M.J., Wear resistance of Al_2O_3–CNT ceramic nanocomposites at room and high temperature. *Ceram. Int*. 39, 5821, 2013.
124. Lee, K., Mo, C.B., Park, S.B., Hong, S.H., Mechanical and electrical properties of multiwalled CNT–alumina nanocomposites prepared by a sequential two-step processing of ultrasonic spray pyrolysis and spark plasma sintering. *J. Am. Cream. Soc*. 94, 3774, 2011.
125. Thomson, K.E., Jiang, D., Yao, W., Ritchie, R.O,, Mukherjee, A.K., Characterization and mechanical testing of alumina-based nanocomposites reinforced with niobium and/or carbon nanotubes fabricated by spark plasma sintering. *Acta Mater.* 60, 622, 2012.
126. Cumings, J., Zettl, A., Low-friction nanoscale linear bearing realized from multiwall carbon nanotubes. *Science* 289, 602, 2000.
127. Arsecularatne, J.A,, Zhang, L.C., Carbon nanotube reinforced ceramic composites and their performance. *Recent Pat. Nanotechnol*. 1, 176, 2007.

Part 3

FUNCTIONAL AND APPLIED CERAMICS

Ashutosh Tiwari, Rosario A. Gerhardt and Magdalena Szutkowska (eds.) Advanced Ceramic Materials, (299–300) © 2016 Scrivener Publishing LLC

8

Application of Organic and Inorganic Wastes in Clay Brick Production: A Chemometric Approach

Milica V. Vasić[1], Zagorka Radojević[1], and Lato Pezo[2]*

[1]Institute for Testing of Materials IMS, Belgrade, Serbia
[2]University of Belgrade, Institute of General and Physical Chemistry, Belgrade, Serbia

Abstract

The goal of this study was the research on the usage capability of various industrial wastes in clay bricks. Changes in product's behavior were studied in terms of relative differences in ceramic-technological parameters compared to samples without waste materials addition. The effects of organic and inorganic wastes were investigated in terms of changes introduced to products during shaping, drying, and firing. Samples with coal dust addition showed the highest sensitivity to drying, whereas the greatest plasticity and shaping moist were detected in samples with 50 wt.% of fly and landfill ashes. Waste material addition quantities and firing temperatures were independent parameters that influenced dependent parameters such as compressive strength, water absorption, firing shrinkage, weight loss during firing, and volume mass. The optimization results demonstrated that sunflower hulls, wood sawdust, soybean husks, and saturation sludge are best to be used in solid-brick production. Coal dust, landfill ashes, and neutralization (inorganic) sludge are best to be used in hollow-brick production. Sunflower hulls ash can be added in higher quantity to heavy clay to produce blocks or in lower quantity in roof tiles. The addition of 50 wt.% fly ash allows production of roof tiles.

***Keywords*:** Organic and inorganic industrial wastes, heavy clay bricks, response surface method, second-order polynomial models, artificial neural networks, prediction

**Corresponding author*: latopezo@yahoo.co.uk

Ashutosh Tiwari, Rosario A. Gerhardt and Magdalena Szutkowska (eds.) Advanced Ceramic Materials, (301–333) © 2016 Scrivener Publishing LLC

8.1 Introduction

From the sustainable development point of view, use of mineral raw materials is very important because it reduces consumption of natural resources and energy, utilizes waste materials, lowers emission of hazardous gases (especially carbon dioxide), reconstructs the mines after exploitation of raw materials, and so on [1, 2]. The recent matter of concern in many parts of the world is that there is already a shortage of heavy clay raw materials [3]; therefore, in some countries, use of these materials has been prohibited in construction [4]. The possibility of using waste materials in heavy clay–based raw material mixtures is intensively explored since traditional construction materials allow admixing without significant modifications in the manufacturing process [5–7]. Waste materials that can be used in brick industry are of organic, inorganic, or mixed nature [8].

Organic remains such as sawdust, residues from the tobacco industry [9], the ash created by the firing of rice husks [10], petroleum waste [11], and oil shale [12] are often used. Clay bricks containing organic waste are light-weight elements for building, characterized by very significant primary porosity of ceramic matrix, which together with the system cavities within ensures favorable thermo-technical characteristics. In addition, these elements can be produced in larger formats, maintaining sufficiently high compressive strength. Entering the combustible components generally reduces drying time, and heat release decreases the amount of energy required for the firing process [13]. However, it is necessary to beware of possible problems. During firing a product containing organic waste, it is recommended that retention at a temperature of 600 °C is 2 h for complete combustion of organic carbon [14]. Black nuclei can occur in case of high content of organic matter as well as vitrification, which may block the combustion inside the matrix [13]. A problem that should also be taken into account is the content of flue gases [15]. Besides, high energy can cause deformation of firing curve, and a high-speed warm-up can cause destruction of products, followed by a danger that the energy released in the kiln can be impossible to control [13].

Among inorganic raw materials, researchers studied the possibility of applying the remains of natural stone and fly ash, metallurgical waste, residue from the production of pine, waste blocks [16, 17], etc. Inorganic waste is considered to be hazardous due to the presence of toxic elements, which can be fixed within a heavy clay matrix after thermal treatment. Including this waste is considered to be an effective low-expense technique for fixing toxic species in usable products, or a simple way to reduce the residual volume which would usually be disposed off [5]. Inorganic additives create

fewer problems to the environment, but they can negatively alter plasticity of clay and increase the amount of shaping moist [9]. Also, microelements can introduce problems if they are leachable out of fired product [5].

Secondary raw materials of mixed nature presented in research earlier were, for example, sludge from the production of recycled paper [14], dried sludge from the purification of drinking water [10], and contaminated marine and river sediments [16, 17].

Each particular case of brick production initiation requires preliminary examinations and definition of the optimal raw materials mixture and technological parameters. All of the above-mentioned aspects must be taken into account so that the products can fulfill the Europopean Norms (EN) standards demands. For example, lowering clay mineral content in raw materials by adding sand is the cheapest way to reduce moist to the level required for shaping, and therefore the energy spent only to dry the products [18]. Such an effect is also introduced by adding secondary raw materials since it lowers fine fraction content.

In this study, a representative plastic heavy clay raw material was chosen, to which different industrial waste materials were added. Neutralization sludges from galvanizing industry were proved to be useful in the brick industry in our previous study [5]. The coal of pure quality is generally used in most of the power plants, and the remaining results are large amounts of fly and bottom ashes of varying properties. These ashes have not been utilized effectively, although much research has been done on this subject [4, 19]. The possibility of using these ashes as secondary raw material in heavy clay bricks is well known, so they are also included in this study. For both neutralization sludge and coal combustion residues, it is common that their usage reduces environmental problems and the total cost of raw material disposition. The physical and chemical properties of fly and bottom ashes may be quite variable as they are influenced by the kind of coal used, particle size, and the type of coal-burning process. Therefore, several of every kind of ashes was tested in this work for use in brick industry. Using these ashes as raw materials in bricks production also includes advantages of saving firing energy of remained carbon [19].

Wastes of organic nature were added to increase porosity and insulation ability of the products, while improving mechanical strength of the matrix by introducing combustion energy. Soybean crust, wood sawdust, sunflower hulls, and their ash are used as they do not represent a great concern to the environment and are already used for other purposes. Use of agricultural waste presents an innovative way to produce heavy clay bricks, but rather modest concentrations are usually added – up to 10 wt.% [9, 20]. Sunflower husk was never tested as a secondary raw material in the brick industry

before. Only sunflower husk ash can be found in the literature since solid residues of biomass combustion are rarely considered to be used or recycled [21]. On the other hand, waste coal dust and saturation sludge from sugar factory are produced in large quantities and often disposed of in landfills. This coal is of a brittle nature, and therefore its mining and transportation produce much coal dust. As it is environmentally hazardous, especially because of possibility to explode and also its toxic nature, it can be used in many ways – as a fuel or binder, but it is never tested as a supplementary material in the brick industry. In the sugar industry, as the result of processing of the diffusion juice of beets after straining and alkalization with lime milk, in the first phase of gas saturation using CO_2 and later, after filtration, a sludge that contains large amounts of finely granulated calcite occurs. This saturation sludge, not usable in industry, is presented in only one research work that aimed to test the production possibility of facing bricks [22].

In the present research, chemical content of used materials and loss on ignition (LOI) are determined. After adequate mixing of wastes and heavy clay raw materials and shaping of laboratory products, the mixture was fired in temperatures 850 °C, 900 °C, 950 °C, and 1000 °C. Quality of the fired products is determined based on mechanical and ceramic-technological tests as a function of the firing temperature. Second-order polynomial (SOP) models, with a defined firing temperature and additive material concentration, were used for calculation of 10 response variables (compressive strength of blocks and cubes – *CSB* and *CSC*; water absorption of blocks, cubes, and tiles – *WAB, WAC*, and *WAT*; tiles firing shrinkage – *FS*; weight loss during firing – *WLFB, WLFC*, and *WLFT*; and volume mass of cubes – *VMC*) on the basis of experimental results. Analysis of variance (ANOVA) was used to test the effects of waste materials concentrations on fired products properties and to compare the differences.

This study is based on mathematical optimization of different brick products using various industrial wastes separately. The main aim of this research was to determine the optimum process conditions (regarding firing temperature) and to find the best possible use of certain waste material in brick production. On the basis of response surface method (RSM), fuzzy synthetic evaluation (FSE) algorithm, using trapezoidal function, with defined optimal interval values of fired products parameters, was used depending on a final usage of the raw material in heavy clay brick industry [23]. Technological characteristics of prepared products are accompanied by shaping moist, plasticity of used masses for extrusion forming, shrinkage, and sensitivity to drying. The porosity-changing effect is determined by water absorption and volume mass of the fired products. In this way, the influence of addition of organic and inorganic industrial wastes on shaping, drying, and firing of

the heavy clay products is determined. Developed empirical models gave a reasonable fit to experimental data and successfully predicted technological parameters. In the case of brick production, nonlinear models are found to be more suitable due to variability in chemical composition of raw material and nonlinear behavior during firing. Generally, the heterogeneous nature of the heavy clays implied a complex material–process–product relationship [24]. Artificial neural network (ANN) models are recognized as a good modeling tool since they provide the solution to the problems from a set of experimental data and are capable of handling complex systems with nonlinearities and interactions between decision variables [25]. The performance of the ANN was compared with that of SOP models.

The main aim of this research was to determine the influence of addition of organic and inorganic industrial wastes on the quality of heavy clay products and also to test their usability in getting light-weight products and elegantly resolve environmental problems, while spending unwanted waste. The focus of this study was to determine the optimal addition of organic and inorganic industrial wastes depending on a final usage of the raw material in heavy clay brick industry. Optimization algorithm used in this study is concerned with finding the maxima of objective functions, subject to constraints. Described mathematical models, applied together, will be extremely helpful in preserving the raw natural resources and lowering the industrial waste and energy consumption.

8.2 Materials and Methods

8.2.1 Raw Materials and Laboratory Brick Samples

Plastic heavy clay raw material, containing enough clay minerals to be used to produce roof tiles, was sampled from a brick factory in Vlasotince (Serbia). After addition of chosen secondary raw materials, the masses were mixed, sufficiently moistened, and left in sealed nylon bags to homogenize. Afterward, the laboratory samples (plates $120 \times 50 \times 14\,mm^3$, no perforation cubes $30 \times 30 \times 30\,mm$ and hollow bricks $55.5 \times 36 \times 36\,mm$) were extruded under vacuum in a laboratory-type Händle machine. The shaped samples were then dried, fired, and tested in the same way as the starting representative samples [5, 25, 26]. The parameters monitored are related to characteristics of the raw materials (chemical composition and quantity of waste materials addition) and properties of fired products (weight loss during firing, water absorption, firing shrinkage, compressive strength, and volume mass). All of the tests were done in the same way as described in our previous studies [5, 25, 26].

Waste materials mixed to starting representative heavy clay were as follows:

- Two samples of sludge remained from hot-dip galvanizing industry in Ćuprija (Serbia) after wastewater neutralization (added by 3 wt.% to gain samples S1 and S3 and 6 wt.% in samples S2 and S4).
- Sludge remained from hot-dip galvanizing industry in Stalać (Serbia) after wastewater neutralization (added in 5 and 10 wt.% quantities to gain samples S5 and S6).
- Coal dust remained after washing of coal in industrial tanks in Vreoci, Serbia (added in 3 and 6 wt.% to gain samples CD1 and CD2).
- Coal dust remained after washing of coal in industrial tanks in Obrenovac, Serbia (added in 3 and 6 wt.% to gain samples CD3 and CD4).
- Fly ashes remained in thermal power plant in Obrenovac, Serbia (added in 50 wt.% to gain samples FA1, FA2, FA3, FA4, and FA5),
- Landfill bottom ashes remained in thermal power plant in Obrenovac, Serbia (added in 50 wt.% to gain samples LA1, LA2, LA3, and LA4).
- Soybean crust (6 wt.% in sample S) from edible oil factory in Zrenjanin (Serbia).
- Wood sawdust (2.5 wt.% in sample WS) from Vojvodina.
- Sunflower hulls from edible oil factory in Zrenjanin, Serbia (added in 5 and 10 wt.% to gain samples SF1 and SF2).
- Sunflower hulls ash from edible oil factory in Zrenjanin, Serbia (added in 5 and 10 wt.% to gain samples SFA1 and SFA2).
- Saturation sludge from sugar factory in Crvenka, Serbia (added in 5 and 10 wt.% to gain samples SS1 and SS2).

8.2.2 Macro Oxides Content of the Used Raw Materials

Contents of major elements were determined using energy-dispersive X-ray fluorescence (EDXRF) (XRF spectrophotometer ED 27 2000 – Oxford). X-ray tube with a silver target anode was used as the source of excitation. Energy-dispersive Si (Li) cooled by liquid nitrogen was used as detector. SMART digital pulse processor was used. The samples were mixed and/or milled to homogenize, and each of them was tested for three times, and the average values were taken into account.

8.2.3 Response Surface Method

RSM was selected to estimate the main effect of the process variables on the properties of fired laboratory products. The accepted experimental design was taken from [27]. The independent variables were firing temperature and industrial waste materials added in different ratios. The dependent variables observed were the responses *CSB*, *CSC*, *WAT*, *WAB*, *WAC*, *FS*, *WLFT*, *WLFB*, *WLFC*, and *VMC*. Ten SOP models were developed to relate ten responses to two independent process variables for every group of waste materials. The model was obtained for each dependent variable (or response), where factors were rejected when their significance level was $p < 0.05$ (confidence limit 95%). All mathematical methods were performed using StatSoft Statistica, for Windows, ver. 10. ANOVA analysis was used to test the effects of waste materials concentrations on fired products properties.

As a way of easier interpretation, in Table 8.1 are shown wastes used in this research, with the quantity and annotations of both wastes and prepared brick laboratory samples, whose origin and usage reasons were described in detail in [23].

Table 8.1 Used symbols to annotate wastes used and brick samples.

Symbol of waste added	Waste added	Waste quantity (wt.%)	Symbol of samples prepared
SĆ1	Neutralization sludge from Ćuprija, Serbia	3 6	S1 S2
SĆ2	Neutralization sludge from Ćuprija, Serbia	3 6	S3 S4
SSt	Neutralization sludge from Stalać, Serbia	3 6	S5 S6
CDV	Coal dust from Vreoci, Serbia	3 6	CD1 CD2
CDO	Coal dust from Obrenovac, Serbia	3 6	CD3 CD4
FAO1 FAO2 FAO3 FAO4 FAO5	Fly ashes from Obrenovac, Serbia	50 50 50 50 50	FA1 FA2 FA3 FA4 FA5

(*Continued*)

Table 8.1 Cont.

Symbol of waste added	Waste added	Waste quantity (wt.%)	Symbol of samples prepared
LAO1 LAO2 LAO3 LAO4	Landfill ashes from Obrenovac, Serbia	50 50 50 50	LA1 LA2 LA3 LA4
SV	Soybean crust from Zrenjanin, Vojvodina region, Serbia	6	S
WSV	Wood sawdust from Vojvodina region, Serbia	2.5	WS
SFZ	Sunflower hulls, Zrenjanin	5 10	SF1 SF2
SFAZ	Sunflower hulls ash, Zrenjanin	5 10	SFA1 SFA2
SSC	Saturation sludge from Crvenka	5 10	SS1 SS2

8.2.4 Fuzzy Synthetic Evaluation Algorithm

FSE algorithm was applied for optimal process parameters calculation. This method was intended to be used to solve a sequence of simple problems whose solutions converge to the solution of the original problem [28, 29]. According to our previous research, FSE algorithm, with trapezoidal membership function, is the most appropriate method to optimize the brick production process, on the basis of predefined optimal range of values [25, 30]. Optimization was performed using Microsoft Excel 2007 in order to determine the workable optimum conditions for firing of heavy clay bricks.

Trapezoidal membership function could be written as follows:

$$A(x,\min(x),m,n,\max(x)) = \begin{cases} \min(x) \le x < m, & \dfrac{x-\min(x)}{m-\min(x)} \\ m \le x < n, & 1 \\ n \le x < \max(x), & 1-\dfrac{x-n}{\max(x)-n} \end{cases} \tag{8.1}$$

where x is the value of *CSB*, *CSC*, *WAT*, *WAB*, or *WAC*, or *SM*, ΔSk, ΔGk or *PC*, while the values of m and n are the function parameters. Interval m–n is the expected optimal values range for output variables, chosen for certain products groups.

Optimization was done concerning the firing phase. Optimal values of tested parameters, relative to those of fired representative sample (RS), are assigned on the basis of our experience on this subject and presented in Table 8.2. The brick products are roughly divided to solid bricks (Group I), hollow blocks (Group II) and roof tiles (Group III).

8.2.5 Artificial Neural Network modeling

According to StatSoft Statistica's recommendations, the database is randomly divided into training data (60%), cross-validation (20%), and testing data (20%). The cross-validation dataset was used to test the performance of the network while training was in progress as an indicator of the level of generalization and the time at which the network has begun to overtrain. Testing dataset was used to examine the network generalization capability.

To improve the behavior of the ANN, both input and output data were normalized according to the following equation:

$$q_{i\,norm.} = \frac{q_i - \min(q_i)}{\max(q_i) - \min(q_i)} \tag{8.2}$$

where q_i is ith case, with measured compressive strength (*CS*), water absorption (*WA*), firing shrinkage (*FS*), weight loss during firing (*WLF*), and volume mass of cubes (*VMC*). Normalized variables gained values in the range of 0–1 and have no physical meaning.

In order to obtain a good network behavior, it is necessary to make a trial-and-error procedure and also to choose the number of hidden layers, and the number of neurons in hidden layer(s). The use of only one layer is advisable because more layers exacerbate the problem of local minima [25, 31].

A multilayer perceptron models (MLP) consisted of three layers (input, hidden, and output), which is the most common, flexible, and general-purpose kind of ANN. Such a model has been proved quite capable of approximating nonlinear functions [25, 31], giving the reason for choosing it in this study. The network consists of one layer of linear output neurons and one hidden layer of nonlinear neurons. The MLP neural network learns using an algorithm called "backpropagation". The Levenberg–Marquardt

Table 8.2 Optimal parameters concerning fired brick products

	***Eq. (1)* annotation**	***WLFT***	***WLFC***	***WLFB***	***FS***	***WAT***	***WAC***	***WAB***	***CSC***	***CSB***	***VMC***
Min		5.21	5.12	5.03	0.06	7.86	7.74	8.22	19.33	16.55	1.11
Max		8.74	8.57	8.73	2.57	15.13	14.40	13.74	64.82	28.47	2.15
Group I	*m*	5.00	5.00	5.00	0.15	11.50	11.50	11.50	24.00	18.00	1.62
	n	8.50	8.50	8.50	0.25	13.70	13.70	13.70	30.00	20.00	1.81
Group II	*m*	4.90	4.90	4.90	0.65	9.00	9.00	9.00	38.00	22.00	1.76
	n	7.50	7.50	7.50	0.95	13.00	13.00	13.00	45.00	24.00	2.00
Group III	*m*	4.70	4.70	4.70	1.20	8.30	8.30	8.30	58.00	26.00	1.85
	n	6.50	6.50	6.50	1.50	10.5	10.5	10.5	64.00	28.00	2.10

algorithm is proved to be the fastest and particularly adapted for networks of moderate size. During this iterative process, input data are repeatedly presented to the network [32] .

The first estimation of the number of neurons can be obtained from the following equation [33, 34]:

$$m = n \cdot (x+1) + y \cdot (n+1) \tag{8.3}$$

where x and y represent the number of input and output neurons, respectively; n is the number of neurons in the hidden layer; and m is the number of weights (connections between layers) in the neural network. m can be taken as the number of training exemplars divided by 10. Some suggestions regarding the number of hidden neurons are as follows: this number should be between the sizes of the input and output layers, and it should be 2/3 the size of the input layer, plus the size of the output layer, or less than twice the size of the input layer [34].

In this work, the ANN procedure of StatSoft Statistica was used to model the ANN, and the number (n) of hidden neurons varied from 5 to 13 (proposed by the program used). There were $x = 10$ inputs, $y = 10$ outputs, and $m = 115–283$ weight coefficients (depending on n). The Broyden–Fletcher–Goldfarb–Shanno (BFGS) algorithm, implemented in StatSoft Statistica's evaluation routine, was used for the ANN modeling. The information is transferred between the layers through a "transfer" or "activation" function. This function is typically nonlinear for the hidden layers and linear for the output layers. Most common nonlinear activation functions used in StatSoft Statistica ANN calculation are: logistic, sigmoid, hyperbolic, and tangent functions (also exponential, sine, softmax, and Gausian). In most applications, hyperbolic tangent function behaves better as compared to the other functions [31].

Coefficients associated with the hidden layer (both weights and biases) are grouped in matrices W_1 and B_1. Similarly, coefficients associated with the output layer are grouped in matrices W_2 and B_2. If Y is the matrix of the output variables, f_1 and f_2 are transfer functions in the hidden and output layers, respectively, and X is the matrix of input variables, it is possible to represent the neural network by using matrix notation as follows [35]:

$$Y = f_1(W_2 \cdot f_2(W_1 \cdot X + B_1) + B_2) \tag{8.4}$$

Weights (elements of matrices W_1 and W_2) are determined during the training step, which updates them using optimization procedures to

minimize the error function between network and experimental outputs [33, 34], evaluated according to the sum of squares (SOS) and the BFGS algorithm, used to speed up and stabilize convergence [36].

After defining the architecture of ANN, the training step is initiated. The training process was repeated several times in order to get the best performance of the ANN, due to a high degree of variability of parameters. It was accepted that the successful training was achieved when learning and cross-validation curves (SOS vs. training cycles) approached zero. Testing was carried out with the best weights stored during the training step. Correlation coefficient r and SOS were used as parameters to check the performance (i.e. the accuracy) of the obtained ANN.

After the best-behaved ANN is chosen, the model is implemented using an algebraic system of equations to predict *CS*, *WA*, *FS*, *WLF*, and *VMC*, by substitution of the corresponding weights and coefficients matrices in Eq. (8.4). This step can be easily achieved in some spreadsheet calculus (e.g. Microsoft Office Excel).

8.3 Results and Discussion

8.3.1 Characteristics of Raw Materials

Macro oxides content and LOI of the used materials are shown in Table 8.3. The representative heavy clay sample (RS) was of usual composition for its purpose, with particularly high content of Fe_2O_3 and relatively low content of carbonates [37]. RS was composed mostly of quartz and illite, relatively low amount of feldspars, carbonates, illite and chlorites, and minor amounts of montmorillonite and kaolinite. According to LOI, it is expected that calorific values decrease in the next series: wood sawdust (WSV), soybean crust (SV), sunflower hulls (SFZ), (inorganic) sludge (SC and SSt), saturation sludge (SSC), coal dust (CD), landfill ashes (LAO), fly ashes (FAO), and sunflower hulls ash (SFAZ). Of course, it is necessary to bear in mind that the LOI values, except for combustion of organic matter, also include decomposition of carbonates, whose decomposition is an endothermic process. Carbonates content in secondary raw materials was the highest for SSC, followed by inorganic sludge and landfill and fly ashes, whereas the lowest is detected in WSV.

Alkali oxide content was very high in SFAZ and significant in SFZ, while other additives contained relatively low concentrations. Inorganic sludge and then also fly and landfill ashes contained Fe_2O_3 in the highest quantities. Fe was almost not detected in organic materials. The content of SiO_2

Table 8.3 Macro oxides content of the used raw materials.

	SiO_2	Al_2O_3	Fe_2O_3	ZnO	Na_2O	K_2O	MgO	CaO	TiO_2	MnO	P_2O_5	SO_3	LOI
RS	58.73	13.62	11.41	0.00	0.32	2.99	1.34	2.36	1.73	0.17	0.00	0.32	7.01
SĆ1	0.64	0.21	31.33	0.63	0.21	0.00	0.74	19.23	0.00	0.22	0.34	0.12	46.33
SĆ2	0.29	0.13	28.14	1.18	0.35	0.00	1.19	28.64	0.00	0.25	0.26	0.14	39.43
SSt	1.14	0.37	40.15	0.96	3.41	0.00	1.43	11.34	0.00	0.16	0.31	0.17	40.56
CDV	37.45	11.07	11.37	0.00	0.87	0.87	1.58	5.85	0.37	0.05	0.08	0.15	30.29
CDO	47.06	12.96	2.79	0.00	0.69	1.13	2.84	3.15	0.47	0.07	0.03	0.97	27.84
FAO1	53.32	21.33	6.27	0.58	0.45	1.23	2.75	7.66	0.64	0.02	0.01	0.81	4.93
FAO2	53.89	19.93	5.98	0.71	0.66	1.22	2.44	8.31	0.55	0.03	0.04	0.63	5.61
FAO3	57.26	18.11	10.13	0.34	0.36	0.59	1.98	6.96	0.42	0.03	0.02	0.96	2.84
FAO4	53.84	21.36	6.41	0.12	0.44	1.21	2.70	7.61	0.56	0.03	0.03	0.78	4.91
FAO5	57.99	18.88	6.95	0.21	0.43	1.16	2.21	8.61	0.57	0.03	0.02	1.10	1.84
LAO1	49.54	10.69	5.59	0.00	0.81	1.28	3.82	13.45	0.72	0.00	0.05	1.32	12.73
LAO2	54.8	16.54	5.95	0.00	0.84	1.24	1.54	6.71	0.75	0.03	0.07	0.12	11.41
LAO3	51.11	13.65	6.14	0.11	0.71	1.01	2.18	10.13	0.32	0.01	0.04	0.64	13.95
LAO4	50.21	15.05	5.72	0.14	0.63	1.25	2.45	9.52	0.55	0.01	0.06	0.54	13.87
SV	0.00	0.00	0.00	0.00	0.12	5.12	0.00	1.44	0.00	0.00	0.13	0.00	93.19
WSV	0.07	0.00	0.00	0.00	0.21	0.51	0.42	0.54	0.00	0.00	0.03	0.02	98.2
SFZ	0.11	0.00	0.00	0.00	0.36	3.63	0.00	1.01	0.00	0.00	0.67	0.00	94.22
SFAZ	1.64	0.00	0.00	0.00	5.13	78.5	0.00	14.13	0.00	0.00	0.00	0.00	0.60
SSC	4.47	1.58	0.94	0.00	0.00	0.00	2.57	49.14	0.00	0.00	0.00	0.00	41.30

in fly ash was lower than that in RS, but the situation with Al_2O_3 was *vice versa*. Landfill bottom ash was rich in Ca content, as also stated in the literature [19].

8.3.2 Changes Observed in Shaping and Drying in the Air

The chosen representative heavy clay material needed 22.62% of moist to be added to obtain the matrix of optimal plasticity for shaping. After tests were performed according to the Pfefferkorn method [38], the heavy clay is determined as high plastic with a plasticity coefficient of 31.1. During drying in the air, critical point of Bigot's curve [38] showed that the material was highly susceptible to drying according to ΔGk, which was 10.96% (ΔSk is determined to be 6.65%). The differences introduced by adding the industrial waste during shaping and drying, the data rarely presented in the literature, are shown in Figure 8.1. According to most of the results, higher correlation is observed between pairs *SM*–*PC* and ΔSk–ΔGk.

In the production of bricks from primary raw materials (heavy clay), the rule is that the *SM*, ΔSk, ΔGk, and *PC* parameters are positively correlated and that with increasing content of clay minerals, they all grow [25]. If secondary raw materials are introduced, the situation can be rather different. *SM* and *PC* mostly increase when wastes are added to the representative clay, meaning that further drying process would require higher amount of energy. The addition of LA1, LA3, and LA4 required more than 30% of water for shaping. Most of the mixtures belonged to highly plastic materials, except for CD3 and CD4, which were slightly plastic. Most of the mixtures were highly susceptible to drying, except for the ones with fly and landfill ashes, which belonged to susceptible group [25].

Addition of inorganic sludge, gaining the samples S1, S2, S3, S4, S5, and S6, increased all of the parameters of concern. No data were found in the literature on this subject and on addition of high Fe and Ca concentration industrial sludge. In the study of loess heavy clays (high carbonates content), it is determined that Fe_2O_3 content influences *PC* and ΔGk positively and total carbonates content negatively [38]. Since Fe in heavy clay is mainly within $Fe(OH)_3$, the same as in tested sludge [5], the conclusion that high Fe content improves plasticity is confirmed. The highest influence showed SSt, while SĆ1 and SĆ2 were closer, according to shaped bricks behavior (Figure 8.2).

With addition of FA and SFA, the results are similar: SM and PC increase, wheras ΔSk and ΔGk decrease. The proposed explanation of decrease in sensitivity to drying is improved binding of the particles due to pozzolanic reaction in contact with moist [39]. The other researchers also concluded that moist diffusion in bricks is improved with addition of fly

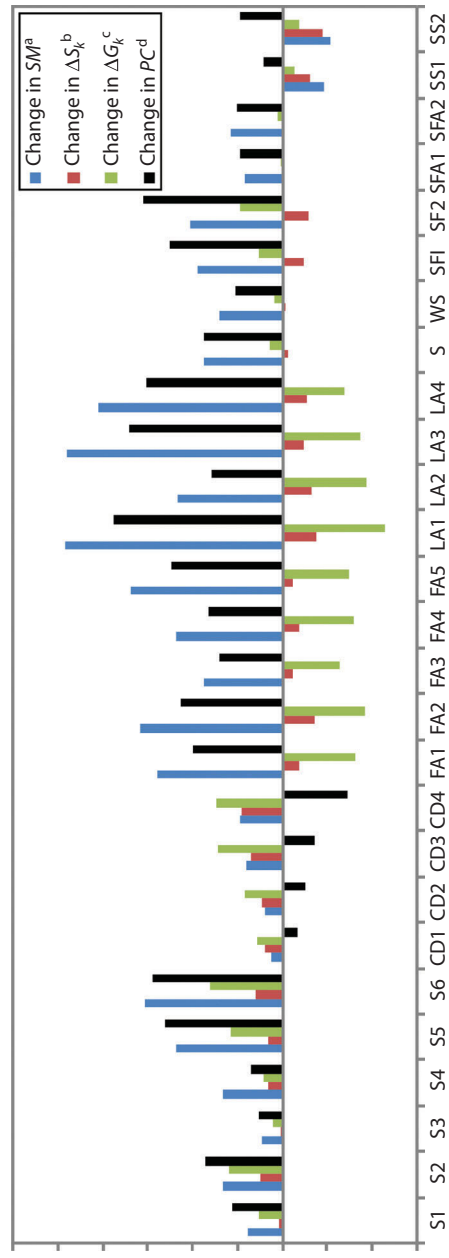

Figure 8.1 Changes in shaping and drying with waste material addition. [a]*SM* – shaping moist, [b]*ΔSk* – shrinkage in Bigot's curve critical point, [c]*ΔGk* – weight loss in Bigot`s curve critical point, [d] *PC* – plasticity coefficient by Pfefferkorn

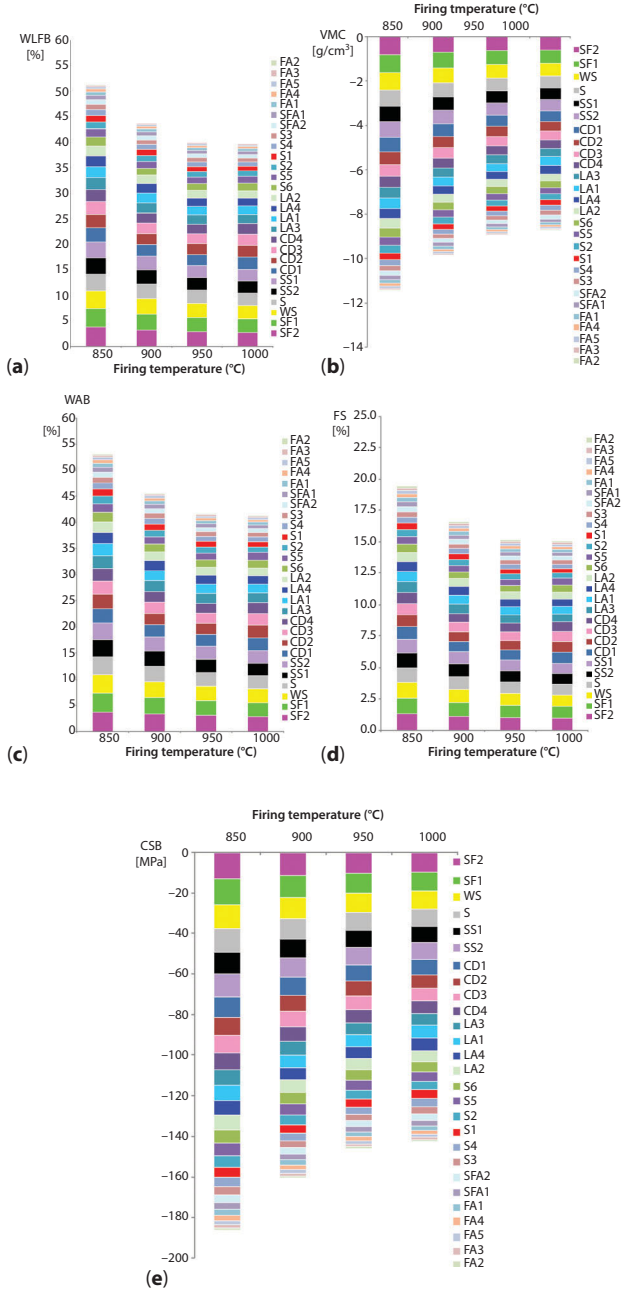

Figure 8.2 Changes of observed parameters during firing of products with waste materials addition.

ash [15]. A high quantity of water is needed in heavy clay and ash mixture to make the matrix plastic enough to be extrudable, and so *SM* and *PC* increase. The conclusion during the other study is that with 50 wt.% of fly ash, decrease in plasticity is about 34%, and that additives must be used to improve this parameter [4]. The ash used in that research contained less CaO and MgO [40], which are found to be the most influential on plasticity. The reason could also be alkalis, which were present in relatively high amount in our research. Since LAO1 contained the most of alkali and alkaline earth oxides, it showed the highest changes in parameters that describe shaping process and drying in the air in the sample LA, whereas additive FAO3 used in sample FA3 showed *vice versa* behavior.

The addition of SSC caused decrease in all of the parameters, except in *PC*, which was different than in other authors' experiments [22]. It is known that fine-grained calcite decreases plasticity [25], but used material contained also coarser particles. Concerning that after contact with the atmosphere the samples were intensively covered by "pop-corns", this conclusion is confirmed. Since it is known that the matrix containing microcracks and micropores dries slower, the conclusion is that the SSC addition does not introduce strain to the matrix [41] because the material contained a mixture of large and small calcite grains which adapted to the RS matrix. CDV and CDO acted *vice versa*: the only parameter that dropped is *PC* because of particles coarser compared to FA and SFA. Still, *SM* and *PC* change very slightly. CDV contained higher amounts of organic matter, carbonates, and total Si, Al, and Fe oxides. This is why all of the parameters of concern were slightly higher compared to the addition of CDO.

The addition of some organic wastes (SFZ, SFAZ, WSV, and SV) decreases shrinkage during drying in the air, while increasing the other three parameters. Cellulose fibers absorb the water within existing channels, and it is the main cause of the increased need of water. Also, the presence of soluble organic compounds in water increases the plasticity of the samples [9]. The fibrous wastes, because of its size distribution and the presence of greater particles, acted partly as plasticity-decreasing additives and conditioned the decline in drying shrinkage. On the other hand, slightly increased plasticity and shaping moist caused slight increase in sensitivity to drying (ΔGk), followed by decreasing shrinkage to a critical point in Bigot's curve (ΔSk). Concerning the amount of cellulose fibers and the quantities of materials added to RS, the influence on shaping and drying characteristics is weaker in the line: SFZ, S, WSV, and SFAZ (Figure 8.1). According to the available literature data, plasticity increased for 11.5% [9]; however, in this case, the increase is lower – about 6.8%.

8.3.3 Characteristics of Fired Products

The results concerning starting, representative heavy clay samples, after firing, are shown in Table 8.4. Weight loss during firing, firing shrinkage, compressive strength, and volume mass mostly increased with firing temperature, whereas water absorption decreased. According to the results and decades of experience in this field, it is concluded that this material is adequate for production of bricks and roof tiles and that it showed the capacity to be mixed with secondary raw materials, thereby, besides lowered quality, obtaininf the products that could satisfy EN regulations.

Changes that were introduced to the representative heavy clay material by wastes additions are shown in Figure 8.2 in sequence from the highest to the lowest effects on observed characteristic. All of the wastes have contributed to the growth of *WLF*, *FS*, and *WA* and decline in *CS* and *VMC*. Increase of *WA* indirectly showed increase of open porosity and lightweight products formation [42]. The influence of firing temperature was *vice versa*: temperature increase caused decrease of *WLF*, *FS*, and *WA* as well as increase of *CS* and *VMC*. Consolidation of the matrix by firing at higher temperatures is expected, and therefore open porosity declined, while closed pores are formed [42]. The same correlations are obtained when testing a huge number of heavy clay materials [25].

Organic wastes showed higher influence on final laboratory products. As for the firing temperature and the observed properties, based on the results shown in Table 8.4, it is evident that the increase in temperature reduces the level of influence of a specific waste, being most denominated at 850 °C, while at higher temperatures (950 °C and 1000 °C), the differences introduced were similar.

The waste materials introduced congruent changes to parameters concerned – increase of *WLF*, *FS*, and *WA* and decrease of *CS* and *VMC* in the same order: SF2, SF1, WS, S, SS2, and SS1; followed by CD1, CD2, CD3, and CD4; then LA3, LA1, LA4, LA2, S6, S5, S2, S1, S4, S3, SFA2, and SFA1; and FA1, FA4, FA5, FA3, and FA2.

The addition of organic waste to bricks, especially the ones with the highest LOI values, mostly affected the changes of parameters concerned. The changes to bricks' quality are caused by the addition of wastes depending on their amount in the mixtures as well as their calorific values, because the heat of combustion improves the mechanical properties of the matrix. Also, the chemical composition of starting materials influenced on how the addition of waste affected the final products, the reactions that occur during firing, and the process of vitrification. Certainly, the impact depended

Table 8.4 Characteristics of fired products made of representative raw material.

Temp.	*WLFT*	*WLFC*	*WLFB*	*FS*	*WAT*	*WAC*	*WAB*	*CSC*	*CSB*	*VMC*
850 °C	5.07	5.03	4.89	−0.10	10.25	10.48	10.06	41.92	29.56	1.944
900 °C	5.16	5.00	4.98	0.26	9.81	9.64	9.38	53.35	28.12	1.962
950 °C	5.29	5.05	5.05	0.74	8.68	8.56	8.50	51.06	28.16	2.172
1000 °C	5.31	5.06	5.06	1.58	7.68	7.59	8.06	65.66	27.71	2.079

more on organic matter than on fluxes content. Thus, for example, the organic wastes supplemented in the highest amounts (10 wt.%) were SFZ (sample SF2) and SSC (sample SS2), but sunflower husks provided greater LOI because they contain more organic matter than saturation sludge and so influenced the change in weight loss during firing. Wood sawdust (WSV) is added in the lower quantity than SFZ, so despite its higher LOI value, it had lower influence on the products. Among organic wastes, the lowest quantity of burnable matter is found in coal dust, so it showed the least impact on the products, especially in the case of the sample from the plant in Obrenovac. The other study results showed that facing bricks with saturation sludge addition were of higher compressive strength compared to starting heavy clay material samples [22], but this could be because the used contained more clay minerals than RS so that fine-grained carbonates reacted with them and improved consolidation of the matrix. Sunflower husks ash behaved as inorganic additive since it contained low amount of organic matter. According to research reported in the literature, the theoretical sintering temperature when adding sunflower husk ash was determined to be too high for a cost-effective production [21]. The case we tested was different because of the very high content of fluxes (Table 8.3) [40] and showed that this mixture can be used even in roof tiles production.

Among the inorganic additives used, the greatest impact is noticed with landfill ashes, especially due to the large amount mixed to RS (50 wt.%). The most influential of the pattern is LA3, which was expected given the LOI value. LA1 contained the highest total content of fluxes, and therefore it was next in the series. LA4 showed a higher LOI value and content of fluxes than LA2, and therefore its impact was more important. Landfill ashes are followed by inorganic sludge, which showed high values of LOI related mostly to carbonate contents. Among these sludge, SĆ2 had the lowest content of burnable matter, but its influence on the products was similar. LOI and fluxes content were higher in SĆ1 than in SSt (Table 8.3) but showed a lesser effect, possibly because of higher microelement content, which improved physical consolidation of the matrix due to fixing of microelements within a heavy clay matrix after thermal treatment [5]. Also, concentration of SĆ2 was more influential than SĆ1 (Figure 8.2). Fly ash introduced the lowest changes to observed fired products properties and thus were involved in obtaining the highest value of compressive strength and volume mass, among all of the products. Having the middle content of fluxes and among the lowest LOI values, they possibly gave the highest quality products because of microelements content and better binding of the particles due to the pozzolanic reaction of water and alkali particles of fly ash during drying [5, 39].

8.3.4 RSM and ANOVA Analysis

In this study, ANOVA was conducted to show the significant effects of the independent variables (firing temperature and the content of different waste materials additives) on the responses. The effect of each variable is tested by *F*-test and the level of statistical significance of result (expressed by *p*-value). The models obtained are not shown due to the large volume of data, but the most important data and conclusions are presented in Table 8.5 and in the following text. SOP models were made individually for every parameter that described fired laboratory products, but coefficients of determination (r^2) are shown in the obtained range for all of them. Very good fitting (high r^2 values, statistically significant at $p < 0.05$, by 95% confidence limit) showed that the models adequately represented experimental data.

In most of the cases, among used independent parameters, firing temperature showed the highest influence on fired products characteristics. Concentrations of added waste materials were mostly relatively low, and therefore significant temperature influence is expected. Also, firing

Table 8.5 Overview of SOP models and ANOVA results.

Waste material	The most influential parameters in SOP models*	r^2
SĆ	T	0.913–0.998
SSt	T and T^2	0.913–0.996
CDV	[CDV] and $[CDV]^2$	0.918–0.999
CDO	$[CDO]^2$, T and T^2	0.918–0.986
FAO	T	0.955–0.999
LAO	T	0.970–0.998
SV	T	0.990–0.999
WSV	T	0.991–0.998
SFZ	T and [SFZ]	0.913–0.998
SFAZ	[SFAZ]	0.922–0.996
SSC	T	0.896–0.999

*Statistically significant at $p < 0.05$ level, 95 % confidence limit,
[*X*] – concentretion of material *X*

temperature is known as a very influential parameter [27, 28]. Among all of the wastes, inorganic and organic sludges contained the highest carbonates concentrations (Table 8.2), and thus the firing temperature showed greater impact than the additives concentration [25].

It must be mentioned that in some of the samples (and SOP models), concentration was not a changeable parameter (different LAs and FAs were all added in a quantity of 50 wt.%, SV is added in 6 wt.% only, and WSV in 2.5 wt.%), so it could not show any influence. It is interesting that it was not the sample of fly and landfill ashes that influenced brick properties, but the temperature.

In some mixtures, certain parameters were the most influenced by waste material concentration. Thus, for example, when adding CDV to heavy clay, its concentration changed all of the responses most significantly, while CDO content introduced the most changes only to *WLF*, *FS*, and *WA* parameters. Also, SFZ concentration introduced the greatest changes in *CS* and *VMC*, and SFAZ in all of the tested parameters, while the rest were affected by firing temperature more. Among all wastes that were added in different concentrations, coal dust and sunflower hulls contained the most organics and total fluxes, which, besides relatively low content, introduced significant changes to the products by energy released and burned matter content. Still, in the case of CDO, the firing temperature influenced compressive strength and volume mass more because of lower organic matter content and LOI value, compared to CDV and SFAZ (Table 8.2). At the same concentrations of additives, CDV has brought major changes in the properties of fired products. SFAZ concentration effect is expected since it contained very high concentration of K_2O and also high content of total fluxes, which introduced higher influence than the firing temperature in all of the tested parameters. It seems that fluxes concentration in waste materials above 10 wt.% brought more changes to *WLF*, *FS*, and *WA* and that high LOI values influenced *CS* and *VMC* more.

After the whole discussion, it is important to mention some practical aspects that are seen after the experiments. On the samples with residues from the production of sunflower oil (hulls and ashes) after firing, separation (diffusion) of oil is noticed on the surface, during which emerged occurrence of oil spots. As a result, it is not recommendable to use these wastes in the brick industry, although they showed good performance in terms of technical characteristics. Samples with saturation sludge from sugar factory, after accelerated aging in steam or some time under the influence of atmosphere, the phenomenon of intense "popcorn limes" occurred because CaO reacted and turned into $Ca(OH)_2$, and that lowered

mechanical resistance, and negatively affected the appearance of the products. In contrast, samples in which inorganic sludge were added appeared nice and homogenous in a dark red color due to the increased content of Fe_2O_3. Despite the large amount of fly and landfill ashes, the samples looked good and consistent and had ditched "brick red" color.

8.3.5 Neurons in the ANN Hidden Layer

Determination of the appropriate number of hidden layers and the number of hidden neurons in each layer is one of the most critical tasks in the ANN design. The number of neurons in a hidden layer depends on the complexity of the relationship between inputs and outputs. As this relationship becomes more complex, more neurons should be added [31].

The optimum number of hidden neurons in this research was chosen upon minimizing the difference between predicted ANN values and desired outputs, using *SOS* during testing as performance indicator (Figure 8.2). Results of *CSB*, *CSC*, *WAT*, *WAB*, *WAC*, *FS*, *WLFT*, *WLFB*, *WLFC*, and *VMC* during training, testing, and validation are presented. Used MLP are marked according to StatSoft Statistica's notation, MLP followed by the number of inputs, the number of neurons in the hidden layer, and the number of outputs. According to ANN performance, from Table 8.6 (sum of r^2 and SOSs for all variables in one ANN), it was noticed that the optimal number of neurons in the hidden layer is 6 (network MLP 12-6-10.), when obtaining high values of r^2 and also low values of *SOS*. It is noticed that a greater number of neurons increases the structure complexity but does not necessarily significantly improve the network behavior [36] (during testing step MLP 12-6-10, gained $r^2 = 1.000$, $SOS = 0.004$). The goodness of fit between experimental measurements and model calculated outputs represented as ANN performance (sum of r^2 between measured and calculated *CS*, *WA*, *FS*, *WLF*, and *VMC* for each ANN) and also the *SOS* between measured and calculated technological parameters, during training, testing, and validation steps, are shown in Table 8.7. The *SOS* between the experimental and the network predicted values was used as the iteration termination criterion, as StatSoft Statistica's default. As soon as the cross-validation *SOS* starts to increase, the training step is terminated; otherwise, the training step ends after a fixed number of epochs or training cycles [31].

Table 8.6 shows ANN performance data expressed as the sum of r^2 and *SOS*, for all variables in one ANN, while Table 8.7 presents r^2 for each variable (*CSB*, *CSC*, *WAT*, *WAB*, *WAC*, *FS*, *WLFT*, *WLFB*, *WLFC*, and *VMC*) during training, testing, and validation steps.

Table 8.6 ANN summary.

Net. name	Train. perf.	Test. perf.	Valid. perf.	Train. error	Test. error	Valid.n error	Train. Algor.	Error func.	Hidden activ.	Output activ.
MLP 12-6-10	1.000	0.998	0.997	0.000	0.004	0.003	BFGS 57	SOS	Logistic	Identity

Table 8.7 Coefficient of determination for each variable.

Cycle	WLFT	WLFC	WLFB	FS	WAT	WAC	WAB	CSC	CSB	VMC
Train.	1.000	1.000	1.000	1.000	1.000	1.000	1.000	1.000	0.999	1.000
Test.	1.000	1.000	1.000	1.000	1.000	1.000	1.000	0.993	0.992	0.993
Valid.	0.998	0.998	0.998	0.998	0.998	0.998	0.998	0.997	0.995	0.996

8.3.6 Simulation of the ANNs

Process outputs *CSB*, *CSC*, *WAT*, *WAB*, *WAC*, *FS*, *WLFT*, *WLFB*, *WLFC*, and *VMC* can be calculated by Eq. (8.4), using matrices W_1 and B_1, and matrices W_2 and B_2, which represent system, incorporating coefficients associated with the hidden layer (both weights and biases). Output variables are calculated by applying transfer functions f_1 and f_2 (from Figure 8.2) in the hidden and output layers, respectively, onto the matrix of input variables X using Eq. (8.4). The algebraic system of equations is easily evaluated in a spreadsheet (i.e. Microsoft Excel) to predict *CSB*, *CSC*, *WAT*, *WAB*, *WAC*, *FS*, *WLFT*, *WLFB*, *WLFC,* and *VMC*, using Eq. (8.4), with shown calculated weights and biases matrices. Table 8.8 presents the elements of matrix W_1 and vector B_1 (presented in "bias" column), and Table 8.9 presents the elements of matrix W_2 and vector B_2 ("bias" raw) for hidden layer.

The ANN model was used to predict experimental variables (*CSB*, *CSC*, *WAT*, *WAB*, *WAC*, *FS*, *WLFT*, *WLFB*, *WLFC*, and *VMC*) and showed the highest match obtained so far for such systems [25]. Figure 8.3 shows simulated curves in comparison with experimental data for the best found MLP 12-6-10 neural network. It can be noted from Tables 8.6 and 8.7 that the networks were able to predict reasonably well all process outputs for a broad range of the process variables, shown in Figure 8.3. The predicted values were very close to the desired values in most cases, although *CSB*, *CSC*, *FS*, and *VMC* prediction was not as good as that for *WAT*, *WAB*, *WAC*, *FS*, *WLFT*, *WLFB*, and *WLFC* in terms of r^2 value, for both SOP and ANN models. *SOS*s obtained with the ANN model are of the same order of magnitude as experimental errors for *CSB*, *CSC*, *WAT*, *WAB*, *WAC*, *FS*, *WLFT*, *WLFB*, *WLFC*, and *VMC* reported in the literature [25].

The mean and the standard deviation of residuals have also been analyzed. The mean of residuals were as follows: 0.164 for *CSB*, 0.123 for *CSC*, 0.026 for *WAT*, 0.051 for *WAB*, 0.042 for *WAC*, 0.069 for *FS*, 0.031 for *WLFT*, 0.012 for *WLFB*, 0.042 for *WLFC*, and 0.017 for *VMC*, while the standard deviations of residuals were as follows: 0.008 for *CSB*, 0.001 for *CSC*, 0.001 for *WAT*, 0.002 for *WAB*, 0.002 for *WAC*, 0.003 for *FS*, 0.003 for *WLFT*, 0.001 for *WLFB*, 0.003 for *WLFC*, and 0.002 for *VMC*. These results showed a good approximation to a normal distribution around zero with a probability of 95% (2·SD), which means a good generalization ability of the ANN model for the range of experimental values of *CSB*, *CSC*, *WAT*, *WAB*, *WAC*, *FS*, *WLFT*, *WLFB*, *WLFC*, and *VMC* shown in Figure 8.2.

Table 8.8 The elements of matrix W_1 and vector B_1.

	Temp.	FA1	FA2	FA3	FA4	FA5	LA1	LA2	LA3	LA4	S	WS	Bias
1	0.232	0.850	−0.981	0.178	−1.995	−0.094	2.678	−0.791	−1.403	−0.608	−0.191	0.100	−0.450
2	−0.936	0.451	−0.752	0.315	−0.409	0.498	0.055	−0.503	−0.388	0.205	−0.522	0.056	−0.443
3	−2.083	0.927	−1.105	0.258	−1.532	0.925	1.589	0.407	−1.120	1.448	−0.784	0.412	−1.394
4	−1.392	0.619	−1.486	0.313	−1.447	0.274	0.443	0.055	−0.928	−0.025	−1.012	0.269	1.595
5	−0.912	1.497	−1.179	2.297	−1.009	1.229	0.202	0.214	−0.634	1.620	−0.758	1.583	0.546
6	−1.098	1.756	−1.392	2.149	−0.927	1.224	0.051	−0.417	−0.555	1.593	−0.898	1.451	−0.175

Table 8.9 The elements of matrix W_2 and vector B_2.

	1	2	3	4	5	6	Bias
WLFT	0.636	–0.105	0.716	0.648	–0.120	–0.716	0.167
WLFC	0.081	0.399	–0.405	0.017	0.432	0.553	0.099
WLFB	0.603	0.651	–0.100	0.738	–0.610	0.342	0.142
FS	–0.333	0.047	0.459	–0.280	–0.027	–0.718	0.228
WAT	–0.119	0.665	0.636	–0.100	–0.714	–0.601	0.144
WAC	0.430	–0.310	0.052	0.420	0.484	–0.010	0.114
WAB	0.669	–0.109	0.676	0.629	0.312	–0.736	0.163
CSC	0.020	0.422	–0.309	0.061	–0.655	0.489	0.682
CSB	0.744	0.603	–0.113	0.671	–0.564	0.320	0.616
VMC	–0.263	0.017	0.429	–0.329	–0.034	–0.688	0.681

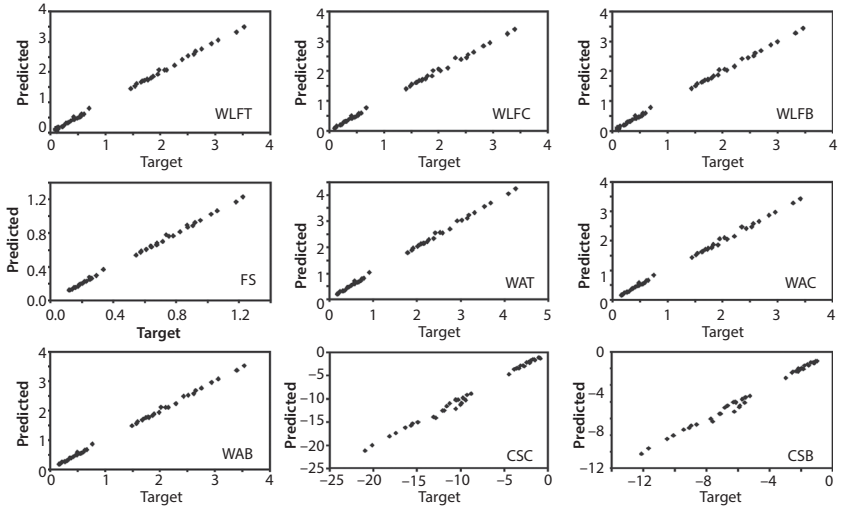

Figure 8.3 Target and predicted *CSB*, *CSC*, *WAT*, *WAB*, *WAC*, *WLFT*, *WLFB,* and *WLFC* (MLP 12-6-10).

The SOP models using StatSoft Statistica 10 were also developed, and SOS and r^2 values are presented in Table 8.5. It can be seen that these r^2 values are slightly lower than those associated with the ANN model. This agrees with other authors [33, 34, 36]. Although the ANN model is more complex (148 weights biases for *CSB*, *CSC*, *WAT*, *WAB*, *WAC*, *FS*, *WLFT*,

WLFB, *WLFC*, and *VMC* model, for 10 different ANN) than SOPs, the ANN model performed better because of the high nonlinearity of the developed system [36]. Tables 8.6 and 8.7 showed that the ANN model gained much better results compared to SOPs (Table 8.5), regarding the r^2 comparison between experimental and calculated outputs.

8.3.7 Principal Component Analysis

The PCA allows a considerable reduction in a number of variables and the detection of structure in the relationship between measured process parameters and different heavy clays additives that give complimentary information. All samples have been produced with different additives and various conditioning treatments as described by experimental design described in [23]. For visualizing the data trends and the discriminating efficiency of the used descriptors for shaping, drying in the air, and ceramic-technological characteristics, two scatter plots of samples using the first two principal components (PCs) issued from PCA of the data matrix are obtained (Figures 8.2 and 8.3). The results revealed good diversity between various samples, expressed by their distinctive positions of points in factor space.

PCA of behavior of samples during shaping and drying in the air showed that the first two PCs accounted for 89.45% of the total variability, which could be considered as adequate presentation of the data, Figure 8.1. *SM* (23.2%), Δ*Sk* (23.2%), Δ*Gk* (26.3%), and *PC* (27.3%) contributed almost equally to first PC calculation, whereas second PC mostly consisted of *SM* and Δ*Sk* (contribution of 35.6% and 34.3%, respectively).

The highest Δ*Gk* and Δ*Sk* values were observed in samples CD1, CD2, CD3, and CD4, while the greatest *PC* and *SM* were noticed in LA1, LA2, LA3, and LA4 and also in FA1, FA2, FA3, FA4, and FA5. The lowest *PC* and *SM* as well as the lowest Δ*Gk* and Δ*Sk* were observed for SS1 and SS2 samples.

PCA of fired products characteristics showed that there is a neat separation for four used temperatures, Figure 8.4. Quality results show that the first two PCs, accounting for 88.27% of the total variability, can be considered sufficient for data representation for ceramic-technological characteristics. *WAT* (12.6%), *WAC* (12.6%), and *WAB* (12.6%) have been found to be most influential for the first-factor coordinate calculation, whereas the contribution of *WLFT* (18.7%), *WLFC* (20.1%), *WLFB* (16.7%), and *CSC* (26.2%) have been the most important variables for the second-factor coordinate calculation.

The influence of processing parameters can be observed in Figure 8.5: temperature is rising along the *CSC* vector (on the contrary direction

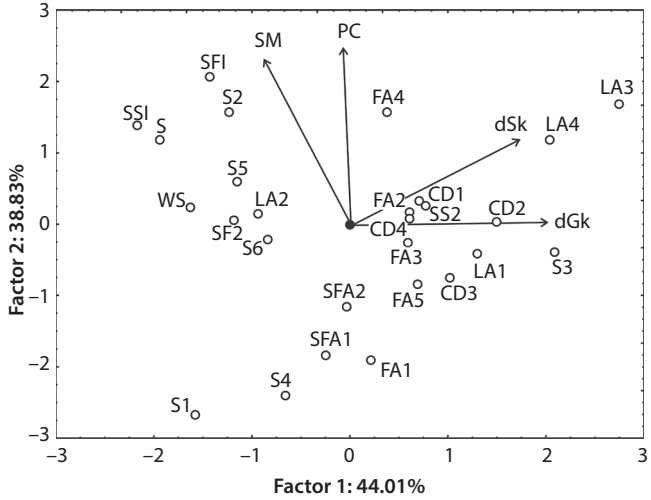

Figure 8.4 PCA graphic, showing the behavior in shaping and drying in the air.

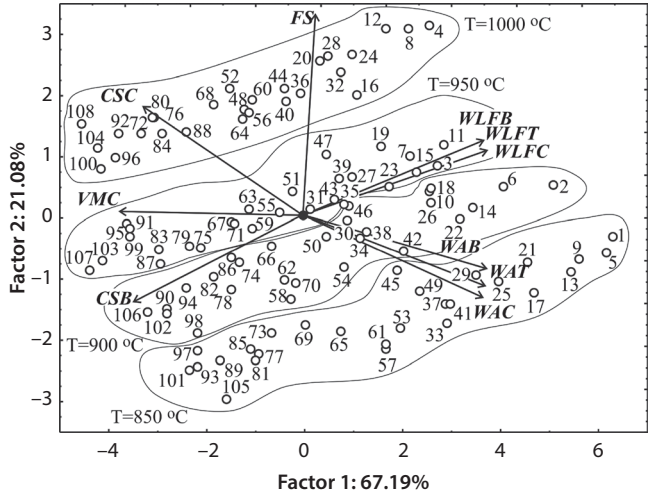

Figure 8.5 PCA of fired products ceramic-technological characteristics.

to *WAT*, *WAB*, and *WAC* vectors). Samples were numbered as follows: $1 + i \cdot 4$, $2 + i \cdot 4$, $3 + i \cdot 4$, and $4 + i \cdot 4$ (for 850 °C, 900 °C, 950 °C, and 1000 °C, respectively), with $i = 0$–26 (total 27 samples × 4 firing temperatures = 108 samples) representing the effects of SĆ1, SĆ2, SSt, CDV, CDO, FAO1, FAO2, FAO3, FAO4, FAO5, LAO1, LAO2, LAO3, LAO4, SV, WSV, SFZ, SFAZ, and SSC additions, to gain 27 samples (Table 8.1). Sample

numbers are listed in the order of lowering the influence to brick quality parameters: SF2 ($i = 0$), SF1 ($i = 4$), WS ($i = 8$), S ($i = 12$), SS2 ($i = 16$), and SS1 ($i = 20$); followed by CD1 ($i = 24$), CD2 ($i = 28$), CD3 ($i = 32$), and CD4 ($i = 36$); then LA3 ($i = 40$), LA1 ($i = 44$), LA4 (i = 48), LA2 ($i = 52$), S6 ($i = 56$), S5 ($i = 60$), S2 ($i = 64$), S1 ($i = 68$), S4 ($i = 72$), S3 ($i = 76$), SFA2 ($i = 80$), and SFA1 ($i = 84$); and FA1 ($i = 88$), FA4 ($i = 92$), FA5 ($i = 96$), FA3 ($i = 100$), and FA2 ($i = 104$).

The influence of different additives can be observed mostly along the *CSB*, *WLFT*, *WLFB*, and *WLFC* vectors, as can be seen in Figure 8.5. Lower *i* value is reserved for higher *WLF* (right side of the PCA plot), whereas large *i* represented higher *CSB* value (on the left side of graphic).

PCA (Figure 8.5) revealed high correlations among tested parameters. *WLF* are positively correlated to *WA* parameters (correlation coefficient $r = 0.6$) and *FS* ($r = 0.4$) but negatively correlated to *CS* parameters ($r = -0.5$) and *VMC* ($r = -0.7$), statistically significant at $p < 0.001$ level, 95% confidence limit.

8.3.8 Optimization

In order to enable more comprehensive comparison between the investigated samples, FSE has been introduced, and standard scores (SS) were calculated. Graphics presented in Figure 8.6 show the FSE analysis for

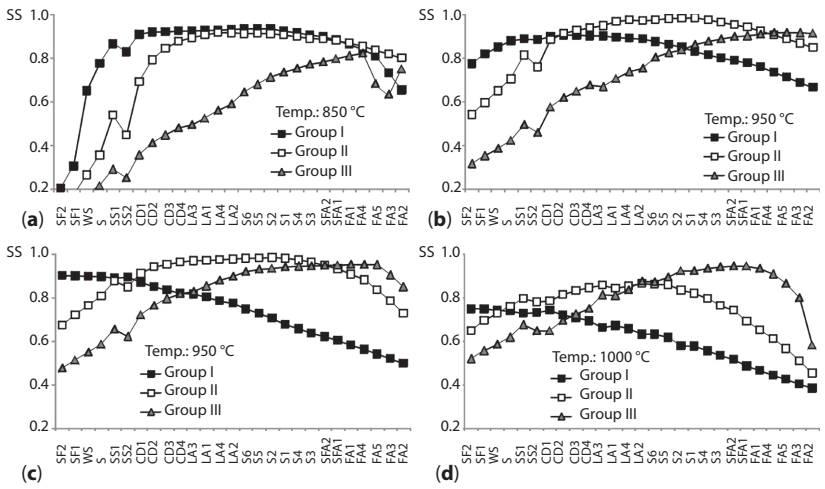

Figure 8.6 FSE analysis for ceramic-technological characteristics for different waste materials additions, when firing at 850, 900, 950 and 1000 °C.

ceramic-technological characteristics of heavy clay samples with different additives. These samples were fired at different temperatures and scored according to optimal values shown in [24]. Samples in Figure 8.5 are placed in line of lowering the influence to fired products characteristics, as determined in [43].

It is concluded that increased firing temperature allows production of more demanding (higher-quality) products, which is the known fact. For laboratory conditions, 850 °C is quite a low temperature, and therefore it mainly can be used to produce only Group I, except, possibly, to samples with less influence of additives (FAO addition). The addition of FA and firing at 900 °C can even be a good combination for roof tiles, while the addition of CD, LAO, sludge, and SFA FAO1 I can give hollow block. At an even higher temperature (950 °C), the addition of SFA can be good for the production of tiles, while Groups I and II remain the same, according to SS, as at 900 °C. While firing at 1000 °C, even the addition of soy flakes and saturation sludge can give Group II, while inorganic sludge can be used for the production of roof tiles.

The optimization results showed that sunflower hulls (added in 5 and 10 wt.%), wood sawdust (2.5 wt.%), soybean husks (6 wt.%), and saturation sludge (5 and 10 wt.%) are best to be used in solid-bricks production and optimally fired at 900–950 °C. Coal dust (3 and 6 wt.%), landfill ashes (50 wt.%), and neutralization (inorganic) sludge (3 and 6 wt.%) are best to be used in hollow-bricks production and fired at 900–950 °C. Sunflower hulls ash (5 and 10 wt.%) can be added to heavy clay in higher quantity to produce blocks (900–950 °C) or in lower quantity to produce roof tiles (950–1000 °C). Fly ash addition of 50 wt.% allows roof tiles production.

8.4 Conclusions

Waste materials used in this study are listed according to the level of the impact on the properties of fired brick products (weight loss during firing, firing shrinkage, and water absorption increase; and compressive strength and volume mass decrease) in the following series: sunflower hulls from oil factory, wood sawdust, soybean crust, saturation sludge from sugar production, coal dust from thermal power plant, landfill ashes, sludge remained after wastewater neutralization in hot-dip galvanizing industries, sunflower hulls ash, and different fly ashes.

Analyzed wastes are confirmed to be usable as secondary raw materials in the brick industry, but with the additions of organic matter one should be cautious because of possible problems at the finished product after aging. In

particular, the visual and mechanical deteriorations occurred with the addition of residues from the production of sunflower oil and sugar. The incorporation of fly ash and neutralization sludge was the most beneficial, with compressive strength values similar to bricks without waste. Relatively great drop of compressive strength with the addition of wood sawdust, soybean crust, saturation sludge, coal dust, and landfill ashes was also acceptable in terms of such products' usability and quality according to the EN standards.

The optimization results showed that sunflower hulls (added in 5 and 10 wt.%), wood sawdust (2.5 wt.%), soybean husks (6 wt.%) and saturation sludge (5 and 10 wt.%) are best to be used in solid-bricks production and optimally fired at 900–950 °C. Coal dust (3 and 6 wt.%), landfill ashes (50 wt.%), and neutralization (inorganic) sludge (3 and 6 wt.%) are best to be used in hollow-bricks production and fired at 900–950 °C. Sunflower hulls ash (5 and 10 wt.%) can be added to heavy clay in higher quantity to produce blocks (900–950 °C) or in lower quantity to produce roof tiles (950–1000 °C). Fly ashes addition of 50 wt.% allows roof tile production.

Taking into account that a considerable amount and a wide variety of data were used in the present work to obtain the ANN model, and considering that the model turned out to yield a sufficiently good representation of these data, this ANN model can be expected to be very useful in practice for the design and control of the brick production process. The model could be even improved by increasing the laboratory experiments database or by making industrial analysis in as many as possible brick factories.

Acknowledgments

The authors wish to express their gratitude to the Serbian Ministry of Education, Science and Technological Development, for financial support of this research, included in projects III45008 and TR31055, project cycle 2011–2014.

References

1. Kaden, M., Controlling the residual oxygen content of kiln gases. *Ziegelindustrie,* 8, 26, 2005.
2. Xuanye, Z., Guansheng, L., Juan G., Investigation of application possibilities for high-calcium industrial wastes in bricks. *Ziegelindustrie*, 11, 35, 2005.
3. Zhang, L., Production of bricks from waste materials – a review. *Constr. Build. Mater.*, 47, 643, 2013.

4. Lingling, X., Wei, G., Tao, W., Nanru, Y., Study on fired bricks with replacing clay by fly ash in high volume ratio. *Constr. Build. Mater.*, 19, 243, 2005.
5. Arsenović, M., Radojević, Z., Stanković, S., Removal of toxic metals from industrial sludge by fixing in brick structure. *Constr. Build. Mater.*, 37, 7, 2012.
6. Demir, I., Orhan, M., Reuse of waste bricks in the production line. *Build. Environ.*, 38, 1451, 2013.
7. Pappu, A., Saxena, M., Asolekar, S.R., Solid wastes generation in India and their recycling potential in building materials. *Build. Environ.*, 42, 2311, 2007.
8. Lefort, V., Poorteman, M., Kermel, C., Libert, D., Cambier, F., Reduction of VOC released by pore-forming precursors during firing of clay ceramic. *J. Clean. Prod.*, 13, 1131, 2005.
9. Demir, I., Effect of organic residues addition on the technological properties of clay bricks. *Waste Manage.,* 28, 622, 2008.
10. Chiang, K.-Y., Chou, P.-H., Hua, C.-R., Chien, K.-L., Cheeseman, C., Lightweight bricks manufactured from water treatment sludge and rice husks. *J. Hazard. Mater*., 171, 76, 2009.
11. Pinheiro, B.C.A., Holanda J.N.F., Processing of red ceramics incorporated with encapsulated petroleum waste. *J. Mater. Process. Technol.*, 209, 5606, 2009.
12. Hajjaji, M, Khalfaoui, A., Oil shale amended raw clay: firing transformations and ceramic properties. *Constr. Build. Mater*., 23, 959, 2009.
13. Ruppik, M., Use of organic and inorganic pore-forming agents in the brick and tile industry. *Ziegelindustrie*, 59, 22, 2006.
14. Sutcu, M., Akkurt, S., The use of recycled paper processing residues in making porous brick with reduced thermal conductivity. *Ceram. Int.,* 35, 2625, 2009.
15. European Commission, BREF document – Reference Document on Best Available Techniques in the Ceramic Manufacturing Industry, 2007.
16. Romero, M., Andres, A., Alonso, R., Viguri, J., Rincon, J. Ma., Sintering behaviour of ceramic bodies from contaminated marine sediments. *Ceram. Int*., 34, 1917, 2008.
17. Samara, M., Lafhaj, Z., Chapiseau, C., Valorization of stabilized river sediments in fired clay bricks: Factory scale experiment. *J. Hazard. Mater*., 163, 701, 2009.
18. Van Wijck, H., Marks, H. Consequences of using additives for reducing the amount of mixing water needed in the heavy clay ceramic industry (Considerations related to energy savings and technical production aspects). KGK magazine 2, text available at http://www.kgkmagazine.nl/files/papertcki.pdf, 2008.
19. Tiwari, M., Sahu, S.K., Bhangare, R.C., Ajmal, P.Y., Pandit, G.G., Elemental characterization of coal, fly ash, and bottom ash using an energy dispersive X-ray fluorescence technique. *Appl. Radiat. Isotopes,* 90, 53, 2014.
20. Barbieri, L., Andreola. F., Lancellotti, I., Taurino, R., Management of agricultural biomass wastes: Preliminary study on characterization and valorisation in clay matrix bricks. *Waste Manage*., 33, 2307, 2013.

21. Quaranta, N., Unsen, M., López, H., Giansiracusa, C., Roether, J.A., Boccaccini, A.R., Ash from sunflower husk as raw material for ceramic products. *Ceram. Int.*, 37, 377, 2011.
22. Nestertsov, A.I., Lightening of red-burning clays in the production of ceramic materials. *Glass. Ceram*., 66, 7, 2009.
23. Arsenović, M., Radojević, Z., Jakšić, Ž., Pezo, L., Mathematical approach of industrial wastes application in clay brick production – Part I: testing and analysis. *Ceram. Int*., 41, 4890, 2015.
24. Arsenović, M., Optimization and prediction of the quality of materials, process and final properties of heavy clay products by mathematical modeling of the characteristic parameters, PhD dissertation, Faculty of Technology and Metallurgy, University of Belgrade, Belgrade, 2013.
25. Arsenović, M., Pezo, L., Stanković, S., Radojević, Z., Sensitivity analysis of mathematical models for final product properties: link to DTG curve. *Ceram. Int*,. 39 (6), 6277, 2013.
26. Pezo, L., Arsenović, M., Radojević, Z., 2014. ANN model of brick properties using LPNORM calculation of minerals content, *Ceram. Int*., 40 (7A) 9637, 2014.
27. Arsenović, M., Stanković S., Radojević Z., Pezo L., Prediction and fuzzy synthetic optimization of process parameters in heavy clay brick production. *Ceram. Int.*, 39 (2), 2013, 2013.
28. Arsenović, M., Stanković, S., Pezo, L., Mančić, L., Radojević, Z. Optimization of the production process through response surface method: bricks made of loess. *Ceram. Int.*, 39 (3), 3065, 2013.
29. Arsenović, M., Pezo, L., Radojević, Z., Stanković, S., Serbian heavy clays behavior: application in rough ceramics. *Hem. Ind.*, 67 (5), 811, 2013.
30. Brlek, T., Pezo, L., Voća, N., Krička, T., Vukmirović, Đ., Čolović, R., Bodroža-Solarov, M., Chemometric approach for assessing the quality of olive cake pellets. *Fuel Process. Technol.*, 116, 250, 2013.
31. Taylor, B.J., *Methods and Procedures for the Verification and Validation of Artificial Neural Networks*. Springer Science and Business Media, Inc., USA, 2006.
32. Grieua, S., O. Faugeroux, A. Traoré, B. Claudet, J.-L. Bodnar, Artificial intelligence tools and inverse methods for estimating the thermal diffusivity of building materials. *Energ. Buildings*, 43, 543, 2011.
33. Trelea, I. C., A. L. Raoult-Wack, G. Trystram, Note: application of neural network modeling for the control of dewatering and impregnation soaking process (osmotic dehydration). *Food Sci. Technol. Int.*, 3, 459, 1997.
34. Pezo, L.L., B.Lj. Ćurčić, V.S. Filipović, M.R. Nićetin, G.B. Koprivica, N.M. Mišljenović, Lj.B. Lević, Artificial neural network model of pork meat cubes osmotic dehydratation. *Hem. Ind.,* 67 (3), 465, 2013.
35. Kollo T., D. von Rosen, *Advanced Multivariate Statistics with Matrices (Mathematics and Its Applications)*, Springer, the Netherlands, 2005. http://dx.doi.org/10.1007/1-4020-3419-9.

36. Basheer, L. A. M. Hajmeer, Artificial neural networks: fundamentals, computing, design and application. *J. Microbiol. Meth*., 43, 3, 2000.
37. Gliozzo, E., Iacoviello, F., Foresi, L.M., Geosources for ceramic production: the clays from the Neogene–Quaternary Albegna Basin (Southern Tuscany). *Appl. Clay Sci.,* 91–92, 105, 2014.
38. Arsenović, M., Pezo, L., Mančić, L., Radojević, Z., Thermal and mineralogical characterization of loess heavy clays for potential use in brick industry. *Thermoch. Acta*, 580, 38, 2014.
39. Koseoglu, K., Polat, M., Polat, H., Encapsulating fly ash and acidic process waste water in brick structure. *J. Hazard. Mater.*, 176, 957, 2010.
40. Arsenović, M., Radojević, Z., Jakšić, Ž., Pezo, L., Mathematical approach of industrial wastes application in clay brick production – Part II: optimization. *Ceram. Int*., 41, 4899, 2015.
41. Cultrone, G., Sebastián, E., Elert, K., José de la Torre, M., Cazalla, O., Rodriguez–Navarro, C., Influence of mineralogy and firing temperature on the porosity of bricks. *J. Eur. Ceram. Soc.*, 24, 547, 2004.
42. Xu, Y., Yan, C., Xu, B., Ruan, X., Wei, Z., The use of urban river sediments as a primary raw material in the production of highly insulating brick. *Ceram. Int.*, 40, 8833. 2014.
43. Arsenović, M., Radojević, Z., Stanković, S., Lalić, Ž., Pezo, L., What to expect from heavy clay? *Ceram. Int*., 39(2), 1667, 2013.

9

Functional Tantalum-based Oxides: From the Structure to the Applications

Sebastian Zlotnik, Alexander Tkach* and Paula M. Vilarinho

CICECO-Aveiro Institute of Materials, Department of Materials and Ceramic Engineering, University of Aveiro, Aveiro, Portugal

Abstract

Due to stability and lack of toxicity metallic tantalum (Ta), its pentavalent oxide (Ta_2O_5) and tantalate complex oxides become commercially attractive in a number of technologies. Particularly, alkali tantalates with perovskite-like structures, including potassium tantalate, $KTaO_3$, sodium tantalate, $NaTaO_3$, and lithium tantalate, $LiTaO_3$, are encouraging functional materials within the ferroic family of lead-free compounds. Their versatile properties make them potential players in microelectronics, photocatalytic processes or medicine. The scientific and technological importance of the Ta compounds is reviewed in this chapter. The structure, chemical and physical properties of alkali tantalates are described in details. The difference in their functional properties, which are also strongly dependent on the synthesis conditions, is emphasized. The fabrication of these compounds as ceramics with the desired density, stoichiometry, structure and material stability that is always fundamental to ensure the durability and reliability of the compound with particular function is shown to be still challenging. A look over the possible applications of alkali tantalates for electronic components, photocatalysis and tissue engineering is presented.

Keywords: Tantalum-based oxides, perovskites, alkali tantalates, crystallographic structure, functional properties, biomaterials, photocatalysts

**Corresponding author*: atkach@ua.pt

Ashutosh Tiwari, Rosario A. Gerhardt and Magdalena Szutkowska (eds.) Advanced Ceramic Materials, (337–384) © 2016 Scrivener Publishing LLC

9.1 Functional Materials: Current Needs

It is predicted that in 2025 [1]:

1. *Solar is the largest source of energy on the planet*. Methods for harvesting, storing and converting solar energy are so advanced and efficient that it becomes the primary source of energy on our planet.
2. *Electric air transportation takes off*. Light-weight aerospace engineering coupled with new battery technologies power electric vehicle transportation – on land and in the air.
3. *Digital everything … everywhere*. From the smallest personal items to the largest continents, everything, everywhere will be digitally connected, and responsive to our wants and likes.

At the same time it is known that technology, design, engineering and advanced materials are required for these predictions to become reality. These needs have been the driving force behind the current development of materials and the current vital importance of functional materials.

The difference between a device and a functional material arises from the fact that the functional material preserves its functional property even when its volume is split, while the device is normally a multicomponent instrument that fails when it is disintegrated [2]. The definition of functional materials reflects the ability of a material to perform a certain function under a determined stimulus [3]. Although this unspecific definition includes a wide spectrum of materials and a wide range of material properties and applications, the classification of functional materials is usually related to materials, whose function is associated with their electric, magnetic, and or optical properties. Additionally, functional materials are normally related with such applications as information technology, electrical energy conversion, biologics and biomedics, space technology, among others [3].

Functional materials are found in all material classes: ceramics, metals, polymers and composites. Functional ceramic materials consist of a huge group of inorganic compounds that by definition are non-metallic and non-water soluble. This family in which the main characteristics, such as electricity, magnetism, heat, light or force are used to detect, transform, couple, transport, and store information, are characterized by their major properties [4]. Examples of functional materials applications driven by their responsive nature [5], are:

- *Electrical/magnetic* (for example, *electroceramics* as their primary function is related to the electrical properties), to be

used as insulators, semiconductors, conductors and magnets for capacitors, memories, data and information storage, energy conversion, *etc.*;
- *Optical*, to be used as components for lenses, lasers, fibers due to their good transparency to light with distinct wavelength;
- *Chemical*, to be used as catalysts, sensors;
- *Biological*, to be used as bioceramics, mostly for implants, and as nanomaterials in drug delivery systems.

In some cases other groups are also included, *e.g.* mechanical, thermal and nuclear ceramic materials, especially in the older textbooks. The simplified categories of functional ceramics are illustrated in Figure 9.1. Few examples of materials from each group are listed in the outer shell of the graph. The largest growth segments are electronic ceramics that mainly include ferroelectric (FE), piezoelectric, dielectric, semiconductor, superconducting,

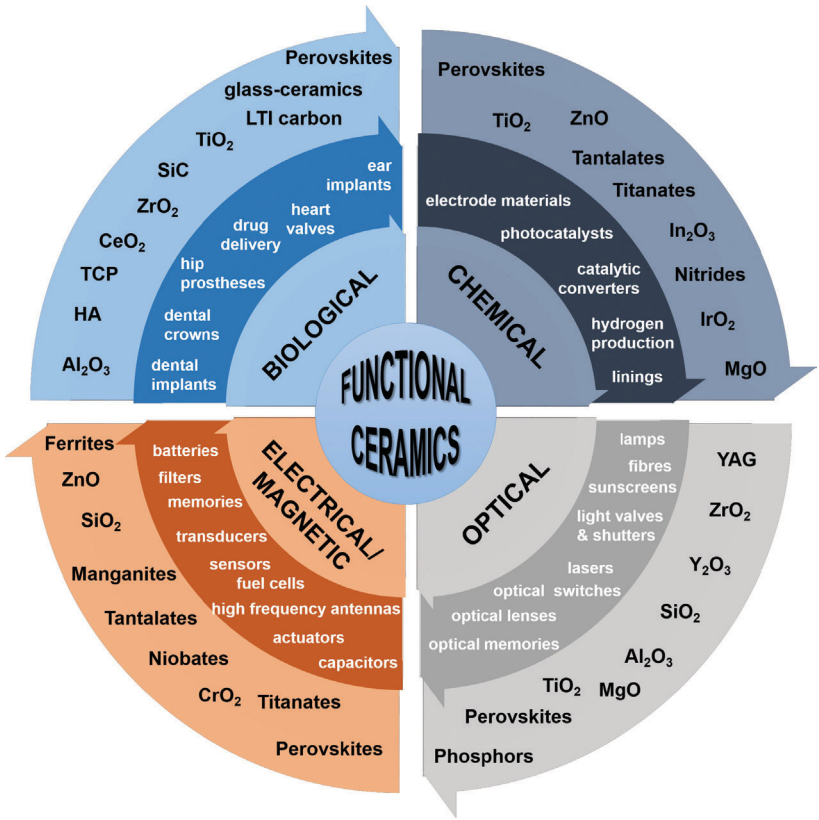

Figure 9.1 Spectrum of functional materials applications. Adapted from Ref. [6].

magnetic, and multiferroic (possessing simultaneously FE and magnetic ordering) materials. However, recently ceramics become used in chemical processing, biological, and environmental-related applications. The dominant compositions are oxides that offer a variety of chemical, physical, structural and microstructural features.

Considering functional oxides, FEs are essential components, being used in a wide spectrum of applications, mainly for microelectronics [3, 7]. A FE material belongs to dielectrics and its main characteristic is that it exhibits an electric dipole moment without an external electric field, which direction can be switched by the application of an alternating field, exhibiting the so-called phenomena of polarization reversal [3]. Ferroelectricity is a temperature dependent property. A FE material with a non-centrosymmetric crystal structure losses its FE behavior above the characteristic temperature designated as Curie temperature (T_C), becoming paraelectric (PE). FEs can be used as memory systems, sensors and actuators, as well as tunable high frequency devices, among others [8–12], in both polar and PE states. Related to ferroelectricity is piezoelectricity, a reversible property leading to a change of dimensions by an electric field and vice versa. Materials possessing this property are widely used as components in medical imaging devices, engine ignition systems, microelectromechanical systems (MEMSs), *etc*. From the group of piezoelectrics, perovskite type titanates, *e.g.* Pb(Zr, Ti)O_3 (PZT) and (Ba, Sr)TiO_3 (BST), account for ~50 % of total sales of electroceramics, being commercially used as capacitors, transducers, thermistors, *etc.* [13].

FE material holds its main functionality in the polar state (below T_C) but is also useful above T_C, in the PE state. In this non-polar phase, a FE is normally characterized by a high dielectric permittivity, which strongly depends on temperature, applied external field and mechanical stress [9]. The dielectric permittivity is important in defining capacitors with high capability to store electrical energy. FEs in PE phase are also useful in tunable microwave devices, *e.g.* phase shifters as components in electronically scanned phased-array antennas for communications and radar applications, because of their low dielectric losses and reasonable tunability (dependence of a dielectric permittivity on the applied bias electric field). In this respect, the incipient FEs (or quantum PEs), such as perovskite type $SrTiO_3$ and $KTaO_3$, are of great interest because they do not possess the phase transition into polar phase at any temperature. Thus, their dissipation factor or dielectric loss can be as low as 10^{-4} to 10^{-5} that is very attractive for microwave applications.

As it is shown above, the most dominant functional materials for electronic, energy, and other applications are perovskite type oxides. The

general chemical formula for the perovskite oxides is ABO_3, where A and B are cations of very different sizes (A are larger than B), and O is an oxygen that bonds to both. The basic perovskite framework is a 3-dimensional array of corner sharing octahedra. The ideal perovskite cubic-symmetry structure has B cation in 6-fold coordination, surrounded by an octahedron of anions, and the A cation in 12-fold cuboctahedral coordination. The stability of the perovskite structure is defined by the tolerance factor:

$$t = \frac{r_A + r_O}{\sqrt{2}(r_B + r_O)} \tag{9.1}$$

where r_A is the radius of the A-site cation, r_B is the radius of the B-site cation, and r_O is the radius of the O [14]. Because of the quite stringent ion size requirements for the stability of the cubic structure, slight buckling and distortion can produce several lower symmetry distorted versions, in which the coordination numbers of A cations, B cations or both are reduced. In such a way, perovskite structures and related ones can incorporate ions of a variety of sizes and charges, as this framework is flexible, allowing for subtle distortions that ease the bond strains created by size mismatch. Majority of the perovskite family compounds has the BO_6 octahedra tilted in various ways, giving deviations from the ideal high-symmetry cubic structure [15]. Thus, the physical properties change due to the corresponding modification of crystal and electronic structures. The perovskite structure is capable to host above 90% of the metallic elements from the periodic table, either on the A or B site, being highly tunable structure through substitution and mixed oxidation states [16, 17]. It leads to a huge number of compounds with extraordinary properties, such as ferroelectricity ($BaTiO_3$, $KNbO_3$, PZT), piezoelectricity (PZT, (K, Na)NbO_3 – KNN), ferromagnetism ($SrRuO_3$), ionic-electronic conductivity ((La, Sr)MnO_3), high electron mobility ($SrTiO_3$), nonlinear optical ($LiNbO_3$, $LiTaO_3$), and catalytic ($NaTaO_3$) properties, *etc.* [16, 18]. Being studied for a long time, the perovskite compounds are still not discovered completely, leading to astonishing explorations from time to time, especially at the interfaces between films and substrate, or between layers in heterostructures [15].

This state of the art of the current needs for functional materials will be used as the stepping stone to introduce the technological importance of tantalum (Ta) and Ta complex oxides in the second part of the chapter. The structure, chemical and physical properties of Ta complex oxides will be described and their relations established in the third part of the chapter. Thereafter, the fourth part of the chapter will describe alkali tantalates

processing, highlighting the different conditions, technologies, and difficulties associated with the processing of these materials as ceramics. The fifth part will end the chapter by a look over the possible future applications of alkali tantalates for photocatalysis and tissue engineering.

9.2 Importance of Tantalum and Tantalum-based Oxides

Ta is a rarely occurring transition metal with unique features. It is one of the refractory metals with high melting temperature, >2000 °C, and low vapor pressure, thus the element is extremely stable. Moreover, Ta has an excellent resistance to corrosion (similar to glass) due to a natural protective oxide layer [19–21]. This oxide layer is normally tantalum pentaoxide, Ta_2O_5, one of the most important compound in optical, electronic, and medical applications [20]. Over the last decades, it is well-recognized as a dielectric material used as a capacitor due to its high dielectric constant. Lately, a 3D nonvolatile memory structure composed of Ta_2O_5 with excellent switching behavior was tested and proposed as an alternative for high density devices based on solid-state memory technology [22]. It can be found in microelectronic components of mobile phones, smartphones, laptop computers and portable music players, *etc.* [23]. Due to its extremely low failure rate, it is used in medical equipment, *e.g.* hearing aids, pacemakers. Ta as a metal is also widely implemented in orthopedic implants because of relatively good biocompatibility in comparison with other metals [21]. Apart from the mentioned applications, it is used in alloys (for aircraft construction) and industrial cutting tools (tantalum carbide) [19, 24, 25].

Recently, Ta_2O_5 has become an interesting material for photocatalytic reactions as a semiconductor material with a band gap ~4 eV [20]. Although its large band gap makes Ta_2O_5 only responsive to ultraviolet (UV) light, the electronic band structure has particular features interesting for H_2 evolution reaction during water splitting, *i.e.* the valence band maximum and the conduction band minimum overlap the redox potentials of H^+/H_2 and O_2/H_2O.

Tantalum oxide-based compounds, the so-called tantalates, represent also an interesting group of materials. They mainly consist of the TaO_3^- and $Ta_2O_6^{2-}$ anions, and are combined with alkali or alkaline earth metal cations. Due to their versatile crystal structure with layered arrangement, the migration of charge carriers is facilitated, leading to high photoactivity [20]. Lithium tantalate is also an important component of lead-free piezoelectrics. There is a demand to explore novel compounds, or engineer

already existing compositions, in order to prevent using lead-based systems, *i.e.* $Pb(Zr_{1-x}Ti_x)O_3$ [26] and to produce materials at low cost and using preferably abundant elements [27]. So far compositions from the solid solution between $PbZrO_3$ and $PbTiO_3$ (PZT) are the most successful perovskite structure materials on the market, being used in piezoelectric actuators, sensors, and transducers [28]. However, the use of PZT that contains more than 60 wt% of lead will be soon severely restricted, due to the lead toxicity [26]. Therefore, there is a need of sustainable materials and manufacturing routes to use lead-free alternatives compatible with the current most restrict environment directives. Due to that, tantalum and niobium oxide-based systems, such as alkali tantalates and niobates, have been considered as one of the group of the most promising compounds on the list of functional materials for future technologies [26, 29].

Alkali tantalate oxides, with general formula $ATaO_3$ (*A* holds for alkali metal ion: Li, Na, or K), contain a number of relevant compounds that possess the perovskite-like structure. Among them are potassium tantalate ($KTaO_3$–KTO), sodium tantalate ($NaTaO_3$–NTO), and lithium tantalate ($LiTaO_3$–LTO), a group of complex oxides with distinguished features. LTO belongs to high temperature FEs, which are necessary in automotive, aerospace, and power-generating industries that require endurance under harsh temperature conditions [30]. $KTaO_3$ is a dielectric with low losses ($\sim 10^{-4} - 10^{-5}$) [31] and stays in the PE state in the whole temperature range, being incipient FE. Low-loss materials can be used as capacitors and microwave electronic device components. Moreover, properties of KTO can be tailored by doping with Li^+ ions. $(K, Li)TaO_3$ solid solution has been investigated for decades, showing attractive macroscopic dielectric response at low temperatures [32–34]. $NaTaO_3$ is also an incipient FE [35–37], and a material with a room temperature (RT) crystal structure tunable by preparation method [38]. That in its turn is useful for optimization of photocatalytic activity of NTO [38]. In the next sections, the crystal and electronic structures as well as thermochemistry of the three alkali tantalate compounds are presented.

9.3 Properties of Alkali Tantalates

9.3.1 Crystal and Electronic Structures

From the group of alkali tanatalates, KTO, LTO, and NTO exhibit diverse properties in a wide spectrum. Table 9.1 presents some of their structural, physical, and chemical characteristics.

Table 9.1 Selected characteristics of $ATaO_3$, where A = K, Li or Na [39-44].

	$KTaO_3$	$LiTaO_3$		$NaTaO_3$			
Molecular weight (g/mol)	268.04	235.89		251.94			
Melting point (°C)	1360	1650		1810			
Transition temperature (°C)	–	660		480	550	630	
Crystallographic data:							
State	PE	FE	PE	PE	PE	PE	PE
Crystal system	cubic	trigonal	trigonal	orthorhombic	orthorhombic	tetragonal	cubic
Space group	Pm3m	R3c	$R\bar{3}c$	Pcmn	Bmmb	P4/mbm	
Lattice parameters	a = 3.9885 Å	a_{hex} = 5.1543 Å, c_{hex} = 13.7835 Å or a_{rh} = 5.474 Å, α_{rh} = 56°10.5' (at RT)		a = 5.4842 Å, b = 7.7952 Å, c = 5.5213 Å (at RT)	a = 7.8453 Å, b = 7.8541 Å, c = 7.8633 Å (at 530 °C)	a = 5.5552 Å, c = 3.9338 Å (at 620 °C)	
Band gap (eV)	3.7	4.5	4.0				
Refractive index *n*	>2.2	>2.1	–				
Linear thermal expansion coefficient (10^{-6} °C^{-1})	6.8	$\alpha_a \sim 16.1$ $\alpha_c \sim 4.1$	–				
Thermal conductivity at RT (W·m^{-1}·°C^{-1})	8.5	4.6	–				
RT – room temperature							

The crystal structure of potassium tantalate is a simple cubic perovskite structure, with a space group $Pm\bar{3}m$. It can be viewed as TaO_6 octahedra, which share vertices forming a 3D-framework, where *K* is located in cuboctahedral voids [45, 46]. In other words, the *O* atoms are positioned on the cube faces, the Ta atoms at the center of the cube, and the *K* atoms at the cube corners. The lattice parameter of KTO was calculated to be $a = 3.9883$ Å [45].

The electronic structure of pure KTO was also calculated using the density functional theory (DFT) [47, 48]. The valence bands are of O *2p* character, while the low lying conduction bands are of Ta *5d*, t_{2g} character (three t_{2g} bands right above the Fermi level); higher lying conduction bands are of Ta e_g, *K d*, and Ta *sp* character [47]. KTO has an indirect band gap, the valence band maxima lies at the *R* point, while the conduction band minima is at the center *Γ* of the Brillouin zone [48], with an experimentally determined value of ~3.6 eV.

The incipient FE KTO remains in the centrosymmetric cubic structure down to very low temperatures, at which quantum fluctuations stabilize its polar soft mode [32]. Thus, KTO possesses highly polarizable lattice that is very sensitive to small amounts of impurities, defects and other external stimuli, leading to relaxor, glass-like and FE behaviors [32]. Because of its low dielectric loss at high frequency, it is a good candidate for microwave electronic applications [31].

NTO belongs also to the family of perovskites and has an orthorhombic structure with a space group *Pbnm* ($a = 5.4768$ Å, $b = 5.5212$ Å, and $c = 7.7890$ Å) at room temperature [49]. On heating, it transforms to orthorhombic, *Cmcm*, at ~447 °C, then to tetragonal, *P4/mbm*, at ~560 °C, and to cubic, $Pm\bar{3}m$, structure at ~630 °C, as refined by neutron powder diffraction studies [49]. The low temperature *Pbnm* structure is created by tilting TaO_6 along the *a*- and *b*-axes with the same angle but in opposite direction, and simultaneously along the *c*-axis with different angle. The high temperature orthorhombic structure *Cmcm* is characterized by simultaneous tilting of the oxygen atom octahedron about two of its tetrad axes, the tilting of successive octahedra being out-of-phase along the *b*-axis, and in-phase along the *c*-axis [49].

The electronic band structure of NTO was recently computed by DFT calculations [50]. It was determined that the lowest valence bands are due to O *2s* states, the states at the top of the valence band are mainly of O *2p* character, while the states at the bottom of the conduction band are of Ta *5d* character. The contribution of Na atoms to Ta *5d* and O *2p* is very minor, indicating the high ionicity between Na and TaO_3 [51]. NTO has a direct band gap at the *Γ*–*Γ* point with the gap value estimated to be ~4.1 eV [50, 51].

Since it was established that the crystal structure of NTO at room temperature is non-centrosymmetric, the first report on NTO by Matthias [52] ascribed NTO to FEs. However, the room temperature ferroelectricity was not confirmed by later measurements [36, 53]. Moreover, recently it was demonstrated by low temperature dielectric studies of NTO that it is in fact an incipient FE [35, 37]. It means that the structural phase transitions are not driven by polar soft phonons from the Brillouin zone center, but by soft phonons from Brillouin zone edge in *M* and *R* points [37]. On the other hand, NTO has received much attention in photocatalysis, being referred as one of the most efficient catalyst due to its crystal structure [54].

LTO (like $LiNbO_3$ - LNO) does not exhibit a typical perovskite structure, but it has an ABO_3 lattice with a sequence of distorted oxygen octahedra joined by their faces along a trigonal, polar *c*-axis [39]. The strong TaO_6 distortion causes that the internal O – Ta – O bond angle and the interoctahedron Ta – O – Ta angle are reduced to ~170° and to 144°, respectively [55]. LTO possesses a non-centrosymmetric *R3c* space group (3 *m* point group) symmetry at room temperature. In contrast to normal perovskites, both Li and Ta cations lie within oxygen octahedra with disorder in the Li positions [56]. This structure is classified as a $LiNbO_3$-type, and can be described as a very distorted derivative of the perovskite one, to which it can be related by a displacive transformation [57].

The electronic band structure of LTO was recently computed using the first principles plane-wave pseudopotential DFT [58]. The density of states was determined revealing that the valence band is mainly composed of O *2p* and Ta *5d* states hybridized with small amount of Ta *s* states, and the conduction band is composed of Ta *5d*, O *s* and Li *s* states. However, the band gap of LTO determined from optical adsorption is reported to fall in a wide range 3.9–5 eV [55]. The differences between the electronic density of states of LTO at the FE and PE configurations were also examined [39]. The results indicate that the electronic structures at these phases are very similar, the lithium is almost completely ionized, and its electronic distribution does not change during the phase transition. The only difference was the band gap value, which becomes larger by ~15% in the FE phase. The same research studied the origin of ferroelectricity in LTO. It was discovered that the driving mechanism behind the FE instability is the hybridization between the *d* state on Ta atom and the *2p* state on O leading to the displacement towards each other (an order–disorder model), and Li is rather passive [39]. In addition, the assessment of the Ta – O distances revealed that the oxygen octahedra in LTO are smaller than that

in KTO, although the Ta atom never displaces to the off-center position in KTO.

LTO is widely produced in the form of crystals, having unique electro-optical, piezoelectric, photoelastic, and nonlinear optical properties. Thus, it is used in laser frequency doubling, nonlinear optics, components for lasers, or other acousto-optic devices [56]. But in comparison with $LiNbO_3$, LTO is mostly implemented as a component in shorter-wavelength applications, and it has longer storage time.

However, it is difficult to grow high quality stoichiometric LTO single crystals. LTO with Li:Ta ratio within 1 ± 0.3% is referred as stoichiometric while most of the commercially available LTO crystals are congruent, containing a large number of non-stoichiometric defects [59]. The main reason of non-stoichiometry in LTO crystals is related to a complex phase diagram with a region of non-stoichiometric solid solubility of LTO at high temperatures toward Ta excess. Thus, it leads to an existence of congruently melting compositions (solid and liquid phases in equilibrium). The main congruent composition of LTO is a composition with approximately 1.5 mol% Li deficiency from the stoichiometric one [59]. The non-stoichiometry in LTO has tremendous effect on the Curie temperature, *i.e.* congruent LTO exhibits a T_C of ~600 °C, while that of stoichiometric LTO is nearly 700 °C. It can be related to point defects, *e.g.* Li vacancies, as well as Ta reduction to Ta^{4+} and its transfer to Li sites (the so-called Ta antisites) [43]. Near-stoichiometric LTO crystals have a structure-sensitive nature due to their low defect density comparing to congruent LTO. As the composition changes from congruent to stoichiometric one, the light absorption edge shifts to shorter wavelengths, being favorable for many optoelectronic applications using UV light [59].

9.3.2 Thermochemistry

It is known that the material stability either mechanical, thermal, or chemical is a key factor of material's durability. The chemical and thermal stabilities are strongly associated with thermodynamic properties such as formation energy of the compound, which is important at the early stage of the materials processing to control the functional properties [57]. Within this context the enthalpy of formation is an important thermodynamic feature [60].

The enthalpies of formation and surface energies of alkali tantalates with perovskite-like structures were recently determined experimentally for the first time [61, 62]. Progress in the calorimetry technique and development in metrology over the last decades have allowed to collect thermodynamic

data on a number of compositions in real conditions [63]. Namely, high-temperature oxide melt solution calorimetry is a powerful technique that allows one to study the thermochemistry of complex oxides and even refractory ceramic materials [64, 65].

Using well-established and suitable thermochemical cycles, the formation enthalpies of alkali tantalates both from oxides and elements were experimentally obtained [61, 62]. The enthalpy of formation from the constituent elements is always large and negative in comparison to the enthalpy of formation from the binary constituent oxides (Table 9.2).

The energetics indicate that the formation enthalpies become more exothermic (more negative) with increase in the size of the alkali cations: $\Delta H_{f\ LTO}^{ox} > \Delta H_{f\ NTO}^{ox} > \Delta H_{f\ KTO}^{ox}$. This is an evidence that KTO is energetically more stable than NTO and LTO. Moreover, an additional study of KTO with different K/Ta ratios (KTO with defect pyrochlore structure) has shown that the defect pyrochlore $K_2Ta_2O_6$ is the most stable compound (see Table 9.2) that explains its formation at reduced temperature synthesis of KTO [62]. There exist only one theoretical study on KTO, evaluating the formation enthalpy using a plane-wave pseudopotential method within a DFT formalism [66]. However, the simulations yield values rather different from those obtained experimentally that may be related to the crystal structure selected for modeling.

The trends in the thermodynamic properties of inorganic compounds can be discussed from different points of view, and in the case

Table 9.2 Energetics of alkali tantalates [61, 62].

Composition	Tolerance factor, *t*	ΔH_f^{ox} (kJ/mol)	ΔH_f^0 (kJ/mol)	γ_{hyd} (J/m^2)
$LiTaO_3$	0.78	–93.74 ± 1.77	–1415.94 ± 2.29	1.04 ± 0.34
$NaTaO_3$	0.94	–147.35 ± 2.46	–1378.00 ± 3.27	1.58 ± 0.29
$KTaO_3$	1.03	–203.63 ± 2.92	–1408.23 ± 3.75	–
$K_{0.87}Ta_{2.23}O_6$	–	–339.54 ± 5.03	–2775.46 ± 6.92	–
$K_{1.13}Ta_{2.18}O_6$	–	–369.71 ± 4.84	–2800.60 ± 6.76	–
$K_{1.30}Ta_{2.14}O_6$	–	–364.78 ± 4.24	–2790.68 ± 6.33	–
$K_2Ta_2O_6$	–	–409.87 ± 6.89	–2819.07 ± 8.42	–

ΔH_f^{ox} – enthalpy of formation from oxides, ΔH_f^0 – enthalpy of formation from elements, γ_{hyd} – hydrated surface energy

of perovskites the tolerance factor, *t*, and the stability index, *s*, are the most common factors used in the prediction of their stability [60, 67]. The former factor considers the relative atomic size of the different ions in a compound, as presented by Eq. (1) initially introduced in 1920s by Goldschmidt [14]. The ionic radii were taken from Shannon's effective ionic radii table [68], and the coordination of 6 was assumed for Li^+, 8 for Na^+, 12 for K^+, and 6 for Ta^{5+}. The latter one is based on the acid–base chemistry, taking into account the ionic potential of the metal cations [67]. However, the trends can only be estimated if experimental data are available.

Figure 9.2 depicts the variation of the enthalpies of formation of $LiTaO_3$, $NaTaO_3$, and $KTaO_3$ with relation to their tolerance factor and stability index. With an increase of the tolerance factor (near $t = 1$ where the structure is less distorted), formation enthalpies become more negative, indicating that the formed perovskite materials are more stable than their binary constituent oxides. Similarly, with a larger *s*, the ΔH_f^{ox} becomes more exothermic. The most stable compounds are then formed by combining a very acidic and a very basic oxide. An acidic oxide is an oxide ion acceptor, and a basic oxide is an oxide ion donor. The basicity of the alkali oxides

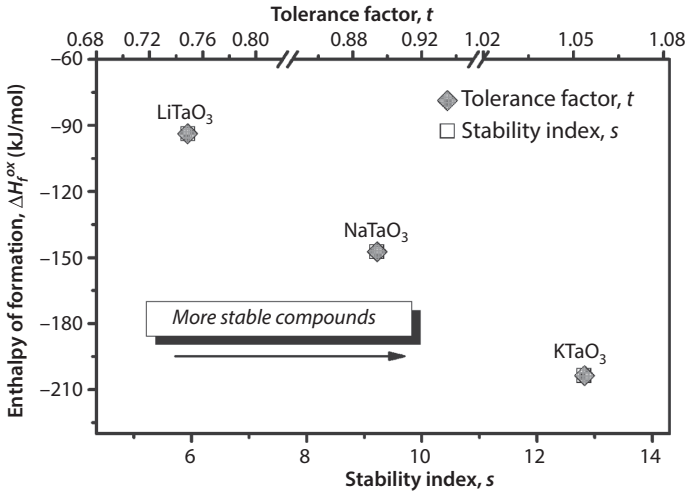

Figure 9.2 The variation of enthalpies of formation of alkali tantalates, $LiTaO_3$, $NaTaO_3$, and $KTaO_3$, as a function of tolerance factor, *t*, and stability index, *s*. With the increase in the tolerance factors and stability index of alkali tantalate perovskites, the formation enthalpies become more negative. Adapted from Ref. [61] with permission from The Royal Society of Chemistry.

increases as: Li_2O (1.00) < Na_2O (1.15) < K_2O (1.40), being based on an optical basicity scale [69]. Therefore, the larger difference in acidity of A_2O (strongly basic) and Ta_2O_5 (strongly acidic) leads to the more exothermic enthalpy of reaction [70]. Thus, the transfer of an oxygen ion from A_2O to Ta_2O_5 forms an A^+ and a TaO_3^- ions, representing a strong (highly exothermic) acid–base reaction [67].

Driven by prospective new applications, nanoparticles with the perovskite structure have been recently raising interest due to the appearance of novel phenomena in these nanomaterials when compared to their bulk counterparts. However, possible applications of these materials are strongly associated with their reactivity and stability, thus the surface and interface energies are fundamental to be known in order to fully discover and understand their potential. The surface energies of an array of binary and ternary oxides (*e.g.* ZrO_2 [71], CeO_2 [72], Mn_3O_4, Mn_2O_3, MnO_2 [73], TiO_2 [74], $PbTiO_3$, $BaTiO_3$ [75], $SrTiO_3$ and $CaTiO_3$ [76]) has also been successfully measured by solution calorimetry.

The heat of solution of the hydrated surfaces was determined, and then corrected for water content. The total water content, n, in $ABO_3{\cdot}nH_2O$ was obtained from thermogravimetric analysis, by weighing the samples before and after the heat treatment. The n normally corresponds to two terms: (i) chemisorbed water, represented by adsorption enthalpies more negative than the enthalpy of water vapor condensation (−44 kJ/mol), and (ii) physisorbed water, being characterized by adsorption enthalpies equal to the enthalpy of water vapor condensation [76]. The surface energy, γ_{hyd}, was calculated by taking into account the drop solution enthalpies of macroscopic and nanosized materials, and difference in their surface area. It corresponds to the thermodynamics of the real surfaces, because under ambient conditions oxides adsorb water molecules very easy. To note as well that the performed experiments consider a range of surface planes and defect structures, thus the measured energies are an average of many planes, edges, kinks, steps, pits, and corners [77]. The data show that the γ_{hyd} of NTO is higher than of LTO (Table 9.2) [61]. It was also observed that the more ionic perovskite possesses more stable structure (more exothermic the ΔH_f^{ox}), higher surface energy, and more tightly bonds to H_2O. These thermodynamic data are potentially important in case of the liquid phase synthesis of the nanoparticles, governing nucleation, growth, Ostwald ripening and nanoparticle stabilization. Besides, the surface energies are directly related to the driving forces of the processes considering solids, such as chemical reactivity, catalysis, coarsening, sintering, *etc.* [78, 79].

9.4 Processing of Alkali Tantalate Ceramics for Electronic Applications

Currently, due to the extensive use of microwaves in radar and communication applications, including military, airport and police radars, satellite communication systems, mobile phones, and wireless computer networks [80] and due to the reaching of the computer clock frequency to the GHz range, one of the most important applications for FE materials is related to microwave microelectronic elements. Thus, cylinders or cubes of dielectric single crystals or ceramics can be used as dielectric resonators or filters. Their linear dimension l is proportional to $1+\sqrt{\varepsilon'}$ [81]. Hence, a high dielectric permittivity ε' of material is particularly important for mobile and satellite communication systems, allowing to reduce the dimensions and correspondingly mass of the dielectric resonators and filters. In addition, if the dielectric constant of the material reveals a dependence on an applied bias electric field E, these elements can be tunable [8, 82–84]. This property, commonly called dielectric tunability, is characteristic of FE materials and is strengthened on approaching the PE–FE phase transition, at which the dielectric constant has a maximum [85]. Thus, applying bias electric field to the FE material of resonator of finite dimensions, it is possible to obtain the desirable resonance frequency proportional to $\varepsilon'(E)^{-1/2}$. Bulk FEs can also be used as parallel plate tunable capacitors or varactors at radio frequencies; as electroded slabs in stack of lens antennas [86]; and as small low cost microwave phase shifters for electronic scanning antennas with high reliability and low complexity [87, 88]. In other words, applying bias electric field, it is possible to obtain desirable capacitance (which is proportional to $\varepsilon'(E)$), desirable steering of the electromagnetic beam, passing through the lens antenna, and desirable phase shift (proportional to $\varepsilon'(0)^{-1/2} - \varepsilon'(E)^{-1/2}$), respectively.

Along with the high dielectric constant and high tunability, low loss (or high quality factor $Q = 1/tan\delta$) and high temperature-stability of the material are also important for microwave elements. However, such microwave application requirements are quite contradictory, because the temperature-stable and low-loss materials (such as diamond or sapphire) have rather small ε' and tunability, whereas high dielectric constant and tunability (usually observed for FEs, such as $BaTiO_3$ and $PbTiO_3$, especially near the phase transition) is accompanied by high temperature coefficient $\tau_\varepsilon = d\varepsilon'/dT$ and loss [89].

$(Ba,Sr)TiO_3$ is currently considered as the main candidate for tunable electronic applications due to the high tunability of the dielectric

permittivity of FE $BaTiO_3$ and low dielectric loss of incipient FE $SrTiO_3$ [86]. However, the dielectric loss of $KTaO_3$, another incipient FE, is reported to be more than 2 times lower from room to liquid nitrogen temperature and about 2 orders of magnitude lower at 5.4 K than that of $SrTiO_3$ [31].

The best KTO single crystals possess loss $\tan\delta \sim 10^{-4}$ in GHz range, whereas the dielectric permittivity continuously increases to ~5000 on cooling toward 0 K [31], becoming dc-electric-field tunable in the low-temperature range [90, 91]. However, there are also numerous reports on KTO single crystals presenting loss $\tan\delta \sim 10^{-3}$ reaching even values of few percents around 50 K associated with unavoidable impurity or lattice defects [32, 91–93]. Thus, the processing of potassium tantalate [32, 94–97] and alkali tantalates in general [35, 98, 99], either in the form of single crystals or polycrystalline materials is known to be not trivial. The most recognizable justifications are: (i) moisture sensitivity of the alkali precursors, (ii) high volatility of the alkali elements, and (iii) strong covalent character of the Ta – O bonds [35, 94–101], which leads to compositional deviations and defects that degrade the functional properties of alkali tantalates.

Overall, the occurrence and apparent stability of the formed phases are strongly dependent on the selected synthesis method and preparation conditions, as starting reagents, temperature, time, and atmosphere. The majority of the research studies on alkali tantalates has been conducted on single crystals [31, 32, 90, 91], and reports on processing of polycrystalline bulk are rather rare [35, 94–99] even though ceramics are cheaper to produce. In the case of KTO, this scarcity probably stems from the difficulty in achieving high-density monophasic and stoichiometric polycrystalline KTO, since KTO sinters in very narrow temperature interval close to the melting point above 1350 °C [102]. Furthermore, the starting reagents have to be carefully dried and potassium evaporation during the heat treatment needs to be controlled to ensure the desired stoichiometry.

The optimization of the dielectric response in functional materials is evidently associated with the precise control of the composition/stoichiometry. Chen *et al.* obtained KTO ceramics by conventional sintering at 1330 °C for 1 h with dielectric permittivity up to only 1000 and dissipation factor about 7.5% at 100 kHz [94], which are much worse than those reported by Geyer *et al.* for KTO single crystals [31]. Axelsson *et al.* could obtain KTO ceramics with dielectric permittivity up to 3100 at 3.6 GHz by conventional sintering at 1340 °C for 1 h but only by adding 5% excess of potassium [95]. At the same time, the dielectric loss values were found to vary between 0.0001 and 0.02, although not only with temperature but also from sample to sample [95]. However, if ceramics are prepared without potassium excess, a potassium-poor $K_6Ta_{10.8}O_{30}$ secondary phase is formed [95, 97], yielding

indeed a strong decrease in the maximum dielectric permittivity [97]. More recently, KTO ceramics were sintered at 1350 °C for 1 h with an initial 2% excess of potassium that was found to be enough to obtain a dielectric permittivity as high as 4000 together with tanδ of 0.0047 ± 0.0023 at 10 kHz [97], as shown in Figure 9.3. Such high permittivity was explained by formation of single phase ceramics with lattice parameters close to that of KTO single crystals and liquid-phase [102] enhanced grain growth compared to the ceramics prepared without initial potassium excess [97]. However, even with initial potassium excess an achieving of high relative density, >90 %, is still challenging for the KTO ceramics prepared by conventional solid-state reaction method [94, 95, 97].

On the other hand, some of the problems faced with the preparation of KTO ceramics by conventional solid-state reaction, like evaporation of potassium or poor ceramic densification, could be overcame when using

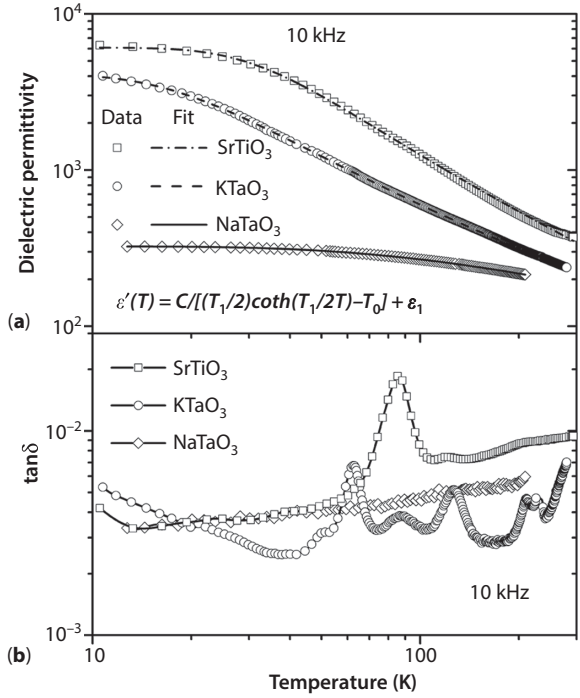

Figure 9.3 Temperature dependence of the real part of the dielectric permittivity ε′ (a) and of the dielectric loss tanδ (b) of $NaTaO_3$, $KTaO_3$, and $SrTiO_3$ ceramics at 10 kHz together with the fit of the ε′(T) experimental data to the Barrett's relation, indicating them as incipient FEs.

pressure-assisted sintering [94, 96]. Chen *et al.* could obtain 92% dense KTO ceramics by hot isostatic pressing at 1300–1310 °C under 20.7 MPa in argon for 1 h, yielding the dielectric permittivity up to 2000 and dissipation factor about 1% at 100 kHz [94]. More recently, pure phase KTO ceramics with relative density ≥95% were obtained by Glinšek *et al.* , using hot pressing of mechanically activated powders at 1250 °C and 25 MPa for 2 h [96]. However, the maximum permittivity they could get using single calcined powders was still about 2500. Just using a double calcination, the dielectric permittivity up to 4080 and dissipation factor between 0.001 and 0.016 at 1 kHz [96] and between 0.004 and 0.0013 in GHz range [103] were obtained in the dense hot-pressed KTO ceramics. This maximum permittivity value is shown in Table 9.3 in comparison to other ceramics and single crystals. Surprisingly, this value is not much superior to that reported for KTO ceramics conventionally sintered at 1350 °C with 2% potassium excess [97].

Processing of $NaTaO_3$ ceramics is also complicated. First, similarly to KTO, the starting reagents have to be carefully dried due to moisture sensitivity of the alkali precursors. Second, the sintering temperature required to obtain NTO ceramics is normally ≥1550 °C [36, 53, 98] that is much higher than that of KTO. These high sintering temperatures strongly promote sodium evaporation and secondary Ta-rich phases, such as $Na_2Ta_4O_{11}$ and $Na_2Ta_8O_{21}$, are frequently present in the sintered NTO ceramics [98], affecting the electrical properties, which are indeed reported only few times. Iwasaki and Ikeda claimed that the dielectric permittivity of NTO increases monotonically on cooling from 923 to 4 K without any peak, although neither the temperature dependence of the dielectric permittivity nor the values of the dielectric permittivity for NTO were reported [36]. Aleksandrowicz and Wojcik presented the temperature dependence of the dielectric permittivity for NTO ceramics from 300 to 1000 K, but values of the dielectric permittivity were very low, from 4 to 11 [53]. König *et al.* have also reported that the density of single-phase $NaTaO_3$ ceramics sintered at temperature as high as 1640 °C was not enough for dielectric characterization, whereas NTO with $Na_2Ta_4O_{11}$ secondary phase, formed due to sodium evaporation above 1550 °C, revealed a room-temperature permittivity of 142 with a negative temperature coefficient of permittivity between 123 and 823 K [98]. Further these ceramics were studied at microwave and infrared ranges, revealing the maximum permittivity obtained on cooling toward 0 K of about 205 [37].

Recently, NTO ceramics were prepared by solid-state reaction from Na_2CO_3 and Ta_2O_5, mixed with Na/Ta ratio = 1.05 to compensate sodium evaporation during sintering [35]. Due to the presence of 5% sodium

Table 9.3 Low-temperature values of the dielectric permittivity ε'_{max} and parameters of the Barrett's relation for the incipient FEs.

Composition	Type	ε'_{max}	T_0 (K)	T_1 (K)	C ($10^3 \times$ K)	ε_1	Reference
$SrTiO_3$	SC	24000	35.5	80	80	–	Müller & Burkard [110]
	CER	6300	34.5	99.3	92.1	–	Tkach *et al.* [111]
$KTaO_3$	SC	3840	13.1	56.9	54.5	47.5	Samara & Morosin [112]
	SC	–	12.9	54.2	55.8	–	Vogt & Uwe [113]
	SC	–	8.02	48.3	61.8	48	Chen *et al.* [94]
	CER	2000	5.22	60.0	48.6	49	Chen *et al.* [94]
	CER	**4000**	**12.0**	**48.1**	**48.7**	**58.4**	**Tkach *et al.*** [97]
	CER	4080	15	56	51	64	Glinsek *et al.* [103]
$NaTaO_3$	**CER**	**324**	**–184**	**85.1**	**58.0**	**67.8**	**Tkach *et al.*** [35]
	CER	205	–326.3	106.9	68.3	25.4	Kamba *et al.* [37]
$CaTiO_3$	CER	331	–111	110	47.7	43.9	Lemanov *et al.* [114]
TiO_2	SC	251	–165.9	135.4	39.5	81.7	Samara & Peercy [115]

SC – single crystals, CER – ceramics

excess a sintering temperature of 1250 °C was found to be enough to obtain NTO dense ceramics revealing a classic incipient FE behavior. A continuous increase of ε' with the temperature decrease in agreement with previous reports on the dielectric response of NTO [36, 53, 98] was observed, while the dielectric loss was kept low ($tan\delta < 0.7$ %), as shown in Figure 9.3. However, in comparison with the previous works on both NTO single crystals and ceramics, NTO ceramics with initial 5% sodium excess revealed higher dielectric permittivity up to 324 [35], as shown in Table 9.3 as well. Such high permittivity can be explained by lack of secondary phases in these ceramics.

In the case of $LiTaO_3$ (LTO) ceramics, the processing challenges are even more serious because besides the densification issue there is a problem to maintain the ceramics integrity under significant thermal stress upon cooling from sintering to room temperature [99]. So the firing parameters, although not always well described, are very important for a successful fabrication of LTO ceramics. Thus, complex and long-time calcination procedures have been used [104–106]. Additionally, to release the stress the temperature variation rate during sintering was reduced to 100 °C/h [105, 106]. Recently, Yang *et al.* [107] reported also a preparation of well-compacted LTO ceramics by conventional sintering at 1300 °C for 3 h. However, in this case also non-trivial LiCl–KCl molten-salt method was used for calcination, performed at 500 °C for 4 h. Finally, Chen *et al.* [99] succeeded to obtain dense (~95%) and monophasic undoped LTO ceramics with rather large grains (~8 μm) using hot pressing at 1250 °C.

Since polycrystalline LTO can substitute LTO single crystals (which use to grow congruently [59]) in many applications, the optimization of the processing conditions is still important. Moreover, since LTO single crystals are widely used in electro-optical devices including digital light modulators, optical shutters and switchers and image memory devices, there is a relevance of having LTO transparent ceramics. The transparent FE ceramics have attracted much attention for their practical advantages such as low production cost and possibility to fabricate materials of wide variety of sizes and shapes with good compositional control, compared to single crystals [108]. Up to now mostly lead-containing transparent ceramics, such as lanthanum modified lead zirconate titanate (PLZT), have been prepared [108]. Due to the fact that lead is harmful to the environment and gradually degrades the optical efficacy and lead-free transparent FE ceramics are much more desirable. However, the reports on the preparation of lead-free transparent FE ceramics are very rare, since it requires at least nanopowders and spark plasma sintering to obtain ceramics with low

porosity and nanometric grain size that result in low scattering and thus transparency [108].

As it was established above, while LTO is a FE with high Curie temperature, NTO and KTO reveal incipient FE or quantum PE behavior. It is well known that for quantum PEs, $\varepsilon'(T)$ dependence can be described by Barrett's relation [109]:

$$\varepsilon'(T) = \frac{c}{\frac{T_1}{2}\coth\frac{T_1}{2T}T_o} + \varepsilon_1 \tag{9.2}$$

which is based on the mean-field theory taking quantum fluctuations into account. C stands for the Curie–Weiss constant, T_1 for the temperature of the crossover between classical and quantum behavior, T_0 for the transition temperature at which the lattice instability would occur in the absence of quantum fluctuations, and ε_1 for the temperature independent component of permittivity. In the limit $T>>T_1$, the Barrett relation transforms into the traditional Curie–Weiss law $\varepsilon'(T) = C/(T - T_0)$, usually applied to regular FEs.

A classical quantum PE is STO with the Barrett's law parameters presented in Table 9.3 both for single crystals [110] and ceramics [111]. Fit of the $\varepsilon'(T)$ dependence measured at 10 kHz on stoichiometric STO ceramics to the Barrett's law [111] is shown in Figure 9.3(a). Figure 9.3(a) depicts also that the Barrett's law can be well applied to the $\varepsilon'(T)$ dependences of KTO ceramics with initial K/Ta ratio of 1.02 [97] and $NaTaO_3$ ceramics with initial Na/Ta ratio of 1.05 [35]. The fitting parameters for these ceramics are also indicated in Table 9.3 together with those for other reported KTO ceramics [94, 97, 103], KTO single crystals [94, 112, 113], and NTO ceramics [35, 98]. While in the case of KTO all the fitting parameters show similar values, there is a big difference in the transition temperature T_0 for NTO ceramics prepared with [35] and without [98] initial sodium excess. This difference that once more strengthens the dependence on the processing procedure and starting precursor stoichiometry can be explained by the formation of secondary phases in NTO ceramics sintered without initial Na excess. On the other hand, the negative values of T_0 mean that the transition to the FE state would never occur in undoped NTO. Nevertheless, there are many materials (like $CaTiO_3$ [114] and TiO_2 [115] with parameters presented in Table 9.3 as well) reported to be incipient FEs with negative T_0. Thus, comparing the maximum dielectric permittivity values and Barrett's law parameters shown in Table 9.3, one can conclude that dielectric response of NTO is close to that of TiO_2.

Looking back to the dissipation factor of KTO ceramics prepared with initial potassium excess of 2% [97], one can conclude from Figure 9.3(b) that it is higher than that in the best KTO single crystals [31, 90], but comparable to that in regular KTO crystals [32, 91–93]. Thus, these KTO ceramics can substitute KTO single crystals in microwave electronic applications. Moreover, the dielectric loss of stoichiometric $SrTiO_3$ ceramics [111] is higher than that of KTO ceramics for all the temperatures below 300 K, except the vicinity of 15 and 60 K. Such behavior resembles that of KTO and STO single crystals [31, 90]. Finally, Figure 9.3(b) depicts also that the dielectric loss for NTO ceramics prepared with the initial sodium excess of 5% [35] is intermediate between that of KTO and STO ceramics. However, it is worthwhile to note that KTO ceramics with 5% of potassium excess revealed also enhanced loss [97]. So, it might be that Na excess amount in NTO ceramics still has to be tuned to give the loss values applicable in microwave components.

9.5 Potential Applications of Alkali Tantalates

9.5.1 Sodium Tantalate as a Photocatalyst

Heterogeneous photocatalysis, with assistance of semiconductor oxides, is an emerging green technology leading to the degradation of organic pollutants [116]. The photodegradation is based on the redox reactions, which occur on light-irradiated semiconductors when their conduction band minimum is below the redox potential of H^+/H_2 (0 V vs. normal hydrogen electrode (NHE)) and valence band maximum is above the redox potential of O_2/H_2O (1.23 V vs. NHE) [20]. Titanates, niobates and tantalates are among such semiconductive materials with suited photophysical properties. However, conduction bands of tantalates consisting of Ta *5d* orbitals are located at a more negative position than those of titanates (Ti *3d*) or niobates (Nb *4d*) that might make tantalates beneficial in photocatalytic reactions [117]. A detailed review on the topic of Ta-based semiconductors for solar water splitting can be found in recent work by Zhang *et al.* [20].

Currently, much attention has also been paid to develop new types of photocatalytic materials, including tantalum oxide based compounds with known photocatalytic activity for water splitting under UV and visible-light irradiation. Although under UV-light irradiation, pure Ta_2O_5 (band gap of 4.0 eV) can only produce a very small amount of H_2 and no O_2 from pure water [118–120], the NiO-loaded mesoporous Ta_2O_5 displays

a relatively high activity for overall water decomposition, >500 μmol/h of H_2 and >250 μmol/h of O_2 [121]. Within the Ta-based compounds, alkali tantalates, ATaO$_3$ (A = Na, Li, or K), have also attracted an interest showing high efficiency for splitting of water into hydrogen fuels [122–131]. It was reported that alkali tantalates showed relatively high activities for photocatalytic water splitting into H_2 and O_2 under UV irradiation [122], and the excess of alkali in the synthetic process of the solid-state reaction even improved the photocatalytic activities of them, following the order: KTaO$_3$ < NaTaO$_3$ < LiTaO$_3$ (H_2: 29 < 160 < 430 μmol/h; O_2: 13 < 86 < 220 μmol/h) [123]. Doping (loading) with NiO [132, 133] and nanosized Au particles [134] was reported to have an efficient function as co-catalysts for photocatalytic water splitting. Among them, NiO/NaTaO$_3$ was the most photocatalytically active system (synthesized via solid state), which produced H_2 and O_2 from pure water with a quantum yield of 28% at 270 nm (~2.2 mmol/h of H_2 and ~1.1 mmol/h of O_2) [133]. Both the hydrothermal [126, 135] and the sol–gel methods [136] produced ATaO$_3$ (A = K, Na) with good crystallinity as well as high surface area, providing higher photocatalytic activity in water splitting than the solid-state produced material. More than 5 mmol/h of H_2 were produced using nanocrystalline NTO [126]. Studies on KTO revealed that small amount of acceptors such as tri- or tetravalent cations was effective for improving the photocatalytic activity [137, 138], *e.g.* NiO/KTaO$_3$ doped with 8 mol% Zr^{4+} exhibited a higher photocatalytic activity than the well-known photocatalyst Pt/TiO$_2$. H_2 formation on this catalyst was 122.3 μmol/h, while on Pt/TiO$_2$ it was 106.1 μmol/h [137]. The increased activity was brought about by an increase in the lifetime of the photoexcited charge, which in its turn was caused by a decrease in the charge density.

Removing non-biodegradable organic pollutants by their degradation is another important aspect, in which heterogeneous photocatalysis can assist. Thus, perovskite tantalates and niobates have been reported also as series of promising photocatalysts to promote oxidative decomposition of organic contaminants under suitable illumination. Other attractive aspects of these compounds are their low toxicity and high stability [139, 140]. It was demonstrated that the sol–gel synthesized alkali tantalates degrade an organic dye, azo type dying agent, methylene blue (MB), with the performance in the following order: NTO> LTO >KTO [141]. Later, NTO (mostly doped one) has become the most extensively investigated photocatalytic material [142–147]. Nanosized NTO powders doped with Sm and La were found to be highly active photocatalysts for the degradation of MB under UV irradiation [142]. Bi-, Cr- and N-doped NTO catalysts were even highly active under visible-light irradiation [143–147]. It was

also proven that the activity of N-doped NTO is significantly higher in Rhodamine B dye degradation under visible light than TiO_2P25 [147].

Due to a lack of direct comparison of degradation efficiency using alkali tantalates with perovskite-like structures, a set of highly crystalline alkali tantalates, LTO, NTO, and KTO, was synthesized at the same conditions, and their photocatalytic degradation (PCD) of MB, was assessed. MB is a model dye, a heterocyclic aromatic chemical compound with the molecular formula $C_{16}H_{18}ClN_3S$. It is largely used in the industry in the dyeing of paper, linen and silk textiles as well as in the painting of bamboo and wood [148, 149]. It is one of the most difficult dye contaminant to degrade [141, 150].

The PCD of the LTO, NTO, and KTO powders was evaluated in liquid-solid phase, by monitoring the degradation of MB using a UV–Vis spectrometer [151]. The UVA-light source was a germicidal lamp (Philips PL-S 9W, NL), having an irradiance of approximately 13 W m^{-2} and a maximum emission at ~365 nm. The MB concentration in the liquid was determined, taking advantage of the Lambert–Beer law, by measuring the absorbance in a spectrometer at a wavelength of 665 nm (characteristic peak that decreases in intensity with increasing irradiation time indicating degradation degree), using distilled water as a reference. The extent of MB photodegradation efficiency, ξ, was evaluated as:

$$\xi(\%) = \frac{C_0 - C}{C_0} \cdot 100 \tag{9.3}$$

where C_0 is the initial MB concentration (mg·L^{-1}) and C is the concentration after a certain UVA/visible irradiation time (it was set at 7 h). The photocatalytic decomposition of organic pollutants in water generally follows the Langmuir–Hinshelwood mechanism [152]. Thus, the reaction kinetics were studied using a pseudo first-order model [153], in which the apparent photocatalysis rate constant, k_{app} (min^{-1}), was determined.

The diffuse reflectance spectra of the as-synthesized powders are depicted in Figure 9.4. The spectra were acquired in the UV–Vis range, and the Kubelka–Munk function was applied with the aim to convert the diffuse reflectance into the absorption coefficient that is proportional to $F(R_\infty)$. As expected, all the compounds show no absorption in the visible region. Their spectra, consisting of a single absorption band below approximately 400 nm, are characteristic of this group of oxides. The energy band gaps, E_g, of the powders calculated by the differential reflectance method are 4.84, 4.07, and 3.65 eV for LTO, NTO, and KTO, respectively, being comparable to the literature reports [55, 123].

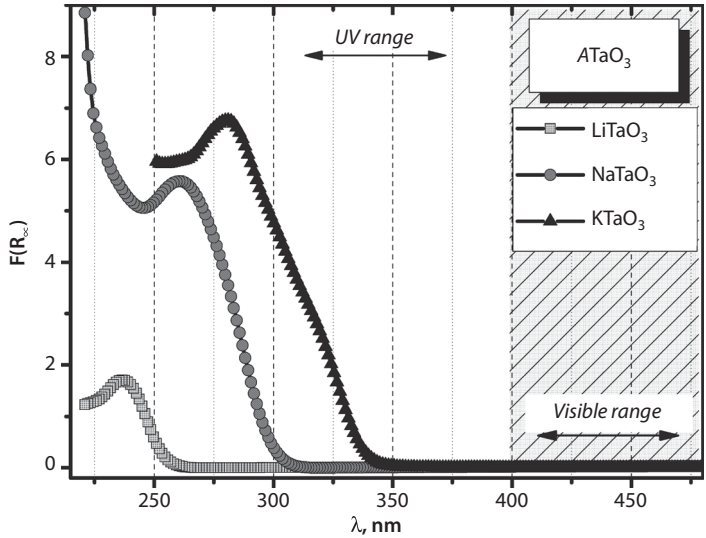

Figure 9.4 Diffuse reflectance spectra versus wavelength of perovskite-like alkali tantalates [154]. The spectra were acquired in the UV–Vis range, with 0.02 nm in step-size and using $BaSO_4$ as reference, and the Kubelka–Munk function was applied with the aim to convert the diffuse reflectance into the absorption coefficient that is proportional to $F(R_\infty)$.

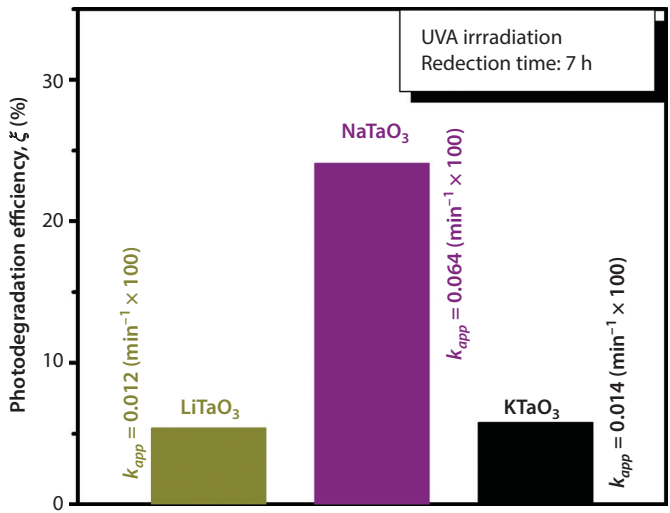

Figure 9.5 Photocatalytic efficiency of alkali tantalates after 7 h of UVA irradiation [154]. The rate constant, k_{app}, was also calculated for the assessed powders, and results are included.

Photocatalytic efficiency (after 7 h) of the as-prepared alkali tantalate powders are shown in Figure 9.5. The alkali tantalates exhibit a PCD with the following order: NTO > KTO > LTO. A reaction kinetics study was conducted as well, and the apparent rate constant, k_{app}, was calculated for the assessed powders, and results are also included in Figure 9.5. NTO is the best photocatalyst (using certain conditions) amongst all tested alkali tantalates, degrading the dye minimum 4 times more efficiently than KTO and LTO. This can be related to the presence of a higher number of active photocatalytic centers on NTO surface, and consequently a higher affinity of the dye to its surface. The MB decomposition rate presented by k_{app} confirms the observed degradation trend.

The effect of catalyst dose (alkali tantalate concentration in a dye) is an important parameter on removal efficiency of the dye. The higher is the number of active sites on the photocatalyst surface, the amount of hydroxyl and superoxide radicals is higher, having influence on the degradation of the dye [144]. Therefore, a comparison with the reported studies is rather difficult. Additionally, a literature on PCD of organic pollutants by alkali tantalates is not very broad, although some works are listed in Table 9.4. Torres-Martínez *et al.* [141] reported a PCD of MB (under UVC-light irradiation) using a set of sol–gel prepared alkali tantalates demonstrating the photocatalytic efficiencies <10% (at 3 h of irradiation time). The rate constant, k_{app}, was calculated to be in the order k_{app} (NTO) > k_{app} (LTO) > k_{app} (KTO). Though the catalyst concentration was ~2 times higher than presented by Zlotnik *et al.* [154], the reaction rates were comparable. It was also demonstrated that even higher catalyst concentration (0.75 $g{\cdot}L^{-1}$) leads to a full MB degradation after 7 h using NTO, with reaction rate ~0.007 min^{-1} [142]. Zhao *et al.* [145] carried out the PCA experiments of MB degradation under UVC-light irradiation using NTO powders prepared by hydrothermal method. The degradation of ~20% MB was already achieved within 40 min, but the experiments were conducted with 20 $mg{\cdot}L^{-1}$ concentration of MB, and with a huge amount of photocatalyst, 1 $g{\cdot}L^{-1}$. Thus, 4 times higher concentration of both, dye and catalyst, led to much more accelerated reactions, and a direct comparison with current results is not possible without comparing other factors, *i.e.* reaction rate, surface area of catalyst, *etc*. Two very recent works are also included in Table 9.4, but they were carried out using methyl orange [155, 156].

In principle, a photocatalytic activity of metal oxide semiconductor depends on a number of parameters, *i.e.* surface area, particle size, crystallinity, particle shape anisotropy, local structure, light absorption, and diffusion rates of charge carriers [157, 158]. The morphological aspects, such as surface area and particle/crystallite size, are important factors affecting

Table 9.4 Photocatalytic degradation of organic dyes using alkali tantalate perovskites.

	PCD	Dye	Remarks	Reference
$LiTaO_3$	5.4 % at 420 min **k_{app} = 0.00012 min^{-1}** **(0.25 $g{\cdot}L^{-1}$)** **UVA (365 nm)**	**MB** **(5 $mg{\cdot}L^{-1}$)**	**Solid-state** **SA_{BET}** = 7.6 $m^2{\cdot}g^{-1}$ **E_g** = 4.84 eV	**Zlotnik *et al.*** [154]
	~5 % at 210 min k_{app} = 0.00035 min^{-1} (0.4 $g{\cdot}L^{-1}$) UVC (254 nm)	MB (30 $mg{\cdot}L^{-1}$)	Sol–gel SA_{BET} = 7.3 $m^2{\cdot}g^{-1}$ E_g = 4.8 eV	Torres-Martínez *et al.* [141]
$NaTaO_3$	24.1 % at 420 min **k_{app} = 0.00064 min^{-1}** **(0.25 $g{\cdot}L^{-1}$)** **UVA (365 nm)**	**MB** **(5 $mg{\cdot}L^{-1}$)**	**Solid-state** **SA_{BET}** = 9.0 $m^2{\cdot}g^{-1}$ **E_g** = 4.07 eV	**Zlotnik *et al.*** [154]
	~7 % at 210 min k_{app} = 0.00074 min^{-1} (0.4 $g{\cdot}L^{-1}$) UVC (254 nm)	MB (30 $mg{\cdot}L^{-1}$)	Sol–gel SA_{BET} = 10.6 $m^2{\cdot}g^{-1}$ E_g = 4.0 eV	Torres-Martínez *et al.* [141]
	~100 % at ~350 min k_{app} = 0.0078 min^{-1} (0.75 $g{\cdot}L^{-1}$) UVC (254 nm)	MB (30 $mg{\cdot}L^{-1}$)	Sol–gel SA_{BET} = 4–18 $m^2{\cdot}g^{-1}$ E_g = 3.5–3.6 eV	Torres-Martínez *et al.* [142]

(*Continued*)

Table 9.4 Cont.

	PCD	Dye	Remarks	Reference
	~20 % at 40 min (1.0 g·L^{-1}) UVC	MB (20 mg·L^{-1})	Hydrothermal 300 nm particles E_g = 3.94 eV	Zhao *et al.* [145]
	<40 % at 100 min k_{app} = 0.00048 min^{-1} (1.0 g·L^{-1}) UVC (254&185 nm)	MO (20 mg·L^{-1})	Hydrothermal E_g = 4 eV	Li *at al.* [155]
$KTaO_3$	5.8 % at 420 min **k_{app}** = 0.00014 min^{-1} **(0.25 g·L^{-1})** **UVA (365 nm)**	**MB** **(5 mg·L^{-1})**	**Solid-state** **SA_{BET}** = 6.3 m^2·g^{-1} **E_g** = 3.65 eV	**Zlotnik *et al.*** [154]
	~3 % at 210 min k_{app} = 0.00030 min^{-1} (0.4 g·L^{-1}) UVC (254 nm)	MB (30 mg·L^{-1})	Sol–gel SA_{BET} = 1.9 m^2·g^{-1} E_g = 3.6 eV	Torres-Martínez *et al.* [141]
	~10 % at 80 min (0.5 g·L^{-1}) UV	MO (6.5 mg·L^{-1})	Hydrothermal 100 nm particles SA_{BET} = 4.1 m^2·g^{-1} E_g = 3.62 eV	Liu *et al.* [156]

MB – methylene blue, MO – methyl orange.

the photocatalytic activity by providing more reaction sites. Surface area, SA_{BET}, of NTO is only slightly higher than SA_{BET} of LTO and KTO. The crystallinity of the as-synthesized powders is rather similar (calcination temperature and time were almost the same), thus its effect can also be ignored when comparing their PCD. Thus, here the effect of these features can be neglected while comparing KTO, NTO, and LTO.

The conduction bands of alkali tantalates consist of Ta *5d,* and the band gap of KTO is the narrowest among them. The absorption edge of KTO (~340 nm) is the closest to the maximum wavelength of the used lamp. Thus, this parameter cannot be also the most decisive because NTO is the most effective photocatalyst among the tested, and its absorption edge is ~305 nm, thus located closer to UVC range rather than to UVA.

The surface/interface chemistry of a semiconductor is crucial in photocatalytic processes because the transfer of charge carriers and the adsorption of molecules take place on a surface [159–161]. Therefore, the higher stability of a surface (and its energy) leads normally to a higher catalytic activity [162]. A thermodynamic factor associated with a surface, its energy, was recently measured in some of the alkali tantalates [61], being a 1.6 times higher in NTO than in LTO. This indicates that NTO shows higher affinity to water, yielding a higher catalytic activity.

It is known that a slight modification of structure has a dramatic effect on the concentration and mobility of charge, which directly affects the photocatalytic and photophysical properties of semiconductors [126]. The distorted BO_6 octahedra with shared corners in perovskite-like structures has a crucial impact on the dipole and electronic band structures, which affect the behavior of photogenerated charge carriers [163, 164]. It was reported that the Ta – O – Ta bond angle is one of the key factors influencing photocatalytic activity in alkali tantalates [117, 163, 164]. If the bond angle is closer to 180°, like in NTO and KTO, a migration of excited energy in the crystal occurs easier. In contrast, in perovskite-like LTO the interaction of TaO_6 octahedra is very weak, and the excited energy is localized due to the bond angle of Ta – O – Ta being much lower than 180° [163]. The effect of crystal and electronic structures on photocatalytic activity was investigated in NTO in details [127, 128]. It has to be pointed out that the recombination rate for electron–hole pairs is usually much lower in the systems with an indirect band gap (monoclinic NTO) compared to those with a direct band gap (orthorhombic NTO). The longer lifetime of the free electrons and holes is expected to increase the probability of their participations in photocatalytic reactions as it was demonstrated in the monoclinic NTO due to a favorable delocalization of the excited energy [127, 128].

Within the same experimental conditions, NTO possesses the highest photocatalytic performance among alkali tantalates with perovskite-like structure. Although NTO does not have the narrowest band gap, but its suitable crystal and electronic structures lead to higher mobility of charge carriers and consequently to better photocatalytic performance. The promising photocatalytic activity of alkali tantalates is attributed to a suitable conduction band level and an efficient carrier-delocalization caused by the proper distortion of TaO_6 connections. Additionally, a band gap engineering of NTO by doping with metal or non-metal leads to the appearance of donor or acceptor states (midgap states) between the valence band and the conduction band. Hence, it improves the photocatalytic properties of NTO even to the visible region. It is known that UV light occupies only around 4% of the solar energy spectrum; thus, there is a great interest in developing new visible light-responsive photocatalysts capable of utilizing the more abundant visible light spectrum (~43% of the solar energy range) [150, 163]. Therefore, there is a need to develop and engineer novel visible light-responsive photocatalysts.

9.5.2 Lithium Tantalate as a Piezoelectric Biomaterial

Bone and joint degenerative and inflammatory problems affect millions of people worldwide [165]. Many diseases often require surgery, including total replacement of the natural joint in case of its deterioration [165, 166]. Therefore, orthopedic biomaterials are meant to be implanted in the human body as constituents of devices that are designed to perform certain biological functions by substituting or repairing different tissues such as bone, cartilage or ligaments, and tendons, and even by guiding bone repair when necessary [167].

Synthetic materials used for bone repair can be divided into ceramics, polymers, metals and composites, where at least two classes of materials are combined together [167]. Since ceramics may have a structure that mimics the one of natural bone, they were considered as attractive materials in this respect [168]. This category of materials includes oxides, phosphates, carbonates, nitrides, carbides, carbons, and glasses. Biodegradable and bioactive ceramics, sometimes denoted as second generation bioceramics, have more recently been developed to fulfill specific functions for a given period of time, helping in the self-repair processes of the living organism, and subsequently resorbed [167]. Bioactive ceramics can react with physiological fluids giving rise to a sequence of surface reactions producing a strong bond between the material and the bone. Well-known bioactive ceramics are hydroxyapatite (HA) and certain compositions of glasses and glass

ceramics. Bioactive and biodegradable ceramics are clinically used as bone fillers, bone cements, or for coating metallic implants [167, 169].

Previous biomaterials' development has pursued mimicking bone chemical composition and structure [170]. More recently, interest is growing in a new generation of biomaterials, which seek to influence healing by mimicking the electrical effects in bone. Piezoelectricity is an important property that is defined as a coupling between mechanical stress and electric field, and it has been found in a number of biological materials of different nature [171]. Indeed, it is known that piezoelectricity, and in particular the piezoelectric nature of collagen plays a vital role in the development and maintenance of the natural bone. Thus, piezoelectric materials with good biocompatibility can be considered as a promising alternative for bone tissue regeneration and growth, fracture healing, and ultimately for orthopedic prosthetic implants [172–174]. It is crucial to explore the potential of the piezoelectric biocompatible materials for tissue regeneration to develop biodegradable substrates or platforms able to deliver electrical cues for regeneration without any external energy source.

Two methods can be employed to create a surface charge of bioceramics [175]. First one is to polarize an ionic biomaterial by application of an electric field at elevated temperature to displace cations and anions in opposite directions (*e.g.* polarization by electric field of HA between two Pt electrodes leading to the ordering of lattice OH^- ions due to the reorientation of protons around O^{2-}. Second one is to develop a piezoelectric biomaterial so that a charge is generated under the application of a mechanical stress (*e.g.* composites containing $BaTiO_3$, in which piezoelectric behavior originates from electrical dipole of FE material). Therefore, piezoelectric ceramics as $BaTiO_3$ have been studied *in vitro* and *in vivo* and demonstrated as potential biomaterials [176–178]. The addition of $BaTiO_3$ as a secondary phase to bioactive HA improves the electrical properties, such as dielectric constant, piezo- and pyroelectric coefficients [179, 180], and mechanical properties, namely the fracture toughness [181]. Cell proliferation and growth have been also studied in these composites, demonstrating the enhancement of cell-material interactions during the application of pulsed electric fields [182]. It is proposed that the electrical signal activates extracellular signal molecules during the field application and then those molecules bound to cell surface receptor proteins. The signals can be further transferred via molecular switching mechanisms to intracellular signaling proteins. In this way, the applied electric field enhances cell proliferation on control substrate, *i.e.* the investigated bioceramics.

Besides $BaTiO_3$, alkali tantalates and niobates, as (K, Na)NbO_3, $LiNbO_3$, and $LiTaO_3$, have been reported to be bioactive and biocompatible [183–188]. Studies have shown that KNN, LNO, and LTO piezoelectrics are good candidates as biomaterials for bone repairing. KNN was even patented as material for implants, and toxicology tests showed no presence of any bacterial products [187].

With a different but related perspective, the selective adsorption of biomolecules on charged surfaces and domain boundaries of FE single crystals of LNO and LTO has been demonstrated as well [189], *e.g.* piezoelectric substrate materials in surface acoustic wave (SAW) biosensors, for the detection of small molecules in liquid media [190, 191]. LNO has previously been also quite well exploited for polarization-dependent surface reactivity and biocompatibility [184, 186, 192]. However, only one report is known to describe the cells response to LTO [183]. Christophis *et al.* studied a fibroblast cells adhesion *in vitro* to periodically poled LTO crystals. The approach of using periodically poled substrate domains allowed the cells to select locations of different polarizations and field gradients without being significantly perturbed by chemical differences [183]. It was found that there was no preferential adsorption of cells to either positive or negative polarization, with uniform coverage of ~5 nm throughout the entire sample surface. The cells started spreading after 10 min and were mostly spread after 1 h, this behavior is typical for moderately attractive artificial surfaces such as glass. Interestingly, it was demonstrated that the cells' response is inhibited by the strong field gradients of a domain boundary.

Within this context, the bioactivity of $LiTaO_3$ (and $LiNbO_3$) powders was assessed [185], in order to determine the feasibility of apatite formation on the surface of LTO powders by diverse incubation periods in a simulated body fluid (SBF). Well-crystalline and monophasic LTO powders with surface area ~1.7 m^2/g was synthesized by mixed-oxide method. For assessing the *in vitro* bioactivity of $LiTaO_3$ powders, an acellular SBF with ion concentrations nearly equal to those of the human blood plasma was used, following the Kokubo *et al.* SBF preparation protocol [193].

It was observed that there was no obvious evidence of any precipitated structures for LTO powders incubated for 1 and 3 days in SBF. However, elongated cauliflower-like shape structures were formed in the samples incubated for 7 days and longer. Figure 9.6(a) shows the micrograph of LTO powders and the precipitated structures (21 days incubation time). The EDS spectra of these precipitates showed Ca and P characteristic peaks (evidence of calcium phosphate formation), and the calculated Ca/P atomic ratio was ~1.91, ~1.00, and ~0.68 in the samples incubated for 7,

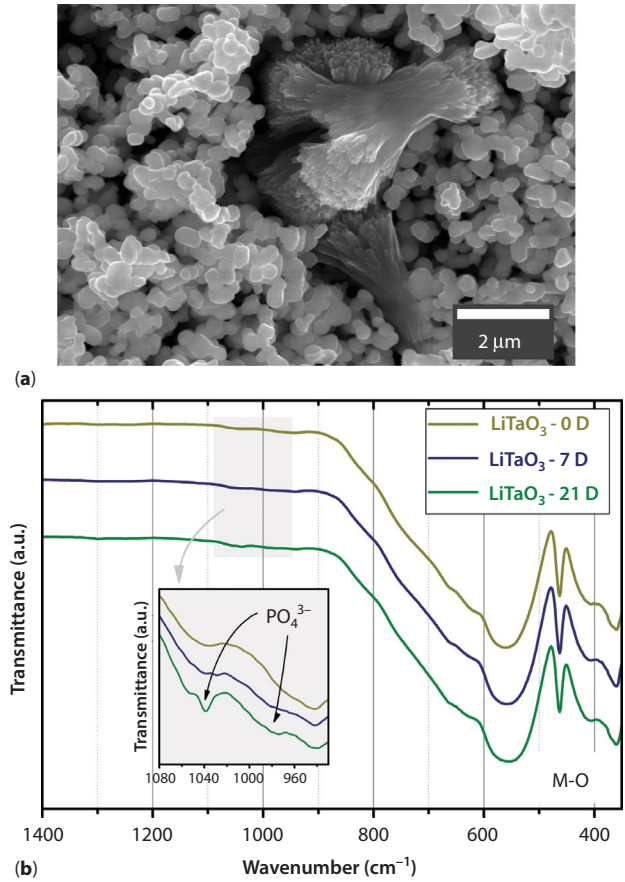

Figure 9.6 (a) SEM micrograph of calcium phosphate precipitates with cauliflower-like morphology in LTO powder incubated for 21 days in SBF. (b) FTIR spectra of LTO powders incubated for 0, 7, and 21 days in SBF; inset shows phosphate bands. Reprinted from Ref. [185], with permission from Elsevier.

14, and 21 days, respectively. Ca/P ratio significantly decreases while the incubation time increases. Composition of the calcium phosphate precipitates, formed on LTO incubated for 7 days, was not a stoichiometric HA (Ca/P = 1.67), but a phosphorous deficient apatite. However, with time they became calcium deficient. Fourier transform infrared spectroscopy (FTIR) confirmed the phosphate formation. The characteristic IR absorption bands of P – O vibrations in phosphate groups, PO_4^{3-}, were identified at 1040 and 960 cm^{-1}. Figure 9.6(b) presents FTIR spectra of LTO powders incubated for 7 and 21 days in SBF, as well as-prepared LTO (0D).

Inductively coupling plasma spectrometry indicated that Ca and P ions concentrations decrease in SBF as the incubation time increases. The Ca ions were depleted from SBF in the amount of ~40 and ~60 mg/L for 7 and 21 days, respectively, whereas the amount of P ions was ~15 and ~25 mg/L for 7 and 21 days, respectively. This is related to the formation of the apatite structures at the surface of LTO. The Ca and P ion concentrations decreased markedly after 3 days of incubation. Simultaneously, there is a quick raise of Li ions concentration in SBF solution of ~45 mg/L just after 1 day of incubation. Li ion concentration is then stabilized, reaching ~65 mg/L after 21 days. These results indicate the lithium dissolution from LTO powders, and the dissolution rate was estimated to be ~6 mg/L per day during the first week of the incubation [185].

In what concerns, the mechanism of apatite formation was proposed. The lixiviation of Li ions from the powders originates the negative surface charges that act as anchor sites for the positively charged Ca^{2+} ions to which the negative PO_4^{3-} ions attract forming the apatite structure nuclei [185]. The observed Li lixiviation from LNO and LTO powders can be viewed as a limitation for practical applications, restricting the use of LNO and LTO powders, unless they are submitted to a pre-lixiviation before use. However, the utilization of dense compact forms (ceramics, films, substrates) of LNO and LTO with properly functionalized surfaces is suggested as viable alternatives [185].

9.6 Conclusions

The non-toxic nature and stability of pentavalent oxide (Ta_2O_5) and tantalate complex oxides make commercially attractive for the range of technologies. Principally, alkali tantalates with perovskite-like structures are encouraging functional materials within the ferroic family of lead-free compounds. Their versatile properties make them potential players in microelectronics, photocatalytic processes, or medicine. The difference in their functional properties is also strongly dependent on the synthesis conditions. The fabrication of these compounds as ceramics with the desired density, stoichiometry, structure, and material stability that is always fundamental to ensure the durability and reliability of the compound with particular function is shown to be still challenging. A look over the possible applications of alkali tantalates for electronic components, photocatalysis, and tissue engineering is presented.

Acknowledgements

We thank Prof. Alexandra Navrotsky and Dr. Sulata K. Sahu (UCDavis, USA), Dr. David M. Tobaldi and Prof. M. Helena Fernandes (UA, Portugal) and Prof. Abilio Almeida (IFIMUP, Portugal) for their valuable collaboration.

References

1. Thomson Reuters Predicts the Top 10 Innovations for 2025, Press Releases, 2014.
2. Cao, W., Multifunctional Materials: The Basis for Adaptronics, in: *Adaptronics and Smart Structures*, Janocha, H. (Ed.), pp. 29–53, Springer Publishing, Berlin Heidelberg, 2007.
3. Vilarinho, P.M., Functional Materials: Properties, Processing and Applications, in: *Scanning Probe Microscopy: Characterization, Nanofabrication and Device Application of Functional Materials*, Vilarinho, P.M., Rosenwaks, Y., and Kingon, A. (Eds.), pp. 3–33, Springer, Netherlands, 2005.
4. Boch, P., and Baumard, J.-F., Ceramic Compounds: Ceramic Materials, in: *Ceramic Materials: Processes, Properties and Applications*, Boch, P., and Nièpce, J.C. (Eds.), pp. 3–28, ISTE, London, 2007.
5. Carter, C.B., and Norton, M.G., *Ceramic Materials: Science and Engineering*, pp. 527–689, Springer, New York, 2007.
6. Colomban, P., Poudres sur mesure: la clé des céramiques fiables? *L'Industrie Céramique*, 815, 250, 1987.
7. Setter, N., Damjanovic, D., Eng, L., Fox, G., Gevorgian, S., Hong, S., Kingon, A., Kohlstedt, H., Park, N.Y., Stephenson, G.B., Stolitchnov, I., Taganstev, A.K., Taylor, D.V., Yamada, T., and Streiffer, S., Ferroelectric Thin Films: Review of Materials, Properties, and Applications. *J. Appl. Phys.*, 100, 051606, 2006.
8. Gevorgian, S.S., and Kollberg, E.L., Do We Really Need Ferroelectrics in Paraelectric Phase Only in Electrically Controlled Microwave Devices? *IEEE Trans. Microw. Theory Tech.*, 49, 2117, 2001.
9. Gevorgian, S., Introduction: Overview of Agile Microwave Technologies, in: *Ferroelectrics in Microwave Devices, Circuits and Systems*, Gevorgian, S. (Ed.), pp. 1–19, Springer Publishing, London, 2009.
10. Gevorgian, S., and Deleniv, A., Ferroelectric Devices, in: *Ferroelectrics in Microwave Devices, Circuits and Systems*, Gevorgian, S. (Ed.), pp. 175–223, Springer, London, 2009.
11. Nagarajan, V., Ganpule, C.S., and Ramesh, R., Nanoscale Phenomena in Ferroelectric Thin Films, in: *Ferroelectric Random Access Memories Fundamentals and Applications*, Ishiwara, H., Okuyama, M., and Arimoto, Y. (Eds.), pp. 47–68, Springer Publishing, Berlin Heidelberg, 2004.

12. Scott, J.F., Ferroelectric Nanostructures for Device Applications, in: Handbook of Advanced Dielectric, Piezoelectric and Ferroelectric Materials: Synthesis, Properties and Applications, Ye, Z.-G. (Ed.), pp. 541–569, Woodhead Publishing Limited, Cambridge, UK, 2008.
13. Carter, C.B., and Norton, M.G., Some History – Ceramic Materials, in: *Ceramic Materials: Science and Engineering*, pp. 15–32, Springer Publishing, New York, 2007.
14. Goldschmidt, V.M., Die Gesetze der Krystallochemie. *Naturwissenschaften*, 14, 477, 1926.
15. Johnsson, M., and Lemmens, P., Perovskites and Thin Films – Crystallography and Chemistry. *J. Phys.: Condens. Matter.*, 20, 264001, 2008.
16. Schlom, D.G., Chen, L.-Q., Pan, X., Schmehl, A., and Zurbuchen, M.A., A Thin Film Approach to Engineering Functionality into Oxides. *J. Am. Ceram. Soc.*, 91, 2429, 2008.
17. Wang, F., Grinberg, I., and Rappe, A.M., Band Gap Engineering Strategy via Polarization Rotation in Perovskite Ferroelectrics. *Appl. Phys. Lett.*, 104, 152903, 2014.
18. Fedorov, V., Perovskites, in: *Ceramics Science and Technology*, pp. 257–297, Wiley-VCH Verlag GmbH & Co. KGaA, Weinheim, 2010.
19. Shaw, R., and Goodenough, K., *Niobium-tantalum: April 2011*, British Geological Survey, Keyworth, 2011.
20. Zhang, P., Zhang, J., and Gong, J., Tantalum-based Semiconductors for Solar Water Splitting. *Chemical Society Reviews*, 43, 4395, 2014.
21. Chen, Q., and Thouas, G.A., Metallic Implant Biomaterials. *Mater. Sci. Eng., R*, 87, 1, 2015.
22. Wang, G., Lee, J.-H., Yang, Y., Ruan, G., Kim, N.D., Ji, Y., and Tour, J.M., Three-dimensional Networked Nanoporous Ta_2O_{5-x} Memory System for Ultrahigh Density Storage. *Nano Lett.*, 15, 6009, 2015.
23. Larsen, E.M., *Tantalum*, McGraw-Hill Professional, New York, 2014.
24. Kikuchi, R., Yamamoto, T., and Nakamoto, M., Preliminary Information of Laboratorial Tantalum Recovery and Considerations for a Potential Solution for Conflict Mineral and Wildlife Conservation. *Environ. Nat. Res. Res.*, 4, 31, 2014.
25. Manhart, A., Buchert, M., Bleher, D., and Pingel, D., Recycling of Critical Metals from End-of-life Electronics, in: *IEEE*, Berlin, 2012, pp. 1–5.
26. Rödel, J., Webber, K.G., Dittmer, R., Jo, W., Kimura, M., and Damjanovic, D., Transferring Lead-free Piezoelectric Ceramics Into Application. *J. Eur. Ceram. Soc.*, 35, 1659, 2015.
27. Kalil, T., and Wadia, C., *Materials Genome Initiative for Global Competitiveness*, National Science and Technology Council, Washington, DC, 2011.
28. Panda, P.K., and Sahoo, B., PZT to Lead Free Piezo Ceramics: A Review. *Ferroelectrics*, 474, 128, 2015.
29. Valant, M., Axelsson, A.-K., and Alford, N., Review of Ag(Nb, Ta)O_3 as a Functional Material. *J. Eur. Ceram. Soc.*, 27, 2549, 2007.

30. Shrout, T.R., Zhang, S.J., Eitel, R., Stringer, C., and Randall, C.A., High Performance, High Temperature Perovskite Piezoelectrics, in: 14th IEEE International Symposium on Applications of Ferroelectrics, ISAF-04, IEEE, 23–27 Aug. 2004, pp. 126–129.
31. Geyer, R.G., Riddle, B., Krupka, J., and Boatner, L.A., Microwave Dielectric Properties of Single-crystal Quantum Paraelectrics $KTaO_3$ and $SrTiO_3$ at Cryogenic Temperatures. *J. Appl. Phys.*, 97, 104111, 2005.
32. Samara, G.A., The Relaxational Properties of Compositionally Disordered ABO_3 Perovskites. *J. Phys.: Condens. Matter*, 15, R367, 2003.
33. Tkach, A., Almeida, A., Moreira, J.A., Espinha, A., Chaves, M.R., de la Cruz, J.P., and Vilarinho, P.M., Lithium-induced Dielectric Relaxations in Potassium Tantalate Ceramics. *J. Phys. D: Appl. Phys.*, 44, 315406, 2011.
34. Tkach, A., Almeida, A., Moreira, J.A., Chaves, M.R., Espinha, A., and Vilarinho, P.M., Polar Behaviour Induced by Lithium in Potassium Tantalate Ceramics. *J. Phys.: Condens. Matter*, 24, 045906, 2012.
35. Tkach, A., Almeida, A., Moreira, J.A., Perez de la Cruz, J., Romaguera-Barcelay, Y., and Vilarinho, P.M., Low-temperature Dielectric Response of $NaTaO_3$ Ceramics and Films. *Appl. Phys. Lett.*, 100, 192909, 2012.
36. Iwasaki, H., and Ikeda, T., Studies on the System $Na(Nb_{1-x}Ta_x)O_3$. *J. Phys. Soc. Jpn.*, 18, 157, 1963.
37. Kamba, S., Goian, V., Bovtun, V., Nuzhnyy, D., Kempa, M., Spreitzer, M., König, J., and Suvorov, D., Incipient Ferroelectric Properties of $NaTaO_3$. *Ferroelectrics*, 426, 206, 2012.
38. Hu, C.C., Tsai, C.C., and Teng, H., Structure Characterization and Tuning of Perovskite-like $NaTaO_3$ for Applications in Photoluminescence and Photocatalysis. *J. Am. Ceram. Soc.*, 92, 460, 2009.
39. Inbar, I., and Cohen, R.E., Comparison of the Electronic Structures and Energetics of Ferroelectric $LiNbO_3$ and $LiTaO_3$. *Phys. Rev. B*, 53, 1193, 1996.
40. Adachi, M., Akishige, Y., Asahi, T., Deguchi, K., Gesi, K., Hasebe, K., Hikita, T., Ikeda, T., Iwata, Y., Komukae, M., Mitsui, T., Nakamura, E., Nakatani, N., Okuyama, M., Osaka, T., Sakai, A., Sawaguchi, E., Shiozaki, Y., Takenaka, T., Toyoda, K., Tsukamoto, T., and Yagi, T., $NaTaO_3$, 1A-4, in: *Oxides*, Shiozaki, Y., Nakamura, E., and Mitsui, T. (Eds.), pp. 1–14, Springer-Verlag, Berlin Heidelberg, 2001.
41. Adachi, M., Akishige, Y., Asahi, T., Deguchi, K., Gesi, K., Hasebe, K., Hikita, T., Ikeda, T., Iwata, Y., Komukae, M., Mitsui, T., Nakamura, E., Nakatani, N., Okuyama, M., Osaka, T., Sakai, A., Sawaguchi, E., Shiozaki, Y., Takenaka, T., Toyoda, K., Tsukamoto, T., and Yagi, T., $LiTaO_3$ [F], 2A-2, in: *Oxides*, Shiozaki, Y., Nakamura, E., and Mitsui, T. (Eds.), pp. 1–104, Springer-Verlag, Berlin Heidelberg, 2001.
42. Adachi, M., Akishige, Y., Asahi, T., Deguchi, K., Gesi, K., Hasebe, K., Hikita, T., Ikeda, T., Iwata, Y., Komukae, M., Mitsui, T., Nakamura, E., Nakatani, N., Okuyama, M., Osaka, T., Sakai, A., Sawaguchi, E., Shiozaki, Y., Takenaka, T.,

Toyoda, K., Tsukamoto, T., and Yagi, T., $KTaO_3$ Survey, 1A-5, in: *Oxides*, Shiozaki, Y., Nakamura, E., and Mitsui, T. (Eds.), pp. 1–5, Springer-Verlag, Berlin Heidelberg, 2001.
43. Volk, T., and Wöhlecke, M., Introduction, in: *Lithium Niobate: Defects, Photorefraction and Ferroelectric Switching*, Volk, T., and Wöhlecke, M. (Eds.), pp. 1–7, Springer-Verlag, Berlin Heidelberg, 2009.
44. Wang, X.P., Wang, J.Y., Zhang, H.J., Yu, Y.G., Wu, J., Gao, W.L., and Boughton, R.I., Thermal Properties of Cubic $KTa_{1-x}Nb_xO_3$ Crystals. *J. Appl. Phys.*, 103, 033513, 2008.
45. Zhurova, E.A., Ivanov, Y., Zavodnik, V., and Tsirelson, V., Electron Density and Atomic Displacements in $KTaO_3$. *Acta Crystallogr. Sect. B: Struct. Sci.*, 56, 594, 2000.
46. Ishihara, T., Baik, N.S., Ono, N., Nishiguchi, H., and Takita, Y., Effects of Crystal Structure on Photolysis of H_2O on K-Ta Mixed Oxide. *J. Photochem. Photobiol., A*, 167, 149, 2004.
47. Jellison, G.E., Paulauskas, I., Boatner, L.A., and Singh, D.J., Optical Functions of $KTaO_3$ as Determined by Spectroscopic Ellipsometry and Comparison with Band Structure Calculations. *Phys. Rev. B*, 74, 155130, 2006.
48. Neumann, T., Borstel, G., Scharfschwerdt, C., and Neumann, M., Electronic Structure of $KNbO_3$ and $KTaO_3$. *Phys. Rev. B*, 46, 10623, 1992.
49. Kennedy, B.J., Prodjosantoso, A.K., and Howard, C.J., Powder Neutron Diffraction Study of the High Temperature Phase Transitions in $NaTaO_3$. *J. Phys.: Condens. Matter.*, 11, 6319, 1999.
50. Modak, B., Srinivasu, K., and Ghosh, S.K., Band Gap Engineering of $NaTaO_3$ Using Density Functional Theory: A Charge Compensated Codoping Strategy. *Phys. Chem. Chem. Phys.*, 16, 17116, 2014.
51. Ece Eyi, E., and Cabuk, S., Ab Initio Study of the Structural, Electronic and Optical Properties of $NaTaO_3$. *Philos. Mag.*, 90, 2965, 2010.
52. Matthias, B.T., New Ferroelectric Crystals. *Phys. Rev.*, 75, 1771, 1949.
53. Aleksandrowicz, A., and Wójcik, K., Electrical Properties of Single Crystals and Ceramic Samples of $NaTaO_3$. *Ferroelectrics*, 99, 105, 1989.
54. Kudo, A., and Miseki, Y., Heterogeneous Photocatalyst Materials for Water Splitting. *Chem. Soc. Rev.*, 38, 253, 2009.
55. Wang, H., Wu, F., and Jiang, H., Electronic Band Structures of $ATaO_3$ (A = Li, Na, and K) from First-principles Many-body Perturbation Theory. *J. Phys. Chem. C*, 115, 16180, 2011.
56. Wood, I.G., Daniels, P., Brown, R.H., and Glazer, A.M., Optical Birefringence Study of the Ferroelectric Phase Transition in Lithium Niobate Tantalate Mixed Crystals: $LiNb_{1-x}Ta_xO_3$. *J. Phys.: Condens. Matter*, 20, 235237, 2008.
57. Navrotsky, A., Energetics and Crystal Chemical Systematics among Ilmenite, Lithium Niobate, and Perovskite Structures. *Chem. Mater.*, 10, 2787, 1998.
58. Yang, J., Long, J., and Yang, L., First-principles Investigations of the Physical Properties of Lithium Niobate and Lithium Tantalate. *Physica B Condens. Matter.*, 425, 12, 2013.

59. Hatano, H., Kitamura, K., and Liu, Y., Growth and Photorefractive Properties of Stoichiometric $LiNbO_3$ and $LiTaO_3$, in: *Photorefractive Materials and Their Applications 2*, Günter, P. and Huignard, J.-P. (Eds.), pp. 127–164, Springer, New York, 2007.
60. Stølen, S., and Grande, T., Trends in Enthalpy of Formation, in: *Chemical Thermodynamics of Materials*, Stølen, S., Grande, T., and Allan, N.L. (Eds.), pp. 197–227, John Wiley & Sons, Ltd, Chichester, 2004.
61. Sahu, S.K., Zlotnik, S., Navrotsky, A., and Vilarinho, P.M., Thermodynamic Stability of Lead-free Alkali Niobate and Tantalate Perovskites. *J. Mater. Chem. C*, 3, 7691, 2015.
62. Zlotnik, S., Sahu, S.K., Navrotsky, A., and Vilarinho, P.M., Pyrochlore and Perovskite Potassium Tantalate: Enthalpies of Formation and Phase Transformation. *Chem. Eur. J.*, 21, 5231, 2015.
63. Navrotsky, A., Progress and New Directions in Calorimetry: A 2014 Perspective. *J. Am. Ceram. Soc.*, 97, 3349, 2014.
64. Navrotsky, A., Thermochemistry of Complex Perovskites. *AIP Conf. Proc.*, 535, 288, 2000.
65. Navrotsky, A., Thermochemical Insights into Refractory Ceramic Materials Based on Oxides with Large Tetravalent Ccations. *J. Mater. Chem.*, 15, 1883, 2005.
66. Shigemi, A., Koyama, T., and Wada, T., First-principles Studies of Various Crystallographic Phases and Neutral Atomic Vacancies in $KNbO_3$ and $KTaO_3$. *Phys. Status Solidi C*, 3, 2862, 2006.
67. Navrotsky, A., Repeating Patterns in Mineral Energetics. *Am. Mineral.*, 79, 589, 1994.
68. Shannon, R., Revised Effective Ionic Radii and Systematic Studies of Interatomic Distances in Halides and Chalcogenides. *Acta Crystallographica Section A*, 32, 751, 1976.
69. Duffy, J.A., Acid–Base Reactions of Transition Metal Oxides in the Solid State. *J. Am. Ceram. Soc.*, 80, 1416, 1997.
70. Navrotsky, A., Chemical Bonding, in: *Physics and Chemistry of Earth Materials*, Navrotsky, A. (Ed.), pp. 172–272, Cambridge University Press, Cambridge, 1994.
71. Radha, A.V., Bomati-Miguel, O., Ushakov, S.V., Navrotsky, A., and Tartaj, P., Surface Enthalpy, Enthalpy of Water Adsorption, and Phase Stability in Nanocrystalline Monoclinic Zirconia. *J. Am. Ceram. Soc.*, 92, 133, 2009.
72. Hayun, S., Shvareva, T.Y., and Navrotsky, A., Nanoceria – Energetics of Surfaces, Interfaces and Water Adsorption. *J. Am. Ceram. Soc.*, 94, 3992, 2011.
73. Birkner, N., and Navrotsky, A., Thermodynamics of Manganese Oxides: Effects of Particle Size and Hydration on Oxidation-reduction Equilibria among Hausmannite, Bixbyite, and Pyrolusite. *Am. Mineral.*, 97, 1291, 2012.
74. Park, T.-J., Levchenko, A.A., Zhou, H., Wong, S.S., and Navrotsky, A., Shape-dependent Surface Energetics of Nanocrystalline TiO_2. *J. Mater. Chem.*, 20, 8639, 2010.

75. Costa, G.C.C., Saradhi Maram, P., and Navrotsky, A., Thermodynamics of Nanoscale Lead Titanate and Barium Titanate Perovskites. *J. Am. Ceram. Soc.*, 95, 3254, 2012.
76. Sahu, S.K., Maram, P.S., and Navrotsky, A., Thermodynamics of Nanoscale Calcium and Strontium Titanate Perovskites. *J. Am. Ceram. Soc.*, 96, 3670, 2013.
77. Navrotsky, A., Nanoscale Effects on Thermodynamics and Phase Equilibria in Oxide Systems. *ChemPhysChem*, 12, 2207, 2011.
78. Navrotsky, A., Energetics of Oxide Nanoparticles. *Int. J. Quantum Chem*, 109, 2647, 2009.
79. Castro, R.H.R., and Quach, D.V., Analysis of Anhydrous and Hydrated Surface Energies of Gamma-Al_2O_3 by Water Adsorption Microcalorimetry. *J. Phys. Chem. C*, 116, 24726, 2012.
80. Scott, A.W., *Understanding Microwaves*, Wiley, 1993.
81. Sivasubramanian, V., Murthy, V.R.K., and Viswanathan, B., Microwave Dielectric Properties of Certain Simple Alkaline Earth Perovskite Compounds as a Function of Tolerance Factor. *Japanese Journal of Applied Physics*, 36, 194, 1997.
82. Vendik, O.G., Kollberg, E., Gevorgian, S.S., Kozyrev, A.B., and Soldatenkov, O.I., 1 GHz Tunable Resonator on Bulk Single Crystal $SrTiO_3$Plated with $YBa_2Cu_3O_{7-x}$Films. *Electron. Lett.*, 31, 654, 1995.
83. Wooldridge, I., Turner, C.W., Warburton, P.A., and Romans, E.J., Electrical Tuning of Passive HTS Microwave Devices using Single Crystal Strontium Titanate. *IEEE Transactions onApplied Superconductivity*, 9, 3220, 1999.
84. Misra, M., Murakami, H., and Tonouchi, M., Electrically Tunable Compact High-T_cSuperconducting CPW Resonator. *Electron. Lett.*, 39, 990, 2003.
85. Lines, M.E., and Glass, A.M., *Principles and Applications of Ferroelectrics and Related Materials*, Clarendon Press, 1977.
86. Tagantsev, A.K., Sherman, V.O., Astafiev, K.F., Venkatesh, J., and Setter, N., Ferroelectric Materials for Microwave Tunable Applications. *J. Electroceram.*, 11, 5, 2003.
87. Varadan, V.K., Ghodgaonkar, D.K., Varadan, V.V., Kelly, J.F., and Gilkerdas, P., Ceramic Phase Shifters for Electronically Steerable Antenna Systems. *Microwave J.*, 35, 116, 1992.
88. Babbit, R.W., Koscica, T.E., and Drach, W.C., Planar Microwave Electrooptic Phase Shifters. *Microwave J.*, 35, 63, 1992.
89. von Hippel, A., Breckenridge, R.G., Chesley, F.G., and Tisza, L., High Dielectric Constant Ceramics. *Industr. Eng. Chem.*, 38, 1097, 1946.
90. Vendik, O.G., Ter-Martirosyan, L.T., and Zubko, S.P., Microwave Losses in Incipient Ferroelectrics as Functions of the Temperature and the Biasing Field. *J. Appl. Phys.*, 84, 993, 1998.
91. Ang, C., Bhalla, A.S., and Cross, L.E., Dielectric Behavior of Paraelectric $KTaO_3$, $CaTiO_3$, and $(Ln_{1/2}Na_{1/2})TiO_3$ under a DC Electric Field. *Phys. Rev. B*, 64, 184104, 2001.

92. Trybuła, Z., Miga, S., Łoś, S., Trybuła, M., and Dec, J., Evidence of Polar Nanoregions in Quantum Paraelectric $KTaO_3$. *Solid State Commun.*, 209–210, 23, 2015.
93. Zlotnik, S., Vilarinho, P.M., Costa, M.E.V., Moreira, J.A., and Almeida, A., Growth of Incipient Ferroelectric $KTaO_3$ Single Crystals by a Modified Self-flux Solution Method. *Cryst. Growth Des.*, 10, 3397, 2010.
94. Chen, Z.X., Zhang, X.L., and Cross, L.E., Low-temperature Dielectric-properties of Ceramic Potassium Tantalate ($KTaO_3$). *J. Am. Ceram. Soc.*, 66, 511, 1983.
95. Axelsson, A.K., Pan, Y.Y., Valant, M., and Alfordz, N., Synthesis, Sintering, and Microwave Dielectric Properties of $KTaO_3$ Ceramics. *J. Am. Ceram. Soc.*, 92, 1773, 2009.
96. Glinšek, S., Malič, B., Rojac, T., Filipič, C., Budič, B., and Kosec, M., $KTaO_3$ Ceramics Prepared by the Mechanochemically Activated Solid-state Synthesis. *J. Am. Ceram. Soc.*, 94, 1368, 2011.
97. Tkach, A., Vilarinho, P.M., and Almeida, A., Role of Initial Potassium Excess on the Properties of Potassium Tantalate Ceramics. *J. Eur. Ceram. Soc.*, 31, 2303, 2011.
98. König, J., Jančar, B., and Suvorov, D., New $Na_{0.5}Bi_{0.5}TiO_3$–$NaTaO_3$-based Perovskite Ceramics. *J. Am. Ceram. Soc.*, 90, 3621, 2007.
99. Chen, C.-F., Llobet, A., Brennecka, G.L., Forsyth, R.T., Guidry, D.R., Papin, P.A., and McCabe, R.J., Powder Synthesis and Hot-pressing of a $LiTaO_3$ Ceramic. *J. Am. Ceram. Soc.*, 95, 2820, 2012.
100. Pertosa, P., Hollinger, G., and Michel-Calendini, F.M., Covalency Effects in Transition-metal Perovskitelike Compounds: Partial Densities of *p* and *d* States and Photoelectron Valence-band Spectra. *Phys. Rev. B*, 18, 5177, 1978.
101. Elissalde, C., Villesuzanne, A., Hornebecq, V., and Ravez, J., Prediction of Ferroelectric Properties in Niobates and Tantalates Based on Covalency Considerations. *Ferroelectrics*, 229, 1, 1999.
102. Reisman, A., Holtzberg, F., Berkenblit, M., and Berry, M., Reactions of the Group-VB Pentoxides with Alkali Oxides and Carbonates. 3. Thermal and X-ray Phase Diagrams of the System K_2O or K_2CO_3 with Ta_2O_5. *J. Am. Chem. Soc.*, 78, 4514, 1956.
103. Glinšek, S., Nuzhnyy, D., Petzelt, J., Malič, B., Kamba, S., Bovtun, V., Kempa, M., Skoromets, V., Kužel, P., Gregora, I., and Kosec, M., Lattice Dynamics and Broad-band Dielectric Properties of the $KTaO_3$Ceramics. *J. Appl. Phys.*, 111, 104101, 2012.
104. Huanosta, A., and West, A.R., The Electrical Properties of Ferroelectric $LiTaO_3$ and Its Solid Solutions. *J. Appl. Phys.*, 61, 5386, 1987.
105. Bennani, F., and Husson, E., Impedance Spectroscopy Analysis of Pure and Ni-doped Lithium Tantalate. *J. Eur. Ceram. Soc.*, 21, 847, 2001.
106. Masaif, N., Jebbari, S., Bennani, F., and Jennane, A., New Study of Defect Structure in Nonstoichiometric Lithium Tantalate. *Ferroelectr. Lett.*, 32, 7, 2005.

107. Yang, T., Liu, Y.-G., Zhang, L., Hu, M.-L., Yang, Q., Huang, Z.-H., and Fang, M.-H., Powder Synthesis and Properties of $LiTaO_3$ Ceramics. *Adv. Powder Technol.*, 25, 933, 2014.
108. Kong, L.B., Huang, Y., Que, W., Zhang, T., Li, S., Zhang, J., Dong, Z., and Tang, D., Transparent Ceramic Materials, in: *Transparent Ceramics*, Kong, L.B., Huang, Y., Que, W., Zhang, T., Li, S., Zhang, J., Dong, Z., and Tang, D. (Eds.), pp. 29–91, Springer International Publishing, Switzerland, 2015.
109. Barrett, J.H., Dielectric Constant in Perovskite Type Crystals. *Phys. Rev.*, 86, 118, 1952.
110. Müller, K.A., and Burkard, H., $SrTiO_3$: An Intrinsic Quantum Paraelectric below 4 K. *Phys. Rev. B*, 19, 3593, 1979.
111. Tkach, A., Vilarinho, P.M., Senos, A.M.R., and Kholkin, A.L., Effect of Nonstoichiometry on the Microstructure and Dielectric Properties of Strontium Titanate Ceramics. *J. Eur. Ceram. Soc.*, 25, 2769, 2005.
112. Samara, G.A., and Morosin, B., Anharmonic Effects in $KTaO_3$-ferroelectric Mode, Thermal-expansion, and Compressibility. *Phys. Rev. B*, 8, 1256, 1973.
113. Vogt, H., and Uwe, H., Hyper-Raman Scattering from the Incipient Ferroelectric $KTaO_3$. *Phys. Rev. B*, 29, 1030, 1984.
114. Lemanov, V.V., Sotnikov, A.V., Smirnova, E.P., Weihnacht, M., and Kunze, R., Perovskite $CaTiO_3$ as an Incipient Ferroelectric. *Solid State Commun.*, 110, 611, 1999.
115. Samara, G.A., and Peercy, P.S., Pressure and Temperature Dependence of the Static Dielectric Constants and Raman Spectra of TiO_2 (Rutile). *Phys. Rev. B*, 7, 1131, 1973.
116. Houas, A., Lachheb, H., Ksibi, M., Elaloui, E., Guillard, C., and Herrmann, J.-M., Photocatalytic Degradation Pathway of Methylene Blue in Water. *Appl. Catal., B*, 31, 145, 2001.
117. Kato, H., and Kudo, A., Photocatalytic Water Splitting into H_2 and O_2 Over Various Tantalate Photocatalysts. *Catal. Today*, 78, 561, 2003.
118. Sayama, K., Arakawa, H., and Domen, K., Photocatalytic Water Splitting on Nickel Intercalated $A_4Ta_xNb_{6-x}O_{17}$ (A = K, Rb). *Catal. Today*, 28, 175, 1996.
119. Huang, Y., Xie, Y., Fan, L., Li, Y., Wei, Y., Lin, J., and Wu, J., Synthesis and Photochemical Properties of La-doped $HCa_2Nb_3O_{10}$. *Int. J. Hydrogen Energy*, 33, 6432, 2008.
120. Xing, J., Fang, W.Q., Zhao, H.J., and Yang, H.G., Inorganic Photocatalysts for Overall Water Splitting. *Chem. Asian J.*, 7, 642, 2012.
121. Takahara, Y., Kondo, J.N., Takata, T., Lu, D., and Domen, K., Mesoporous Tantalum Oxide. 1. Characterization and Photocatalytic Activity for the Overall Water Decomposition. *Chem. Mater.*, 13, 1194, 2001.
122. Kato, H., and Kudo, A., New Tantalate Photocatalysts for Water Decomposition into H_2 and O_2. *Chemical Physics Letters*, 295, 487, 1998.
123. Kato, H., and Kudo, A., Water Splitting into H_2 and O_2 on Alkali Tantalate Photocatalysts $ATaO_3$ (A = Li, Na, and K). *J. Phys. Chem. B*, 105, 4285, 2001.

124. Zielinska, B., Mijowska, E., and Kalenczuk, R.J., Synthesis and Characterization of K-Ta Mixed Oxides for Hydrogen Generation in Photocatalysis. *Int. J. Photoenergy*, 2012, 525727, 2012.
125. Torres-Martínez, L.M., Gómez, R., Vázquez-Cuchillo, O., Juárez-Ramírez, I., Cruz-López, A., and Alejandre-Sandoval, F.J., Enhanced Photocatalytic Water Splitting Hydrogen Production on RuO_2/La:$NaTaO_3$ Prepared by Sol–Gel Method. *Catal. Commun.*, 12, 268, 2010.
126. Liu, J.W., Chen, G., Li, Z.H., and Zhang, Z.G., Hydrothermal Synthesis and Photocatalytic Properties of $ATaO_3$ and $ANbO_3$ (A = Na and K). *Int. J. Hydro. Energy*, 32, 2269, 2007.
127. Hu, C.-C., and Teng, H., Influence of Structural Features on the Photocatalytic Activity of $NaTaO_3$ Powders from Different Synthesis Methods. *Appl. Catal., A*, 331, 44, 2007.
128. Lin, W.H., Cheng, C., Hu, C.C., and Teng, H., $NaTaO_3$ Photocatalysts of Different Crystalline Structures for Water Splitting into H_2 and O_2. *Appl. Phys. Lett.*, 89, 211904, 2006.
129. Torres-Martínez, L.M., Juárez-Ramírez, I., and Figueroa-Torres, M.Z., Semiconductor Nanomaterials for Organic Dye Degradation and Hydrogen Production via Photocatalysis, in: *Nanomaterials for Environmental Protection*, Kharisov, B.I., Kharissova, O.V., and Rasika Dias, H.V. (Eds.), John Wiley & Sons, Inc., Hoboken, NJ, 2015, pp. 193–203.
130. Xu, D., Yang, S., Jin, Y., Chen, M., Fan, W., Luo, B., and Shi, W., Ag-decorated $ATaO_3$ (A = K, Na) Nanocube Plasmonic Photocatalysts with Enhanced Photocatalytic Water-splitting Properties. *Langmuir*, 31, 9694, 2015.
131. Grewe, T., Meier, K., and Tüysüz, H., Photocatalytic Hydrogen Production over Various Sodium Tantalates. *Catal. Today*, 225, 142, 2014.
132. Kato, H., and Kudo, A., Photocatalytic Decomposition of Pure Water into H_2 and O_2 Over $SrTa_2O_6$ Prepared by a Flux Method. *Chem. Lett.*, 28, 1207, 1999.
133. Kato, H., and Kudo, A., Photocatalytic Water Splitting into H_2 and O_2 over Various Tantalate Photocatalysts. *Catalysis Today*, 78, 561, 2003.
134. Iwase, A., Kato, H., and Kudo, A., Nanosized Au Particles as an Efficient Cocatalyst for Photocatalytic Overall Water Splitting. *Catal. Lett.*, 108, 2006.
135. Lee, Y., Watanabe, T., Takata, T., Hara, M., Yoshimura, M., and Domen, K., Hydrothermal Synthesis of Fine $NaTaO_3$ Powder as a Highly Efficient Photocatalyst for Overall Water Splitting. *Bull. Chem. Soc. Japan*, 80, 423, 2007.
136. Hu, C.-C., and Teng, H., Influence of Structural Features on the Photocatalytic Activity of $NaTaO_3$ Powders from Different Synthesis Methods. *Appl. Catal. A: Gen.*, 331, 44, 2007.
137. Ishihara, T., Nishiguchi, H., Fukamachi, K., and Takita, Y., Effects of Acceptor Doping to $KTaO_3$ on Photocatalytic Decomposition of Pure H_2O. *J. Phys. Chem. B*, 103, 1, 1999.
138. Mitsui, C., Nishiguchi, H., Fukamachi, K., Ishihara, T., and Takita, Y., Photocatalytic Decomposition of Pure Water over NiO Supported on KTa(M)O_3 (M = Ti^{4+}, Hf^{4+}, Zr^{4+}) Perovskite Oxide. *Chem. Lett.*, 28, 1327, 1999.

139. Shi, H., and Zou, Z., Photophysical and Photocatalytic Properties of $ANbO_3$ (A = Na, K) Photocatalysts. *J. Phys. Chem. Solids*, 73, 788, 2012.
140. Jiang, L., Qiu, Y., and Yi, Z., Potassium Niobate Nanostructures: Controllable Morphology, Growth Mechanism, and Photocatalytic Activity. *J. Mater. Chem. A*, 1, 2878, 2013.
141. Torres-Martínez, L.M., Garza-Tovar, L.L., and López, E.M., Photocatalytic Degradation of Methylene Blue in Water by UV-irradiated $ATaO_3$ (A = Li, Na, K) Sol-gel, in: *Eco-materials Processing and Design*, Watari, K. and Lee, S.-W. (Eds.), pp. 197–211, John Wiley & Sons, Inc., New York, 2006.
142. Torres-Martínez, L.M., Cruz-López, A., Juárez-Ramírez, I., and Meza-de la Rosa, M.E., Methylene Blue Degradation by $NaTaO_3$ Sol-gel Doped with Sm and La. *J. Hazard. Mater.*, 165, 774, 2009.
143. Kanhere, P.D., Zheng, J., and Chen, Z., Site Specific Optical and Photocatalytic Properties of Bi-doped $NaTaO_3$. *J. Phys. Chem. C*, 115, 11846, 2011.
144. Liu, D.-R., Jiang, Y.-S., and Gao, G.-M., Photocatalytic Degradation of an Azo Dye using N-doped $NaTaO_3$ Synthesized by One-step Hydrothermal Process. *Chemosphere*, 83, 1546, 2011.
145. Zhao, Y.-X., Liu, D.-R., Li, F.-F., Yang, D.-F., and Jiang, Y.-S., Preparation, Characterization and Photocatalytic Activity of N-doped $NaTaO_3$ Nanocubes. *Powder Technol.*, 214, 155, 2011.
146. Su, Y., Wang, S., Meng, Y., Han, H., and Wang, X., Dual Substitutions of Single Dopant Cr^{3+} in Perovskite $NaTaO_3$: Synthesis, Structure, and Photocatalytic Performance. *RSC Adv.*, 2, 12932, 2012.
147. Qi, L., and Li, X., N-doped $NaTaO_3$: Novel Visible-light-driven Photocatalysts Synthesised by a Sol–Gel Method. *J. Sol-Gel Sci. Technol.*, 69, 625, 2014.
148. Zhao, J., and Yang, X., Photocatalytic Oxidation for Indoor Air Purification: A Literature Review. *Build. Environ.*, 38, 645, 2003.
149. Das, D.P., Biswal, N., Martha, S., and Parida, K.M., Solar-light Induced Photodegradation of Organic Pollutants over CdS-pillared Zirconium-titanium Phosphate (ZTP). *J. Mol. Catal. A: Chem.*, 349, 36, 2011.
150. Yunjun, Y., and Jingfei, L., Synthesis, Property Characterization and Photocatalytic Activity of the Novel Composite Polymer Polyaniline/Bi_2SnTiO_7. *Molecules*, 17, 2752, 2012.
151. Tobaldi, D.M., Pullar, R.C., Gualtieri, A.F., Seabra, M.P., and Labrincha, J.A., Sol-gel Synthesis, Characterisation and Photocatalytic Activity of Pure, W-, Ag- and W/Ag Co-doped TiO_2 Nanopowders. *Chem. Eng. J.*, 214, 364, 2013.
152. Fu, H., Pan, C., Yao, W., and Zhu, Y., Visible-light-induced Degradation of Rhodamine B by Nanosized Bi_2WO_6. *J. Phys. Chem. B*, 109, 22432, 2005.
153. Kumar, S., Khanchandani, S., Thirumal, M., and Ganguli, A.K., Achieving Enhanced Visible-light-driven Photocatalysis Using Type-II $NaNbO_3$/CdS Core/Shell Heterostructures. *ACS Appl. Mater. Interfaces*, 6, 13221, 2014.
154. Zlotnik, S., Tobaldi, D.M., Seabra, M.P., Labrincha, J.A., and Vilarinho, P.M., Alkali Niobate and Tantalate Perovskites as Alternative Photocatalysts. *Chem. Phys. Chem.*, submitted.

155. Li, F.-F., Liu, D.-R., Gao, G.-M., Xue, B., and Jiang, Y.-S., Improved Visible-light Photocatalytic Activity of $NaTaO_3$ with Perovskite-like Structure via Sulfur Anion Doping. *Appl. Catal., B*, 166–167, 104, 2015.
156. Liu, X., Lv, J., Wang, S., Li, X., Lang, J., Su, Y., Chai, Z., and Wang, X., A Novel Contractive Effect of $KTaO_3$ Nanocrystals via La^{3+} Doping and an Enhanced Photocatalytic Performance. *J. Alloys Compd.*, 622, 894, 2015.
157. Lan, J., Zhou, X., Liu, G., Yu, J., Zhang, J., Zhi, L., and Nie, G., Enhancing Photocatalytic Activity of One-dimensional $KNbO_3$ Nanowires by Au Nanoparticles under Ultraviolet and Visible-light. *Nanoscale*, 3, 5161, 2011.
158. Wang, R., Zhu, Y., Qiu, Y., Leung, C.-F., He, J., Liu, G., and Lau, T.-C., Synthesis of Nitrogen-doped $KNbO_3$ Nanocubes with High Photocatalytic Activity for Water Splitting and Degradation of Organic Pollutants Under Visible Light. *Chem. Eng. J.*, 226, 123, 2013.
159. Osgood, R., Photoreaction Dynamics of Molecular Adsorbates on Semiconductor and Oxide Surfaces. *Chem. Rev.*, 106, 4379, 2006.
160. Thompson, T.L., and Yates, J.T., Surface Science Studies of the Photoactivation of TiO_2 New Photochemical Processes. *Chem. Rev.*, 106, 4428, 2006.
161. Luttrell, T., Halpegamage, S., Tao, J., Kramer, A., Sutter, E., and Batzill, M., Why is Anatase a Better Photocatalyst than Rutile? Model Studies on Epitaxial TiO_2 Films. *Sci. Rep.*, 4, 4043, 2014.
162. Tong, H., Ouyang, S., Bi, Y., Umezawa, N., Oshikiri, M., and Ye, J., Nano-photocatalytic Materials: Possibilities and Challenges. *Adv. Mater.*, 24, 229, 2012.
163. Shi, J., and Guo, L., ABO_3-based Photocatalysts for Water Splitting. *Prog. Nat. Sci. Mat. Int.*, 22, 592, 2012.
164. Li, P., Ouyang, S., Xi, G., Kako, T., and Ye, J., The Effects of Crystal Structure and Electronic Structure on Photocatalytic H_2 Evolution and CO_2 Reduction over Two Phases of Perovskite-structured $NaNbO_3$. *J. Phys. Chem. C*, 116, 7621, 2012.
165. Amini, A.R., Laurencin, C.T., and Nukavarapu, S.P., Bone Tissue Engineering: Recent Advances and Challenges. *Crit. Rev. Biomed. Eng.*, 40, 363, 2012.
166. Navarro, M., Michiardi, A., Castaño, O., and Planell, J.A., Biomaterials in Orthopaedics. *J. R. Soc. Interface*, 5, 1137, 2008.
167. Salinas, A.J., Esbrit, P., and Vallet-Regi, M., A Tissue Engineering Approach based on the Use of Bioceramics for Bone Repair. *Biomater. Sci.*, 1, 40, 2013.
168. Vallet-Regí, M., and Ruiz-Hernández, E., Bioceramics: From Bone Regeneration to Cancer Nanomedicine. *Adv. Mater.*, 23, 5177, 2011.
169. Hench, L.L., Bioceramics. *J. Am. Ceram. Soc.*, 81, 1705, 1998.
170. Best, S.M., Porter, A.E., Thian, E.S., and Huang, J., Bioceramics: Past, Present and for the Future. *J. Eur. Ceram. Soc.*, 28, 1319, 2008.
171. Bystrov, V.S., Seyed Hosseini, E., Kopyl, S., Bdikin, I.K., and Kholkin, A.L., Piezoelectricity and Ferroelectricity in Biomaterials: Molecular Modeling and Piezoresponse Force Microscopy Measurements. *J. Appl. Phys.*, 116, 066803, 2014.
172. Fukada, E., and Yasuda, I., On the Piezoelectric Effect of Bone. *J. Phys. Soc. Jpn.*, 12, 1158, 1957.

173. Teng, N.C., Nakamura, S., Takagi, Y., Yamashita, Y., Ohgaki, M., and Yamashita, K., A New Approach to Enhancement of Bone Formation by Electrically Polarized Hydroxyapatite. *J. Dent. Res.*, 80, 1925, 2001.
174. Dubey, A.K., and Basu, B., Pulsed Electrical Stimulation and Surface Charge Induced Cell Growth on Multistage Spark Plasma Sintered Hydroxyapatite-Barium Titanate Piezobiocomposite. *J. Am. Ceram. Soc.*, 97, 481, 2014.
175. Baxter, F.R., Bowen, C.R., Turner, I.G., and Dent, A.C.E., Electrically Active Bioceramics: A Review of Interfacial Responses. *Ann. Biomed. Eng.*, 38, 2079, 2010.
176. Jianqing, F., Huipin, Y., and Xingdong, Z., Promotion of Osteogenesis by a Piezoelectric Biological Ceramic. *Biomaterials*, 18, 1531, 1997.
177. Hwang, K.S., Song, J.E., Jo, J.W., Yang, H.S., Park, Y.J., Ong, J.L., and Rawls, H.R., Effect of Poling Conditions on Growth of Calcium Phosphate Crystal in Ferroelectric $BaTiO_3$ Ceramics. *J. Mater. Sci. Mater. Med.*, 13, 133, 2002.
178. Park, Y.-J., Hwang, K.-S., Song, J.-E., Ong, J.L., and Ralph Rawls, H., Growth of Calcium Phosphate on Poling Treated Ferroelectric $BaTiO_3$ Ceramics. *Biomaterials*, 23, 3859, 2002.
179. Dubey, A.K., Basu, B., Balani, K., Guo, R., and Bhalla, A.S., Dielectric and Pyroelectric Properties of HAp-$BaTiO_3$ Composites. *Ferroelectrics*, 423, 63, 2011.
180. Dubey, A.K., Basu, B., Balani, K., Guo, R., and Bhalla, A.S., Multifunctionality of Perovskites $BaTiO_3$ and $CaTiO_3$ in a Composite with Hydroxyapatite as Orthopedic Implant Materials. *Integr. Ferroelectr.*, 131, 119, 2011.
181. Chen, X.M., and Yang, B., A New Approach for Toughening of Ceramics. *Mater. Lett.*, 33, 237, 1997.
182. Dubey, A.K., Gupta, S.D., and Basu, B., Optimization of Electrical Stimulation Parameters for Enhanced Cell Proliferation on Biomaterial Surfaces. *J. Biomed. Mater. Res. Part B Appl. Biomater.*, 98B, 18, 2011.
183. Christophis, C., Cavalcanti-Adam, E., Hanke, M., Kitamura, K., Gruverman, A., Grunze, M., Dowben, P., and Rosenhahn, A., Adherent Cells Avoid Polarization Gradients on Periodically Poled $LiTaO_3$ Ferroelectrics. *Biointerphases*, 8, 1, 2013.
184. Carville, N.C., Collins, L., Manzo, M., Gallo, K., Lukasz, B.I., McKayed, K.K., Simpson, J.C., and Rodriguez, B.J., Biocompatibility of Ferroelectric Lithium Niobate and the Influence of Polarization Charge on Osteoblast Proliferation and Function. *J. Biomed. Mater. Res. A*, 103, 2540, 2014.
185. Vilarinho, P.M., Barroca, N., Zlotnik, S., Félix, P., and Fernandes, M.H., Are Lithium Niobate ($LiNbO_3$) and Lithium Tantalate ($LiTaO_3$) Ferroelectrics Bioactive? *Mater. Sci. Eng., C*, 39, 395, 2014.
186. Marchesano, V., Gennari, O., Mecozzi, L., Grilli, S., and Ferraro, P., Effects of Lithium Niobate Polarization on Cell Adhesion and Morphology. *ACS Appl. Mater. Interfaces*, 7, 18113, 2015.

187. Nilsson, K., Lidman, J., Ljungstrom, K., and Kjellman, C., Biocompatible Material for Implants, US 09/673,815, assigned to St. Jude Medical AB, Jarfalla, SE, 2003.
188. Wang, Q., Yang, J., Zhang, W., Khoie, R., Li, Y.-M., Zhu, J.-G., and Chen, Z.-Q., Manufacture and Cytotoxicity of a Lead-free Piezoelectric Ceramic as a Bone Substitute – Consolidation of Porous Lithium Sodium Potassium Niobate by Cold Isostatic Pressing. *Int. J. Oral Sci.*, 1, 99, 2009.
189. Länge, K., Rapp, B., and Rapp, M., Surface Acoustic Wave Biosensors: a review. *Anal. Bioanal. Chem.*, 391, 1509, 2008.
190. Shiokawa, S., and Moriizumi, T., Design of SAW Sensor in Liquid. *Jpn J. Appl. Phys.*, 27, 142, 1988.
191. Kondoh, J., Matsui, Y., and Shiokawa, S., New Biosensor Using Shear Horizontal Surface Acoustic Wave Device. *Jpn J. Appl. Phys.*, 32, 2376, 1993.
192. Li, J., Mou, X., Qiu, J., Wang, S., Wang, D., Sun, D., Guo, W., Li, D., Kumar, A., Yang, X., Li, A., and Liu, H., Surface Charge Regulation of Osteogenic Differentiation of Mesenchymal Stem Cell on Polarized Ferroelectric Crystal Substrate. *Advan. Healthcare Mater.*, 4, 998, 2015.
193. Kokubo, T., and Takadama, H., How Useful Is SBF in Predicting In Vivo Bone Bioactivity? *Biomaterials*, 27, 2907, 2006.

10

Application of Silver Tin Research on Hydroxyapatite

Ewa Skwarek

Department of Radiochemistry and Colloid Chemistry, Maria Curie-Sklodowska University, Lublin, Poland

Abstract

One of the biggest challenges in the advanced materials area is biomaterials. On the other hand, growing antibiotic resistance of microorganism demands from the science community continuous search for new bioactive substances and target drugs with high biocompatibility and antibacterial properties. Although the mechanism of antibacterial activity of silver nanoparticles is not completely clear, the literature reports that electrostatic attraction between the negatively charged bacterial cells and the positively charged silver nanoparticles plays a key role in its antibacterial activity. To obtain new compounds with high biocompatibility and desired properties, silver ions are either deposited on biomaterials or embedded in their structure. One of these materials, examined the best and possessing phenomenal biological, bone-creative properties and high biocompatibility, is hydroxyapatite (HAP) $Ca_{10}(PO_4)_6(OH)_2$. This chapter constitutes the literature survey about the silver nanoparticles' characteristics, structure, synthesis, properties, and implementation of HAP with embedded silver and the use of modern scientific methods: X-ray powder diffraction, transition electron microscopy, and scanning electron microscopy, for determination of structure, morphology, and optical properties of the examined materials. The research provides results on the characteristics of the colloid HAP/silver/electrolyte solution. System and measurements of zeta potential, surface charge density, and adsorption from the solution are discussed.

***Keywords*:** Hydroxyapatite, silver, adsorption, surface charge density, zeta potential

Corresponding author: ewunias@hektor.umcs.lublin.pl

Ashutosh Tiwari, Rosario A. Gerhardt and Magdalena Szutkowska (eds.) Advanced Ceramic Materials, (385–418) © 2016 Scrivener Publishing LLC

10.1 Introduction

Iron as a noble metal has been known for ages, and its treatment properties were appreciated already by the ancients. In Ancient Greece, Rome, or Babylon, silver vessels were used, or if they were not available, silver coins were put into ordinary vessels so that water or wine kept in them was not spoiled. The Egyptians used silver to activate wounds healing.

The tradition of using silver sets to consume dishes was continued into the middle Ages. Then, silver was the attribute of wealth and belonging to the noble class. What is more, if protected against food infection with microorganisms? On the other hand, using silver vessels and cutlery resulted in agrarian—the disease caused by silver depositions in tissues and under the skin. Such skin and membranes become grey-blue, and "as agrarian" afflicted mostly aristocrats, there is still the name "blue blood", which suggests aristocratic origin. Also in the twenty-first century, there were found some cases of agrarian in people who overdosed colloidal silver (due to its regular admission in the amount of at least 0.014 mg Ag/kg of body mass every day) or in poor countries in miners who work in silver mines as their organisms absorb large amounts of silver dust. Overcoloring of skin can affect the whole body or only some areas. Though not having negative effects on the health conditions, it cannot be removed (contrary to the orange color of skin caused by excessive consumption of β-carotene which disappears).

In the twentieth century, during the world wars, antibacterial properties of silver were exploited to counteract infections. Powdered, colloidal silver was put into contaminated wells to destroy, among others, pathogens causing typhoid fever or malaria. Silver salts are also applied to cure burns and wounds.

10.1.1 Properties of Silver

In natural state, silver occurs in the filamentous or feathery state. It contains a significant amount of gold or mercury. It can be obtained as a by-product during smelting of other metals, e.g. copper or lead from their sulfide ores. It is of white luster. It is soft and malleable, so it is easy to polish and is ductile [1].

Silver is characterized by the best electrical and heating conductivity of metals and forms alloys with various metals. Its vapors are blue and are composed of monoatomic molecules. Ozone is eatable of direct reaction with silver. On the surface, there is formed a black coating which dissolves acids (in diluted nitric acid in cold and in concentrated sulfuric acid in hot).

Silver is mainly employed to mint coins and in production of tableware, etc. Pure silver cannot be used because it is too soft. In production, its alloys with copper are applied. The amount of silver in the alloy is used as its "hallmark". This is the content of pure silver per 1000 parts of alloy. For the above-mentioned usage, the 800 hallmark silver is used [1, 2]. It is also used for protection, e.g., of copper alloys against corrosion. In the laboratory, there are silver vessels used while working with alkaline alloys to which silver is more resistant compared to other metals, e.g., Fe, Ni, and Pt [1]. Preparations containing colloidal silver are applied as very effective disinfection agents in treatment of respiratory track phlogistic states. The silver ions are characterized by its deadly action against microorganisms.

$$2Ag + H_2O + \tfrac{1}{2} O_2 = 2Ag^+ + 2OH^-$$

The above reaction shows transition of metallic silver into the solution containing dissolved oxygen [3].

One of commonly known compounds is nitrate (V) silver, the so-called lunar caustic, which is a white substance blacking in the light accompanied by release of atomic silver [4].

$$AgNO_3 \xrightarrow[\text{light}]{} Ag + NO_2 + O$$

It is soluble in water and possesses antiseptic properties. It can be obtained by dissolution of silver in nitric acid and evaporation of the silver solution. Nitrate is used in the form of rods or plates for cauterization (pointwise burning of skin excrescences). It can also be used for dyeing of eyelashes and eyebrows, and then its admissible concentration cannot exceed 4% [3, 4].

10.1.2 Application of Silver

In modern times, silver is used for production of mirrors, in photographic and electrical industries, in jeweler's croft (jewelry, ornaments). Its biocidal and disinfection properties are still appreciated. Therefore, Ag found its application in household goods (toilets, washing machines) as well as coating of silica carriers, in which Ag acting biocidal and Si deodorizing are very effective disinfection agents combating over 90% of microorganisms. In cosmetology, there is applied colloidal silver which is pure metallic silver found in clear water. As silver molecules have the same charge, they repel each other, so they are in constant motion and do not drop on the bottom as well as do not flout over the surface. Efficiency of the

solution action increases with the decreasing size of colloidal silver molecules. The sizes of colloidal silver molecules are from 1.5 to 5 nm, but the sizes of viruses are 15–150 nm and of bacteria 350–1000 nm; therefore, it can easily penetrate into pathogens and destroy them effectively. Silver is a trace element which ensures proper functioning of our organism. In trace amounts, it strengthens our immunological system in combating various kinds of bacteria and viruses. With the age, the ability to assimilate silver by our organism drops. Lowering its level results in increasing morbidity [5].

Silver combined with other compounds is used in rejuvenating preparations containing hyaluronic acid and colloidal silver [6]. The preparation is able to minimize skin inflammation and act against free radicals. Silver is used in the preparations regulating the work of sebaceous glands protecting against seborrhea and increasing the level of skin moistening [7–9]. Because of its microdermabrasion properties, silver is used in creams for reducing scars and wrinkles. These cosmetics can be used for any kind of skin [8].

Colloidal silver is safe for our organism; it does not accumulate in it. Contrary to antibiotics, it is capable of killing pathogens and their mutation. Antibiotics are characterized by limited action against pathogenic organisms. They can destroy at most 6 pathogens, whereas colloidal silver can annihilate about 650 various pathogens contrary to antibiotics; colloidal silver is a natural compound occurring in our organism, which destroys the cause of the disease, and it does not have any negative effect. Silver's oxidizing activity results in immediate destruction of pathogenic organisms, but antibiotics are not effective against viruses. What is more, in relation to bacteria, they can inhibit their partition (bacterium does not perish). Silver possesses the properties of a catalyst. When it oxidizes pathogen, it loses its pathogenic properties, but silver can destroy another such organism. One molecule of antibiotic is used for each eliminated pathogen. Main advantages of colloidal silver, owing to which it is used in medicine, are its colorless and odorless nature, nontoxicity, being not addictive, does not undergo accumulation, is bioassimilable, kills parasites, destroys fungi and mould, does not irritate mucous membranes, does not contain free radicals, can be taken by pregnant women and breast-feeding mothers, and does not interact with drugs. Colloidal silver is used to cure infections and diseases like AIDS and diseases induced by staphylococci and streptococci. It can be applied locally in skin diseases and internally in colds. Its very important feature is that it does not cause any side effects in oral or intravenous therapy. However, it should be kept in mind that the solution of colloidal silver must be prepared in

accordance with the procedure. Colloidal silver belongs to a group of natural antibiotics, and its action consists in discriminating the enzymatic system which is used by unicellular pathogens in oxygen metabolism. Pathogens and their mutations are not capable of creating resistance to colloidal silver. It is also applied to cure wounds as it stimulates the skin reconstruction process. It stimulates bone cells to regenerate and reconstruct bones.

Colloidal silver can be used orally, intravenously, locally, to gargle the throat, and in eye and ear drops. Externally, it can be applied in the cases of acne, solar burns, skin changes, skin mycosis, cuts and open wounds, skin inflammation, and insect bites. Internally, it can be applied in the cases of gonorrhea, furuncles, flu, catarrh, poisoning with toxins, rosella, pneumonia, septicemia, diabetes, and yeast infection [5].

Nanosilver exhibits a large characteristic surface area. It can be prepared in various ways. In a chemical way, reducers and suitable stabilizers for silver salt reduction are used. Hazardous byproducts can be formed in this reaction, but it is quick and relatively simple. The physicochemical method uses ultrasounds, microwaves, or irradiation. However, in a biological way, nanomolecules are synthesized from natural plant and fungous extracts or bacterial ones. Biodeadly action is associated with oxidizing properties of silver. It deactivates enzymes of bacteria and other unicellular microorganisms causing necrobiosis only after a few minutes. Moreover, silver nanomolecules act as a catalyst. They block a bacterial cell owing to its tight surrounding. The bacterium is deprived of motion and loses ability to conjugation, adhesion to other cells. In the presence of active oxygen, there are formed disulfide bridges between the thiol groups of cysteine, which disturbs the flow of electrons and run of the respiration chain as well as synthesis of components for building a cellular wall. The cell is deprived of abilities to respire, its genetic material oxidizes, and as a result it perishes. The mechanism of binding silver with bacterial DNA, not damaging hydrogen bonds, is not known. What is only known is that it hinders development and synthesis of DNA threads and thus cell partition. In the case of fungi, the water balance is disturbed, and in viruses, Ag catalyzes decomposition of protein–lipid background (Figure 10.1).

The areola of the electrically charged molecule of nanosilver exhibits the lack of two electrons which allows attracting pathogens and taking over electrons from them resulting in microorganism's damage. However, silver does not impair healthy body cells due to their electrical neutrality and cellular membrane structure. Therefore, Ag nanomolecules are an effective antibiotic with a wide range of action: bactericidal, virucidal,

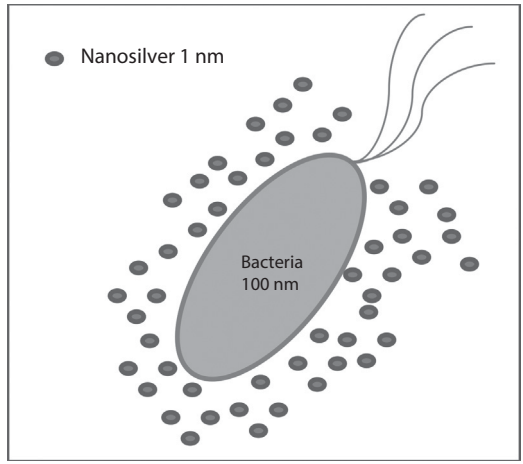

Figure 10.1 Scheme of antibacterial action of nanosilver/bacteria (about 100 nm size) encircled with silver nanomolecules (1 nm nanomolecules outnumber).

and mycocidal. However, as follows from the studies, not all bacteria are sensitive to interaction of silver with the cellular wall. For instance, staphylococcus characterized by large resistance absorbs only 12% of silver nanomolecules (whereas 95% of other bacteria undergo degradation).

The question arises if nanomolecular silver exhibits stronger bioactivity than its ions. Therefore, the cells of *Chlamydomonas reinhardtii* were subjected to the action of both Ag^+ and Ag. It is proved that during the first hour, silver ions (originating from $AgNO_3$) are characterized by larger toxicity toward the living cells, but after about 2 h, silver nanomolecules (10–200 nm diameter) are more effective.

Besides long-known antimicrobial property, due to its oxidizing ability, silver can neutralize effectively gaseous contaminations. There is a serious problem in livestock lodgings where enormous amounts of gases from bedding and animal excrements are released into the atmosphere. The studies carried out in 2011 using the aqueous suspension of silver nanomolecules showed change of physicochemical and microbiological properties of bedding composed of straw and sawdust. The bedding spread with silver in breeding broilers emitted less ammonia and contained a fewer number of microorganism catalytic coatings. Silver exhibits similar action toward gaseous contaminants and microorganisms, and it is more effective compared to titanium coatings. Antibacterial activities of silver nanomolecules are affected by coarseness of coating surface as well as dose and size of molecules [10].

10.1.3 Hydroxyapatite (HAP)–Silver

The most important publications on combination of hydroxyapatite (HAP) and silver will be described below [11]. The aim of the research presented by Ciobanu *et al.* was evaluation of $Ca_{10-x}Ag_x(PO_4)_6(OH)_2$ nanomolecules (Ag/HAP-NPs) with respect to their antibacterial and antifungal actions. Resistance of bacterial pathogens to antimicrobial agents appeared lately and became a main health problem. The paper presents the method of synthesis of nanocrystalline HAP with the silver admixture at 100 °C in the deionized water and the estimation of the action of Ag/HAP-NPs against the gram-positive and gram-negative bacteria as well as fungal strains. Specific antimicrobial activity revealed in the qualitative test indicates that the compounds obtained by the authors react differently with the already mentioned microorganisms (probably due to differences in the structure of cellular walls of microorganisms); synthesis of Ag/HAP by the co-precipitation method uses cheap and nontoxic compounds. On the other hand, there were determined the experimental conditions of inspecting morphology and size of the Ag/HAP nanomolecules with the increasing concentration of Ag. The X-ray powder diffraction (XRD) studies confirm the presence of the peak characteristic of HAP, whereas the energy-dispersive X-ray spectroscopy (EDX) and X-ray photoelectron spectroscopy (XPS) spectra show the presence of silver in the samples. The presence of any other phase was not detected. Additionally, the antimicrobial activity of the Ag/HAP nanopowder was estimated. The obtained results of investigations indicate that the compound being analyzed can be an effective alternative to antibiotic therapy as it reveals a specific range of antimicrobial activity. It is capable of inhibiting the initial stage of development of microbial biofilm but does not exhibit it toward the biofilm being formed which is more difficult to eradicate and more resistant.

In the study of Erakowic *et al.* [12], HAP coatings were modified with lignin to achieve corrosive stability and porous surface enabling osteogenesis. The addition of silver known for antimicrobial properties seemed to be the best strategy to avoid infection. The coatings of silver/hydroxyapatite (Ag/HAP) and silver/hydroxyapatite/lignin (Ag/HAP/Lig) were prepared by cataphoretic deposition on titanium from the ethanol suspension sintered at 900 °C in argon. This system was characterized by means of XRD, scanning electron microscopy (SEM), field-emission SEM (FESEM), and attenuated total reflectance Fourier transform infrared spectroscopy (ATR-FTIR). Corrosive stability of electrodeposited coatings was estimated *in vitro* in the Kokubo's simulated body fluid (SBF) at 37 °C using the electrochemical impedance spectroscopy (EIS). Biological activity was

estimated by immersion in SBF, thus estimating formation of HAP on the coating surface. The structure of crystals of newly formed HAP carbonate of plate habit was detected already after 7 days and showed bioactivity increase. Both coatings were characterized by good biological stability during a prolonged time of immersion. Of these two, the coating Ag/HAP/Lig possessed a homogeneous surface, smaller coarseness, and lower value of contact angle. The analyses XRD, ATR-FTIR, SEM, and FESEM indicate formation of a new phase in both studied coatings, which means an effective biogrowth of HAP during immersion in the SBF solution. The biogrowth manifests itself in the form of new plate-shaped crystals of properties indispensable for biological activity. On the other hand, transformation of HAP to other phases of calcium phosphates after sintering at 900 °C was thwarted owing to the presence of lignin in the composite Ag/HAP/Lig as confirmed by the results of XRD and ATR-FTIR. The SEM and FESEM analyses also show that the surface of the Ag/Hap/Lig coating is more homogeneous, compact, and less coarse. However, the low value of the contact angle in SBF (determined in the lying drop test) proves better wettability compared to the Ag/HAP coating. As follows from the presented results, the Ag/HAP/Lig coating deposited electrophoretic ally on titanium is a promising candidate for future development of biologically active materials.

In a study by Michiyo Honda *et al*. [13], to prevent bacterial growth and biofilm formation on HAP discs, silver-containing (1–20 mol%) hydroxyapatite (Ag/HAP) powders were synthesized using an ultrasonic spray pyrolysis (USSP) technique. The XRD peaks were very broad, indicating low crystallinity, and this induced the release of Ag^{+} ions from Ag/HAP powders. In addition, a gradual increase in Ca^{2+} ion release was observed. These results suggest that dissolution of Ca^{2+} ion in Ag/HAP triggered the release of Ag^{+} ions. The antimicrobial efficacy of Ag/HAP disc was tested against *Staphylococcus aureus*. The samples with Ag contents of more than 5 mol% were found to be highly effective against bacterial colonization and biofilm formation *in vitro*. *In vivo* antibacterial tests using bioluminescent strains also showed reductions in the viability of bacteria with Ag/HAP (5 mol%) discs. Biocompatibility tests using a modified Transwell insert method showed that Ag/HAP (5 mol%) discs have negative effects on osteoblast proliferation. These results indicate that Ag/HAP (5 mol%) is characterized by effective antibacterial activity and good biocompatibility both *in vitro* and *in vivo* together with good biocompatibility, thus confirming its utility as a bactericidal material. A series of silver-containing HAP powders were synthesized using the USSP technique. The microstructures of Ag/HAP powders, as observed by SEM and transmission electron microscopy

(TEM), showed microspheres with the diameters of 0.5–2.0 μm and exhibited very similar morphology, despite the Ag content, while the cores of the spherical particles were translucent. The release of Ag^+ ions from each Ag/HAP powder was sustained over a period of 30 days, resulting in dissolution of Ca with powders of low crystallinity. A study on antimicrobial effects has shown that Ag/HAP powders with the contents of more than 5 mol% of Ag exhibit good antibacterial activity. The relative inhibition zone dose-dependently increased with Ag ion contents, and biofilm formation was inhibited by the release of Ag^+ ions from the Ag/HAP disc. In addition, the Ag/HAP disc diminished bacterial growth *in vivo*. However, no significant cytotoxicity was observed for Ag/HAP discs using the modified Transwell insert method. It was concluded that Ag/HAP discs have good biological properties and antibacterial activities *in vitro* and *in vivo*. Therefore, Ag/HAP powders and/or discs are promising for bone tissue engineering and may be applied as bactericidal biomaterials.

In a study, Aurora Mocanu *et al.* [14] nanohydroxyapatite doped with zinc (0.2 wt%), silver (0.25 wt%), and gold (0.025 wt%) has been obtained by an innovative wet chemical approach, coupled with a reduction process for silver and gold. The synthesized multi-substituted nanohydroxyapatite was freeze-dried and calcined at 650 °C. It was characterized by XRD, FTIR, and imaging techniques: TEM, SEM, and AFM. Then, nanohydroxyapatite was mixed with previously synthesized silver nanoparticles in the amount of 9 wt% to give a novel material (Ag/HAP). The silver nanoparticles were prepared by the reduction of silver nitrate with glucose in alkaline medium. TEM and UV–Vis confirmed the formation of silver nanoparticles with an average size of 12 nm. Furthermore, organic matrix composites were obtained from a filler made of HAP and/or Ag/HAP and a mixture of monomers (such as bis-GMA and TEG-DMA), which were polymerized at various compositions in the silver nanoparticles content up to 5.4 wt%. Antibacterial activities of these composites were investigated against several different pathogenic species: *Escherichia coli*, *S. aureus*, *Staphylococcus* spp., *Bacillus cereus*, and *Candida albicans*, using the Kirby–Bauer disk-diffusion method. Antibacterial activities are enhanced with increasing of silver content within composites. These effects clearly reveal that silver nanoparticles can be effectively utilized in combination with multi-substituted HAP and polymeric matrix, both used as carriers, in order to improve their efficiency against various pathogenic species. These composites can be considered a promising antimicrobial material for coating of orthopedic and dental implants or used as bone cements in surgical applications.

The aim of the research presented by Radovanovic *et al.* is to synthesize HAP [15] powders doped with Ag^+ or Cu^{2+} by a hydrothermal method in

order to obtain biomaterial with an antimicrobial effect. The synthesis was performed with two contents of dopant (Ag^+ or Cu^{2+}) by considering both the antimicrobial activities and biocompatibility of the powders. The doped HAP was annealed at 1200 °C for 2 h in order to investigate the influence of doping with Ag^+ and Cu^{2+} on the creation of the biphasic HAP/tricalcium phosphate and determine the antimicrobial activity and biocompatibility of the obtained biphasic powders. Analyses of all powders, undoped and Hap doped and HAP/tricalcium phosphate, were performed by FESEM, XRD, atomic absorption spectroscopy (AAS), and EDS. The *in vitro* antibacterial activities of the powders were evaluated against *S. aureus*, *E. coli*, *Pseudomonas aeruginosa* and *C. albicans*. All powders showed good antimicrobial activity, but generally the powders of doped HAP/tricalcium phosphate had more uniform results against all pathogenic microorganisms than those HAP doped. *In vitro* biocompatibility tests, MTT and DET, were used to evaluate the biocompatibility of Ag^+- and Cu^{2+}-doped HAP/tricalcium phosphate with MRC-5 human fibroblast cells. These tests confirmed that powders do not have a cytotoxic effect. The HAP/tricalcium phosphate powders doped with the lower content of Ag^+ and Cu^{2+} showed especially good biocompatibility. Antimicrobial and biocompatibility tests recommend the Ag^+- and Cu^{2+}-doped HAP /tricalcium phosphate as promising material for use in reconstructive surgery of bone.

In a study by Dubnikan *et al.* [16], silver-doped HAP containing different amounts of Ag (0.5 and 0.8 wt %) was prepared using wet chemical precipitation method. In the synthesis process, CaO, H_3PO_4, and $AgNO_3$ were used as raw materials. Porous HAP and Ag/HAP scaffolds via viscous mass-foaming technique were prepared from as-synthesized powders, and obtained samples were sintered at different temperatures. According to the XRD data and SEM microstructure analysis, silver ions from Ag/HAP structure were excluded, and additional silver phase during the sintering process was formed. Impact of sintering temperature (1000 °C and 1200 °C) on the porosity, density, specific surface area, and mechanical properties of porous HAP and Ag/HAP scaffolds was evaluated. Total porosity of 71% (at 1000 °C) and 54% (at 1200 °C) was achieved. Incorporation of Ag into the HAP structure resulted in the decrease of porous scaffold compressive strength by 30–50% compared to pure HAP porous scaffolds. Increasing the sintering temperature of porous scaffolds up to 1200 °C, it was possible to obtain samples with 2–4 times higher compressive strength, compared to samples sintered at 1000 °C.

In a study, Li *et al.* [17] suggested that a novel multifunctional Ag_3PO_4-loaded HAP material can remove the typical pollutants from water. The Ag_3PO_4/ HAP composites were synthesized facilely via *in situ* precipitation

of Ag_3PO_4 on the pre-existing HAP nanowires. By optimizing the composition of Ag_3PO_4 and HAP, the material could achieve an optimal photocatalytic activity to decompose rhodamine B (RhB), methyl orange (MO), and methylene blue (MB) under visible light irradiations with enhanced pH stability. Besides, the adsorption of Pb (II) on the Ag_3PO_4/ HAP reached a maximum capacity of 250 mg/g, and this value was approximately three times as that of pure HAP. Furthermore, the composite material exhibited excellent antibacterial activities toward gram-negative bacterium (*E. coli*) and gram-positive bacterium (*S. aureus*). The results highlighted the cooperative effects between Ag_3PO_4 and HAP. Simultaneous removals of dyes, toxic metal ions, and bacteria with a high efficiency followed an easy approach to the purification of contaminated water via the rationally designed material, in which the Ag_3PO_4/ HAP composite might be developed as a general water treatment material with multiple functions.

The aim of the study by Ciobanu *et al.* [18] was to obtain a novel HAP - based material with high biocompatibility. The structural properties of the samples were well characterized by XRD, SEM, and XPS. The XRD studies revealed the characteristic peaks of HAP in each sample. Other phases or impurities were not observed. The SEM observations suggest that the doping components have no influence on the surface morphology of the samples, which reveals a homogeneous aspect of the synthesized particles for all samples. The presence of calcium (Ca), phosphorus (P), oxygen (O), and silver (Ag) in the Ag/HAP is confirmed by EDX and XPS analyses. Nanocrystalline silver-doped HAP stimulated viability and potentiated the activation of murine macrophages.

The aim of the research presented by Jegatheeswaran *et al*. was to prepare HAP [19] nanocomposite particles simply in the presence of polyethylene glycol (PEG) and fabricated with silver via a sol–gel route. Their physicochemical and biological properties were investigated. The objective of this study is to inspect the crystallinity and antibacterial activity of these composite materials. PEG was applied to promote biocompatibility and biodegradability of HAP. Silver nanoparticles were used for improving its bactericidal efficacy while applying composites. The nanosized HAP composite particles with PEG and nanosilver were incorporated to increase the crystalline nature of the nanocomposite. The structure of nanocomposite particles was studied by XRD, FTIR, high-resolution SEM, EDS, and TEM analyses. Silver nanoparticles loaded on the synthesized HAP/PEG showed a synergistic antibacterial effect against the gram-negative bacterium *E. coli*. The controlled release of Ag+ ion from HAP /PEG/Ag nanocomposite has given good antibacterial efficacy evidenced by epi-fluorescence microscopy images during different hours.

In the study by Shi *et al*. [20], Ag-doped HAP nanocrystal has been elaborately prepared with the optimal doping concentration from 0.27 to 2.2 ppm, exhibiting non-cytotoxicity with simultaneous effective bacteria reduction ability. Ultra-trace Ag-doped HAP nanocrystals possess higher protein adsorption than pure HAP ones due to the trace doping-induced less negative surface potential. The ultra-trace Ag-doped HAP nanocrystals showed effectively antibacterial ability, non-cytotoxicity, and enhanced adsorbability that made them ideal materials for various biocompatible and antibacterial applications.

In the study by Zamperini *et al*. [21], pure HAP and HAP decorated with silver (Ag/HAP) nanoparticles were synthesized and characterized, and a series of ultra-trace Ag-doped HAP nanocrystals have been elaborately prepared with the optimal doping concentration from 0.27 to 2.2 ppm, exhibiting non-cytotoxicity with simultaneous effective bacteria reduction ability. Ultra-trace Ag-doped HAP nanocrystals possess higher protein. The antifungal effect of Ag/HAP nanoparticles in a distilled water solution was evaluated against *C. albicans*. The origin of the antifungal activity of Ag/HAP is also discussed. The results obtained showed that the HAP nanorod morphology remained the same with Ag ions decorations on the HAP structure, which were deposited in the form of nanospheres. The interactions that occurred between the structure and its defect density variation in the interfacial Ag/HAP and interfacial HAP region with the fungal medium resulted in antifungal activity. The reaction mechanisms involved oxygen and water adsorption, which formed an active complex cluster. Decomposition and desorption of the final products as well as the electron/hole recombination process contribute largely to fungicidal effects.

In the research presented by Ciobanu *et al*. (2013), synthesis [22] of nanosized particles of Ag/HAP with antibacterial properties is of great interest for the development of new biomedical applications. This study was the evaluation of $Ca_{10-x}Ag_x(PO_4)_6(OH)_2$ nanoparticles (Ag/HAP-NPs) were for their antibacterial and antifungal activities. Resistance to antimicrobial agents by pathogenic bacteria has emerged in the recent years and became a major health problem. A method for synthesizing Ag-doped nanocrystalline HAP is as follows. A silver-doped nanocrystalline HAP was synthesized at 100 °C in deionized water. Also, Ag/HAP-NPs are evaluated for their antimicrobial activity against gram-positive and gram-negative bacteria and fungal strains. The specific antimicrobial activity revealed by the qualitative assay is that the compounds interact differently with the microbial targets probably due to the differences in the microbial wall structures.

In the study by Ciobanu *et al.* [23], synthesis of nanosized particles of Ag-doped HAP with antibacterial properties is of great interest in new biomedical applications. A method for Ag-doped nanocrystalline HAP synthesis is proposed. A silver-doped nanocrystalline HAP was synthesized at 100 °C in deionized water. Other phases or impurities were not observed. Silver-doped HAP nanoparticles (Ag/HAP) were obtained by setting the atomic ratio of Ag/[Ag + Ca] at 20% and [Ca + Ag]/P as 1.67. The XRD studies demonstrate that powders made by co-precipitation at 100 °C exhibit the apatite characteristics with good crystal structure, and no new phase or impurity is found. The SEM observations suggest that these materials present a little different morphology, which reveals a homogeneous aspect of the synthesized particles for all samples. The presence of calcium (Ca), phosphorus (P), oxygen (O), and silver (Ag) in the Ag/HAP is confirmed by the EDX analysis. FTIR and FT-Raman spectroscopies revealed that the presence of various vibrational modes corresponds to phosphates and hydroxyl groups. The strain of *S. aureus* was used to evaluate the antibacterial activity of $Ca_{10-x}Ag_x(PO_4)_6(OH)_2$ ($x = 0$ and 0.2). The *in vitro* bacterial adhesion study indicated a significant difference between HAP ($x = 0$) and Ag/HAP ($x = 0.2$). The Ag/HAP nanopowder showed higher inhibition.

The aim of the research presented by Jadalannangari *et al.* was to synthesize silver-doped HAP [24] ($Ag_xCa_{100-x}(PO_4)_6(OH)_2$) nanorods using a modified sol–gel method at a low temperature of 100 °C. Silver concentration was varied as $x = 1$, 3, and 5. XRD studies showed that the synthesized silver-doped hydroxyapatite (Ag/HAP) was fully crystalline with hexagonal structure and an average crystallite size of 25 nm. At all the doping concentrations, the nanoparticles were rod shaped with an average length of 110–180 nm and a diameter of 20–25 nm as determined from the TEM studies. These compounds were tested for their antimicrobial activities against *E. coli* (MTCC 2345) and *S. aureus* (MTCC 737). Antimicrobial activity was observed for all the three silver-doping concentrations with the highest activity for $x = 3$, in terms of the zone of inhibition and the percentage reduction in the number of colonies. The hemolysis ratios for $x = 1$ and 3 Ag/HAP samples were below 2%, indicating that they are highly compatible and can be a promising biomaterial for tissue-engineering applications in orthopedics.

The aim of the research presented by Vukomanovi *et al.* was to develop a new approach [25] for the synthesis of silver (Ag) nanoparticles and their combination with HAP to form composites via a sonochemical process. The Ag particles, obtained using a nitrate precursor, are cubic in structure, spherical in shape, and up to 20 nm in size. The use of precursors with a lower temperature of thermal decomposition (acetates and lactates) leads

to a change of the morphological and structural properties, resulting in the formation of both hexagonal and cubic Ag phases. In the case of the HAP/Ag composites investigated in this study, both the

structural and morphological properties of the Ag nanoparticles were affected by the tinplating effect of the HAP. The formation mechanism and growth of the Ag particles on their own and within a HAP/Ag composite are discussed in terms of the sonification process and the thermal reduction steps used. In this work, homogeneous sonochemical precipitation was optimized as a new method for the synthesis of silver (Ag) nanoparticles and their composites with HAP. As a result, the composite particles obtained as the final outcome were composed of (a) Ag ions incorporated into the apatite structure, (b) smaller Ag particles embedded within the apatite plates, and (c) larger Ag particles attached to the surface of these plates. Moreover, the structure of the smaller and larger Ag particles in these systems is different (cubic and hexagonal). The optimization of the synthesis process revealed that the obtained properties of this material can be controlled by applying a particular type of the silver precursor, that is, by making the selection with regard to its thermal properties that control the particle growth. A selection of precursors with a lower decomposition temperature enables the initiation of a rapid reduction process and formation of small Ag seeds during the sonication step. A second, thermal reduction step is a slow process that uses the sonochemically formed seeds for the formation of hexagonal Ag particles. The HAP surface has a special role in the formation of Ag particles within the HAP/Ag composite, preventing their aggregation and contributing to their growth. A comparison between sonochemical and classical precipitation shows that the sonochemical approach makes it possible to control the phase composition in the system obtained before the reduction process and to influence the rate of silver reduction. Consequently, the structural and morphological properties of the metallic and metal/apatite composite nanoparticles are affected, which results in the formation of materials with an unusual design with the ability to provide very interesting activity against bacteria.

In a study by Noda *et al.* [26], a novel thermal spraying technology was developed for a silver-containing hydroxyapatite (Ag/HAP) coating with antibacterial activity to reduce the incidence of implant-associated infections. In this study, we determined the concentration of Ag ions that exhibit antibacterial activity in fetal bovine serum (FBS) and antibacterial activity of the Ag/HAP coating in FBS. The minimum inhibitory concentration (MIC) of Ag ions for several bacteria in FBS was in the range of 4.0–7.9 ppm. When 10 ppm of Ag was added (as $AgNO_3$ solution), 0.01 ppm of free Ag ions was detected. As the MIC of Ag ions approached

the concentration that enabled formation of free Ag ions in FBS, the antibacterial activity of added Ag can be attributed to the free Ag ions. The Ag/HAP coating showed strong antibacterial activity in FBS as well; the Ag concentration in FBS was 26 ppm for the antibacterial test of the Ag/HAP coating. Because the Ag/HAP coating can release sufficient free Ag ions in FBS, the Ag/HAP coating was observed to show a strong antibacterial effect in the studied biological medium.

In the study by Erakovic *et al.* [27], HAP coatings were modified with lignin in order to attain corrosion stability and surface porosity that enables osteogenesis. Incorporating silver, well known for its antimicrobial properties, seemed the best strategy for avoiding possible infections. The Ag/HAP and Ag/HAP/Lig coatings were cataphoretically deposited on titanium from ethanol suspensions, sintered at 900 °C in Ar, and characterized by XRD, SEM, FESEM, ATR-FTIR, and XPS. The corrosion stability of electrodeposited coatings was evaluated *in vitro* in the Kokubo's SBF at 37 °C using EIS. Bioactivity was estimated by immersion in SBF to evaluate the formation of HAP on the coating surface. A microcrystalline structure of newly formed plate-shaped carbonate HAP was detected after only 7 days, indicating enhanced bioactive behavior. Both coatings had good corrosion stability during a prolonged immersion time. Of the two, the Ag/HAP/Lig coating had a homogeneous surface, less roughness, and low values of contact angle.

10.2 Materials and Methods

10.2.1 Synthesis of Hydroxyapatite Using the Co-precipitation Method

Pure HAP powder was prepared by co-precipitation of 0.75 M $Ca(NO_3)_2 \cdot 4H_2O$ solution and 1 M $(NH_4)HPO_4$ solution. To prepare the above solutions, the following reagents were used: $Ca(NO_3)_2 \cdot 4H_2O$ produced by POCh, $(NH_4)_2HPO_4$ of 99% purity produced by POCH, and 25% NH_4OH analytically pure produced by Chempur.

The solution of diammonium hydrophosphate was brought to the pH 10 value using ammonia water. The 200 ml calcium nitrate solution was put into a three-necked round-bottom flask and heated at 100 °C for 30 min with continuous stirring. After 30 min, the 200 ml phosphate solution of pH 10 was added dropwise for successive 2 h while stirring continuously. While adding drop by drop, the solution pH was checked so that its value was maintained at 10. The pH value was adjusted with ammonia water.

The obtained deposit of HAP was washed and centrifuged using redistilled water up to obtaining the constant value of conductivity, which for this synthesis was about 6.5 μS/cm. The centrifuged HAP powder was dried for 24 h at 100 °C. The powder obtained in this way is designated HAP in the paper.

10.2.2 Synthesis of Silver-doped Hydroxyapatite

Silver-doped HAP was obtained by means of co-precipitation of 0.75 M $Ca(NO_3)_2 \cdot 4H_2O$ and $AgNO_3$ solutions from 1 M $(NH_4)_2HPO_4$ solution. Using appropriate proportions of the mixture of solutions containing calcium and silver ions, Ag-HAP powder of the molar silver ions and calcium ions were obtained at a ratio of 0.4 and 0.8, respectively. In the synthesis, the following reagents were used: $Ca(NO_3)_2 \cdot 4H_2O$ produced by POCH; $AgNO_3$ analytically pure produced by Eurochem BGD and of 99.8% purity, produced by POCH; $(NH_4)_2HPO_4$ of 99% purity produced by POCH; and 25% NH_4OH analytically pure produced by Chempur.

At first, solutions of tetra aqua calcium nitrate (V) and silver nitrate of the concentration 1 M were prepared dissolving suitable weighed amounts of salt in redistilled water. Then, using ammonia water, the phosphate solution was adjusted to the basic pH 10.

In order to prepare silver-doped HAP of the molar ratio of Ag^+ and Ca^{2+} ions 0.4, the $Ca(NO_3)_2 \cdot 4H_2O$ and $AgNO_3$ solutions were put into the three-necked round-bottom flask and heated in water bath for 30 min at 100 °C stirring continuously. Then, 200 ml of $(NH_4)_2HPO_4$ solution of earlier adjusted pH was added dropwise for 2 h. During the synthesis, pH was checked to be 10.

The obtained Ag/HAp powder was washed several times with redistilled water and centrifuged. When the value of conductivity of the solution over the Ag/Hap deposit did not decrease and was about 8 μS/cm, the obtained material was dried for 24 h at 100 °C. The synthesis of HAP of the silver ions content being 0.8 was conducted in the analogous way. The powders obtained in this way are designated HAP/0.4 Ag and HAP/0.8 Ag.

10.2.3 Characteristics of Surfaces of Obtained Materials

Crystalline structure of the material was determined using the XRD method by means of a diffractometer equipped with the rtg generator of the ISO-DEBYFLEX 3003-60 kV type by the Seifert Analytical X-ray firm, the system KMW 3000C by the Oxford Diffraction firm. The measurement data were collected, analyzed, and processed using the XRAYAN program.

In order to determine parameters of porous structure of sample surfaces, a standard method such as nitrogen low-temperature adsorption–desorption was applied. The measurements were performed using the automatic adsorption analyser of the ASAP (Accelerated Surface Area and Porosimetry) 2405 produced by Micromeritics Instruments, Co. Adsorption isotherms were measured after the sample degassing under the reduced pressure at 150 °C.

The zeta potential of HAP dispersions was determined by electrophoresis with Nano series ZS90 by Malvern. Prior to the zeta potential measurements, the suspensions containing 100 ppm solid concentration were ultrasonificated. In order to measure the zeta potential, 0.01 g of powdered HAP was added to 100 ml of $NaNO_3$ of the concentration 10^{-3} M, and the mixture was subjected to ultrasonification for 3 min. Then, the solution pH was adjusted to 10 using the 0.1 M NaOH solutions, and the zeta potential of the suspension was measured. After the measurements, the solution pH was reduced to the value 9 using the 0.1 M HNO_3 solution, and the zeta potential was measured again. The measurements were also made for the pH values 8, 7, 6, 5, and 4. Analogous measurements were made for the concentrations of the background electrolyte being 10^{-2} and 10^{-1} M.

The zeta potential of HAP suspension was also measured in the solution of background electrolyte of the concentration 10^{-3} M containing silver ions originating from $AgNO_3$. Therefore, there were weighed four samples of HAP prepared by the wet method of the mass 0.01 g, and each of them was placed in 100 ml solution containing $AgNO_3$ and $NaNO_3$ in such proportions that concentration of silver ions should be 10^{-6}, 10^{-5}, 10^{-4}, and 10^{-3} M, respectively. Each suspension was subjected to ultrasonification for 3 min. Then, the zeta potential was measured for the pH value of 4–10 changing by one unit.

Measurements of zeta potential were made for HAP-containing admixture of silver in relation to calcium 0.4 and 0.8, respectively. Similarly to pure HAP, the potential was measured in the solution of $NaNO_3$ electrolyte at its three concentrations: 10^{-3}, 10^{-2}, and 10^{-1} M in the pH range of 4–10 (change by one unit of pH).

Surface charge density and adsorption measurements were performed simultaneously in the suspension of the same solid content, to keep the identical conditions of the experiments in a thermostated Teflon vessel at 25 °C. To eliminate the influence of CO_2, all potentiometric measurements were performed under nitrogen atmosphere. pH values were measured using a set of glass REF 451 and calomel pHG201-8 electrodes with the Radiometer assembly. The surface charge density was calculated from the difference of the amounts of added acid or base to obtain the same pH value of suspension as for the background electrolyte $NaNO_3$.

Adsorption of Ag^+ ions was determined by the radioisotope method using labeled ^{110}Ag and calculated from difference between initial and final concentrations of ions in solution per unit mass of sample. Radioactivity of ^{110}Ag gamma sources was determined using 2480 Automatic Gamma Counter (Perkin Elmer, USA). Adsorption of ions was studied by the method of radioactivity loss from the solution using the potentiometric titration set.

10.3 Results and Discussion

10.3.1 The Results of XRD and Surface

The materials obtained from the synthesis were analyzed to date their composition, crystalline structure, and surface characteristics. Therefore, the XRD method allowing to establish the crystalline structure of samples was applied.

As follows from Figure 10.2, peaks characteristic of HAP overlaps those with inbuilt Ag^+ ions regardless of silver content. Possibly, increase in the

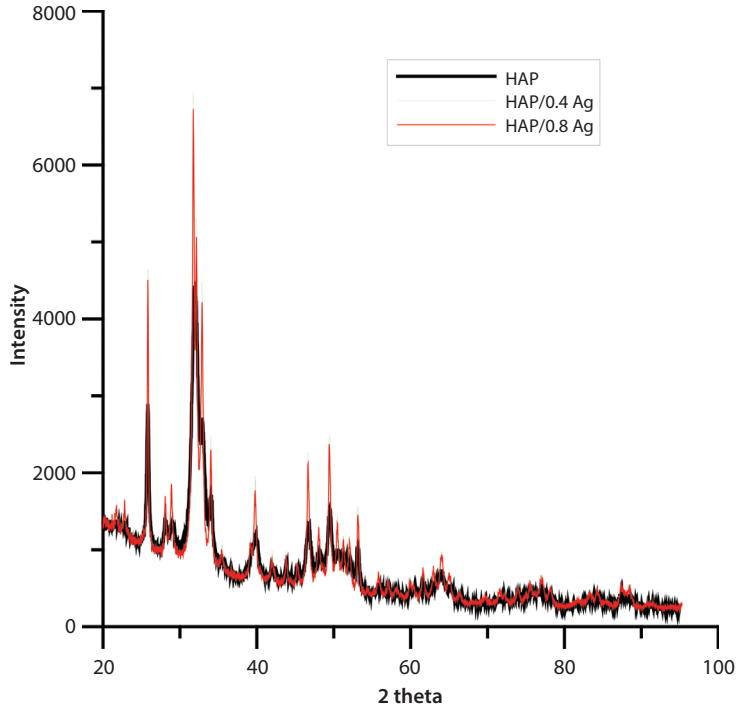

Figure 10.2 Diffractogram of the HAP sample with the adsorbed silver.

number of silver ions would affect the crystalline structure of studied samples. Besides this crystalline phase, no other one was detected for the studied samples. The size of crystallites counted using the Rietveld method was also very similar HAP = 31 nm, HAP/0.8 Ag = 36 nm, HAP/0.4 Ag = 33 nm.

Figure 10.3 shows the peaks characteristic of the crystalline form of HAP as evidenced by the following peaks and their intensities: 25.9–100%, 32.96–55%, 39.84–20%; 46.7–40%, and 49.5–30%, which is consistent with the phase analysis conducted based on the ASTM data. However, it should be structured. Possibly, annealing at a higher temperature, e.g. 800 °C or 1200 °C, would favorably affect crystallographic structure but would diminish the specific surface area.

The diffractograms of HAP with adsorbed Ag^+ ions presented in Figure 10.3 indicate the presence of additional peaks. As follows from the figure, in the case of HAP/Ag, silver phosphate constitutes only 58.1% of the surface area and HAP 41.9%. The size of silver phosphate crystallites is 79.5 nm and that of HAP 31 nm. The specific surface area of the obtained samples was determined by means of the apparatus ASAP Micromeritics, Inc., USA. The results presented in Table 10.1 for all studied systems are very similar to all studied sizes confirming the XRD results of insignificant effects of the silver ions' presence on the HAP surface.

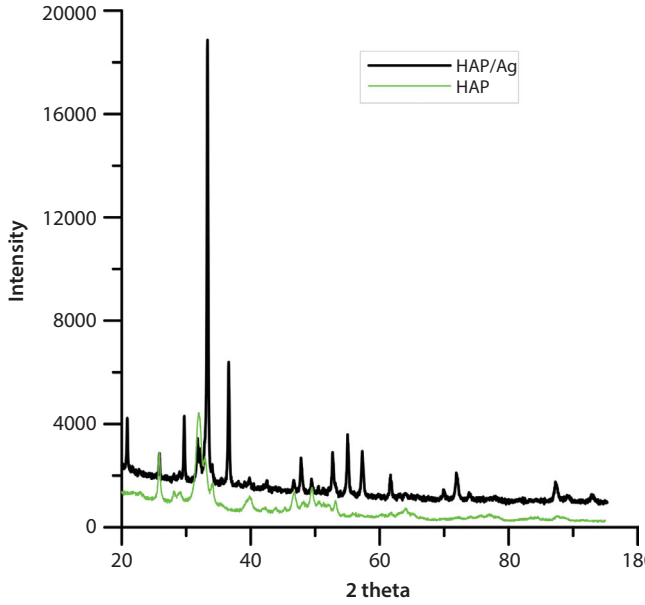

Figure 10.3 Diffractogram of the HAP sample with adsorbed silver.

Table 10.1 Structural parameters of HAP obtained from low-temperature nitrogen adsorption–desorption.

HAP	HAP	HAP/ 0.4 Ag	HAP/ 0.8 Ag	HAP/ Ag
Surface area from BET [m^2/g]	55	54	55	52
Surface area from Langmuir isotherm [m^2/g]	80	78	80	77
Total pore volume from adsorption 1.7 nm < d < 300 nm by BJH method [cm^3/g]	0.32	0.35	51.77	0.32
Total pore volume from desorption 1.7 nm < d < 300 nm by BJH method [cm^3/g]	0.32	0,35	55.94	0.32
Average pores radius from adsorption, BET method [nm]	23.50	26.17	23.91	24.46
Average pores radius from adsorption, BJH method [nm]	24	26.93	25.12	26.34
Average pores radius from desorption, BJH method [nm]	23	25.11	23.41	24.84

HAP = hydroxyapatite, HAP/Ag after adsorption.

The surface area of pure HAP and both silver-doped HAP powders was similar being: for HAP 55 m^2/g, for HAP/0.4 Ag, and 54 m^2/g and for HAP/0.8 Ag 55 m^2/g, which confirms the XRD results of a small effect of the presence of silver ions on the HAP surface. For better evidence of the changes caused by adsorbed or inbuilt silver ions on the surface of HAP, the HAP sample was analyzed after adsorption measurements. As follows from Table 10.1, both total pore volume and the specific surface area of the HAP sample after silver adsorption decreased due to silver adsorption on the HAP surface resulting in pores closing.

10.3.2 Zeta Potential at the Hydroxyapatite/$NaNO_3$ Electrolyte Solution Interface

Knowledge of the zeta potential value enables prediction of colloidal systems' stability. The zeta potential allows to determine electrostatic interactions among the colloidal particles, and thus, it can be referred to the colloidal systems' stability. The HAP zeta potential allows characterizing

the double electrical layer at the HAP/electrolyte solution interface. The particles of HAP in the electrolyte possess the electrical charge, and the zeta potential allows determining part of the charge in the double-diffusion layer. The results are presented in Figure 10.4. The figure of the zeta potential dependence indicates that the value of the zeta potential changes insignificantly with the pH increase for a given concentration of the electrolyte. The dependence of the zeta potential on the pH function allows to assume that pH_{IEP} has the value of <4 and is lower than pH_{PZC} as the zeta potential depends additionally on the part of the surface charge, which is affected by calcium or phosphate ions adsorbing on or desorbing from the crystal lattice. Then, the same action was done for HAP prepared by co-precipitation of the $Ca(NO_3)_2{\cdot}4H_2O$ and $(NH_4)HPO_4$ solutions. The diagram (Figure 10.4) presents the results of zeta potential measurements.

The zeta potential was also measured at the interface HAP electrolyte solution $NaNO_3$ containing additionally Ag^+ ions. The results of

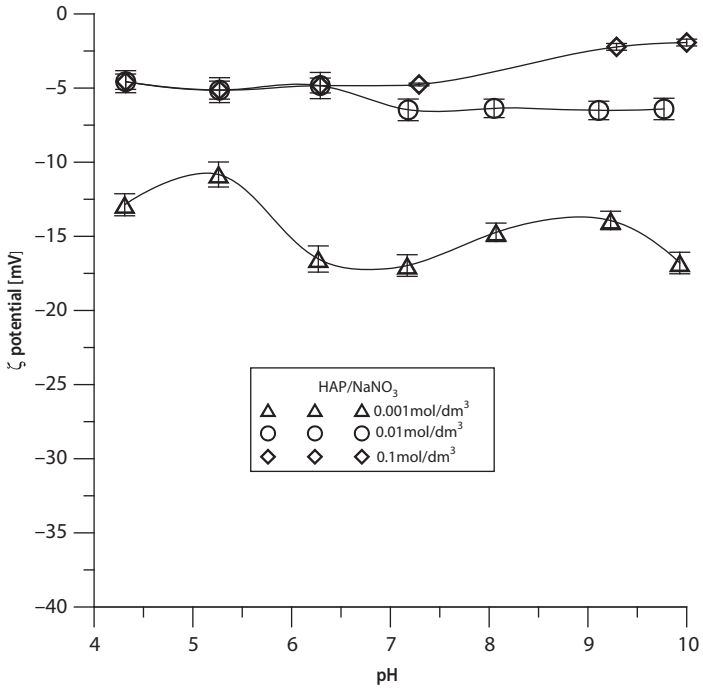

Figure 10.4 The diagram of dependence of the zeta potential of HAP prepared by co-precipitation of the $Ca(NO_3)_2 \cdot 4H_2O$ and $(NH_4)HPO_4$ solutions on pH in the sodium nitrate solutions of the concentrations 10^{-3}, 10^{-2}, and 10^{-1} M.

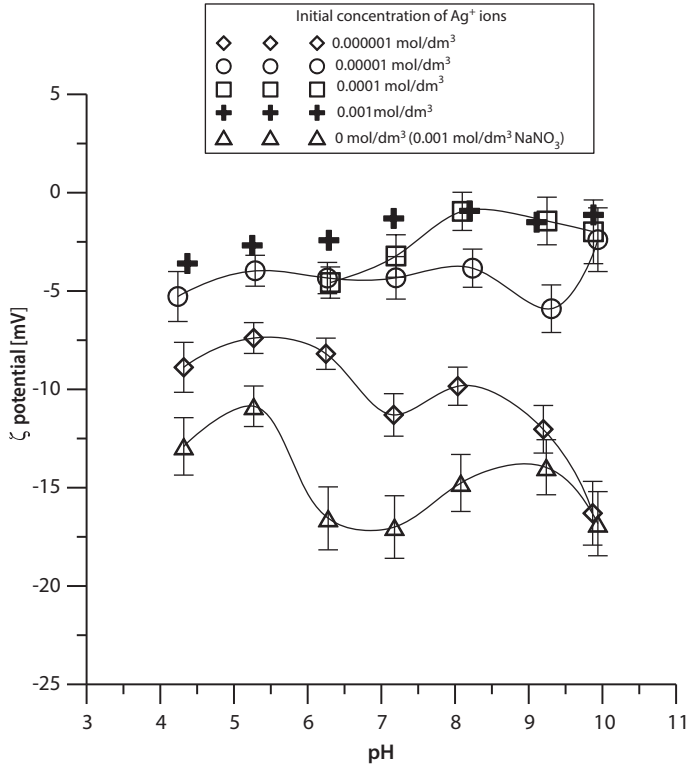

Figure 10.5 The dependence of the zeta potential of HAP obtained by the wet method on pH in the 10^{-3} M solution of $NaNO_3$ electrolyte containing Ag^+ ions at appropriate concentration.

measurements are presented in the diagram. The presence of silver ions in the HAP/electrolyte suspension affects the value of the zeta potential. The increase in the zeta potential value can be seen. Silver ions replacing hydrogen ions change the character of HAP surface enhancing its basic character (Figure 10.5).

Measurements of the zeta potential were made for silver-doped HAP compared to calcium being (HAP/0.4 Ag) (Figure 10.6) and (HAP/0.8Ag) (Figure 10.7). The results are presented in the diagram. The course of the zeta potential in the pH function is quite interesting. The value of zeta potential increases and then decreases, which may be due to the presence of Ag^+ ions in the structure of these adsorbents because the dependence course for pure HAP is different.

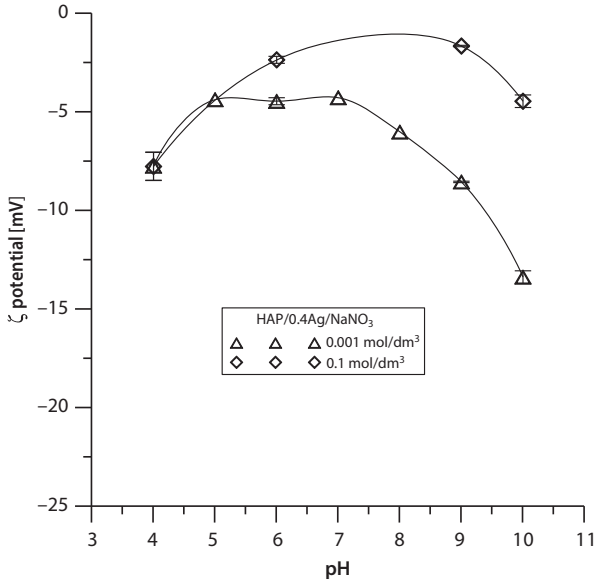

Figure 10.6 The dependence of the zeta potential of AgHAp ($x_{Ag} = 0.4$) on pH in the $NaNO_3$ solutions of the concentrations 10^{-3}, 10^{-2}, and 10^{-1} M.

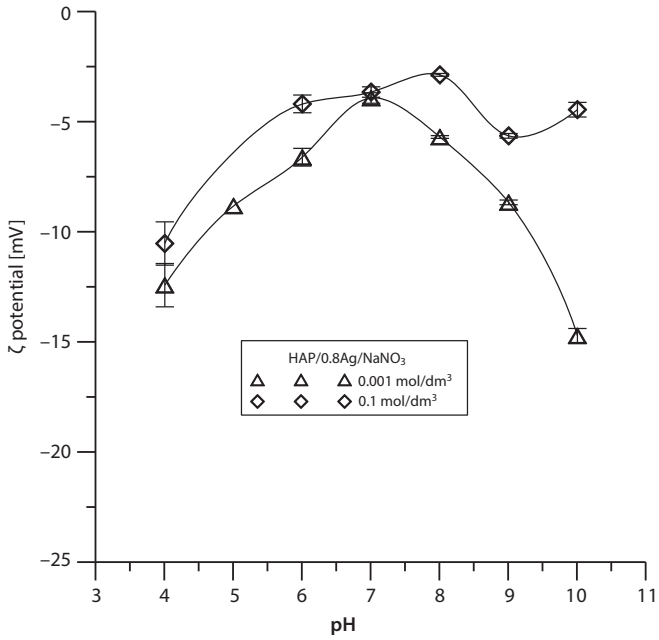

Figure 10.7 The dependence of the zeta potential of AgHAp ($x_{Ag} = 0.8$) on pH in the $NaNO_3$ solutions of the concentrations 10^{-3}, 10^{-2}, and 10^{-1} M.

10.3.3 Surface Charge Density

Surface charge density in the HAP/electrolyte solution as well as silver-doped HAP/electrolyte solution systems was determined by the potentiometric titration method. This method allows to determine acid–base properties of functional groups on the surface of the studied solid, and its advantage is possibility of determination of potential creating ions (H^+ and OH^-) concentration in a simple way. As follows from Figures 10.8–10.10, the value of pH_{PZC} for pure HAP is 7.38, but for the samples, HAP/0.4 Ag and HAP/0.8 Ag 6.53 and 6.91, respectively. The presence of silver ions in the HAP structure results in the shift of pH_{PZC} toward higher values of pH and increases the contribution of positively charged groups in surface charge formation.

Figure 10.11 presents the effect of silver ions concentration on surface charge density in the pH function at the HAP/$NaNO_3$/Ag interface. As can be seen, the increase in adsorption of silver ions causes drop in the surface chargé density at pH > 6. This is due to the release of hydrogen ions from the surface of HAP functional groups.

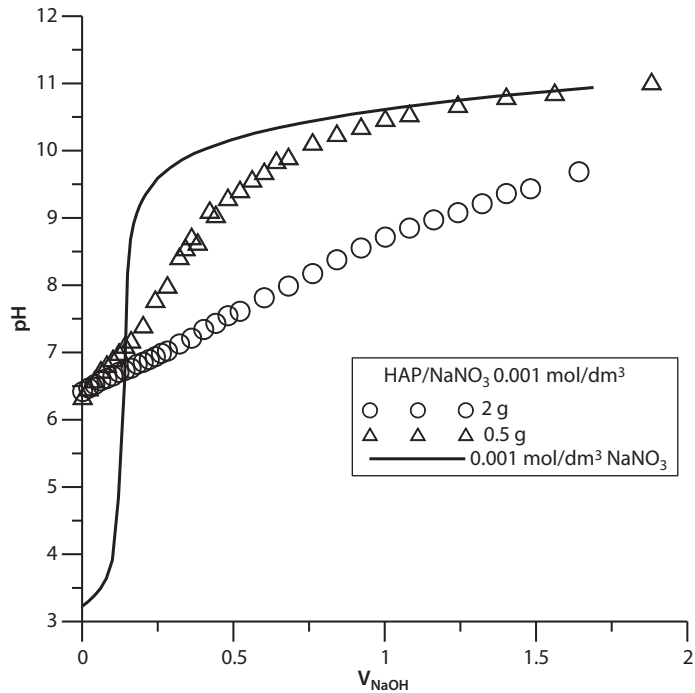

Figure 10.8 The dependence of pH on $V_{(NaOH)}$ for the HAP/electrolyte system.

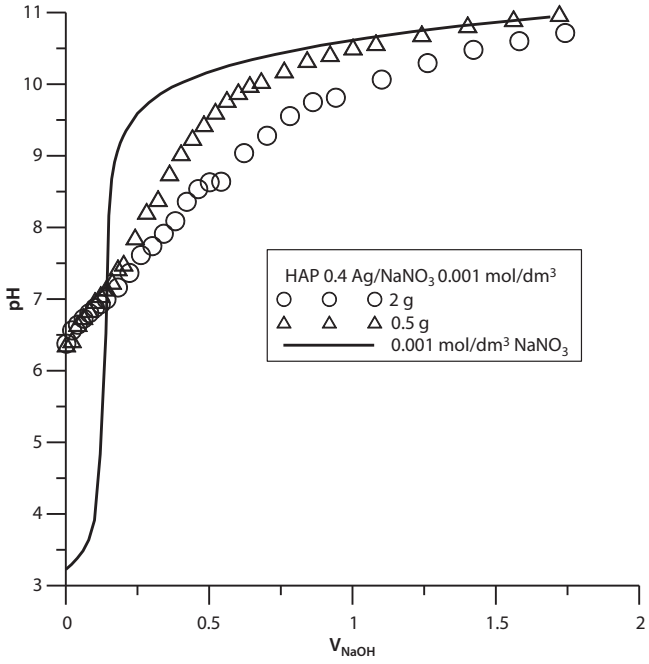

Figure 10.9 The dependence of pH on $V_{(NaOH)}$ for the HAP 0.4 Ag/electrolyte system.

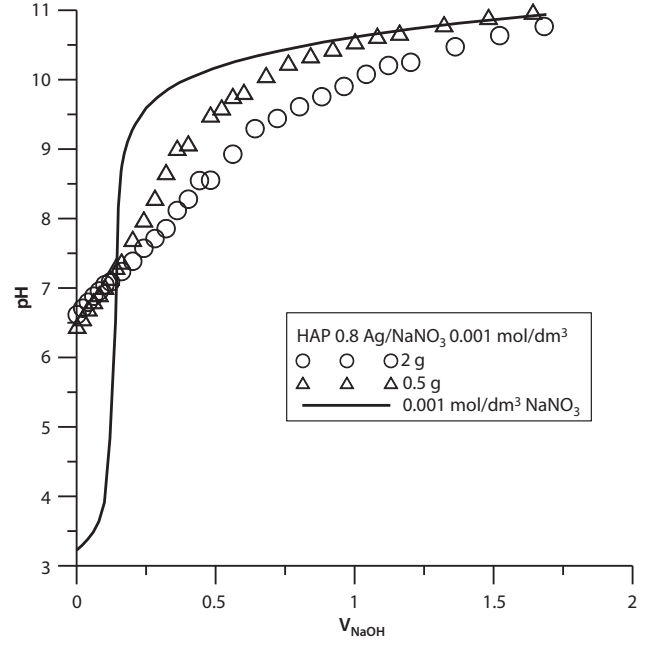

Figure 10.10 The dependence of pH on $V_{(NaOH)}$ for the HAP 0.8 Ag/electrolyte system.

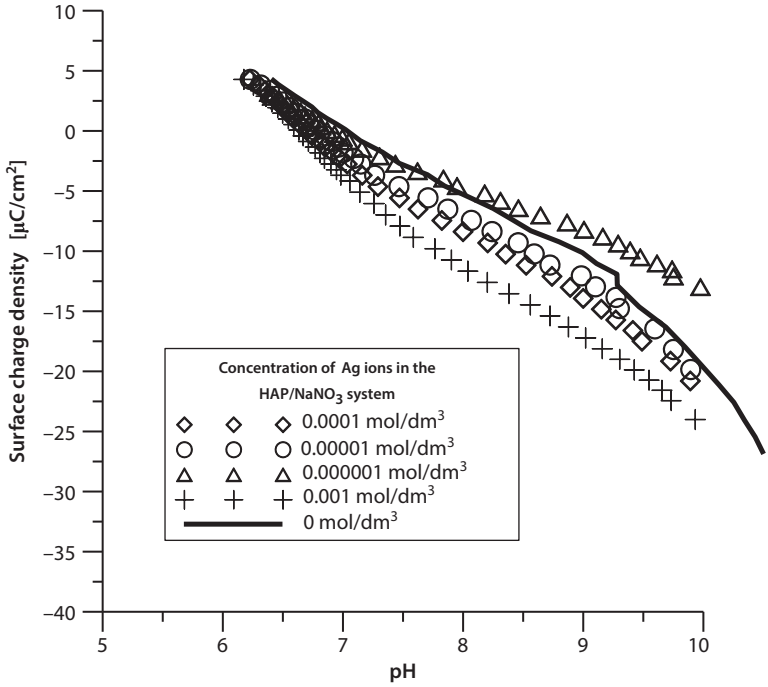

Figure 10.11 The dependence of surface charge density on pH for the HAP/electrolyte/Ag system.

10.3.4 Adsorption of Silver Ions on Hydroxyapatite

Many authors describe the absorption of anions and cations on the HAP [28–32]. Adsorption of silver ions (from the silver ^{110}Ag isotope) on HAP prepared by the co-precipitation of $Ca(NO_3)_2{\cdot}4H_2O$ and $(NH_4)HPO_4$ method was determined. The $NaNO_3$ solution of the concentration 10^{-3} M was used as an electrolyte. The measurements were made by examining the reduction of solution radiation and using the potentiometric titration set.

The results obtained from the measurements of radioactivity of taken up samples allowed to determine the amount of adsorption (Figures 10.12–10.15). Silver ions adsorption increases with the increasing pH value reaching the constant value over pH_{PZC} of the pure HAP sample which is evident in all initial concentrations of silver. This can be explained by the reactions of silver ions exchange with H^+ ions of the hydroxyl groups and with calcium ions Ca^{2+} of HAP. Obtaining of adsorption dependecies in the pH function in the studied adsorption system is difficult because in the HAP suspensions, measurement can be made in the small pH range of 5–11. Above pH 6, HAP dissolves largely and silver ions can precipitate in the form of sediment at pH > 9.

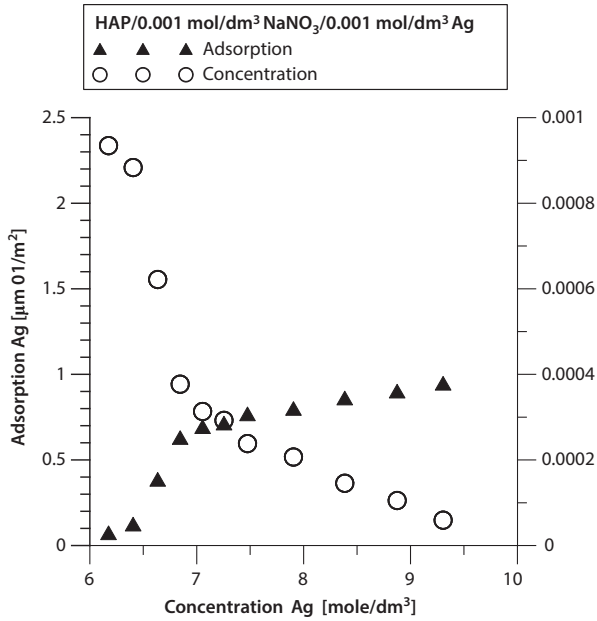

Figure 10.12 Dependence of density of Ag^+ adsorption on pH for the HAP/0.001 mol/dm^3 $NaNO_3$ + 0.001 mol/dm^3 Ag^+.

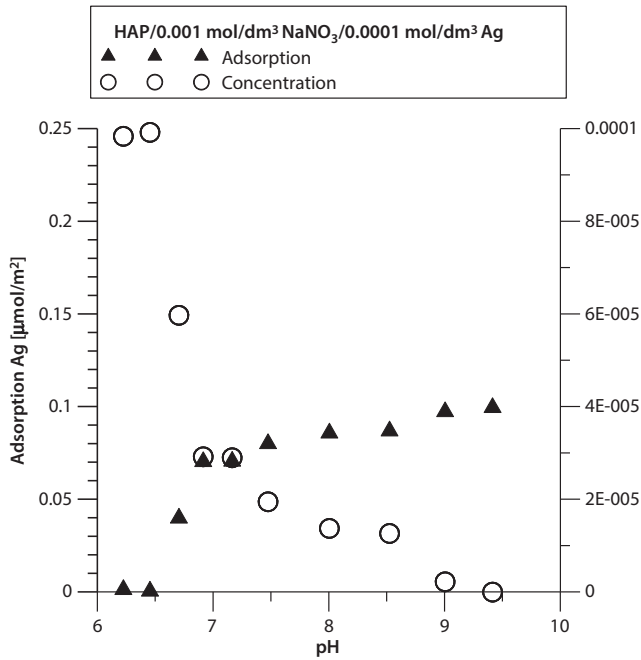

Figure 10.13 Dependence of density of Ag^+ adsorption on pH for the HAP/0.001 mol/dm^3 $NaNO_3$ + 0.0001 mol/dm^3 Ag^+.

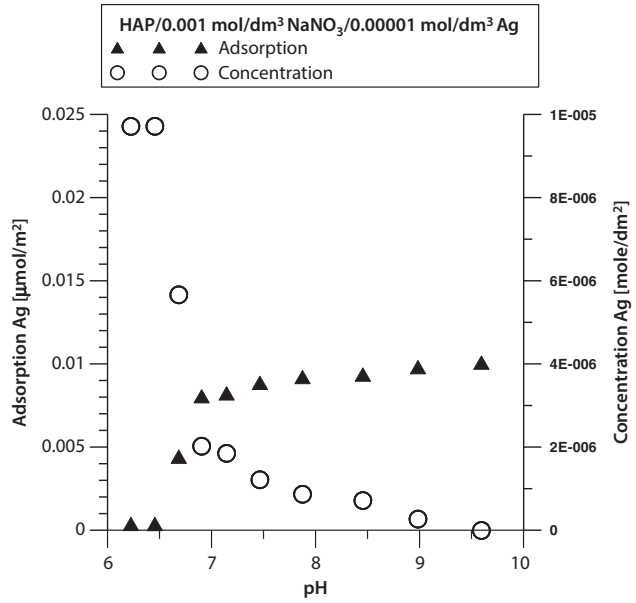

Figure 10.14 Dependence of density of Ag^+ adsorption on pH for the HAP/0.001 mol/dm^3 $NaNO_3$ + 0.00001 mol/dm^3 Ag^+.

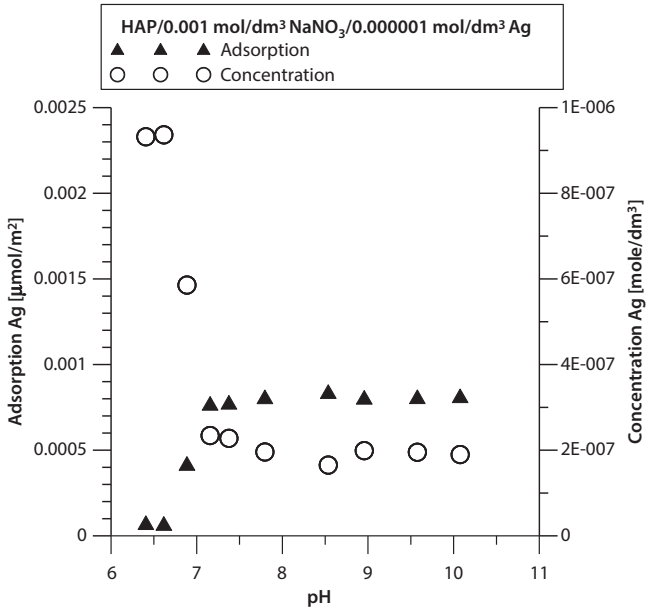

Figure 10.15 Dependence of density of Ag^+ adsorption on pH for the HAP/0.001 mol/dm^3 $NaNO_3$ + 0.000001 mol/dm^3 Ag^+.

10.3.5 Kinetics of Ag^+ Ions Adsorption on the Hydroxyapatite Surface

The rate of adsorption process is affected by several factors, among others: structure and size of adsorbed molecules, kind of the solvent, or adsorbent structure (porous) nonporous. Adsorption at the solid/solution interface is composed of two stages:

1. Transport of the substance adsorbing from the volumetric phase to the adsorbent surface - depends on the kind of solvent and substance being adsorbed and is based on diffusion of the adsorbate toward the external adsorbent surface and then internal diffusion inside the adsorbent capillaries.
2. Adsorption of the substance on the adsorbent surface - the process proceeds quickly. Most part of adsorbate passes to the surface layer in a relatively short time.

Studies of kinetics of silver ions adsorption at the HAP/electrolyte solution interface concern not only the adsorption process of ions but also pH change resulting in the change of electrical double-layer structure. The paper presents the measurements of kinetics of adsorption on HAP prepared by co-precipitation of Ca $(NO_3)_2 \cdot 4H_2O$ and $(NH_4)HPO_4$ as well as the concentrations of Ag^+ ions being 0.000001 M (Figure 10.16) and 0.001 M (Figure 10.17).

Figure 10.17 presents the diagrams of silver ions adsorption dependence as well as changes of pH in the time function of making measurements for the

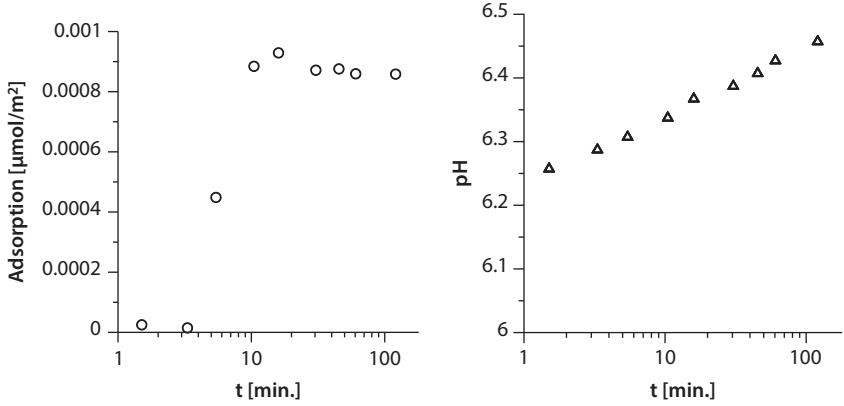

Figure 10.16 Kinetics of Ag^+ ions adsorption on the HAP from the 0.001 mol/dm^3 $NaNO_3$ solution with Ag^+ ions initial concentration of 0.000001 mol/dm^3.

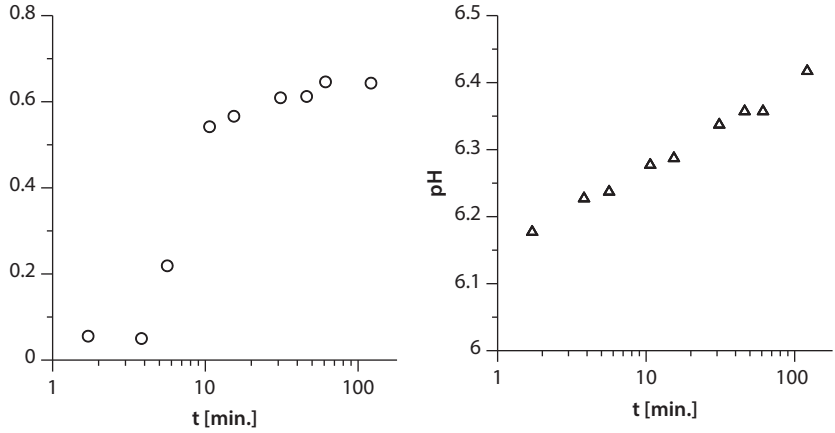

Figure 10.17 Kinetics of Ag^+ ions adsorption on the HAP from the 0.001 mol/dm^3 $NaNO_3$ solution with Ag^+ ions initial concentration of 0.001 mol/dm^3.

two initial concentrations of silver ions, pH increases establishing the value after 10 min, adsorption also increases in time, and then stabilizes after 15 min. In the case of higher initial concentration of the adsorbed Ag ions, which is 0.001 M, adsorption and pH of the suspension increase in time. This evidences diffusion of ions inside crystals or recrystallization of HAP. The latter mechanism is confirmed by the results of specific surface area measurements.

10.4 Conclusion

The results of the research on the effects of silver's presence on properties of HAP and Ag adsorption at the HAP/electrolyte solution are as follows:

1. The studies of the samples HAP, HAP/Ag, HAP/0.4 Ag, and HAP0.8 Ag using the XRD and nitrogen adsorption and desorption methods showed that there were obtained crystal samples forming porous particles.
2. The points characteristic of the double layer for the obtained compounds: HAP pH_{PZC}=7.38 and $pH_{IEP} < 4$; HAP/0.4 Ag $pH_{PZC} = 6.53$ and $pH_{IEP} < 4$ as well as HAP/0.8 Ag $pH_{PZC} = 6.91$ and $pH_{IEP} < 4$. Thus, the presence of silver ions has a larger effect on the surface tension than the zeta potential.
3. Adsorption of Ag ions increases with the increasing pH. This effect can be seen for all studied Ag initial concentrations.

4. The presence of Ag^+ ions in the solutions increases the zeta potential values.
5. Adsorption of silver ions results in the surface properties of HAP, e.g. diminishes the specific surface area, but the presence of silver ions in the HAP/0.4 Ag and HAP/0.8 Ag syntheses does not change the surface structure.
6. The XRD analysis showed the formation of calcium phosphate phase due to adsorption of silver ions HAP/Ag.

The chapter has been about the silver nanoparticles characteristics, structure, synthesis, properties, and implementation of HAP with embedded silver and the use of modern scientific methods. The properties and the most popular applications in the medical fields were discussed.

Although the described topic is very interesting, it is quite new and up to now has been well specified in the scientific literature. However, a lot of researches still need to be done to fill a big gap in the area of modern nanotechnology, finding applications in many fields of science and industry. Nanomaterials with Ag/HAP are very broad field of science, and many of its interesting aspects were omitted in this chapter. It was due to the fact that they were not directly connected with discussed topic.

This chapter can be treated as a source of collected documents, devoted to development of application of silver tin research on HAP, and can be useful for people interested in this area and their applications in medical fields.

References

1. Bielański, A., *General and Inorganic Chemistry,* State Scientific Publishers, Warsaw, 2007.
2. Trzebiatowski, W., *Inorganic Chemistry*, State Scientific Publishers, Warsaw, 1965.
3. Cox, P.A., *Short Lectures Inorganic Chemistry*, Scientific Publishers PWN, Warsaw, 2006.
4. Molski, M., *Beautiful Chemistry*, Scientific Publishers UAM, Poznań, 2005.
5. Available at: www.medserwis.pl, 2015.
6. Haibo Wang, B.S., *Hydroxyapatite Degradation and Biocompatibility*, Dissertation, 2004.
7. Available at: www.studioessenza.pl, 2015.
8. Available at: www.chantarelle.pl, 2015.
9. Sopyan, I.R., Singh, R., Hamdi, M. Synthesis of nanosized hydroxyapatite powder using sol-gel technique and its conversion to dense and porous bodies, *Ind. J. Chem.*, 47A, 1626, 2008.

10. Mroczek-Sosnowska, N., Jaworski, S.A., Siennicka, A., Gondek, A. Unique properties of silver nanomolecules, *Pol. Poul. Bre.,* 2, 6, 2013.
11. Ciobanu, C.S., Iconaru, S.L., Chifiriuc, M.C., Costescu, A., Le Coustumer, P., Predoi, D., Synthesis and antimicrobial activity of silver-doped hydroxyapatite nanoparticles, *BioMed. Res. Int.*, ID 916218, 1, 2013.
12. Erakowić, S., Jankowić, A., Veljović, D., Palcevskis, E., Mitrić, M., Stevanović, T., Janaćković, D., Mišković-Stanković, V., Corrosion stability and bioactivity in simulated body fluid of silver/hydroxyapatite and silver/hydroxyapatite/lignin coatings on titanium obtained by electrophoretic deposition, *J. Phys. Chem. B*, 117(6), 1633, 2012.
13. Honda, M., Kawanobe, Y., Ishii, K., Konishi, T., Mizumoto, M., Kanzawa, N., Morio, M., Aizawa, M., *In vitro* and *in vivo* antimicrobial properties of silver-containing hydroxyapatite prepared via ultrasonic spray pyrolysis route, *Mat. Sci. Eng. C*, 33, 5008, 2013.
14. Mocanu, A., Furtos, G., Rapuntean, S., Horovitz, O., Flore, C., Garbo, C., Danisteanu, A., Rapuntean, G., Prejmerean, C., Tomoaia-Cotisel, M., Synthesis: characterization and antimicrobial effects of composites based on multi-substituted hydroxyapatite and silver nanoparticles, *Appl. Surf. Sci.*, 298, 225, 2014.
15. Radovanovic, Z., Jokic, B., Veljovic, D., Dimitrijevic, S., Kojic, V., Petrovic, R., Janackovi, D., Antimicrobial activity and biocompatibility of Ag+ and Cu^{2+} doped biphasic hydroxyapatite/-tricalcium phosphate obtained from hydrothermally synthesized Ag^{+}- and Cu^{2+}-doped hydroxyapatite, *Appl. Surf. Sci.*, 307, 513, 2014.
16. Dubnikan, A., Zalite, V., Preparation and characterization of porous Ag doped hydroxyapatite bioceramic scaffolds, *Ceram. Int.*, 40, 9923, 2014.
17. Li, Y., Zhou, H., Zhu, G., Shao, C., Pan, H., Xu, X., Tang, R., High efficient multifunctional Ag_3PO_4 loaded hydroxyapatite nanowires for water treatment, *J. Haz. Mat.*, 299, 379, 2015.
18. Ciobanu, C.S., Iconaru, S.L., Pasuk, I., Vasile, B.S., Lupu, A.R., Hermenean, A., Dinischiotu, A., Predoi, D., Structural properties of silver doped hydroxyapatite and their biocompatibility, *Mater. Sci. Eng. C*, 33, 1395, 2013.
19. Jegatheeswaran, S., Sundrarajan, M., PEGylation of novel hydroxyapatite/PEG/Ag nanocomposite particles to improve its antibacterial efficacy, *Mater. Sci. Eng. C,* 51, 174, 2015.
20. Shi, C., Gao, J., Wang, M., Fu J., Wang, D., Zhu, Y., Ultra-trace silver-doped hydroxyapatite with non-cytotoxicity and effective antibacterial activity, *Mater. Sci. Eng.* C, 55, 497, 2015.
21. Zamperini, C.A., André, R.S., Longo, V.M., Mima, E.G., Gergani, C.E., Machado, A.L., Varela, J.A., Longo, E. Antifungal applications of Ag-decorated hydroxyapatite nanoparticles, *J. Nanomater.*, ID 174398, 9, 2013.
22. Ciobanu, S.C., Iconaru, S.L., Chiriuc, A.C., Costescu, A., Le Coustumer, P., Predoi, D., Synthesis and antimicrobial activity of silver-doped hydroxyapatite nanoparticles, *BioMed Res. Int.*, ID 916218, 10, 2013.

23. Ciobanu, C.S., Massuyeau, F., Violeta, L., Predoi, C., Predoi, D. Structural and physical properties of antibacterial Ag-doped nano-hydroxyapatite synthesized at 100 °C, *Nano. Res. Lett*., 6, 613, 2011.
24. Jadalannagari, S., Deshmukh, K., Ramanan, S.R., Kowshik, M., Antimicrobial activity of hemocompatible silver doped hydroxyapatite nanoparticles synthesized by modified sol–gel technique, *Appl. Nanosci.,* 4, 133, 2014.
25. Vukomanovi, M., Bracko, I., Poljan, I., Uskokovi, D., Suvorov, S., Suvorov, D., The growth of silver nanoparticles and their combination with hydroxyapatite to form composites via a sonochemical approach, *Cryst. Growth Des.*, 11, 3802, 2011.
26. Noda, I., Miyaji, F., Ando, V., Miyamoto, H., Shimazaki, T., Yonekura, Y., Miyazaki, M., Mawatari, M., Ashdin, T.H., Next generation antibacterial hydroxyapatite coating: antibacterial activity of Ag ions in serum, *Bioc. Devel. Appl.,* 1, ID D101102, 3, 2011.
27. Erakovic, S., Jankovic, A., Veljovic, D., Palcevskis, E., Mitric, M., Stevanovic, T., Janackovic, D., Miskovič-Stankovic, V., Corrosion stability and bioactivity in simulated body fluid of silver/hydroxyapatite and silver/hydroxyapatite/lignin coatings on titanium obtained by electrophoretic deposition, *J. Phys. Chem. B*, 117, 1633, 2013.
28. Skwarek, E., Janusz, W., Sternik, D., Adsorption of citrate ions on hydroxyapatite synthesized by various methods, *J. Radioanal. Nucl. Chem.*, 299(3), 2027, 2013.
29. Skwarek, E., Adsorption of Zn on synthetic hydroxyapatite from aqueous solution, *Sep. Sci. Tech.,* 49(11), 1654, 2014.
30. Skwarek, E., Thermal analysis of hydroxyapatite with adsorbed oxalic acid, *J. Therm. Anal. Cal.*, 122(1), 33, 2015.
31. Skwarek, E., Adsorption of Cs^+ at the hydroxyapatite/aqueous electrolyte interface, *Ads. Sci. Tech.,* 33(6–8), 575, 2015.
32. Janusz, W., Skwarek, E., Złotucha, A., Reszka, M., The study of the acid–base properties of the surface groups at the hydroxyapatite/$NaClO_4$ solution Interface, *Pol. J. Chem.*, 82, 57, 2008.

Also of Interest

Check out these published volumes in the Advanced Materials Series

Advanced Electrode Materials
Edited by Ashutosh Tiwari, Filiz Kuralay and Lokman Uzun
Forthcoming 2016. ISBN 9781119242529

Advanced Molecularly Imprinting Materials
Edited by Ashutosh Tiwari and Lokman Uzun
Forthcoming 2016. ISBN 978-1-119-33629-7

Intelligent Nanomaterials (2nd edition)
Edited by Tiwari, Yogendra Kumar Mishra, Hisatoshi Kobayashi and Anthony P. F. Turner
Forthcoming 2016. ISBN 978-1-119-24253-6

Advanced Composite Materials
Edited by Ashutosh Tiwari, Mohammad Rabia Alenezi and Seong Chan Jun
Forthcoming 2016. ISBN 978-1-119-24253-6

Advanced Surface Engineering Materials
Edited by Ashutosh Tiwari, Rui Wang, and Bingqing Wei
Forthcoming 2016. ISBN 978-1-119-24244-4

Advanced Ceramic Materials
Edited by Ashutosh Tiwari, Rosario A. Gerhardt and Magdalena Szutkowska
Forthcoming 2016. ISBN 978-1-119-24244-4

Advanced Engineering Materials and Modeling
Edited by Ashutosh Tiwari, N. Arul Murugan and Rajeev Ahuja
Published 2016. ISBN 978-1-119-24246-8

Ashutosh Tiwari, Rosario A. Gerhardt and Magdalena Szutkowska (eds.) Advanced Ceramic Materials, (425–428) © 2016 Scrivener Publishing LLC

Advanced 2D Materials
Ashutosh Tiwari and Mikael Syväjärvi
Published 2016. ISBN 978-1-119-24249-9

Advanced Materials Interfaces
Edited by Ashutosh Tiwari, Hirak K. Patra and Xumei Wang
Published 2016. ISBN 978-1-119-24245-1

Advanced Bioelectronics Materials
Edited by Ashutosh Tiwari, Hirak K. Patra and Anthony P.F. Turner
Published 2015. ISBN 978-1-118-99830-4

Graphene
An Introduction to the Fundamentals and Industrial Applications
By Madhuri Sharon and Maheswar Sharon
Published 2015. ISBN 978-1-118-84256-0

Advanced Theranostic Materials
Edited by Ashutosh Tiwari, Hirak K. Patra and Jeong-Woo Choi
Published 2015. ISBN: 978-1-118-99829-8

Advanced Functional Materials
Edited by Ashutosh Tiwari and Lokman Uzun
Published 2015. ISBN 978-1-118-99827-4

Advanced Catalytic Materials
Edited by Ashutosh Tiwari and Salam Titinchi
Published 2015. ISBN 978-1-118-99828-1

Graphene Materials
Fundamentals and Emerging Applications
Edited by Ashutosh Tiwari and Mikael Syväjärvi
Published 2015. ISBN 978-1-118-99837-3

DNA Engineered Noble Metal Nanoparticles
Fundamentals and State-of-the-art-of Nanobiotechnology
By Ignác Capek
Published 2015. ISBN 978-1-118-07214-1

Advanced Electrical and Electronics Materials
Process and Applications
By K.M. Gupta and Nishu Gupta
Published 2015. ISBN: 978-1-118-99835-9

Advanced Materials for Agriculture, Food and Environmental Safety
Edited by Ashutosh Tiwari and Mikael Syväjärvi
Published 2014. ISBN: 978-1-118-77343-7

Advanced Biomaterials and Biodevices
Edited by Ashutosh Tiwari and Anis N. Nordin
Published 2014. ISBN 978-1-118-77363-5

Biosensors Nanotechnology
Edited by Ashutosh Tiwari and Anthony P. F. Turner
Published 2014. ISBN 978-1-118-77351-2

Advanced Sensor and Detection Materials
Edited by Ashutosh Tiwari and Mustafa M. Demir
Published 2014. ISBN 978-1-118-77348-2

Advanced Healthcare Materials
Edited by Ashutosh Tiwari
Published 2014. ISBN 978-1-118-77359-8

Advanced Energy Materials
Edited by Ashutosh Tiwari and Sergiy Valyukh
Published 2014. ISBN 978-1-118-68629-4

Advanced Carbon Materials and Technology
Edited by Ashutosh Tiwari and S.K. Shukla
Published 2014. ISBN 978-1-118-68623-2

Responsive Materials and Methods
State-of-the-Art Stimuli-Responsive Materials and Their Applications
Edited by Ashutosh Tiwari and Hisatoshi Kobayashi
Published 2013. ISBN 978-1-118-68622-5

Other Scrivener books edited by Ashutosh Tiwari

Nanomaterials in Drug Delivery, Imaging, and Tissue Engineering
Edited by Ashutosh Tiwari and Atul Tiwari
Published 2013. ISBN 978-1-118-29032-3

Biomedical Materials and Diagnostic Devices Devices
Edited by Ashutosh Tiwari, Murugan Ramalingam, Hisatoshi Kobayashi and Anthony P.F. Turner
Published 2012. ISBN 978-1-118-03014-1

Intelligent Nanomaterials (first edition)
Processes, Properties, and Applications
Edited by Ashutosh Tiwari Ajay K. Mishra, Hisatoshi Kobayashi and Anthony P.F. Turner
Published 2012. ISBN 978-0-470-93879-9

Integrated Biomaterials for Biomedical Technology
Edited by Murugan Ramalingam, Ashutosh Tiwari, Seeram Ramakrishna and Hisatoshi Kobayashi
Published 2012. ISBN 978-1-118-42385-1

Index

Ashutosh Tiwari, Rosario A. Gerhardt and Magdalena Szutkowska (eds.) Advanced Ceramic Materials, (419–424) © 2016 Scrivener Publishing LLC